DYNAMIC CHARACTERISTICS AND PERFORMANCE ASSESSMENT OF REINFORCED CONCRETE STRUCTURAL WALLS

A THESIS SUBMITTED TO
THE GRADUATE SCHOOL OF NATURAL AND APPLIED SCIENCES
OF
MIDDLE EAST TECHNICAL UNIVERSITY

BY

İLKER KAZAZ

IN PARTIAL FULFILLMENT OF THE REQUIREMENTS
FOR
THE DEGREE OF DOCTOR OF PHILOSOPHY
IN
CIVIL ENGINEERING

FEBRUARY 2010

Approval of the thesis:

DYNAMIC CHARACTERISTICS AND PERFORMANCE ASSESSMENT OF REINFORCED CONCRETE STRUCTURAL WALLS

submitted by **İLKER KAZAZ** in partial fulfillment of the requirements for the degree of **Doctor of Philosophy in Civil Engineering Department, Middle East Technical University** by,

Prof. Dr. Canan Özgen ______________________
Dean, Graduate School of **Natural and Applied Sciences**

Prof. Dr. Güney Özcebe ______________________
Head of Department, **Civil Engineering**

Prof. Dr. Polat Gülkan ______________________
Supervisor, **Civil Engineering Dept., METU**

Examining Committee Members:

Assoc. Prof. Dr. Ahmet Yakut ______________________
Civil Engineering Dept., METU

Prof. Dr. Polat Gülkan ______________________
Civil Engineering Dept., METU

Assoc. Prof. Dr. Erdem Canbay ______________________
Civil Engineering Dept., METU

Assoc. Prof. Dr. Halis Günel ______________________
Architecture Dept., METU

Assist. Prof. Dr. Abdulkadir Cüneyt Aydın ______________________
Civil Engineering Dept., Atatürk University

Date: 26.02.2010

I hereby declare that all information in this document has been obtained and presented in accordance with academic rules and ethical conduct. I also declare that, as required by these rules and conduct, I have fully cited and referenced all material and results that are not original to this work.

Name, Last name : İlker Kazaz

Signature :

ABSTRACT

DYNAMIC CHARACTERISTICS AND PERFORMANCE ASSESSMENT OF REINFORCED CONCRETE STRUCTURAL WALLS

Kazaz, İlker

Ph.D., Department of Civil Engineering

Supervisor: Prof. Dr. Polat Gülkan

February 2010, 379 pages

The analytical tools used in displacement based design and assessment procedures require accurate strain limits to define the performance levels. Additionally, recently proposed changes to modeling and acceptance criteria in seismic regulations for both flexure and shear dominated reinforced concrete structural walls proves that a comprehensive study is required for improved limit state definitions and their corresponding values. This is due to limitations in the experimental setups, such that most previous tests used a single actuator at the top of the wall, which does not reflect the actual loading condition, and infeasibility of performing tests of walls of actual size in actual structural configuration. This study utilizes a well calibrated finite element modeling tool to investigate the relationship between the global drift, section rotation and curvature, and local concrete and steel strains at the extreme fiber of rectangular structural walls. Functions defining more exact limits of modeling parameters and acceptance criteria for

rectangular reinforced concrete walls were developed. This way a strict evaluation of the requirements embedded in the Turkish Seismic Code and other design guidelines has become possible. Several other aspects of performance evaluation of structural walls were studied also. Accurate finite element modeling strategies and analytical models of wall and frame-wall systems were developed for seismic response calculations. The models are able to calculate both the static and dynamic characteristics of wall type buildings efficiently. Seismic responses of wall type buildings characterized with increasing wall area in the plan were analyzed under design spectrum compatible normal ground motions.

Keywords: Structural Walls, Performance Limits, Strain, Plastic Rotation, Plastic Hinge Length, Finite Element Modeling, Turkish Seismic Design Code, Seismic Demand, Period Formula, Frame-wall Interaction, Approximate Methods

ÖZ

BETONARME PERDELERİN DİNAMİK ÖZELLİKLERİ VE PERFORMANS DEĞERLENDİRMESİ

Kazaz, İlker
Doktora, İnşaat Mühendisliği Bölümü
Tez Yöneticisi: Prof. Dr. Polat Gülkan

Şubat 2010, 379 sayfa

Yer değiştirmeye dayalı tasarım ve değerlendirme yöntemlerinde kullanılan analitik araçlarla performans düzeyini tanımlamak için doğru gerilme değerlerine ihtiyaç duyulmaktadır. Ayrıca son zamanlarda yönetmeliklerde hem kesme ve hem de eğilme etkisi altındaki betonarme perdelerin modelleme ve kabul kriterleri için önerilen değişiklikler de hasar sınır durumlarının tanımlanması ve karşı gelen gerilme değerlerinin belirlenmesi için kapsamlı bir çalışmaya ihtiyaç duyulduğunu göstermektedir. Bu durum sınırların belirlenmesinde kullanılan deneysel düzeneklerin yetersizliğinden kaynaklanmaktadır. Birçok deney perdeye tepe noktasından uygulanan tek bir yüklemeyle gerçekleştirilmekte ve gerçek boyutlarda ve yapı içinde gerçek konumundaki etkilere maruz elemanlar üzerinde deneyler kolaylıkla yapılamamaktadır. Bu çalışma çok iyi kalibre edilmiş bir sonlu elemanlar modelleme programını kullanarak dikdörtgen kesitli betonarme perdelerin global ötelenme, kesit dönmesi ve eğriliği ve perde uçlarındaki beton ve çelik gerilmeleri arasındaki ilişkiyi incelemektedir. Dikdörtgen kesitli perde elemanları için mevcut değerlerden daha doğru olduğuna inanılan modelleme parametreleri ve kabul kriteri fonksiyonları teklif edilmektedir. Türk Deprem Şartnamesi ve bazı diğer hesap kılavuzlarında verilen şekil değiştirme ile ilgili hükümlerin geçerliği irdelenmektedir. Bu çalışmada yapısal duvarların performans değerlendirmesine dair birçok konu da irdelenmiştir. Perde ve perde-çerçeve sistemler için sismik hesaplarda kullanılmak üzere sonlu eleman modelleme stratejileri ve analitik hesap yöntemleri geliştirilmiştir. Geliştirilen modeller perdeli yapıların hem dinamik hem de statik özelliklerini etkin bir şekilde hesaplamaktadır. Plan alanına göre perde alanı arttırımı esas alınarak, perdeli yapıların doğrusal olmayan sismik hesapları tasarım tepki spektrumuyla uyumlu yer hareketi kayıtları kullanılarak zaman tanım alanında hesap yöntemi ile gerçekleştirilmiştir.

Anahtar Kelimeler: Yapısal Perde, Performans Limitleri, Birim Gerilme, Sonlu Elemanlar Yöntemi, Plastik Dönme, Plastik Mafsal Yöntemi, Türk Deprem Yönetmeliği, Sismik Talep, Periyot Formülü, Perde-Çerçeve Etkileşimi, Yaklaşık Metodlar

To my family…

ACKNOWLEDGMENTS

I would like to express my gratitude to my supervisor Prof. Dr. Polat Gülkan who has supported me throughout my thesis with his patience and knowledge whilst allowing me the room to work in my own way.

This dissertation would not have been a real fulfillment without the support of many people. I would like to thank my committee members, especially Assoc. Prof. Dr. Ahmet Yakut, who was abundantly helpful and offered invaluable assistance, support and guidance from the preliminary to the concluding level of the study. The author wishes to express his gratitude also to Assoc. Prof. Dr. M. Altuğ Erberik and old friends M. Selim Günay, Bora Acun and Tuğba Eroğlu for fruitful discussions that worked out a solution most of the time.

I would like to thank my friends at Structural Mechanics Laboratory; Dilek Okuyucu, Abdullah Dilsiz, Emrah Yenier, Özgür Avşar, Bilge Erdoğan, Vesile Akansel and Barış Erdil for their warm friendship during my assistantship at METU. I also thank to Mr. Hüseyin Güler for colorful conversations on the other aspects of life, which have been an escape for me to refresh my mind.

I would like to express my deepest appreciation to my parents for their confidence in me and for the support, love and understanding that they have provided me throughout my academic life. Finally, I would like to thank my little lambkin Defne Zeynep and wonderful wife Emriye without whose support and patience this study would not have been successful.

This study was supported by the State Planning Organization (DPT) Grant No: BAP-08-11-DPT2002 K120510-DK-13.

TABLE OF CONTENTS

LIST OF TABLES

LIST OF FIGURES

CHAPTER 1

INTRODUCTION

1.1 GENERAL

Structural walls are used extensively in low- and moderate- rise buildings to resist lateral loads induced by wind or earthquakes. Unlike other structural members such as beams and columns when robust structural walls were utilized in the structural system to resist the lateral earthquake loads, they dominate the response of the entire structure. The seismic performance of many buildings, therefore, closely linked to the behavior of the reinforced concrete walls.

Understanding behavior of structural walls requires experimental as well as analytical investigations. Nearly all the conclusion and derivations on structural walls come from the tests of isolated shear walls of variable aspect ratios (squat to slender walls), defined as the ratio of height to the length of the wall (H_w/L_w). Although vast amount of experimental and analytical information is available on the behavior of structural walls tested and simulated under severe earthquake loading conditions, due to limitations in the experimental setups, such that most previous tests used a single actuator at the top of the wall and did not simulate well the actual moment distribution expected in a multi-story system subjected to seismic loading, and inability of analytical models especially to include the critical shear-flexure interaction effects entails this study to undertake the analytical investigation of structural walls. Additionally, previous research has evaluated the seismic response of walls, few studies have specifically focused on the performance (or damage) of structural wall systems.

After the 90s due to increased interest in performance-based earthquake engineering, a significant amount of research has been conducted on performance-based seismic design or limit-states design procedures that have the simple aim of specifying structural performance for predefined seismic intensity levels. Structural walls have also been investigated extensively in this process (Wallace, 1994; Kowalsky, 2001; Paulay, 2002, Priestley et al., 2007). The general aim in these studies is to establish a relation between the expected displacement demands (drift ratio limits, ductility demand) on the building system to the local deformations on the wall cross section (curvatures and rotation), the magnitude and distribution of wall normal strain. The analytical methods adopted in these studies that assumed linear distribution of wall curvature and other simplified modeling assumptions requires reinvestigation of such elements under flexural, shear and combined loading actions that is induced by the seismic action. As an example to this situation, the strain distribution in concrete at the base of a rectangular wall specimen used in the model verification by Orakcal (2004) were shown in Figure 1.1. Even though analytical predictions obtained by an improved version of the Multiple-Vertical-Line-Element Model (MVLEM) agree well with the measured response in average, the model requires extensive calibration. It is also obvious from the figure that the plain sections do not remain plane any more in large inelastic action and the analytical predictions significantly underestimate the concrete strain at the extreme compression fiber. This situation leads to anticipation of unconservative deformation capacities of reinforced concrete members when displacement based design and assessment are utilized in the evaluation of such members. For instance, the modeling and acceptance criteria in the recently enforced Turkish Seismic Design Code (TSC, 2007) lay down concrete compressive and steel tensile strain limits in the performance assessment of concrete members, but the correctness of these values has not been extensively checked.

The recent efforts that aim to enhance the accuracy and reliability of wall provisions also justify the necessity of this study. Such an example is a newly completed standard, ASCE/SEI 41-06 (2006), Seismic Rehabilitation of Existing Buildings, which proposes changes to acceptance and modeling criteria for walls controlled by both flexure and shear in FEMA 356 (2000). The main goal of proposed changes to wall provisions of ASCE/SEI 41 (Section 6.7) was to update the modeling and acceptance parameters for walls to make them more consistent with experimental results (ASCE/SEI 41 update, 2007).

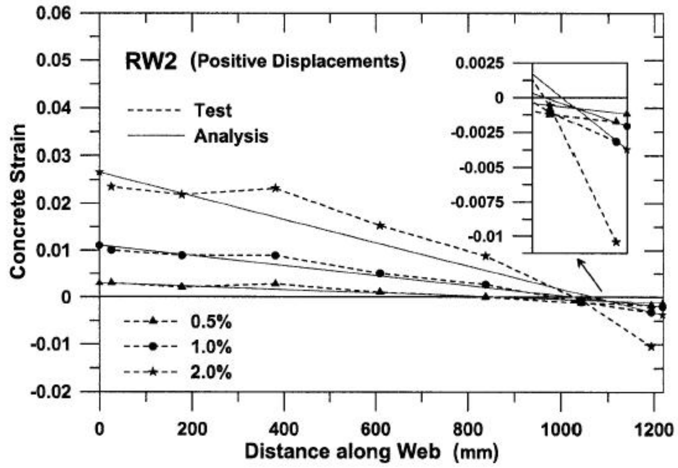

Figure 1.1 Comparison of predicted and measured average concrete strains at the base of the wall at applied peak top roof drifts (adopted from Orakcal, 2004)

Analytical procedures are widely used in performance evaluation of reinforced concrete structures and components. However, state-of-the-art of structural wall modeling underlines the inadequacy of traditional strategies in obtaining reliable wall response. In the last decades the international benchmark studies that were organized to investigate the modeling problems on structural walls revealed the inadequacy of the various modeling techniques used in structural walls. The first is the Seismic Shear Wall International Standard Problem (SSWISP) conducted by NUPEC (Nuclear Power Engineering Corporation of Japan) in between 1995 and 1996 (OECD/NEA/CSNI, 1996). The results of each experiment were presented to research community for blind prediction under different benchmark projects. The participants were asked to predict the measured global response quantities such as displacements, forces, moments, accelerations as well as local quantities like rebar strains at different levels to figure out the local weaknesses during the course of dynamic experiments. To achieve capturing local as well as global behavior necessitates the use of finite element methodology. The results of this benchmark led the research community to question accuracy of stress analyses methods due to inadequate ability in predicting both the peak strength and ductility response of structural walls under seismic actions. Many distinguished experts in the field fell short in predicting the response. The variation of predictions on the structural ductility was very significant and ranges from 35 to 180 percent of the displacement recorded by NUPEC. Figure 1.2 summarizes the results of the participants.

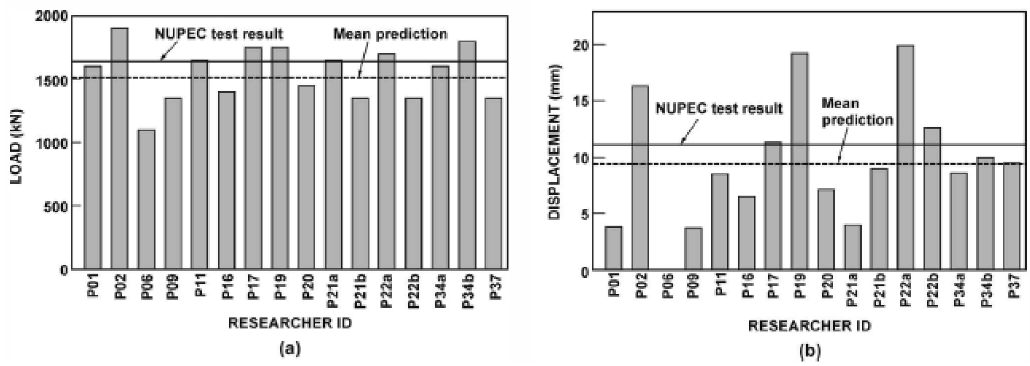

Figure 1.2 Predictions on NUPEC wall by the participants,
(a) Strength, (b) Displacement

The second benchmark project that also has inspired this study is named as "Safety Significance of Near-Field Earthquakes" organized by International Atomic Energy Agency (IAEA) in between 2002 and 2005 (Kazaz et al., 2006a). The same tendency in excessive variation of predicted seismic deformations was also valid in this project especially when the blind prediction of the response was asked. Figure 1.3 presents the maximum displacement response blind predictions (results were not known to the participants) of CAMUS wall of participants under a given earthquake record. In a blind prediction exercise there is significant difficulty in predicting the displacements. It must be mentioned that the best estimations were obtained by teams that used solid continuum elements in the finite element discretization of the shear wall. Information about the experimental programs of these walls and the development of their accurate finite element models are described in Chapter 2.

The difficulties with predicting ductility and strength, as it became obvious in these benchmark projects, has stimulated this study to investigate reliable modeling criteria of structural walls and to evaluate the validity of procedures and displacement limits used in the performance assessment of this type of structures.

The accurate prediction of deformation demands of any structural system is important from various aspects including:

- Judging the validity of applied design in proportioning the reinforcement and the dimensions whether it is adequate in satisfying the imposed deformation demands.
- Quantification of seismic demands to assess the damaging potential of ground motions on wall type structural systems.

- Assessment of the performance of existing structures under code specified performance criteria.
- Improving the effectiveness and accuracy of displacement based design and assessment procedures by examining proposed plastic rotation and strain limits.

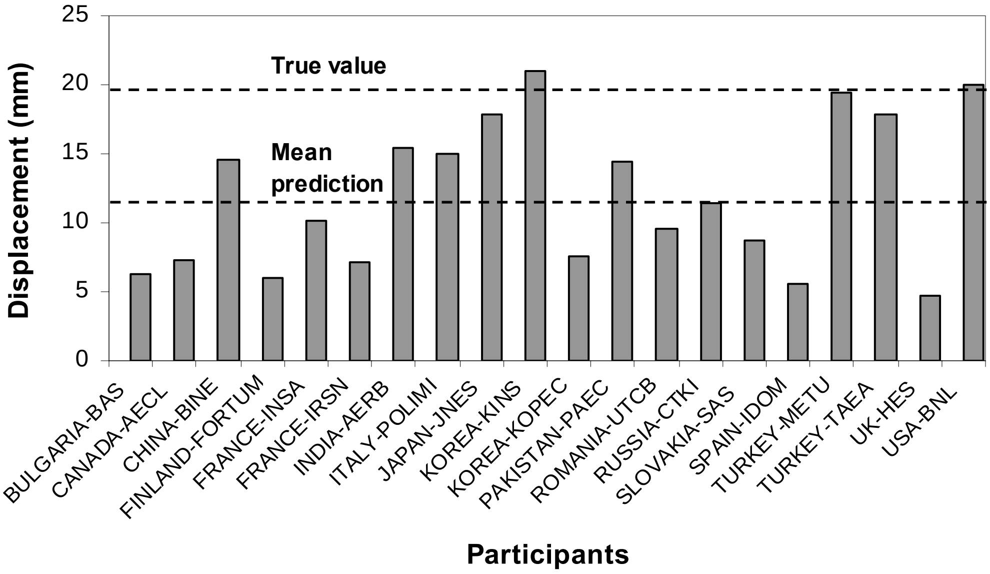

Figure 1.3 Maximum displacement predictions of CAMUS wall

The merit of this research will be the utilization of current *non-linear finite element analyses* (NLFEA) procedures in the field of *earthquake engineering* to investigate the *seismic behavior* of *reinforced concrete structural walls*. NLFEA can serve as a tool in the reliable assessment of the strength and behavior of structures in cases where it is expensive and labor intensive to carry out experimentation, especially dynamically. Vecchio (1998) explains the relevance and value of non-linear finite element procedures for analysis and design of reinforced concrete structures as well as the reasons for caution when applying them. One of the most important reasons for a cautious attitude towards NLFEA procedures in the field of structural engineering is the reliable modeling of non-linear behavior of reinforced concrete, particularly in shear critical conditions which is the case most of the times in the analysis of structural walls. It was observed that any procedure or modeling strategy that is well suited to a certain structure or loading condition can perform poorly in another case. Different problems can require different element formulation, constitutive material laws, load application and finite element mesh generation.

In summary, detailed and comprehensive analytical investigation of structural walls is required to find out:

1. Limitations due to load application and scale of the experimental setup, and
2. Limitations in the analytical approaches used in the evaluation of structural walls.

1.2 REVIEW OF PREVIOUS STUDIES

The subject tiers of this study is composed several items each of which has its own specific literature. The relevant literature of each main topic is covered in related chapter. In this introduction part, only a general literature review is given with regards to modeling and performance assessment of structural walls.

1.2.1 Analytical Modeling of RC Structural Walls

Various analytical models based on different approaches have been proposed to predict the inelastic response of RC structural walls. The modeling strategies of RC structural walls can be classified in two major groups:

- ***Macroscopic models***: These models are phenomenological in nature and tend to simulate the global behavior of the entire large-sized wall element by means of an analogous structural idealization (Colotti, 1993). The derivations are based on observed test results, so usually valid only for specific conditions upon which the derivation of the model is based (Vulcano and Bertero, 1987).

There are three main types of macro-models being used for reinforced concrete structural walls. These are the equivalent beam-column element model, the equivalent truss element model, and the vertical line element model. The beam-column elements extensively used to model reinforced concrete members. The behavior of the element is characterized traditionally by the elasto-plastic force-deflection (moment-rotation) response lumped at the hinges developing at member ends. Introduction of fiber section formulation into beam-column element provided considerable flexibility and ease in the use of the element (Taucer et al., 1991), yet could not solve the problems related to inadequate shear behavior, which is crucial in the modeling of structural walls (Vulcano and Bertero, 1987). Another limitation of the beam elements is that the rotations occur around the point lying on the centroidal axis of the wall impeding the fluctuation of the neutral axis. The equivalent truss element model, also named as strut-and-tie model, depends on the inclined compression struts that are parallel to the direction of cracking. Although the procedure yields conservative estimates of the strength when compared with test evidence (ASCE-ACI Committee 445, 1998), it is not accurate and limited to monotonic loading because of difficulties in defining the structural topology and the properties of the truss elements under cyclic loading.

Vertical line element models are specifically developed for the analysis reinforced concrete shear walls. This model was originally proposed by Kabeyasawa et al. (1984) on the basis of the experimentally observed behavior of a seven-story RC frame-wall structural system. The model shown in Figure 1.4(a) is idealized a wall member as three vertical line elements with infinitely rigid beams at the top and bottom floor levels. Axial springs at each side and a rotational spring at the center are for representing flexural behavior, while the horizontal spring is for modeling shear behavior. Element still assumes uniform distribution of curvature (plane sections remains plane after deformation). The hysteretic behavior of the elements constituting the wall model is simulated by adopting empirical relations developed on the basis of experimental studies (Vulcano, 1992).

Different versions of model was developed basically changing the number of axial springs. The increase in the number of springs is also reflected in the name of the model by evolving from three vertical line element model (TVLEM) to multiple vertical line element model (MVLEM). Vulcano et al. (1988) removing the rotational spring in the center stated that to obtain an improved estimation of flexural behavior at least four axial springs will be used in the model. Linde (1993) proposed a simpler model with three axial springs and one horizontal spring and developed kinematic formulation of the model. Recently, Orakcal et al. (2004) proposed a new version of MVLEM in which the only difference being in the behavior of the nonlinear springs as shown on the model in Figure 1.4(b). The modeling approach involves implementing refined hysteretic uniaxial stress-strain laws instead of simplified force-deformation rules to track nonlinear responses. By this way the analytical responses are directly related to physical material behavior (stress-strain curve) and provide a more robust modeling approach, where model improvements result from improvement in constitutive models and refinement in the spatial resolution of the discrete model.

An inherent shortcoming of MVLM models is that the shear and flexural displacement components of the wall are described independently. Although model effectively calculates the flexural response, shear response is not adequately described, particularly for high shear stresses. It is known experimentally (Vallenas et al., 1979) that the behavior of walls is strongly influenced by interaction between axial force, flexure and shear.

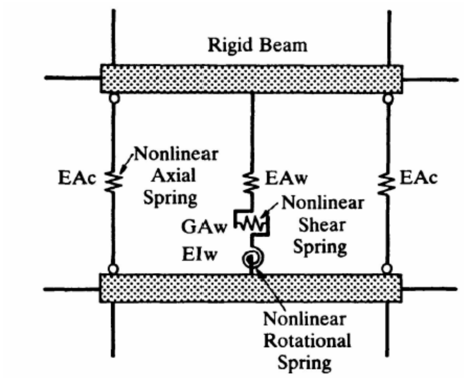

a) Three Vertical Line Element Model (TVLEM) (Kabeyasawa et al., 1984)

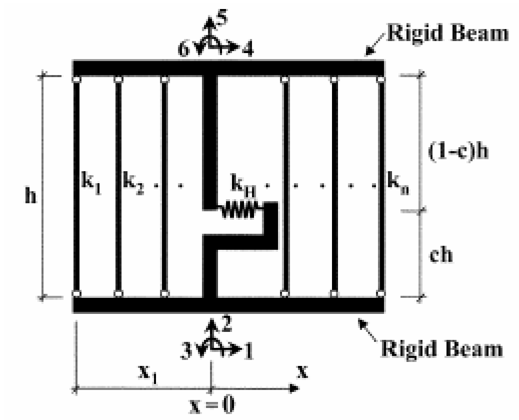

b) Multiple Vertical Line Element Model (MVLEM) (Orakcal et al., 2004)

Figure 1.4 Idealization of a wall member

- ***Microscopic models***: These models are based on discretization of the continuum through finite element procedures by the application of solid mechanics principals. Stress and strain is calculated at every point of the material. There exist various shell and solid elements implemented in finite element codes with different element formulations affecting the accuracy of the simulation results (ASCE-ACI, 1993). Special features of finite element analysis applied to reinforced concrete may include constitutive relationships, failure theories, multi-axial stress theories, modeling of reinforcement, behavior on the interface between reinforcement and concrete, crack representation, mechanisms of shear transfer, cyclic and dynamic loading effects, and the time-dependent effects of creep, shrinkage, and temperature variation. It is criticized that in practice the use of nonlinear finite element analysis for the investigation of the strength and deformation properties of reinforced concrete structural walls is restricted to the analysis of isolated and coupled walls due to very long computation times and complexities involved in the analysis.

Cervenka and Gerstle (1972) were first to make a finite element study of the several shear panels which Cervenka (1970) had tested experimentally. A large number of sophisticated constitutive models that can successfully capture behavior at the material level have been developed, as summarized in state-of-the-art reports by ASCE-ACI (1982, 1993) and CEB (1996). Ayoub and Filippou (1998) and Kwak and Kim (2004a) described the implementation of an orthotropic concrete constitutive model in the finite-element analysis of reinforced concrete shear walls. The emphasis was on the evaluation of the effect of orthotropic model parameters on the monotonic load-displacement relation of shear panels and walls under different stress states. Less has been reported on the successful application of these material models to predict the behavior of structural components under cyclic loading.

With the advancement of modeling techniques and computational power, more successful cyclic loading analyses of reinforced concrete have been conducted in the nineties. These include simulations of shear test panels designed to have a uniform stress state for the verification of constitutive models (Schnobrich et al. 1991; Stevens et al. 1991; Rose et al. 1999, Palermo and Vecchio, 2004; Kwak and Kim, 2004b), and simulations of structural members (Okamura and Maekawa 1991; Sittipunt and Wood 1995; Elmorsi et al. 1998; Vecchio, 1999). These models demonstrated reasonable agreement with experimental results.

A significant research milestone in the field of constitutive modeling of members subjected to shear and torsion is the development of the compression field theory (CFT) (Collins and Mitchell, 1980). The CFT assumes that after cracking, there will be no tensile stresses in the concrete. Test on reinforced concrete elements (Vecchio and Collins, 1986; Belarbi and Hsu, 1994) demonstrated that even after extensive cracking, tensile stresses still existed in the cracked concrete and that these stresses significantly increased the ability of cracked concrete to resist shear stresses. The modified compression field theory (MCFT) (Vecchio and Collins, 1986) is a further development of the CFT that accounts for the influence of the tensile stresses in the cracked concrete. It is recognized that the local stresses in both the concrete and the reinforcement vary form point to point in the cracked concrete, with high reinforcement stresses but low concrete tensile stresses occurring at crack locations. A somewhat different procedure to account for tensile stresses in diagonally cracked concrete has been developed by Hsu and his coworkers at the University of Houston (Belarbi and Hsu, 1994, 1995). The procedure is called the rotating angle softened-truss model (RA-STM). Like the MCFT, this method assumes that the inclination of the principal stress direction, θ, in the cracked concrete coincides with the principal strain direction. For typical elements this angle will decrease as the shear is increased. Hence the name “rotating angle” was given (ASCE-ACI Committee 445, 1998).

Vecchio (1989) developed a two-dimensional nonlinear finite-element program for reinforced concrete membrane elements based on the modified compression field theory. Selby and Vecchio (1997) expanded the applicability of the modified compression field theory for general three-dimensional analysis of reinforced concrete solids for the solution of problems in which confinement and lateral expansion effects are important. Recently, Palermo and Vecchio (2007) presented nonlinear finite-element analyses results of several reinforced concrete shear wall experiments using well-established MCFT analysis method. The emphasis is on the simplest form of modeling available for continuum FE analysis, utilizing low-powered elements and smearing of the material properties.

Kwan and Billington (2001) evaluated the reliability of material models available in commercial, nonlinear finite-element codes or models that may be easily implemented or modified within such codes. Lefas and Kotsovos (1990) using a reliable finite element program investigated the influence of several parameters on the observed behavior and strength characteristics of structural walls. Among the parameters investigated in the study were the arrangement and amount of vertical and horizontal reinforcement, the detailing of edge members, the height to length ratio, the axial load and concrete strength. The reliability of the NLFE analysis systems had been tested by comparing analytical predictions with published information obtained experimentally (Barda et al., 1977; Cardenas et al., 1980; Oesterle et al., 1980; Maier and Thurlimann, 1985; Wiranidata and Saatcioglu., 1986) for a wide range of RC structural walls.

1.2.2 Performance Assessment and Limits of Structural Walls

The foundation of performance-based design concepts are established in three documents: SEAOC Vision 2000 (1995); ATC 40 (1996); and FEMA 273 (1996) (later FEMA 356, 2000). The documents attempted to develop procedures that can be used as seismic provisions in building codes (Ghobarah, 2001). FEMA 356 (2000) and ASCE/SEI 41 (2006) documents incorporate rational evaluation procedures for structural displacement capacities corresponding to specific performance criteria. The limits defined in terms of chord rotations and story drifts based on the results of experimental studies were adjusted to conform to mathematical modeling approaches used in nonlinear static (pushover analysis) and dynamic (time-history analysis) procedures. In the ATC 40 (1996) document, performance-based design refers to the methodology in which structural criteria are expressed in terms of achieving a performance objective. The document is limited to concrete buildings and emphasizes the use of the capacity spectrum method (Freeman et al., 1975). The procedure involves determining the capacity and demand spectra. To construct the capacity spectrum, the force–displacement curve of a structure is determined using nonlinear static (pushover) analysis. The forces and displacements are converted to spectral accelerations and spectral displacements using a substitute SDOF system (Gülkan and Sozen, 1974; Shibata and Sozen, 1976).

In the last decade based on the knowledge inherited from the documents listed above in relation to performance-based earthquake engineering, direct displacement-based design have matured to a stage where seismic assessment of existing structures or design of new structures can be carried out to ensure that particular deformation-based criteria are met (Priestley, 2000). Within this scope several researches had been conducted for the improvement of the displacement based design procedures. Wallace and Moehle (1992) investigated the ductility and detailing requirements at the boundary elements of structural walls via developing an analytical procedure that is based on comparing directly the expected displacement capacities and displacement demands for the building. The seismic displacement demand is obtained using the analytical procedure developed by Sozen (1989). Then the calculated deformation demand is related to local deformations (curvatures and rotations at the base of the wall) utilizing plastic hinge analysis method developed for cantilever members by Park and Paulay (1975). Wallace (1994) introduced the same analytical framework with minor modifications for the displacement based design of RC shear walls. By this way the structural response in terms of displacement is related to strain-based limit state, which in turn is assumed to be related to the level of damage.

Especially in the last decade the pioneering work in the field of displacement-based design were mostly conducted by Priestley and his coworkers (Priestley, 1993; Priestley and Kowalsky, 1998; Sullivan et al., 2006; Priestley et al., 2007). It has been found possible to express the yield and ultimate curvatures of different reinforced concrete structural members by simple expression based on moment-curvature responses obtained from sectional analysis. Combining these findings with simplified analysis approach based on the concept of plastic hinge of length L_p, several expression in regards to deformation limits were derived for different structural members and shear walls as well. The procedure found wide spread application on structural walls due to availibilty of these members as isolated cantilevers.

Paulay (2002) redefined some traditionally used structural properties employed in the simplified plastic hinge analysis by exemplifying on a sample frame-wall structure. Kowalsky (2001) investigated 1997 Uniform Building Code (ICBO, 1997) from the perspective of achieving performance-based earthquake engineering of structural wall buildings. It is shown that although strain limits are present in the 1997 UBC, the drift ratio limits generally govern design. The conflict between assumed force reduction factors and actual ductility demand at the design limit state controlled by drift is also explored. Sullivan et al. (2006) described the essentials of a direct displacement-based design of frame-wall structures. The effect of link beams connects from frames directly on to the ends of walls is emphasized.

In addition to these studies that were concentrated on defining limit states for design and assessment, several other studies were performed to investigate the seismic performance of structural wall buildings and to compare the static analysis results with dynamic analysis results (Mwafy, 2000; Tremblay et al., 2001). Mwafy (2000) investigated the relationship between the lateral capacity, the design force reduction factor, the ductility level and the overstrength factor of reinforced concrete frame-wall buildings. The lateral capacity and the overstrength factor were estimated by means of inelastic static pushover as well as time-history collapse analysis. Kim (2004) investigated the performance of reinforced concrete shear wall buildings designed under current codes and standards of practice and to propose a rational procedure for determining the Response Modification Factor, R. Kazaz et al. (2006b) analyzed a well calibrated finite element model of 5-story shear wall test specimen under a suite of ground motions for validating the accuracy of capacity spectrum method in estimating the actual performance of shear walls. It was found that the existing expressions for the equivalent viscous damping lead to underestimation of seismic deformation demands on isolated structural walls. Seneviratna and Krawinkler (1997) used plastic hinge rotation demands at the base as a measure of structural damage, and empirical relationships were provided to estimate these demands from spectral displacements of the first mode SDOF system.

1.3 OBJECT AND SCOPE

Reinforced concrete provisions such as in FEMA356 and ASCE/SEI 41 include modeling parameters and numerical acceptance criteria for both flexure and shear controlled wall members. The criteria are defined in terms of plastic hinge rotations and total drift ratios for the governing behavior modes of flexure (ductile members) and shear (brittle members), respectively. Strain limits are defined for concrete in compression and steel in tension at serviceability and damage-control limit states as a vital component of direct displacement-based design procedures. The recently enacted Turkish Seismic Code (2007) specifies limiting strain values associated with different performance levels. On one side deformations are specified in relation to global parameters such as drifts, and on the other local damage indicators are used to determine the performance. When results of nonlinear pushover analyses are evaluated according to either of the acceptance criteria whether the local and global response will correspond to similar performance states is debatable because little calibration has been made and field data has been totally ignored.

This study utilizes a well calibrated finite element modeling tool to investigate the relationship between the global drift, section rotation and curvature, and local concrete and steel strains at the extreme fiber of rectangular structural walls. The validity of finite element modeling strategy has been verified with simulations of various shear wall test results. Pushover analyses of isolated structural walls under inverted triangular and uniform load patterns have been performed. The parameters of the investigation were the axial load ratio, cross section length, wall height and flexural reinforcement ratio. Functions defining more exact limits of modeling parameters and acceptance criteria for rectangular reinforced concrete walls will be developed. As an indicator of the damage state of the wall, strains at the compressive and tensile boundaries of the wall will be related to performance criteria.

Additionally, the performance of structural walls designed according to current seismic code specifications will be investigated by conducting nonlinear time history analyses with recorded ground motions as seismic input. Seismic deformation demands, defined as inter-story drift in the global sense, curvature ductility at the section and strain at the boundaries as local measures, will be investigated as a function of amount of shear walls in the system.

1.4 ORGANIZATION OF THE STUDY

This study has been built on multi-tiered investigations. Several aspects of the modeling and performance assessment issues on shear walls have been covered in detail. The accuracy of the assessment procedure depends on modeling assumptions and analytical framework, which incorporates the mathematical discretization of the structure, quantification of seismic demands and effective treatment of utilized analytical procedures. All the shortcomings due to these effects should be identified.

Chapter 2 is devoted to the description of the finite elements and materials models to model the concrete and steel and verification of the finite element modeling strategy for structural walls by comparing the simulated response with the measured response of several wall specimens that are available in the literature. Essentials of finite element modeling of reinforced concrete structural walls will be given with aspects of material and geometric nonlinearities to be used in comprehensive parametric studies.

In Chapter 3, the procedures for the ground motion selection for nonlinear time history analyses available in the literature are considered and seismic intensity measures that depend on the frequency content characteristic of ground motions are defined. To quantify the seismic demands on wall type structures, intensity measures will be defined in terms of response spectral representations of input ground motions. It is displayed that the presented ground motion intensity measures correlates well with the calculated seismic deformation demands. The ground motions to be used as seismic input in the analyses are selected in this chapter.

Chapter 4 is devoted to establishing an analytical framework for the parametric investigation of shear walls. The elements of presented framework is composed of development of simple lumped-parameter structural models of wall and frame-wall systems for NLFEA, determination of the parameters that affect the shear wall response and identification of procedures to include these effects in the analyses. Simple analytical procedures used in the analyses of bearing wall and frame-wall structures are investigated and isolated wall models representative of global structural effects in both types of structural configurations are developed. A thorough investigation of these simplified models is necessary in order to determine the parameters of the study. The models are also used to derive useful information about the dynamic and static characteristics of wall type structures.

Chapter 5 presents the results of analyses carried out on the finite element models of the isolated walls to investigate the available deformation limits in FEMA 356 (2000) and TSC (2007). A parametric study taking in to account wall length and height, so as wall aspect ratio, axial load level and the amount boundary element reinforcement as parameters is conducted. The results of nonlinear static analyses were used to indentify several issues related to performance assessment of structural walls. Typical plastic hinge lengths that must be used in plastic hinge analyses of cantilever walls are determined and an equation is proposed for its calculation. The calculated rotations are compared with FEMA limits and new limits are established. For the newly established performance levels curvature and drift limits are presented. The strain limits corresponding to these performance levels are also determined. Finally the extreme fiber concrete and steel strains corresponding to rotation limits in FEMA 356 are determined and compared with the strain limits in TSC.

In Chapter 6, synthesizing all the information obtained from the previous steps regarding the ground motion and the structural modeling aspects, dynamic time history analysis of generic frame-wall structures are performed to investigate the seismic deformation demands on wall type structures. The calculated seismic deformation demands are evaluated on the basis of performance limits defined in FEMA 356 provisions.

Chapter 7 is a summary and recapture of the principal conclusions of the study.

CHAPTER 2

VERIFICATION OF THE FINITE ELEMENTS AND NONLINEAR PROCEDURE FOR ANALYSIS

2.1 INTRODUCTION

In this study ANSYS finite element program was used to simulate the static and dynamic behavior of seismic load bearing structural walls. Towards this end, it must be asserted that any other finite element code can in principle be used in the simulations, and the conclusions and methods would be very similar. However, each code has its own special features in terms of element types and material models, and needs to be used properly. Users of these powerful tools must be familiar with the capabilities of the elements formulated and implemented specifically for the analyses of reinforced concrete structures and at least the general theory of the finite element method and constitutive material laws.

In this context the objective of this chapter is to ascertain the adequacy of familiar monotonic plastic material models in predicting the response of shear-critical members as the name of the investigated structural members implies and discuss any modifications for improved results within ANSYS code.

This chapter is devoted to extensive simulation studies in order to create reliable finite element models of shear walls in ANSYS program. Comparing the measured and simulated response of several shear wall experiments, different aspects of material and finite element modeling issues will be discussed and addressed in consideration with simulation of concrete with ANSYS. The results of shear wall tests that were conducted by different researchers previously have been used in this study. The specimens in these tests were subjected to different types of loading conditions such as monotonically increasing static loading, quasi-static cyclic loading and seismic loading on a shake table. The results of simulation process are used to establish guidelines of finite element modeling and analysis of shear walls using ANSYS, which is extremely important in the upcoming parametric study in Chapter 4 for obtaining reliable and meaningful results from the analysis. All the efforts in this section are to achieve the following objectives:

- To develop nonlinear finite element models that can predict the response of flexural and/or shear dominated shear wall components under different loading conditions.
- To investigate the local stress and strain conditions resulting from these diverse combination of behavior types and loading conditions.
- To highlight different aspect of finite element modeling of concrete structures with ANSYS program since although ANSYS is widely used in research, no study, even ANSYS own manual, provides a comprehensive guidelines about its capabilities and disabilities about the analyses of reinforced concrete.

Especially in the last decade with the advent of personal computers, codes that incorporate NLFEA procedures become daily analyses tools of most engineers. A particular segment of the technical literature is devoted to studies where ANSYS has been the principal instrument for analysis.

Mirmiran et al. (2000) tested carbon fiber wrapped cylinders subjected to uniaxial compression and performed the numerical analyses with ANSYS software. Kachlakev (2002) used ANSYS to study the effects of shear strengthening of deficient beams by comparing the behaviors of two full-scale reinforced concrete beams (a reinforced concrete beam with no shear stirrups; and a reinforced concrete beam externally reinforced with Glass Fiber Reinforced Polymer (GFRP) on both sides of the beam). Three-dimensional finite element models are developed using a smeared cracking approach for the concrete and three dimensional layered elements for the FRP composites. Similarly, Santhakumar et al. (2004) presented the results of numerical study to simulate the behavior of CFRP (Carbon Fiber Reinforced Polymer) retrofitted reinforced concrete (RC) using ANSYS. Thomas and Ramaswamy (2006) reported the details of the finite element analysis of eleven shear critical partially prestressed concrete T-beams having steel fibers over partial or full depth. The ANSYS model accounted for the nonlinear phenomenon, such as, bond-slip of longitudinal reinforcements, post-cracking tensile stiffness of the concrete, stress transfer across the cracked blocks of the concrete and load sustenance through the bridging of steel fibers at crack interface. Chansawat (2003) used ANSYS in simulating the behavior of full-scale reinforced concrete beams strengthened with glass and carbon-fiber reinforced polymer laminates for shear and flexure. It was reported that the analysis results agree well with those from the experiments. The predicted crack patterns at failure strongly resemble the failure modes observed for the full-scale tests. Chansawat et al. (2006) performed three-dimensional nonlinear finite element analyses of the Horsetail Creek Bridge strengthened with fiber-reinforced polymers using ANSYS to examine the structural behavior.

Binici (2003) conducted finite element analyses of 15 slab specimens, strengthened with CFRP laminates and subjected to shear and combined shear and moment transfer experimentally, in ANSYS to provide further insight to the mechanics of load transfer, cracking and local stress conditions.

Sigfússon (2001) investigated the seismic capacity of low-rise residential shear wall buildings in Iceland by using ANSYS. Li (2004) simulated the tested response of unreinforced masonry (URM) walls strengthened with near surface mounted FRP (fiber reinforced polymer) bars for improving the structural behavior. Kazaz et al. (2006) using ANSYS simulated the seismic response of a 5-story reinforced concrete shear wall specimen on shake table subjected to progressive damage under sequential application of ground motions. Farvashany et al. (2008) built and loaded seven large-scale high-strength concrete (HSC) shear wall specimens to failure under in plane constant axial load and increasing horizontal loads. The test specimens were approximately 1/3 scale of a prototype wall. The experimental results of walls tested in this research as well as those reported by other researchers were compared with the ultimate resistance predicted by an interactive event simulator developed in ANSYS.

2.2 FINITE ELEMENTS AND CONCRETE MATERIAL MODEL

Finite element models of the experimental specimens and analytical structures are generated using the solid, bar and beam finite elements from ANSYS element library. Detailed description of these finite elements and concrete material models used in this study are given in APPENDICES A and B, respectively. Key aspects of the element formulation that influence the calculated results are identified. These items include the shear locking, extra shape function and shear transfer coefficients. In this chapter accurate determination of the values to be assigned to these parameters and inclusion in finite element models are studied by simulating the results of experimental specimens. The plasticity models that can be used to model concrete compressive behavior in ANSYS are discussed in APPENDIX

B. For that purpose essential expressions used to define von Mises, Drucker-Prager and multilinear plasticity models are given for the sake of accurate determination of the material constants. The damage mechanics of concrete behavior is discussed in relation to five parameter Willam-Warnke concrete model.

2.2.1 Combined Material Model

The concrete constitutive model making use of two yield surfaces by combining any of the plasticity models described in APPENDIX B for compressive loading and Willam-Warnke (CONC) model for tensile loading regimes can be adopted.

In ANSYS when plasticity based models are combined with the Willam-Warnke concrete material option (CONC), the plasticity check is done before the cracking and crushing checks. Yielding or cracking of any material point within the model is evaluated on the basis of principal stresses. This assumption leads the condition of the problem to reduce a plane stress situation approximately. In Figure 2.1 material models that were described above is plotted on the same graph in order to visualize what the combined yield surface will be look like. In view of this and simplification of the problem to a plane stress condition, it is obvious from Figure 2.1 that in the quadrants for tension-tension and tension-compression the Willam-Warnke model will prevail until the cracking of concrete. Upon cracking a plane of weakness will form orthogonal to the crack direction which reduces the principal stress at this direction to zero as the solution converges. Following the stress relaxation upon cracking in the quadrant tension-compression both models will interact. In the quadrant compression-compression purely plastic behavior will be valid. This explanation leads to the following conclusion. Considering the crack concrete with zero tensile stress in the direction perpendicular to crack face, the equivalent stress calculation depends totally on the compressive strength of concrete for σ_2=0. While selecting the material parameters for Drucker-Prager material model to be used in combination with Willam-Warnke concrete model in ANSYS for biaxial stress state, it must be ensured that these parameters result in close estimation of the actual compressive strength of concrete (f_c). This is to say that when either a state of tension-compression or compression-compression exists it is more correct to model the concrete plasticity with equi-biaxial yield surface defined by Eq. (B.19), which is given in APPENDIX B, in squat shear wall analysis since this equation is valid in compressive regime. The surface defined by Eq. (B.22) approximates the von Mises yield surface.

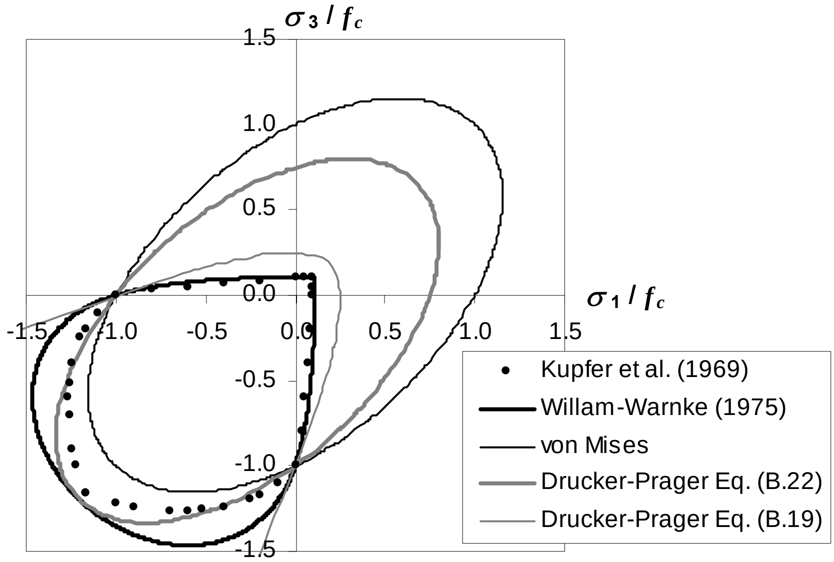

Figure 2.1 Trace of the five parameter Willam-Warnke, two parameter Drucker-Prager and one parameter von Mises material models in biaxial stress space

2.2.2 Compressive Envelope Curves for Concrete in Compression

When full stress-strain curve of concrete is not determined from material tests or it is required to determine the stress-strain curve of confined concrete, the analytical curves proposed by different researchers can be used. Depending on the characteristic compressive strength value (f_{ck}), concrete stress-strain relation curve for confined and unconfined concrete can be determined. For the ascending branch of plain concrete Hognestad (1951) parabola can be used. Since the von Mises plasticity model depends on elasto-plastic representation of the material behavior curve, the nonlinear stress-strain curve of the concrete in uniaxial compression is bilinearized as given in Figure 2.2. The limiting compressive stress f_c'' is taken to be the average compressive stress equal to $0.85f_c$ (Swammy and Qaureshi, 1974). Due to bilinearization the concrete modulus of elasticity reduces. The elastic modulus of the concrete can be calculated by $E_c = 4770\sqrt{f_{ck}}$ as proposed by ACI 318-08 (2008).

For the case of Drucker-Prager model inserting f_c and f_{bc} into Eqs. (B.20) and (B.21), parameters of Drucker-Prager yield surface are calculated as α and τ_o, respectively. The yield surface has the same pattern as plotted in Figure 2.1 utilizing Eq. (B.22). It is now required to express these parameters in terms of Mohr-Coulomb parameters, c and ϕ. Since

Drucker-Prager model in ANSYS uses outer cone approximation, using Eq. (B.15) these parameters for the cohesion and the friction angle are calculated.

For multi-linear plasticity model (MISO), the material base curve was represented with five line segments (more segments can be defined) as shown in Figure 2.2. This is the only model that can be used to represent the strain-softening branch of concrete stress strain curve. When confinement is applied to concrete both strength and ductility enhancement is obtained. To quantify the effect of confinement on concrete various analytical confined concrete models were proposed in the literature (Sheikh and Uzumeri, 1982; Park et al., 1982; Mander et al., 1988, Saatcioglu and Razvi, 1990; Martinez-Rueda and Elnashai, 1997). The models proposed by Mander et al. (1988) and Saatcioglu and Razvi (1990) is given in APPENDIX C.

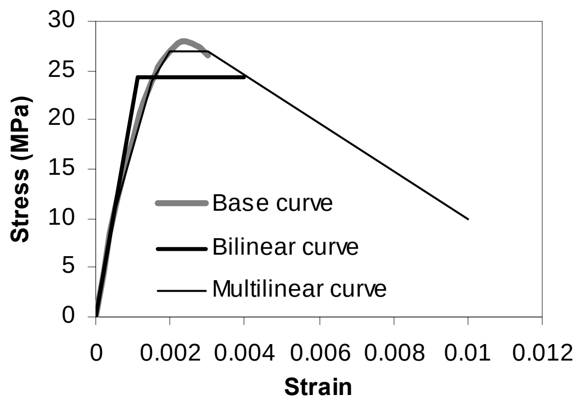

Figure 2.2 Bilinearized and multilinear uniaxial stress-strain curves of concrete

2.2.3 Cyclic Response of Concrete Material Model and SOLID65 Element

The behavior SOLID65 element under cyclic loading was investigated. Multilinear isotropic plasticity model with a descending branch for concrete in compression is combined with Willam-Warnke failure criterion in tension to simulate the behavior of a 200x200x200 mm cubic concrete block as shown in Figure 2.3. The idealization in material behavior like elastic unloading may not be a suitable approach for modeling the cyclic behavior of concrete since concrete exhibits stiffness degradation under cyclic loading (Mirmiran et al., 2000). Nevertheless, for small-to-medium range plasticity of concrete in compression as will be shown later simulations gives satisfactory results.

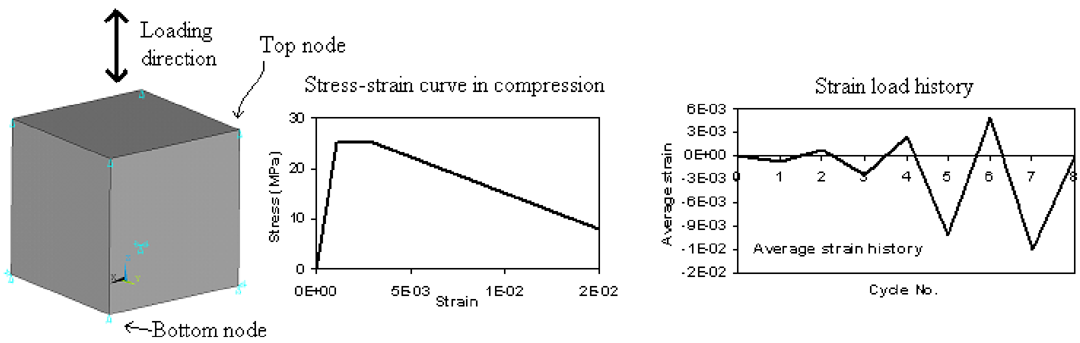

Figure 2.3 Rectangular cross-section of a column Cubic element, material properties and cyclic loading history

The displacement load history displayed in Figure 2.3 was applied at the top nodes of the cubic element, which is constrained at the base nodes appropriately to prevent any reaction against lateral spreading. Effect of ESF (Extra shape functions) on element behavior was investigated. The stress-strain output calculated at the top and bottom nodes are summarized in Figure 2.4. As seen in Figure 2.4(a) when ESF is turned off a constant strain distribution assumed with the element. When the block compressed 2.4 mm at the ultimate cycle imposing a strain of -2.4/200 = -0.012, this strain is constant within the element at both integration points. In the case where ESF's are utilized, deformation localizes at either top or bottom nodes depending on the loading type. While for cyclic load history strain localizes at the top node as displayed in Figure 2.4(b), for static compressive loading significant crushing takes places at the bottom material points as seen in Figure 2.4(c).

The average stress-strain output at the element centroid is plotted in Figure 2.5 for the cases where ESF is activated and deactivated using element options. The unloading and reloading stiffness is same as the initial stiffness of the material curve. The average stress-strain curve obtained by utilizing ESF displays more rapid strength degradation tendency compared to curve without ESF. This is very similar to localized failure phenomena observed in experimental studies on stress-strain curve of concrete under compression. Experimental studies (Bazant, 1989; Lertsrisakulrat et al., 2001; Watanabe et al., 2004) displayed that three (or two) different zones develops on the concrete cylindrical specimens subjected to axial compression, failure zone, a transition zone and an unloading zone. The failure pattern depends on the aspect ratio of the specimens. Different stress-strain curve is defined for each zone. The average stress strain curve is obtained by combining the curves for each segment. In the experiments, a stress-local strain curve measured in the no-crack zone (unloading zone) exhibited unloading behavior until the end of the loading test as shown in Figure 2.4(c) for top node.

The behavior modes displayed in Figure 2.4(b) and (c) evolve when softening property in the material curves is defined. If bilinear isotropic plasticity is utilized for the behavior of concrete in compression, or more explicitly if no softening is considered in concrete, using ESF should not matter to response, constant strain output is obtained at each material point within the element.

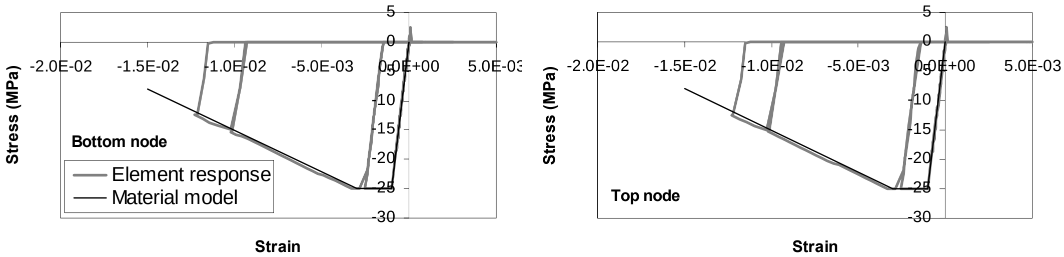

(a) Extra displacement shapes formulation turned off

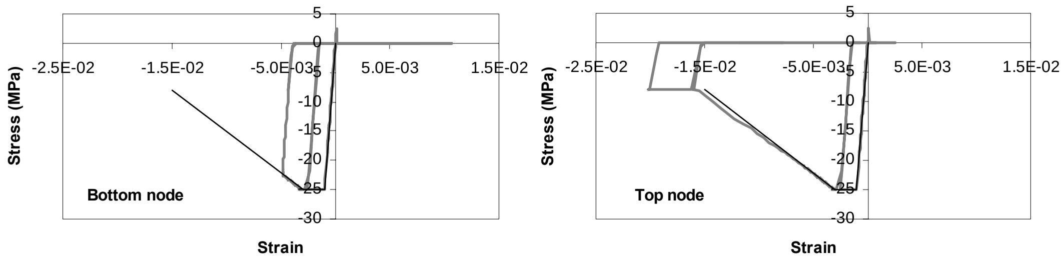

(b) Extra displacement shapes formulation turned on

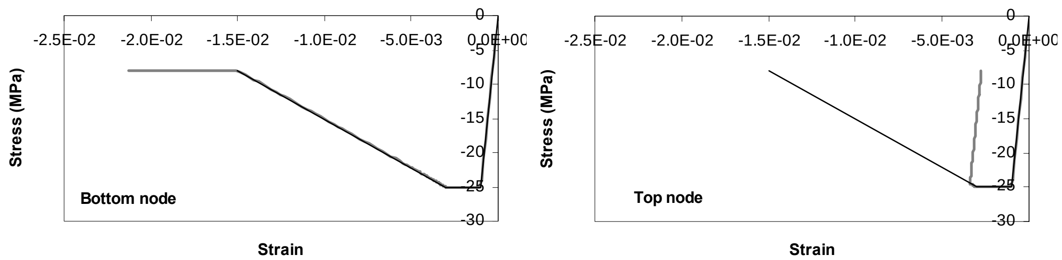

(c) Static compression loading with ESF turned on

Figure 2.4 Effect of ESF on the stress-strain response output at the top and bottom nodes of cubic concrete element (Thin line displays the material curve input to the program)

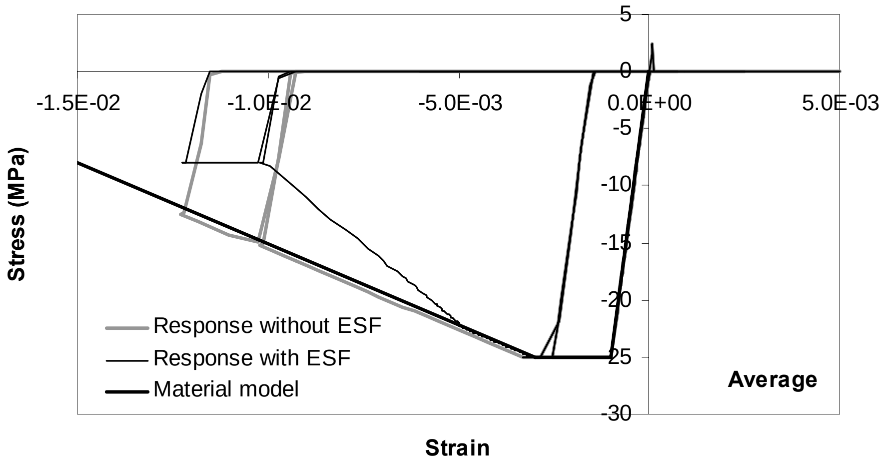

Figure 2.5 Average stress-strain calculated within the element by averaging the stress-strain response at the bottom and top nodes

2.3 STEEL MATERIAL MODEL

In the design of reinforced concrete structures, rebar properties do not need to be known exactly. ASTM A615 only requires that that the yield stress of Grade 60 bars needs to be exceed 424 MPa (60 ksi). For analyses purpose, e.g. finite element analyses, an actual value of the yield stress is needed to be provided for a more accurate prediction of actual structural response.

The typical stress-strain relationship for the reinforcing steel obtained from uniaxial tests displays that steel has definite yield point and a significant yield plateau. Strain hardening starts at the end of this plateau. The most important properties of the σ-ε curve of the reinforcing steel are (a) the yield strength (f_{sy}), (b) the ultimate strength (f_{su}), and (c) ultimate strain capacity (ε_{su}). The monotonic steel response may be defined by a few material parameters as identified in Figure 2.6. In this figure E is the elastic modulus, ε_{sh} is the strain at which strain hardening initiates.

A review of tests on reinforcing bars conforming ASTM specifications (1999) was conducted by Malvar and Crawford (1998). It was shown that there is a significant variability in strain data defining the borderlines of different regions on the stress-strain curve given in Figure 2.6. It was also reported that the measured strains of same grade but different dimension bars are also different.

TS 500 (2003) states that the reinforcement should satisfy the requirements of TS 708. It was required in TSC (2007) that reinforcing steel with strength exceeding that of S420 shall not be used reinforced concrete structural elements. The rupture strain of reinforcement to be used shall not be less than 10%. The mechanical properties of bars made of S420 steel is given as 420 MPa for yield strength, 550 MPa for ultimate strength and minimum strain of 0.1 at the rupture in TSC.

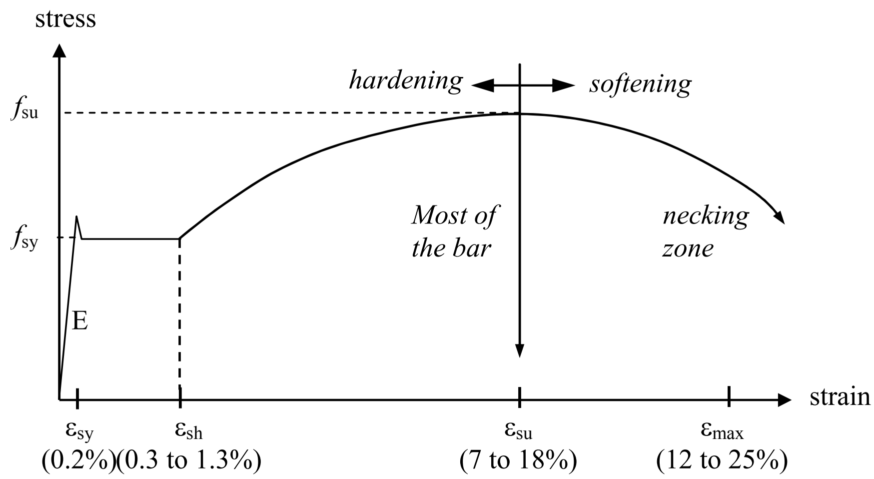

Figure 2.6 Typical stress-strain curve for ASTM A615 Grade 60 steel

Response of reinforcing steel subjected to reversed cyclic loading exhibits isotropic strain hardening, characterized by increasing strength under increasing inelastic strain demand (Lowes, 1999). It was experimentally (Vallenas, 1979; Ma et al.) found that the yielding strength is higher in compression than tension.

In an effort to summarize all the foregoing discussions, Figure 2.7 is plotted, defining the simplified steel stress-strain curve to be used in the analyses. Using the typical stress-strain curves representing ASTM A615 Grade 60 and S420 (BÇ-III) reinforcing bars, a bilinear stress-strain curve was fitted to these curves ignoring the yield plateau. For general engineering applications, the elasto-plastic constitutive relationship, either with or without strain hardening, is normally adopted for ductile reinforcing steel (Powanusorn, 2003). Uniaxial behavior of longitudinal and transverse steels was modeled with a bilinear isotropic hardening using von Mises yield criterion based on this curve. Modulus elasticity of the steel material was taken as 200000 MPa. The yield stress and tangent modulus at the strain hardening is taken as 420 MPa and 2000 MPa, respectively. Using a strain hardening stiffness helps achieving a better convergence behavior.

The steel model used in this study does not consider any modifications or adaptations to take into account bar fracture and slip between steel and concrete due to deterioration of bond. Nevertheless, in a simulation example at the end of this chapter application of bond-slip in finite element analyses is displayed. In regions of variably oriented loading or relatively high shear loading, critical shear and diagonal tension may develop in wall members. The formation of a significant diagonal-tension crack activates resistance to vertical shear by dowel action in the main longitudinal reinforcement, subsequent aggregate interlock along the diagonal crack, and resistance in vertical stirrups (Chen, 1982). This loading of the cracked reinforced concrete volume is referred to as shear friction, and activation of reinforcement perpendicular to the bar axis at a crack surface is referred to as dowel action (Lowes, 1999). Most research into the shear-friction response of reinforced concrete elements indicates that even for this type of loading axial rather than dowel action dominates the response of the reinforcement perpendicular to the crack surface (Laible et al., 1977; Paulay and Loeber, 1977). While most researchers agree on this, there are studies that suggest the dowel action of reinforcing steel may not be negligible and may contribute between twenty-five and thirty-five percent of the slip resistance at a crack surface (Hofbeck et al., 1969). In the current investigation, nonlinear shear behavior due to the dowel action of reinforcing steel is neglected and reinforcing steel is modeled as an uniaxial element.

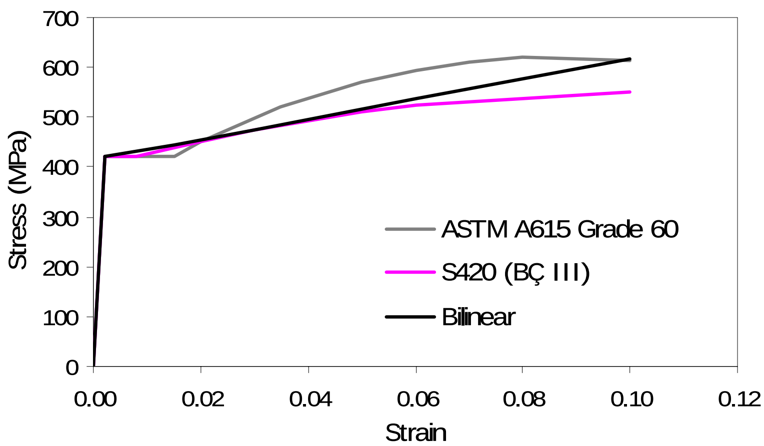

Figure 2.7 Stress-strain diagram of reinforcing steel used in the analyses

2.3.1 Modeling of Bar Buckling

For walls with moderate amounts of boundary longitudinal reinforcement, ties are required to inhibit buckling. Cyclic load reversals may lead to buckling of boundary longitudinal reinforcement even in cases where the demands on the boundary of the wall do not require special boundary elements. Additionally, the confined concrete models are applicable only if premature buckling of longitudinal reinforcement is prevented. Buckling of the reinforcement also affects the drift capacity of reinforced concrete sections.

Dhakal and Maekawa (2002), Gil-Martin et al. (2008), Berry and Eberhard (2005) are among the researches recently studied the subject. Dhakal and Maekawa (2002) proposed a unique relationship between the average stress and average strain of reinforcing bars including the effect of buckling. They found that the average compressive stress-strain relationship including the softening in the post-buckling range can be completely described in terms of the product of square root of yield strength (f_y) and the slenderness ratio, L/D, of the reinforcing bar. L is the unconfined length of the longitudinal reinforcement between the two transverse reinforcement and D is the diameter of the longitudinal bar.

The general layout of the proposed average monotonic compressive stress-strain model is sketched in Figure 2.8. An intermediate point (ε^*,σ^*) is established, after which a constant negative stiffness equal to 0.02E_s, is assumed until the average stress becomes equal to 0.2f_y. to make model applicable to bars with all types of material model, the stress at and before the intermediate point are normalized with respect to the stress computed from the point wise stress-strain relationship at the corresponding strain value. The following equations relating the average compressive stress with the average compressive strain of reinforcing bar are proposed:

$$\frac{\sigma}{\sigma_l} = 1 - \left(1 - \frac{\sigma^*}{\sigma_l^*}\right)\left(\frac{\varepsilon - \varepsilon_y}{\varepsilon^* - \varepsilon_y}\right); \qquad \text{for } \varepsilon_y < \varepsilon \le \varepsilon^* \qquad (2.1)$$

$$\sigma \ge 0.2 f_y; \qquad \sigma = \sigma^* - 0.02 E_s \left(\varepsilon - \varepsilon^*\right); \qquad \text{for } \varepsilon > \varepsilon^* \qquad (2.2)$$

Here , σ_l and σ_l* are the point wise stresses corresponding to ε (current strain) and ε* (strain at intermediate point), respectively. Similarly, ε_y and E_s are the yielding strain and Young's modulus of the reinforcing bars. The coordinates of the intermediate point (ε^*,σ^*) can be calculated by

$$\frac{\varepsilon^*}{\varepsilon_y} = 55 - 2.3\sqrt{\frac{f_y}{100}}\frac{L}{D}; \qquad \varepsilon^*/\varepsilon_y \geq 7 \tag{2.3}$$

$$\frac{\sigma^*}{\sigma_l^*} = \alpha\left(1.1 - 0.016\sqrt{\frac{f_y}{100}}\frac{L}{D}\right); \qquad \sigma^* \geq 0.2 f_y \tag{2.4}$$

The coefficient a takes the value of 1.0 for linear hardening bars and 0.75 for perfectly elasto-plastic bars.

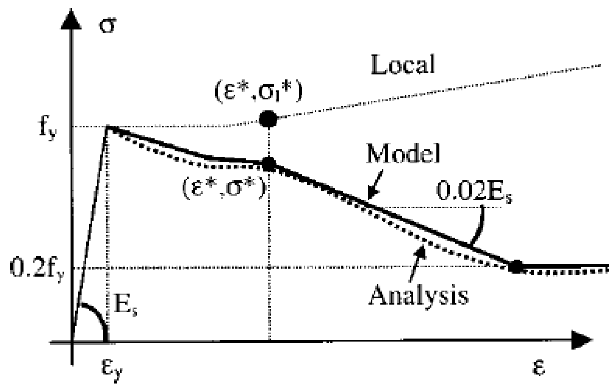

Figure 2.8 Schematic representation of proposed model (Dhakal and Maekawa, 2002)

The bar buckling model is utilized in some static analyses case in this chapter and in parametric study in Chapter 5. The steel material model for the longitudinal bars at the boundary elements of compression region of shear walls is calibrated in accordance with the model presented here.

2.3.2 Effect of Tension Stiffening

It is well known that behavior of reinforcing steel bars surrounded by concrete is different than the bare steel bars. The stress-strain curve of a mild bar tested in a bare condition exhibits a long plateau after yielding. However, the average stress-strain curve of mild steel bars embedded in concrete does not show such a yield plateau. The apparent yield stress is lower than the yield stress of a bare bar. Belarbi and Hsu (1994) based on experimental data from reinforced concrete panels proposed a simple bilinear material law for steel bars embedded in concrete. The parameters affecting the average stress-strain curve of steel bars embedded in concrete found to be the surrounding concrete tensile strength (f_{ctk}), the volumetric ratio of the embedded steel with respect to surrounding concrete core volume and the yield strength of the steel (f_y). Figure 2.9 summarizes the necessary equations for bilinear model to modify the stress-strain relation of reinforcing steel and an example curve with f_y = 420, f_{ctk} = 2 MPa and ρ_s=0.01.

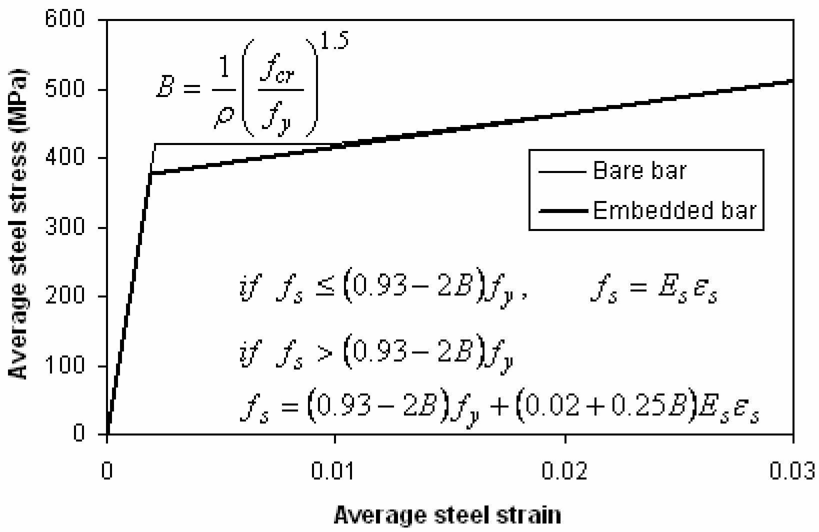

Figure 2.9 Average stress-strain relation of steel embedded in concrete

2.4 CAUSES OF WALL RESISTANCE AND FAILURE MECHANISM

The behavior of a shear walls can be governed by purely flexural or shear effects, or a combination of these two effects. The principal source of energy dissipation in a laterally loaded cantilever wall should be the yielding of the flexural reinforcement in the plastic hinge regions, normally at the base of the wall (Paulay, 1986). To achieve this behavior, shear walls must be designed according to shear strength that yields lateral shear strength higher than that required to develop flexural yielding in the vertical boundary reinforcement of the walls. Nevertheless, there are cases where the governing behavior modes leading to failure change due to large shear wall cross section area.

The walls characterized by small height-to-width ratio are encountered in low-rise buildings or in the lower stories of medium to high-rise buildings. Walls having height-to-width ratio less than two is classified as squat walls. The flexural moment capacity of these walls may be very large, even when a minimum amount of vertical reinforcement used. Due to small height, very large lateral forces must be applied on the wall to develop the flexural strength at the base. However, until the flexural mechanism is actuated significant shear actions may be introduced. Web concrete crushing, diagonal tension or compression and sliding shear are the failure modes observed due to squatness. Diagonal tension or diagonal compression is identified as the most common failure modes observed in squat shear walls. Diagonal tension failure occurs when insufficient horizontal shear reinforcement is placed in the web section of the wall. Diagonal compression failure occurs when the shear stress on the web is large. In the latter case, the concrete in the toe region crashes, followed by a sliding shear plane extending along the base of the wall (Palermo and Vecchio, 2002). Lefas and Kotsovos (1990) stated that it is the strength of the compressive zone that is the main contributor to shear resistance and not the “cracked” concrete in regions subjected to predominantly tensile stress conditions. When it comes to modeling of these elements, the effects of these response modes become more pronounced.

Figure 2.10 illustrates schematically the shear resistance mechanism at the lower part of the compressive zone of a shear walls. If two extreme conditions observed in structural walls are considered, which is flexure dominated behavior as observed in slender walls and shear controlled failure modes due to squatness in shear walls, following generalization can be done about the properties of the material model for concrete.

The response of concrete in the compression region of flexure controlled shear wall can be represented with uni-axial stress-strain relation of concrete. An enhancement in the compressive strength of concrete at this region due to confinement effect around the wall boundary element can be also taken in to account. This kind of flexural behavior, which consists of initial yielding of the reinforcement in tension with subsequent plasticity of the concrete in compression, has many successful applications (Cervenka, 1972; Sittipunt and Wood; 1995; Kazaz et al., 2006). Even in some applications neglecting the plasticity of concrete in compression, i.e. only considering the cracking of concrete and yielding of reinforcement, has yielded adequate prediction of the actual response (Franklin, 1970).

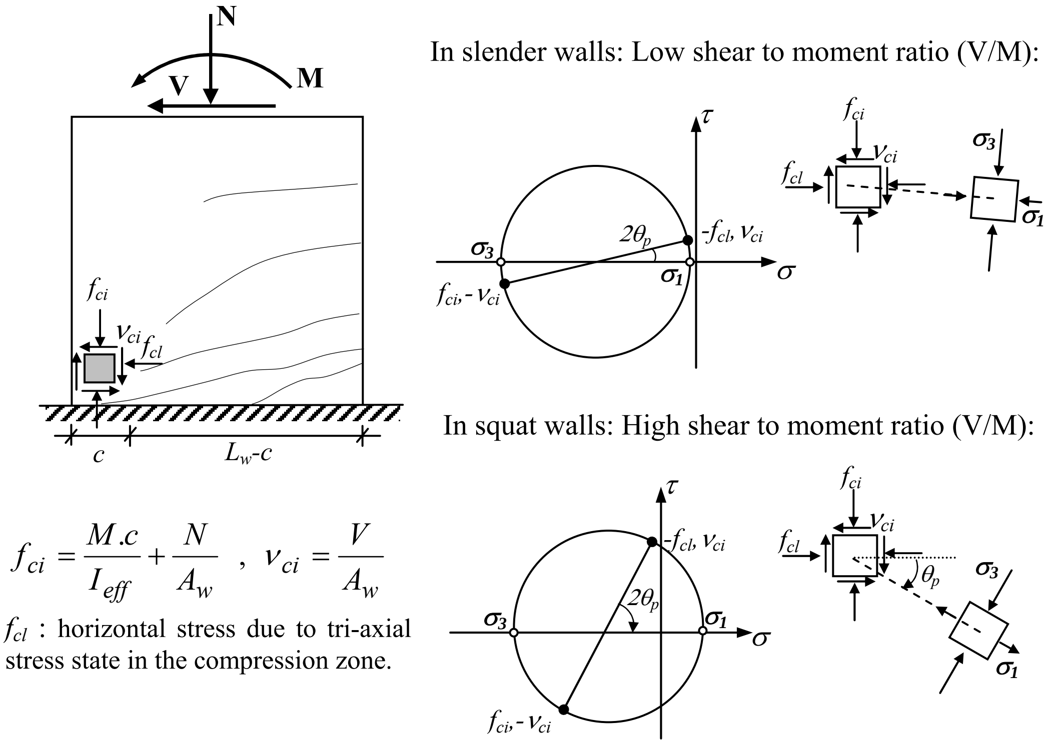

Figure 2.10 Schematic representation of failure mechanism of the walls

On the other hand at high shear to moment situations accompanied by nominal axial stress as observed in squat walls, starting from very early stages of loading diagonal tension and compression would have developed on the web wall. The concrete stress in the web zone was high. The flow of compressive stresses diagonally resulted in maximum compressive stresses and strains to occur at the compression toe located at the lower left part of the web wall. A biaxial tension-compression situation (situations likely to produce shear mechanisms) develops at this region as shown in Figure 2.11. Vecchio and Collins (1986, 1993) based on extensive experimental studies on shear panels showed that compressive strength of concrete subjected to biaxial tension-compression decreases. The principal compressive stress in concrete was found to be a function not only of the principal compressive strain but also of the co-existing principal tensile strain. More clearly, cracked concrete subjected to high tensile strains in the direction normal to the compression is softer and weaker than concrete in a standard cylinder test, see Figure 2.11. Vecchio and Collins (1986) introduced a softening factor as a function of principal tensile and compressive strain to decrease this peak compressive stress and strain of unconfined concrete for simplified shear design. This factor has the form:

$$\beta = \frac{f_{c2\max}}{f_c} = \frac{1}{0.8 + 170\varepsilon_1} \leq 1.0 \tag{2.5}$$

where ε_1 is the principal tensile strain and taken as positive, $f_{c2\max}$ is the softened peak compressive strength. It is obvious that increasing ε_l will reduce β. The stress-strain relationship of concrete is given by

$$f_{c2} = f_{c2\max} \cdot \left[2\left(\frac{\varepsilon_2}{\varepsilon_c^{'}}\right) - \left(\frac{\varepsilon_2}{\varepsilon_c^{'}}\right)^2 \right] \tag{2.6}$$

and the effective modulus of elasticity due to weakening is

$$E_c = \frac{2f_{c2\max}}{\varepsilon_c} \tag{2.7}$$

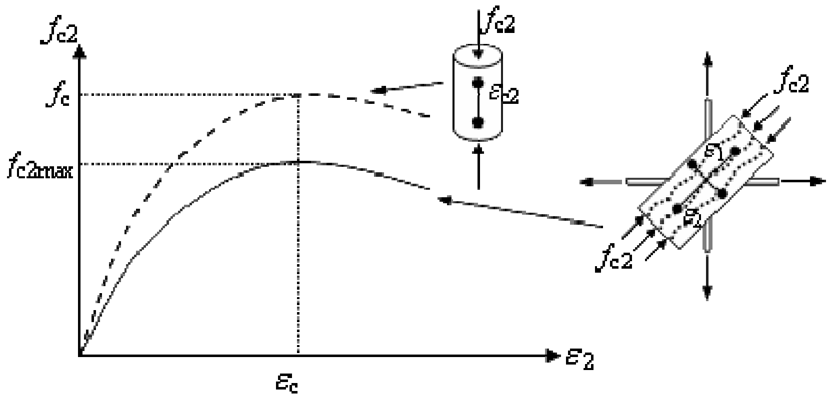

Figure 2.11 Stress strain curve for cracked concrete in compression

Compressive stress strain relationship of diagonally cracked concrete can be modified in one of two ways (Vecchio and Collins, 1986; Belarbi and Hsu, 1995; ASCE-ACI Committee 445, 1998). The loading can be assumed to be proportional, causing both the principal compressive strain, ε_3, and the principal tensile strain, ε_1, to increase simultaneously. Modifications were made to both the peak stress and the strain at peak stress. This method is suitable for static-monotonic analyses, since the initial stiffness is not affected. In the second case, it is assumed that concrete was sequentially subjected to extensive tensile strains first and than the principal compressive strain is increased. While this second case is not a realistic situation for concrete under monotonic loading, it is a better approach for concrete that has already cracked or under cyclic loading. Only the stresses are modified in the second case.

Kwan and Billington (2001) utilizing a commercial finite element code investigated the effects of various nonlinear material models and their associated parameters on the cyclic response of reinforced concrete structural members. A significant outcome of their research is that although the adopted material models are able to represent flexure dominated behavior well, they can only indicate when shear-dominated hysteretic behavior is likely. They stated that further improvements are required in modeling cyclic shear deterioration in concrete constitutive model in order to capture the shear dominated behavior.

This indicates that analyses and design of reinforced concrete members under shear and torsional effects requires special treatment of concrete material properties and laws. Rational and realistic models for response governed by shear are few and seem not to have gained excessive application in finite element practice (Vecchio and Collins, 1986; Belarbi and Hsu, 1995; Hsu and Zhu, 2002). Moreover, results of several prediction exercises revealed the inadequacy of customary analysis procedures for such elements (OECD/NEA/CSNI, 1996).

2.5 NONLINEAR TIME HISTORY ANALYSES PROCEDURE IN ANSYS

In the nonlinear transient dynamic analysis solution phase we encountered some problems related to ANSYS software. Direct application of ground motion is not possible within the program. The only form of acceleration input is to create acceleration field acting on all the nodes of model. Thus, the structural response of the model to the base excitation is calculated using the concept of effective earthquake forces (Chopra, 2000). Lumping masses at the floor levels for the wall, the absolute floor displacement vector, $\mathbf{u}^t$, under the ground displacement u_g is computed from Eq. (2.8) (Figure 2.12(a)).

$$\mathbf{u}^t(t) = \mathbf{u}(t) + u_g(t).\mathbf{1} \tag{2.8}$$

where **1** is a vector of order *N* with each element equal to unity and in general terms called influence vector *(ι)* that represents the displacements of the masses resulting from the static application of a unit ground displacement. For external dynamic forces $F_i(t)$ the general form of the equation of dynamic equilibrium can be written in the form:

$$[M].\{\ddot{u}\} + [C].\{\dot{u}\} + [K].\{u\} = \{F(t)\} \tag{2.9}$$

In the earthquake (base) excitation case, $F(t) = 0$ since no external dynamic force is applied and the equation of dynamic equilibrium becomes

$$[M].\{\ddot{u}\} + [C].\{\dot{u}\} + [K].\{u\} = -[M].\{\iota\}.\ddot{u}_g(t) \tag{2.10}$$

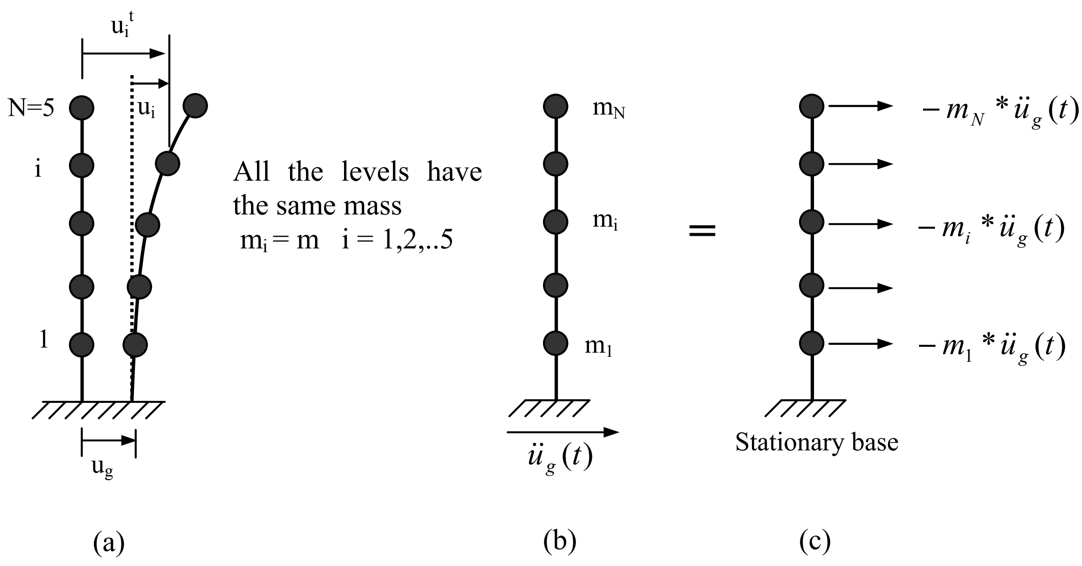

Figure 2.12 *(a)* Lumped mass system, *(b)* Ground excitation, *(c)* Effective earthquake forces

Comparing Eq. (2.9) with Eq. (2.10) shows that the equations of motion for the structure subjected to ground acceleration, $\ddot{u}_g(t)$ in Figure 2.12(b) and externally applied dynamic load, $m_i.\ddot{u}_g(t)$ in Figure 2.12(c) at the level of each mass are one and the same.

The accelerations calculated with Eq. (2.10) are relative accelerations; so for computing the total acceleration related to any mass, Eq. (2.8) must be utilized.

In view of the discussions presented above, acceleration data is entered in the form of an array to the program before the start of solution, and in the solution phase for each time integration step (Δt), corresponding acceleration is called in from the array within a small loop covering the whole time history data points. Due to application of this acceleration field at any particular instant, all the masses are multiplied with the ground acceleration value and the resulting force is applied to the structure as an external dynamic loading, which is the right hand side term in Eq. (2.10). For the given instant governing equations of motion are solved statically including the time integration effects in the calculations. In the ANSYS program Newmark and HHT (Hilber et al., 1977) time integration methods can be employed for the solution of the equations of motion that are in the same form as Eq. (2.10). In nonlinear analysis the stiffness matrix [K] is a function of unknown displacements, so Newton-Raphson Procedure, which is an iterative method to solve nonlinear equations, is also used.

In particular, it is desirable to have a controllable numerical damping in the higher frequency modes, since using finite elements to discretize the spatial domain, the results of these higher frequency modes are less accurate. However, the addition of high frequency *numerical damping* should not incur a loss of accuracy nor introduce excessive numerical damping in the important low frequency modes. In the full transient analysis, the HHT time integration method (Chung and Hulbert, 1993) has the desired property for the numerical damping. The Newmark parameters are related to the four input parameters α, δ, α_f, and α_m used in the HHT method as follows

$$\begin{aligned} \alpha &= \frac{1}{4}(1+\gamma)^2 \\ \delta &= \frac{1}{2}+\gamma \\ \alpha_f &= \frac{1-\gamma}{2} \\ \alpha_m &= \frac{1-3\gamma}{2} \end{aligned} \tag{2.11}$$

where γ is the amplitude decay parameter. In ANSYS either the four input parameters should be input or they should be defined using γ only. When the amplitude decay parameter (γ) equals to zero, method reduces to constant average acceleration. If both α_m

and α_f are zero when using this alternative, the HHT method is same as Newmark method. For the value of amplitude decay parameter Broderick et al. (1994) tried the values in the range of 0.1 and 0.3 and concluded that $\gamma = 0.1$ provides the desired numerical damping to eliminate the higher mode noise especially observed in the force and acceleration responses of the model.

The numerical damping is useful in eliminating the high frequency noise, however to account for the energy dissipation due to many different effects such as material damping, joint friction and radiation damping at the support viscous damping should be defined also. The viscous damping is input by means of Rayleigh damping constants ($[\mathbf{C}] = \alpha[\mathbf{M}] + \beta[\mathbf{K}]$); i.e. it was assumed that both mass- and stiffness-proportional damping was present in the system (Chopra, 2000).

2.6 ACCURACY AND VERIFICATION BY SHEAR WALL TEST RESULTS

To ascertain the adequacy of finite elements and associated material models described above in the analyses of structural walls, a series of shear wall experiments were modeled. The wall specimens in these experiments are representative of typical shear walls in terms of aspect ratio, reinforcement amount, axial load ratio and loading conditions. Different loading schemes, monotonic and cyclic static, dynamic loading, were employed in these tests, so as to make it possible to investigate the effect different loading types in finite element analyses. During the course of numerical simulations of each shear wall experiments different aspects of finite element modeling issues and used solid finite element and material models are discussed. The purpose of this extensive treatment for aligning experiment and analysis is to build confidence for the deep-cutting critique and revised recommendations that will form the basis of Chapter 5.

The analyses of walls that are carried out in this thesis are briefly summarized below.

- CAMUS wall: 1/3 scale 5-story lightly reinforced concrete shear wall was tested on shaking table under sequential application of ground motions of increasing amplitude (Combescure, 2002).
- NUPEC wall: Large scale 1-story H shaped squat wall was tested on shaking table under sequential application of ground motions of increasing amplitude (OECD/NEA/CSNI, 1996). The specimen is proved to be very useful in identifying the shear dominated effects in squat walls as well the dynamic properties.

- Walls tested by Lefas et al. (1990): Thirteen large scale wall models were tested under the combined action of a constant axial and a horizontal load monotonically increasing to failure.
- Portland Cement Association (PCA) structural walls (Oesterle et al. 1976): 1/3 scale isolated reinforced concrete walls representative of full-size walls subjected to cyclic load of increasing amplitude.
- Wall tested by Thomsen and Wallace (1995): Rectangular slender wall designed using a displacement-based design methodology tested under cyclic loading.

In the simulations several issues and problems related to finite element analyses of reinforced concrete structures are addressed. These problems are related to element technology of SOLID65 and material models used to model concrete. Strategies and procedures are proposed for the solution of these problems. In the following sections detailed explanations of finite element modeling of these walls and comparison of calculated and measured response are given.

2.6.1 CAMUS Wall: IAEA Benchmark Project (CAMUS Experiment)

The investigation seismic response of CAMUS wall utilizing NLFEA has been conducted under the IAEA (International Atomic Energy Agency) CRP (Coordinated Research Project) “Safety Significance of Near-Field Earthquakes”. The detailed explanation of numerical simulations of CAMUS wall can be found in Kazaz et al. (2006a). Only the best estimate results will be given here. The experimental program consisted of testing a model with scale 1/3 representative of a 5- story reinforced concrete building on the major Azalee shaking table of Commissariat a l’Energie Atomique (CEA) in the Saclay Nuclear Center, France. The specimen, named CAMUS1, had a total mass of 36 tons with the additional masses attached to it. Walls have no openings and are linked by square slabs measuring 1.7mx1.7m. A heavily reinforced concrete footing allows the anchorage to the shaking table. The total height of the model is 5.10 m. Walls have thickness of 6 cm. The dimensions of the different parts and the mass distribution are shown in the sketches given in Figure 2.13.

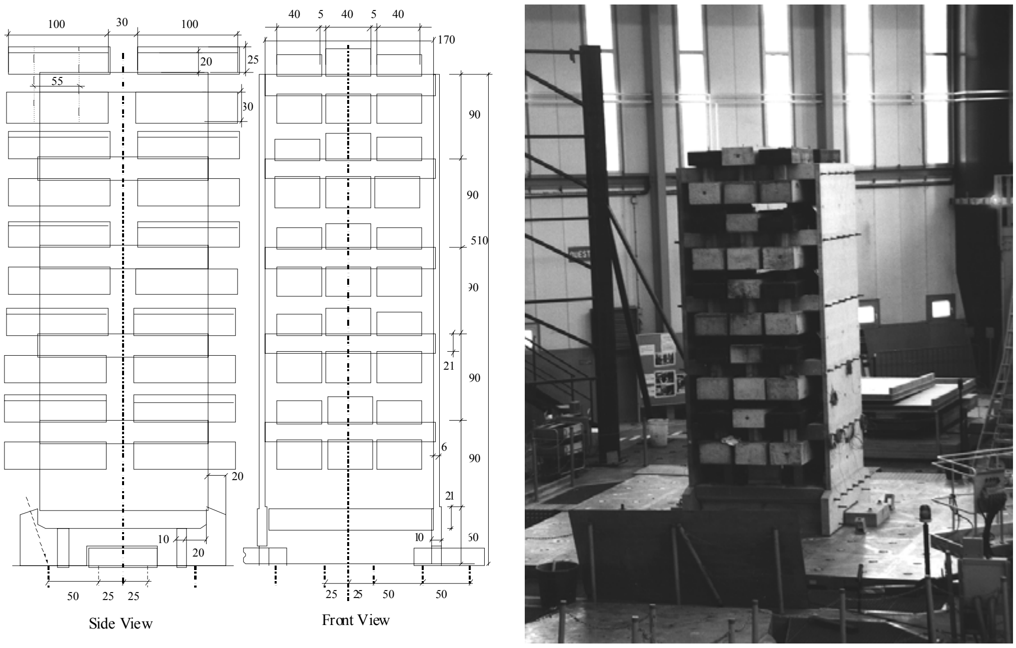

Figure 2.13 View of the CAMUS specimen and sketch of the walls and masses (Combescure, 2002), (units are in cm)

The specimen has reinforcement details that follow the French PS92 seismic design code (Combescure, 2002) with minor adaptation in order to increase the shear safety factor. The distribution and the detailing of the reinforcement are quite different from those in conventional design practice where generally mesh reinforcement is used in the web along with the main longitudinal reinforcement at wall ends. The longitudinally reinforced regions through the 1.7 m wide walls are two edge regions in 10 cm width and the central region with 30 cm width. The amount of reinforcement decreases gradually as it goes to upper stories. The addition of central reinforcement is to limit the risk of sliding shear failure. For transverse reinforcement, bars with 3-mm diameter were used at a spacing of 6 cm along the height of the wall where longitudinal reinforcement is used. The amount of steel at each level and details of reinforcement in elevation are shown in Figure 2.14.

The acceleration waveform of the ground motions are given in Figure 2.15. It is worth noting that these ground motions were applied sequentially to the same specimen so any accumulation of inelasticity from previous runs was retained in the subsequent runs.

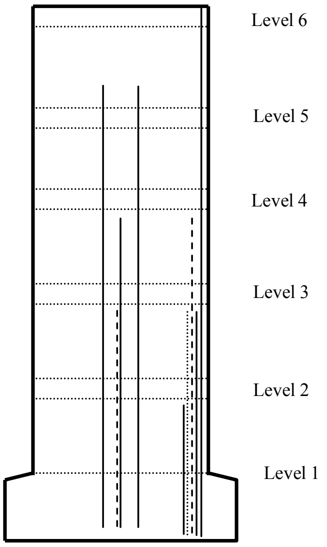

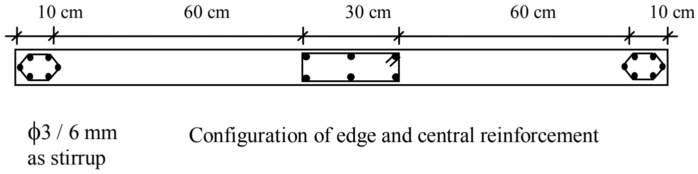

Longitudinal Reinforcement amount at each level

Level	*Edge of the wall (mm^2)*	*Center of the wall (mm^2)*
1	289.4	138
2	188.9	138
3	94.4	110.2
4	28.3	78.4
5	15.9	78.4
6	15.9	Nothing

Figure 2.14 The amount and detailing of reinforcement in elevation of single wall

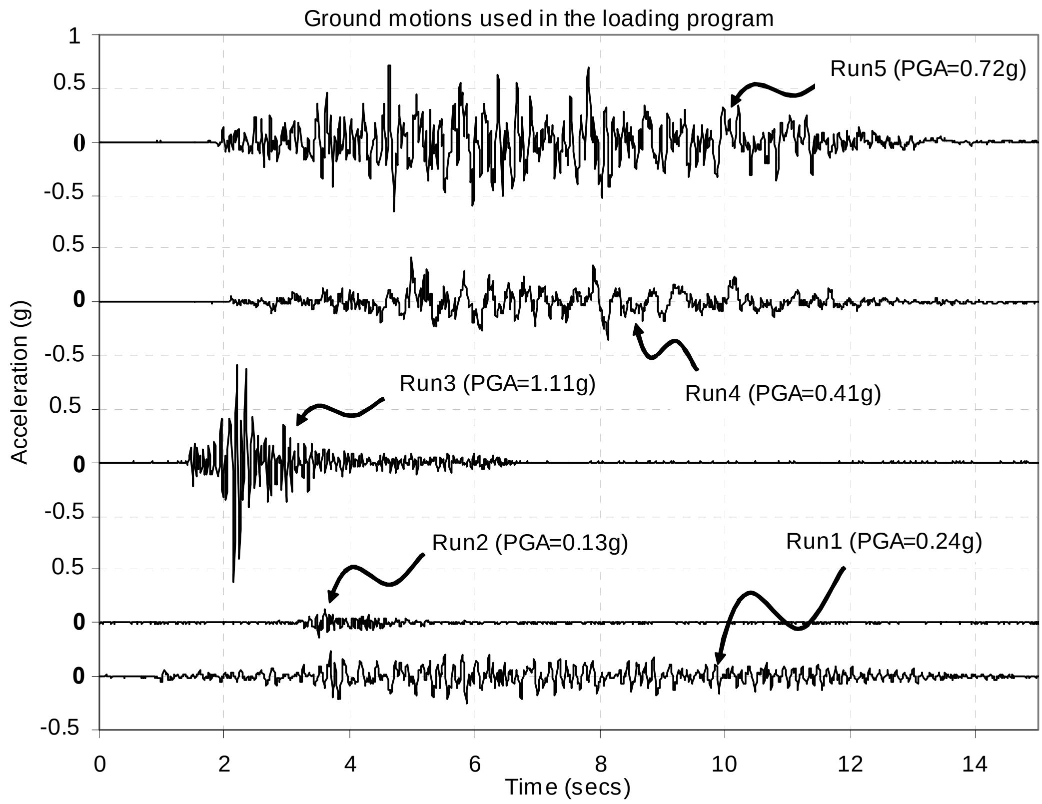

Figure 2.15 Nice and San Francisco signals used in the experiments

2.6.1.1 Steel and Concrete Material Models

In the light of the experimental results, the compressive and tensile strength and the modulus of elasticity of the concrete were taken as 35 MPa, 3.8 MPa and 30 000 MPa, respectively. The stress-strain curve of the concrete in compression was represented with three segments as a multilinear isotropic hardening material as shown in Figure 2.16. In nonlinear analysis of reinforced concrete, the shear transfer coefficient must be assumed. For closed cracks (β_c), the coefficient is assumed to be 1.0, while for open cracks (β_t) it should be in the suggested range of 0.05 to 0.5, rather than 0.0, to prevent numerical difficulties (Hemmaty, 1998). A value of 1.0 was used for the open cracks, which resulted in acceptably accurate predictions. It will be shown later than this value can vary significantly depending on the element formulation. Only one bilinear curve was used to represent the material property of the four different reinforcing bars. The yield stress was taken as 500 MPa (an average value) at 0.002-strain value and the stress at the failure is assumed to be 525 MPa with 0.34 % strain hardening.

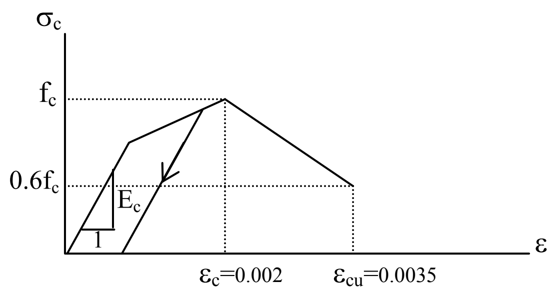

Compressive behavior of concrete

Figure 2.16 Material behavior of concrete

2.6.1.2 Modeling of the Specimen

The modeling work of CAMUS wall has been discussed in great detail in Kazaz et al. (2006). The results of this modeling study especially useful in displaying the effect of boundary condition modeling on the response of test structures. The flexibility of the shaking table and the connectivity of the shear wall specimen to the shaking table found to have significant influence on the dynamic properties of the test specimen, which made them vital components of the model.

Using the symmetry of the model only one wall was modeled. The shake table was modeled as rigid beam with equivalent mass and support stiffness. The table and walls were modeled with element SOLID65. The masses of each story were lumped uniformly at the level of each floor by using special mass elements, MASS21. The solid beam below the wall in Figure 2.17 that models the shaking table was found to be adequate. The wall foundation was not fully anchored to the table at its base (Figure 2.18); the anchorage was provided in the middle of basement for a partial length only, approximately 1/3 of the wall length. At the two ends, the gap between the wall and table can be described as a contact surface problem. This region was filled with elastic mortar with unknown properties. At the two ends, steel anchor bars with 36 mm diameter were used to provide additional fixity to the wall.

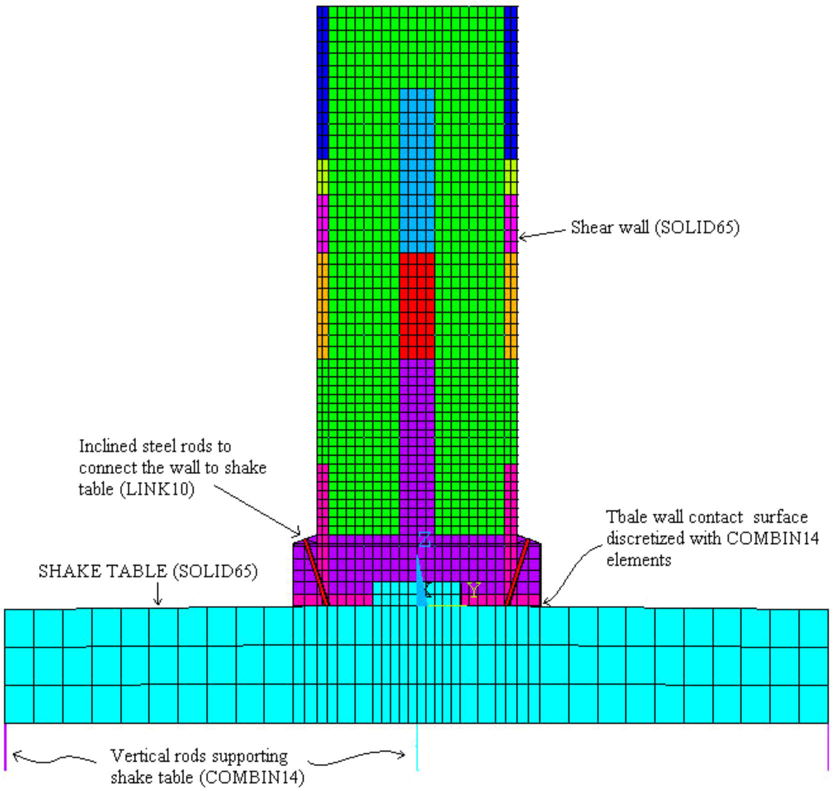

Figure 2.17 The models created in ANSYS

The system was found to be more flexible than assumed. Once the wall is pushed in one direction one pair of steel bars becomes ineffective and the other pair acts only in tension. So the tension-only spar element, LINK10, is considered to be appropriate to model the steel bars. As shown in Figure 2.18, the four inclined steel rods that connect the mock-up to the shaking table were modeled with LINK10, which is a three-dimensional spar element, having the unique feature of a bilinear stiffness matrix resulting in uniaxial tension-only (or compression-only) property. The tension-only option was activated in order not to allow any stiffness contribution when the element was in compression.

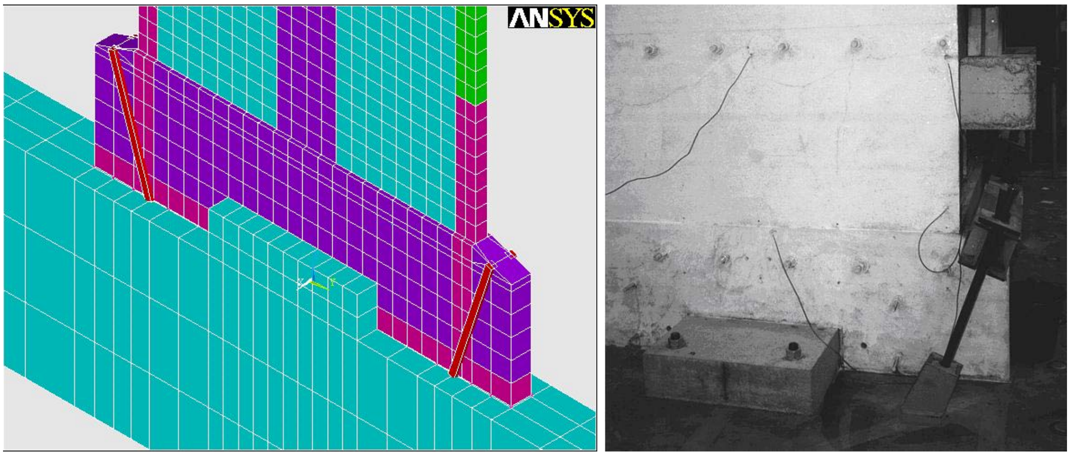

Figure 2.18 Modeling of boundary conditions

In the numerical model vertical rods supporting the shaking table were included and assigned a stiffness to capture the measured vertical frequencies. For these rods, a spring element, COMBIN14, was used. The elastic constant of each spring element was taken as K = 400 MN/m (in accordance with the experimentally measured response) in the numerical computations. The contact surface between the wall and table was discretized with spring elements, COMBIN14, having elastic stiffness of 20000 N/mm. At the free ends of the wall these springs were placed between the wall and table. These springs significantly influence the first mode natural frequency of the system. While assigning zero stiffness to these springs leads to a first natural frequency of 7.1 Hz, assuming very rigid stiffness, i.e. fixed wall-table connection leads system dynamic response to be around 8.1 Hz. These contact spring elements are also crucial for other purposes because without them or when their stiffness is below a certain limit, sliding shear failure initiates on the plane of wall just vertically above the rigidly connected region under high lateral loads.

2.6.1.3 Modal and Static Analyses

Several different boundary conditions were applied to the model and the first bending and vertical modes were computed as tabulated in Table 2.1. As evidenced from the results contained in Table 2.1, both boundary conditions exert considerable influence on the modal response of the model. The flexibility of the connection between the table and the wall affects the first mode significantly but has minor influence on the vertical mode. In the light of all these preliminary analyses it was realized that creating a model incorporating both boundary conditions in the table base and table-wall connection is vital for reproducing the experimental results as close as possible.

Surprisingly, the static analysis results indicated that the table supporting system flexibility has negligible effect on the load deformation pattern. On the other hand, flexibility of the table-wall connection region appears to be a significant factor influencing the initial stiffness and post elastic behavior of the load-deformation relation.

The model was first subjected to statically applied inverted triangular lateral load at the level of each floor to simulate first mode response. Pushover curve that presents base shear force versus top displacement (roof) for one of the two walls (left wall) is given in Figure 2.19. The limiting point where the structure reached the state of instability due to excessive damage corresponds to the limit that indicates the capacity of the model. The computed and experimentally measured maximum response quantities for each dynamic run are also plotted on Figure 2.19. The pushover curve is a powerful tool to visualize the global nonlinear behavior of the structures, and it provides very useful hints about the global behavior of the test specimen in the absence of more elaborate analyses such as nonlinear time history analyses. Examination of Figure 2.19 reveals good agreement between the capacity curve of structure and the peak global response obtained from the dynamic tests. The information presented in Figure 2.19 reveals that the structure remained in the elastic range under the ground motion applied in Run 2 whereas all other cases resulted in inelastic behavior of varying degrees. Needless to say, the largest deformation was measured in Run 5 not Run 3, the strongest shaking intensity, due to sequential application of ground motions. This figure displays also the results of the time history analyses, which are discussed next.

Table 2.1 Modal Frequencies (Hz) due to different boundary conditions

Boundary Conditions	1st Bending Mode	2nd Bending Mode	3rd Bending Mode	1st Vertical Mode
Support & Connection Flexible	7.275	32.664	54.856	22.685
Fixed Support & Flexible Connection	7.858	36.483	-	42.270
Flexible Support & Rigid Connection	8.080	33.095	57.405	22.872
Fixed Support & Rigid Connection	8.868	38.609	-	43.397
Fixed Based Wall	9.190	39.991	-	44.704

For Runs 3 and 5, while the calculated peak displacements are in good agreement with the measured quantities, the calculated base shear is larger, especially for Run3, than the measured ones. As discussed previously, the measured base shears are in some sense calculated, i.e. they are computed from the measured accelerations by multiplying them with the floor masses above certain wall section. Besides, the effect of additional vertical force generated in the dynamic test as a result of opening and closing of cracks was not included in the calculation of measured base shear. However, it is fundamentally known that as the axial load increases on a section, the moment and shear capacity also changes (increasing when the axial load level is low). It is known that in Run 3 and 5, the vertical force on the base section of the wall nearly doubles both in traction and compression due to opening and closing of the cracks on the wall. This miscalculation of the measured base shear force is considered to be the primary reason of the discrepancy between the calculated and measured global response for Run 3 and Run 5. So it was decided to perform two more pushover cases; one is for the triangular load case in which the effective mass of the system was increased 1.6 times ($g_{effective} = 1.6g$) due to vertical excitation (to show the effect of the axial force on the response) and the other one is representative of the uniform (rectangular) loading that is considered as an upper bound case for the load path. The increased effective mass is calculated as the total maximum vertical force at the base (the measured axial compression at Level 1 in Run 3 plus the weight of the structure (165 kN)) divided by the weight of the structure (270 kN/165kN). The resulting load-deformation curves are presented in Figure 2.19. The results support the expectations; the effect of both vertical force and load pattern is very significant on the load-deformation curve. This situation again proves the complexity of the problem and the necessity of comprehensive analysis.

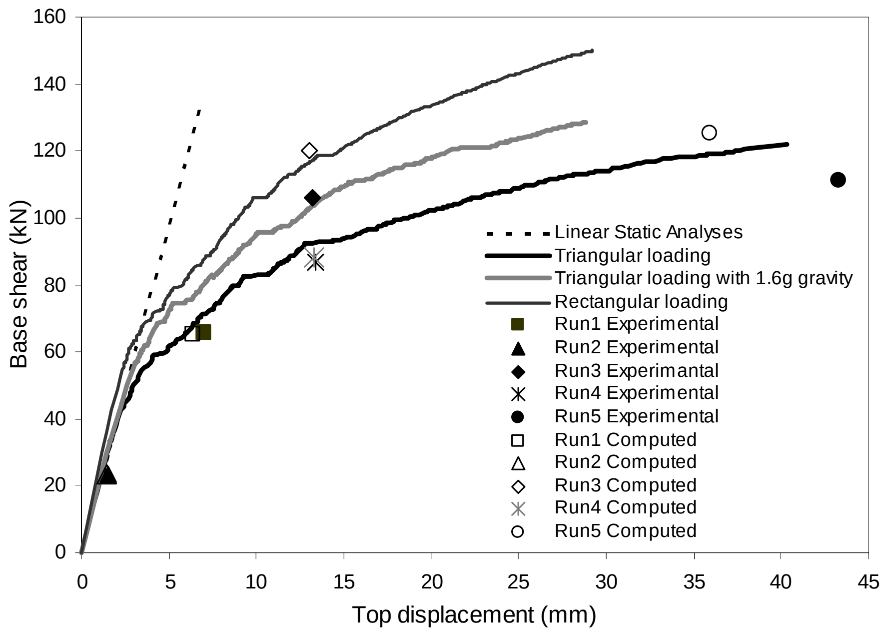

Figure 2.19 Pushover curve of a single wall

2.6.1.4 Time History Analyses

The reference acceleration histories measured on the shaking table were applied to the model at the level of the shaking table. Time history analyses were carried out only for strong motion duration of the given ground motion records. The analyses for Runs 1-5 were carried out in a sequential order to represent the actual loading history. Top displacement was measured from the node at the top corner of the model. The shear forces at different levels of the structure were calculated by taking the sum of horizontal forces (y-component) of elements at a section. The bending moments were calculated by taking moments of vertical force components (z-component) of elements at a section about the center of section. This damping was input by means of Rayleigh damping constants; i.e. it was assumed that both mass- and stiffness-proportional damping was present in the system. The first two modes each with 2 percent damping were used to define α and β.

Time histories for top horizontal displacement, shear force and bending moment at level 1 (base of the shear wall), moment-curvature relationship at the base of wall, strains in the external rebars for Runs 1 to 5 were computed and are summarized in Figure 2.20. The corresponding test measurements are also superimposed on the numerical plots. There is a fairly good match between the experimental (measured) and computed (calculated) results. These comparisons revealed the adequacy of the model for the purpose of simulating an experiment realistically by means of analytical tools.

2.6.1.5 Local Results

Time history results of several parameters were derived from the computational phase including accelerations and external rebar strains on each level. The damage progress, in other words the crack development started from the base of the structure as hairline cracks and moved to the upper levels. As it was expected from the ground motions and evident from the experimental and computed results, non-linearity becomes pronounced significantly first in Run 3. The moment-curvature relations plotted for the four levels in Figure 2.21 show that the second, third and fourth floor levels deformed into non-linear range after Run 3.

In Figure 2.22, the strain concentrations in different regions of the wall computed during Run3 are shown. Due to progressive cracking of concrete and yielding of reinforcement under sequentially applied increasing seismic excitations, the system deformed further. This preliminary damage accumulation is the reason why the test specimen has exhibited such large deformations in Run 4 opposing the expectations. Run5 is the ultimate loading applied to the specimen that led to excessive damage and failure of reinforcement at different sections. The special design of steel allowing the damage to spread among different stories rather than localizing it to a particular section of the wall helped the structure survive such an intense sequential loading history. Yielding of the reinforcement occurred in the stories 1 to 4, but it was excessive in the lower two stories. It is evident that in the regions where the longitudinal steel is reduced, larger deformations were observed. The number of rebars changes at 10 cm below each story level along the height of the wall. For this reason, the cracks on the wall initiate from these interruption regions and progress diagonally between the stories. Smeared crack model that is used to model and detect the damage, the location of the damage and to some degree the level of damage experienced by the structure gave reasonable results when handled carefully. The main crack pattern shown in Figure 2.24 at the end of testing program supports this statement.

(a) Run1 Top Displacement

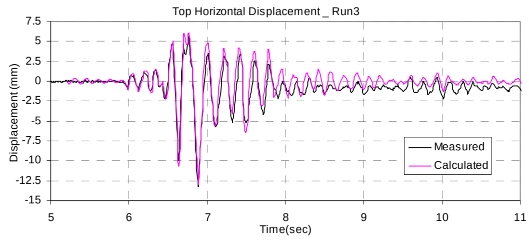

(b) Run3 Top Displacement

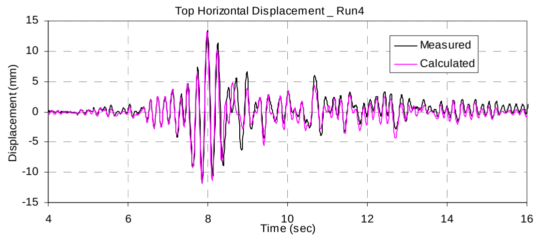

(c) Run4 Top Displacement

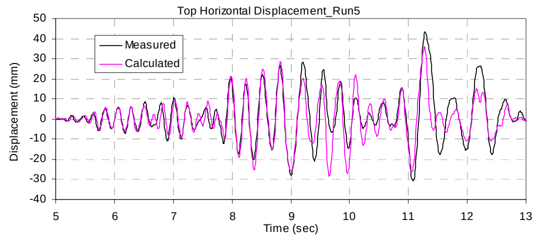

(d) Run5 Top Displacement

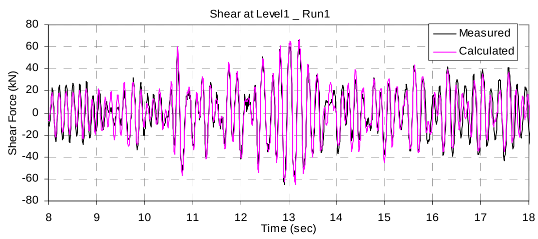

(e) Run1 Base Shear

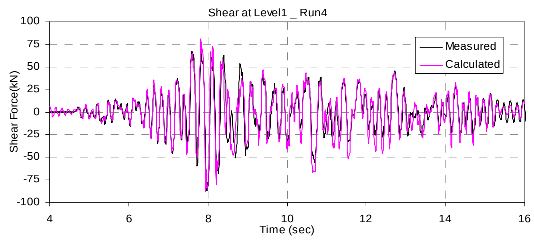

(f) Run4 Base Shear

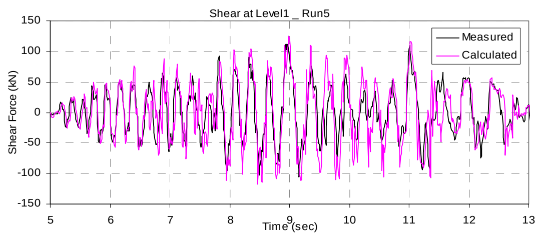

(g) Run5 Base Shear

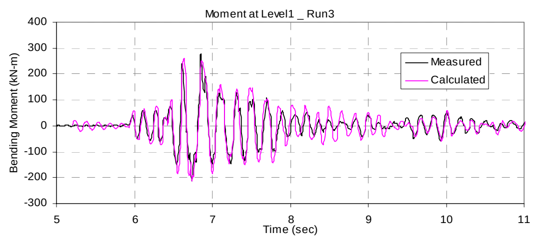

(h) Run3 Bending Moment

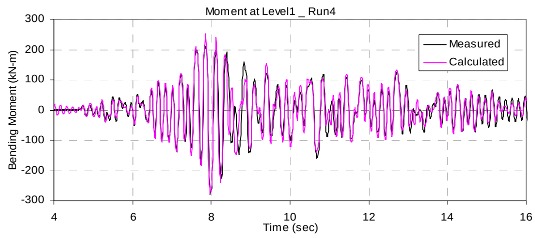

(i) Run4 Bending Moment

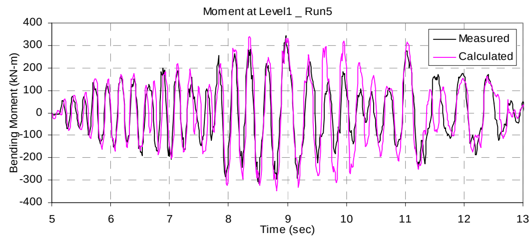

(j) Run5 Bending Moment

Figure 2.20 Comparison of experimentally measured and numerically calculated global response parameters, such as displacement, base shear and bending moment

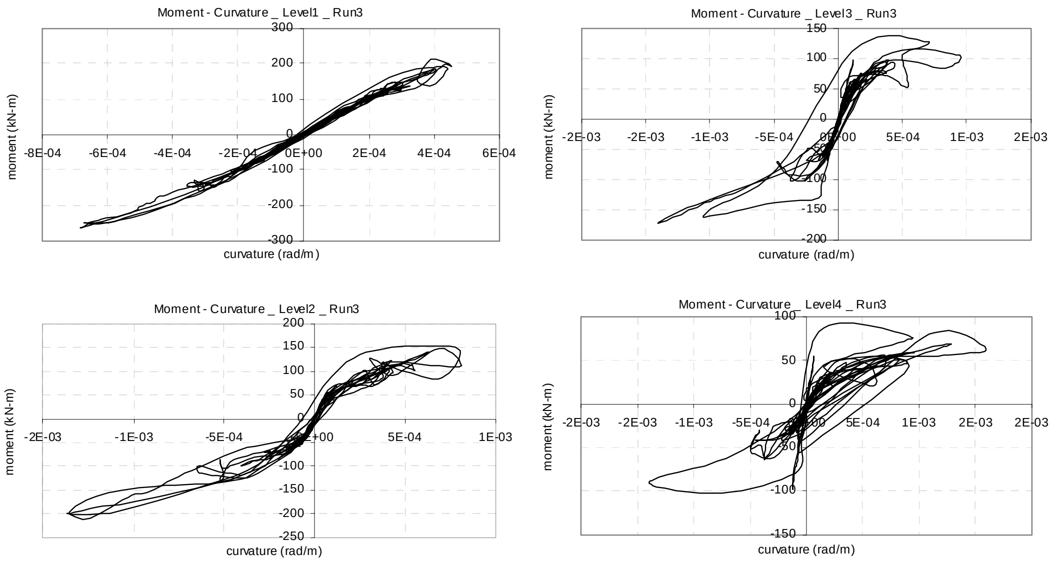

Figure 2.21 Moment-curvature relationship of levels 1-2-3-4 after Run3

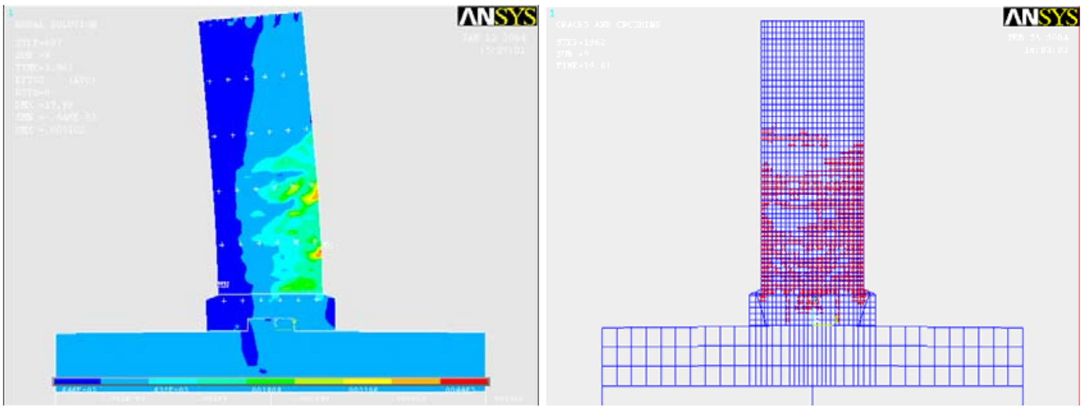

Figure 2.22 Strain distribution and crack pattern developed in the model in Run3

Since strains at a section or a point are the indicators of damage experienced, examining the strains measured on the external rebars from the experimental phase and comparing them with the calculated ones reveals the damage pattern and location in the structure. Level 3 seemed to be the most critical section as evidenced by the experimental results. In the computations very high strains, denoting excessive damage, were obtained at levels 2, 3 and 4. The comparison of strains measured on the external rebars for Run3 and 5 is given in Figure 2.23 and Figure 2.24. During the ultimate Run5, the steel yielded at all sections, and this was accompanied by the failure of the longitudinal reinforcement at level

3. The strains obtained from the simulations showed the same deformation tendency with an exception that the computed strains could not reach the failure limit (2.5 percent) at level 3 but at level 4. So, in experimental stage while the failure initiated at level 3, in the model the first failure indication was observed at level 4. But this is within our expectations since we know that the measured strains at upper levels (3 and 4) is very high and there is a slight difference between these strains showing that initiation of failure at a level is a matter of instant. Another difference in our computations from the measured ones is that, the computed steel strains at level 2 are much greater than the experimental ones in Run5. This can be explained within the experimental procedure itself and the instrumentation of the wall, as all the experimental measurements were made on the left wall, while it is known that the main crack pattern that was observed on the right wall at the end of the testing program was different than that on the left (Figure 2.24). It is known, at least by visual inspection that, there was an excessive damage on right wall at level 2 indicating high strains, which agrees with the computations. The local results (strains) that were computed agree well with the crack pattern on the right wall.

After the failure of reinforcing bars at level 3 in Run5, the response of the system changed drastically. Natural period of the system increased to more than double (from 0.137 sec to approximately 0.3 sec) due to stiffness degradation in the system. This is a big challenge from the modeling point of view. The analytical model and the material laws we employed in the analysis is not equipped to retrieve a failure situation in the reinforcing bars. This is probably the reason why the maximum experimental top displacement (43.3 mm) could not be captured in the computations (36 mm) of Run 5 as good as the previous cases (Figure 2.20(d)). The FE model and the assigned non-linear material properties can be improved to retrieve such a failure situation by adopting bond slip occurring between the concrete and rebars and spalling of concrete due to degradation in quality.

In order to observe the effect of the concrete cracking on the loading history, Run4 was performed on the virgin, uncracked structure. The results were as shown in Figure 2.25. While the cracked model reached a top displacement of 13.2 mm, the virgin model could only reach a translation of 6.35 mm at the top. This exercise not only proved the significance of concrete cracking and yielding of reinforcement on the behavior, but also verified the reliability of the numerical model and the software used.

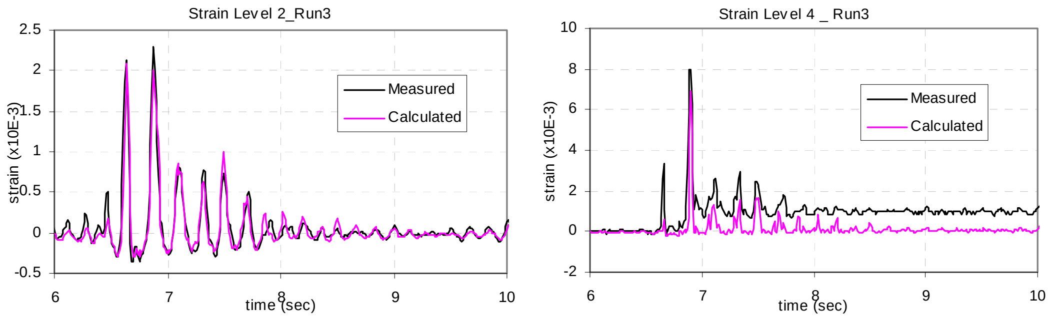

Figure 2.23 Strain time histories compared with experimental ones for Run3 at levels 2&4

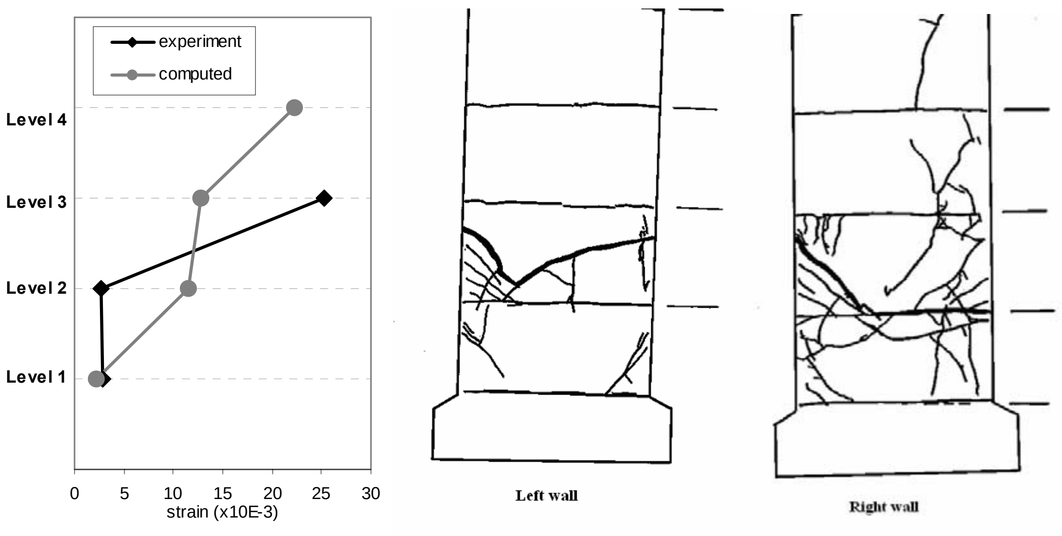

Figure 2.24 Maximum strains computed at each level compared with experimental ones for Run5 and main crack patterns on right and left wall

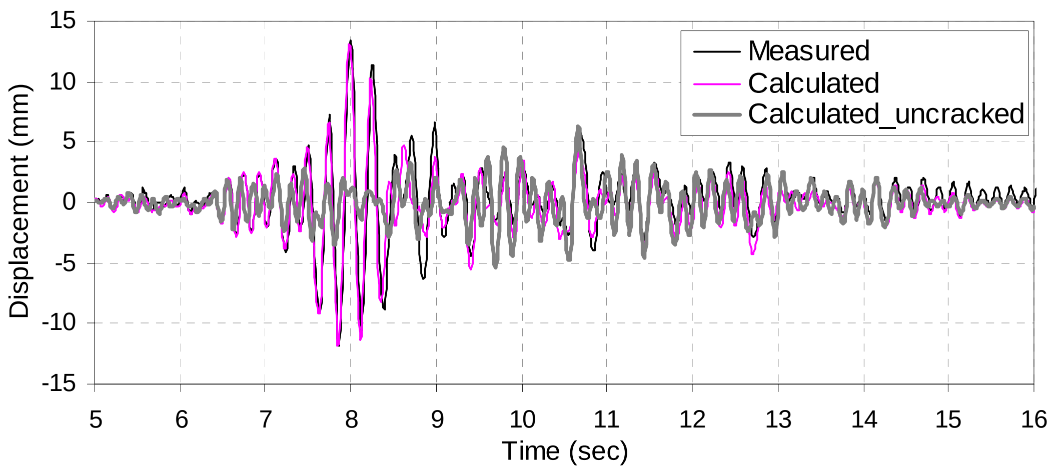

Figure 2.25 Effect of cracking of concrete and yielding of steel on the top displacement

2.6.2 NUPEC Shear Wall

In order to shed light on the behavior of squat shear walls, the response of a large-scale flanged shear wall structure tested on a shaking table in Japan is re-examined here using simple plasticity models combined with the tensile cracking criterion for concrete. The shear wall specimen was a part of experimental program carried out by NUPEC (Nuclear Power Engineering Corporation) in the early 1990s to study the seismic design and performance of shear walls in nuclear reactor buildings (OECD/NEA/CSNI, 1996). It was a single story flanged shear wall with h_w/l_w = 0.67. In the experiment it was observed that the wall response was dominated by shear effects and significant strength loss led to the failure of the specimen as a result of sliding shear developed near the base of the web wall. The structure has been investigated by other researchers (Vecchio, 1998; OECD/NEA/CSNI, 1996).

Analyses and design of reinforced concrete members under shear and torsional effects requires special treatment of concrete material properties and laws. Rational and realistic models for response governed by shear are few and seem not to have gained excessive application in finite element practice (Vecchio and Collins, 1986; Belarbi and Hsu, 1995). Moreover, results of several prediction exercises revealed the inadequacy of customary analysis procedures for such elements (OECD/NEA/CSNI, 1996).

Following this introduction, the geometrical and the material properties and the loading program of the NUPEC specimen are described briefly and its finite element discretization is explained. Several static analyses under monotonically increasing lateral loads are carried out to identify the most effective material constants. Static analyses proved to be crucial for material identification and were important in providing insight for the behavior of the structure before attempting complicated nonlinear time history analyses. Finally effectiveness of the utilized plasticity models is verified by re-calculating the measured seismic response of the specimen.

2.6.2.1 Specimen Description:

The Nuclear Power Engineering Corporation of Japan (NUPEC) conducted an extensive experimental investigation for the seismic safety of nuclear facilities in the early 1990s. For this purpose, two full-scale flanged shear walls (ISP shear walls) were subjected to a series of seismic excitations on a shaking table. Two specimens (U-1 and U-2) with the same design specification were prepared and tested by applying the same input signals in order to ascertain the reproducibility of the test. The specimen used for the analyses in this article was code-named U1 (OECD/NEA/CSNI, 1996).

Figure 2.26 shows the dimensions of the test specimens. The web wall had a thickness of 75 mm, a flange wall center to center length of 3000 mm, the clear height of 2020 mm, and a shear span ratio of 0.8. The flange walls were 100 mm thick and 2980 mm long. The steel percentage in the web was 1.2%, both horizontally and vertically. D6 bars (deformed bar, nominal diameter 6.35 mm) at a spacing of 70 mm were used in the web wall both for the vertical and horizontal reinforcement. D6 bars at 175 mm spacing are used for the vertical reinforcement of the flange walls. As an exception, D6 bars at 70mm spacing were used for the vertical reinforcement at the intersections of the web wall and the flange walls. Additional lead weights were fixed at the upper and lower surfaces of the top slab as shown in Figure 2.26. The total additional weight was 92.9 t, and the total weight of the specimen including the top slab amounted to 122.0 t.

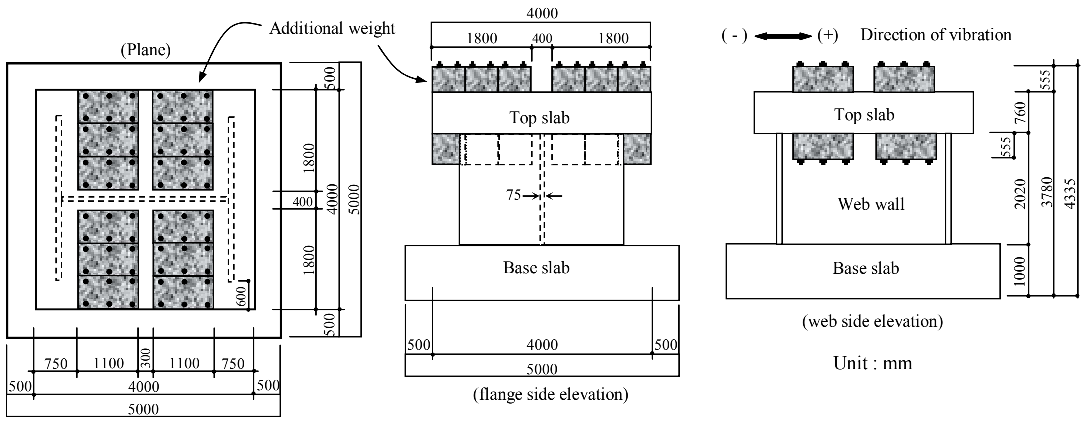

Figure 2.26 Dimensions of the specimen, [Kitada et al., 2000]

2.6.2.2 *Seismic Input Motion:*

The objective of the vibration test program was to identify the dynamic response characteristics of the specimens ranging from their elastic state to their inelastic ultimate state by applying input accelerations at increasing amplitudes. The seismic tests were carried out by applying artificial earthquake motions that had flat acceleration controlled region over the frequencies ranging from 14 to 4 Hz (0.07-0.25 s period) corresponding to the initial frequency (13.2 Hz) and softened response frequencies, in order to avoid any response amplification induced by changes in the stiffness of the specimen by shifting to higher response regions of the spectrum. In the test, the specimens were excited in only one horizontal direction. The vibration test-runs were executed with five input acceleration levels. These runs were executed as RUN-1 to RUN-5 sequentially by increasing input acceleration levels of the same artificial wave. The 5 percent damped acceleration response spectra of the input motions RUN-4 and RUN-5 are given in Figure 2.27. Their spectral similarity is noted. For the detailed description of the structure, material properties, loading program and structural response reference to OECD (1996) and Kitada et al. (1996) is made.

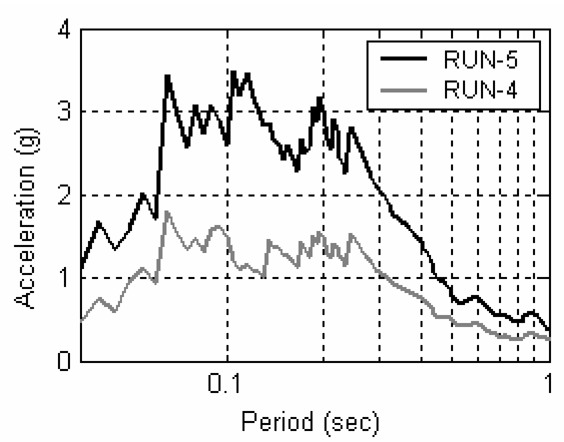

Figure 2.27 Five percent damped response spectrum of input acceleration for RUN-4 and -5

2.6.2.3 Test Results

The measured fundamental frequency of the specimen prior to the loading program was around 13.2 Hz. Upon sequential application of the seismic excitations and due to resulting continuous degradation on the mechanical properties of the structure, measured fundamental frequency reduced to approximately 7 Hz before final loading (RUN-5) when extensive damage in the structure was caused. Table 2.2 shows the change of natural frequency and the equivalent viscous damping ratio observed.

The visual state of cracks for the specimen after the final step (RUN-5) is shown in Figure 2.28. Initial shear cracks at the mid portion of the web wall were observed after

RUN-2 and horizontal cracks of the flange walls were observed after RUN-4. The sliding shear failure occurred 30 cm above the bottom of the web wall in Run-5 resulting in significant loss of in the strength and stiffness of the specimen.

Table 2.2 Change of frequency and equivalent viscous damping ratio

Test	Frequency (Hz)	Equivalent damping ratio (%)
Before RUN-1	13.2	1.1
Before RUN-3	11.3	2.5
Before RUN-4	9.9	3.0
Before RUN-5	7.7	4.0

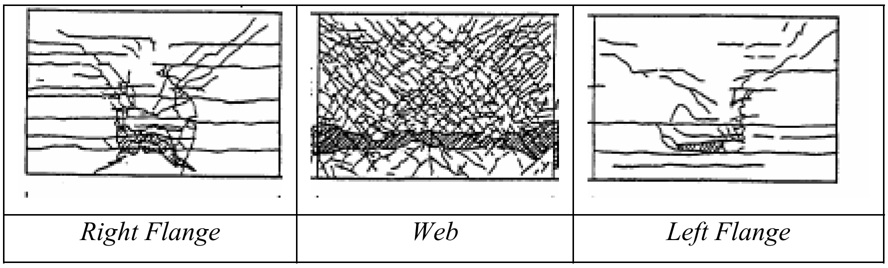

Figure 2.28 Visual observations of cracks and final web crushing failure of the wall (OECD/NEA/CSNI, 1996)

2.6.2.4 Finite Element Modeling

To effectively use the computer resources a model representing half of the specimen was created and symmetry boundary conditions were applied, see Figure 2.29. The element SOLID65 represents the web, flanges, base and top slabs. The LINK8 element is used to model reinforcement discretely. Concrete elements with 200x200x37.5 mm dimension were used in the web wall. The reinforcement mesh in the wall has a grid spacing of 70x70 mm. In order to produce coinciding nodes for concrete and rebar elements due to mesh density, the original reinforcement mesh at 70 mm spacing was replaced by a grid where the bars are configured at 200 mm spacing. The rebar areas were recalculated to keep the total percentage of reinforcement unchanged as 1.2 percent. This is equivalent to using smeared reinforcement modeling since the contribution of smeared reinforcement within the solid element is evaluated at nodes via integration points. As shown later no difference arises in the predicted response between the adopted stratagem and the smeared reinforcement model. When a concrete panel is reinforced by a dense reinforcing mesh and the change of internal forces from one bar to the next is very small, their net effect may be considered as "smeared". For monotonic loading conditions this modeling technique was found to be effective. However, in order to calculate rebar stresses accurately, discrete reinforcement modeling was preferred in model generation. Modeling the reinforcement as discrete and smeared had its effect on the load deformation response.

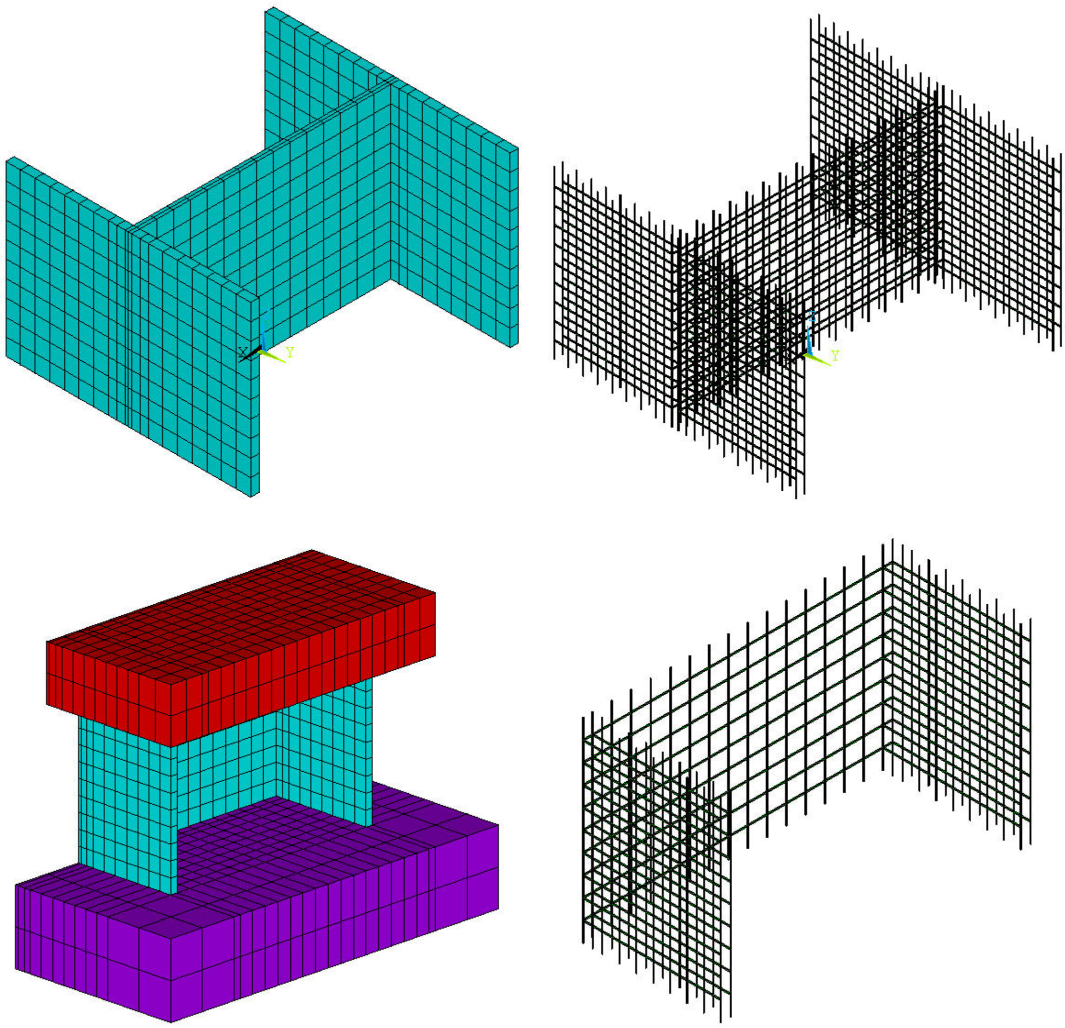

Figure 2.29 Finite element model and the reinforcement grid of full and reduced NUPEC wall specimen

The additional masses are modeled with point mass elements (MASS21) that are assigned to mid section nodes of the top slab. The effect of gravity force is kept constant during the analyses. The lateral load is distributed equally to the mid section nodes of the top slab in the horizontal direction.

2.6.2.5 Calculation of the Material Parameters:

Bilinear isotropic work hardening plasticity (BISO) is utilized for the material model of the steel reinforcement. The modulus of elasticity and yield strength used for steel is 184,400 MPa and 384 MPa, respectively. In the analyses the strain hardening of the steel is attributed a value of 1 % (E_{sp}=0.01E_s) to achieve better convergence.

The concrete material properties were provided by NUPEC. The experimental concrete stress-strain curve was used to determine the constants of the material models mentioned above. The uni-axial compressive strength of the concrete (f_c) was taken as 28.6 MPa, the mean value of the concrete cylinder tests, and the tensile strength as 2.4 MPa. The initial modulus of elasticity and the Poisson's ratio were 22,900 MPa and 0.2, respectively. Since the von Mises plasticity models depend on elasto-plastic representation of the material behavior curve, the nonlinear stress-strain curve of the concrete in uniaxial compression is bilinearized as given in Figure 2.30. The limiting compressive stress f_c'' is taken to be the average compressive stress equal to 0.85f_c corresponding to 23.8 MPa. Due to bilinearization the concrete modulus of elasticity reduces to 20,700 MPa. Using this value the first mode frequency of the model was calculated as 12.9 Hz, which is very close to measured fundamental frequency of the specimen given in Table 2.2. After model generation, modal analysis becomes crucial to verify the correctness of the finite element model.

For the case of Drucker-Prager model, inserting f_c=23.8 MPa and f_{bc}=1.2f_c into Eqs. (B.20) and (B.21), parameters of Drucker-Prager yield surface are calculated as $\alpha = 0.0825$ and τ_o = 11.78 MPa, respectively. The yield surface has the same pattern as plotted in Figure 2.1 utilizing Eq. (B.22). It is now required to express these parameters in terms of Mohr-Coulomb parameters, c and ϕ. Since Drucker-Prager model in ANSYS uses outer cone approximation, using Eq. (B.16) these parameters are calculated as 9.72 MPa and 11.54^o for the cohesion and the friction angle, respectively. For multi-linear plasticity model (MISO), the material base curve was represented with five line segments as shown in

Figure 2.30. This is the only model that can be used to represent the strain-softening branch of concrete stress strain curve.

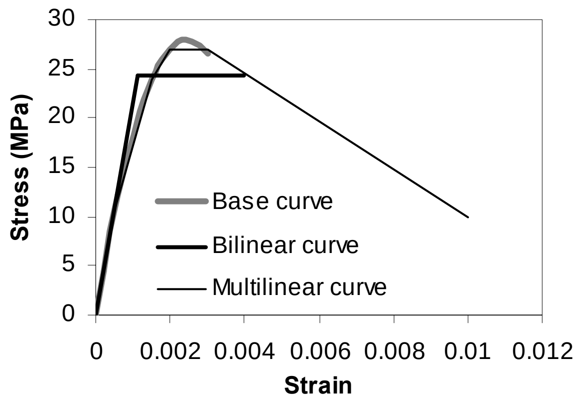

Figure 2.30 Bilinearized and multilinear uniaxial stress-strain curves of concrete

2.6.2.6 Finite Element Model Calibration: Mesh Size and Element Options

At the beginning it was emphasized that finite element analyses results are significantly affected by the adopted constitutive material laws. However, this statement is valid given that the effects due to numerical discretization are negligible. The properties of the model such as the mesh density and the element characteristics are also important aspects of the nonlinear finite element analysis procedure. SOLID65 element has been instrumented with several features to increase the accuracy of the calculations and overcome restriction due to element behavior. However, these are case sensitive properties and needed to be calibrated depending on the application.

Rarely is the first FE analysis satisfactory. After trial runs differences between the calculations must be clarified. Since the displacement field within the element is calculated using linear interpolation functions and 2x2x2 Gauss-quadrature integration scheme, it must be ensured that the mesh used is sufficiently fine to capture the behavior accurately. An extra model that is composed of concrete elements 70x70x37.5 mm in size was created as shown in Figure 2.31, and the reinforcing bars were discretized in their actual amount and location to check the mesh size dependency of the results. Moreover, the eight-noded solid element exhibits shear locking, which is a defect associated with the linear element interpolation functions that contain no quadratic terms resulting in spurious shear strain. Element is excessively stiff to display the bending modes of displacement, if the finite element mesh is not fine enough. The "incompatible modes" formulation for modeling bending was invoked to avoid shear locking in the model. In ANSYS theory manual the formulas are referred as “extra shape functions (ESF)”. Mesh size dependency and shear transfer effects were also investigated.

The multilinear plasticity model with strain-softening behavior as plotted in Figure 2.30 was used in the calculations. The models were loaded by prescribed displacements at the mid section nodes of the top slab in all the analyses. The effect of gravity force is kept constant during the analyses. The Newton-Raphson method with line search and adaptive descent iterations was used in all computations.

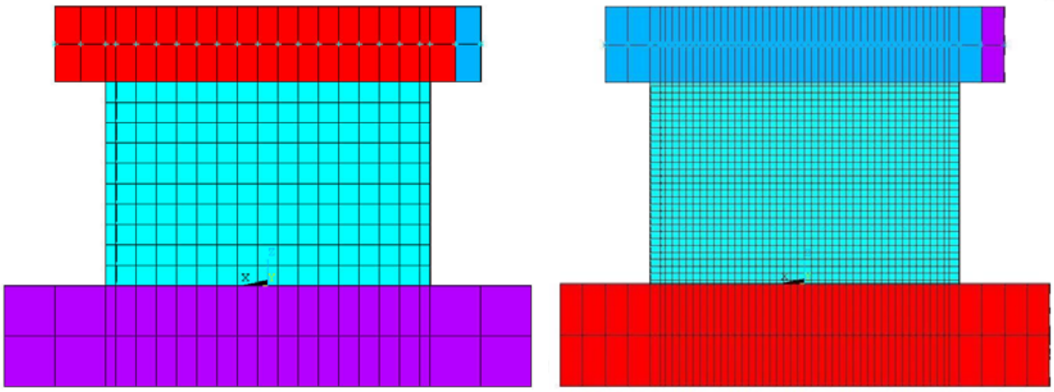

Figure 2.31 Finite element meshes

The comparison of results of the three models was given in Figure 2.32(a). It is seen that there is a considerable difference between the results of the fine and coarse mesh models (when no ESF utilized) in terms of both displacements and forces at the peak level. However, the coarse model utilizing extra element shapes is in good agreement with the fine mesh model curve giving a slightly higher ultimate displacement limit to strength degradation. The reported values for experimentally observed drift ratio limits on squat walls at the peak load is in the range of 0.007~0.008 (Duffy et al., 1994). The calculated displacements are less than (0.005~0.007) the given limits. The initial stiffness of the models were found to be 837, 780 and 798 kN/mm for coarse mesh with no ESF, fine mesh with no ESF and coarse mesh with ESF, respectively. Since the three curves approximately have the same global stiffness until crushing strain is exceeded, the differences in the peak range indicate to a mesh size problem in local modeling. As it was stated previously, the finite element solutions are known to have spurious sensitivity to the mesh size and have difficulty when the softening property in the post-peak response is used in constitutive models.

The ISP wall has a large flexural capacity and adequate horizontal reinforcement to develop diagonal compression failure under monotonic loading. Plastic behavior in compression was observed to develop in the zone near the base of the wall. Analyses results indicated that the strains calculated in the compression region of fine mesh model are larger than the strains in coarse model at the same location. As the size of element in fine mesh is nearly three times smaller than the element in coarse mesh, the strains are much more sensitive to nodal deformations from which they are calculated. Consequently, smaller elements detect the softening earlier than the larger ones. Since the global behavior is affected by local response in the compression zone of the web wall, mesh density in the localized damage region significantly affects the accuracy of the results.

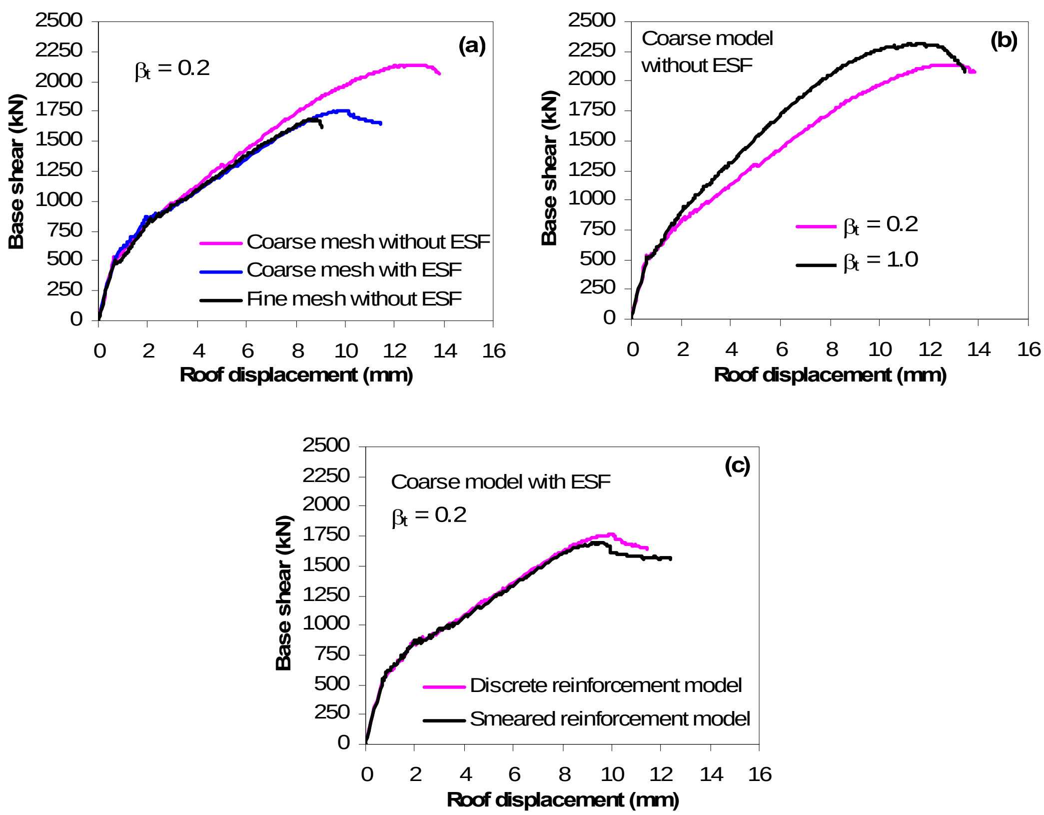

Figure 2.32 Numerical prediction of load-deflection response of the specimen indicating the influence of a) mesh size, b) shear transfer coefficient of concrete, and c) reinforcement modeling

Preliminary analyses also displayed that numerical values assigned to shear transfer coefficients for open (β_t) and closed (β_c) cracks can play a significant role on the load-deflection response of the model. A shear transfer coefficient, β_t, is used to introduce a shear strength reduction factor for loading conditions which induce sliding (shear) across the crack face. Typical shear transfer coefficients range from 0.0 to 1.0, with 0.0 representing a smooth crack (complete loss of shear transfer) and 1.0 representing a rough crack (no loss of shear transfer). In line with previous studies (Hemmaty, 1998) values of 0.2 and 1.0 were adopted as shear transfer coefficients for open and closed cracks, respectively. The effect of shear transfer coefficient is obvious in Figure 2.32(b).

In Figure 2.32(c), the comparison of analytical prediction of load-deflection response of the specimen indicating the influence of reinforcement modeling as discrete and smeared form is given. It is seen from this figure that both modeling strategy yields equivalent responses for monotonically increasing loads.

It was decided that the adopted mesh size of the coarse model in Figure 2.31 and solid finite elements with extra element shapes formulation in the model is appropriate for further analysis purposes.

2.6.2.7 Calculation of NUPEC Wall- Static Case

The force displacement response of the NUPEC wall was calculated by using the three plasticity models described above. The finite element model plotted in Figure 2.31 was used in the analyses. ESF were included in element interpolation functions. Shear transfer coefficients for open and closed cracks were taken as 0.2 and 1.0, respectively. A displacement controlled loading scheme was adopted. Displacement was applied on the mid-section node of the top slab. The calculated response curves are presented in Figure 2.33. Given in this figure is also the load-displacement backbone curve plotted as an outer envelope to the five experimental hysteresis curves. For DP and VM models the calculations were stopped when net section yielding had occurred resulting in large displacements for small increments of load.

For all the material models, the ultimate displacement at the peak load of the specimen was calculated in the range of 10 mm, which is 16 percent smaller than the displacement value at the initiation of strength degradation in the experimental response curve. All curves are very similar. It is displayed in the Figure 2.33 that the calculated response curves slightly underestimate the actual response over a certain region after the cracking load is exceeded ($F_{cr} \approx 600$ kN). Tests on reinforced concrete elements (Vecchio and Collins, 1986; Bentz, 2005) have demonstrated that even after extensive cracking, tensile stresses may still exist in the cracked concrete and that these stresses significantly increase the ability of the cracked concrete to resist shear stresses. Since the cracking was handled by reducing the tensile stresses in the crack plane to zero i.e. tension stiffening is ignored, this led to such an underestimation.

Comparison of the predicted and experimentally measured response revealed that beyond 6 mm roof drift the predicted response overestimates the measurement. This is within expectations since the response obtained from monotonically increasing static loading was compared with a response that is cyclic in nature, which may cause stiffness and strength deterioration in concrete. In order to capture the experimentally measured response, it is required either to modify the finite element model or calibrate the material model to incorporate the effects of load history and concrete mechanics.

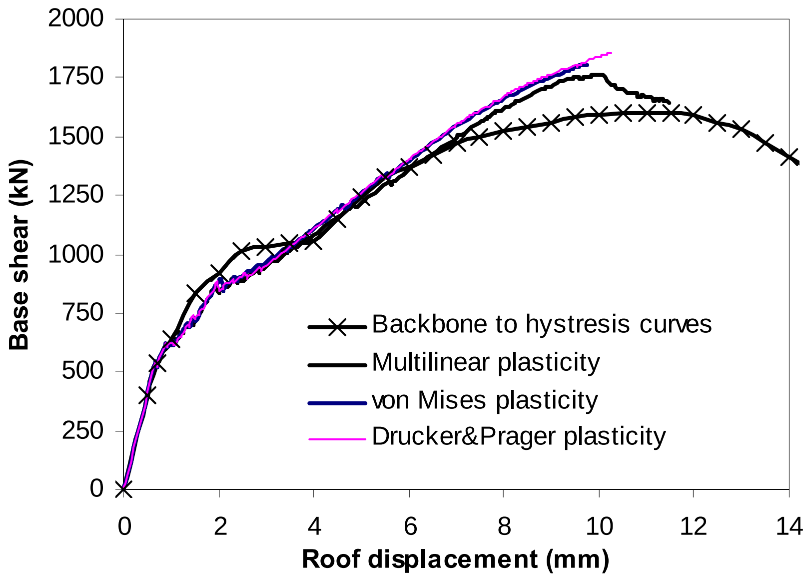

Figure 2.33 Comparison of calculated load-deflection curves with the experimental dynamic back bone curve plotted against the hysteretic curves of the five experiments

At this point, the analytical response of the specimen will be investigated a little bit in detail. A snapshot of the principal strains from the analyses phase when the top slab displacement is approximately 5.5 mm is displayed in Figure 2.34. The tensile strain developed at the lower left region of the web wall is around 0.004. The inclination angle of the principal compressive strains (ε_3) is approximately 45 degrees. Tracking the ratio of principal tensile strain to principal tensile stress ($\varepsilon_1/\varepsilon_3$) from the analysis results at the compression region, the curves in Figure 2.35 showing the ($\varepsilon_1/\varepsilon_3$) ratio with respect to increasing deformation were obtained for the results of three plasticity models. Under increasing shear forces, both the principal compressive strain, ε_3, and the principal tensile strain, ε_1, increases proportionally. Prior to yield of the reinforcement, the ratio $\varepsilon_1/\varepsilon_3$ remains reasonably constant for the three cases. For the range of interest all three curve yields a ratio of approximately -2.

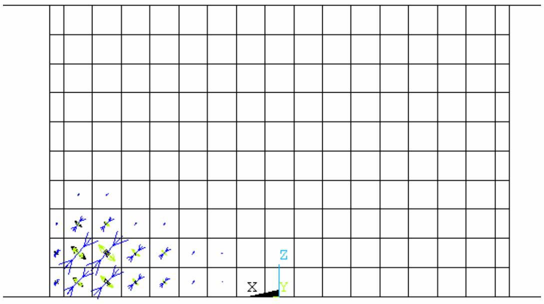

(a) plastic strains

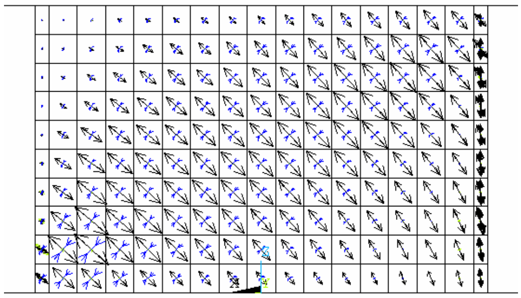

(b) total strains

Figure 2.34 Vector plot displaying the direction of principal strains developed in the web at top displacement of 5.5 mm

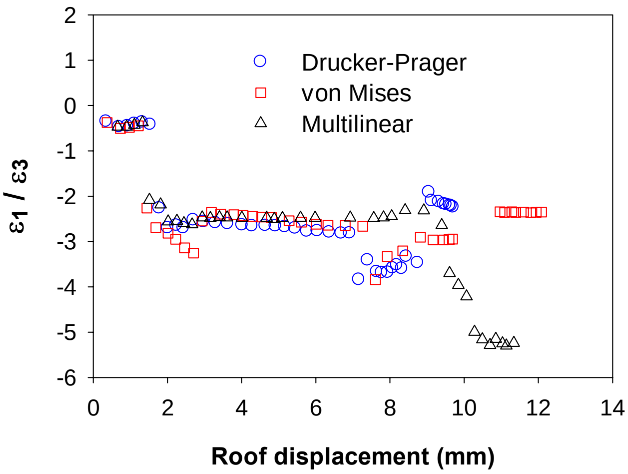

Figure 2.35 The ratio of principal tensile strain to principal tensile stress ($\varepsilon_1/\varepsilon_3$) during the analysis at the compression region

As also was supported in Figure 2.35, the ratio ($\varepsilon_1/\varepsilon_3$) remains reasonably constant prior to yield of reinforcement. Modifications were made to both the peak stress and the strain at peak stress. Distributing the ($\varepsilon_1/\varepsilon_3$) ratio, Eq. (2.5) yields a stress softening factor $\beta \approx 0.72$. The original and modified stress-strain curves of concrete were plotted in Figure 2.36. The concrete peak stress has a value of f_{c2} = 20.5 MPa (0.72x28.6 MPa). For the bilinear case this reduces to $(f_{c2})_{ave}$ = 17.5 MPa by applying the factor of 0.85. However, it will be shown next that a reduction in concrete stiffness must be taken into account for accurate prediction of response in the dynamic analyses. The modulus of elasticity of the softened concrete reduces to approximately 15,000 MPa (0.72x20700 MPa).

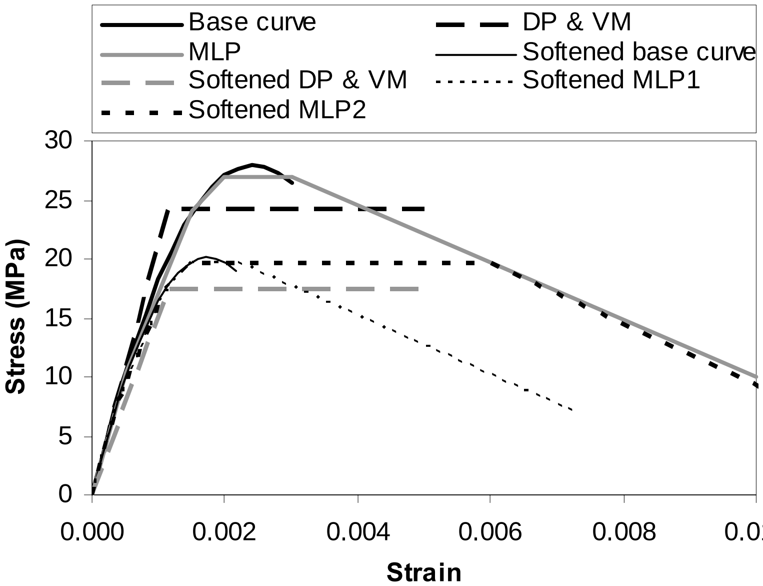

Figure 2.36 Concrete stress-strain curve for original and softened states

For von Mises and multilinear plasticity material models the softened curves given in Figure 2.36 is used in the analyses. Assuming the concrete strength as 17.5 MPa and the stress state biaxial, the new set of material constants for the DP model can be calculated as 7.144 MPa and 11.54^o for the cohesion (c) and the friction angle (ϕ), respectively. The load-deflection curves calculated with softened material models were given in Figure 2.37. For multilinear plasticity, the softened material curve designated as MLP1 in Figure 2.36 was used firstly. In Figure 2.37 it is seen that the load-deflection curve calculated with

MLP1 model experiences a premature softening. The softened multilinear curve in the yield plateau is extended to intersect with the descending branch of the original curve, which corresponds to softened multilinear curve designated as MLP2 in Figure 2.36. Such a modification in the descending branch of stress-strain curve was also proposed by Hsu and Zhu (2001) based on the long yield plateau observed in panel tests. Now the multilinear plasticity model can successfully mark the location where the strength degradation started in the experimental curve in Figure 2.37.

There was a problem in calculation of the descending branch of the load-deflection curve. The solution has experienced significant convergence problems. Nevertheless, considering the drift at 100 percent of ultimate load as the most appropriate definition of ultimate drift limit from engineering point of view, the results provides considerable insight on the displacement capacity of the specimen.

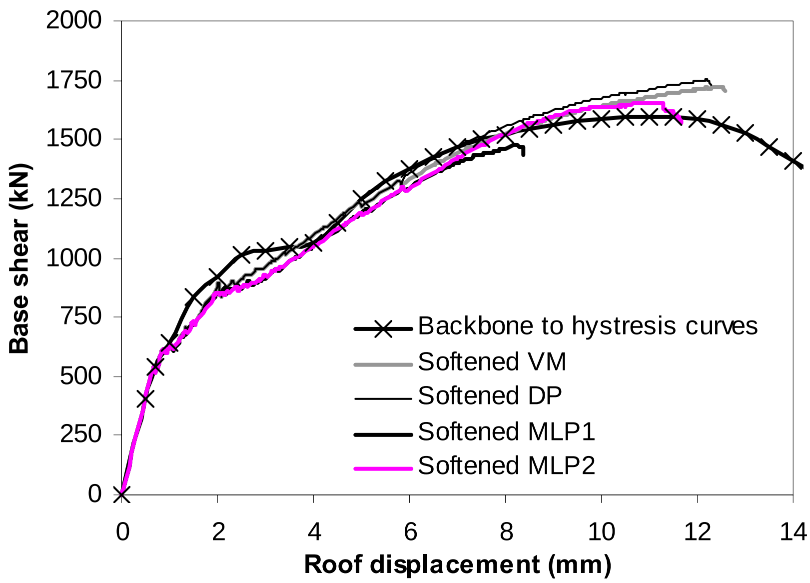

Figure 2.37 Recalculated load-deflection curves plotted in comparison with the backbone curve plotted against the hysteretic curves of the five experiments

The plastic shear strain plot in the plane of web wall at the last step of loading displays the sliding shear failure mode observed in the experiment can also be reproduced in the calculations. In Figure 2.38, after concrete failure is initiated at the tip, it spreads horizontally to the base of the web. The situation is much more severe in the experiment due to cyclic nature of the loading that causes diagonal cracking in both directions and generating softening at both lower tips of the web wall. Crushing of the web concrete spreads rapidly over the entire length of the wall. Diagonal compression failure results in dramatic and irrecoverable loss of strength.

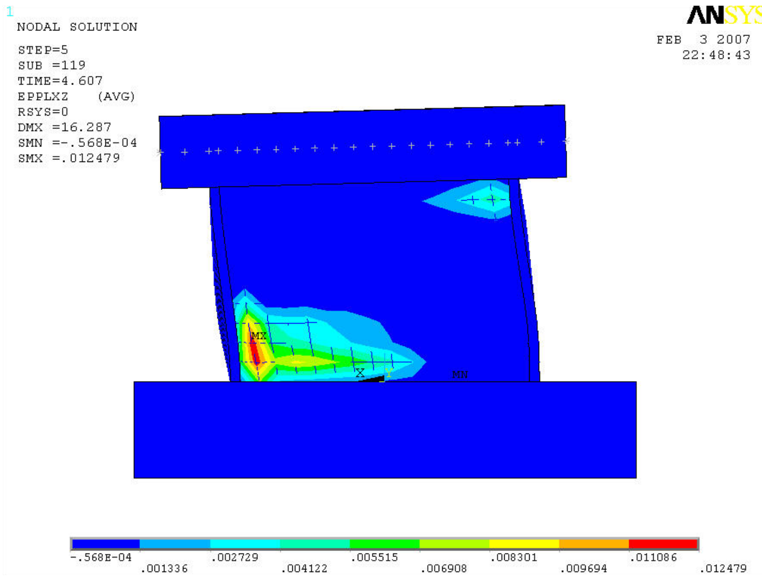

Figure 2.38 Plastic shear strain developed initiation of sliding shear at the base of the web wall.

2.6.2.8 Dynamic Analyses

The derivation of the most correct material parameters was discussed in detail in the above sections. It was displayed that compression softening has a significant impact on accurate estimation of dynamic load-deformation envelope of the structure. Adopting the reduced bilinear curve for von Mises and Drucker-Prager plasticity with material properties of f_c=17.5 and E_c=20,700 MPa in Figure 2.36, nonlinear time history analyses were carried out. Five table motions were applied on the model sequentially. The damping ratio for each analysis was specified with Rayleigh damping constants (alpha and beta) that yielded the values given in Table 2.2. The dynamic analyses procedure described in Section 2.5 was utilized.

The computed top slab displacement and horizontal acceleration response were plotted in Figure 2.39 and Figure 2.40, respectively. Accelerations were converted to inertia forces. For the sake of brevity, only the nonlinear time history results obtained in RUN-5 were discussed here, because the preceding tests had resulted in elastic to moderately inelastic response on the structure only, and the simulations were insensitive to material models and their parameters until the conclusion of RUN-4. In Figure 2.39(c), two displacement response curves were calculated and plotted for RUN-5. In the first case response was calculated by using the bilinear elasto-plastic curve with elastic modulus E_c = 20,700 MPa as described above. Significant variance was observed between the experimental and predicted response as the displacement level of 5 mm was exceeded. This must be attributed to inadequacy of the material model in accounting for the past damage history that cause reduction in the stiffness of the model. In ANSYS stiffness degradation is due only to cracking of concrete. The plasticity models can not be used to model stiffness and strength degradation of concrete directly. To account for stiffness degradation, the stress-strain curve used in this last analysis was altered with one with the same yield strength (f_c = 17.5 MPa) but with a reduced modulus of E_c = 15,000 MPa. It is important to note here that cracks and plastic actions developed in the model during the previous loading history were stored as initial conditions for the finite element model. Not only significant enhancement was provided but also the experimentally measured response was replicated quite well. In Figure 2.41 the hysteric response calculated in RUN-5 was compared with the experiment. These yield very similar patterns. Cumulative dissipated energy in measured and calculated hysteresis loops was also plotted in Figure 2.41 to display the good matching more clearly. In Figure 2.42, total strain developed at the tip of the outer face of the flange-web wall intersection during RUN-5 was plotted.

The analysis was interrupted due to non-convergence several times in RUN-5. Since the displacement level of 12 mm was surpassed when strength degradation was observed (see Figure 2.37), it was decided to terminate the execution. The analysis could not be continued. This point was very close to the time where the saturation of the instruments initiated in the experiment due to failure of the specimen.

In Table 2.3 the predicted response maximum values were tabulated. The values in parentheses are the experimental counterparts of the calculated values.

It can be concluded that by analyzing a preliminary simplified model, useful insight could be gained into the behavior. Preliminary nonlinear static analyses helped in understanding the various aspects of the nonlinear dynamic response before going through the final nonlinear transient dynamic analysis.

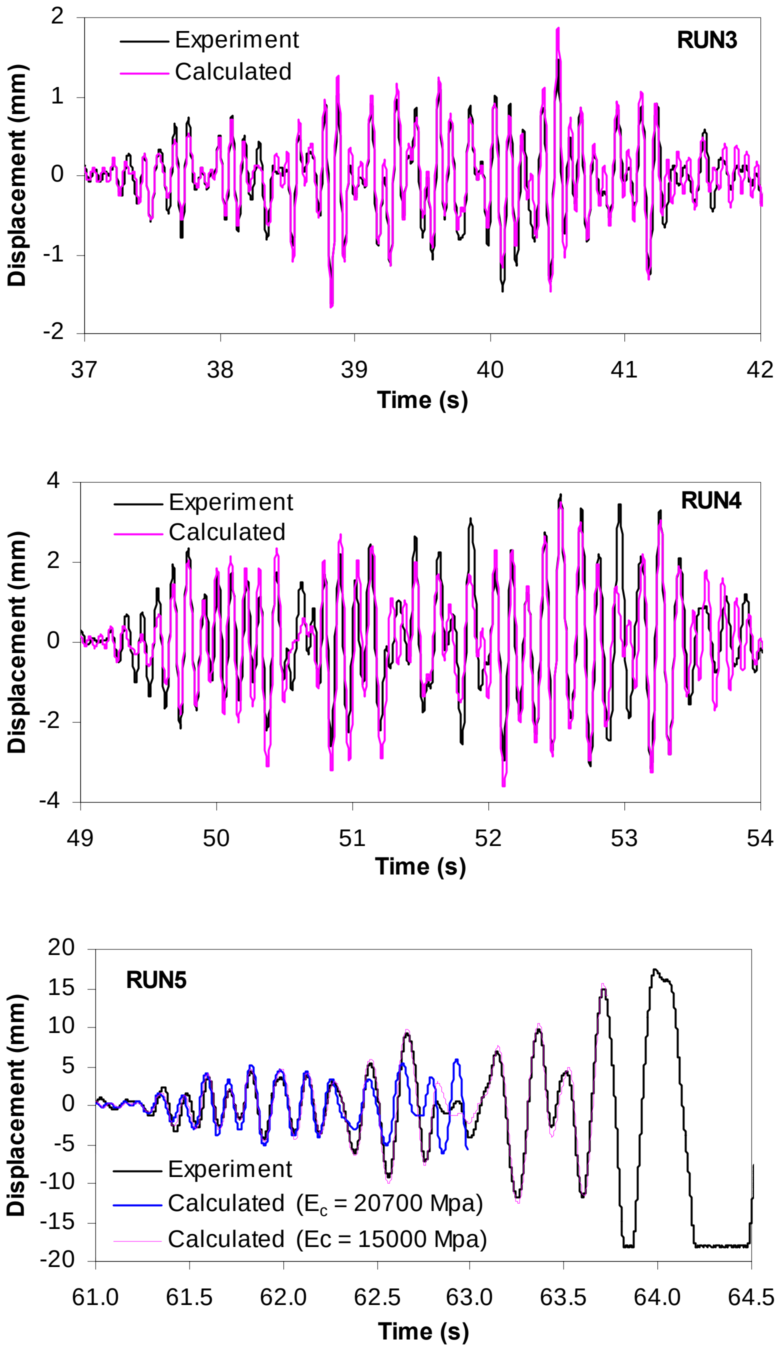

Figure 2.39 Displacements measured and calculated on top slab

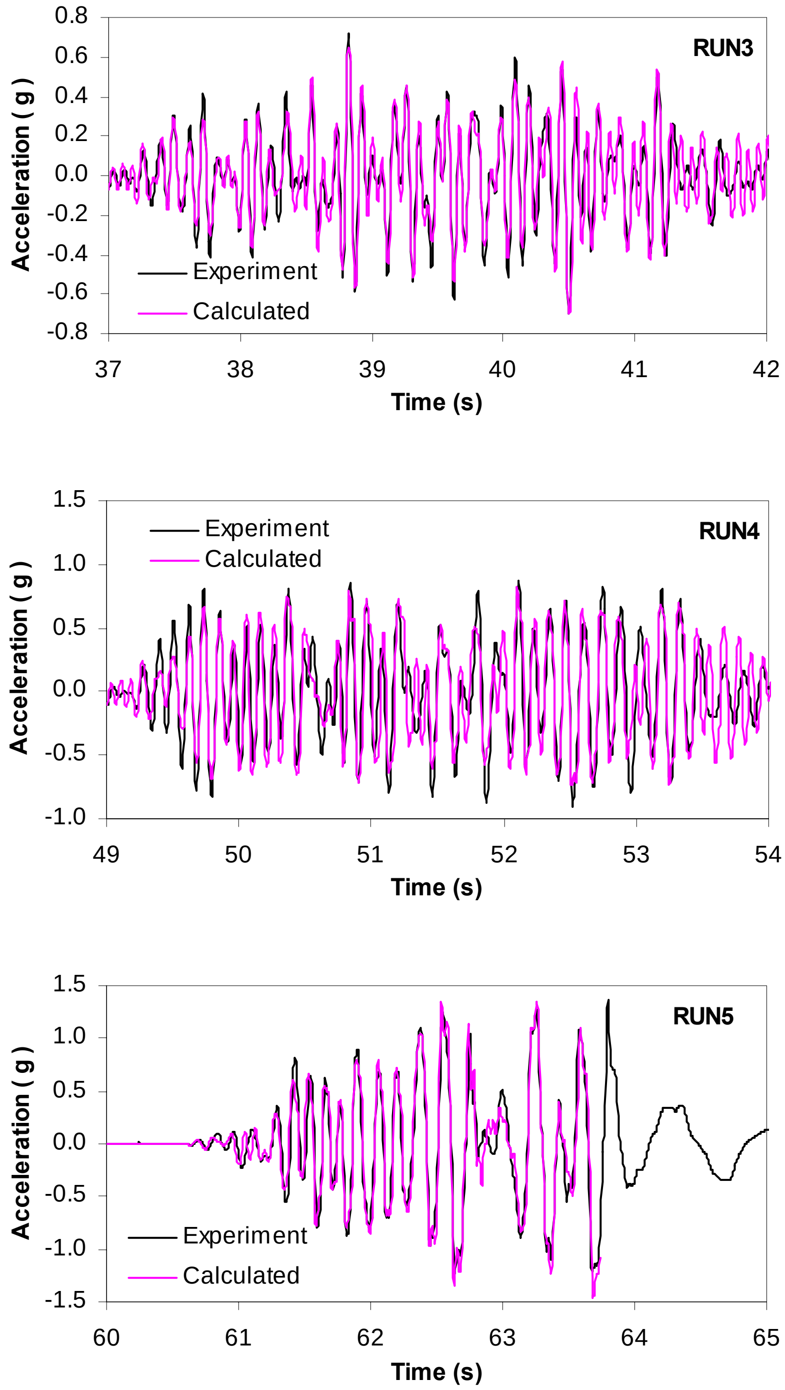

Figure 2.40 Accelerations measured and calculated on top slab

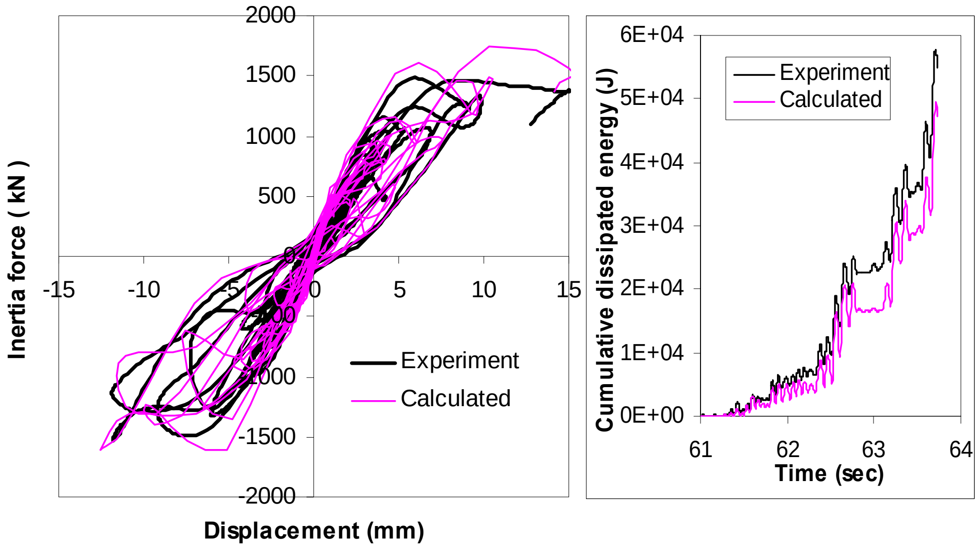

Figure 2.41 Hysteresis and cumulative dissipated energy comparison plots for RUN-5

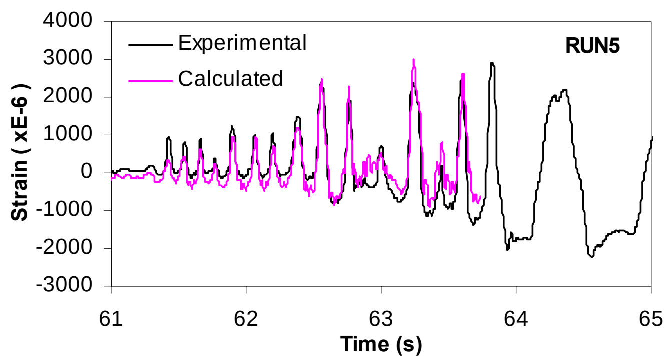

Figure 2.42 Comparison of strain in the outer face of the flange-web wall intersection developed in RUN-5

Table 2.3 Summary of computed time history results

	Top slab horizontal response acceleration and inertial force		Top slab horizontal response displacement	Horizontal rebar strain in web wall ($x10^{-6}$)	Vertical rebar strain in flange wall bottom ($x10^{-6}$)	
	g	kN	mm		Left flange	Right flange
RUN1	0.19 (*0.21*)	231 (*253*)	0.29 (*0.29*)	20 (*9*)	146 (*45*)	143 (*-37*)
RUN2	0.38 (*0.41*)	460 (*485*)	0.55 (*0.58*)	35 (*24*)	-89 (*-92*)	-90 (*-72*)
RUN2D	0.57 (*0.62*)	683 (*739*)	1.26 (*1.05*)	437 (*126*)	-99 (*-159*)	-100 (*-125*)
RUN3	0.70 (*0.72*)	840 (*856*)	1.87 (*1.63*)	562 (*679*)	-186 (*-222*)	-77 (*144*)
RUN4	0.91 (*0.90*)	977 (*1069*)	3.61 (*3.72*)	605 (*1021*)	765 (*1036*)	924 (*893*)
RUN5[a]	1.46 (*1.37*)	1743 (*1628*)	15.72 (*15.0*)	2646 (*>5000*)	2999 (*2632*)	3123 (*2885*)

[a]Analysis stopped due to non-convergent solution.

2.6.3 PCA Rectangular Walls (Oesterle et al., 1978)

Two specimens with rectangular cross sections from the first series of tests conducted by PCA (Portland Cement Association) in mid seventies to investigate the behavior of large isolated reinforced concrete walls were analyzed here. Controlled variables in the first series of tests were the wall cross-sectional shape, amount of flexural reinforcement and confinement levels in boundary elements.

Test specimens were approximately 1/3 scale representations of full-size walls. The walls had a height of 4.57 m and length of 1.9 m. The thickness of the walls was 102 mm. The boundary region was taken to extend 190 mm from each end of the wall. Two walls differ only in terms of amount of the flexural reinforcement at the boundary regions. The ratio of flexural reinforcement area to gross concrete area of boundary element in the first wall, referred as R1 in the Oesterle et al. (1976), was 0.0147. The second wall, R2, had reinforcement ratio of 0.04 at the boundary elements. In both of the walls the amount of vertical and horizontal reinforcement in the web was 0.0025 and 0.0031, respectively. While wall R2 had very well confined boundary elements (ρ_s = 0.02) in the lower 1.83 m of the wall height, wall R1 was constructed with no confinement.

As a part of experimental program, reversing loads were being applied to isolated walls. No axial load was applied in this series of test. Each specimen was loaded as a vertical cantilever with forces applied through the top slab. The test specimens were loaded in a series of increments.

The finite element models of the specimens are shown in Figure 2.43. Two models with fine and coarse meshes created in order to check the mesh size dependency. Both walls have the same reinforcement detailing as displayed with the reinforcement cage in Figure 2.43. Concrete was descriticized with SOLID65 elements. Reinforcement was modeled discretely with LINK8 elements.

Concrete strength of 45 MPa, an experimentally given average value for both specimens, was adopted in the analyses. The experimental Young modulus of 28000 MPa was also used in the analyses. The stress-strain curves for confined and unconfined concrete were developed in accordance with APPENDIX C. Multilinear isotropic work hardening plasticity was used to define the curves. Although bars of different sizes with slightly different yield strengths and post-yield characteristics (strain and stress at rupture) were employed in the experimental specimens, a fixed bilinear kinematic hardening plasticity model with 500 MPa yield strength, 200000 MPa of elastic modulus and strain hardening stiffness of $0.0075E_s$ was used for all the steel material.

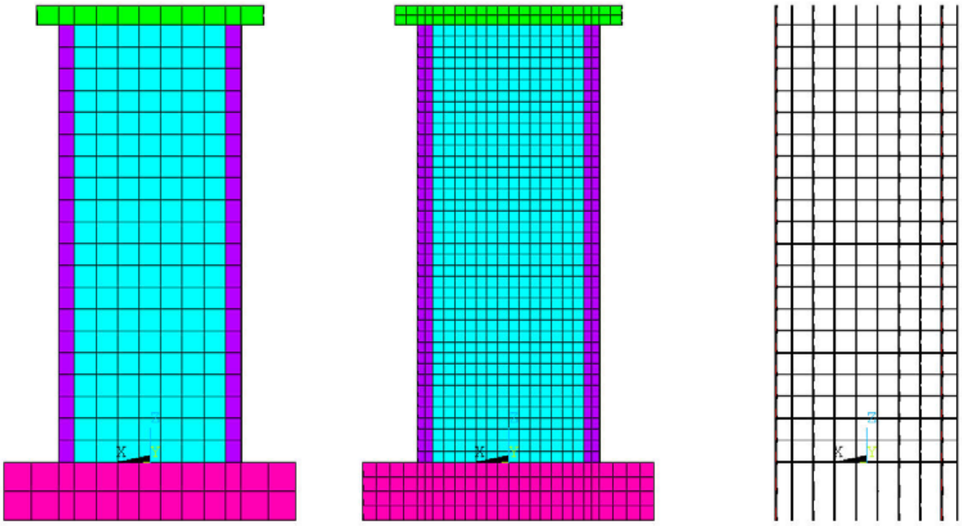

Figure 2.43 Finite element models of PCA R1 and R2 rectangular walls

Static analyses of wall R1 was performed by taking into account different aspects of element technology and finite element modeling as defined in the preceding sections. The result of these analyses was summarized in Figure 2.44. As seen in the figure, to get the closest results with respect the experimentally measured ones ESF should be turned on in the SOLID65. Analysis without ESF in SOLID65 yielded overly stiff response especially after the global yielding of the wall. For the model without ESF only it was possible to get results close to experimental ones when the shear transfer coefficient, β_t, in the model was taken close to zero. At first sight this was attributed to shear locking phenomena. However, as the resultant load-displacement curve of fine model has displayed, indicated with curve number 1 in Figure 2.44, no improvement in the post yield stiffness of the model was observed with regards to coarse model. It is expected that as the mesh becomes finer the effect of shear locking will diminish. Checking the model in detail, the strain distribution along the height of the wall provided a prognosis to the situation.

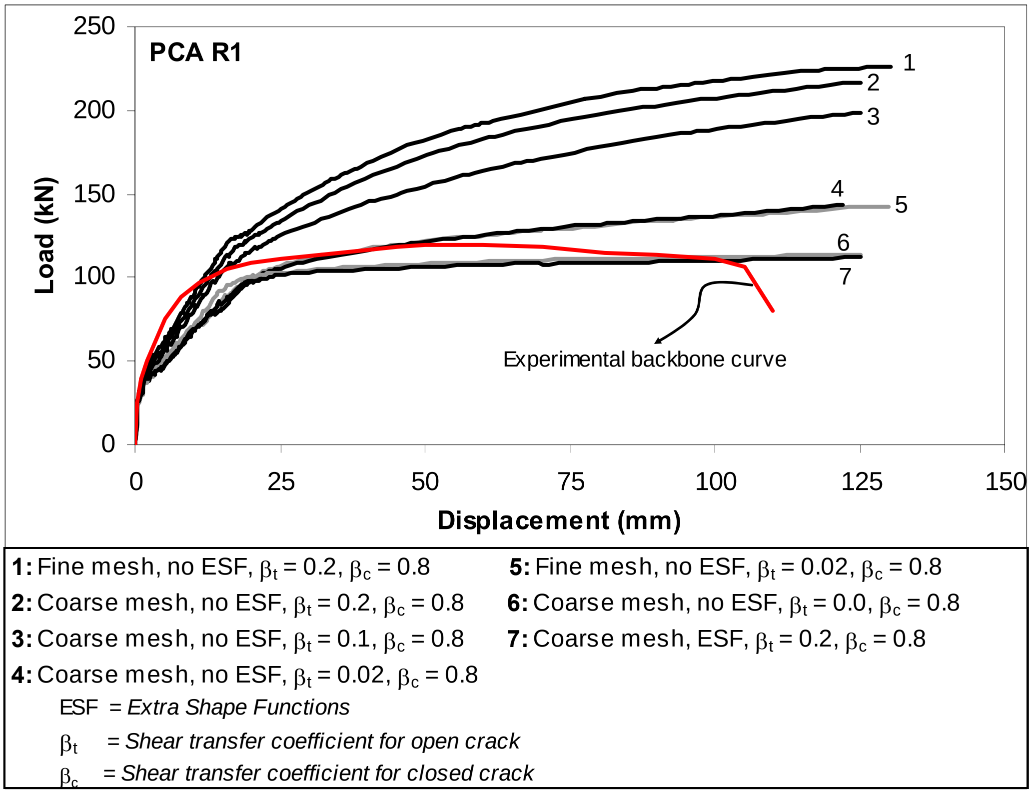

Figure 2.44 Result of static analyses of wall R1 in comparison with experimental hysteresis curve

The contour plots of vertical strain after the analyses in models 2, 4 and 7 in reference to Figure 2.44, at 1.5 mm (initiation of flexural cracking), 20 mm (initiation of global yielding) and 100 mm (excessive deformation range) of displacement levels are given in Figure 2.45. The first thing noticed especially at the third column of the Figure 2.45 is the shift in the location of the concentration of yielding in the tensile boundary region along the wall height. For the three models under consideration, up to global yielding while the yielding starts and progresses at a section very close to base, in the model without ESF (β_t = 0.2), Figure 2.45(a), after the global yield level is exceeded the yielding shifts upwards. Since the moment capacity of section is constant and the lever arm of the top applied force reduces due to shift in the location of yield section, a larger force is calculated.

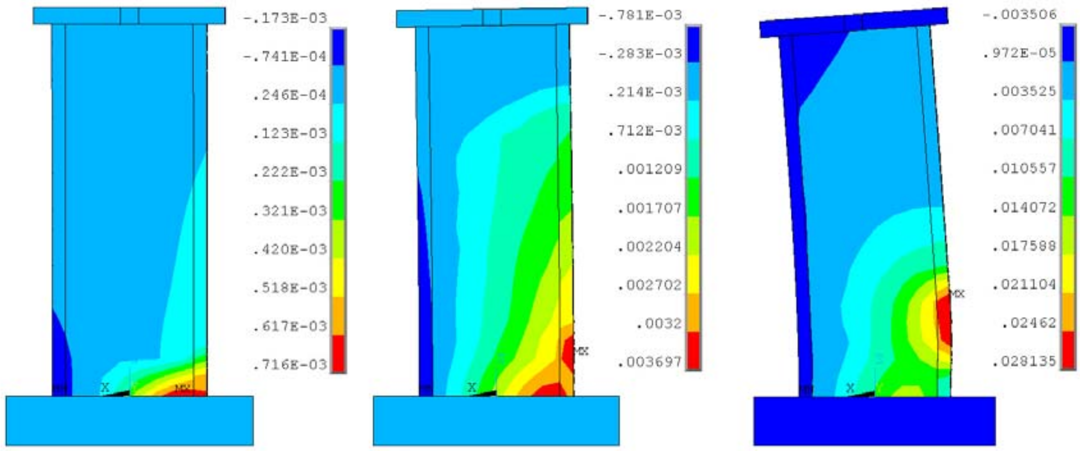

(a) Model without ESF formulation and $\beta_t = 0.2$.

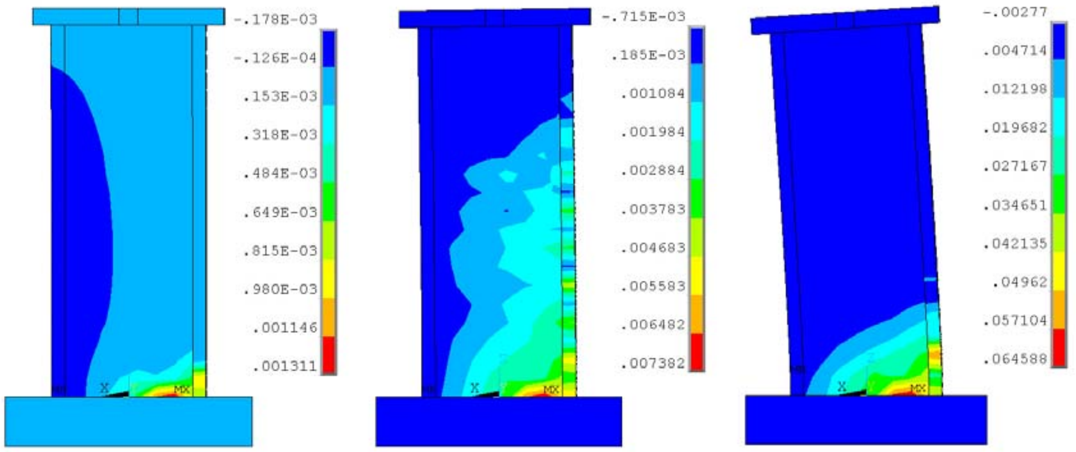

(b) Model with ESF formulation and $\beta_t = 0.2$.

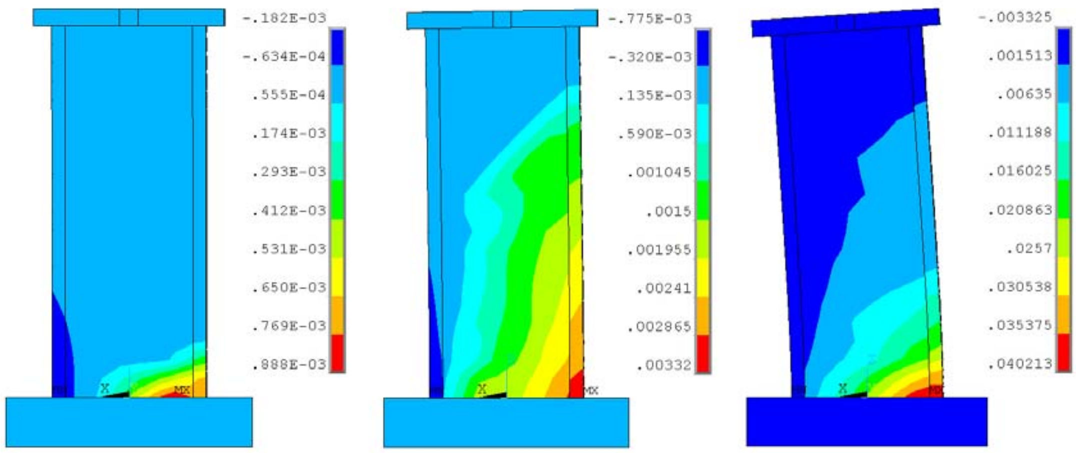

(c) Model without ESF formulation and $\beta_t = 0.02$.

Figure 2.45 Distribution of vertical strain (nodal averaging) in the boundary elements of R1 model for different finite element characteristics

The situation can be verified with simple sectional analyses. The tested wall has very simple geometry and loading. The moment capacity of the section at the initial yielding and ultimate load was calculated as 378 kN.m and 552 kN.m for the given reinforcement detailing and material properties. For the given geometry and loading, assuming that the yielding occurs at the base of wall, the peak load that the wall can sustain is calculated as 552/4.57 = 120.8 kN, which is very close to experimentally measured peak load capacity of the wall (118.3 kN). However, due to reduction in the moment arm as a result of shear locking phenomena nearly two times larger base shear capacity can be obtained.

Monotonic and cyclic static FE analyses of R2 wall were performed. In Figure 2.46 results of three models with different assumptions are plotted together with the experimental load-deflection envelope curve. The displacement capacity at the ultimate load predicted quite well for all models. As observed in the case of R1, the model without ESF and $\beta_t = 0.15$ yielded stiffer response than the experimental one after global yielding of the wall. For this case, while at the ultimate displacement level the strength was calculated 35 percent larger than the actual strength of R2 wall, the deviation in the R1 wall was much larger, approximately 93 percent. For lightly reinforced slender walls (where flexural response governs) and low axial load ratios ESF should be turned on. Figure 2.47 displays the comparison of calculated hysteretic response with the experimental one. Both the static and cyclic analyses provide good estimates of the experimental response.

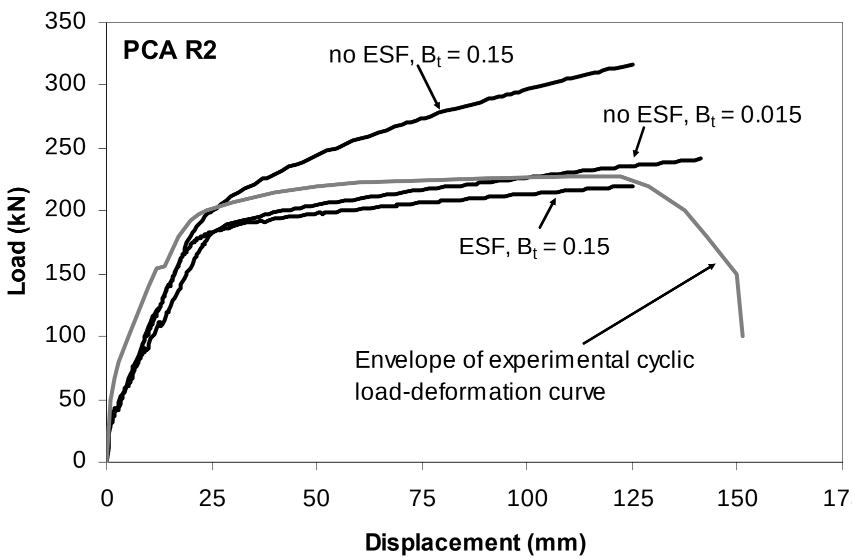

Figure 2.46 Result of static analyses of wall R2 in comparison with experimental hysteresis curve

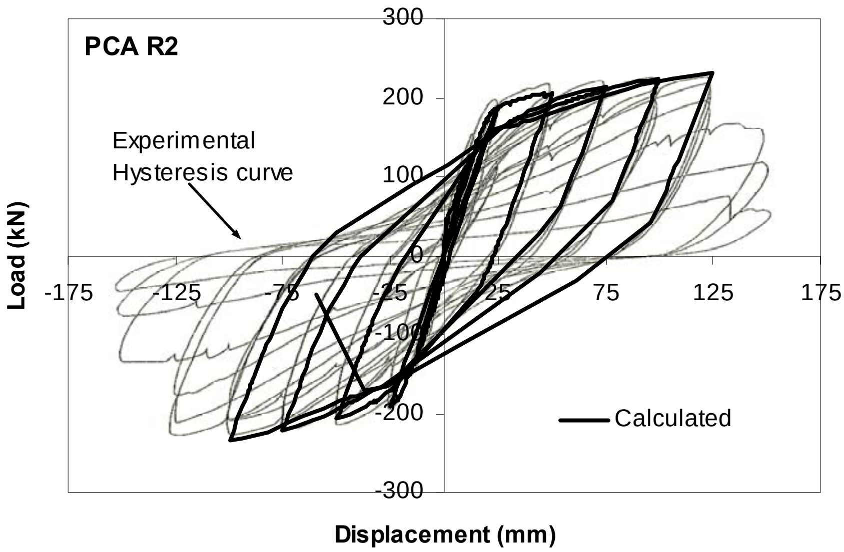

Figure 2.47 Comparison of calculated hysteretic response with the experimental one.

2.6.4 Thomsen and Wallace (1995) Rectangular Wall

The wall specimen with rectangular cross section (RW2) tested by Thomsen and Wallace (1995) and later used by Orakcal (2004) to calibrate and asses the proposed analytical shear wall model is analyzed. The wall was 3.66 m tall and 102 mm thick. Well-detailed boundary elements were provided at the edges of the wall over the bottom 1.22 m of the wall. In Figure 2.48 the detailing of the reinforcement in the cross section is shown. The volumetric ratio of the longitudinal reinforcement in the boundary element is approximately 0.033. The average compressive strength of concrete at the time of testing was measured to be 42.8 MPa. The longitudinal bars was type of Grade 60 (f_y = 414 MPa). Detailed material properties can be found in Orakcal (2004). The specimen was loaded cyclically by hydraulic actuators at the top. An axial stress of approximately $0.075A_gf_c$ was maintained throughout the duration of the test.

The finite element model of the wall specimen is displayed in Figure 2.49. The actual longitudinal reinforcements (8 - #3, A_{bar} = 73.1 mm^2) in the boundary elements was discretized with 6 equivalent rebar (A_{bar} = 97.5 mm^2) that gives the same amount of reinforcement in the boundary element. In the model, SOLID65 and LINK8 elements were used for concrete and reinforcing bars, respectively. This is done to provide coincident nodes between the concrete and bar elements for the used mesh pattern. Using the material constants and cross sectional details provided above and utilizing the procedures described in the proceeding sections, analytical material curves for concrete and steel were calculated and incorporated into the finite element model. The material curves are plotted in Figure 2.49(b).

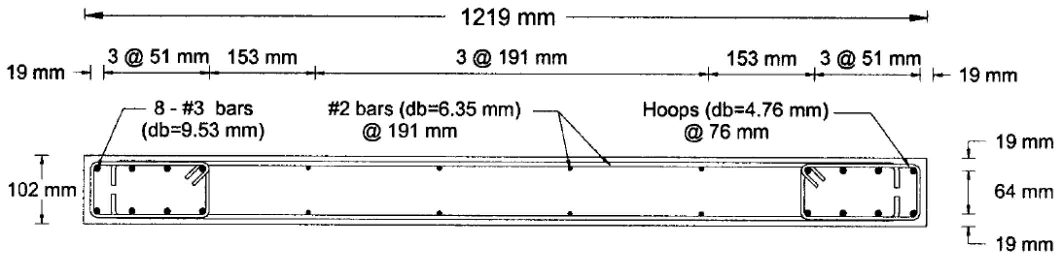

Figure 2.48 Wall cross sectional view (Orakcal, 2004)

Monotonic and cyclic static analyses were performed on the finite element model. The model is loaded with a prescribed displacement at the top mid node. By this way not only a better convergence behavior was obtained but also the initiation of the strength degradation in the load –deformation response can be detected. With force controlled loading schemes the behavior can not be tracked after the ultimate strength point. The effect of ESF and shear transfer coefficient on the load-deformation response of the wall was also checked on this model. The results of static analyses including these effects were displayed in Figure 2.50. In this figure calculated load-deformation curves are plotted together with the experimental cyclic response envelope curve for comparison. As studied and verified in the case of PCA wall specimens, in the analysis case where the elements with EFS were used and β_t was taken as 0.2 and in the analysis case where no ESF was used and β_t = 0.02 was assumed, the predicted load deflection curves are very similar and very close to the experimental one. The point where the strength degradation initiates was also predicted with a reasonable error. The predictions with the model without ESF overestimated the ultimate load capacity 22 percent, where the error is smaller compared to PCA wall case. The better performance is attributed to existence of axial load on the specimen as discussed previously.

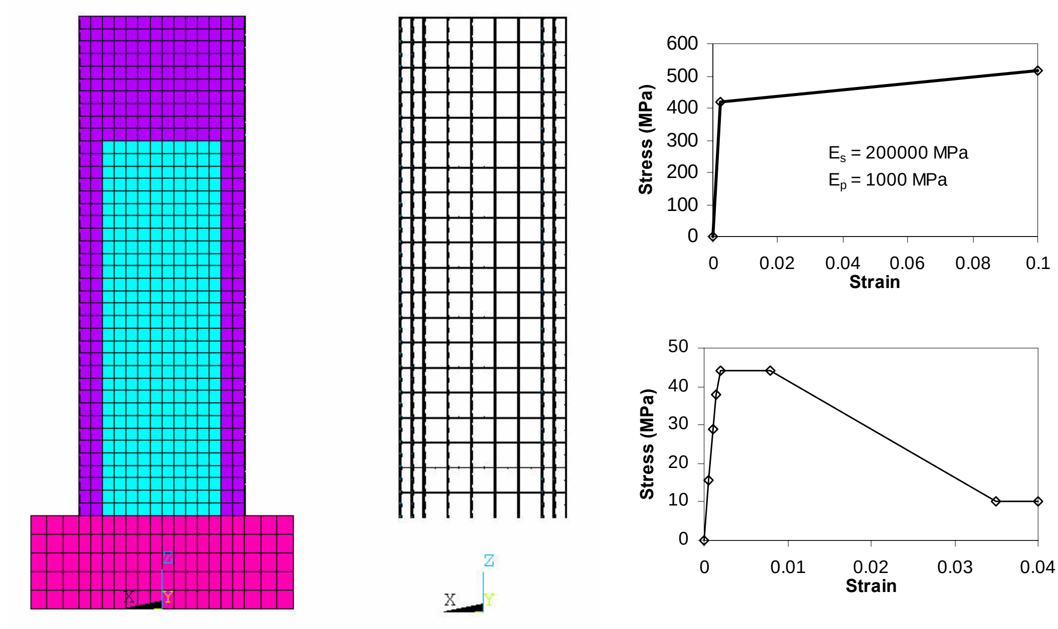

(a) (b)

Figure 2.49 (a) Finite element model and reinforcement mesh of the RW2 specimen, (b) steel and confined concrete material models

Using the finite element model utilizing no ESF in the SOLID 65 element options and with a minor shear transfer coefficient, cyclic load analysis was performed. While the multilinear curves with descending branch after the peak strain can be effectively used to define concrete stress-strain relation in static analyses, a bilinear curve is preferred in cyclic analysis to improve the convergence. It is worth to mention that analysis with ESF was conducted but significant convergence problems even at very early stages of the nonlinearity were encountered in cyclic loading. It is recommend here that in the analyses that includes reversing loads, when SOLID65 was used in the FE model the ESF will be turned off. In deed under loads cyclic in nature it is difficult to perform analyses with SOLID65 either with ESF is on or off when significant inelastic actions exist in the problem. Nevertheless it is possible to get a solution in the cases where no ESF was utilized by relaxing the convergence criteria when convergence problems encountered. The result of analysis is plotted in Figure 2.51. The agreement in the predicted and measured responses even surprised the author. This situation is attributed to fact that the analyses of the structural wall performed here is a slender flexural member with reasonable amount of axial load nearly without any shear effect, behavior of which can be predicted easily.

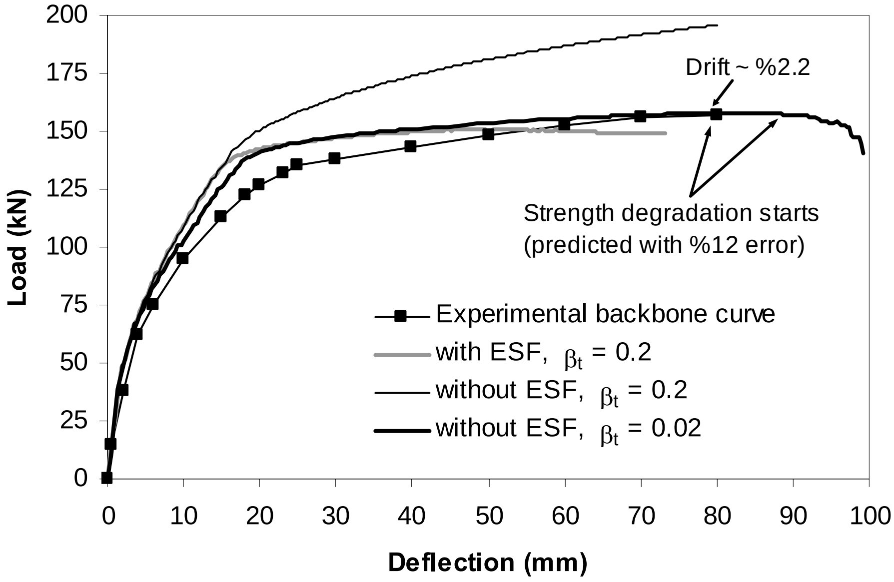

Figure 2.50 Static analyses results compared with cyclic envelope curve

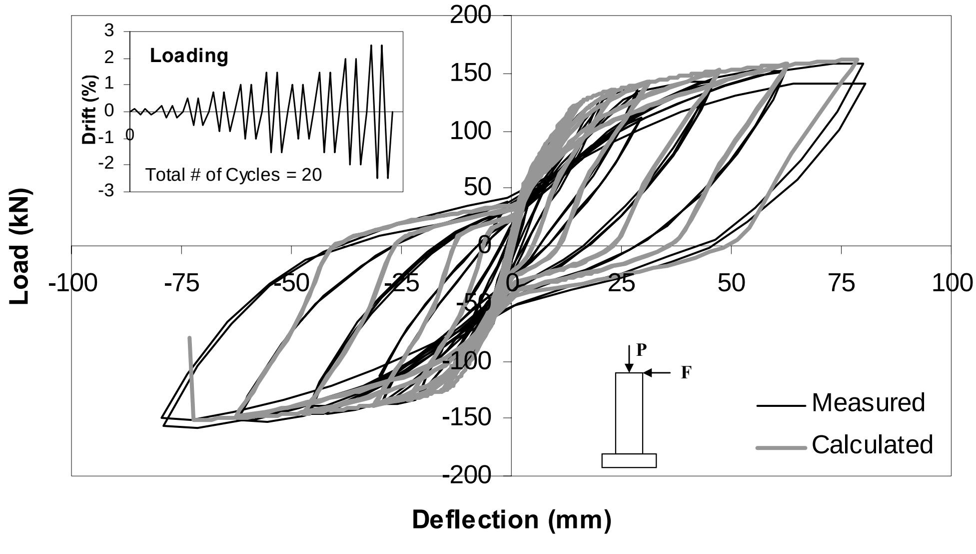

Figure 2.51 Comparison measured and calculated response of RW2. The measured response was corrected for pedestal movement, so as the applied displacement loading was adjusted accordingly.

The local response was also predicted with reasonable accuracy as well. Figure 2.52 displays the contour plot of vertical strain, stress and crack pattern at top deflection of 80 mm. The orientation of cracks indicates to flexural response. First flexural cracks develop and they are inclined at the web representing the stress state. As it can be remembered the concrete strength is taken to be 42.8 MPa, but the vertical stress plot in Figure 2.52 indicates to a stress level of 63.6 MPa. This situation can be attributed to the enhancement in the strength of concrete at the boundary element due to multi-axial stress state. Figure 2.53 compares the analytical and experimental curvature distribution at the base of the wall at drift levels of 1 and 2 percent. The predictions aggress reasonably well with the experimental ones even at very high deformations. An important observation in regards to this figure is the inadequacy of the "plane section remains plane" assumption in estimating the concrete strains at the extreme fiber at the compression region of flexural members. While the experimental result indicate to a concrete compressive strain of 0.012 at drift of %2 and finite element analysis predicted this accurately, the undistorted section assumption (Euler beam) yields only 0.005 strain value for the same level of tension steel strain (ε_s = 0.03). This leads to a great underestimation in evaluating the damage of concrete at the compression zone.

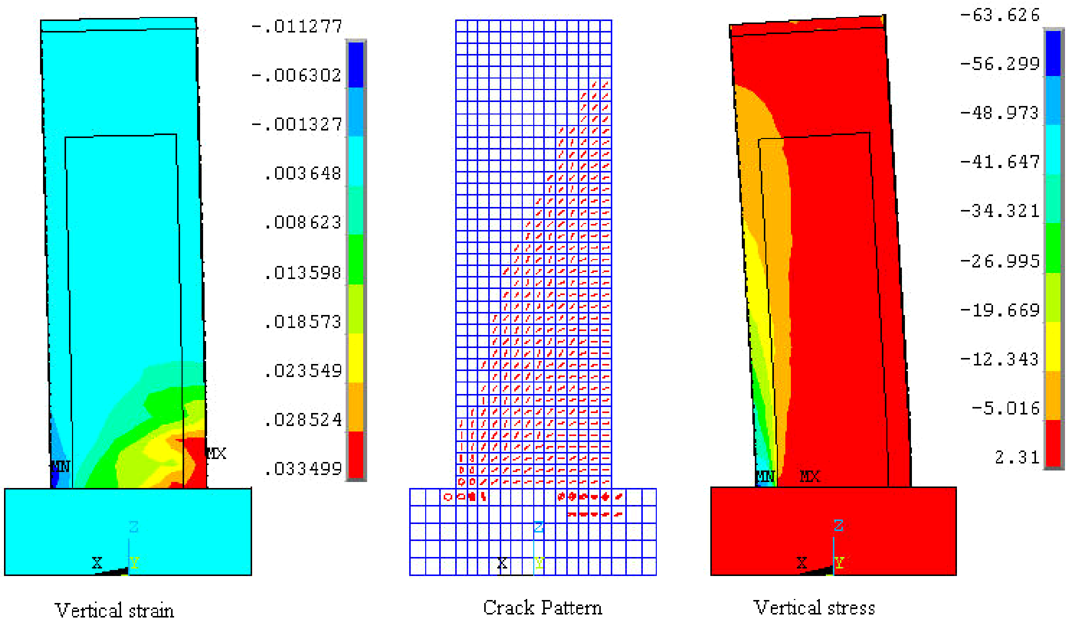

Figure 2.52 Distribution of vertical stress and strain at roof displacement of 80 mm (at %2.2 drift)

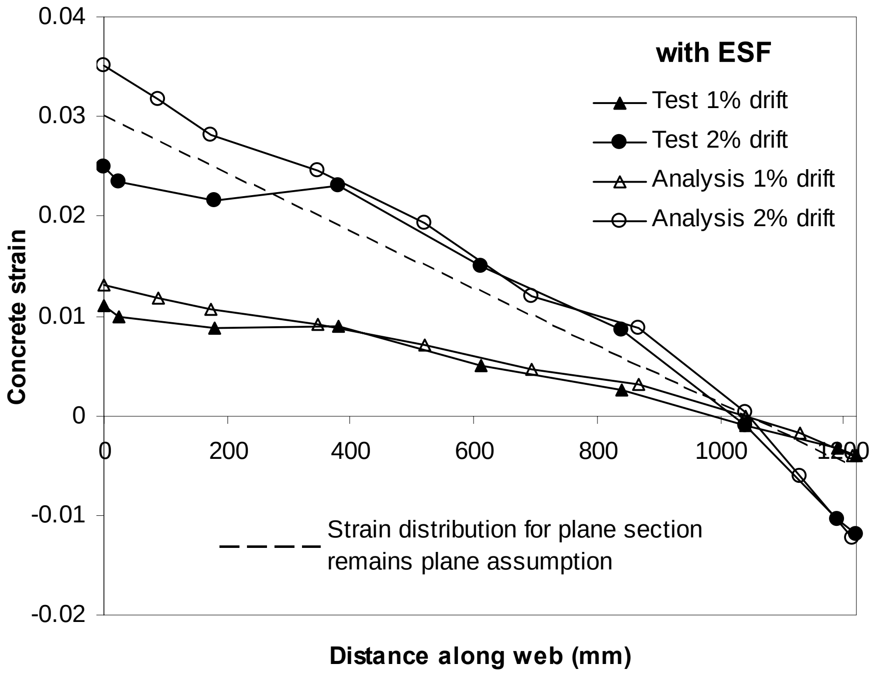

Figure 2.53 Comparison of measured (measured by LVDT's over a 229 mm gauge length) and calculated concrete strain at the base of the wall

2.6.5 Walls Tested by Vallenas et al. (1978)

Vallenas et al. (1978) presented the results of eight earthquake simulation tests on 1/3 scale RC wall sub-assemblage model specimens. In the experimental program Vallenas et al. tested four three-story wall specimens, two of which were framed wall and the other two were rectangular walls and after incipient failure, all the specimens were repaired and retested. The aim was to understand and model the behavior of reinforced concrete structural walls subjected to high shear earthquake loading conditions. The specimens represented the lower portion of the shear walls of wall-frame structural systems of ten- and seven-story buildings. Walls are designed to resist the total lateral load in the buildings. Dimensions of the specimens correspond to one-third the dimensions of the walls existing in the designed prototype buildings. The experiments simulated, in a pseudo-static manner, the dynamic loading conditions which could be induced in sub-assemblages of buildings during actual earthquake shaking. In the proceeding analytical work, analytical models for the behavior of structural walls under high shear stresses are presented. These models consider a breakdown of the overall deformations into three components: flexural, shear, and fixed end deformations. It was reported that the damage to the walls was concentrated on the first story. It included crushing of the concrete in the panel, buckling of the wall and column reinforcement, and, after rupturing of the confining reinforcement, crushing of the concrete in the column under compression and shear. Damage also included large residual tensile cracks, especially in the boundary elements.

The rectangular wall was 3.047 m high and had a length of 2.142 m. Thickness of the wall was 114 mm. Over the 279 mm length at the edges, boundary elements were formed. The volumetric ratio of the longitudinal reinforcement in the boundaries was 0.05. The amount of reinforcing steel in the vertical and horizontal direction was 0.0028. The rectangular wall investigated here was loaded monotonically. The typical sub-assemblage of a rectangular wall designed in a seven-story building is shown in Figure 2.54(a) together with the main geometric dimensions. The critical loading condition applied on the structure, as displayed in Figure 2.54(a), corresponds to response spectrum analysis of entire building using the ground motion of the 1971 San Fernando earthquake. The simplified loads were normalized to the ultimate moment capacity of the wall. The axial load in the walls kept constant. The test set up employed in this study is one of the most realistic one that was used in the experimental programs on shear walls as far as to the knowledge of the author.

Finite element of the model is displayed in Figure 2.54(b). Reinforcement was assumed to be smeared in the element volume. Extra displacement shapes option was turned on in the SOLID65 element formulation. Shear transfer coefficient was taken as 0.2. The concrete strength reported as 28 MPa. The confined concrete stress-strain curves that were calculated in accordance with the models described previously was given in Figure 2.55. As seen, hoops used at 34 mm spacing significantly enhanced the deformation capacity of the boundary element. Although such ductile stress-strain behavior curves were calculated for the boundary elements in compression, a more conservative curve compared to Mander et al. (1988) and Saatcioglu and Razvi (1992) models were adopted. Indeed whether concrete may sustain such levels of deformations is a questionable issue but beyond the target of this study.

Using the loading configuration shown in Figure 2.54(a), load-deformation response of the model was calculated and plotted in Figure 2.56. As done in the test, when the displacement at the top is 37 mm the model is unloaded and after reloading at the displacement of 56 mm the analyses ended due to “negative tangent stiffness matrix” error as a result of Newton-Raphson algorithm can no more track the nonlinear material curves in the softening regime. An interesting observation in Figure 2.56 is the occurrence of zigzags (small drops in the load) on the load-deformation curves nearly at the same time for both measured and predicted responses. At 25.5, 37 and 55 mm displacement these fluctuations were observed. The specimen was severely damaged at the end of experiment. The concrete lost its integrity, the reinforcing steel at the boundary has ruptured and out of plane buckling of the wall occurred by the end of test. The critical point in the response of specimen is where the unloading took place due to stability problem in the wall.

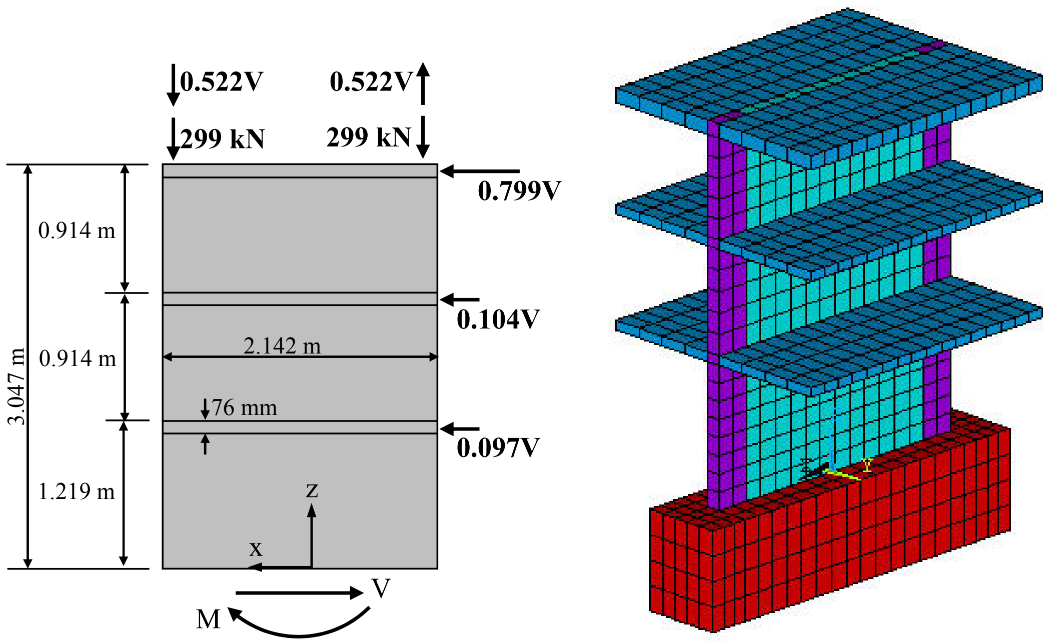

Figure 2.54 (a) Loading conditions of sub-assemblage rectangular structural wall, (b) Finite element model of the specimen

Interpretation of stress and strains in NLFEA requires sound understanding of the deformations from the experimental phase. Most of the time strains from FE analysis tend to overestimate the real word strains. The wall tested by Vallenas et al. (1978) provides a good example of such a situation, so it will be investigated in detail in order to legalize the strain calculations performed here. The strain distributions depicted from the analyses of Vallenas et al. (1978) wall specimen is displayed in Figure 2.57. The contour plots are given for top displacement level of ~37 mm (drift of %1.26). For the same level of deflection in the experiment it was reported that the failure was initiated by the unsymmetric spalling of the concrete cover at the boundary element in compression and at this point the *average strains* at the base of the boundary element was recorded as 0.00298 and 0.0047 by two clip gages installed at the region. As seen in Figure 2.57 the predicted vertical strains at the toe of compression strut are in the order of 0.028 and 0.015 in terms of element and nodal outputs, respectively, where the elements results are calculated at the integration points and the nodal results average the component tensor or vector data at nodes used by more than one element. There is a significant difference between the predicted and experimental values. Is it so or a new perspective is required to evaluate the strains? Most of the time experimental strain measurements are obtained by using displacement readings that are derived by measuring rather a long distance between two points on the specimen if they were not obtained from localized strain gage readings. The difference between the initial and final readings divided by the gage length yields the average strain in the region along the gage length. This may lead to significant misinterpretations of the actual strains since the effect of localization is ignored.

In the experimental program, the strain measurement were obtained by a pair of clip gages mounted near the centerline of the edge columns as displayed in Figure 2.58 (Vallenas et al., 1979 and Wang et al., 1975). The small dots shown in this figure represent the steel pins embedded inside the concrete. The deformation measured between two adjacent pins divided by the original distance between these two pins gives the average concrete strain between them. As shown in the lower corner of Figure 2.58, the lower end of the clip gage K11 was mounted on the pin embedded inside the column, 25 mm away form the footing. The lower end of the clip gage C11 was attached to the surface of the footing. The gage configurations are displayed more clearly at the sectional view at the left corner of the Figure 2.58. The strain readings by K11 and C11 were 0.00298 and 0.0047 respectively. The gage lengths of C11 and K11 were 355 and 381 mm, respectively, so the average concrete strains calculated over these lengths. The difference between the readings in gages K11 and C11 primarily represent either the concrete strains at the boundary element over the 25 mm length from the surface of the footing or occurred as a result of measurement error. Assuming that the measurements were taken correctly then the concrete compressive strain calculated over the 25 mm length region laying between the lower ends of gages K11 and C11 is approximately 0.029, which is calculated as,

$$\varepsilon = \frac{(381 \times 0.0047 - 355 \times 0.00298)}{25} = 0.0293$$

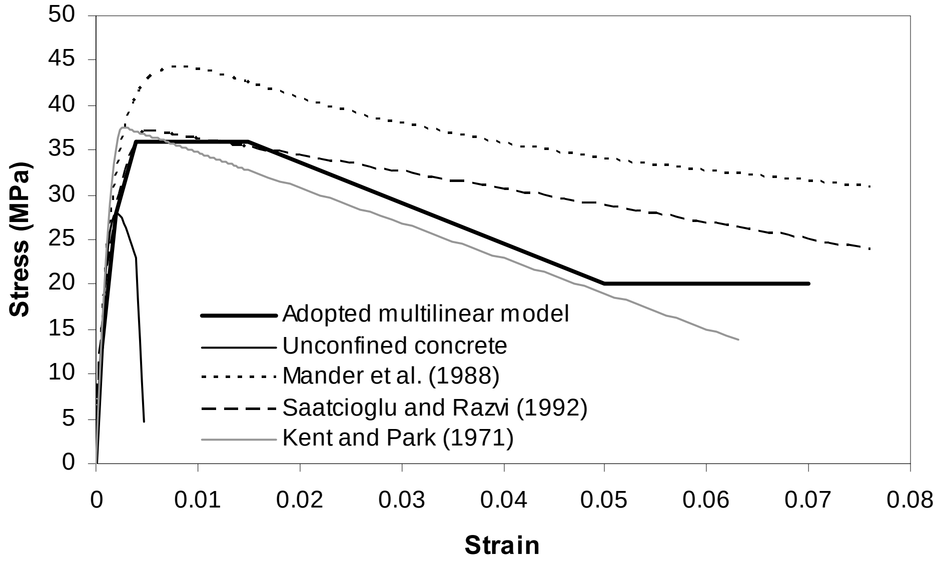

Figure 2.55 Confined concrete stress-strain relation

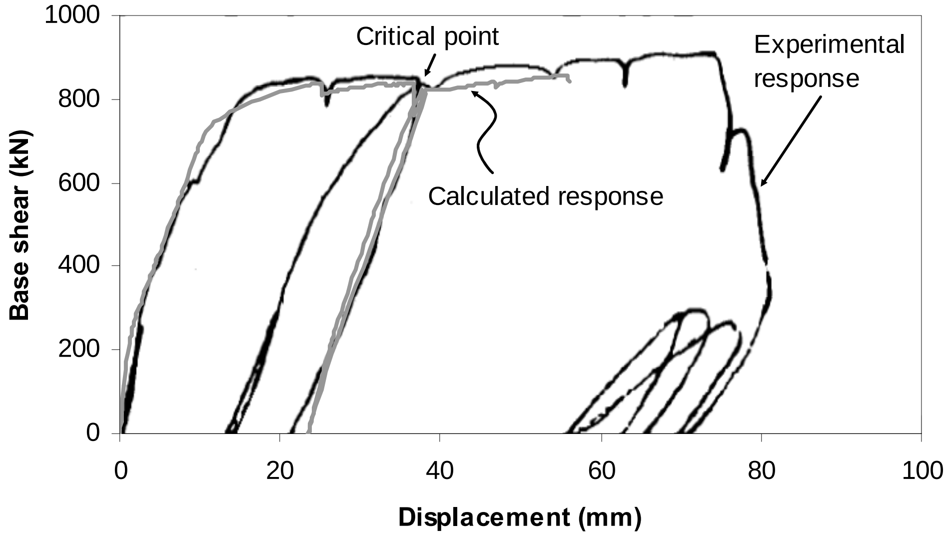

Figure 2.56 Analytical and experimental load-deformation curves of the specimen tested by Vallenas et al. (1979)

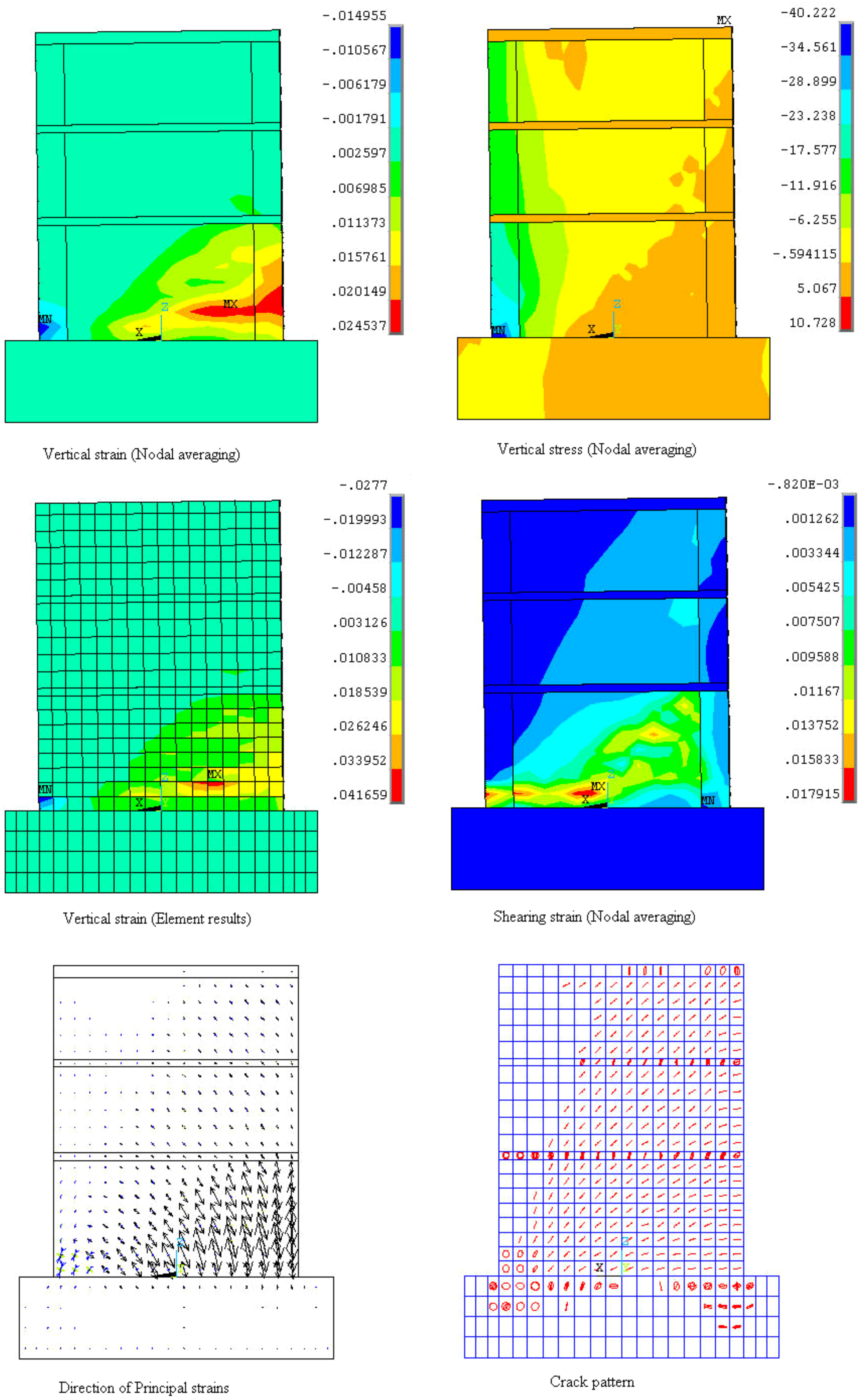

Figure 2.57 Contour plots of stress and strains, crack pattern and principal strains

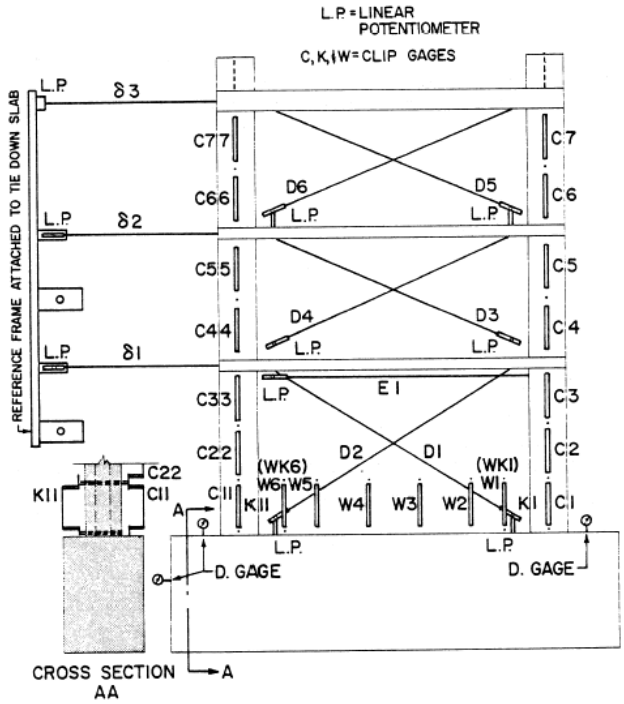

Figure 2.58 External instrumentation of the wall specimen tested by Vallenas et al. (1978)

The calculated strain value is very close to the strain output at the integration point of the element at the bottom compressive corner. The problem may be also elaborated starting from finite element analyses results and progressing towards experimental results as well by evaluating the finite element analyses results in the same manner as done in the experiments. If the strain outputs from the finite elements over the gage length are averaged, the strain corresponding to measurement of C11 (0.0047) becomes 0.00522. The finite element analyses results calculated at the element center (average) at the outer edge and center line of the boundary element (column) is plotted in Figure 2.59 along the height of first story column. The strain distribution displayed in the figure indicates to a very severe crushing situation especially at the lowest 150 mm region of the wall. Since the wall boundaries are very well confined (hoop at 34 mm spacing, ρ_s = 0.01) the specimen can sustain such levels of concrete compression strains. The deformed shapes from the analyses phase and test taken by photogrammetric methods are compared in Figure 2.60. Both patterns have significant resemblances. The strains recorded by gages K11 and C11 at the failure were reported to be 0.0072 and 0.0097.

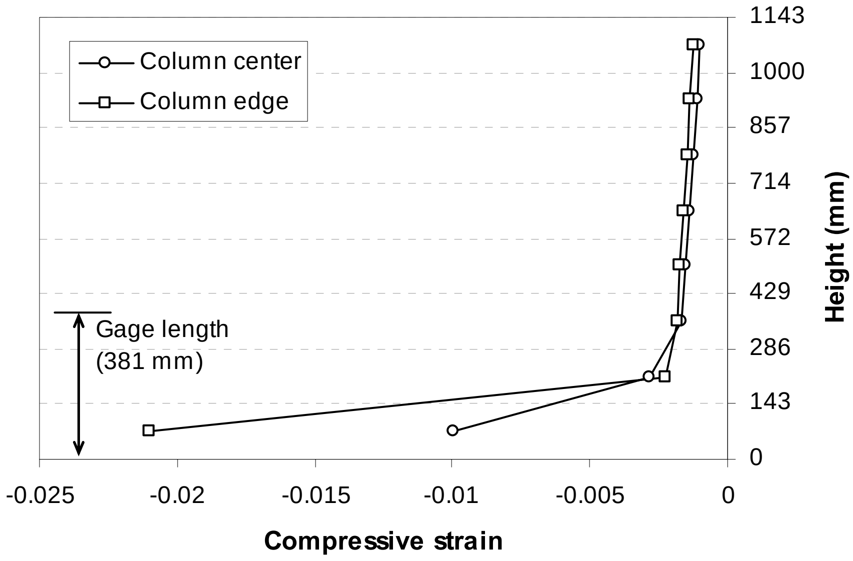

Figure 2.59 Compressive strain distribution along the boundary element in the first story

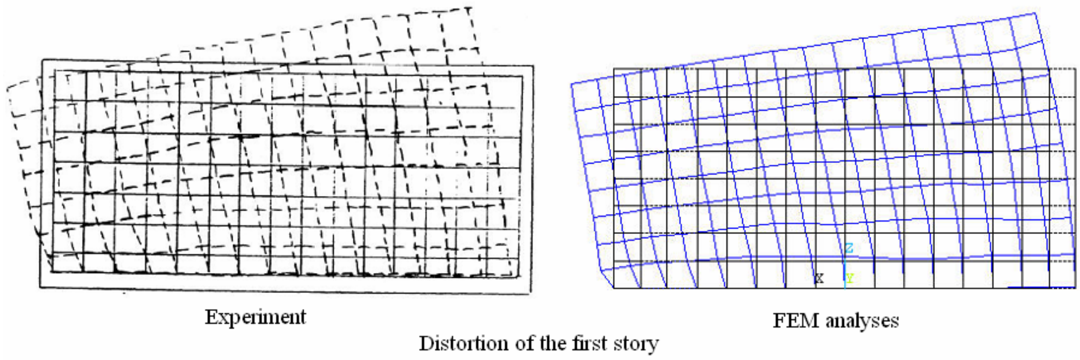

Figure 2.60 Deformed shapes depicted from experimental and analyses phases

2.6.6 Walls Tested by Lefas et al. (1990)

2.6.6.1 Experimental Program

The experimental work involved the testing of 13 structural walls with constant thickness and rectangular cross section. Two types of walls were tested in the program with respect to aspect ratio (h/l), where Type I walls had h/l = 1 and Type II had h/l = 2. Drawings displaying the dimensions and the arrangement of vertical and horizontal reinforcement of two types of walls were given in Figure 2.61. Table 2.4 gives the properties of reinforcement bars. In Table 2.5 amount of main flexural, confinement and web reinforcement is presented for each wall.

Three levels of axial load corresponding to 0.0, 0.1 and 0.2 of the uni-axial compressive strength of the wall cross section were adopted in the testing program. These load levels assumed to be representative of the amount of axial load at the base of the wall of a single story, a medium-height and a high-rise building, respectively. First the total constant axial load was applied and then the specimen was incrementally loaded with horizontal load. The experiment was force-controlled. The tests were not continued after the ultimate strength level exceeded.

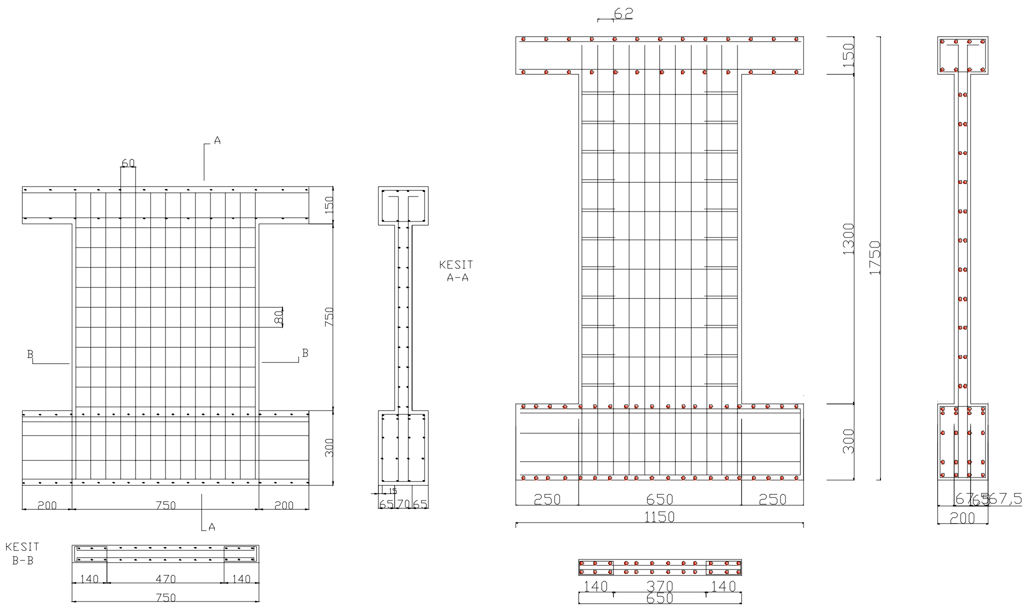

Figure 2.61 Geometry and reinforcement details of Type I and II wall specimens

Table 2.4 Properties of reinforcement bars

Steel type	Yield strength, f_{sy} (MPa)	Ultimate strength, f_{su} (Mpa)
8 mm high-tensile bar	470	565
6.25 mm high-tensile bar	520	610
4 mm mild-steel bar	420	490

Table 2.5 Experimental data of walls tested in the program

Specimen	Reinforcement percentage (%)				f_{ck} (MPa)	Axial load	
	ρ_{horz}	ρ_{vert}	ρ_{flex}	ρ_{conf}		***P*** **(kN)**	$P / f_{ck}bl$
SW11	1.1	2.4	3.1	1.2	44.5	0	0.0
SW12	1.1	2.4	3.1	1.2	45.6	230	0.1
SW13	1.1	2.4	3.1	1.2	34.5	355	0.2
SW14	1.1	2.4	3.1	1.2	35.8	0	0.0
SW15	1.1	2.4	3.1	1.2	36.8	185	0.1
SW16	1.1	2.4	3.1	1.2	43.9	460	0.2
SW17	0.37	2.4	3.1	1.2	41.1	0	0.0
SW21	0.8	2.5	3.3	0.9	36.4	0	0.0
SW22	0.8	2.5	3.3	0.9	43.0	182	0.1
SW23	0.8	2.5	3.3	0.9	40.6	343	0.2
SW24	0.8	2.5	3.3	0.9	41.1	0	0.0
SW25	0.8	2.5	3.3	0.9	38.6	325	0.2
SW26	0.4	2.5	3.3	0.9	25.3	0	0.0

2.6.6.2 Finite Element Models and Analyses

The finite element models of the Type I and Type II walls are shown in Figure 2.62. Using the material properties given in Table 2.5, material curves for confined and unconfined concrete were calculated. As seen in Figure 2.63, which is plotted for Type I walls, the calculated confinement effect provides insignificant ductility to the concrete after the peak strength. The tensile strength of concrete was taken as 10 percent of the compressive strength. For the material of steel, a bilinear curve was calculated by taking into account the tension stiffening as outlined in Section 2.4.2. The yield strength of 8 mm and 6.25 mm tensile bars was reduced from 470 MPa to 425 MPa and from 520 MPa to 445 MPa, respectively. At first stage reinforcement was modeled as smeared in the element volume. The models only consist of SOLID65 elements. ESF was allowed in the element formulation.

In all experiments, the top slab acted as the distributor of the applied vertical and horizontal loads. The vertical load was applied first on the models. Succeeding horizontal load was applied as nodal forces to the nodes lying on the surface of right side of the top slab. The load-deformation response curves for Type I and Type II walls are displayed in Figure 2.64 and Figure 2.65, respectively. The response of Type II walls was predicted with a reasonable accuracy. However, as seen in Figure 2.64 the calculated results overestimate the experimentally measured response of Type II walls. The finite element analyses that were conducted by Kotsovos et al. (1992) for the same group of wall specimens has also indicted to stiffer response of the numerical model, which was attributed time-dependent effects in the course of the loading history. Since a few minutes were waited to take readings and mark the progress of damage on the wall, a drop in the load can be observed during testing. Kotsovos et al. (1992) modified the response curves to incorporate these effects, but still a stiffer nonlinear response was calculated. The results presented in Figure 2.64 and referred as "bond-slip model" is discussed next.

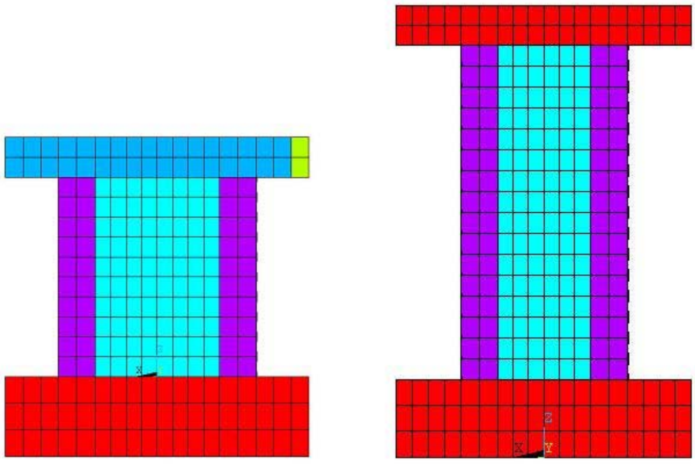

Figure 2.62 Finite element models of the Type I and II walls

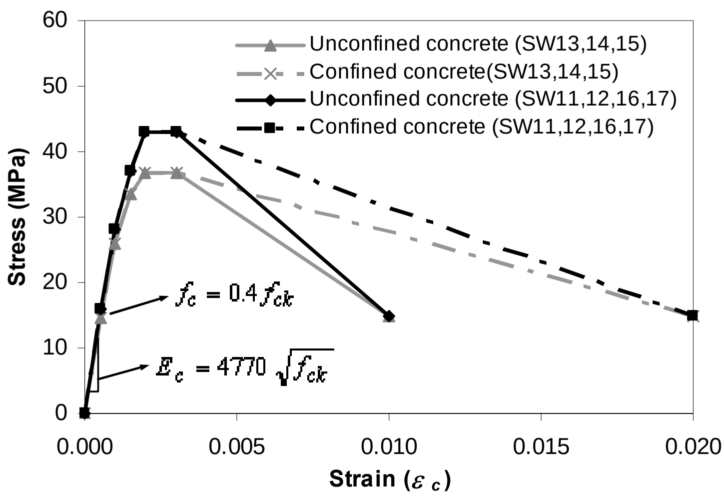

Figure 2.63 Concrete material curves for Type I walls

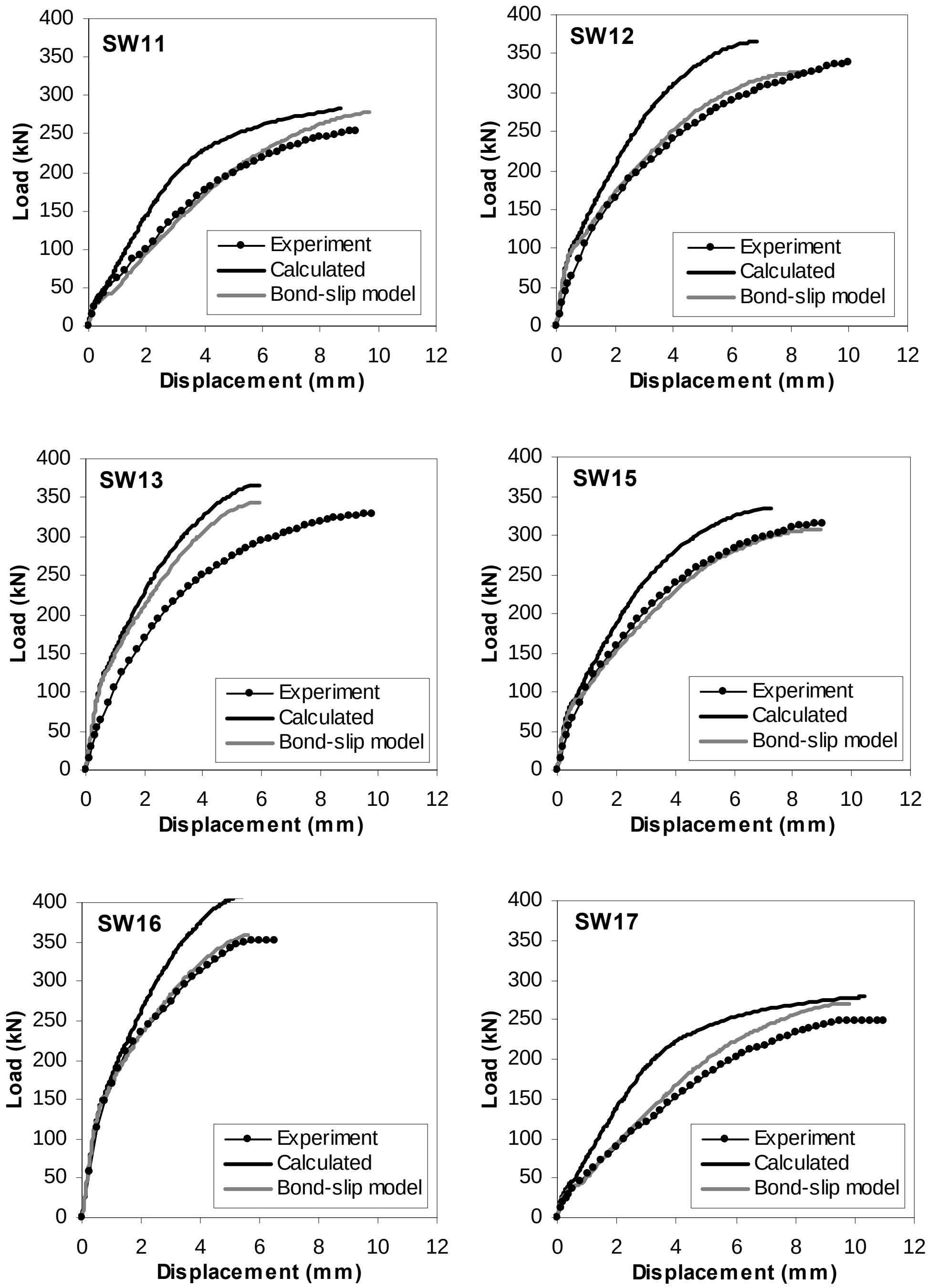

Figure 2.64 Load-deformation response of Type I walls

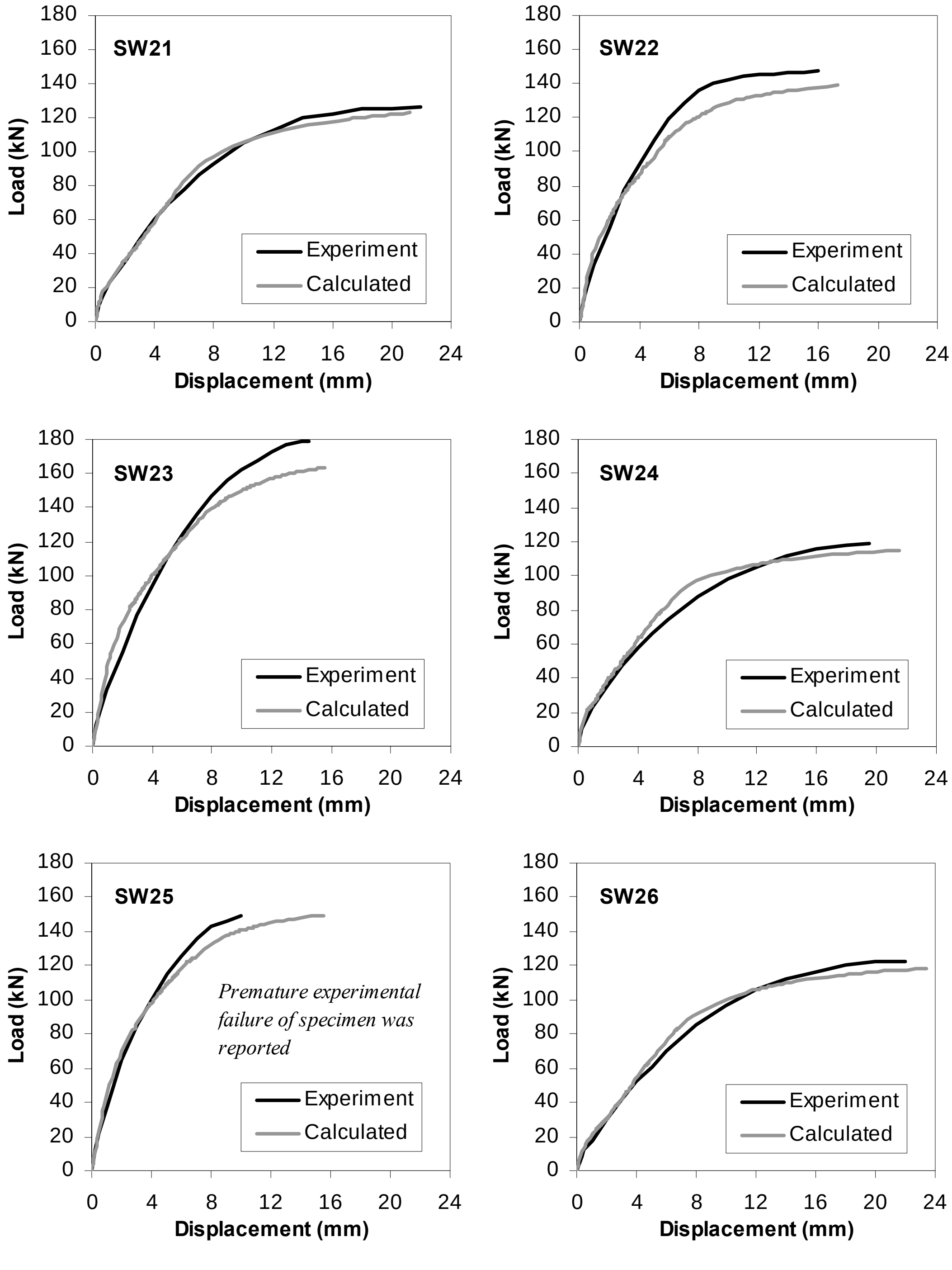

Figure 2.65 Load-deformation responses of Type II walls

2.6.6.3 *Finite Element Modeling with Bond-slip*

This study considered that bond-slip between the concrete and steel might have caused to such a response. A new finite element model with discrete reinforcement and bond-slip elements was constructed.

As described schematically in Figure 2.66, the discrete bond-slip elements between the nodes of steels element, modeled with LINK8 elements, and concrete were discretized using COMBIN39 nonlinear spring elements. This kind of approach was adopted by Ngo and Scordelis (1967) and Thomas and Ramaswamy (2006), previously. The bond-slip behavior of COMBIN39 elements were defined with Mirza and Houde's (1979) bond-slip model. Mirza and Houde (1979) conducted tension tests on a typical steel bar embedded into concrete as shown in Figure 2.67 by keeping the concrete area (A_c) and rebar diameter (d), i.e. steel area (A_s), as variables. In a tension test the force in the steel bar is transferred progressively to the concrete by bond stresses. When the tensile stresses at a certain distance from ends exceed the tensile strength of concrete, cracks develops in the concrete. If the length of concrete prism between newly formed cracks is longer than the stable crack spacing, same conditions as before develop, resulting in new cracks. As the result of experiments, Mirza and Houde (1979) proposed the following relation between the steel stress and average bond-slip

$$\Delta_s = 0.0003684 \cdot k_1 f_s^{k_2} \left(A_c / A_s\right)^{k_3} \tag{2.12}$$

where, Δ_S is the average bond slip (mm), f_s is the instantaneous stress in the rebar (MPa), A_s is the area of the rebar and A_c effective concrete area surrounding the rebar. The influence of the steel stress was noted to be almost linear (k_2 was found to vary between 1.0 and 1.2). For simplicity, k_2 was set equal to 1.0 and the value of k_3 was found to be 0.33. The corresponding k_1 coefficient can be computed using Eq. (2.13) or can be taken as 0.2 mm/MPa.

$$k_1 = 5.690 \cdot 10^{-7} f_s^{\,2} + 6.645 \cdot 10^{-5} f_s + 1.774 \cdot 10^{-1} \tag{2.13}$$

The slip-steel stress relation for different reinforcing steel bars used in the specimen was calculated in accordance with the described model. The steel stresses were converted to force multiplying by the steel area since COMBIN39 admits force-deformation data as described in Section A.3.4. As seen in Figure 2.64, the correlation of predictions with experimental results improved significantly. The implementation of bond-slip model to ANSYS reinforced concrete analyses was demonstrated for comprehensiveness of the study, otherwise no bond-slip behavior is anticipated for the rest of analyses that will be conducted.

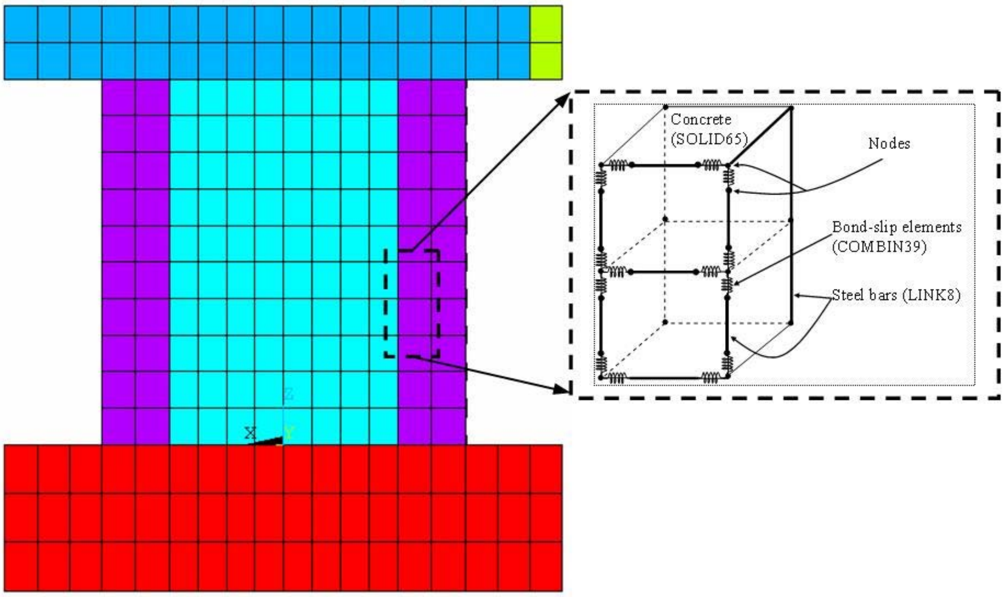

Figure 2.66 Finite element model of Type I walls with bond-slip

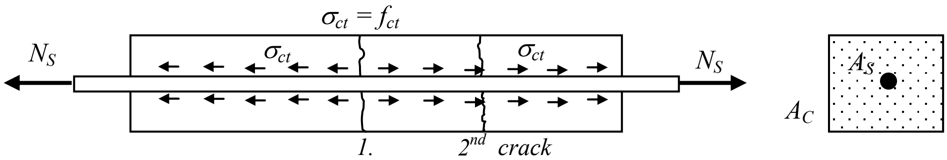

Figure 2.67 Development of crack in concrete in a tension test

2.6.6.4 Local Results

The steel strains were measured during the experiment. The strain gages were implemented on the vertical rebars at the boundary elements at the base level of the wall, just above the footing. Lefas et al. (1990) reported that the vertical reinforcement exhibited considerable post-yield deformations prior to failure. The strains measured at the base of the walls on the vertical rebars in the compressive and tensile boundary elements are plotted in Figure 2.68.

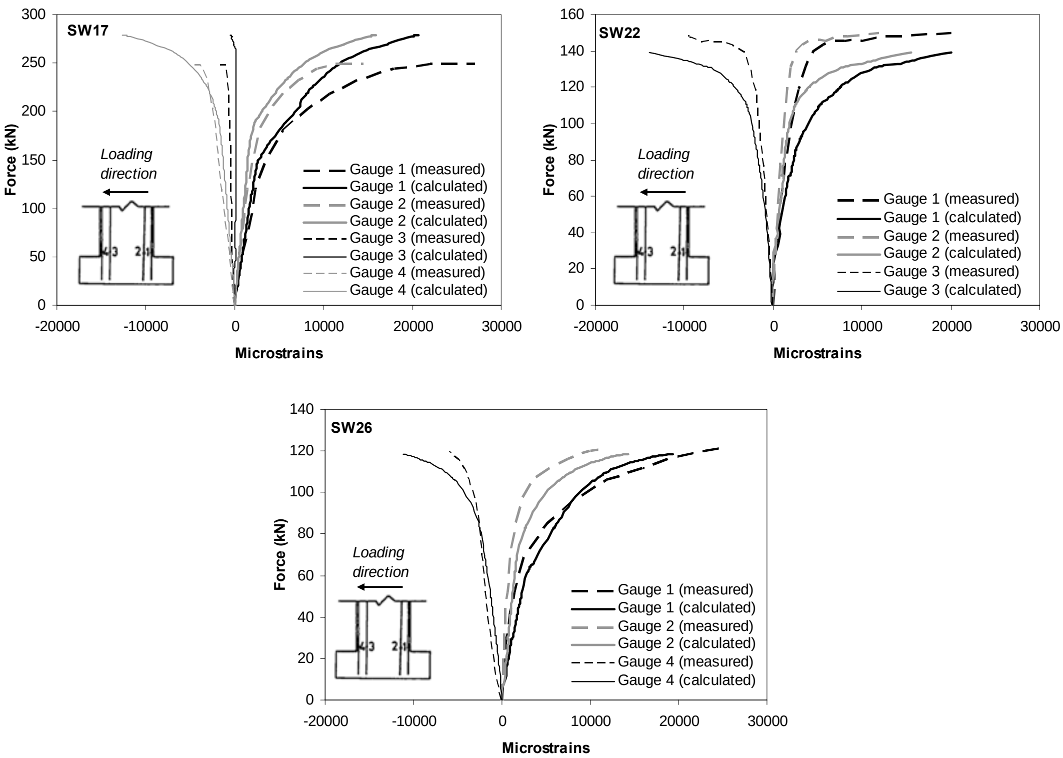

Figure 2.68 Comparison of analytical and experimental strains at the base of the wall

The strains presented by Lefas et al. (1990) and obtained here from the simulations agree well for the tension case. In general, the calculated compressive concrete strains overestimate the measured compressive steel strains as seen in Figure 2.68. For example, the compressive strain in the external rebar (gauge 4) of SW17 reported to be approximately 0.0045 at the ultimate, where as the calculated concrete strain is 0.013 approximately. Moreover, the compressive steel strains at the ultimate for Type I walls (h/l = 1) were smaller than the strains reported for Type II walls (h/l = 2). It is known that the main resisting mechanism to the applied lateral load in the squat walls is the development of diagonal compression strut depressing on the boundary element on the compression side. However, pictures that were presented in the paper displaying the state of damage of the wall at the end of tests conflicts with damage indicated by the measured strains. As displayed in Figure 2.69, the compressive region of Type I walls exhibits severe spalling and crushing damage during the test compared to Type II walls. Such a discrepancy between the measured and calculated strains might have been due to an interruption in the data acquisition as a result of damage to strain gages or due to buckling of the reinforcement, which is evident in Figure 2.69, but nothing was declared about such situations by Lefas et al. (1990) in their paper. The compressive strut is evident in the Figure 2.70, resulting in triaxial stress state at the compressive boundary element.

Figure 2.69 Damaged walls; Type I walls experiences more damage than Type II walls at the compression zone (adopted from Lefas et al, 1990)

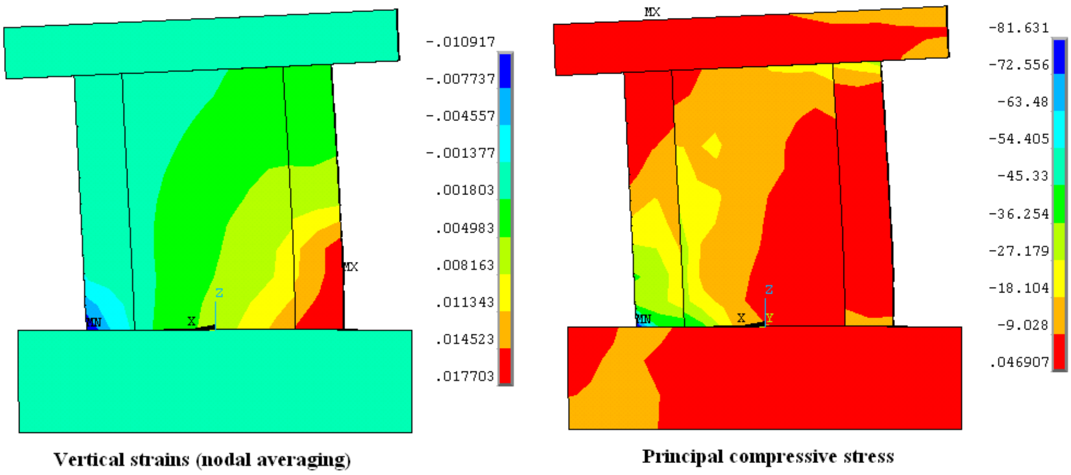

Figure 2.70 Vertical strain and principal compressive stress plot at the ultimate load of SW17. The compressive strut is evident in the figure, resulting in triaxial stress state at the compressive boundary element. The concrete compressive strength is reported to be 41.1 MPa for this specimen.

2.7 LESSONS LEARNED FROM SIMULATION STUDIES

2.7.1 Meshing

A finite element mesh consisting of 12-20 elements along the length of the wall proved to yield satisfactory results. For slender walls this number may be reduced to 10 when ESF functions are utilized. Meshes consisting of more than 15 and 20 elements along the length of the wall should be considered fine mesh for slender and squat walls respectively. Along the height of the wall the length of elements can be larger than horizontal element edge length without violating aspect ratio rule. The ratio of lengths of edges of a brick element should not be larger than two in general.

When ESF functions are utilized in the SOLID65 element formulation, fine meshes may lead to localization of crushing damage (softening) at particular elements leading premature failure indication in the model. When fine mesh is used in the model, ESF should be turned off. For slender walls (H/L > 3) when ESF are turned off, for the shear transfer coefficient for open cracks a value very close to zero should be adopted. This number may be zero, but may cause convergence problems. For squat walls a value equal to 0.2 for shear transfer coefficient may be used.

2.7.2 Convergence Problems

Significant convergence problems in the solution of nonlinear problems may be experienced in ANSYS due to excessive cracking and crushing (softening regime after peak strength) of concrete. Several convergence–enhancement tools, such as automatic time steeping, line search, adaptive decent, is available in ANSYS program to help the solution of nonlinear problems. To overcome convergence problems either the load is applied in small increments or the force and displacement convergence criteria is loosened or both are done simultaneously. If the amplitude of the applied load is within the likely limits of the member capacity, this should improve the convergence significantly. Simple hand calculations or analyses should be performed to estimate magnitude of the applied loads. For example, if the model is loaded with displacements, the drift ratio that will be experienced by the model is in the range of 1-3% depending on the aspect ratio of the wall (slender or squat). Similarly, moment capacity calculated from sectional analyses can be used to determine the amplitude of applied lateral loading.

If increasing the number of substeps does not work, convergence criteria may be loosened. In most of the analyses performed here, the default force based convergence criterion created convergence problems after onset of first cracking. The convergence norm, against which the unbalanced forces are checked, is calculated within the program as *NORM = VALUE x TOLER*. The parameters are input with *CNVTOL* command. The default value of *VALUE* is the SRSS of the applied loads (or, for applied displacements, of the Newton-Raphson restoring forces). Tolerance, *TOLER*, about *VALUE* defaults to 0.005 (0.5%) for force and moment, and 0.05 (5%) for displacement when rotational DOFs are not present. In the analyses performed in this study the default values are suppressed and according to adopted N-mm units system the *VALUE* and *TOLER* adjusted such that they yield force and displacement norms (*F_NORM* and *D_NORM*) equal to 5000~10000 N and 0.015~0.025 mm respectively. An example command line read as

CNVTOL,F,1E6,0.0075,2

CNVTOL,U,10,0.002,2

These norms were found to be satisfactory in overcoming cracking related convergence problems. If the solution still does not converge, after checking the displacement and force convergence norms that are reported after each equilibrium iterations in the output window the criteria for the problematic one may be loosened further.

Another way to handle convergence issue is using multiple load step files corresponding to each region on the curve. With multi-frame restart option this method also improves convergence.

2.7.3 Static Analysis Procedure

The second problematic region on the load deformation curve is the peak load region. When the peak load capacity of the member is reached, under force type loading analysis can not be continued into softening regime. A pushover algorithm that allows tracking the force-deformation response after the ultimate strength level was developed utilizing multiple load step analyses procedure. The procedure uses four load steps. The actions in each load step summarized below.

LS1: Apply the vertical load (F_{vert}). *TIME* will be equal 1.0 by default at the end of load step. The ANSYS program uses time as a tracking parameter in all static and transient analyses, whether they are or are not truly time-dependent. The advantage of this is that you can use one consistent "counter" or "tracker" in all cases, eliminating the need for analysis-dependent terminology. For example, if the analyses stop at *TIME* = 0.65 due to any reason before the full load step is finished, this means 65% percent of the load is applied.

LS2: Apply the lateral forces of any pattern on the model (F_{horz}). The applied load should be larger than the peak load capacity of the model. The analysis stops when the applied load is very close to ultimate strength of the structure. Analysis may be restarted several times in this load step until it is ensured that the model can not sustain any more load increment. Enter the postprocessor and read the time of the last converged substep (eg., *TIME* = 1.783) and the value of displacement at a node at the top or roof of the model (Δ_{top}).

LS3: This is a dummy load step to change the loading scheme from force-controlled to displacement-controlled one. The applied horizontal load is reduced by a factor (*TIME*-1), where TIME is obtained from the last converged step of LS2. This will reduce the applied load to the level of the last converged step [$F_{peak} = F_{horz}$ x (*TIME*-1)]. After issuing restart command apply the reduced forces to the previously loaded nodes and apply the roof displacement (Δ_{top}) as displacement loading at a node where it was read. The solution is same as the last converged substep of LS2. *TIME* becomes 2.0 after the solution of this step. The displacement boundary condition was introduced at the top of the structure.

LS4: Scale the Δ_{top} with a factor 2-5 or more depending on the expected displacement capacity of the member and apply it again to the same node as displacement loading. The imposed displacement boundary condition at the top while ensures the pushover to propagate in the prescribed direction also acts as a tuner by adjusting the level of applied lateral load as well. A support reaction that may be positive or negative depending on the increasing or decreasing tendency in the load deformation curve develops at the node of prescribed displacement. This means if the peak strength of the model is not reached, load continues to increase. At this load step the magnitude of lateral load may be taken as the same as in previous step or reduced further 0 to 15 percent [*factor* x F_{horz} x (*TIME*-1)] depending on the expected behavior in the post-peak regime. For squat walls a reduction helps convergence since after peak strength, gradual strength degradation occurs. A loose convergence criteria and enough number of substeps should be preferred in this load step.

The pushover procedure outlined here is utilized in the parametric studies conducted in Chapter 5 and Chapter 6. Under force controlled loading scheme the analyses provide results only for a limited ductility or drift range without such a procedure.

CHAPTER 3

GROUND MOTION EVALUATION AND SELECTION

3.1 INTRODUCTION

Seismic performance investigation of structures requires the use of recorded natural ground motions or their artificially produced representatives for use in nonlinear time history analyses. Due to complex interrelation between the energy dissipation properties of structures and the dynamic characteristics of seismic ground motions, the quality and adequacy of results of inelastic dynamic analyses depends strongly on the comprehensiveness of the employed ground motion data set, as much as it depends on the mathematical modeling of the structural and material behavior. This stipulates the necessity of a reliable ground motion intensity measures for the ground motion selection criteria and evaluation of its damage potential to bridge the gap between the seismic loading and structural response.

Earthquake ground motion selection for nonlinear time history analysis is a subject that has aroused interest in the research community especially in the last decade, after the number of well recorded earthquakes increased and high quality data obtained from these recordings. One another reason that gave boost to research on ground motion selection is the rapid development in the field of performance based earthquake engineering that is applied in design and assessment. However, the results presented by different researchers displayed that there is still lack of a common criterion reached for the ground motion selection. This is mainly due to variations in the characteristics of ground motion records that compose the data sets or bins used by different researchers, since each based the selection on different criteria. For example, the ground motions data sets can be formed according to a particular scenario earthquake that takes into account magnitude-distance

(M-R) relation (selection in terms of geophysical parameters), or alternatively considering the ground motion characteristics such as peak ground acceleration (PGA) or peak ground velocity (PGV) (selection in terms of strong-motion parameters). Even the distinctions in approaches can lead to different emphasis at the outputs, to be applicable in engineering practice they should have results that indicate to a common point. So it is required to find out the common sides of used criterions in ground motion selection, reflecting the engineering judgment of the experts of the field, so as to offer a unified approach for the ground motion selection.

When an earthquake occurs, the amplitude, phasing (seismic waves arrive to a site like trains, with different frequencies arriving at different times), and frequency content of the shaking depend strongly both on source characteristics (e.g., magnitude, rupture mechanism, fault plane orientation with respect to site, occurrence or non-occurrence of surface rupture) (Stewart et al., 2001) and the properties (stiffness, strength, layering) of the soil or rock strata between the recording site and the source (Newmark and Hall, 1969). Due to all these counted reasons, each ground motion recorded at a particular site displays different characteristics in terms of amplitude (peak ground acceleration – PGA and peak ground velocity – PGV), frequency content (existence of different wave components in the composition of record) and phasing of the arriving waves. When all these parameters are considered it is unlikely that any one record will be adequate to account for the seismic hazard. For instance, response predictions calculated from ground motions with similar intensity defined in terms of single intensity measure like PGA or spectral acceleration at the fundamental period ($Sa(T_1)$) of the structure resulted in significant variability. It is usually necessary to examine a group of records. Several intensity measures were proposed to identify the damage potential of a ground motion due to any one of these seismic parameters.

It was well identified from seismic response studies of engineering structures that the structural damage is caused mainly by three important seismic parameters: the amplitude and the frequency content of the seismic ground motion, and the duration of the strong ground shaking. When inelastic response of multi-degree of freedom (MDOF) structural systems is considered several researchers (Derecho et al., 1978b; Anderson and Bertero, 1987; Tso et al., 1993; Seneviratna and Krawinkler, 1997; Medina and Krawinkler, 2003) agreed that what matters to increased structural damage among any two ground motion with the same intensity (either in terms of ground motion parameters such as peak ground acceleration (PGA) or spectral acceleration at the fundamental period of the structure, $Sa(T_1)$) is the frequency content of the ground motion. Following from this fact, different researchers (Zhu et al, 1988b; Stewart et al., 2001; Cordova et al., 2000; Baker and Cornell, 2005) have concluded that the nonlinear response of structures is strongly dependent on the phasing of the input ground motion and on the detailed shape (frequency content) of its spectrum, things that are closely related to magnitude (M) of the earthquake and site-to-source distance (R).

Seneviratna and Krawinkler (1997) stated that due to inherent variability of the input ground motions, the demand estimation and related response modification factors need to be computed using a statistical analysis of the inelastic dynamic response of MDOF systems to a suite of ground motions with reasonably similar frequency content. This requires the introduction of a criterion to identify the frequency content among different ground motions.

In this study, particularly, ground motion frequency content has been considered to be the most significant factor contributing to inelastic response of reinforced concrete structures for ground motion with similar intensity. In the following sections, methods for identifying the frequency content of the ground motion discussed and its effect on nonlinear response of SDOF and MDOF systems is evaluated.

3.2 FREQUENCY CONTENT OF A RECORDED EARTHQUAKE GROUND MOTION

3.2.1 Geophysical Parameters Effecting Frequency Content

Most accepted method for the ground motion classification procedure is to use magnitude-distance bins that represent different earthquake scenarios, for example, a large earthquake (M>6.7) occurring at a far distance (R>35km) from the site of the structure. Ground motions are selected so as to match the elastic response spectra (probabilistic hazard response spectrum) at a particular damping ratio to represent the potential seismic hazard defined by the characteristics of the site and source.

Wide range of frequency wave components exist in the composition of any recorded ground motion time-history. The power attained to these wave components at different frequencies varies due to a number of geophysical parameters as accounted above resulting in different spectral shapes. The geophysical parameters that influence the shape of the spectrum (frequency content) mainly are the earthquake magnitude (M), path effects both in terms of source-to-site distance (R) and travel path geology, and the local geological conditions at the recording site. A ground motion accelerogram composed of wave components with limited frequency range has its destructive power on the structures whose natural periods coincides with the predominant period of the record (Kazaz et al., 2006b). These types of records generally exhibit large amplitude (PGA) high frequency oscillations. On the other hand, an accelerogram rich in broad band of frequencies with moderate level amplitude can constitute significant seismic hazard for a wide range of structural periods. Figure 3.1 displaying the theoretical acceleration source spectrum model proposed by Atkinson and Silva (2000) illustrates the amplification of wave components in different frequencies due to increasing earthquake magnitude especially in the low frequency content.

Additionally local site conditions may play significant effect on frequency content of the recorded ground motion. The differences in the shape of earthquake response spectra for different geological conditions such as rock and soils sites have been identified long time ago (Seed et al., 1976; Mohraz, 1976; Newmark and Hall, 1982) and entered the design codes of many countries. This effect displays itself as an amplification or deamplification of particular wave components due to soil nonlinearity especially in softer soils with the level of input motion, rather than a change in the content of these waves. Local site conditions affect peak ground amplitude values.

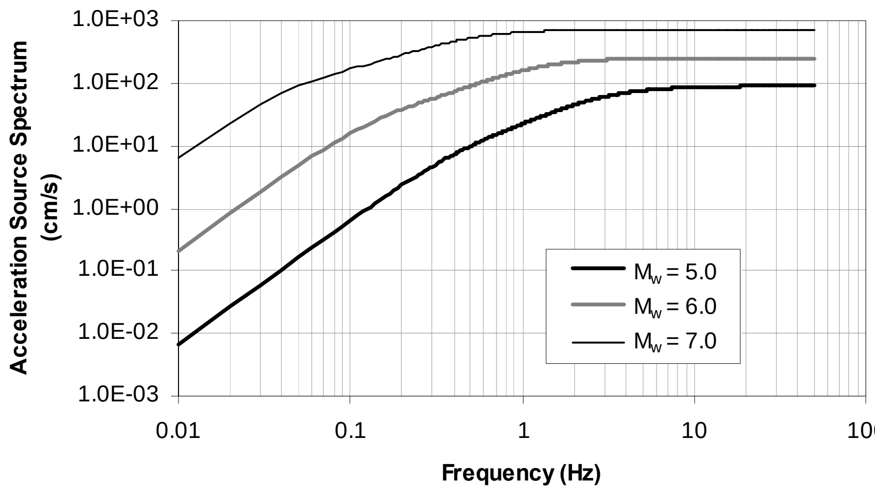

Figure 3.1 Acceleration source spectrum model by Atkinson and Silva (2000)

Among many of the studies available Sabetta and Pugliese (1996) declares the dependence of spectral shape (frequency content) on magnitude (M) and nearly independence on distance (R). Magnitude is a source parameter and the primary factor that determines the frequency composition of radiating waves. Distance is the parameter that causes the attenuation of the amplitude of ground motion and has negligible effect on the frequency content. In support of this statement, Figure 3.2 shows the normalized spectral shapes, using the spectral acceleration attenuation equation proposed by Boore and Atkinson (2008) and constructed from median values predicted for different magnitude, distance and site class categories. It is clear from the figure that while magnitude and site classification significantly affect the frequency content (Figure 3.2(a) and Figure 3.2(b)), source-to-site distance has only minor effect on the spectral shape (Figure 3.2(c)).

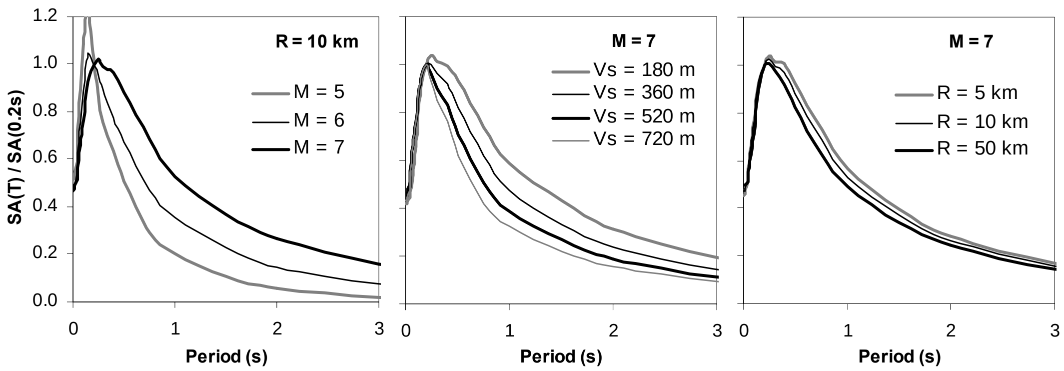

Figure 3.2 Response spectral shapes normalized to the ordinate at 0.2 s
a) for soil sites at 10 km from earthquakes of magnitude 5, 6 and 7, b) for magnitude 7 earthquake at 10 km from the source on different soil profiles represented with shear wave velocities and c) for magnitude 7 earthquake at distances 5, 10 and 50 km from the site. Boore and Atkinson (2008) spectral attenuation model was used.

3.2.2 Magnitude-distance Dependence of Spectral Shape and Demand Predictions

Even though the strong influence of earthquake magnitude on the frequency content and duration of the ground motion very well identified, in some of seismic response studies performed by significant researches (Shome et al., 1998; Medina and Krawinkler, 2003, Iervolino and Cornell, 2005), it was concluded that ground motions selected either arbitrarily or carefully from narrow magnitude-distance bins defining the scenario seismic hazard do not affect the median demand prediction provided that the records are scaled to match the elastic median response spectrum of the bin at the fundamental period of the structure.

Naturally it is expected that nonlinear response measures from a suite of records display wide dispersion even the ground motions used were chosen from a narrow magnitude and distance interval. Shome et al. (1998) stated that, upon their quest to answer the question whether scaled records will produce different nonlinear structural response statistics than those of unscaled records of the same "intensity", using ground-motion bins of narrow magnitude and distance interval that were normalized (or scaled) to the bin-median spectral acceleration at the fundamental period of the structure (i.e. $Sa(T_1)$) reduces the dispersion about median DM predictions compared to unscaled bins (or sets) with the same median damage measures. Moving from this point forward, the most efficient strategy proposed for nonlinear demand prediction from a given event (M and R) is to first use an available attenuation relation to estimate the median spectral acceleration defining the seismic intensity and then to scale the ground motions to the same magnitude of the spectral acceleration of the considered period before carrying out the nonlinear analysis. They also compared the results of the proposed scaling procedure with that of alternative scaling measures and declared the superiority of the proposed method over the alternatives. They also found that the dispersion in the central tendency of the demand measure is significantly large when the scaling methods based on peak ground motion characteristics. The most significant hindrance for the generalization of their results is that their derivations depend strictly on the study of a single MDOF structure which is a simplified stick model. Another crucial conclusion of their study is that upon proper scaling of ground motions the number of runs required the estimate the median response can be reduced by a factor of about 4.

Medina and Krawinkler (2003), declaring the dependence of ground motion frequency content on magnitude and distance, stated that records must be selected in narrow magnitude and distance bins for the scenario earthquake defining certain hazard level in order to reduce bias in the calculated demands. They used 'ordinary ground motions' that are exempt from abnormal characteristics such as the ones posed by near fault ground motion records like directivity-induced velocity pulses. They assumed that the spectral acceleration at the first mode period of the structure ($Sa(T_1)$) (more specifically, the pseudo-spectral acceleration) is the primary ground motion intensity measure (IM). However, they observed that even records are chosen in relatively narrow bins, large dispersion in frequency content still observed. The median spectral shapes for the ground motion bins are comparable as shown in Figure 3.3 and dispersion is rather insensitive to the magnitude-distance combination (bin), but is large at all periods except the scaling period ($Sa(T_1)$). Following from this fact, they concluded that the effect of frequency content on the prediction of demand is dominated by the dispersion of spectral values rather than the median shape of the spectrum.

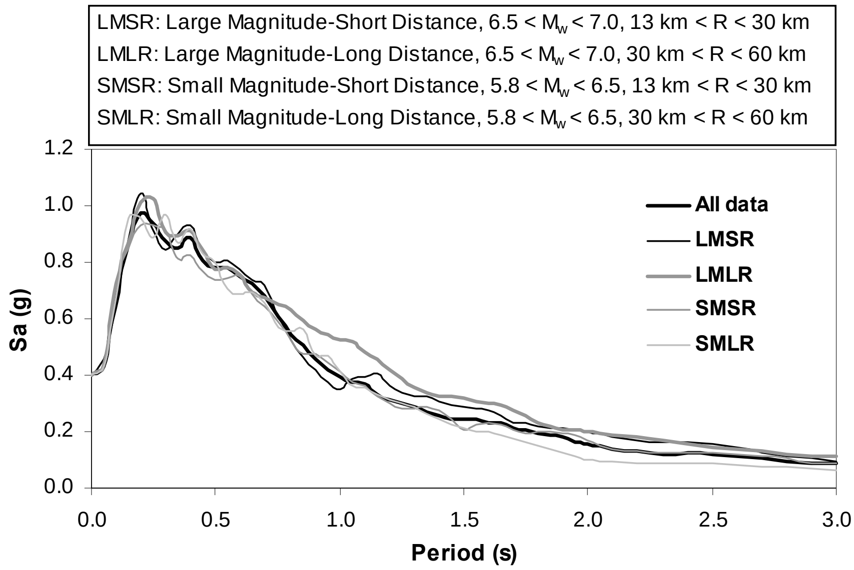

Figure 3.3 Median spectral shapes of four M-R bins, all the ground motions scaled to same PGA.

Recently, Iervolino and Cornell (2005) in their study addressing the question of selection and amplitude scaling of accelerograms for predicting the nonlinear seismic response of structures investigated the characteristics that should be taken into account in accelerograms selection, efficient ways of scaling of records in order to get scenario (target) intensity, and the sufficient size of record sets to obtain reliable demand measures. They also took into consideration the structural period and backbone sensitivity in nonlinear demand prediction. The ground motions selected for the study was organized under two general groups, the target set and arbitrary set, each having five sub-bins. The arbitrary set records were selected simply at random from a catalog with a comparatively wide magnitude and distance range. The target sets for the record selection study were designed to be representative of a specific scenario event (M and R) that might be the realistic threat to a particular site, here a moment magnitude 7 at 20 km, defined as the closest distance to fault rupture. All the records were from 5 events in the magnitude range of 6.7 to 7.4 and in the narrow distance range of 20 ± 5 km. As done in the previous studies (Shome et al. 1998), for each structure considered, these records in the sample target sets were scaled to their overall median spectral acceleration at the first-mode period.

Depending on the results calculated, Iervolino and Cornell (2005) stated that M and R play at most only minor roles in affecting nonlinear displacements of structures and found no consistent evidence to suggest that it is necessary to take great care in the selection of records with respect to such factors, a general conclusion quantified in various ways in the studies of Shome et al. (1998), Carballo and Cornell (2000), Medina and Krawinkler (2003), and Jalayer (2003). This is to say nonlinear structural displacements are insensitive to R and the slightly sensitive to M. It was also mentioned that, cases that may display some sensitivity to magnitude include tall buildings with important second-mode effects and very short period systems.

As seen, except the well established attenuation phenomena of the ground motion amplitude as moving far away from the source, no clear indiscrimination can be made on the frequency content and the duration of strong ground motion depending on the magnitude and distance. In fact, a ground motion intensity measure when evaluated from the structural engineer point of view must be instructive in terms of possible earthquake loads applied on the structure rather than its seismological properties. Iervolino and Cornell (2005) states that "*Lack of knowledge of the influence of seismological parameters on the structural response has driven the seismologists to be prudent and assume that all features (magnitude, faulting style, etc.) matter to structural response, and so they do their best to provide records accordingly*". That is to say priority must be given to the consequences (PGA, PGV, $Sa(T_1)$) of the earthquake event in ground motion selection rather than it's causes (M and R).

3.2.3 A Key to the Frequency Content: Response Spectrum

There are several ways to identify the frequency content of a ground motion. Ground motion frequency content can be solely determined independent on structural characteristics such as Fourier spectrum analyses or it can be determined coherently together with the dynamic properties of structures utilizing spectral analyses of single-degree-of-freedom oscillators. It was widely accepted (Rathje et al., 1998; Cordova et al., 2001; Baker and Cornell, 2005) that significance of frequency content can be best identified through the use of acceleration response spectrum of a ground motion record since it incorporates the knowledge of the structure. It is also admitted that frequency content of ground motion is reflected in the shape of acceleration response spectrum (Baker and Cornell, 2005 and 2006).

In order to understand why spectral shape could affect the structural response, it is compulsory to understand the response of a MDOF structure ranging from elastic to inelastic stage. Elastic response of MDOF structure is characterized by the first mode period and quantified in terms of spectral acceleration calculated at this period ($Sa(T_1)$). However besides several parameters, inelastic behavior of multi-degree-of-freedom structures exposed to earthquake base excitations is governed by two major phenomenons, which are namely reduction in stiffness as a result of degradation in the mechanical properties of the structure due to reversed cyclic excursions and excitation of higher modes contributing to dynamic response. While the former leads to lengthening of the structural period resulting in softer response with increased displacement demands, the later causes alterations in the inertia force distribution resulting in increased base shear demand. Under continues inelastic yield excursions Kazaz and Yakut (2006) displayed that fundamental vibration period of a shear wall structure can increase to a value that is two times of the initial. Thus, given two records with the same $Sa(T_1)$ value, the record with higher Sa values at periods other than T_1 will tend to cause larger displacement demands in inelastic systems. It will be shown that response of MDOF structures is highly sensitive to peaks and valleys on the acceleration response spectra.

In Figure 3.4(a), elastic acceleration response spectrum for Ito-Oki EW component record (PGA is 0.198g) used in analyses of CAMUS wall and its scaled forms are given. Roof displacements obtained from nonlinear time history analysis results yielded 1.78 mm, 6.22 mm, 11.39 mm and 25.01 mm top displacements for peak ground accelerations of 0.198g, 0.386g, 0.482g and 0.578g, respectively. Increasing PGA 25 percent (from 0.382g to 0.482g) caused 83 percent increase in global displacement, whereas increasing it 50 percent (from 0.382g to 0.578g) resulted in 300 percent increase in global response. The explanation for this situation is that as the intensity of the ground motion increases, the elongation in the period (T_f) also increases due to increased level of inelastic deformations. Due to shift in the fundamental elastic period (T_i), the system moves to high amplitude acceleration region and is exposed to larger earthquake forces. For yielding systems, when ground motions conforming to the above description were encountered and the yield level was exceeded, global deformation demands increased dramatically. If the yield path or elongation path of the period coincides with the ascending leg of the spectrum, this means significant deformations can be induced on the structure depending on the base shear strength. ($\eta = V_y/W$). Meantime, if elongation path is on the descending leg of the spectrum, although the fundamental period (T_i) can coincide with very high spectral accelerations, unexpectedly low global responses can be obtained depending on the slope of spectrum along the yield path.

The ground motion Run2 and its scaled forms are good examples of the situation described above, and the illustration made for the Ito-Oki case is also done for Run2 in Figure 3.4(b). Note that, for nearly the same level of PGA the linear deformation potential of the Run2 record is larger than Ito-Oki ground motion. Two ground motions have PGA of 0.578g and 0.6g, and spectral acceleration of 0.748g and 1.216g at the fundamental period of the structure, $Sa(T_i)$, for Ito-Oki and Run2 records, respectively. But the inelastic deformations obtained from two cases were totally different; revealing that the structure subjected to Run 2 motion scaled to 0.6g remained almost linear (Δ_{top}=6.70 mm) after the excitation, where as significant inelasticity was imposed on the structure in Ito-Oki case (Δ_{top}=25.01 mm).

As the above example demonstrated, during nonlinear dynamic analysis initial frequency of the system decreased from 7.2 Hz to 6~3 Hz depending on the level of inelastic deformations attained by the structure due to intensity of the applied ground motion. It is obvious that different ground motions will yield different spectral shapes. The slope of the spectrum can be positive (ascending) or negative (descending) beyond the initial period of the structure as seen in Figure 3.4. An ascending spectrum is expected to yield larger inelastic demand on the structure compared to a descending one, even if the spectral acceleration corresponding to elastic period of the structure is smaller for ascending type spectrum.

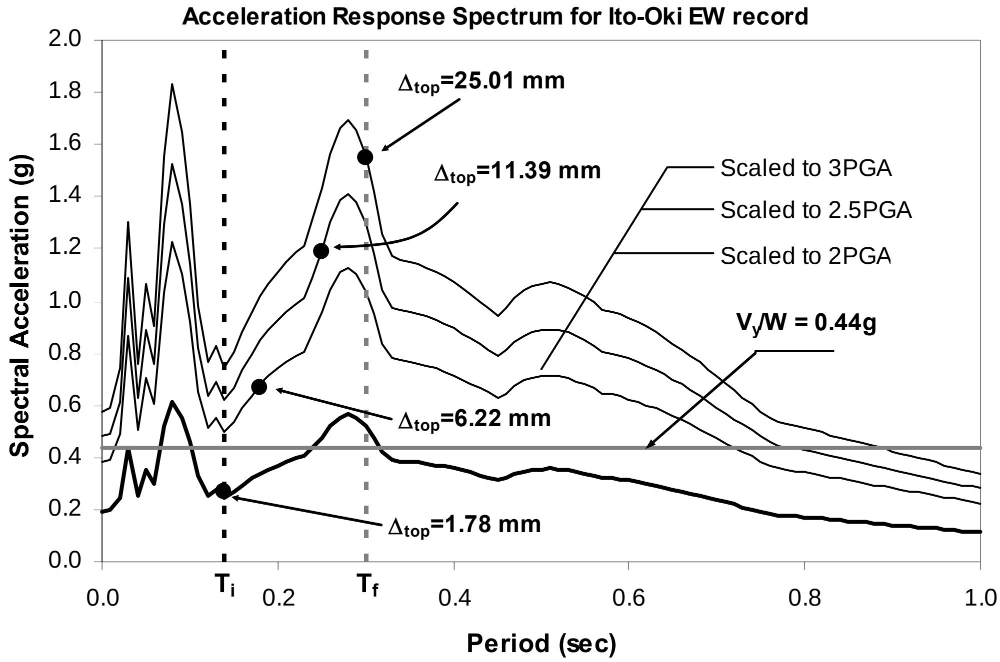

(a) Ito-Oki EW record

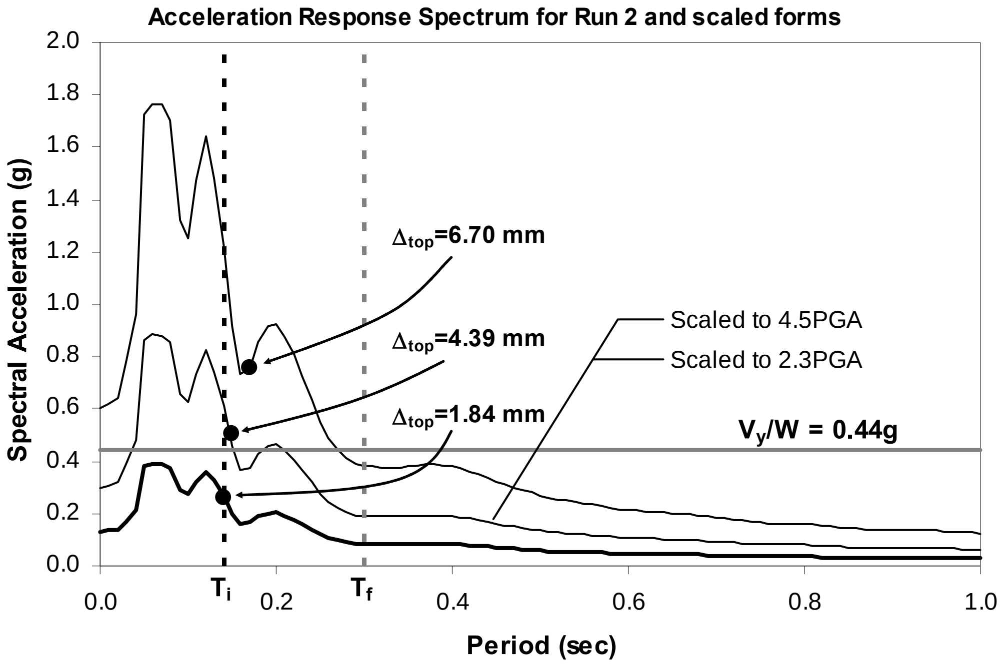

(b) Run2

Figure 3.4 Effect of period elongation on structural response

Previously, Derecho et al. (1978b) in a parametric study on a 20-story isolated cantilever structural wall investigated various structural and ground motion parameters in terms of their effects on the dynamic inelastic response of isolated walls. Among the structural parameters considered are fundamental period (T_1), yield level (M_y or V_y), yield stiffness ratio (α), character of the hysteretic force-displacement loop (reloading and unloading stiffness) damping, stiffness and strength taper, and degree of base fixity. Also considered are the three parameters characterizing strong-motion accelerograms: duration, intensity, and frequency content. Doing so, they aimed to identify the most significant variables that gave way to calculation of estimate of strength and deformation demands in critical regions of structural walls as affected by the significant parameters.

For input motions they selected a small number of accelerograms from among the recorded and artificially generated accelerograms in a previous study by Derecho et al. (1978a). In that preceding study, the accelerogram classification was performed in terms of the general features of its velocity spectra relative to the initial fundamental period of the structure. They classified ground motions into three groups according to shape of velocity response spectrum. A " peaking (0)" classification indicates that the 5%-damped velocity response spectrum for this accelerogram shows a pronounced peak at or close to the fundamental period of the structure considered (in this case, T_1 = 1.4 sec.). A "peaking (+)" classification indicates that the peak in the velocity spectrum occurs at a period value greater than that of the fundamental period of the structure. A "broad-band" classification refers to an accelerogram with a 5%-damped velocity spectrum which remains more or less flat over a region extending from the fundamental period of the structure to at least one second greater.

All the structures analyzed were subjected to 10 seconds of ground motion. Housner's (1959) "spectral intensity" measure, defined as the area under the 5%-damped relative velocity response spectrum between periods of 0.1 and 3.0 seconds, was used to normalize the input motions multiplying by a factor to yield spectrum intensity equal to some percentage of reference spectrum intensity, SI_{ref}. The reference spectrum intensity used was that corresponding to the first 10 seconds of the NS component of the 1940 El Centro record (SI_{ref} = 178 cm). Velocity spectrum of normalized ground motions are displayed in Figure 3.5.

Recognizing that the extent of yielding is a function of the earthquake intensity, the yield level of the structure, and the frequency characteristics of the input motion, it was stated that these factors must be considered in selecting an input motion for a given structure to obtain a reasonable estimate of the maximum response. For the same intensity and duration of the ground motion, significant increases in response can result from an input motion having the appropriate frequency characteristics relative to the period and yield level of the structure. It was stated that when significant yielding that would appreciably alter the effective period of vibration is expected in a structure, an input motion with a velocity spectrum of the “broad band ascending” type is likely to produce more severe deformation demands than other types of motion of the same intensity and duration. For cases where only nominal yielding is expected, “peaking” accelerograms tend to produce more severe deformations. The considerations are important in determining near-maximum, or in specifying input motions for use in the analysis of particular types of structures.

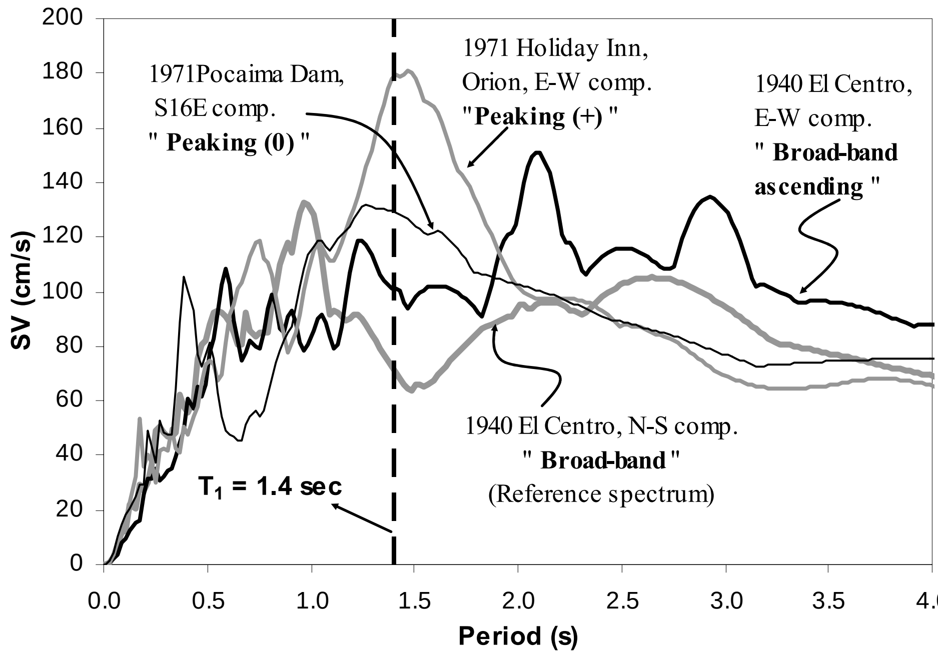

Figure 3.5 Velocity response spectrum of ground motions used in the study of Derecho et al. (1978) describing the characteristics of the ground motions according to spectral shape.

It was found that the effect of ground motion duration was not too significant on the response and its major effect is to increase the cumulative inelastic plastic deformations. They notified that shear force fluctuates more rapidly compared to the moment at the base of the wall or deformation at the top, which is an indication of the greater sensitivity of the shear force to higher modes of response. Because of this, the maximum base shear force is strongly dependent on the ground motion. The criticality of response with respect to shear will depend on the relationship of the frequency characteristics of the input motion to the significant higher effective mode frequencies of the yielded structure.

3.3 METHODS TO IDENTIFY THE SPECTRAL SHAPE

In the view of above discussion, it is seen that evaluating the frequency content of a seismic ground motion is a two sided issue; one is due to characteristics of a specific earthquake (magnitude, faulting type, source distance, etc.) each accelerogram has its own inherent frequency nature, and complementary to this fact structural response is directly related to the frequency content of ground motion through the dynamic properties (natural vibration period) of the structure. So, ground motion frequency content can be solely determined independent on structural characteristics or by utilizing spectral analyses of single-degree-of-freedom oscillators, it can be determined coherently together with the dynamic properties of structures. Three procedures become more pronounced at this stage to analyze the frequency content:

- *Fourier spectrum:* The ground motions can be expressed as a sum of harmonic (sinusoidal) waves with different frequencies and arrivals (phases). The Fourier amplitude spectrum (FAS) is capable of displaying the frequency content of the ground motion.

A Fourier spectrum where the amplitudes are accumulated in a narrow band of frequencies implies that the motion has a dominant frequency (period) that can produce a smooth, almost sinusoidal time history. Meanwhile, a broadband spectrum corresponds to a motion that contains distinct frequencies producing a more jagged irregular time history.

For any given time series (*f(t)*) with finite duration (t_d), Fourier spectrum is

$$F(\omega) = \int_0^{t_d} f(t) e^{i\omega t} dt \tag{3.1}$$

and the Fourier amplitude is

$$|F(i\omega)| = \left\{ \left[\int_0^{t_d} f(t) \cos \omega t \right]^2 + \left[\int_0^{t_d} f(t) \sin \omega t \right]^2 \right\}^{1/2} \tag{3.2}$$

with the Fourier phase angle

$$\varphi(i\omega) = \frac{\left[\int_0^{t_d} f(t)\sin\omega t dt\right]}{\left[\int_0^{t_d} f(t)\cos\omega t dt\right]} \tag{3.3}$$

- *Elastic response spectrum:* Under a postulated ground motion, a plot of the absolute peak values of response quantities (acceleration, velocity and displacement) as a function of vibration period (or frequency) of a SDOF system for a fixed viscous damping ratio, ξ, is called elastic response spectrum.

Spectral intensity measures are the most widely used intensity indicators to determine the damageability of a ground motion since they incorporate the structural characteristics to the decision process.

- *From amplitude parameters*, ground motion acceleration to velocity ratio (A/V).

Next a spectral intensity measure will be introduced. Then it will be displayed that A/V ratio defined in terms of ground motion parameters can be used to differentiate the ground motions according to frequency content.

3.4 A SPECTRAL INTENSITY MEASURE FOR DEMAND PREDICTION

Researchers like Malhotra (2002) and Cordova et al. (2000) stated that seismic hazard intensity measures quantified on the basis of acceleration response spectrum ordinate of the first mode structural period may result in significantly different inelastic response, depending on the slope of the spectra at lengthened periods, such as the situation illustrated in Figure 3.4. Cordova et al. (2000) proposed a second intensity parameter to account for the spectral shape (or frequency content) as the ratio of spectral accelerations at two periods, first mode period (T_1) and longer period (T_f) that represents the inelastic (damaged) structure. While, the spectral acceleration at the first mode period, $Sa(T_1)$, correlates well with the level of elastic structural response reflecting the spectral intensity, the parameter $R_{Sa} = [Sa(T_f)/Sa(T_1)]$ reflect the spectral shape so as the damage potential in the inelastic phase of the response. However, the parameter is sensitive to peaks and valleys in the spectrum, which reduces the reliability of the proposed intensity measure.

Kazaz et al. (2006b) investigated the seismic performance of CAMUS wall described in the previous chapter by performing nonlinear time-history analysis under a suite of ground motions of diverse intensity. The result of these analyses led to several useful and interesting observations. In parallel to findings of the previous researchers, it is seen that ground motions that have an increasing spectral trend beyond the fundamental period of the structure, produced higher seismic demands as compared to decreasing or broad trends. It can be proposed that the shape of the response spectrum along the period elongation path (increasing or decreasing trend in the spectral acceleration) reveals the damage potential or severity of the seismic demand in view of seismic capacity of the structure. There exist several spectral intensity measures that quantify the damage potential of ground motions (Housner, 1959; Martínez-Rueda, 1998). Housner proposed a spectral intensity defined as the area under the velocity spectrum over a period range from 0.1 to 2.5 s.

$$I_H = \int_{T=0.1s}^{2.5s} S_V(T,\xi)dT \tag{3.4}$$

In analogy with Housner's equation [Eq. (3.4)], for short-to-medium period range of the spectrum and for stiff structural walls, following relation for the new intensity measure was proposed relying on the hypothetical acceleration response spectra plotted in Figure 3.6 (Kazaz and Yakut, 2006):

$$I_a = \int_{T_i}^{T_f} Sa(T,\xi)dT \tag{3.5}$$

Eq. (3.5) calculates the area below the acceleration response spectrum between the fundamental period (T_i) and calculated elongated period (T_f). Normalizing the calculated area by dividing to the area below the yield base acceleration level (A_y), a dimensionless intensity measure can be obtained, which is given by Eq. (3.6).

$$I_a = \frac{1}{(T_f - T_i)A_y} \int_{T_i}^{T_f} Sa(T,\xi)dT \tag{3.6}$$

By utilizing response frequency analysis, the softened period (apparent response period) of the CAMUS wall structure was calculated for each ground motion case from the calculated top acceleration and displacement response. When the softened period was plotted against the damage index (I_d: global top displacement) a perfect correlation was obtained. A linear trend was observed between the damage experienced by the structure and elongation in the fundamental mode period (Figure 3.7) which may be attributed to dynamic behavior of shear-wall type structures. Figure 3.7 also supports the findings of the previous research, Lestuzzi et al.(2004) and Brun et al. (2003), that the final stiffness reduces to 30~15 percent of the initial stiffness due to structural deterioration for shear walls. Depending on these analyses results, the upper limit for the period elongation of medium height shear walls can be taken as $T_f^{max} \approx 2T_i$.

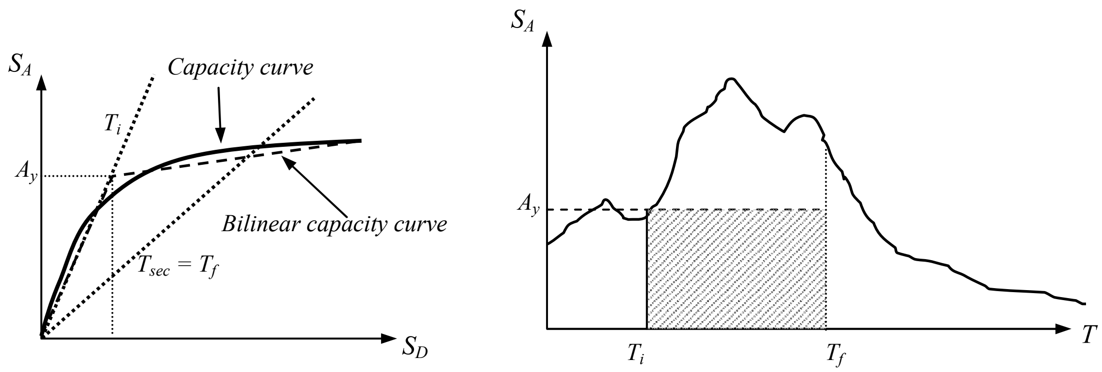

Figure 3.6 Pictorial description of the spectral intensity measure $\boldsymbol{I_a}$

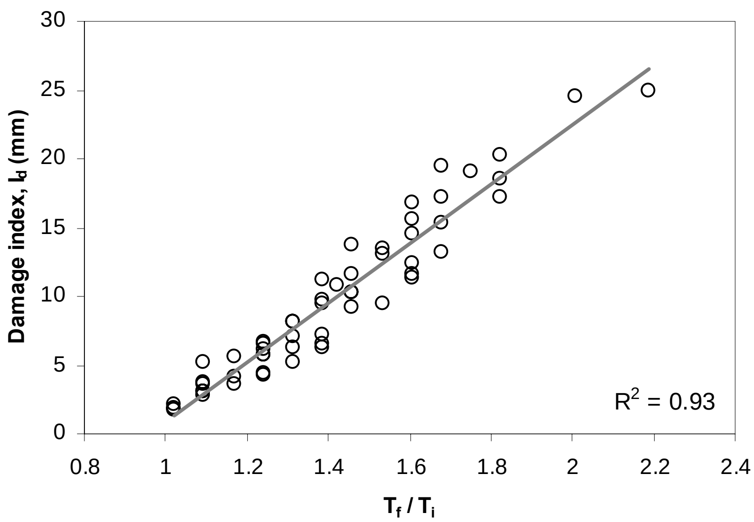

Figure 3.7 Correlation of elongated period normalized with respect to initial period with selected Damage Index.

In Figure 3.8, the proposed intensity measure (***I*$_a$**) was calculated by using the elongated periods for each dynamic analyses cases and plotted against the damage index, I_d, top displacement. It sis seen that the proposed spectral intensity measure is useful in comparative evaluation of damage potential of ground motions.

As it is understood from the above explanations, the impediment of the proposed procedure is the estimation of the softened period that will hold for the effective period of SDOF system. If no knowledge of the lengthened period exists a value equal to $2T_i$ can be adopted or the value of T_f can be calculated using the procedures defined in the works of Kazaz and Yakut (2006) and Kadas et al. (2008). Improved spectral intensity formulations that were tested for wide range of structural configurations are available in Kadas et al. (2008).

This spectral intensity measure is especially useful in getting a notion about the possible level of inelasticity that the system will experience when there is a number of candidate ground motions available to be used as seismic input in nonlinear time history analyses, so reducing the number of ground motions by evaluating their severity for the structure under consideration.

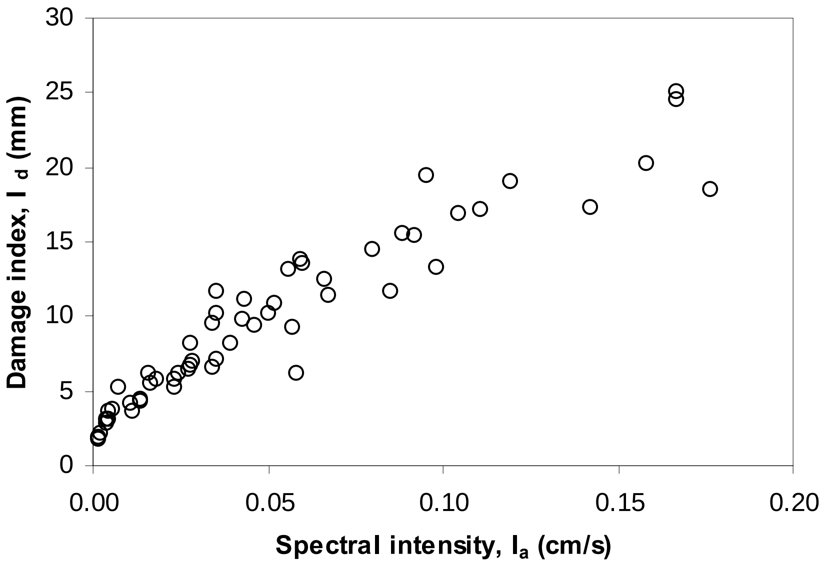

Figure 3.8 Correlation of the intensity measure with the top displacement

3.5 A/V RATIO

In the earlier earthquake engineering practice, the maximum horizontal ground acceleration is the parameter usually specified for design and a realistic estimate of the ground velocity is obtained from the mean *V/A* ratios of the group with the larger peak ground acceleration. Together with appropriate amplification factors peak ground acceleration and velocity is used to construct the elastic design spectrum (Newmark and Hall, 1982). This philosophy was adopted in some design codes like 1985 Canadian Code to construct the elastic design spectrum (Basham et al., 1985). At this point it has to be mentioned that in the research literature both terminologies of A/V and V/A ratio were adopted in several studies. Nevertheless, for the sake of consistency through the text and to provide the reader with instant comparison among the values presented, the terminology acceleration to velocity ratio (A/V) and units of (s^{-1}) is used while referring to results in different studies, even (V/A) and different units were used in the original study.

3.5.1 Past Research on A/V Ratio

In earthquake engineering literature, A/V is generally used to emphasize the effect of local soil conditions on the ground motion parameters (Mohraz et. al, 1972; Mohraz, 1976; Seed et al., 1976; Zhu et al., 1988a). In the early seventies the Unites States Atomic Energy Commission funded a comprehensive study conducted by Mohraz et al. (1972) for Newmark Consulting Engineering Services to investigate the vertical and horizontal elastic response spectra for nuclear facilities. In this study V/A ratio was calculated and averaged for rock and alluvium sites using recorded ground motion time history of two horizontal and one vertical component from fourteen earthquakes. The average values obtained for A/V ratio were 13.79 and 8.05 for rock and alluvium sites respectively.

Later in a significant study by Mohraz (1976), the effects of geological conditions on the elastic spectra and also on the ground motion parameters, such as peak ground acceleration (A), velocity (V) and displacement (D) and A/V ratio were investigated. Mohraz considered four site conditions: alluvium deposits, rock deposits, sites with less than 10 m of alluvium underlain by rock deposits, and sites located on 10 m to 60 m of alluvium underlain by rock deposits. This classification was done due to only a few stations shear wave velocities estimates were available at the instant of the study. A total of 54 earthquake records (three components from each record) from 46 stations in 16 seismic events were considered in that study. Mohraz performed a detailed statistical study on the ratios of the ground motion parameters and the average A/V values calculated for each of the four site conditions for the group with the larger peak ground acceleration were found to be 7.57, 14.30, 10.44 and 11.70 respectively for the sites classified above. The values indicate that the A/V ratio for rock sites is substantially higher than those for alluvium. The ratios for the two alluvium layers underlain by rock are between those for rock and alluvium. Although the calculated average A/V ratio for two alluvial sites underlain by rock are close, sites with thicker alluvium layer produced larger A/V ratio which is opposite to expectations. However, investigation of the records composing these two site class data bins explains the situation. The records from stations on less than 10 m of alluvium underlain by rock deposits were all from San Fernando earthquake (1971) with M_w=6.5. On the other side, the half of the records from stations on 10 to 60 m of alluvium underlain by rock deposits were recorded in events with magnitude smaller than 6. Since smaller event are richer in high frequency content affecting A much more than V, the A/V ratio calculated from small earthquakes posses larger values. So the discrepancy above arises from this situation, for which any explanation brought by Mohraz (1976). These findings give the clues how magnitude of earthquake and site geology affects the A/V ratio.

Contemporaneously Seed et al. (1976) studied the influence of local geological conditions on the attenuation of peak accelerations and peak velocities with increasing distance from the source of energy release for earthquakes with a magnitude of about 6.5 occurring in the western part of the United States. Three site categories classified as: rock sites, where rock was considered to be shale-like or sounder in characteristics, as evidenced by a shear-wave velocity greater than about 760 m/s, stiff soil conditions, where rock as defined above was overlain by less than about 45 m of stiff clay, sand and gravel, deep cohesionless soil conditions where rock as defined above was overlain at least 76 m of generally cohesionless soils. They investigated the relationships between the A/V ratio for different geological conditions and distances from the source of energy release. The results indicted that while there is some variation in the A/V ratio with distance from source, the values of this ratio vary considerably with local geological conditions. The calculated A/V ratio for rock, stiff soil conditions and deep cohesionless soils took the values 14.85, 8.58 and 7.02 respectively. The degree of agreement between these results of independent studies was noteworthy. The results of these studies were presented in Table 3.1.

Depending on the results presented in Table 3.1, it can be said that the A/V ratios from different studies characterizing rock and soft soil sites are quite similar. These values are representative of an event approximately 6.5 in magnitude. A/V ratio for the sites of soil deposits with varying thickness underlain by rock formations is difficult to determine.

Table 3.1 Ground motion acceleration to velocity ratio from different studies

		Based on Mohraz et al. (1972)		
Site condition	Rock	Alluvium		
A/V (s^{-1})	13.79	8.05		
		Based on Mohraz (1976)		
Site condition	Rock	Less than 10 m alluvium underlain by rocks	10 to 60 m alluvium underlain by rocks	Alluvium
A/V (s^{-1})	14.30	10.44	11.70	7.57
		Based on Seed et al. (1976)		
Site condition	Rock	Stiff soil conditions	Deep cohesionless soils	
A/V (s^{-1})	14.85	8.58	7.02	

A/V ratio was also used to identify the characteristic period (where constant acceleration and constant velocity plateaus meet) of impulsive and harmonic type ground motions (Seed et al., 1976; Shimazaki and Sözen, 1984; Tso et al., 1992; Sucuoğlu and Nurtuğ, 1995). In these studies the differences in predominant period of the ground motions were attributed mainly to different geological conditions indicated by larger A/V values for rock sites and smaller A/V ratios for soil sites. However, even the ground motions were selected among the ground motions recorded on similar geological conditions in order to minimize the influence of local geological conditions on ground motion characteristics, there is still significant variation observed in the A/V ratio (Zhu et al., 1988a). So before further elaborating the effect of A/V ratio on the structural damage, the parameters that contribute to A/V ratio must be identified clearly.

Sucuoğlu et al. (1998) investigated the effect of A/V ratio together with the effective duration of ground motion on the damage potential of strong ground motions and concluded that these two basic ground motion intensity parameters significantly influence the damage potential of earthquake ground motions. They also argued that these two parameters were not represented appropriately by the spectral definitions of earthquake excitations in seismic design codes.

Acceleration to velocity ratio (A/V) has been extensively studied particularly as a measure of the frequency content of the ground motion. Zhu et al. (1988a) discussed the significance of A/V ratio as a parameter for ground motion characterization from a seismological point of view. Tso et al. (1992) have concluded that this ratio provides indications of the dynamic characteristics of earthquake ground motion. It was also concluded that the A/V ratio of ground motions correlates well with the magnitude-epicentral distance relationship of motion and gives an indication of the relative frequency content and duration of ground motion.

Local geological condition also has an effect on the A/V ratio with the lowest value for deep cohesionless soil, higher for stiff soil and the highest for rock. In terms of structural responses, this ratio reflects information regarding the significant frequency content of the input earthquake motions.

The logic lying behind the A/V ratio is that, relative highness of velocity with respect to acceleration is an indication of existence of long period wave components that reflects the magnitude and frequency content of the earthquake and cause structural damage since natural period of medium to long period structures can overlap periods of these waves resulting in dynamic amplification of displacements.

The destructiveness of apparent pulses in acceleration and velocity traces of recorded ground motions has been long ago identified by different researchers. Long acceleration pulses which yield large ground velocities lead to significant structural response (Hudson, 1979). Anderson and Bertero (1987) pointed out that wide acceleration pulses are especially damaging, if the time duration of the pulse is large compared with the natural period of the structure.

In favor of these findings, Kazaz et al. (2006b) analyzed the nonlinear behavior of an isolated shear wall through dynamic investigation and observed that ground motions with evident acceleration pulse produce significantly larger displacements than the ground motion with very large PGA and highly irregular high frequency accelerogram. It was also reported that ground motions with larger predominant period causes larger displacement demands on short period systems.

Sucuoğlu and Nurtuğ (1995) stated that ground motion records with a dominant acceleration pulse usually possess high V/A ratio. If the peak ground velocity is reached immediately following the dominant acceleration pulse in the accelerogram, then the V/A ratio indicates the average duration of the pulse. It is related to the duration of dominant acceleration pulse in impulsive ground motions and dominant acceleration period in nearly harmonic ground motion records. The coherent long-period waves cause the PGV/PGA ratio to become larger, thus making the constant acceleration part of response spectra longer.

Akkar and Özen (2005) compared it with other ground motion intensity measures to estimate the structural damage. They investigated the influence of peak ground velocity on deformation demands of SDOF systems. Total of 60 ground motions were used in that research. The ground motions were recorded on firm sites (site class C and D according IBC 2000). Ground motions are grouped in three bins that were organized with respect to different PGV velocity ranges. The bins are organized such that the first bin is composed of records with PGV less than 20 cm/s, second bin consist records with PGV ranging from 20 to 40 cm/s and in the third group the ground motions have PGV ranging from 40-60 cm/s.

They calculated the correlation coefficient between the spectral displacement and PGV, so as PGA and PGA/PGV ratio at period T_i for a spectral period range of 0.1-4 s. They concluded that PGV has much better performance as a ground motion intensity measure in decreasing the dispersion in deformation demands due to record-to-record variability compared to both PGA and PGA/PGV ratio. However, they misinterpreted a very significant point in the evaluation of A/V. While both PGA and PGV are ground motion amplitude parameters and PGV in some sense reveals information about the frequency content of ground motion (large PGV indicates wide acceleration pulses), PGA/PGV ratio only tells about the frequency content of the ground motion (e.g., (PGA=150 cm/s^2)/(PGV=15 cm/s)=10 s^{-1} or (PGA=450 cm/s^2)/(PGV=45 cm/s)=10 s^{-1}). As calculated both ground motions have the same acceleration to velocity ratio, but they are far different in terms of destructive power. So, their conclusion is disputable. .

3.5.2 Limits of A/V Ranges

Due to large dispersion in the peak ground motion amplitude values, even if they were recorded at the same seismic event, the calculated acceleration to velocity ratio value can vary significantly. Relying on two previously conducted studies, the limits of A/V ranges are identified. Zhu et al. (1988a) stated that review of the previous studies and examination of earthquake records reveal the three categories of earthquake ground motions may be identified,

a) '*normal*' ground motions having significant energy content over a broad range of frequencies and exhibiting a highly irregular acceleration pattern;
b) ground motions exhibiting large amplitude, high frequency oscillations in the strong-motion phase of the motion;
c) ground motions containing a few severe, long duration acceleration pulses.

Depending on this classification of ground motions, Zhu et al. (1988a) selected 36 horizontal ground motions from western United States earthquakes and categorized them in three groups each containing 12 ground motions based on their A/V ratio. A/V ranges defining each group is presented in Table 3.2.

Table 3.2 Limits of A/V ranges due to Zhu et al. (1988a)

Bin	**A/V range**
Normal A/V range	0.8 g/m/s ≤ A/V ≤ 1.2 g/m/s
High A/V range	< 1.2 g/m/s
Low A/V range	> 0.8 g/m/s

The highly irregular acceleration pattern in ground motions of the first category would generally result in intermediate A/V ratios and acceleration spectra similar to the standard design spectrum defined by Newmark and Hall (1982) that is generally associated with so-called 'normal' severe earthquake ground motions at moderate distances from the causative fault. Therefore, A/V ratio is a useful, yet simple, parameter to distinguish 'abnormal' ground motions from 'normal' ground motions. This classification disregards any implication of earthquake magnitude on A/V ratio.

Meskouris et al. (1991), regarding damage potential of ground motions according to characteristics such as strong motion duration, central period and quotient of maximum ground acceleration to maximum ground velocity, has proposed a classification of probable records into one of the three types (S, M, and L) as given in Table 3.3. L-type motions (low frequency, long duration, high energy) are characterized by a great number of load reversals and accordingly high demands on nonlinear reserves, while S-type records (high frequency, short duration, and low energy) do not pose as serious a threat to structural integrity.

While for S- and M-type excitations usual response spectrum based design and analysis techniques in conjunction with detailing requirements are sufficient, the damage evaluation of important buildings subject to L-type excitations should be investigated by nonlinear direct integration.

The A/V classification performed by these previous researchers only establish general limits to evaluate the damage potential due to this classification, noticing Meskouris et al. (1991) provides information about the duration of the ground motion also. However, A/V ratio can be classified to represent the seismic intensity of a particular seismic hazard scenario taking into consideration of magnitude and site effects. At the rest of this study all the efforts will be due to achieve this task.

Table 3.3 Proposed classification of ground motions by Meskouris et al. (1991)

	S-Type	M-type	L-type
Duration t_d (s)	< 10	$10 < t_d < 15$	> 15
Central Period T_o (s)	< 1.0	$1.0 < T_o < 1.2$	> 1.2
A_g / V_g (g/m/s)	< 1.0	0.8 to 1.2	< 0.8

3.5.3 Identification of A/V Ratio due to Magnitude and Site Effects

In previous section limits were established on A/V ranges to interpret the severity of any ground motion due to frequency content. How these limits conform to the available ground motion data is a matter of issue. It is given that for a given site and earthquake source, the three parameters that can vary are magnitude, distance and frequency content. If we decompose these parameters to an individual level we get the following picture. The spectral shape (frequency) content is dependent on magnitude and nearly independent on distance. However, local site conditions may play significant effect on frequency content of the recorded ground motion and affect both PGA and PGV. Since the maximum ground velocity is a much more stable parameter with a more determinate upper bound than the maximum ground acceleration (Newmark and Hall, 1969) and the integration process tends to dilute high-frequency components of the motion and enhance low-frequency components, A/V ratio calculated from these parameters will be more sensitive to PGA.

Two significant and vital issues arise at this point due to complex relation between the earthquake magnitude and site amplification, the lingering uncertainty as to whether the degree of amplification varies with the level of input motion and the influence of frequency content of ground motions on site amplification. Without entering too much into the field of seismologist, an answer will be sought.

In order to shed more light on this issue a simple statistical analyses conducted and interesting conclusions derived. From COSMOS web site ground motion information including magnitude (M), distance (R), shear wave velocity at the upper 30 m of the site ($V_{s\text{-}30}$), PGA and PGV values are downloaded. Data of 2584 strong ground motion horizontal components from 99 earthquakes of magnitudes ranging from 4 to 7.9 is downloaded. This data was subjected to a simple statistical evaluation. Figure 3.9(a) displays increasing trend in the amplitude of ground motion with the increasing earthquake magnitude. In Figure 3.9(b) the amplitude of ground motion is plotted with respect to closest distance to fault rupture displaying the attenuation effect of distance.

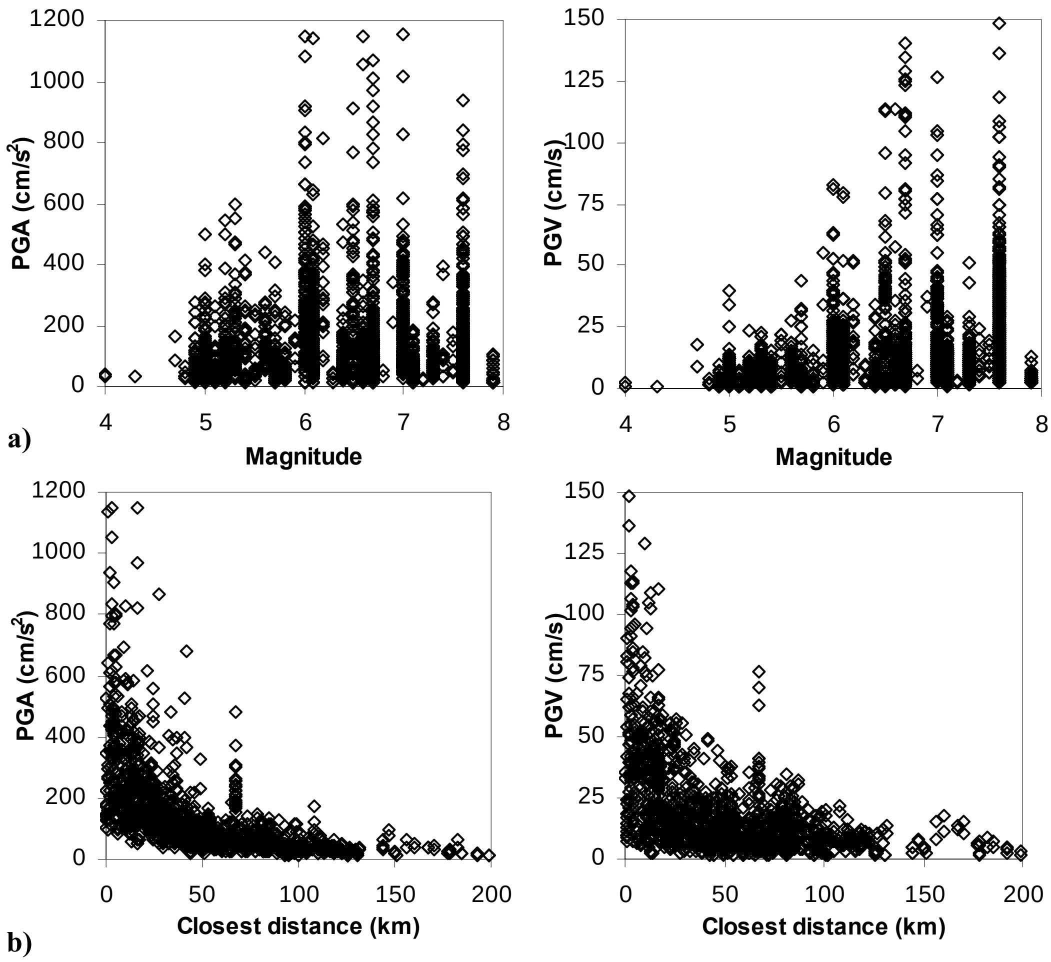

Figure 3.9 Histograms of data downloaded from COSMOS site showing the relation of PGA and PGV with M and R.

Naming the three parameters affecting the frequency content of ground motion as magnitude, site to source distance and geological conditions at the site, the relation of these parameters with frequency content as defined by A/V ratio in this study is plotted in Figure 3.10. Figure 3.10(a) gives the plot of A/V ratio against magnitude showing the magnitude dependence of frequency content. Figure 3.10(b) displays the A/V ratio plotted against the distance. Although it is not reflected so powerful in the figure, the trend in densely clouded data points displays a slightly decreasing trend. This trend can be attributed to the fact that the attenuation of velocity with distance is generally slower than the attenuation of acceleration and as the distance increase the high frequency content filters out leading to more stable A/V ratio. Therefore, the A/V ratio would be low for ground motions at a large distance from a major earthquake; and it would be high for motions near an earthquake source. In Figure 3.10(c), the variation of A/V ratio with shear wave velocity is plotted. Shear wave velocity is used to define the site class. From this figure no clear discrimination can be made with regards the influence of site geology on frequency content of the ground motion except the reality that there is a significant variation.

It is obvious that these figures inherit crude statistical information, however reminding that the intention in plotting these figures is not to display an exact relation, it's rather to declare a tendency observed between the frequency content of ground motion defined in terms of A/V ratio and magnitude. From these figures it is possible to declare the pronounced affect of earthquake magnitude on the frequency content. However, to throw more light on this blurred subject, combining Figure 3.10(a) and Figure 3.10(c) into a figure will be beneficial. In Figure 3.11, A/V ratio is disaggregated in to bins classified with shear wave velocity and plotted with respect to magnitude. Serving to this purpose ground motions were sorted into the 5 categories according to $V_{s\text{-}30}$ values as defined by Choi and Stewart (2005). The ranges defined by Choi and Stewart (2005) essentially match the NEHRP site categories, except that NEHRP C and D are subdivided into three bins (C_{hv}, CD and D_{lv}) to better capture the variation of site nonlinearity with $V_{s\text{-}30}$. Being not so obvious, Figure 3.11 reveals the hidden information with regards to site effect. The trend lines fitted to data displays that as the site get stiffer the A/V ratio increases. Despite this observation, the dispersion in the data is significant.

In the ground motion selection, no restrictions were put on the amplitude of the ground motion (neither PGA nor PGV), since as the inspection of the naturally recorded ground motions will reveal both PGA and PGV can display significant variation even though they are recorded during a particular seismic event at a certain distance from the focus. At this point, to eliminate this variability, seismologist developed predictive equations to calculate the attenuated values of both ground motion amplitude parameters (PGA, PGV) and accordingly spectral ordinates (SA, SV, SD) as one moves away from the source for a particular earthquake magnitude.

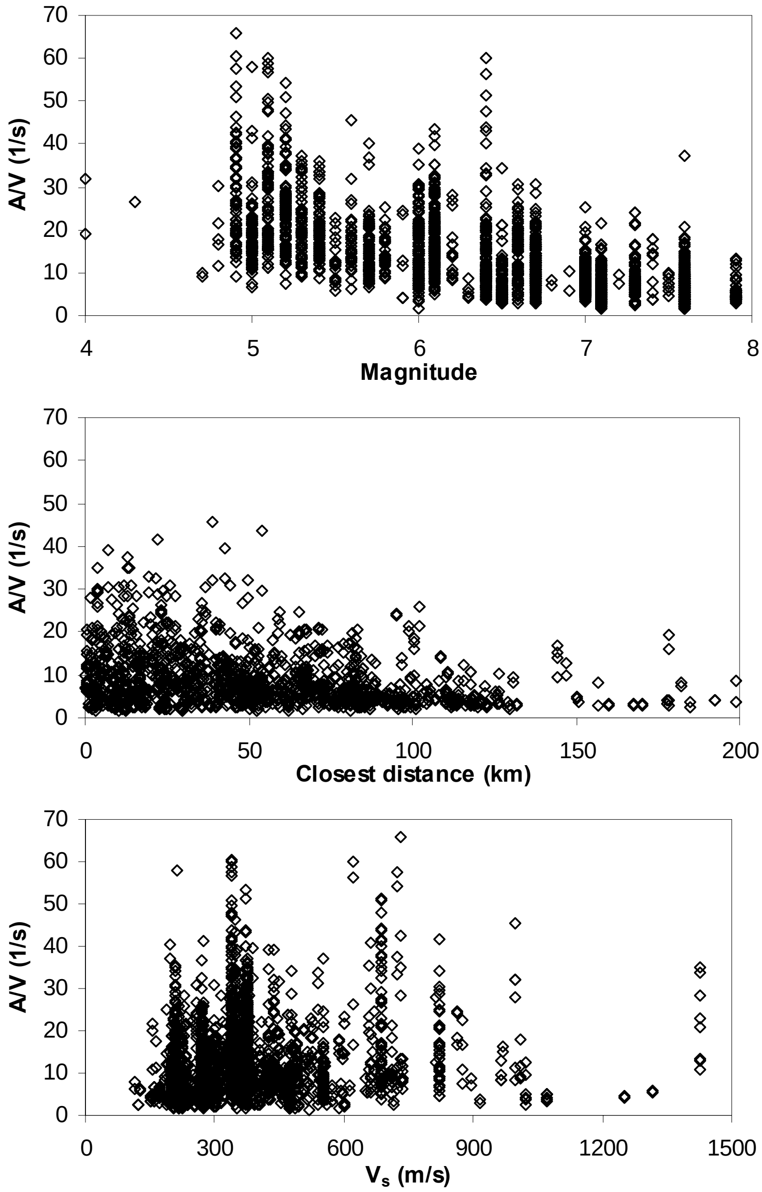

Figure 3.10 Effect of magnitude, distance, soil profile on frequency content defined in terms of A/V ratio

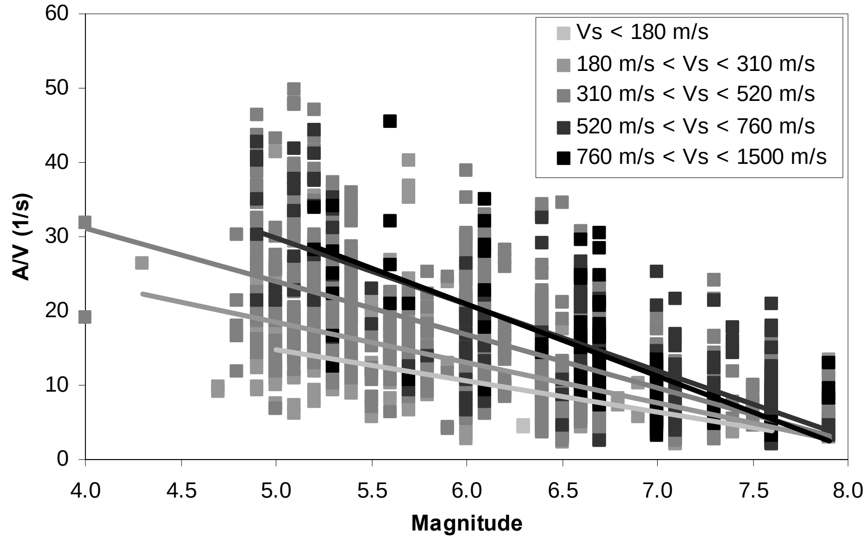

Figure 3.11 A/V ratio disaggregated into magnitude and site information.

Ground motion attenuation relationships provide estimates of intensity measures that typically apply for broadly defined site conditions such as rock or soil. Actual conditions at strong motion recording sites are highly variable with respect to local ground conditions, possible basin effects, and surface topography, and hence estimates from attenuation relationships necessarily represent averaged values across the range of possible site conditions (Stewart et al., 2001). Recently Akkar and Bommer (2007a-b) developed equations for the prediction of PGV and PGA using the strong motion database from the seismically active areas of Europe and the Middle East. Using these equations, first PGA and PGV are calculated for stiff and soft soil sites for varying magnitude and distance combinations. Then dividing the calculated amplitude values each other A/V ratio is calculated as a function of magnitude and distance. In Figure 3.12, the predicted A/V ratio for closest distance of 5 and 30 km is plotted on the same figure with the mean values of A/V ratios calculated for each event downloaded from COSMOS site. The predicted A/V curves for rock and soil sites agree well with the upper and lower bounds of mean A/V. It is displayed that A/V ratio, i.e. frequency content of ground motion, is affected only insignificantly by the source-to-distance but significantly by the magnitude of earthquake. Nevertheless, for smaller magnitude events there is evidence that distance influence the frequency content of ground motions.

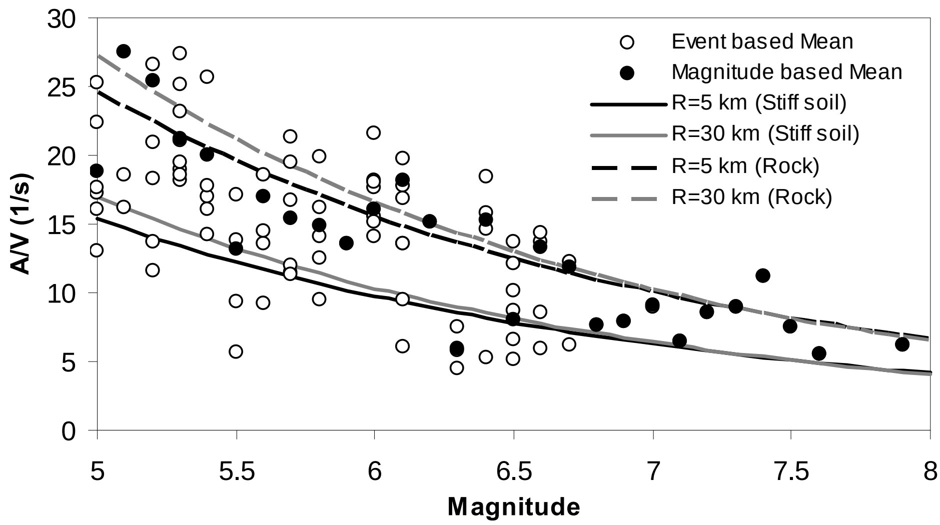

Figure 3.12 Magnitude dependence of A/V ratio

The following conclusions can be derived from the data presented here. A/V ratio is a simple yet effective parameter in ground motion frequency content identification. A/V ratio displaying a decreasing tendency with increasing magnitude reveals the existence of long period wave components, which can be very damaging for medium to long period structures. However, it must not be missed out that A/V ratio does not reveal any information about the amplitude of the ground motion, i.e. two ground motion accelerograms recorded far- and near-field of the causative fault may have similar A/V ratios, but they will have totally different ground motion amplitudes. The term 'near-field' is not used to represent the disputed 'near-fault' term that produces abnormal ground motions. Maybe the most important observation from this figure is the requirement to establish certain limits on the A/V ratio as function of magnitude. Considering the classification in Table 3.2, ground motions in normal range are produced by moderate-to-large magnitude earthquakes. For instance, ground motions selected from an event with magnitude 6.7 must have A/V value equal to approximately 8 s^{-1} with a certain standard deviation such as ±2. Finally, when a ground motion selected considering any one of the amplitude parameters either PGA or PGV, the other one must be checked if it is within the limits imposed by A/V ratio. This procedure will assure the incorporation of the effect of frequency content directly to the selection criteria.

3.6 GROUND MOTION DATA SETS

Next to validate the general observations and trends on A/V, ground motions used in serious studies were investigated. Ground motion sets from previous research (Akkar and Özen, 2005; Medina and Krawinkler, 2003; Iervolino and Cornell, 2005; Zhu et al., 1988a) was reanalyzed and used to investigate the central tendency and dispersion in the demand predictions of SDOF systems. The originally formed ground motion bins reflecting the selection criteria of the researchers were reorganized according to frequency content.

General characteristics of the ground motion data sets and the conclusions from the previous studies are summarized briefly next.

3.6.1 Data Characteristics of the Ground Motions Used in This Study

In none of the studies till today the ground motions are selected considering the frequency content directly. For statistical analyses the data sets used by four different research studies was used. The selection criteria, number of ground motions, bin data used in these studies is summarized in Table 3.4. Total number of ground motions records is 228. There are only 15 ground motions used in common. So the combined ground motion data set includes 213 distinct records. Data is gathered from both COSMOS and PEER ground motion sites.

The four data sets composed by different researchers are analyzed for magnitude and acceleration to velocity ratio relation, and plotted in Figure 3.13. The ground motion data set used by Akkar and Özen (2005) reveals the same tendency between the magnitude and A/V ratio as it was exposed above figures except 3 data points above A/V=25 level. They used a wider magnitude interval than the other studies. Medina and Krawinkler (2003) used a data composed of ‘ordinary’ ground motions records in magnitude range of 5.8 to 6.9. The scatter in data is not as wide as observed in Akkar and Ozen (2005). Narrow magnitude distance selection criteria used by Iervolino and Cornell (2005) displays its effect on the narrower scatter in observed in A/V ratio. Moreover, the decreasing tendency of A/V ratio with increasing magnitude is also observed here although a narrow magnitude interval selected. The data set composed by Zhu et al. is dominated by the ground motion records from San Fernando earthquake of magnitude 6.6 occurred in 1971. 26 out of 36 ground motions were recorded during San Fernando earthquake. A significant deficiency of their selection is that they used ground motions recoded on both rock and stiff soil. In Figure

3.14, it is displayed how rock site effects the A/V ratio. Their study is the only one that uses rock site records. It is reported by Boore and Joyner (1997) that the amplifications on rock sites can be in excess of 3.5 at high frequencies, in contrast to the amplifications of less than 1.2 on very hard rock sites. It can be also concluded from the figure that ground motions from soil sites reflect the characteristic frequency content of an earthquake due to magnitude better than rock sites, A/V ratio of approximately 6.5, a reasonable average for such an earthquake.

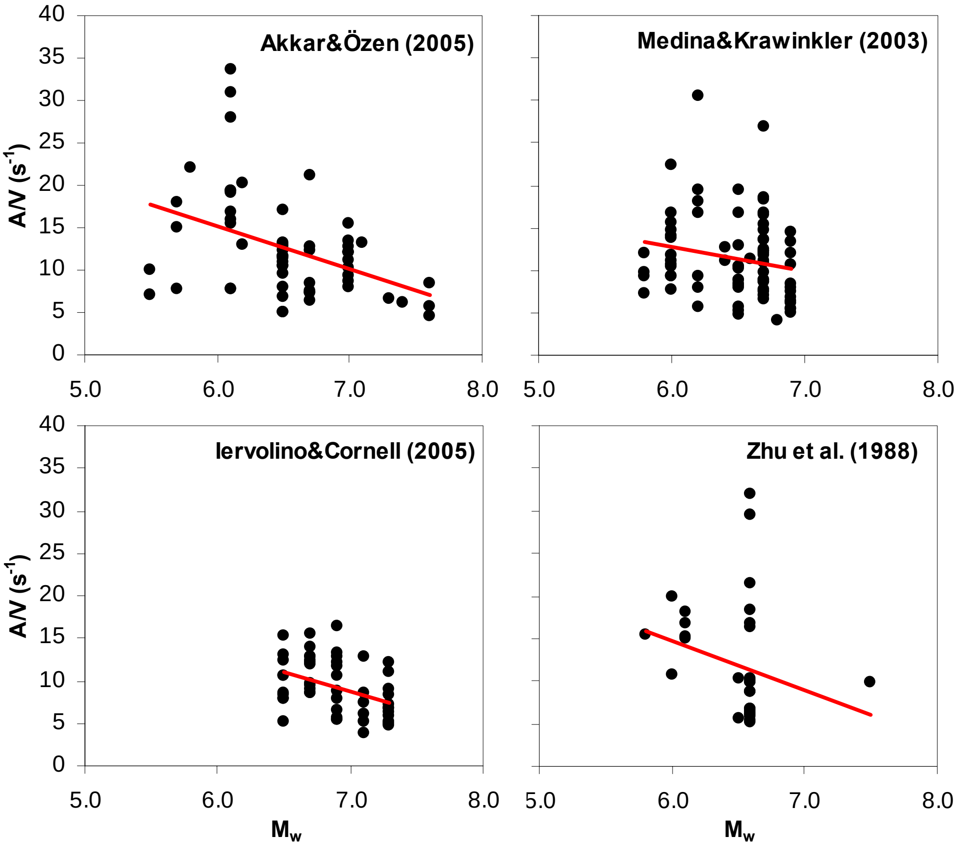

Figure 3.13 Magnitude-A/V relation of ground motions in different data bins

Table 3.4 Characteristics of the ground motion data sets

Study	Total number of ground motions	Ground motion classification criteria	Bins		Scaling methods
			Bin name	No. of ground motions in the bin	
Zhu et al. (1988)	36	A/V ratio	Low A/V (< 0.8 g/m/s)	12	Ground motions were scaled to 0.2 g peak ground acceleration
			Normal A/V (0.8 g/m/s < A/V < 1.2 g/m/s)	12	
			High A/V (> 1.2 g/m/s)	12	
Akkar and Ozen (2005)	60	PGV	PGV < 20 cm/s	20	No scaling
			20 cm/s < PGV < 40 cm/s	20	
			40 cm/s < PGV < 60 cm/s	20	
Medina and Krawinkler (2003)	80	M-R bins	Large Magnitude-Short Distance Bin, LMSR, (6.5 < Mw < 7.0, 13 km < R < 30 km),	20	All ground motions are scaled to a common spectral acceleration at pre-selected period or period of the system used
			Large Magnitude-Long Distance Bin, LMLR, (6.5 < Mw < 7.0, 30 km < R < 60 km),	20	
			Small Magnitude-Short Distance Bin, SMSR, (5.8 < Mw < 6.5, 13 km < R < 30 km),	20	
			Small Magnitude-Long Distance Bin, SMLR, (5.8 < Mw < 6.5, 30 km < R < 60 km),	20	
Iervolino and Cornell (2005)	52	M-R and arbitrary selection	All the records are from 5 events in the magnitude range of 6.7 to 7.4 and in the narrow distance range of 20 ± 5 km.	52	For each structure, the records in the target sets are scaled to their overall median spectral acceleration at the first mode-period.

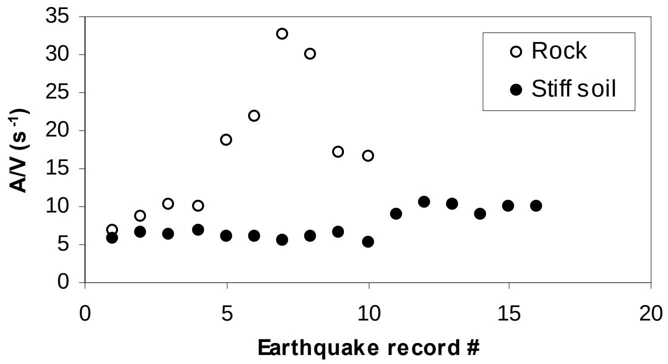

Figure 3.14 A/V ratio of ground motions from 1971 San Fernando earthquake of magnitude 6.6 plotted for rock and stiff soil sites.

3.6.2 Spectral Characteristics of the Used Databases

All the ground motions are scaled to the same PGA level of 0.4g to investigate the spectral shape. The mean 5 percent damped mean spectrum and coefficient of variation in each period are calculated for the used ground motions data sets for both the original classification and the acceleration to velocity ratio based classification. The results are presented in Figure 3.15 to Figure 3.16. At first sight, it is clearly seen in these figures that low A/V ratio group ground motions yield mean spectra with larger acceleration controlled plateau, whereas it is narrowest for the ground motions in the high A/V ratio group. As it is explained previously low A/V is an indication of existence of low frequency wave components in the accelerogram which is disclosed in the spectrum at medium to long periods. Classification of ground motion records based on PGV proposed by Akkar and Özen (2005) is also useful parameter in ground motion frequency content identification. It was reported that PGV correlates well with the earthquake magnitude and since it is calculated from the accelerogram by direct integration, it reveals the apparent or hidden pulses that are low amplitude but long duration or inversely high amplitude but short duration, in manner acting like a magnifier, the frequency content information of the ground motion. Given that the ground motions are scaled to same PGA level, A/V ratio based ground motion classification gives less dispersion.

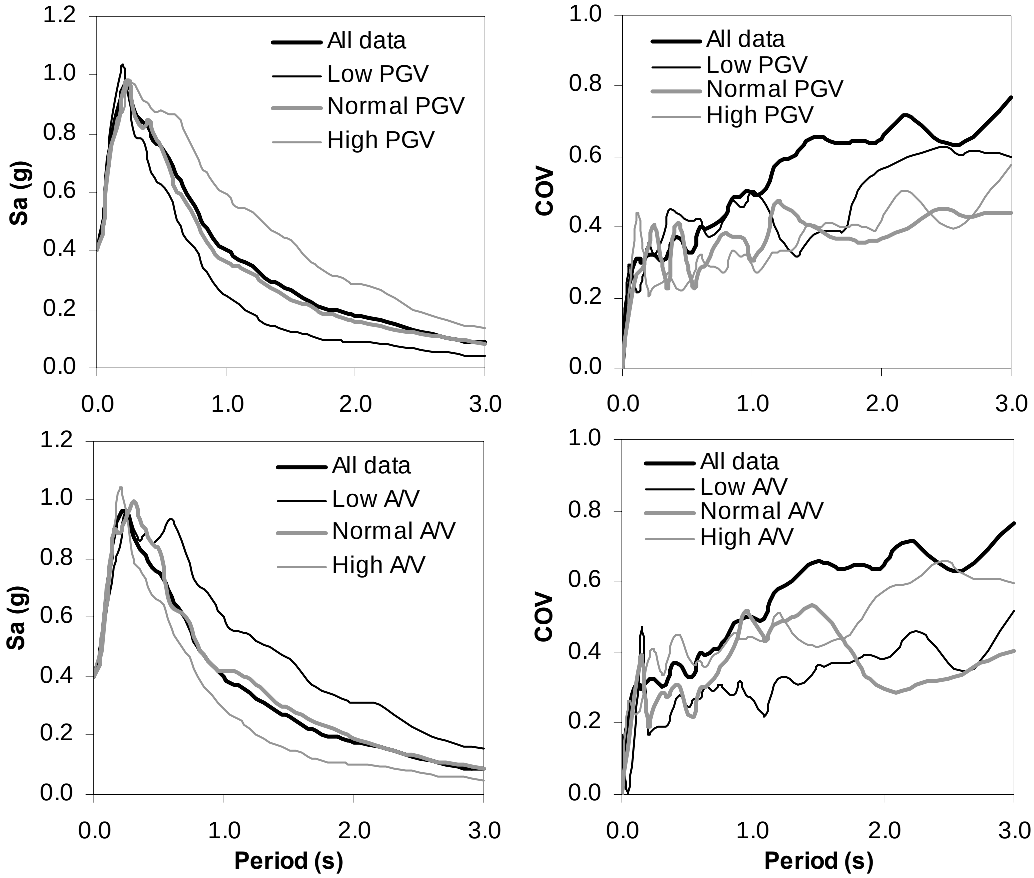

Figure 3.15 Mean spectrum of ground motions in the Akkar and Özen's (2005) database classified in PGV and A/V based bins.

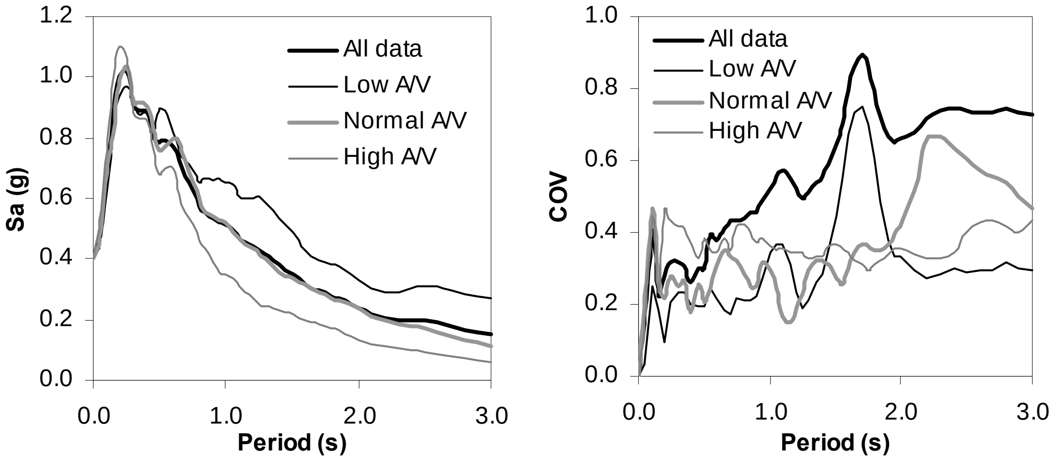

Figure 3.16 Mean spectrum of ground motions in the Iervolino and Cornell (2005) database classified in A/V based bins.

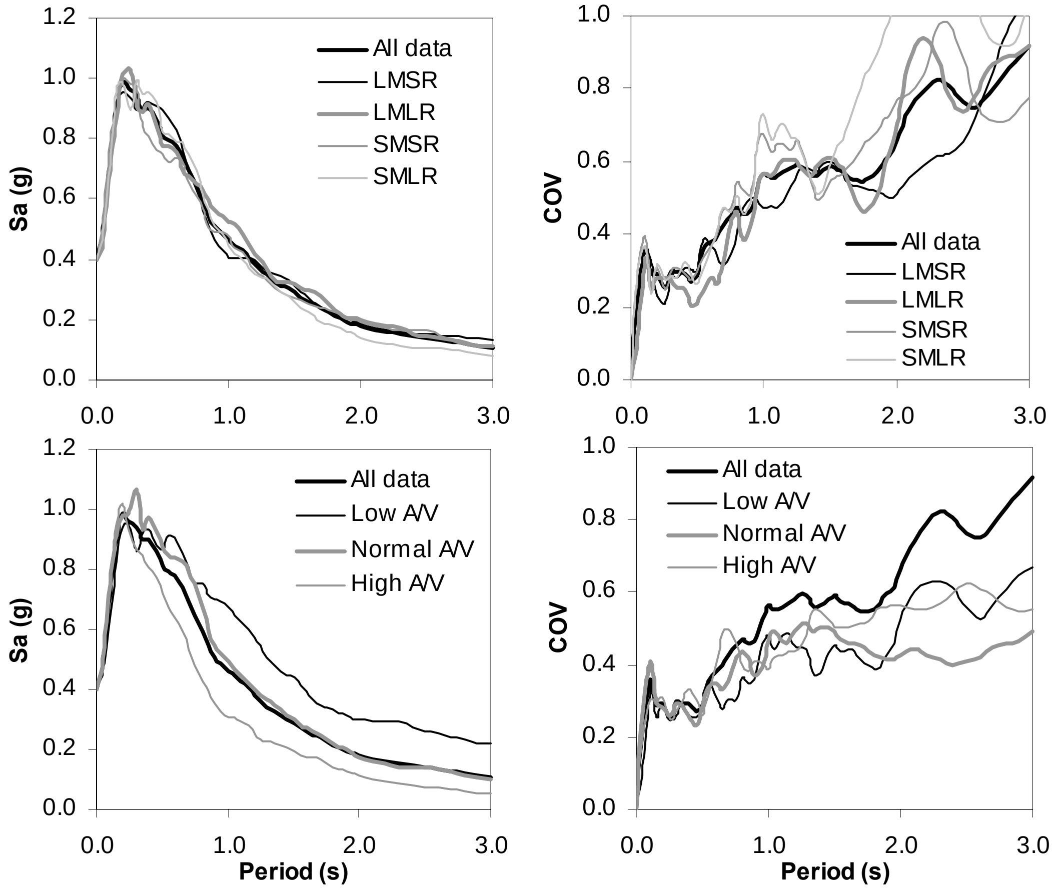

Figure 3.17 Mean spectrum of ground motions in the Medina and Krawinkler's (2003) database classified in M-R (Magnitude-distance) and A/V based bins.

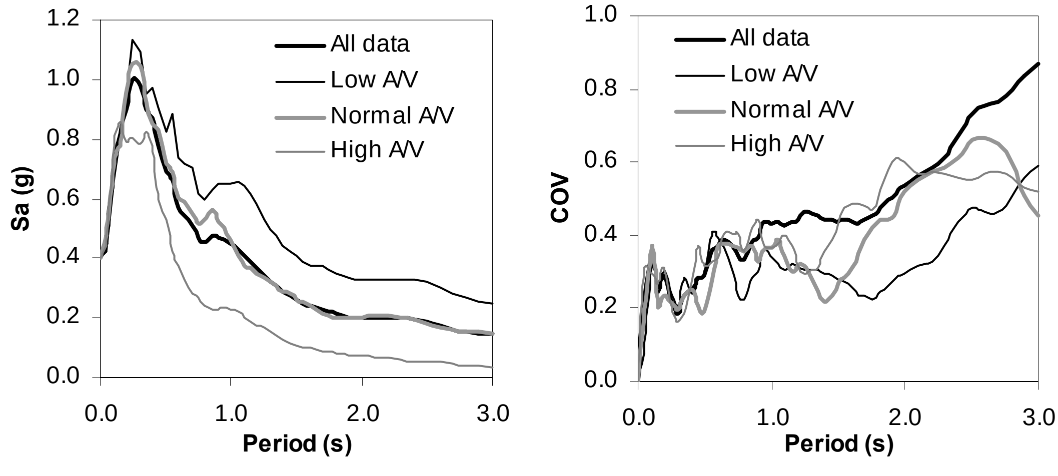

Figure 3.18 Mean spectrum of ground motions in the Zhu et al. (1988) database classified in A/V based bins.

3.7 EFFECT OF FREQUENCY CONTENT ON SEISMIC DEMAND EVALUATION OF SDOF SYSTEMS

In order to investigate the dependence of seismic demand on frequency content of ground motions classified in terms of A/V ratio SDOF analyses were performed. A bilinear elasto-plastic hysteresis model with %3 strain hardening and period dependent strength factors (η=V_y/W) are used. As it is declared at the beginning of this study, the intent of this study is to identify the frequency content as a major seismic intensity measure. Moving from this hypothesis, it is not desired to investigate a whole possible set of systems with same elastic period and varying strengths. Based on field observations, traditional R-μ-T relations avoided and only a representative strength factor is used for each period on condition that at least moderate seismic demands will be applied on the SDOF system. This is to say a constant strength factor is associated with each period (η-T relation). The η-T relation used in this study was calculated from the database used by Akkar et al. (2005) to determine the fragility functions for low- and mid-rise ordinary reinforced concrete buildings. The field data consists of 32 sample buildings representing the general characteristics of two- to five-story substandard reinforced concrete buildings that constitute the most vulnerable construction type in Turkey as well as several other countries prone to earthquakes. In that study, conducting pushover analyses lateral stiffness, strength and deformation capacities of these building were determined. Using the results of pushover analyses strength of each structural configuration is identified. The plot of period versus corresponding strength factor is given in Figure 3.19. At this point, it is crucial to point out that neither the building stock inventory is representative of all structures nor the calculated period dependent strength factors covers the whole set of possible structural strengths. The purpose is to determine the effect of frequency content on yielding systems and do this as simple as possible by producing only relevant outputs. Strength factors derived from two other studies (Mwafy, 2000; Kadas, 2006) performed on generic reinforced concrete frames and frame-wall systems are also introduced in to the same figure. The generic frames used in these studies displays much higher strength compared to database used, even higher than expected. However, to experience moderate or higher level of ductility demands it is decided that the calculated η-T curve is appropriate for obtaining the expected outputs. Traditional maximum displacement ductility is used as a structural damage indicator for SDOF systems.

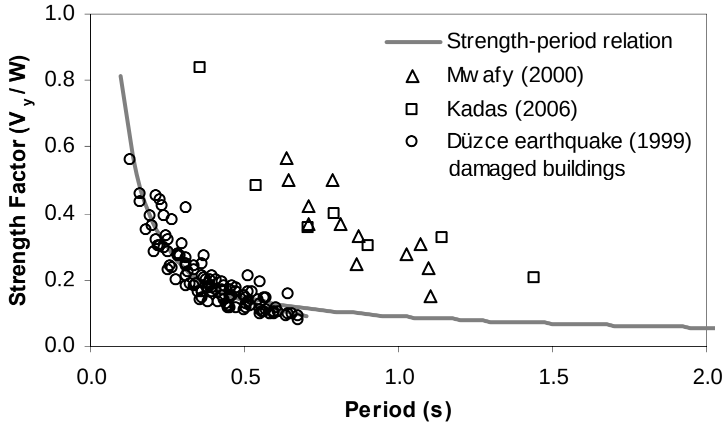

Figure 3.19 Period dependent strength factors derived from damaged building inventory during 1999 Duzce earthquake

Following the traditional way, ground motions were normalized to the same peak acceleration of 0.4g. This scaling resulted in significantly different energy content over the moderate and long period ranges for the three groups of chosen earthquake records with different A/V ranges. The limits of A/V ranges used to group ground motions were given in Table 3.2. As a result, this classification led to substantial differences in the maximum displacement ductility demands among the three groups of accelerograms as displayed in Figure 3.20. Excitation using the low A/V range group of records leads to the greatest ductility demand. Therefore, the common practice of specifying seismic design forces based on peak site acceleration does not lead to consistent control over structural damage for earthquake ground motions in the different A/V ranges.

Alternatively the ground motions were normalized to a common peak ground velocity of 50 cm/s. The calculated displacement ductility demands for each group of A/V ratio is presented in Figure 3.21. Scaling ground motions in this way to the same PGV resulted in ductility demands similar to PGA scaling for normal A/V group ground motions, where as significantly different ductility demands obtained in the low and high A/V group ground motions. Agreement in the normal A/V group results can be attributed to the fact that used scaling levels for PGA and PGV yield an A/V ratio of 8 s^{-1}, which is roughly represent the normal ground motions.

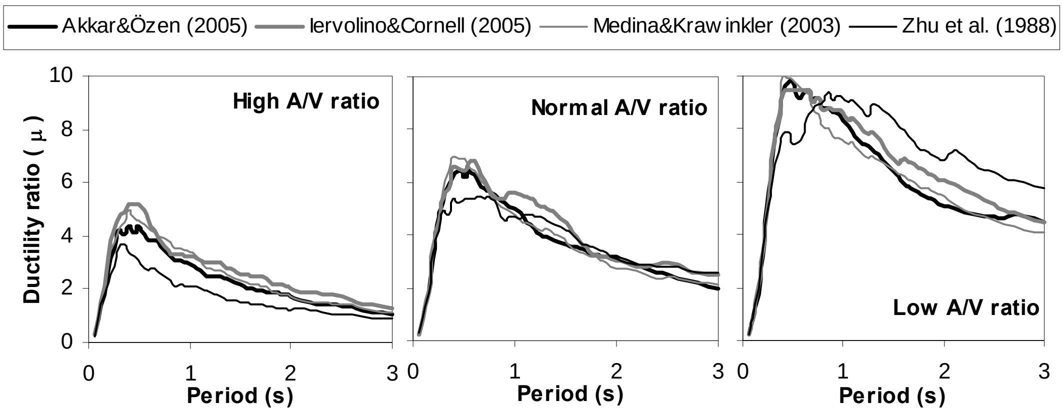

Figure 3.20 Effect of A/V based ground motion classification on the mean ductility demand spectrum of generalized SDOF systems.Ground motions are scaled to 0.4g PGA level.

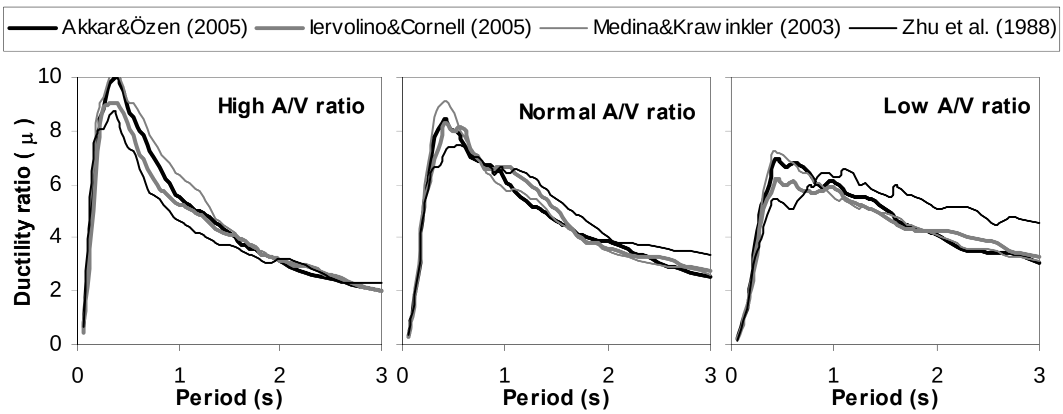

Figure 3.21 Effect of A/V based ground motion classification on the mean ductility demand spectrum of generalized SDOF systems. Ground motions are scaled to 50 cm/s PGV level

Effect of PGA and PGV scaling on mean ductility demands obtained for different A/V groups is displayed in Figure 3.22 by combining all the databases used in this study. An interesting observation in regard to results of inelastic SDOF system analyses with different peak ground amplitude scaling techniques is that the ratio between the displacement ductility calculated by PGA scaling and PGV scaling yields a constant value over the entire range of periods for each A/V group. This ratio obtained for each A/V group is plotted in Figure 3.23. This ratio is sensitive to A/V ratio of the scaling, i.e. ratio of the PGA and PGV levels used in two scaling techniques. The A/V ratio of the scaling is (400 cm/s^2) / (50 cm/s) = 8.0 s^{-1}. When the A/V ratio of the two scaling techniques is in agreement with the A/V ratio of the ground motion data set, the two scaling methods yield similar inelastic displacement demands. In the case analyzed here, since the A/V ratio of the normal ground motions is 9.6, the ratio of inelastic displacements obtained form PGA scaling and PGV scaling should be in the order of 0.83 (8.0/9.6), which agrees with the value in Figure 3.23. Similarly for low and high A/V group ground motions this ratio is calculated as 8.0/6.2=1.29 and 8.0/16.4=0.49, respectively and again in agreement with the curves in Figure 3.23. In the light of this useful observation, Table 3.5 presents typical factors that can be used to convert ductility ratios or displacements obtained from PGA scaling to PGV scaling by multiplying the values obtained from PGA scaled ground motions with this factor.

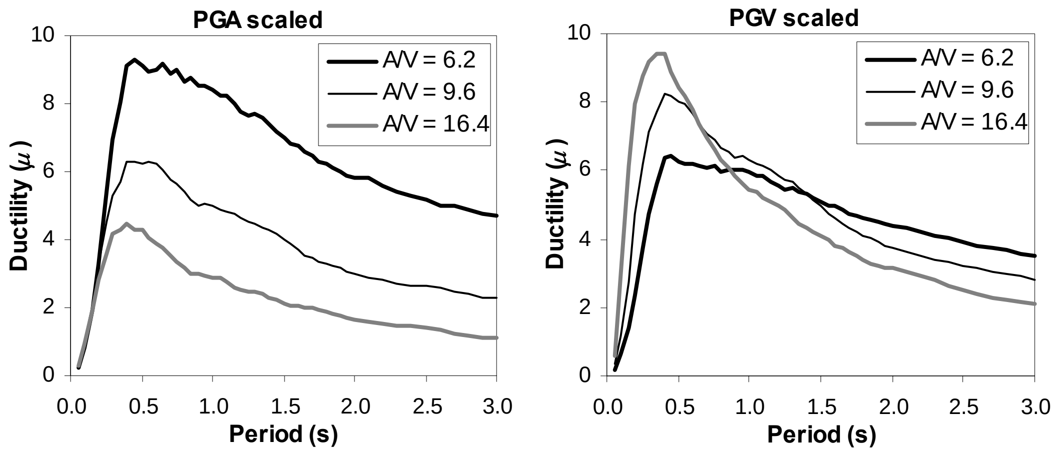

Figure 3.22 Effect of PGA and PGV scaling on mean ductility demands obtained for different A/V groups, represented with the group mean A/V value rather than the group name, by combining all the databases used in this study.

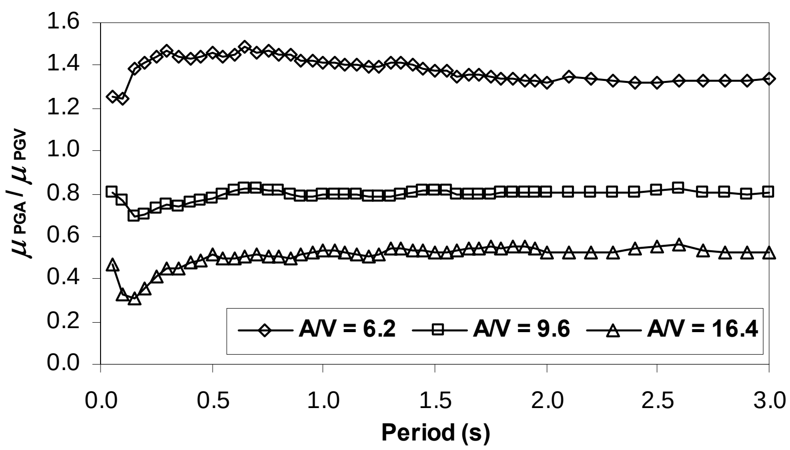

Figure 3.23 Ratio of ductility values calculated for different A/V groups by using PGA scaling and PGV scaling

Table 3.5 Typical factors that can be used to convert ductility ratios or displacements obtained from PGA scaling to PGV scaling

A/V of scaling	A/V = 6.2	A/V = 9.6	A/V = 16.4
6.20	1.00	0.65	0.38
9.60	1.55	1.00	0.59
16.40	2.65	1.71	1.00

3.8 SELECTION OF GROUND MOTIONS

The general aim in ground motion selection is to match the elastic response spectra at a particular damping ratio to represent the potential seismic hazard defined by the characteristics of the site and source. In the current design codes, design earthquake is specified in the form of smoothed acceleration response spectrum and the intensity of the ground excitation is adjusted with only one parameter, peak ground horizontal acceleration, PGA. In engineering practice damage potential of ground motion is evaluated on the basis of peak ground acceleration (PGA) and scaling of ground motions are done accordingly. More precisely, acceleration response spectra display the maximum ground acceleration (effective peak acceleration, EPA) that creates maximum response, and its shape reflects the frequency content of excitation which is assumed to be influenced only from the soil characteristics at the recording site, even though it is well established that the spectral shape is strongly influenced by earthquake magnitude and, to a much lesser extent, by source-to-site distance (Bommer and Pinho, 2006). This statement supports the idea that PGA is alone adequate to display the potential of damageability of a ground motion. However, there are studies that impoverish this idea.

Akkar and Gülkan (2002) examined the records from Kocaeli earthquake (17 August 1999, M_w 7.4) and Bolu–Düzce earthquake (12 November 1999, M_w 7.2), to determine whether they provide clues about the extensive damage on the housing stock in the epicentral region. They reported that peaks of 0.3–0.4g from event 1 seem to be inconsistent with the structural performance, but so is the 0.8g peak recorded during event 2 in Bolu, where the percentage of collapsed buildings was much less than in Izmit (Kocaeli). They found the clues of damage in frequency content characteristics of the two earthquakes. They stated that the component with larger ground velocity correlate better with the component with larger drift demand and the period of the peak velocity pulse matches the structural period where the drift demand is the largest. The fact that ground motions from the Kocaeli earthquake have lower A/V ratio than Düzce earthquake could be added to these observations.

Another reason that was put forward for the inconvenience of peak ground motion parameters as intensity measures arouse in the scaling issue. Previous studies (Nau and Hall, 1984; Shome and Cornell, 1998) have indicated that the use of PGA or PGV to scaling earthquake records is to be discouraged compared with other normalization methods such as the spectral intensity method. This is because scaling procedures based on peak record values do not provide consistent results over the entire range of periods of engineering significance.

Iervolino and Cornell (2005), to form ground motion sets strong enough to investigate the scaling, introduced a strong ground motion criteria as those ones with the maximum average spectral acceleration at the four periods **(0.1, 0.85, 1.5, and 4 sec).** The objective of using this average was to reduce the likelihood of selecting records that happen to be unduly strong at one period and due to there being a large peak in its spectrum. Such records would be present if the selection were done structure-by-structure seeking the strongest records based on the spectrum at a single period. Among records scaled to a common single spectral acceleration level, a record with such a peak will generally cause ***lower*** nonlinear response for structures with that natural period; the common explanation is that as it "softens" it drifts into a regime of lower input energy (Mwafy, 2000; Kazaz and Yakut, 2006). Based on the responses of the models to sets of records that are comparatively strong and records that are arbitrarily selected and then scaled up to match the strength of the stronger records, Iervolino and Cornell (2005) has found no compelling evidence that such scaling induces bias in the response estimation. This scaling conclusion reaches to scale factors as high as 4 and ductility up to 6.

Critics have also been raised against spectral scaling methods. Naeim and Lew (1995) have concluded that the indiscriminate use of spectrum-compatible accelerograms may lead to exaggeration of displacement demand and energy input.

Nevertheless, it was displayed that A/V ratio is an effective parameter in identifying the frequency content and spectral shape, in this way reflecting the damage potential of ground motions on condition that they were scaled to same intensity, here PGA. It was revealed in Figures 3.15-18 that as far as the ground motions are collected in proper bins reflecting the frequency content (A/V bins in that case), scaling with PGA do not introduce any inconsistency in the calculation of mean response spectrum of particular bin.

Now it will be displayed that as far as the ground motions are classified according to frequency content that is represented with three A/V ranges as defined in Table 3.2, scaling with PGA or scaling to match target spectrum do not matters. They lead to similar scale factors.

It is necessary to scale the applied ground motion time histories to an intensity level for direct and logical evaluation and comparison of their damage potential in terms of predefined ground motion intensity measures. This will also help identification of the required intensity, frequency content and the duration of the ground acceleration time histories to be used for the seismic hazard analyses in performance based earthquake engineering.

In the preparation of suites of acceleration time-series to be used as input to dynamic analyses it is generally sought that the records match with the shape of a target spectrum (elastic design spectrum most of the time). In order to implement searches that will produce records likely to meet the spectral matching criteria, or at least to do so with a minimum of manipulation of the records, it is useful to have a tool that allows records to be searched on the basis of the spectral ordinates. Ambraseys et al. (2004) discussed on such a matching criteria that is included in the new European strong-motion data CD-ROM. The records are searched by matching the spectral shape to the shape of the design spectrum. The search is based on the average root-mean-square deviation of the observed spectrum from the target design spectrum:

$$D_{rms} = \frac{1}{N}\sqrt{\sum_{i=1}^{N}\left(\frac{SA_o(T_i)}{PGA_o} - \frac{SA_S(T_i)}{PGA_S}\right)^2} \tag{3.7}$$

where N is the number of periods at which the spectral shape is specified, $SA_o(Ti)$ is the spectral acceleration from the record at period Ti, $SA_s(Ti)$ is the target spectral acceleration at the same period; PGA_o and PGA_s are the peak ground acceleration of the record and the zero-period anchor point of the target spectrum, respectively. The smaller the value of D_{rms} the closer the match between the shape of the record and target spectrum is. Smaller values of D_{rms} can be specified if the spectral matching is being done at short rather than longer spectral response periods (Bommer and Acevedo, 2004).

Assuming the ground motion spectrums should match the elastic response spectra of TSC (2007) that has a 10% probability of exceedance in 50 years defined on Z3 site class with PGA of 0.4g, the D_{rms} values are calculated for the ground motions in database to measure degree of spectral matching. Bommer and Acevedo (2004) reported that values of D_{rms} of the order of 0.15 were needed for matching ordinates in the period range of 0.4-0.8 second, where as values as low as 0.06-0.07 could be used for matching the spectral ordinates from 0.1 to 0.3 seconds. In this study, periods used to calculate the D_{rms} values ranges from 0.3 to 0.8 seconds. Somerville (2005) defined the levels of spectral matching as

• No spectral matching, which may leave critical peaks and troughs that strongly determine nonlinear response – OK when using many records.

• "Loose" spectral matching, which makes the response spectrum approximately follow a smooth target spectrum but leaving peaks and troughs – OK when using a few records.

• "Tight" spectral matching, which makes a smooth response spectrum that lacks peaks and troughs but conforms to a smooth uniform hazard spectrum – OK when using 1 record - minimizes variability but may introduce bias.

In this study "loose' spectral matching that does not involve any modification of the shape of the response spectrum is adopted. Tight spectral matching is not preferred because it modifies the ground motion time-history and produces time histories that are artificially broadband and do not have peaks or troughs in their response spectra. Such peaks and troughs are characteristic of actual ground motions, and nonlinear response of structures is sensitive as described on CAMUS wall specimen previously.

Two different scaling factors are calculated to match the target spectrum. In the first scaling method PGA of the ground motion is scaled to match the spectral ordinate at the zero second period (PGA_o = 0.4g) of the target spectrum. Second approach calculates a scale factor defined as the average of the ratio of spectral ordinates of target and matching spectrums at periods 0.1 s, 0.4 s and 0.85 s. Comparison of the two scale factors is given in Figure 3.24 for the four databases used here. SF_{Spect} yields 25 percent lager scale factors than SF_{PGA} for the range of scale factors 0 to 3.5. The best correlation between the two scale factors was observed in Iervolino and Cornell's (2005) database due to narrow ranges in the selection criteria. This can be attributed to the fact that the ground motions in that bin are from large magnitude earthquakes at a moderate distance from the site, a situation that is in agreement with our target scenario event spectrum. Figure 3.24 also indicates that due to poor correlation between the two scale factors beyond 3, this value can be assumed to be the upper limit for scaling.

$$SF_{PGA} = \frac{PGA_S}{PGA_o} \tag{3.8}$$

$$SF_{Spect} = \frac{1}{3}\left(\frac{SA_S(T=0.1s)}{SA_o(T=0.1s)} + \frac{SA_S(T=0.4s)}{SA_o(T=0.4s)} + \frac{SA_S(T=0.85s)}{SA_o(T=0.85s)} \right) \tag{3.9}$$

After all, the following criteria were introduced to select the most suitable ground motions that conform to elastic design spectrum. It is assumed that

- A/V ratio should be smaller than 10 s^{-1}.
- D_{rms} should be lower than 0.3.
- Scale factors applied to match the spectra is lower than 3.

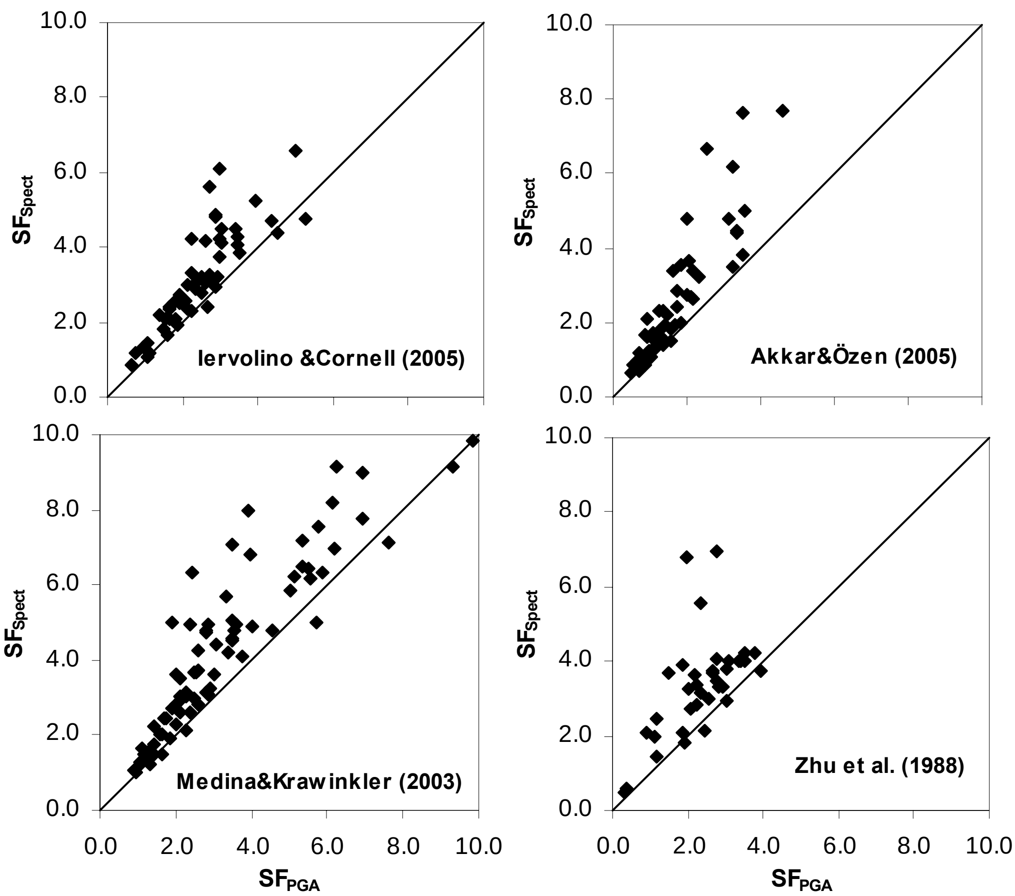

Figure 3.24 Correlation between the two scale factors for each database used here

3.8.1 Selected Ground Motions

Using the criteria introduced above, 215 ground motions are screened for finding the spectrum compatible ones. 23 ground motions obeying the given limitation were found. Among these 23 ground motions, 10 of them selected to be used as seismic input for time-history analyses. The catalog data of these ground motions were presented in Table 3.6. The acceleration, velocity and displacement response spectra of these scaled ground motions were presented in Figure 3.25, Figure 3.26 and Figure 3.27 respectively. In Table 3.7 peak ground values of strong motions were given for both original and scaled forms together with applied scale factors. SF_{Spect} is used to scale the ground motions. Acceleration and velocity spectrum intensities were also tabulated in Table 3.7.

Ground motions yielded an average A/V ratio of 8.2 with standard deviation of 1.0. This value corresponds to lower limit of normal ground motions displaying that the selected ground motions carries a frequency content that should be dangerous for medium period range structures. The ground motions have nearly uniformly distributed peak ground values, yielding values of 480.1 cm/s^2 and 58.9 cm/s in the mean for acceleration and velocity, respectively. The peak values are higher than the values given for mean-plus-one-standard-deviation response spectrum that is compatible with El Centro ground motion, which are 313 cm/s^2 and 33.1 cm/s for acceleration and velocity, respectively. 1940 El Centro earthquake record has been used for long time as a standard for evaluating the earthquake ground motions. Derecho et al. (1978b) used 1.5 times the velocity spectrum intensity, SI_{ref} = 178 cm/s, of this record as reference to scale the ground motion. This scaling procedure yielded a spectrum intensity of 267 cm/s that corresponds to the intensity of broad band ascending ground motions according to their classification. As seen in Tablo 3.6, the ground motions (ground motion No. 1, 2, 3 and 8) that conforms to their classification nearly posses the same intensity (VSI ~ 250 cm/s) in this study. The scaled ground acceleration and velocity time series of the selected ground motions are given in APPENDIX D.

Table 3.6 Catalog data of the selected ground motions

No	Earthquake	Year	M_w	Station	R (km)	PGA (cm/s^2)	PGV (cm/s)
1	Imperial Valley	1979	6.5	Keystone Rd., El Centro Array #2	16.2	309	32.7
2	Kocaeli	1999	7.4	Duzce	17.1	308	50.7
3	Northridge	1994	6.7	Los Angeles, Brentwood V.A. Ho.	23.1	182	24.0
4	Northridge	1994	6.7	Pacoima-Kagel Canyon	10.6	424	50.9
5	Whittier Narrows	1987	6.1	7420 Jaboneria, Bell Gardens	16.4	216	28.0
6	Cape Mendocino	1992	7.1	89324 Rio Dell Overpass - FF	18.5	378	43.9
7	Northridge	1994	6.7	24389 LA - Century City CC North	25.7	218	25.2
8	Northridge	1994	6.7	24283 Moorpark - Fire Sta.	28	189	20.2
9	Loma Prieta	1989	6.9	Hollister Differential Array	25.8	274	35.6
10	Northridge	1994	6.7	LA - Fletcher Dr.	29.5	235	26.2

Table 3.7 Scale and spectral matching factors, corresponding peak ground values and spectral intensity measures

No	Unscaled		SF_{Spec}	SF_{PGA}	D_{rms}	Scaled				
	PGA (cm/s^2)	PGV (cm/s)				PGA (cm/s^2)	PGV (cm/s)	A/V (s^{-1})	ASI[1] (cm/s)	VSI[2] (cm)
1	309	32.7	1.77	1.27	0.23	547	58	9.5	574.1	246.6
2	308	50.7	1.52	1.27	0.17	469	77	6.1	421.5	245.5
3	182	24.0	2.69	2.15	0.16	490	65	7.6	447.6	251.8
4	424	50.9	1.20	0.93	0.09	507	61	8.3	388.3	205.2
5	216	28.0	1.98	1.82	0.26	428	55	7.7	376.0	185.8
6	378	43.9	1.43	1.04	0.18	541	63	8.6	448.4	218.9
7	218	25.2	2.11	1.80	0.27	460	53	8.6	381.4	228.2
8	189	20.2	2.56	2.07	0.23	486	52	9.4	498.8	239.9
9	274	35.6	1.47	1.43	0.29	404	52	7.7	402.8	205.3
10	235	26.2	2.00	1.67	0.21	470	52	8.8	411.3	172.8
					Average	**480.1**	**58.9**	**8.2**		
					Std. (±)	**45.14**	**7.95**	**1.00**		

[1]ASI: Acceleration Spectrum Intensity
[2]VSI: Velocity Spectrum Intensity

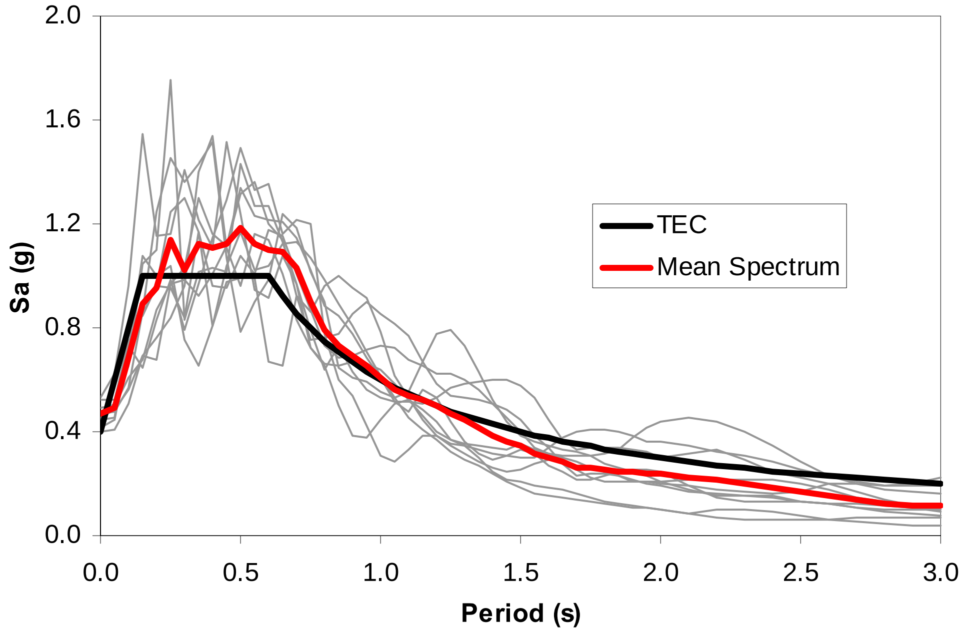

Figure 3.25 Acceleration response spectra of the selected ground motions

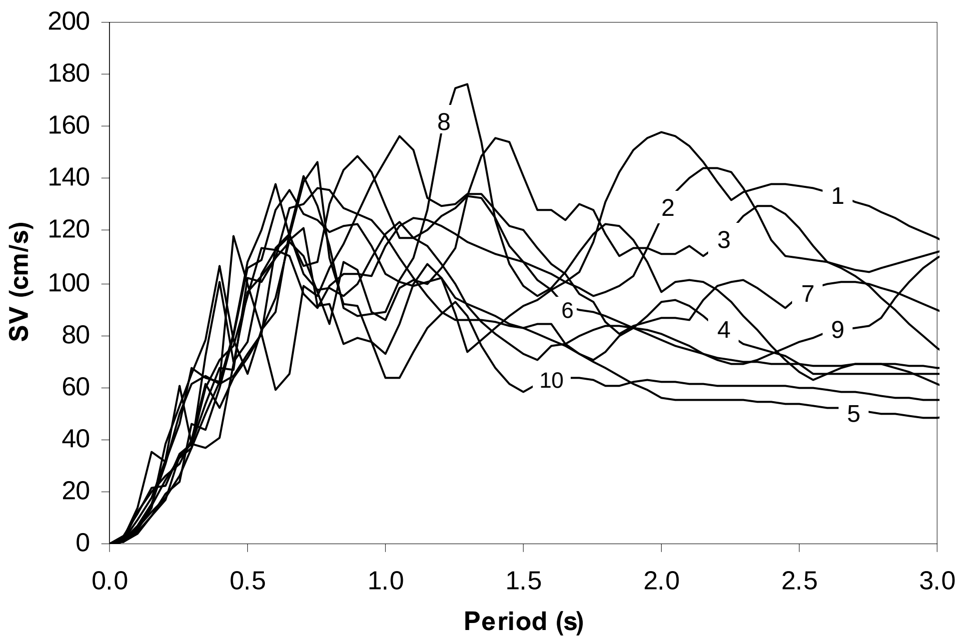

Figure 3.26 Velocity response spectra of the selected ground motions

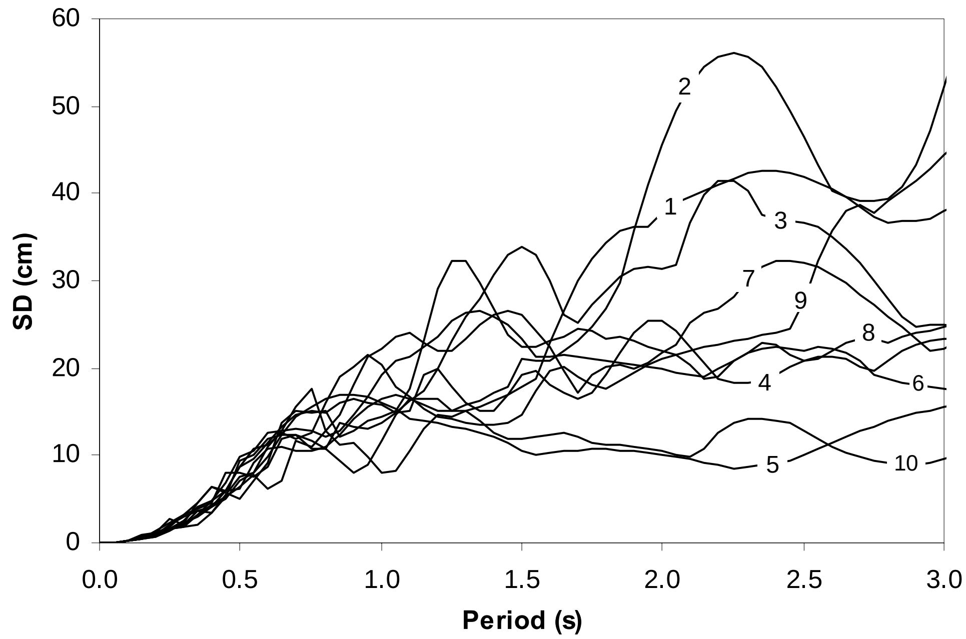

Figure 3.27 Displacement response spectra of the selected ground motions

3.9 CONCLUDING REMARKS

All the ongoing discussion above is to display that the different intensity measures based on geophysical parameters, seismological parameters and structural parameters when evaluated from structural response point of view indicates to a common point; what matters to structural response is the frequency content of ground motion given that the amplitude of the motion is high enough to drive the structure into inelastic range. Spectral shape is a key to the nonlinear response. As displayed previously by others and as demonstrated here, the ascending trend in the spectrum (acceleration and velocity) beyond the fundamental period of the structure is a good indicator for the damageability of the ground motion record. A measure to evaluate this potential was presented in Section 3.4.

Another intensity measure calculated from peak ground motion parameters acceleration to velocity A/V ratio is foreseen as a simple yet effective parameter that might be used to determine the frequency content of ground motions and differentiate it due to magnitude and soil effect. A/V ratio can be classified to represent the seismic intensity of a particular seismic hazard scenario taking into consideration of magnitude and site effects. While the indiscrimination of the frequency content of a ground motion record due to magnitude was obvious, the effect of local site response due to soil nonlinearity on the frequency content as implied by A/V ratio could not be illuminated thoroughly. Theoretically, A/V ratio should take larger values as the site becomes stiffer for a particular earthquake magnitude. In a recent study by Yenier (2009), the limitations of point-source stochastic simulations were investigated in terms of fundamental geophysical parameters. Within this context synthetic ground motions were generated for various magnitude ($5.0 \leq M_w \leq 7.5$), source-to-site distance (1 km $\leq R_{JB} \leq 100$ km), faulting style (shallow dipping and strike-slip) and site class (soft, stiff and rock) bins. In Figure 3.28, the A/V ratios calculated from these ground motions grouped in soft, stiff and rock site bins according to NEHRP site classification are plotted for earthquake magnitude. This figure reveals the hidden information in regard to Figure 3.11, the effect of local site conditions on the A/V ratio. This subject left at this point for future studies.

In Section 3.7 the effect of frequency content of earthquake record on inelastic displacement demands on SDOF systems was investigated. It was displayed that for the ground motions scaled to same PGA amplitude low frequency ground motions produced highest inelastic displacement demands. Effects of scaling based on peak ground values, PGA and PGV, were investigated and it was observed that there is a consistent relation between the ductility demands calculated from the two scaling techniques. For the same group of ground motions, the ratio of mean inelastic displacements calculated from these ground motions by applying PGA scaling and PGV scaling can be evaluated from the ratio of the scaling ($A/V_{scaling} = PGA_{scaling\ level} / PGV_{scaling\ level}$) and the mean A/V_{group} ratio of the group of records.

In Section 3.8 scaling issue was discussed. It was displayed that for the level of scaling up to factor of 3, the PGA scaling and scaling due to spectral matching at periods of 0.1 s, 0.4 s and 0.85 s produces similar scaling factors. Indeed the scale factors produced with PGA scaling can be up to 25% lower than scaling factors obtained from spectral matching. For achieving spectral matching between the target and matching spectrums at the listed periods, an upper limit of 0.3 can be adopted for the D_{rms} values, which display the goodness of matching. 10 of the 23 ground motions records conforming to limitations defined were selected for use in time-history analyses.

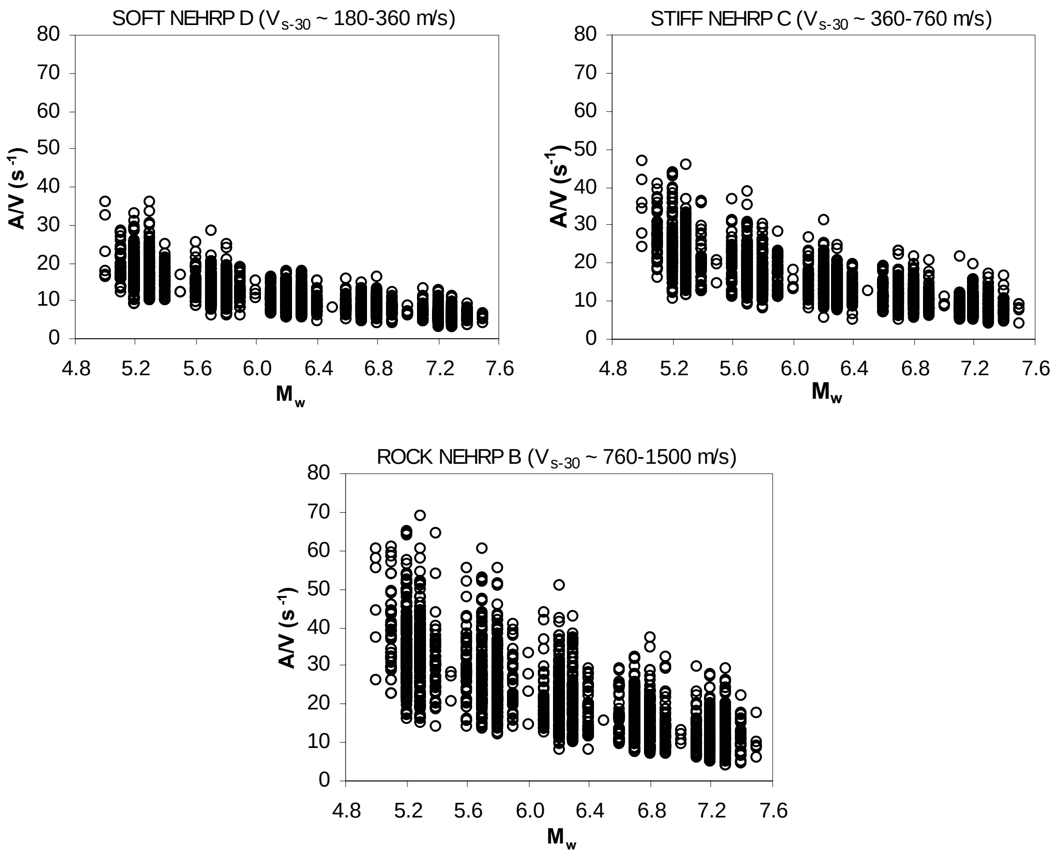

Figure 3.28 Effect of earthquake magnitude and site effect on the A/V ratio (Yenier, 2009)

CHAPTER 4

PARAMETERS AND PROCEDURES OF THE ANALYTICAL FRAMEWORK

4.1 INTRODUCTION

This chapter is devoted to establish an analytical framework for the parametric investigation of shear walls. The elements of presented framework is composed of development of simple lumped-parameter structural models of wall and frame-wall systems for NLFEA, determination of the parameters that affect the shear wall response and identification of procedures to include these effects in the analyses. The parameters affecting the wall response are not only related to characteristics wall properties like length (L_w), height (H_w), axial load ratio (P/P_o), but also 3D structural interaction effects arising from differences between the dominant deformation modes of walls and accommodating structural type (eg. frame-wall interaction). These effects are required to be included in the analyses.

The use of NLFEA for the investigation of the deformations (damage) of structural walls at the micro level (strains) requires simplified modeling techniques to account for 3D global effects in the finite element descritization of the shear walls. In a FE model a wall can be composed of thousands of elements and nodes since 3D continuum finite elements are used. It is neither feasible nor logical to model the entire wall system or frame-wall structure in such type of parametric analyses. Simple analytical procedures used in the analyses of bearing wall and frame-wall structures were investigated and isolated wall models representative of global structural effects in both types of structural configurations were developed. A thorough investigation of these simplified models is necessary in order to determine the parameters of the study. The models can be used to derive useful information about the dynamic and static characteristics of wall type structures.

4.1.1 Types of Concrete Shear Wall Buildings

Structural walls are one of the most commonly used lateral-load resisting systems. The recent code rules nearly lay down a condition to use the minimum amount of shear walls in large portion of newly constructed reinforced concrete structures. The buildings consisting of shear walls as lateral load resisting system can be constructed with different technologies and structural forms used in these buildings to carry vertical and lateral loads can lead to different behavior types. Although the general definition of "concrete shear wall building" is used to hold for variety of buildings types that relies on shear walls as primary lateral load resisting system (FEMA 356 - Table 10-2 *Description of Building Types*), the evaluation of damage to a building requires an understanding on the part of the engineer of the way in which it supports gravity loads, resists earthquake forces, and accommodates related displacements (FEMA 306). According to their behavior under horizontal seismic actions, Eurocode8 and TSC 2007 propose similar classifications for concrete buildings in terms of structural types. The systems with concrete shear walls were classified as (according to TSC 2007 description given in Table 2-5):

"… (1.2) Buildings in which seismic loads are fully resisted by coupled structural walls..
(1.3) Buildings in which seismic loads are fully resisted by solid structural walls..
(1.4) Buildings in which seismic loads are jointly resisted by frames and solid and/or coupled structural walls..........."

Obviously it is not possible to talk about a unique structural type that can be used as a basis to infer conclusions about the behavior of structural walls by using it in the structural analysis. In addition to purpose of providing the necessary lateral load resistance and displacement control over the height of the structure, structural wall can be also designed to compose the vertical load carrying system of the entire system. Depending on these explanations, shear wall buildings can be classified into two broad groups:

1. Shear/Flexural lateral load resisting buildings.
2. Bearing wall buildings

where typical plan views of such type of buildings are as displayed in Figure 4.1.

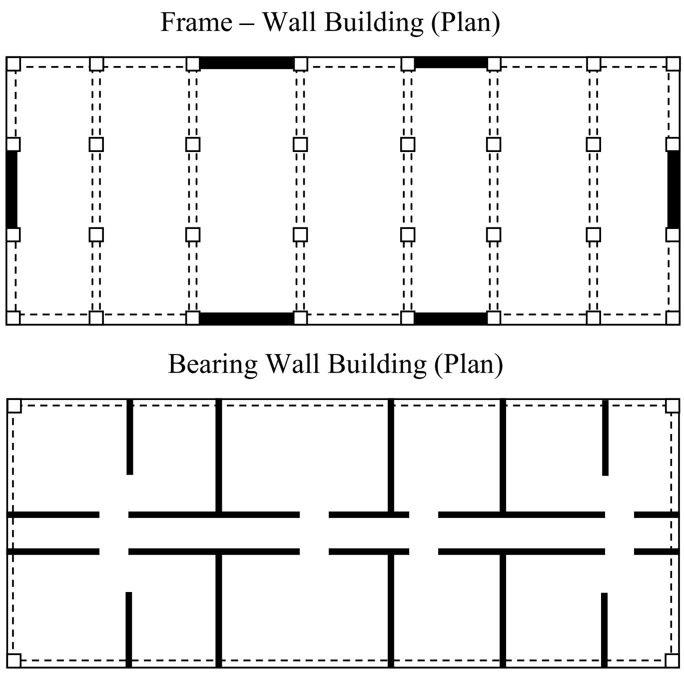

Figure 4.1 Comparison of typical frame-wall and bearing wall building configurations

First category structures utilize both frames and walls to resist earthquake actions in parallel. This particular form of structure is commonly known as frame-wall structure or dual system structure. In this structural form, frames and walls share the total base shear due to applied lateral load on the structure in different proportions. Dynamic behavior of dual systems is considerably different from pure frame or wall structures. Such differences in dynamic behavior are attributed to the interaction that takes place between the frames and walls. As being different than frame-wall design where structural walls are primarily designed for lateral load resistance, walls in bearing wall buildings are also designed to carry vertical forces.

In United States the common type of concrete shear wall building consists of shear wall – flat plate floor systems. Typical plan drawing of such type of buildings located at site in downtown Los Angeles, which is a high seismic region, is shown in Figure 4.2 (Kim, 2004). The lateral load resisting systems of the building are special reinforced concrete shear walls for the transverse direction and special moment resisting frames for the longitudinal direction. The eight shear walls are located at the core in the center of the building plan and along each side. The walls are located at column lines so as not to disturb architectural elements. They are also architectural elements themselves that serve as either elevator cores or stairways. Most of the gravity load is carried by a flat-plate floor system, with no beams, to columns that transfer gravity load down through slab.

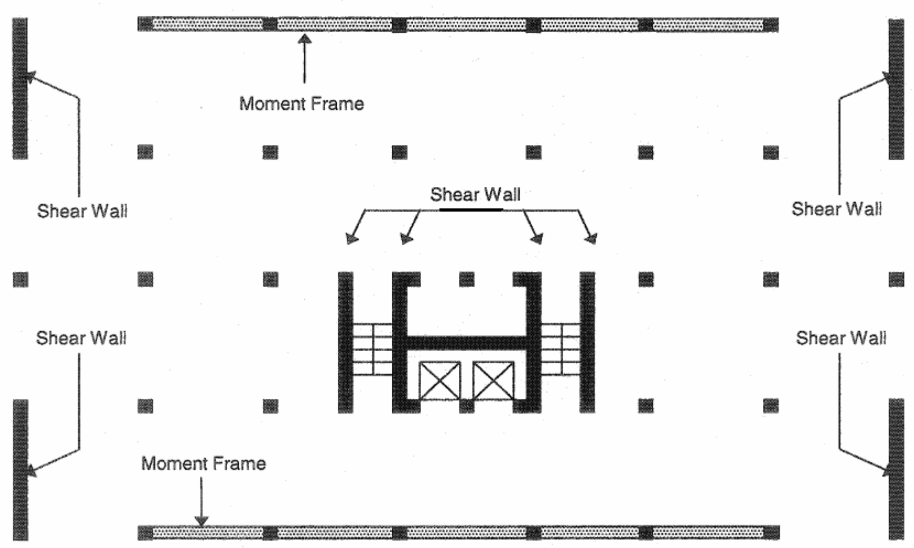

Figure 4.2 Typical US construction of shear wall building (adapted from Kim, 2004).

Box systems are extensively used in countries like Turkey, China, Japan, New Zealand and Chile in high seismicity prone regions. In Turkey shear wall dominant buildings constructed by using a tunnel form system (i.e., box system), so called tunnel form buildings, utilize all wall and slab elements as primary load carrying and transferring members (Balkaya and Kalkan, 2004). Riddle et al. (1987) reports the wall-to-plan area ratio in the range of 4-5% for moderate rise Chilean bearing wall buildings. In general lateral stiffness or strength of structures including structural walls is related with the total wall area in plan. In regards to typical wall area, defined as the ratio of total wall to floor area, Wallace and Moehle (1992) argues that the U.S. construction for concrete buildings 5- to 20-strories tall relies on frames or combined frame-wall systems to resist lateral loads, and the total wall to plan area is typically in the order of 1% for these structures.

4.1.2 Differences in the Behavior Modes of Shear Walls

The inherent free and forced deflected shapes of a cantilever wall and a frame are quite different as shown in Figure 4.3. An isolated structural wall is actually a cantilever of which behavior is controlled by bending moments. The total deflection calculated at the tip of the cantilever is composed of both flexural and shear deformations, but only a minor part due to shear. The amount shear deformation is related to height to width (H_w/L_w) ratio of the structural wall. On the other hand, even though the beam and column members composing the frame are relatively slender compared to a structural wall, the beam-to-column stiffness ratio, ρ, controlling the relative joint rotation in building systems due to the beam to column flexural stiffness contributions at the story levels determines the dominant behavior type (Blume, 1968). This parameter controls the degree of participation of lateral flexural and shear deformations in moment-resisting frame building. The general form of ρ is given by

$$\rho = \frac{\sum (I/l)_{beam}}{\sum (I/l)_{column}} \tag{4.1}$$

where (I/l) represents the rigidity of a member, which is the ratio of member's section moment of inertia to the member's length. When realistic values of ρ, derived from regular reinforced concrete frames with uniform lateral stiffness along the height, is considered, a modal deflected shape in the first mode as shown in Figure 4.3(a) is obtained (Akkar et al., 2005). The mode shape for $\rho = 0$ represents pure flexural behavior. As ρ increases, the behavior is controlled by both shear and flexural displacements. When $\rho = \infty$, the structure acts as a shear frame.

A wall located in any of the structural forms mentioned above will be in an interaction with the structural system causing different behavior modes. The failure mechanism of the wall not only depends on the geometry of the cross section, but also on the way the wall is loaded (FEMA 306). If the wall is subjected to a large moment which produces yielding with low shear, the mechanism will be completely different than if loaded with low moment but large shear. The way the wall undergoes inelastic deformations will determine the path of force redistribution, and entirely dominate the subsequent response of the building (Charney and Bertero, 1982). For instance, in frame-wall systems relative rigidity of frame has significant effect on deformation and strength characteristics of structural walls (Vallenas et al., 1978; Kayal, 1986).

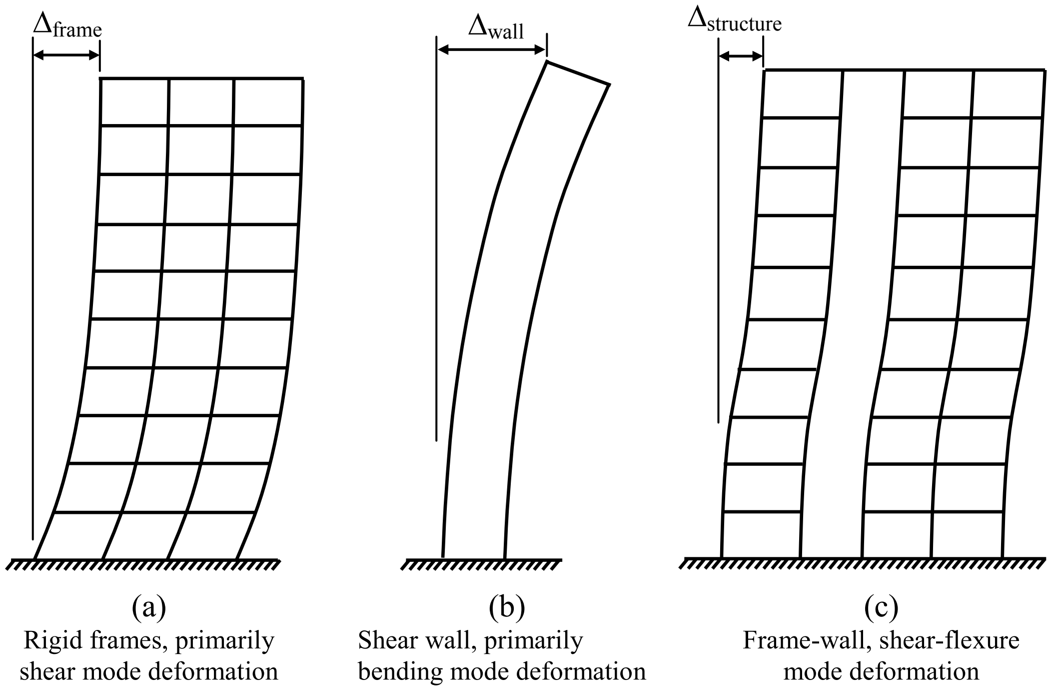

Figure 4.3 Deformation modes of frame-wall structures

4.2 SIMPLIFIED PROCEDURES FOR THE ANALYSES OF SHEAR WALLS

The elastic and inelastic behavior and the failure mechanism of reinforced concrete frame-wall systems (dual systems) were investigated by different researchers in an approximate manner by replacing the structure with a system of idealized mechanical models. The name "frame-wall interaction force" was given to the forces developing in the rigid link beams connecting the wall and frame components of the mathematical model developed and widely used for analyzing frame-wall systems as shown in Figure 4.4 (Khan and Sbarounis, 1964; Emori and Schnobrich, 1981; Charney and Bertero, 1982; Scarlat, 1995). The method involves the floor by floor interaction of planar panels consisting of walls, or frames, or both. The lateral loading is usually distributed between the component structures in proportion to their rigidities at each story. A simple elastic frame-wall model that takes into account the interaction effects was first proposed by Khan and Sbarounis (1964). An iterative procedure was developed in that study to calculate the lateral displacements and forces in the system. The model proposed by Kahn and Sbarounis (1964) depends on the equivalent dual structure concept in which the frames were replaced by an equivalent one-bay frame where each column in the story is assigned the half of the total stiffness of the columns in that story. In the same way, the structural walls were replaced by an equivalent structural wall. Equivalent frame and wall is connected with rigid connection bars ensuring equal horizontal deflections as shown in Figure 4.4.

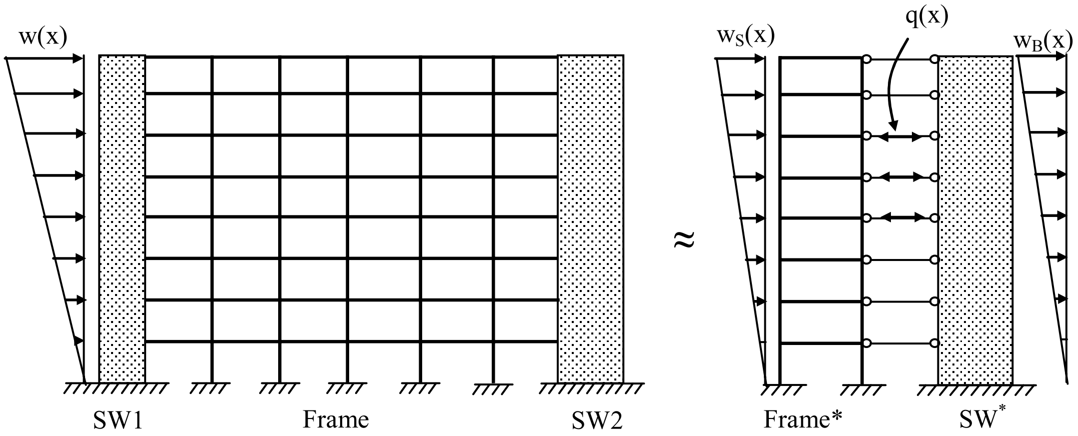

Figure 4.4 Frame wall interaction model after Khan and Sbarounis (1964)

Macleod (1971) developed and proposed another method based on a number of simplifying assumptions as a practical design tool for designing a regular building of average height. Heidebrecht and Smith (1973) derived the differential equation governing the response of frame-wall system based on an analogy to shear-flexure beam. The closed form solution to this equation can be used to calculate the lateral displacements, bending moments, and shear forces under static triangular, uniform and a point top lateral load. Design curves for displacement, moment and shear force distribution over the non-dimensional height of the structure for different frame rigidities were presented in their study. MacGregor et al. (1972) proposed a simplified equivalent frame-wall model that was divided into the frame system and the wall system in which the properties of all same type of members were lumped into a single member in a story, such as frame beams spanning between two adjacent columns, link beams linking the shear walls to the columns and all the shear walls by a single wall having as stiffness and plastic moment capacity equal to the sum of the stiffnesses and plastic moment capacities of the individual walls. The moment rotation relationship for the individual frame members were idealized as elastic-plastic for beams and columns and elastic-strain hardening for the shear walls.

Emori and Schnobrich (1981) presented three mechanical cantilever beam models that were studied by previously and can be used to idealize the structural wall: (1) a concentrated spring model (Otani, 1974); (2) a multiple spring model (Takayanagi and Schnobrich, 1976); and (3) a layered model. The concentrated spring model consists of a flexible elastic line element over the beam length, and a nonlinear rotational spring element at the restrained end of the beam, as shown in Figure 4.5(a). The multiple spring model is a line element model composed of a number of springs in series connected by rigid links. Each subelement may have different values of inelastic properties. The layered model shown in Figure 4.5(c) is a modification or alteration of the concentrated spring model. Instead of the nonlinear spring, a layered cross section of length L_p is assigned to the end of the cantilever beam, so the inelastic flexural action of the cantilever beam is calculated explicitly allowing the contribution of the effect of axial load. The length L_p is chosen as the region where major inelastic action is expected. The entire frame-wall system is therefore idealized as a plane structure composed of two components. One of the systems is the isolated wall. The second system is a substitute frame structure which models the two parallel rigid frames as a frame substructure.

Miranda (1999) adopting the equivalent continuum shear-flexure beam model developed by Heidebrecht and Stafford Smith (1973) calculated the seismic lateral deformation demands in multistory buildings under generalized lateral static loads. Later, Miranda and Akkar (2006) derived the generalized interstory drift spectrum, which extends the drift spectrum to buildings that do not deform laterally like pure shear beams as proposed by Iwan (1997), using the same continuous model that consists of a combination of a flexural beam and a shear beam. Miranda and Reyes (2002) used the same formulation to estimate the maximum lateral drift demands in multistory buildings with nonuniform lateral stiffness primarily responding in the fundamental mode when subjected to earthquake loads.

Sozen (1989) developed a simple analytical tool to calculate the displacement response of shear wall buildings for a given earthquake strong motion. The study concerning with the observed behavior of reinforced concrete shear wall buildings in Vina del Mar during March 1985 Chile earthquake, the model did not suggest that its results should be identical to individual response of large inventory of shear wall buildings, but it was rather intended to show that certain dominant structural properties have led to observed damage on the buildings.

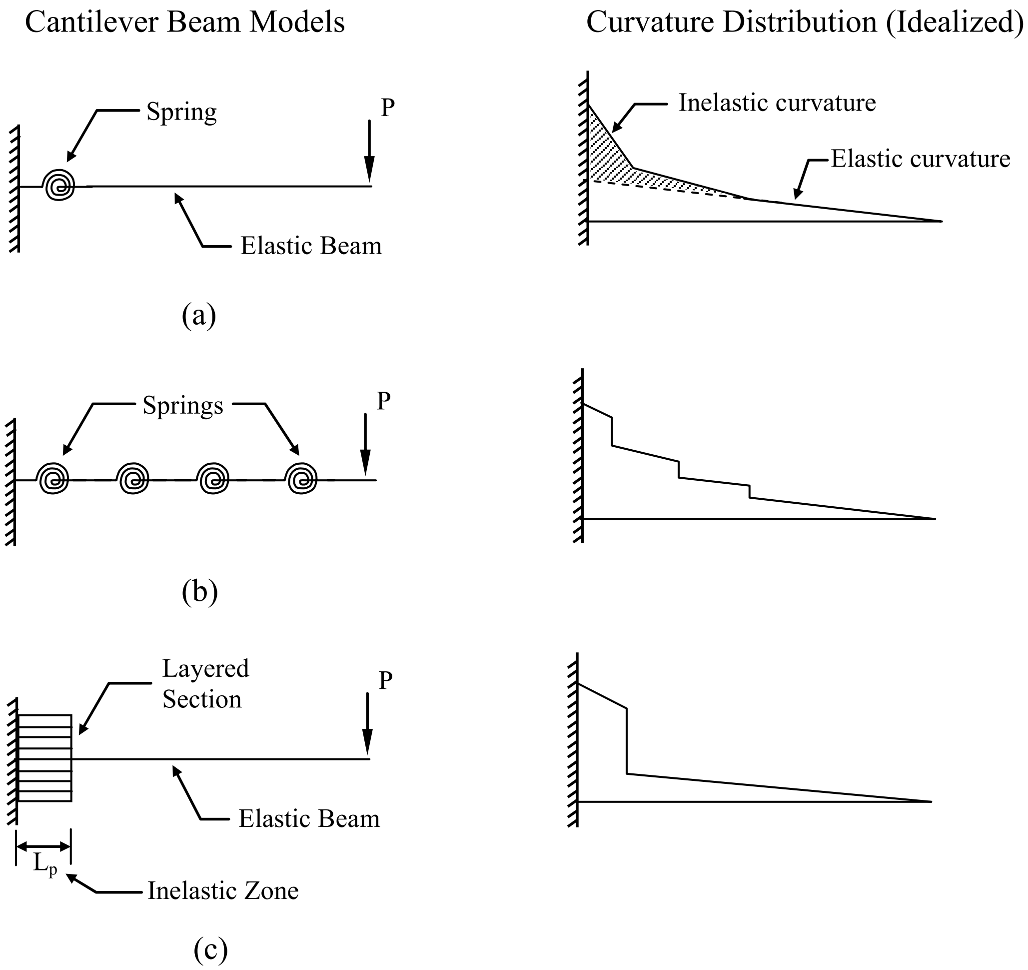

Figure 4.5 Mechanical models used by Emori and Schnobrich (1981) in modeling shear walls to investigate the inelastic behavior of concrete frame-wall structures: (a) Concentrated Spring Model; (b) Multiple Spring Model; (c) Layered Model.

This study focus on two simplified procedures among the studies summarized above for the analyses of structural wall buildings. The models are the isolated cantilever wall model as described by Sozen (1989) and the shear-flexure beam continuum model of Heidebrecht and Stafford Smith (1973). While the former applies to wall dominant structures responding in cantilever mode, the later can be used to model frame-wall systems. Both methods are developed for linear analysis purposes, but here procedures are implemented to extend the range of their applicability to nonlinear range.

4.2.1 Isolated Wall Model

The expression for the fundamental period of a cantilever beam of uniform cross section and uniformly distributed mass is (Clough and Penzien, 1993),

$$T = \frac{2\pi}{3.52}\sqrt{\frac{mH^4}{EI}} \tag{4.2}$$

where

m = mass per unit height

H = Total height

I = Moment of inertia of cross section

Depending on the assumption that the fundamental period of a building, where flexural behavior of structural walls dominates the lateral load response, can be approximated by analysis of an equivalent cantilever, Sozen (1989) derived the following equation to calculate the fundamental period of an uniform concrete cantilever having rectangular cross section and supporting regularly distributed floor load (Figure 4.6) as

$$T = 6.2\frac{H_w}{L_w}N\sqrt{\frac{wh_s}{gE_c p}} \tag{4.3}$$

in which N = number of floors; w = unit floor weight including tributary wall height; h_s = mean story height; E_c = concrete modulus of elasticity; H_w = wall height; and p = wall index, ratio of wall area to floor plan area for the walls aligned in the direction the period is calculated ($p = \Sigma A_w / A_f$, where $A_w = L_w t_w$, L_w is the wall length, t_w is the wall thickness, and A_f is the floor plan area of a typical floor of the building). For cracked section the number in front of the expression given in Eq. (4.3) shall be taken as 8.8.

The expression in Eq. (4.3) can be further simplified by introducing typical values of w = 10.0 kPa (1.02 t/m^2), h_s = 300 cm, g = 981 cm/s^2 and E_c = 25,000 MPa (these are the typical values adopted in study, so the coefficient in this study may differ from the ones in other works) and assuming uncracked section as

$$T = 0.00216\frac{H_w}{L_w}N\frac{1}{\sqrt{p}} \tag{4.4}$$

As seen in Eq. (4.4), it is possible to express the fundamental period of structural wall buildings in terms of three nondimensional parameter: the slenderness ratio of the primary walls (H_w/L_w), the number of stories (N), and the wall index, p (the ratio of wall are to floor area).

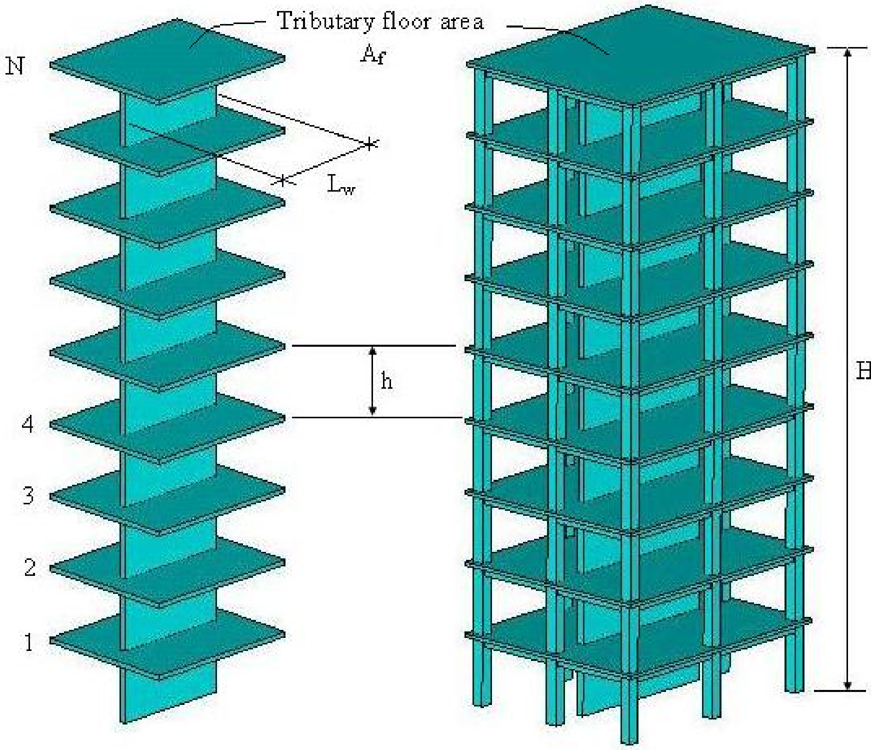

Figure 4.6 Generic shear wall building models

4.2.1.1 *Roof Drift of Wall Type Structures*

The procedure presented by Sozen (1989) exploited by Wallace and Moehle (1992), Wood (1991), Riddell and Vasquez (1992), and Gülkan and Utkutuğ (2003) in later studies to investigate the roof drift demands in shear wall buildings. In a series of technical papers, Wallace presented the general guidelines of a displacement-based analytical procedure for the seismic design of reinforced concrete shear walls (Wallace, 1994; Wallace, 1995a-b). The aim of the procedure is to relate the global and local deformations. The procedure uses a computed strain distribution to determine requirements for transverse reinforcement at wall boundaries for concrete confinement and to restrain buckling of reinforcement.

A step forward after the derivation of Eq. (4.3) is the definition of a ground motion in terms of displacement response spectrum. In the derivation of spectral displacement demands, Wallace (1994) utilized the expression in ATC-3-06 for the spectral acceleration for elastic response. Assuming high seismicity (a seismic coefficient A_v=0.4 representing the effective peak acceleration of the ground) and firm soil site as the site class, the elastic spectral displacement for 5% damping was computed as

$$\begin{aligned} S_d &= 25T^2 \cdots (cm) \cdots\cdots 0.0 \le T \le 0.585\ s \\ S_d &= 15T \cdots (cm) \cdots\cdots 0.585\ s < T \end{aligned} \tag{4.5}$$

Finally for a shear wall building, the elastic displacement calculated for a single degree of freedom oscillator is related to the roof displacement of the actual multi degree of freedom structure by using a factor of 1.5. The roof drift (roof displacement divided by building height, δ_u/H_w) is computed by multiplying Eq. 4.5(a-b) by 1.5 and dividing by the building (or wall) height, H_w,

$$\frac{\delta_u}{H_w} = \frac{1.5(S_d)}{H_w} \tag{4.6}$$

The roof drift is expressed in terms of the wall aspect ratio (H_w/L_w) and wall index, p, by substituting the spectral displacement and the cracked stiffness period T as given in Eq. (4.5) and Eq. (4.3) with front multiplier of 8.8, respectively, into the Eq. (4.6) as

$$\frac{\delta_u}{H_w} = 0.2\frac{H_w}{L_w}\sqrt{\frac{wg}{E_c p h_s}} \tag{4.7}$$

Again substituting the typical values introduced above into the expression in Eq. (4.7), we get for the mean drift ratio

$$\frac{\delta_u}{H_w} = 0.00023\frac{H_w}{L_w}\sqrt{\frac{1}{p}} \tag{4.8}$$

Wallace (1994) stated that the roof drift ratio obtained should tend to be conservative because the cracked stiffness period is based on half the gross-section stiffness and the “typical” values are selected to produce a high drift estimate. For Eq. (4.7), depending on different seismic spectral displacement definition Sozen’s work (1989) yields a front multiplier of 0.25 for the same material and mass characteristics assigned above. Eq. (4.8) is plotted for several aspect ratios as shown in Figure 4.7.

In the most basic form, the isolated shear wall model shown in Figure 4.6(a) can be used as a base model in the NLFEA analyses of structural walls. However, Eq. (4.4) should not be interpreted as a magical formula that gives good results for the period estimation of structures where structural walls are encountered. Certain limitations in regards to aspect ratio of the walls and mass assignment needed to be identified for the determination of dynamic attributes of structural walls. Indeed the period formula given in Eq. (4.4) has a very restricted applicability.

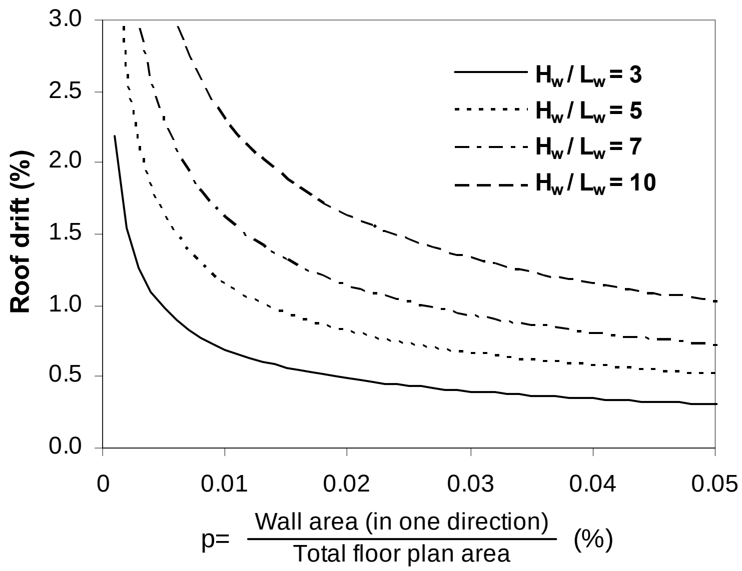

Figure 4.7 Estimate of the roof drift for wall type structures

Then the global deformations imposed on the structure are related to local deformation on the wall cross section by using well-established procedures to account for the distribution of elastic and inelastic deformations over the height of a structural cantilever wall. Based on the model of Figure 4.8, which assumes triangular load distribution, the displacements at the top of the wall can be computed as

$$\delta_u = \delta_y + \theta_p H_w = \frac{11}{40}\phi_y H_w^2 + \frac{1}{2}(\phi_u - \phi_y) H_w L_w \tag{4.9}$$

where δ_y = displacement resulting form elastic deformations; $\theta_p H_w$ = displacements resulting from inelastic deformations; ϕ_y = yield curvature (curvature at first yield of the wall boundary reinforcement); ϕ_u = ultimate curvature; and L_p and θ_p = plastic hinge length and rotation, respectively. For low values of axial load and low steel ratios, the yield curvature can be approximated by

$$\phi_y = \frac{0.0025}{L_w} \tag{4.10}$$

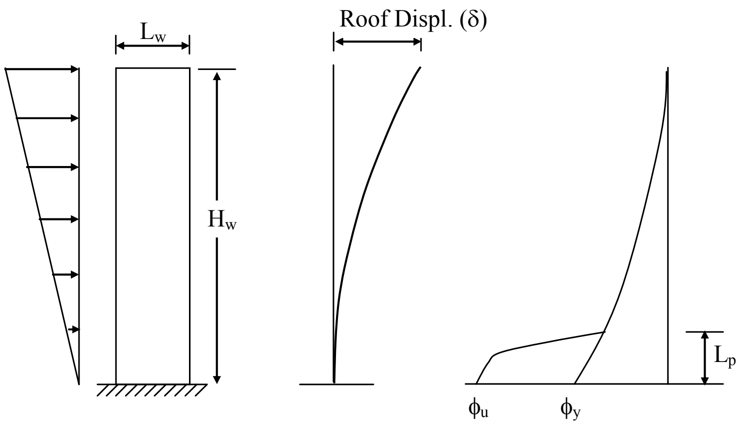

Figure 4.8 Relationship between global and local deformations

The value of ϕ_y increases with increasing steel ratios and axial load. Assuming the plastic hinge is half the wall length (L_p = $0.5L_w$) and using the relation in Eq. (4.10), the deformations imposed on a wall can be derived in terms of the ultimate curvature times the wall length (Wallace and Moehle, 1992) as

$$\phi_u L_w = 0.0025\left[1 - \frac{1}{2}\frac{H_w}{L_w}\right] + 2\frac{\delta_u}{H_w} \tag{4.11}$$

If Eq. (4.9) is substituted in Eq. (4.11), the deformation imposed at the base of the wall can be expressed directly in terms of the building configuration as

$$\phi_u L_w = 0.0025\left[1 - \frac{1}{2}\frac{H_w}{L_w}\right] + 0.00046\frac{H_w}{L_w}\sqrt{\frac{1}{p}} \tag{4.12}$$

Now the detailing requirements such as the concrete confinement required at the boundary element can be evaluated by comparing directly the deformations imposed on the wall cross section with the available flexural deformation capacity of the wall cross section. It was assumed that the wall has rectangular cross section and uniformly distributed reinforcement plus boundary steel. Axial load is centered on the wall web. The longitudinal tension and compression reinforcement is assumed to develop a stress of $\alpha_m f_y$ and γf_y, respectively, to account for possible material over strength and strain hardening (assumed values are α = 1.5 and γ = 1.25). By considering the equilibrium requirement on a rectangular wall cross section, wall deformation capacity is estimated by the relation

$$\varepsilon_{c,\max} = \left[\frac{\left(\rho + \rho'' - \frac{\gamma}{\alpha_m} \rho' \right) \frac{\alpha_m f_y}{f_c} + \frac{P}{A_w f_c}}{\left(0.85\beta_1 + 2\rho'' \frac{\alpha_m f_y}{f_c} \right)} \right] \phi_u L_w \tag{4.13}$$

where $\varepsilon_{c,max}$ = extreme fiber concrete compressive strain; $\rho = A_s/t_w L_w$ = tension steel reinforcing ratio; $\rho' = A_s'/t_w L_w$ = the compression steel reinforcing ratio; $\rho'' = A_s''/t_w L_w$ = the distributed steel reinforcing ratio; f_y = nominal yield stress of the reinforcement; f_c = the compressive strength of the concrete; α_m and γ = factors to account for reinforcement overstrength and strain hardening; P = wall axial load; L_w = wall length; and t_w = web thickness. The equation is valid for rectangular, T-shaped and L-shaped (flanged) walls. A similar expression was also derived for barbell-shaped walls.

For symmetrically reinforced rectangular wall sections, assuming f_c = 25 MPa, f_y = 420 MPa, the extrapolation of above Eq. (4.13) results in following extreme fiber maximum compressive strain curves as shown in Figure 4.9 for different parameters. The concrete compressive strain at the extreme fiber increases as the slenderness of wall increase (larger H_w/L_w ratio).

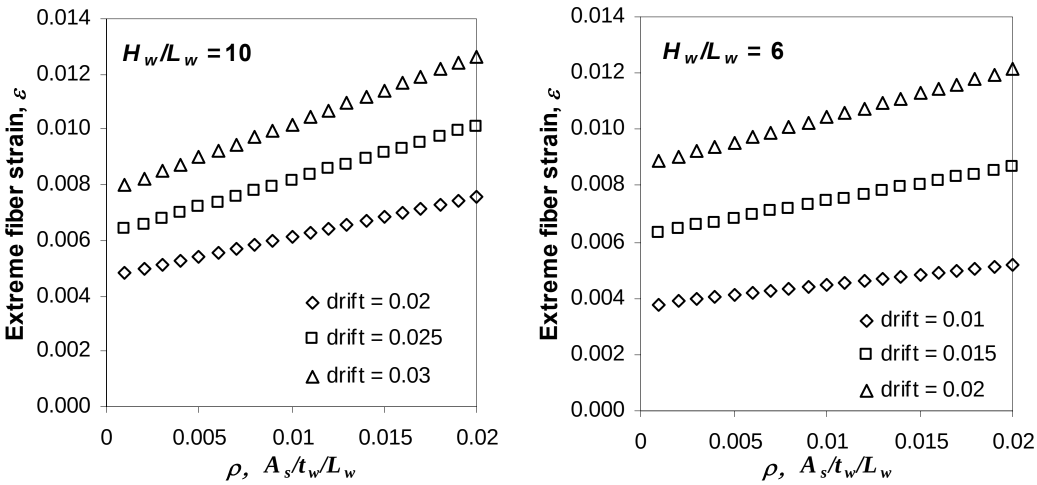

Figure 4.9 Compressive concrete strain at the extreme confined boundary

4.2.1.2 Global Ductility Estimation

Using moment-curvature analyses of cantilever shear walls Kowalsky and Priestly (1998) has shown that yield curvature, serviceability curvature, and ultimate (damage-control) curvature are insensitive to variations of axial load ratio, longitudinal reinforcement ratio, and distribution of longitudinal reinforcement. This implies that the ratio of neutral axis depth (depth to extreme compression fiber) to wall length is essentially constant for a given strain limit state defined by both concrete compression and steel strain limits. For example, if ε_{cu} = 0.018 and ε_s = 0.06, the neutral axis depth ratio becomes 0.2 (c_u=0.2L_w). The results were used to determine available displacement ductility factors for walls of different aspect ratios and drift limits. They stated that drift capacity will generally exceed code levels of permissible drift, and that code drift limits will normally restrict, sometimes severely, the design displacement ductility factor.

Later in a similar framework that was used by Wallace (1994), Kowalsky (2001) examined the seismic provisions of the 1997 Uniform Building Code (ICBO, 1997) from perspective of achieving performance-based earthquake engineering of structural wall buildings. Through the use of design examples and dynamic inelastic time history analysis he concluded that a hybrid design procedure that achieves a performance-based engineering with a force-based approach to specify and control damage in the design process as described in 1997 UBC is not possible. It was also reported that although strain limits are present in the 1997 UBC, the drift ratio limits generally govern the design.

Priestly and Kowalsky (1998) related the curvature ductility (μ_ϕ) of the cross section to the displacement ductility (μ_Δ) at an effective height of 2/3 the total wall height by the expression

$$\mu_\Delta = 1 + 3(\mu_\phi - 1)\frac{3}{4}\frac{L_w}{H_w}\left(1 - \frac{3}{8}\frac{L_w}{H_w}\right) \tag{4.14}$$

Since they claimed that the drift ratio based on the concrete ultimate extreme compression fiber strain of 0.015 will rarely govern the design, they proposed the following relation to calculate the displacement ductility demand based on the maximum allowable drift limits of θ_{max} = 0.02 and 0.025.

$$\mu_\Delta = 1 + 3\left[667\left(\theta_{max} - 0.0015\frac{H_w}{L_w}\right)\right]\frac{3}{4}\frac{L_w}{H_w}\left(1 - \frac{3}{8}\frac{L_w}{H_w}\right) \tag{4.15}$$

The relation given in Eq. (4.15) is plotted in Figure 4.10 for displacement ductility versus aspect ratio for two values of allowable drift ratio.

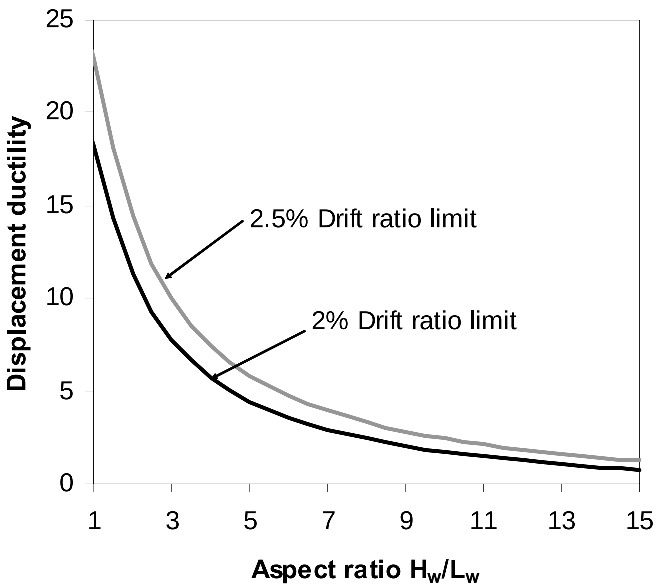

Figure 4.10 Drift limit Ductility levels (Priestley and Kowalsky, 1998)

4.2.1.3 Period of Wall Type Structures (Cantilever Systems)

First of all it is necessary to identify the typical values of periods of shear wall buildings, in order to talk about the range of applicability of the formulas. Figure 4.11 presents the relation between the number of stories and period of shear wall buildings extracted from measured and analytical response of shear wall buildings as performed by different researchers (Wallace and Moehle, 1992; Goel and Chopra, 1998; Lee et al., 2000; Balkaya and Kalkan, 2003). Except the data from Balkaya and Kalkan (2003) all the information given in Figure 4.11 belong the measured response of real life structures. The data by Wallace and Moehle (1992) comes from Chilean shear wall buildings from the city of Vina del Mar as also used by Sozen (1989). These buildings have a wall index of 3% in average and 2% as the lowest. Data by Lee et al. (2000) is from the measured periods of Korean tunnel-form buildings with wall index of 2% approximately. Balkaya and Kalkan (2003) calculated the periods of 80 different tunnel-form building configurations that are typically applied in Turkey by using three-dimensional finite-element modeling. The average ratios of total wall to floor areas in these buildings are 2-3%. The data from Goel and Chopra (1998) covers the measured periods of buildings during eight California earthquakes starting with 1971 San Fernando and ending with the 1994 Northridge earthquake. These buildings have wall indexes ranging from 0.3% to 3%.

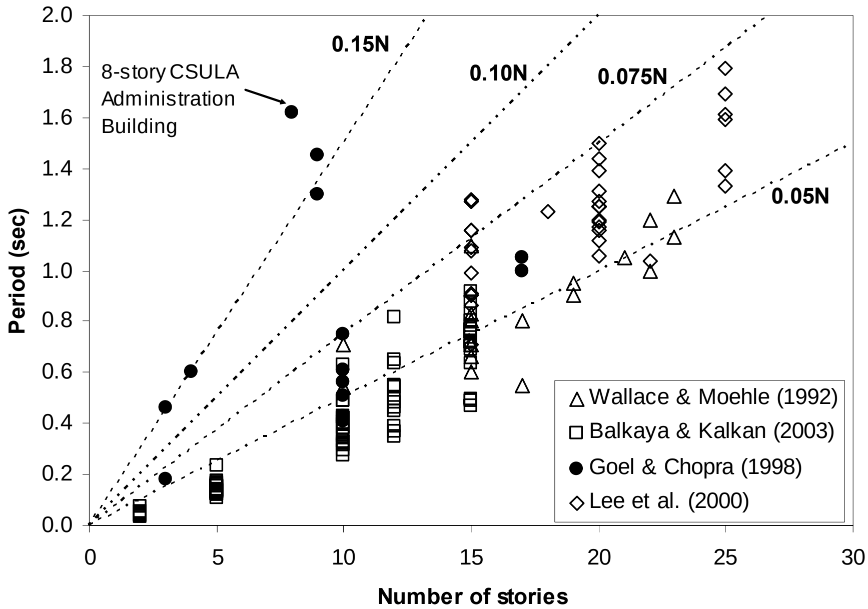

Figure 4.11 Period versus height relation of shear wall buildings

What is noticed at first glance in Figure 4.11 is that the presented data correlates well with the well-known approximate relationship between fundamental period and number of stories of shear wall buildings, $N/20$. These buildings have wall indexes larger than 2%. The outlier points lying on $0.15N$ line are from Goel and Chopra's (1998) building inventory. These buildings have special features in terms of structural systems such as flat-plate system with core walls or vertical irregularities in the plan. For example, one of the outliers, the 8-story CSULA Administration Building with reinforced concrete slab, beams and column as vertical load carrying system and concrete shear walls except between levels 1 and 2 where concrete and steel columns are used as lateral force resisting system, poses a very large fundamental period (T_1 = 1.62 s) due to very soft 1st-story, which has height of 7.26 m as shown in Figure 4.12. Above the 1st-story, the ratio of area of walls in the transverse direction to the floor area is 1.6%, which indeed is an adequate wall index to provide the lateral stiffness.

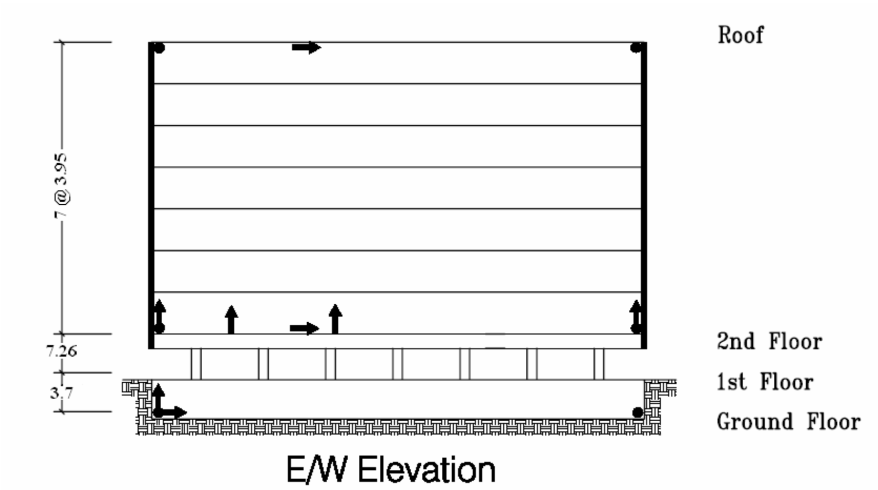

Figure 4.12Los Angeles – 8-story CSULA Administration Building

For further augmenting our understanding on the subject lets assume 4-, 8- and 12-story cantilever wall structures composed of 3, 5 and 8 m walls in length with story height of 3 m. The periods calculated by using Eq. (4.4) for different wall and building height combinations yielding different aspect ratios for isolated shear walls are plotted in Figure 4.13. Restricting the applicable range of calculated period between $0.05N$ and $0.1N$ it can be concluded that the formula given by Eq. (4.4) yields meaningful results for aspect ratios only up to 5 for a very large portion of wall index spectra (p>0.005). As the aspect ratio (slenderness ratio) increases the wall index required to provide adequate stiffness also increases. However, as the 12-story case displayed by no means it is logical to assume an isolated wall model with a wall length of 3 m in buildings taller than 10-story, which corresponds to slenderness ratios larger than 10.

Evidence to such situation was provided by Riddell and Vasquez (1992). They were using Eq. (4.4) and the average amount of wall area of 3%, i.e. p=0.03, for the Chilean buildings, calculated the fundamental period of the generic building as

$$T = 0.0125 \frac{H_w}{L_w} N \tag{4.16}$$

Then combining Eq. (4.16) with the approximate relationship between fundamental period and number of stories, T=0.05N, a typical slenderness was found as 4, or, for a more flexible building with T=0.075N as 6. This limitation should be considered as a rule of thumb of the Sozen's formula while using it. It is obvious that if smaller wall index (p) is adopted in Eq. (4.16), much smaller wall aspect ratios (H_w/L_w) are required to obtain logical period values.

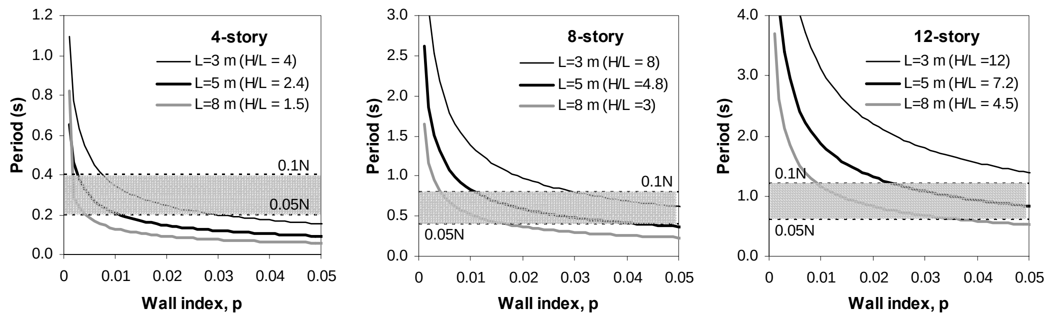

Figure 4.13 Periods calculated for range of wall indexes as a function of wall aspect ratio

This conclusion is important because isolated cantilever idealization of structural walls is a widely used tool (may be the only) in the seismic response assessment of structural walls. Indeed such an idealization of structures carries risks since 3D originated force mechanism build-up in structures due to frame-wall, wall-to-wall and wall-to-slab interactions are all ignored. No structure acts as cantilever unless it is so. Additionally higher mode effects causing amplification in the shear and moments along the height of the walls should come into scene more easily leading to illogically conservative dynamic amplification factors, when such models violating the aspect ratio rule is adopted in analytical studies. The modal mass participating in the first mode of a cantilever is smaller than the frame-wall or coupled wall structure.

4.2.2 Frame-Wall Model: Continuum Approach

The walls can seldom exist in such an idealized configuration described above. If tunnel-form structures are disregarded, since this study excludes them due to distinct load resisting characteristics, walls mostly exist in structures in combination with moment resisting frames. Frame-wall structures can be composed of either (i) structures with walls and frames connected by floor slabs, or (ii) structures with link-beams extending from frames directly to the ends of the walls. The interaction between the frames and walls of structures with link beams is more significant than in the classical form of frame-wall structure in which the frames are parallel to the walls, i.e. walls are located inside a frame (Sullivan et al., 2006). The shear and moment transferred from beams can significantly change the moment profile causing a reduction in the inflection height of the wall. The beam shear forces transferred from both side of the wall affect the axial load on the wall. If the problem is idealized by assuming beams of equal strength and equal length that are framing to the wall from both side, the axial load will not be affected by the beam shears since they will cancel out. However, the beam shears from both sides will form a moment couple which has to be added to moments transferred from beams. Additional 3D effects such as transverse beams' shear forces also contributes to the moments created by the framing shear wall beams as shown in Figure 4.14, a deformed shape view taken from the analyses results of a five-story reinforced concrete frame-wall.

The distribution of the applied lateral load between these two systems in proportion to their relative lateral stiffness and based on the assumptions of small deformations and linear elasticity can lead to serious errors. Because of the inherent difference between the deflected shapes of these two particular systems under lateral loading, frame-wall interaction generally results in reduced lateral displacements at upper floors affecting the distribution of wall moment over the height of the building (Wallace, 1994). Contrarily, over the lower floor levels frame-wall interaction results in an increase in the slope of the moment diagram, and thus an increased shear demand on the wall compared with cantilever walls.

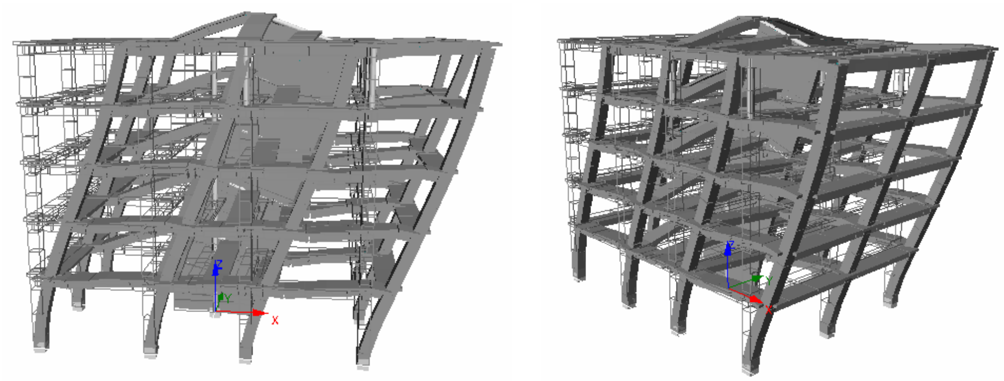

Figure 4.14 Deformed shape of a frame-wall structure displaying the pattern of displacements and rotations for frame and wall components.

Frame wall-interaction poses a serious problem for reinforced concrete structural walls especially in situations where the frame part of the structural system becomes stiffer as compared to the walls. Kayal (1986) investigated the effect of wall-column stiffness ratio, defined as the ratio of the flexural rigidities of the shear wall and the column (EI_w/EI_c), among with additional parameters such as the ratio of beam and column stiffness, load ratio (lateral to vertical load). One of the significant conclusions emerged from this study is that nonlinear idealization of the flexural characteristics of shear walls became more pronounced when shear walls are located in stiff frames since the actual characteristic of shear walls, which is "shear behavior" has to be activated.

In similarity with the isolated cantilever flexural beam used to model structural wall buildings responding primarily in flexure mode, continuum method utilizing combined shear-flexural beam formulation for the analysis of frame-wall and coupled wall systems can be used to investigate the frame-wall interaction problem. Dating back to the 1960s a significant amount of work has been conducted on the continuum approach for the static and dynamic analysis of planar structures consisting of interacting frames and shear walls. Initially the method evolved as a simple yet effective and reliable hand calculation method for the proportioning of structural members in design offices (Heidebrecht and Stafford Smith, 1973). Although in his discussion of the article by Heidebrecht and Stafford Smith (1973), Rosman (1973) claimed that the method had been developed much more completely by himself earlier (Rosman, 1968), this study takes the work of Heidebrecht and Stafford Smith (1973) as its basis. Lately it has been widely used to calculate the dynamic properties of tall buildings and used in studies that deal with the behavior of variety of structures. The method can be easily programmed allowing a reduction in the idealization burden without going through detailed structural modeling by representing each structure with only one parameter (αH) (Miranda and Reyes, 2002).

Since in the shear-flexure beam method, the multistory structure is modeled as an equivalent continuum structure composed of a flexural cantilever (accounts for shear walls) and a shear cantilever (accounts for frames), the forces and moments in the actual structure are assumed distributed along the continua. The continuum model for equivalent shear-flexure beam is given in Figure 4.15. It has to be noted that the beam moments acting on the walls were disregarded in the frame component since they do not have any influence on the lateral deformation. In the figure, $q(x)$ and $m(x)$ represents the action of interaction forces and beam moments transferred on the shear wall, respectively. The subscripts, B and S, refer to the flexural and shear beams, respectively. Although it is possible to assume the action of horizontal forces on the wall as distributed, a concentrated top interaction force is required to maintain the deformation compatibility and force equilibrium between the flexural and shear beams. This is why a point load of magnitude Q was included in the model shown in Figure 4.15.

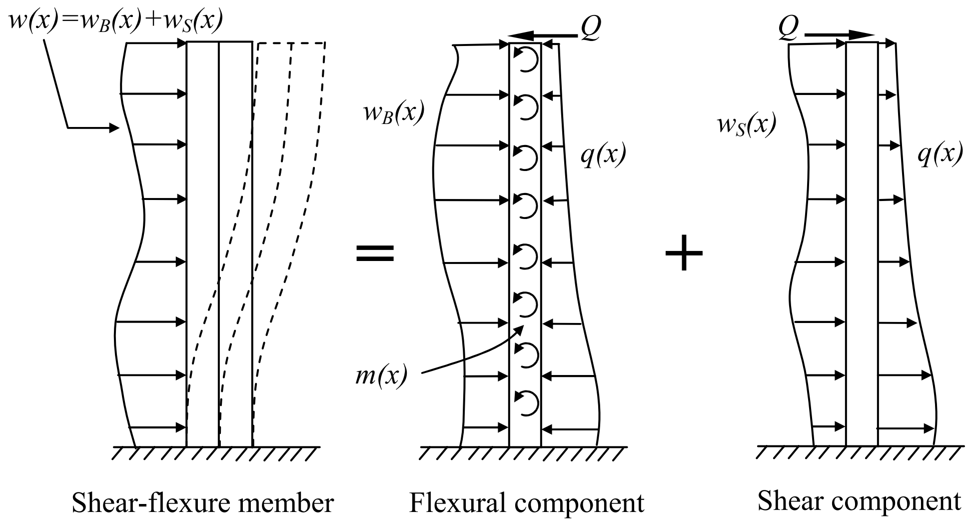

Figure 4.15 Mathematical model of shear-flexural beam, interconnected frame and shear wall (equal deflections at each story levels)

The rigid floor diaphragm provides nearly equal translations at all points of the floor area, however this doesn't necessitates the rotations at member ends be the same also. As shown in Figure 4.15, the deformations of frames and walls when individually considered are same. While the floor diaphragms exhibit very small rotations, the rotations on wall component accumulate as moved upwards and cause additional curves on the beams joining to the wall, especially at the uplift side, if the shift of the neutral axis is considered. So, the mathematical model of a shear-flexure beam used to calculate the response a frame-wall structure will have equal deformations through the continua, but the sectional rotations of each particular member will be different and calculated in accordance with the shear deformation beam theory.

Heidebrecht and Stafford Smith (1973), ignoring the moments transferred from beams to walls, gave the governing equation of the combination beam shown in Figure 4.15 by

$$\frac{d^4 y}{dx^4} - \alpha^2 \frac{d^2 y}{dx^2} = \frac{w(x)}{EI} \tag{4.17}$$

where $w(x) = w_B(x) + w_S(x)$ is the distributed lateral loading function and

$$\alpha^2 = \frac{GA}{EI} \tag{4.18}$$

in which *GA* and *EI* are the shear and flexural rigidities, respectively. While *EI* represents the flexural rigidity of all the flexural members in the systems, interpretation of shear rigidity *GA* being different represents the interstory horizontal shear force required to give a unit horizontal shearing deformation over the 1-story height as explained in APPENDIX E. A complete derivation of Eq. (4.17) is given in APPENDIX E. The main parameter that determines the dominant deformation mode of a shear-flexure beam is the parameter αH. Miranda and Reyes (2002) classified deflected shapes of the structural systems based on this parameter. According to this classification, the deflected shape of structures composed of structural walls as lateral load resisting system can usually be approximated by using values of αH between 0 and 2. The deflected shape of dual systems or braced systems can be calculated by values of αH typically between 1.5 and 6. For buildings composed of only moment-resisting frames the values of αH between 5 and 20 can be used.

A tall structural wall can be considered as vertical cantilever beam, with zero deflection and rotation at the base and free at the top, so the boundary conditions that apply to the solution of the differential equation are $y(0) = y'(0) = M(H) = V(H) = 0$, where H is the height of the structure. The shear force in the shear component (frame) is calculated as

$$V_S(x) = GA\frac{dy}{dx} \tag{4.19}$$

so the shear force at the base of this member becomes zero, which is not correct. The design curves for normalized frame and wall shear forces that were derived for different αH values were plotted in Figure 4.16.

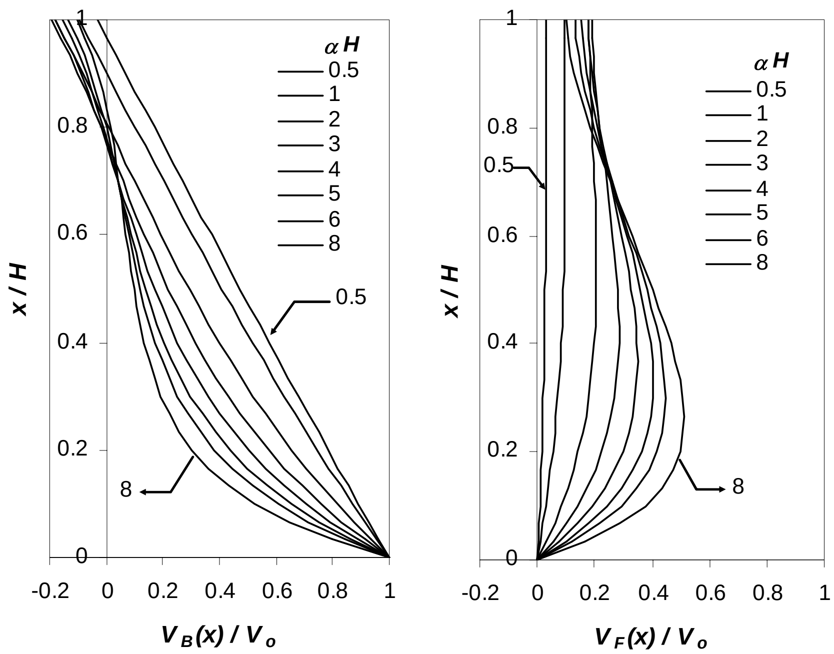

Figure 4.16 Shearing force on flexural (V_B) and shear (V_F) components for uniformly loaded beam. Regardless of relative rigidities of frame and wall components, at the base the entire base shear is attracted by flexural component

The discussion by Coull (1973) of Heidebrecht and Stafford Smith (1973) refers to this issue without any proposal for the solution of the problem. This problem has been often disregarded since it was assumed that the frame members tend to carry much less horizontal load than the wall in the lower levels, so its omission introduces only a minor error in the calculations (Coull, 1973). However, there are cases where frames carry a significant amount of the total base shear. It is also known that the amount of base shear assigned to each component of a dual system on the basis of elastic properties changes considerably after cracking and as a result of progressive yielding in the members, which increase the tendency of frames to carry additional load. Another fact that affects the base shear distribution between the frame and wall components and is disregarded in the analysis of shear walls is the fixed-end assumption. Due to very large moments induced on the foundations of shear walls may rotate, which causes reduction in the shear force in part of the shear wall. A continuum formulation that takes into account foundation flexibility on the interaction between shear walls and frames was presented by Toutanji (1997), but since taking this effect in to account should pose the risk of digressing the subject, fixed based assumption is adopted.

In APPENDIX E derivations of a new shear-flexure beam formula introducing the two refinements into the otherwise well-known formulation for wall-frame systems is given. One is the correction of the shear force boundary condition at the base of the wall, and the other is the additional distributed moment transferred from link beam ends. The primary components of the new formulation are illustrated in Figure 4.17. Referring to Figure 4.17, the structure is assumed to be composed of lower and upper substructures above and below the contra-flexure height of the base story columns. The governing equations for both substructure is derived accordingly and using the extra boundary conditions arising from displacement and force compatibilities at the contra-flexure height, the expression for displacement, shear and moment along the height of the wall are obtained. The method can be used for cases with uniform and non-uniform stiffness along the height of the structure. The expressions for direct estimation of displacement, rotation, shear and moment profiles along the wall are derived for triangular and uniform loading for uniform stiffness case. For non-uniform stiffness case transfer matrix method with necessary modifications in the matrices is adopted. The new formula for the primary substructure (upper part) reads as

$$\frac{d^4y}{dx^4} - \alpha^2 \frac{d^2y}{dx^2} = \frac{w(x)}{EI} \tag{4.20}$$

where $w(x) = w_B(x) + w_S(x)$ and

$$\alpha^2 = \frac{GA + \eta}{EI} \tag{4.21}$$

η holds for the equivalent flexural rigidity of beams framing to wall. This term is especially increase the accuracy of the calculations in cases where the transverse beams have substantial flexural capacity so increase the flexural resistance of the wall by the reactions from transverse beams. Although the governing equation seems to be the same with the previous version, Eq. (4.17), the differences lie in the added beam flexural rigidity term and the nonzero boundary conditions applicable to solution of this equation as given in Eqs. (E.36) to (E.38). The expressions for the distribution of displacement, shear and moment along the height of the walls in frame-wall system are given through Eqs. (E.41) to (E.44).

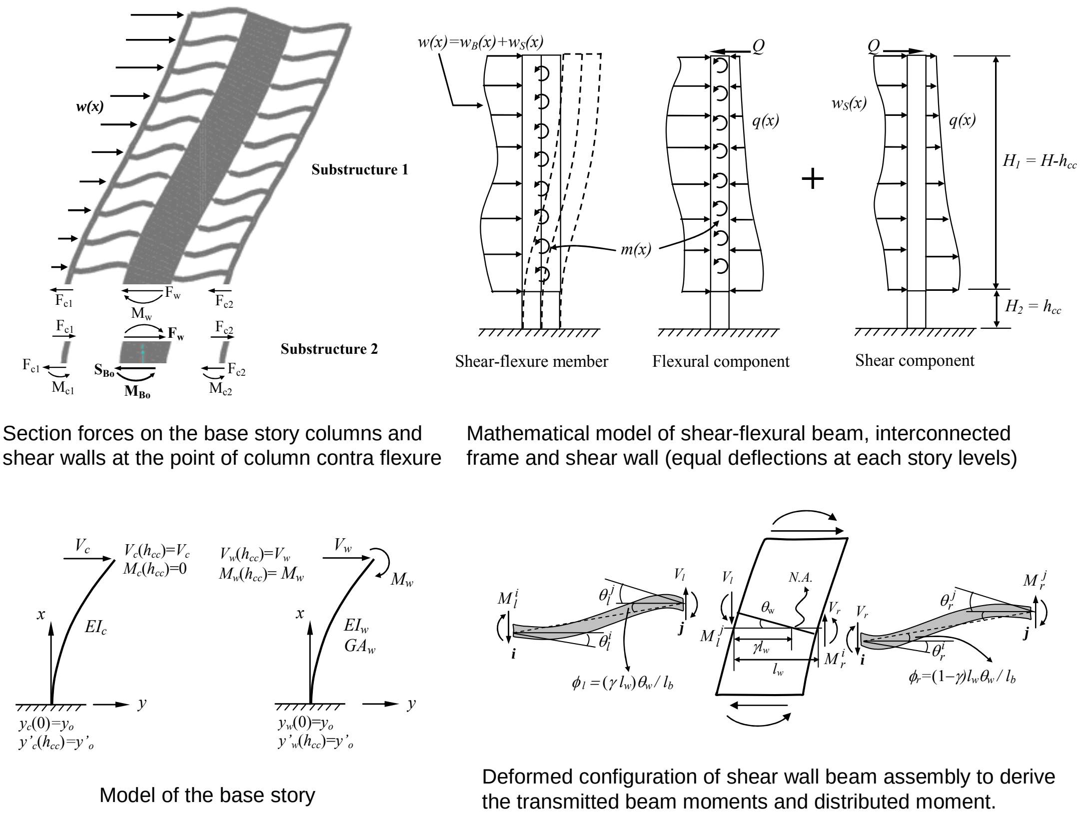

Figure 4.17 Primary components of improved formulation

Now readily available, to show the effectiveness of the new formulation by using the structural configurations shown in Figure 4.18, the share of the walls and frames from the total base shear is calculated for different amounts of wall in the system. Columns are 0.6x0.6 m and beams are 0.6x0.4 m. By replacing the columns with structural walls on the central axis in the longitudinal direction, different frame-wall stiffness ratios are obtained. Two, four and six structural walls in 3 and 5 m length were placed at these locations. Structure is assumed to have 10-stories and height of 30 m. Load was applied uniformly along the height. The normalized wall and frame shear spectrum were calculated and plotted in Figure 4.19. The main difference of the plots presented in Figure 4.19 from the ones shown in Figure 4.16 is that the shear force at the base of both members is calculated correctly. Additional verification examples can be found in APPENDIX E.

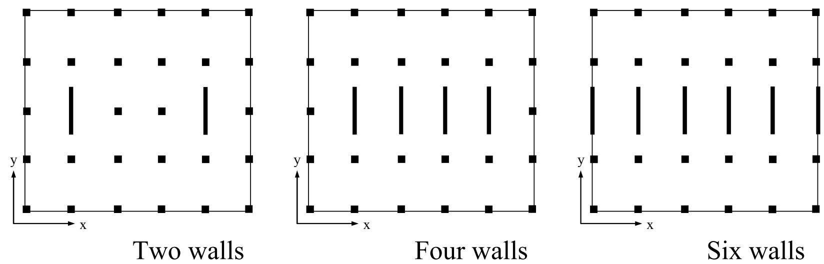

Figure 4.18 Floor plans consisting two, four and six shear walls

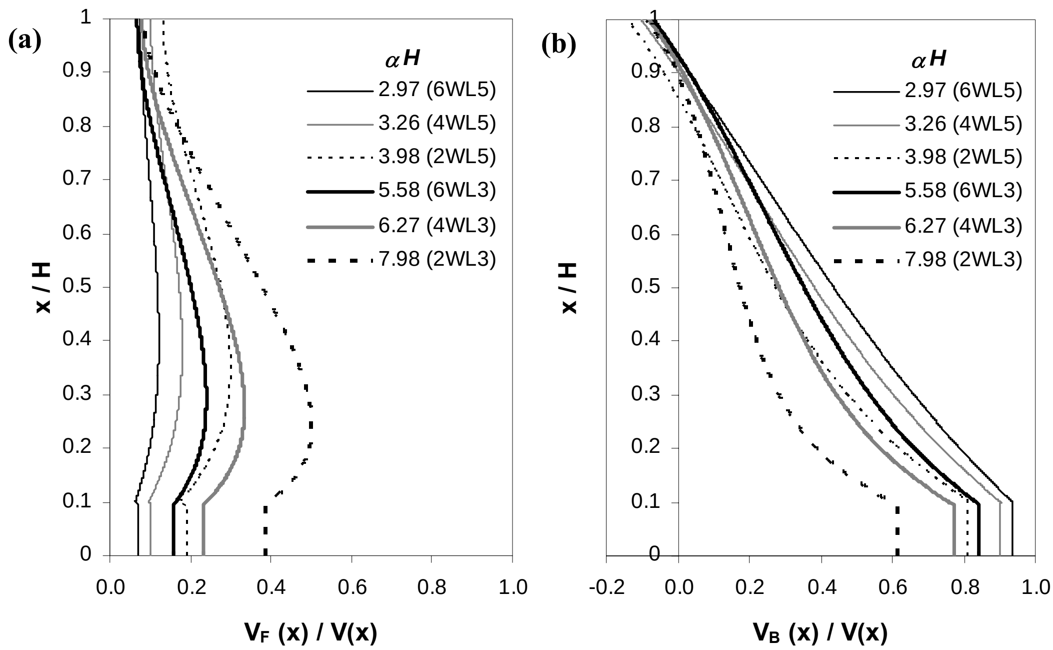

Figure 4.19 Normalized frame (a) and wall (b) forces for different frame to wall ratios under uniform lateral load. (The notations in parentheses in the legend refer to number of walls and their lengths. For instance, “6WL5” means there are total of six walls, each 5 m in length, in the system)

4.2.2.1 *Period Formula for Frame-Wall and Wall Type Structures*

The basic mathematical model of the shear-flexure beam can also be used to determine the dynamic properties of a tall building structure consisting of uniform shear walls and frames. In Heidebrecht and Stafford Smith (1973) the equation governing the free vibration of shear-flexure beam is given by

$$\frac{d^4 y}{dx^4} - \alpha^2 \frac{d^2 y}{dx^2} = -\frac{1}{a^2}\frac{\partial^2 y}{\partial t^2} \tag{4.22}$$

in which

$$a^2 = \frac{EI}{\rho_d A_f} \tag{4.23}$$

and ρ_d is the mass per unit volume of the uniform structure.

The solution of the differential equation given in Eq. (4.22) is available in Timoshenko and Goodier (1970), and Heidebrecht and Stafford Smith (1973) calculates the natural frequencies as

$$\omega = \omega_o \sqrt{1 + \left(\frac{\alpha H}{\lambda_o H}\right)^2} \tag{4.24}$$

in which $\lambda_o H$ takes the values of 1.875, 4.694, 7.855, 10.996 and 14.137 for the first five modes respectively as defined in Timoshenko and Goodier (1970) and ω_o is the natural frequency of a flexural beam with the same mass and stiffness properties, as given by

$$\omega_o = a\lambda_o^{\ 2} \tag{4.25}$$

The α value is calculated in accordance with Eq. (4.21) and H should be taken as the total height of the building, since the dynamic solution for the new formulation is not done in this study. The first natural period of frame-wall systems can be obtained by using $T = 2\pi/\omega$ as

$$T = \frac{2\pi}{\omega_o \sqrt{1 + \left(\frac{\alpha H}{\lambda_o H}\right)^2}} = \frac{2\pi}{\sqrt{\frac{EI}{\rho A_f}} \left(\frac{1.875}{H}\right)^2 \sqrt{1 + \left(\frac{\alpha H}{1.875}\right)^2}} \tag{4.26}$$

and introducing necessary modifications like $A_f = A_w/p = (L_w.t_w)\ /\ p$ and $I = L_w^{\ 3}.t_w/12$, and rearranging we get

$$T = \frac{2\pi h}{1.875}\sqrt{\frac{12\rho}{E}}\frac{H_w}{L_w}N\frac{1}{\sqrt{p\left(1.875^2 + (\alpha H)^2\right)}} \tag{4.27}$$

Upon distribution of typical values used for Eq. (4.4), Eq. (4.27) takes the form in resemblance with Eq. (4.4)

$$T = 0.00406\frac{H_w}{L_w}N\frac{1}{\sqrt{p\left(1.875^2 + (\alpha H)^2\right)}} \tag{4.28}$$

This equation is a more general form as compared to Eq. (4.4) and yields more reliable and realistic period estimations for various types of shear wall buildings with the incorporation αH term.

4.3 PARAMETERS OF STUDY

Several analytical parametric studies were conducted on structural walls to investigate their deformation and strength properties. The parameters (variables) of these research studies were evaluated to form the parameter set of this study. Unlike the one carried out here, which makes use of nonlinear finite element analysis for the investigation of the strength and deformation of reinforced concrete structural walls in both micro and macro level, most of the previous analytical studies conducted on structural walls relies on the lump plasticity modeling of structural walls, which can be legitimized within the scope of these studies. The primary interest of these studies is the global response parameters, such as the drift or plastic rotation and shear strength of the walls.

Wallace and Moehle (1992) and Wallace (1994) studied the ductility and detailing requirements at the boundaries of structural walls with simplified analytical procedure of Sozen (1989) described above. Priestly and Kowalsky (1998) investigated drift and ductility capacity of rectangular structural walls. Kowalsky (2001) examined the ways of implementing displacement based design perspectives of structural walls into traditional force based design code (ICBO, 1997) by relating the strain limit states to a particular drift ratio.

Kongoli et al. (1999) devised a parametric analytical study that adopted the number of walls in a frame-wall building as the fundamental parameter for discussing the effects of walls on the response of frame-wall buildings. This ratio was further quantified as the base shear coefficients of frames wand walls defined as yield strength divided by the total weight of the building.

Lefas and Kotsovos (1990) conducted an analytical work based on the use of a reliable finite element program to investigate the influence of several parameters that affect the behavior and strength characteristics of walls, such as arrangement and amount of vertical and horizontal reinforcement, the detailing of the edge members, the aspect ratio, the axial load and concrete strength.

Derecho et al. (1978a), Derecho and Corley (1984), Ghosh and Markevicius, (1991), Seneviratna and Krawinkler (1997), Amaris (2002), Rutenberg and Nsieri, (2006), Celep and Aydinoglu (2006) are others that was conducted parametric investigation on shear walls for different purposes.

When all these studies were examined, the primary variables affecting wall response were found to be

- the ratio of wall cross sectional area to floor-plan area,
- fundamental period,
- shape of the structural wall cross-section,
- the wall aspect ratio (H_w / L_w) and configuration in the plan,
- the wall axial load ($P/f_c/A_w$),
- percentage of the longitudinal reinforcement (ρ_b), and
- degree of confinement of compression zone concrete.

In the light of discussion that summarizes the outcomes of the previous parametric research on structural walls, it was decided that the primary variables of the parametric study should be

- ***Wall aspect ratio (H_w / L_w):*** Walls of 3, 5 and 8 m in length that are located in four-, eight- and twelve-story structures were analyzed. A constant inter-story height of 3 m was accounted for each structure. Each pair of wall length (L_w) and building height (H_w) corresponds to different wall aspect ratios which are 1.5, 2.4, 3.0, 4.0, 4.5, 4.8, 7.2, 8.0 and 12.0. Height to length ratio of walls significantly affects the behavior modes of the walls. As the height-to-length ratio decreases shear effects become more pronounced.
- ***Wall axial load ratio ($P/f_c/A_w$):*** The common range of axial load ratios in practice with cantilever walls is reported to be in the range $0 \le P/(A_w f_c) \le 0.15$ for short-to-medium height buildings (Priestley et al., 2007). For simple calculation it can be assumed that each

wall resist 1~1.25% axial load ratio per story (Kowalsky, 2001). The axial load ratios used in the parametric study are 0.02, 0.05, 0.1, 0.15 and 0.25.

- ***Wall boundary element longitudinal reinforcement ratio (ρ_b):*** The flexural wall reinforcement ratio, defined as the ratio of total longitudinal steel area (A_s) in the boundary element to the area of boundary region (A_{wb}), in typical rectangular shear wall sections is in the range of $0.005 \leq \rho_b \leq 0.04$. Four different values of boundary element reinforcement ratio were used. These are 0.005, 0.01, 0.02 and 0.04. By changing the amount of flexural reinforcement strength of the wall is adjusted to reflect different design strength reduction factors (R).
- ***Concrete strength:*** For all the walls analyzed in the current study, concrete compressive characteristic strength (f_c) was taken as 25 MPa. Selection of this value can be attributed to two reasons. First of all, since the result of this study is desired to be applicable in the civil engineering industry, on the basis of the ready-mix concrete production statistics of the recent years in Turkey, it was observed that grade C25 (f_c = 25 MPa) concrete compose more than 35% of the concrete production in recent years. In Table 1, Turkey concrete industry's production for last 8 years is given according to percentage of the produced concrete grade with respect to total production.

Secondly, results of previous experimental and parametric studies (Lefas et al., 1990) displayed that concrete strength has negligible influence on strength and deformation characteristics of reinforced concrete structural walls governed by flexure and only minor effect on walls under flexure-shear combined actions. Depending on the results of 13 large-scale panel tests with varying concrete compressive strength Lefas et al. (1990) concluded that the strength and deformational response of the walls were found to be independent of the uniaxial concrete strength within a range of 30 to 55 MPa.

However, behavior of squat walls is governed by shear and Lefas and Kotsovos (1990) stated that it is the strength of compressive zone that is the main contributor to shear resistance and not the "cracked" concrete in regions subjected to predominantly tensile stress conditions. In Chapter 2, the effect of concrete compressive strength was displayed on the response of shear dominated squat wall. Nevertheless, since in a multi-story reinforced concrete shear wall building or frame-wall buildings, the shear effects are not as pronounced as in the experiments due to high aspect ratio (H_w/L_w), a single value can be adopted for concrete strength.

Table 4.1 Turkey's concrete production percentages for different concrete grades*

Year	C 14 (%)	C 16 - 18 (%)	C 20 (%)	C 25 (%)	C 30 + (%)	Total (%)
1998	24.4	45.4	18	8.1	4.1	100
1999	22.7	35.9	27.6	10.3	3.3	99.8
2000	11.5	25.1	41.3	13.2	4.9	96
2001	7	21.3	47.9	18	5.8	100
2002	5.9	21.1	46.9	19.2	6.9	100
2003	4.6	14.7	39.6	25.4	15.7	100
2004	3.3	10.3	40.6	30.7	15.1	100
2005	3.2	8.4	31.2	42.1	15.1	100
2006	2.92	7.66	35.09	36.56	17.77	100
2007	2.85	5.58	26.95	35.25	29.37	100

*Türkiye Hazır Beton Birligi, "*2007 Yılı Hazır Beton Sektörü İstatistikleri*"

4.4 PROTOTYPE FRAME-WALL STRUCTURE

In this section prototype frame-wall structure that is used to identify the static and dynamic characteristics of structural walls and to display the limitations of the employed analytical procedures is introduced. The general plan configuration shown in Figure 4.20(a) is used for all the prototype frame-wall structures. The structure is composed of nine 3-bay frames in the transverse direction and three 8-bay frames in the longitudinal direction. By increasing the number of walls allocated into the central bay in the transverse direction different frame-wall arrangements are obtained as shown in Figure 4.20. By this way different wall indexes are obtained. Later using the stiffness properties of these buildings single wall-equivalent frame models that depend mainly on a specific wall length and a wall index is developed. The purpose is to reduce the size of the finite element models and to create a workable framework for the parametric investigation as will be discussed in detail in Chapter 6.

In this study shear wall of lengths 3, 5 and 8 meters were handled. The building heights that were considered to determine the aspect ratio of the shear walls consists of 4, 8 and 12 story structures. The interstory height is considered to be constant along the height of the building, which is 3 m.

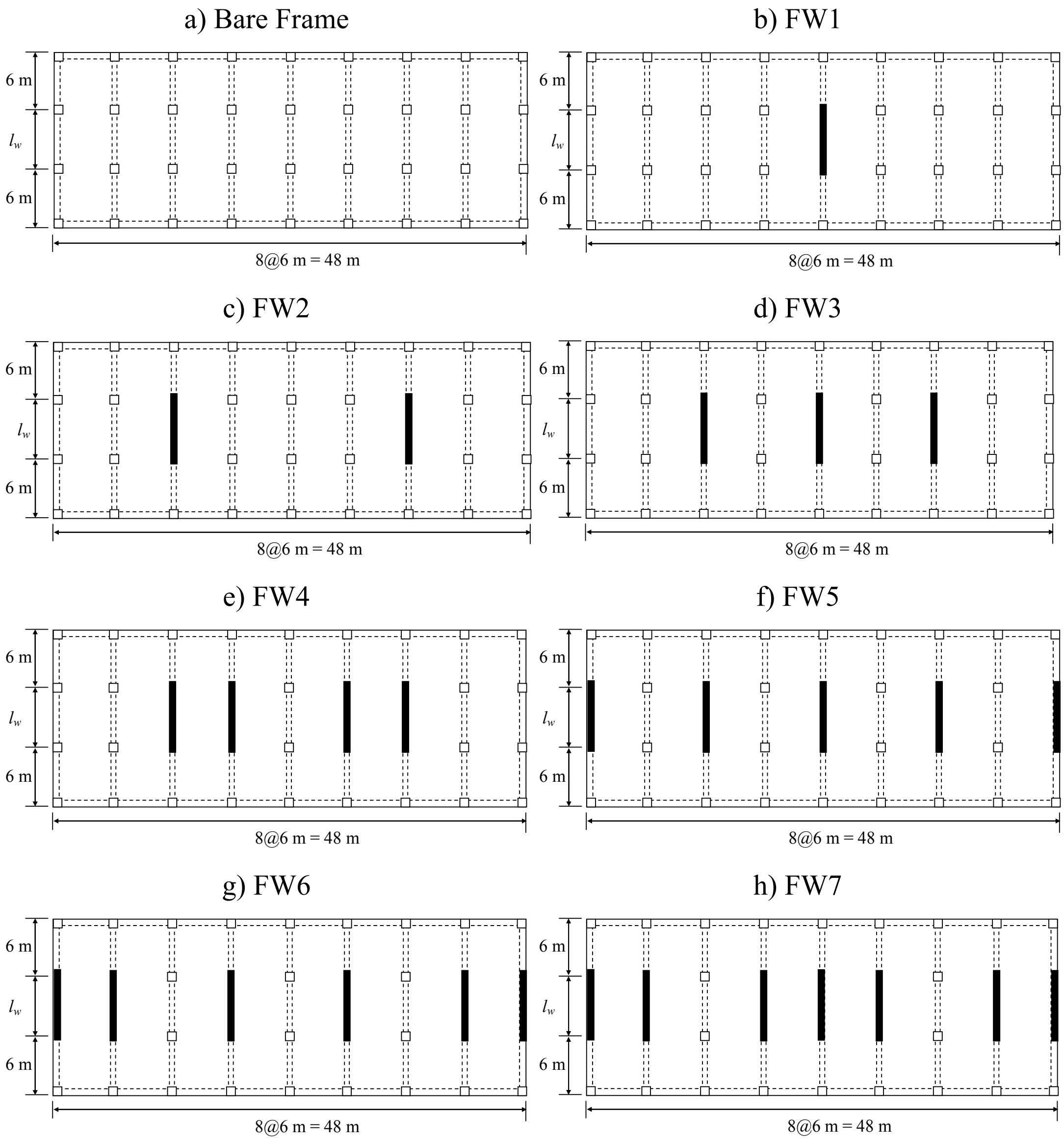

Figure 4.20 Plan view of frame-wall configurations

Assuming the dimensions of the columns are 0.6x0.6 m and the beams are 0.6x0.4 m, the distribution of normalized shear force, moment and displacement distribution on wall component of frame-wall structures for the combination of wall length and number of stories is plotted in Figure 4.21 to Figure 4.23. Robust beam and column elements were used to assure the desired frame-wall interaction develops effectively. Each graph contains seven curves each represented with an αH value. The αH term effectively characterizes the dominant behavior mode of the frame-wall structures. αH values in the graphs are related to number of walls in the system, where in the descending order each value correspond to the structural systems with 1, 2, 3, 4, 5, 7 and 9 walls. Although these figures display the normalized results of linear static analyses with elastic properties (E_c=25000 MPa) they reveal very useful information about the likely distribution of forces and deformations on structural walls of different properties. The following conclusions can be derived from these figures.

- The maximum shear along the wall occurs at the base story under equivalent static lateral load. More interestingly, for the same structural member configuration and plan, the base shear ratio between the walls and frames changes only slightly (decreases) as the number of stories increases. This can be explained in reference to model describing the lower portion (below the contra flexure height of base story columns) of the frame-wall model presented in Figure E.8 of APPENDIX E. Eq. (E.25) states that for the same level of deflection at the contraflexure height the column shears should be same regardless of the building height for structures with the same plan and member configuration and dimension. The slight decrement in the shear ratio of frames and walls as the height increase is due to shift in the location of contraflexure height and the change in the moment profile of the walls.
- The walls are very effective in resisting lateral loads especially in 4-story buildings. For example, two-8 m long wall or three- or four-5 m long walls are adequate to resist all the shear force imposed on a building with nearly 800 m^2 floor area. This corresponds to a wall index of 0.0025 approximately. 3 m long walls are not as much effective as 5 and 8 m long walls in carrying lateral load. A linear distribution of shear force on the shear walls can be assumed in such structures. For the structures with same plan and member configuration and dimension, while the base shear carried by the wall relative to the total base shear remains insensitive to the increasing number of stories, the effectiveness of walls in carrying lateral loads in the upper stories significantly drops as the number of stories and rigidity of frames relative to the walls increase.
- The relative strength of walls and frames should not be interpreted in terms of shear calculated at the base of the structure since in systems where walls are weaker than frames the wall shear may reduce rapidly as moved to upper stories. For mid-rise structures (4-15 stories high) where frames share more than 40% of the total base shear, the maximum frame shear that occurs at mid-stories (2-5) may be 2 to 2.5 times larger than it is at the base of the structure.

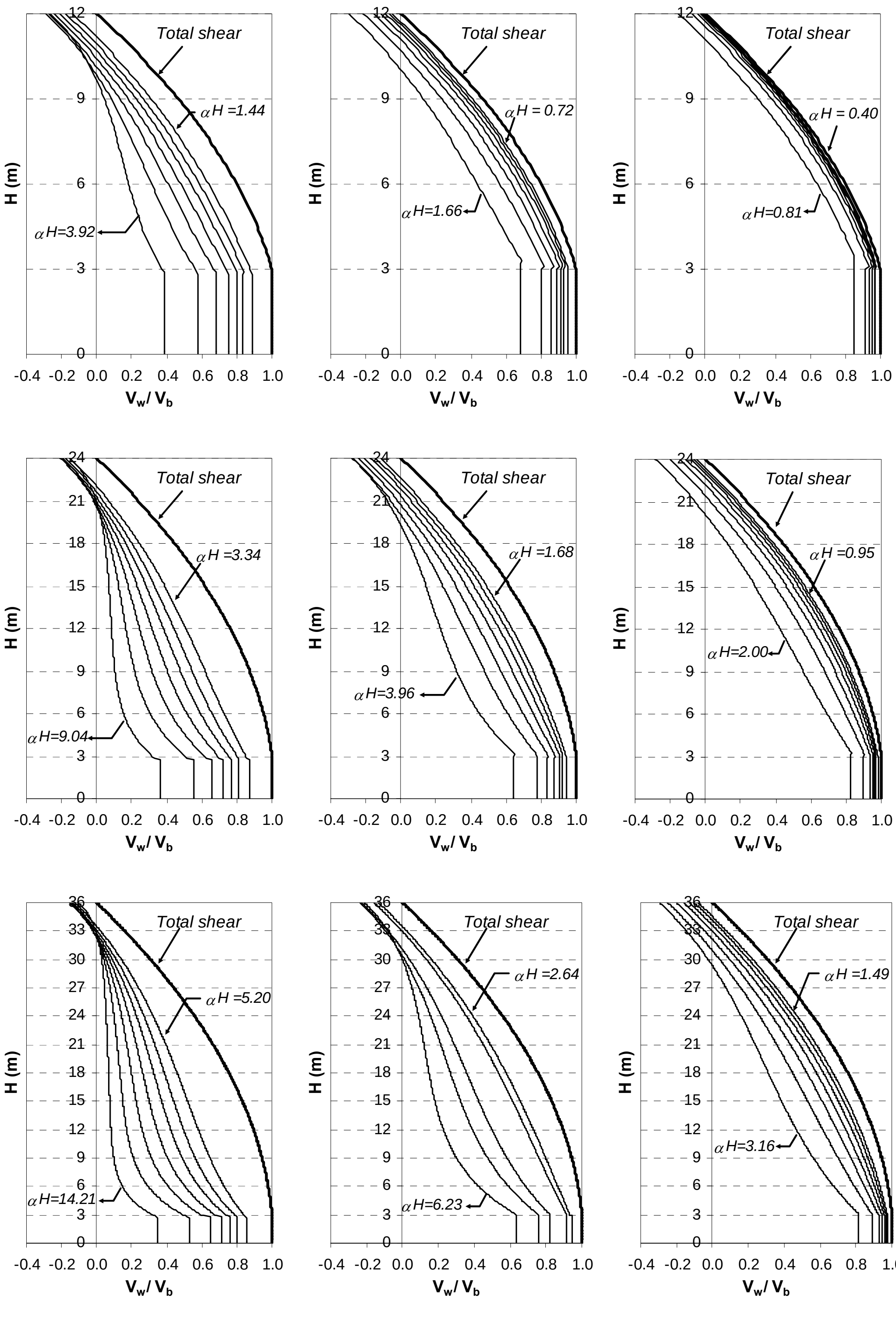

Figure 4.21 Normalized shear force distribution on shear walls obtained from the analysis of the prototype structure with L_w= 3, 5, 8 m (each column respectively) for 4-, 8- and 12-stories (each row respectively).

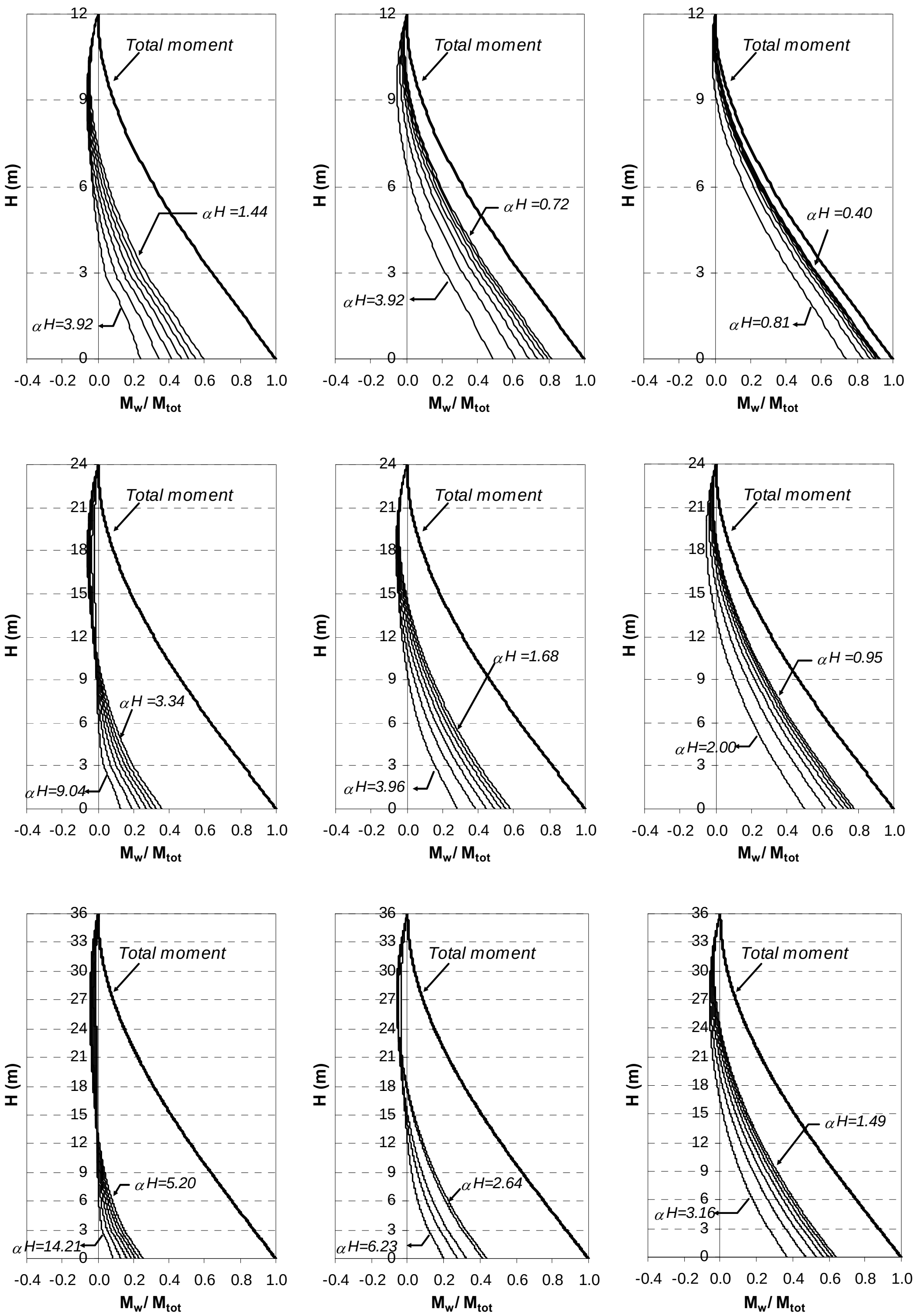

Figure 4.22 Normalized bending moment distribution on shear walls obtained from the analysis of the prototype structure with L_w= 3, 5, 8 m (each column respectively) for 4-, 8- and 12-stories (each row respectively).

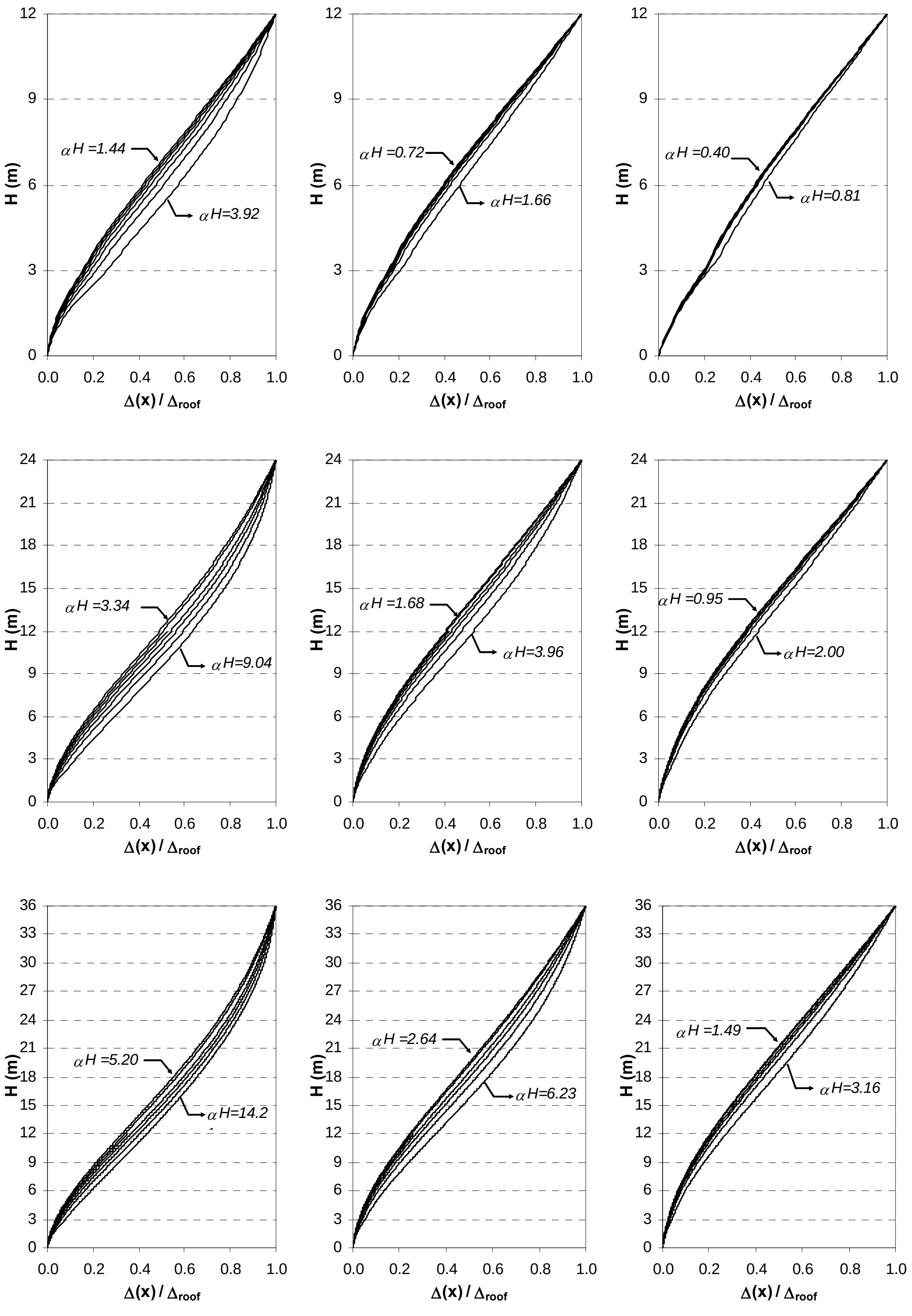

Figure 4.23 Normalized lateral displacement distribution on shear walls obtained from the analysis of the prototype structure with L_w= 3, 5, 8 m (each column respectively) for 4-, 8- and 12-stories (each row respectively).

- As the frame-wall interaction effects develop (as frames become stronger) the inflection height on the walls drops. The moment and shear resistance of 3 m long walls drops significantly as the building height increases, so it has to be disputed that shear wall members with lengths shorter than 3 m should be considered as wall or not depending on the height of the structure.
- The last columns of Figure 4.21, Figure 4.22 and Figure 4.23 tell that even minimum amount of walls was provided in the system by using L_w = 8 m walls, they dominate the entire force and displacement response of the system. This observation suggests that not the quantity but the quality of the structural walls should be sought in the system to evaluate all the necessary strength and deformation characteristics. For the values of αH parameter smaller than 2, walls dominates the behavior of the system. For the values of αH parameter larger than 6, frames dominates the behavior of the system.

Using Eq. (4.28) fundamental vibration period of prototype structures was calculated. The results were plotted in Figure 4.24(a). After a limiting αH value, which is inversely proportional to the wall index (p), estimated periods of frame-wall structures converge to the values given by 0.1N at the upper bound. The formula predicted periods of prototype structures were also compared with more exact values calculated in SAP2000 program by employing the finite element models of the structures. As seen in Figure 4.24(b) both predictions agree quite well.

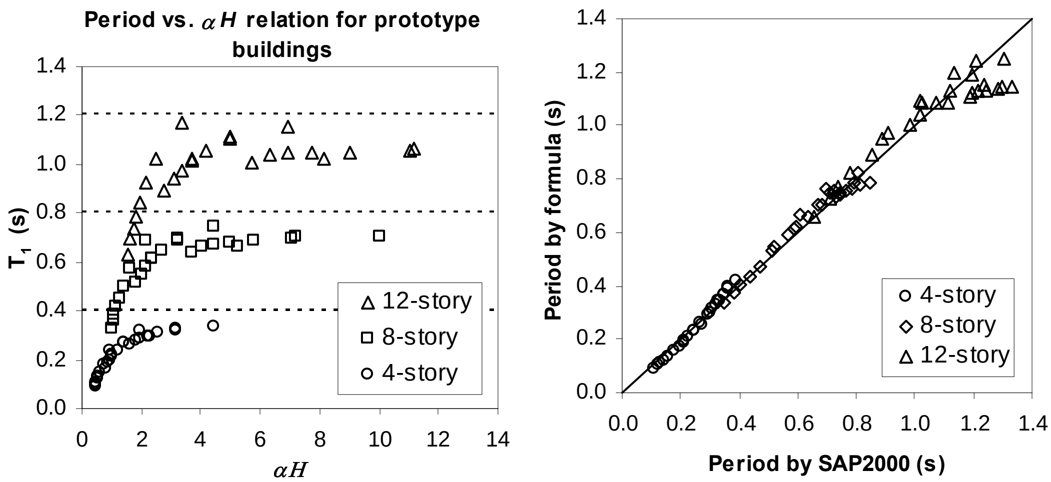

Figure 4.24 a) Fundamental period of prototype structures predicted using Eq. 4.28, b) Comparison of periods predicted with Eq. 4.28 and calculated by using the finite element method

In Figure 4.25 relation between the wall index and the behavior factor αH is plotted for different wall lengths and building heights. This figure suggests that the wall stiffness (taken into account through wall length) is the primary factor affecting the global behavior of frame-wall structures. As the αH decreases system behavior is governed by the walls. The same base curve in the form of $N.c.x^b$ is used to define relation between the wall index and behavior factor, where N is the story number. For particular wall length and plan configuration coefficients b and c are constant regardless of the building height, where height of the building is measured above the inflection height of the base story columns.

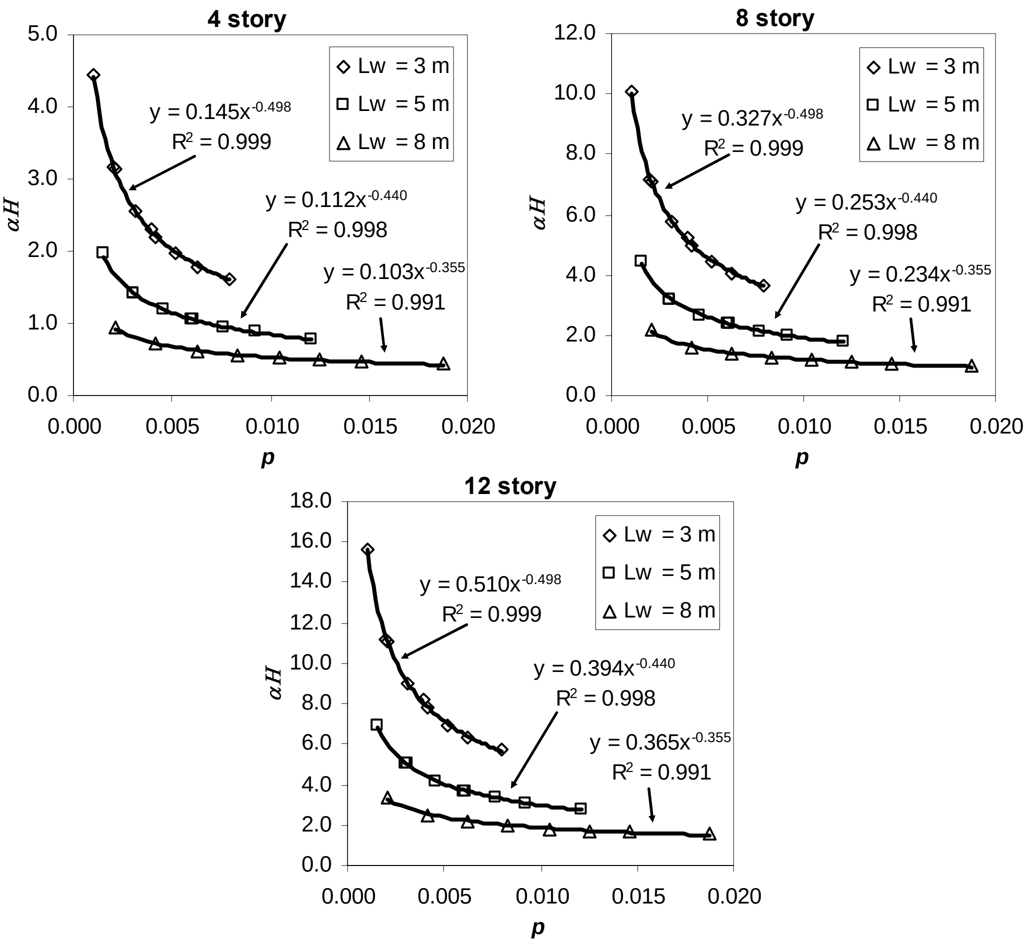

Figure 4.25 Relation between the wall index (p) and behavior factor αH

The data presented in Figure 4.26 represents different frame-wall structures that were obtained by changing the dimensions of wall and frame elements in the plan shown in Figure 4.20, so several structural system scenarios such as weak frame-strong wall and vice versa were included. When more exact value of αH obtained by calculations is not available, the average relation between the total flexural rigidity of walls in the system, EI_w, and αH for 4-, 8- and 12-story frame-wall structures derived under combination of different beam, column and wall member rigidities and given in Figure 4.26 can be used. The equations for the curve-fits to the data were classified according to the number of stories (wall height).

To emphasize one more time, the purpose of this efforts is to draw the outline of the procedure that allows structural walls to be analyzed in an isolated form yet taking into account all the interaction effect such that the wall exists at their actual configuration in a 3D structure.

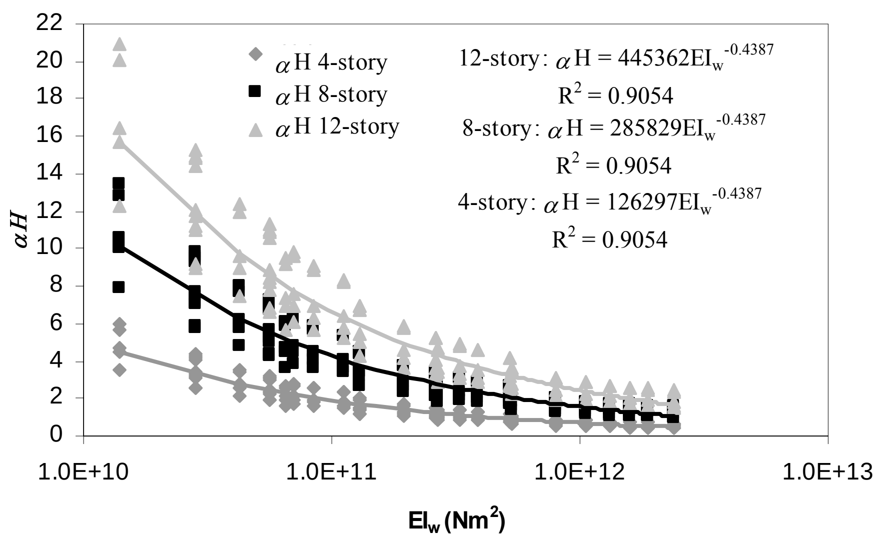

Figure 4.26 The average relation between the total flexural rigidity of walls, EI_w, in the system and αH

4.5 DESIGN OF WALL SYSTEMS FOR PARAMETRIC STUDY

In a parametric study, values of variables can be determined in one of two ways. The values of a variable can be taken as either constant numbers ranging from minimum to maximum values that can be possibly attained by the variable or the values required being determined after a design process since they are affected by other variables of the system. This study utilizes both methods in the determination of variable sets. For instance, the effect of boundary element longitudinal reinforcement amount on the deformation capacity of a reinforced concrete wall member can be calculated considering constant values of volumetric ratio of longitudinal reinforcement such as ρ_b = 0.005, 0.01, 0.02 and 0.04. However, to obtain realistic estimation of seismic deformation demands on a wall structure a relation between dynamic characteristics and strength requirements must be established which requires particular reinforcement detailing application on wall. In frame-wall systems the stiffness and strength must be proportioned systematically among wall and frame components for the sake of reliability of obtained results. The strength assignments of frame and wall components are achieved by using linear continuum theory.

A simple yet straight-forward design procedure, which incorporates the newly derived formulation of frame-wall continuum model, is developed to quantify the seismic shear force distribution among the wall and frame components of the generic frame-wall models and to calculate the amount of flexural reinforcement at the boundary elements of the walls. The procedure also establishes a relation between the wall index and the seismic capacity of the structure so may answer the question for the minimum amount of shear walls required to provide the necessary resistance to control the seismic drift demands.

Using the knowledge produced on dynamic and static characteristic of frame-wall structures, variations in stiffness and yielding strength along the height of the generic single wall-equivalent frame structure models are calculated. The static equivalent triangular lateral load pattern specified in the Turkish Seismic Code (TSC, 2007) is used in the loading of the continuum model. The yielding strength was distributed over the stories so that all stories yield simultaneously under the static design earthquake forces.

The created frame-wall model is characterized by a particular wall index and behavior factor, αH. The stages of model construction can be defined as follows

1. Select a wall length (L_w) and wall index (p).
2. Decide the number of stories (N).

3. Compute the behavior factor (αH) using the selected wall index value and relations presented in Figure 4.25.

4. Compute the period of vibration. The fundamental period of structure (T_1) is determined by utilizing Eq. (4.4) for isolated cantilever wall and Eq. (4.28) for frame-wall structures.

5. For an assumed or given wall index (p) the floor area per wall is calculated as $A_f = pL_w t_w$ for predetermined wall dimensions. In this study a constant wall thickness (t_w) that is equal to 0.25 m is adopted for all the rectangular walls.

6. The story masses are calculated on the basis of $m_s = A_f.(1\ t/m^2)$.

The design procedure is described stepwise in the following sentences.

Step 1: Spectral acceleration coefficient

Using the calculated period based on uncracked section properties, spectral acceleration coefficient, $A(T_1)$, is calculated according to spectral shape given in TSC 2007 and assuming local site class Z3 (firm soil) in seismic zone 1 (Effective ground acceleration coefficient, $A_o = 0.4$).

Step 2: Total Equivalent Seismic Load

Total equivalent seismic load (base shear) acting on the entire frame-wall structure is obtained by

$$V_t = \frac{W\,A(T_1)}{R} \tag{4.29}$$

where W is the total weight of the structure calculated as $NA_f w$. Here N is the total number of stories, A_f is the floor area per floor and w is the story weight per unit floor area with a typical value of 1 t/m^2. R is the seismic load reduction factor (structural behavior factor) given as 6 and 7 for buildings in which seismic loads are fully resisted by solid structural walls and seismic loads are jointly resisted by frames and solid and/or coupled structural walls, respectively, for high ductility systems. For the sake of simplicity and consistency among the analyses results, a constant R equal to 6 is adopted in this study for both structural systems.

Step 3: Calculation of wall base bending moment and shear

Using the expressions derived for moment and shear in the new frame-wall continuum model given in APPENDIX E, the share of the frames and walls from the total shear along the height of the structure is calculated. The total base shear (V_t) is used to calculate the magnitude of the triangularly distributed lateral load applied along the shear-flexure beam model using Eq. 4.30.

$$w_1 = \frac{2V_t H}{(H^2 - h_{cc}^2)} \tag{4.30}$$

Having all the necessary values (w_1, V_o= V_t, αH, EI_w) in hand, the bending moment at the base of the wall can be calculated using the expression derived in APPENDIX E, which is

$$M_{Bo} = \frac{\dfrac{V_o \sinh(\alpha H_1)}{\alpha} - \dfrac{V_o h_{cc}^4}{3EI_c f}\left[\dfrac{\alpha h_{cc}\sinh(\alpha H_1)}{2} + \cosh(\alpha H_1)\right] - \dfrac{w_1}{\alpha^3 H}\left[\alpha h_{cc}\cosh(\alpha H_1) + \sinh(\alpha H_1) - \alpha H\right]}{\left(1 - \dfrac{h_{cc}^3 \beta}{4EI_w f}\right)\alpha h_{cc}\sinh(\alpha H_1) + \left(1 - \dfrac{h_{cc}^3 \beta}{2EI_w f}\right)\cosh(\alpha H_1)} \tag{4.31}$$

After calculating moment at the base of the wall we have all the necessary information to calculate the force and displacement quantities along the height of the building. The shear force on the wall components can be calculated using

$$V_w = \frac{M_{Bo}\beta h_{cc}^2}{2fEI_w} - \frac{V_o h_{cc}^3}{3fEI_c} \tag{4.32}$$

Distribution of shear force among the frame and wall components of a dual system is not constant in all stages of the nonlinear seismic action. As displayed in Figure 4.27 the redistribution of base shear between the frame and wall components of a dual system changes with the impending inelastic actions, such as cracking, yielding that takes place in each primary lateral load resisting components (Emori and Schnobrich, 1981). The reduction in the wall base shear may constitute an amount of 10-15 % after cracking and 30-50% after yielding of the walls with respect to initial elastic state base shear distribution. This situation may cause problems especially in dual systems where frames contributes to the overall lateral resistance more than 25% since they are not designed for this excess shear force arising after redistribution of forces. So, for such systems in the calculation of member forces and moments cracked section stiffness should be used.

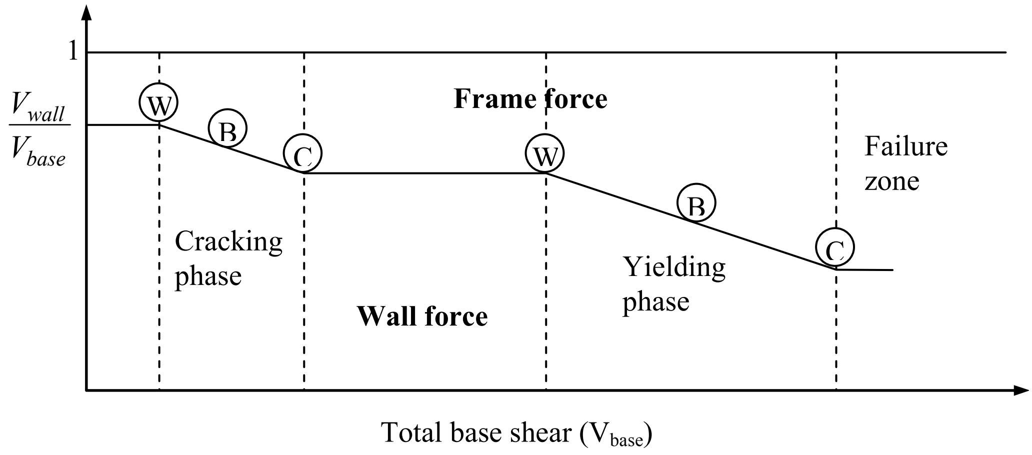

Figure 4.27 Redistribution of base shear between wall and columns of frame-wall structure.

***Step 4**: Design bending moment envelope*

After the frame and wall shears and wall moment at the base of the structure is determined, using the principles of capacity design method reinforcement detailing and strength assignment of wall and frame components can be achieved.

Considering the moment demands that arise during the dynamic response, a linear bending moment envelope is recommended to be used in design rather than bending moment diagrams resulting from code-specified equivalent lateral forces as shown in Figure 4.28 (Paulay and Priestley, 1992). This takes into account the contribution of higher modes to the bending moment along the wall. Additionally from the base of wall in a region that has a height equal to wall length L_w a constant moment distribution is assumed considering the tension shift effect.

Due to uncertainty in the material strengths and strain hardening behavior of vertical flexural reinforcement, the maximum flexural strength, M_o that could be developed in the walls has to be anticipated. The overstrength moment (M_o) develop at the base of the wall, should be taken into account as λM_N, where λ is the overstrength factor due to strength enhancement of the constituent materials. This is an important property that must be accounted for in the design when large ductility demands are imposed on the structure. As higher resistance will be offered by the structure than anticipated when design forces were established, it is expected that ductility demands will reduce (Paulay and Priestley, 1992, Amaris, 2002).

The height of critical region, H_{cr}, above the base of the wall may be estimated as $H_{cr} = \max\left[L_w, \frac{H_w}{6}\right]$ but not greater than $2L_w$. It is also recommended that the critical wall height should not be less than one story height, h_s, for structures less than 6 stories and $2h_s$ for structures higher than 7 stories.

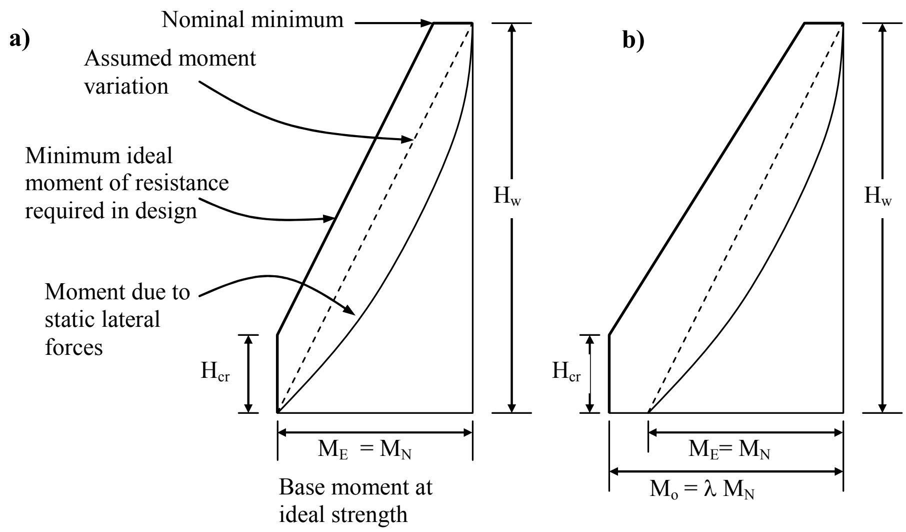

Figure 4.28 Design envelope for bending moments in slender cantilever walls a) Based on design moment equal to nominal moment, recommended by EC8 and TSC 2007 design codes b) Considering the material overstrength (λ), Paulay and Priestley (1992).

Step 5: Calculation of flexural reinforcement at the boundary

The moment distributions given in Figure 4.28 should be also used for the curtailment of the vertical reinforcement. The demand for flexural reinforcement in a cantilever wall is not proportional to the bending moment demand, because axial compression is also present. Even the amount of flexural reinforcement is maintained constant with height, the flexural capacity of the section will reduce with height because the axial compression effects become smaller. Following formula can be used to calculate the moment capacity of rectangular walls designed according to TSC 2007.

$$M_{wy} = (182850L_w - 411610)\rho_b + (1300L_w - 2750)(16.872\frac{P}{P_o} + 0.751) \tag{4.33}$$

where the units of M_{wy} is kN-m and L_w is m. For this formula to be valid, it was assumed that the length of boundary elements is $0.2L_w$ at the edges and flexural reinforcement was distributed uniformly in the boundary element. The percentage of vertical web reinforcement is a constant value equal to minimum value 0.0025 and concrete compressive strength is 25 MPa. Thickness of the wall was assumed to be 0.25 m.

Using the design bending moment calculated with Eq. (4.31), and since the length of the wall element is known, the detailing of the main flexural reinforcement in the boundary element all along the height can be achieved easily.

Turkish earthquake code states that the ratio of the flexural reinforcement at the boundary edge regions to the gross sectional concrete area should be larger than 0.001. This value is 0.002 in the critical height. If the boundary element length is assumed to be $0.2L_w$, then this limitation produces a longitudinal reinforcement ratio of 0.01 in the boundary column, which corresponds to the minimum reinforcement requirement in columns.

Step 6: Shear Safety of Structural Walls

In TSC 2007 and Eurocode8 shear forces obtained from the analysis (V_d) is amplified with a factor of β_v=1.5 to account for possible increase in shear forces after yielding at the base of primary seismic wall due to higher mode effects. TSC 2007 also requires an increase in the design shear force considering the increased moment capacity due to material over strength as described in Step 4 and Figure 4.28. The over strength factor is calculated as the ratio of the flexural strengths of sections at the ultimate to the yield curvatures ($\lambda = M_u/M_y$). The design shear force V_e satisfying the specified requirements is calculated as

$$V_e = \beta_v \lambda V_d \tag{4.34}$$

The factored design shear force will be smaller than the shear strength of wall cross sections, V_r, calculated by Eq.(4.35).

$$V_r = A_{ch}\left(0.65 f_{ctd} + \rho_{sh} f_{yd}\right) \tag{4.35}$$

The amount of shear reinforcement satisfying the condition $V_r > V_e$ is calculated with specified material strengths.

Step 7: Reinforcement Requirements at Wall End Zones

In TSC 2007 the amount of transverse reinforcement for the confinement of boundary elements at wall end zones along the critical wall height is calculated with

$$A_{sh} = 0.05 \frac{s t_w f_{ck}}{f_{ytk}} \tag{4.36}$$

Vertical spacing of hoops and/or cross ties shall not be more than half the wall thickness and 100 mm, nor shall it be less than 50 mm.

4.6 FINITE ELEMENT MODELING OF STRUCTURAL WALLS

4.6.1 Generic Frame-Wall Model

While for linear analysis the continuum shear-flexure beam model yields satisfactory result, to carry out the nonlinear analysis the continuum is required to be descriticized with finite elements. A discrete nonlinear type of simplified frame-wall models presented in Figures 4.4 and 4.15 is developed for the finite element analysis. The developed finite element model of a typical frame-wall system is displayed in Figure 4.29. The model is composed of solid, beam, mass and constraint elements. The wall component is modeled with SOLID65 elements. The reinforcement is assumed to be smeared in the element volume. In Figure 4.29 the different colors at the edge regions of the wall represent the confined boundary elements. The slab extrusions (flanges) at story levels were modeled to take into account the shear mechanism that develops in shear dominated walls (especially ones with larger wall length, L_w) due to interruption of shear flow by the slabs.

The link beams that transmit significant amount of moment on walls, especially as the building height increases, were also modeled. An equivalent moment-curvature relation that takes into account the extra moments transferred on wall due to actual beam end moments and produced by shear couples from tension and compression sides of the wall were assigned for the behavior of these beams. The beams were assumed to be axially rigid and no shear deformation was considered.

Each story was modeled with column elements with idealized story distortion angle-shear force relation. Although beam elements (BEAM188) were used to model columns of the frames, they are shear springs actually.

MASS21 elements were used to assign appropriate masses at the story levels. In vertical the masses were adjusted to yield a vertical load ratio of 1.25% per story. The horizontal mass is calculated by multiplying the tributary area of a single wall and equivalent frame model shown in Figure 4.29 with 1 t/m^2. The tributary area is calculated as a function of αH-p relation presented in Figure 4.25. The procedure was explicitly defined in Section 4.4.

When both solid continuum elements and beam elements were used at the same time in the model, transition between these elements leads problems. Many times a spider web of line elements or constraint equations was used to simplify the transition between the solids and beams. In ANSYS beam and link elements work well for large rotations, but real constants should be applied to input large stiffness values as well as cross sectional and inertia properties. The MPC184 elements use the beam/link approach, but take care of the stiffness and cross sectional properties automatically. The MPC184 elements are created between a "master" node in space, typically where the link beams frames to wall, and the desired nodes on the solid elements of the wall. There are two options for MPC184: rigid link behavior (default, translational DOFs only) and rigid beam behavior (translational plus rotational DOFs). Rigid beam option is utilized.

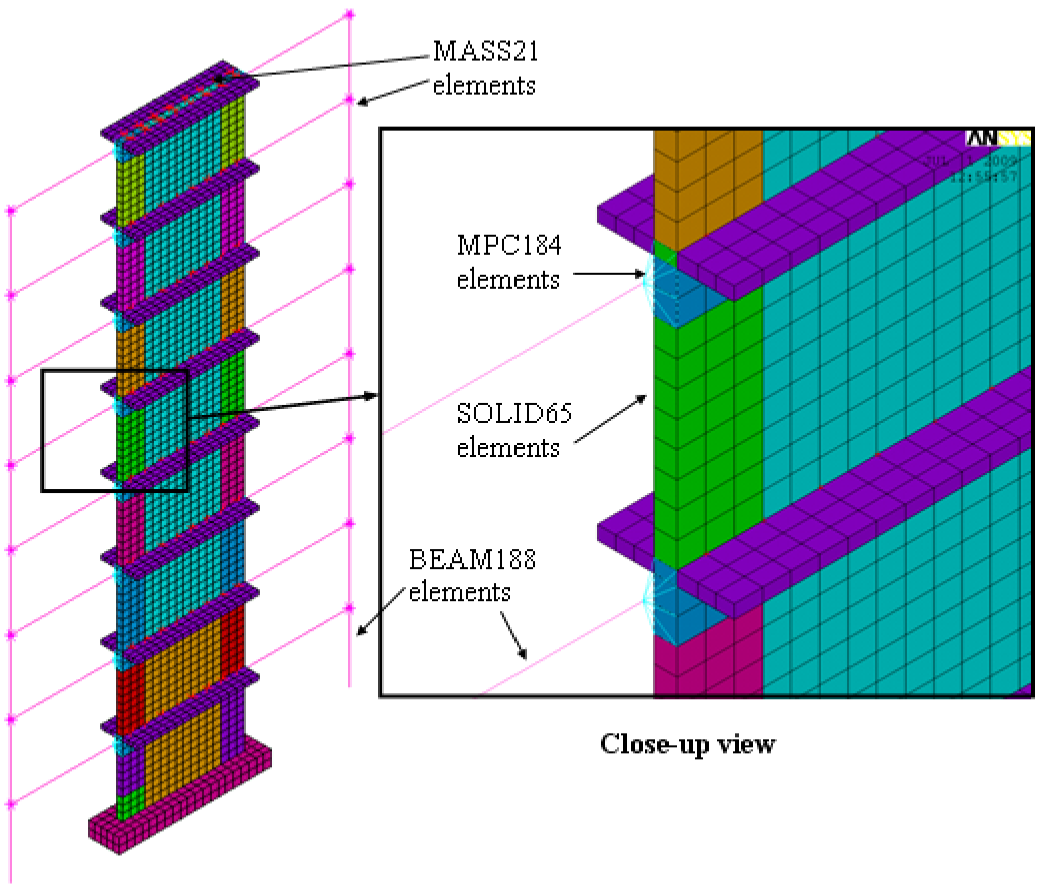

Figure 4.29 Finite element model of the generic frame-wall model

4.6.2 Member Force-Deformation Models

Since the material properties of solid elements were input in the form of stress-strain curves no additional data is required to define the wall behavior. The definition and properties of input material were discussed in great detail in Chapter 2.

To define the behavior of beam elements generalized nonlinear section properties was used. By this way the load deformation behavior of beam elements can be assigned in the form of force-distortion angle (F-γ) or moment-curvature (M-ϕ) relation. For the link beams a bilinear moment-curvature relation, as shown in Figure 4.30, was used. The yield curvature of link beams is calculated by the relation given by Priestley et al. (2007),

$$\phi_{by} = 1.7\frac{\varepsilon_y}{h_b} \tag{4.37}$$

where ε_y is the yield strain of the reinforcement and h_b is the depth of the beam. For the materials and geometries adopted in this study (ε_y = 0.0021 and h_b = 0.6 m) beam curvature at yield takes the value of 0.006 rad/m approximately, which also agrees with the moment-curvature analyses of typical beam sections. The yield moment of beams (M_y) is obtained from the elastic analyses of the model structure under code base shear demand distributed as triangular load over the height of the structure.

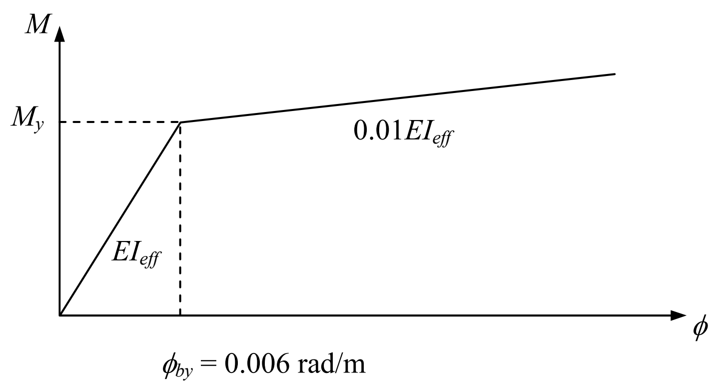

Figure 4.30 Idealized moment-curvature relation of link beams

The story distortion angle (story drift) – shear force relation is idealized with a trilinear skeleton curve as displayed in Figure 4.31. The first bent represents the effect of the cracking and the second one yielding of the story. Analyses results of typical frame–wall structure indicate that yielding of walls and the frames occur at different levels of lateral drift. Priestley (2003), from analysis of typical reinforced concrete beam sections, stated that the current design practice, which assumes beam stiffness is equal to a constant fraction of gross section stiffness, is inappropriate, since effective beam yield curvature can be considered constant, when non-dimensionalized by beam depth and yield strain, indicating that beam stiffness is proportional to strength. A simple expression for yield drift of frames, θ_{yFrame}, was proposed and was calibrated by comparing with results of a large number of beam/column sub-assemblage experiments. The frame yield drift is given as,

$$\theta_{yFrame} = \frac{0.5 l_b \varepsilon_y}{h_b} \tag{4.38}$$

where l_b is the average beam length and h_b is the average depth of the beams at the level of interest. The global yield displacement of the structures is largely determined by the yielding of beams. As given above, yield displacement of beams depends on their span, member depths, and material properties.

When typical values were used (ε_y = 0.0021, h_b = 0.6 m, l_b = 5 m) Eq. (4.38) yields story drift of 0.875%. Aschheim (2002) based on the capacity curves of 4-, 8-, 12-, and 20-story reinforced concrete frames designed presented by Gupta and Kunnath (2000) stated that the roof yields drift range between 0.5 and 0.6% regardless of the number of stories. For the story rotational angle (interstory drift ratio) at yielding a value equal to 0.67% was adopted by Kongoli et al. (1999) as proposed by Akiyama (1987).

In the light of this discussion, the characteristics values used to define the skeleton story drift-shear curves were fixed. The yield story distortion (γ_y) was assumed to be 0.75% and the cracking was assumed to take place at an angle of 0.075%. The cracking load assumed to be 1/3 of the story yield shear. The characteristics values used to define the force-deformation behavior of frames and link beams was assigned on the basis of lateral static earthquake load analysis specified in TSC 2007. The yield strength was distributed over the stories so that all would yield simultaneously under the static design earthquake forces. Distribution of the initial elastic stiffness over the stories was determined so that all would undergo the same yield deflection (drift angle at yielding was set at 1/150) under the specified design load.

The parameters of the shear force-drift relation were input via generalized beam cross section as in the case of link beams. For dynamic analysis, a vertex oriented hysteresis model (while reloading targets yield drift or distortion) was used for both link beams and story shear beams.

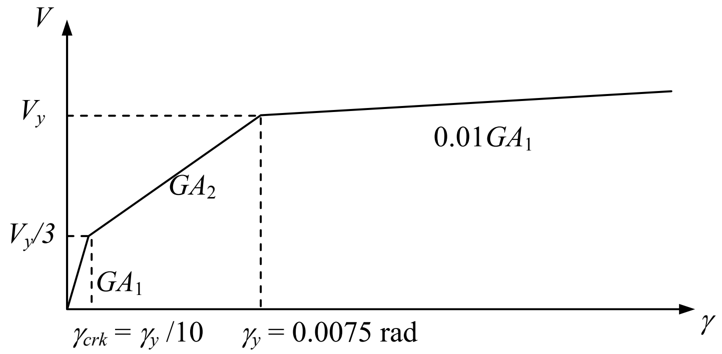

Figure 4.31 Idealized story shear-story drift (distortion) relation

4.6.3 Isolated Wall models

As emphasized many times at different places of this chapter, isolated wall models are the primary research tools in experimental and analytical investigation of structural walls despite the limitations of the model. Cantilever models of structural walls composed of solid finite elements was created. The models were displayed in Figure 4.32(a). A reduced model, which is computationally efficient, was developed and used in analyses to investigate the relation between the local and global deformation demands. In this model by adjusting the lever arm of the applied shear force different moment-shear ratios can be obtained. Changing the primary variables such as the steel amount, axial load ratio and aspect ratio of the walls analyses can be conducted. The model is displayed in Figure 4.32(b).

Each model developed here is intended to be used in different types of analyses for different purposes. The developed wall finite element models and the purpose of their development can be summarized as follows.

Generic frame-wall model: This model is used in time history analyses to investigate the seismic deformation demands under code specified seismic actions. The model allows realizing all the frame-wall interaction effects in the analyses.

Isolated wall model: The simplified mechanical models of cantilever walls are used widely to estimate global drift demands. Local curvature demands are related to global ductility and strains. The reliability of such procedures is validated by using this model.

Reduced wall model: This model is used in parametric studies to investigate the relation between the wall drifts, section rotations and curvatures, since it is computationally efficient model.

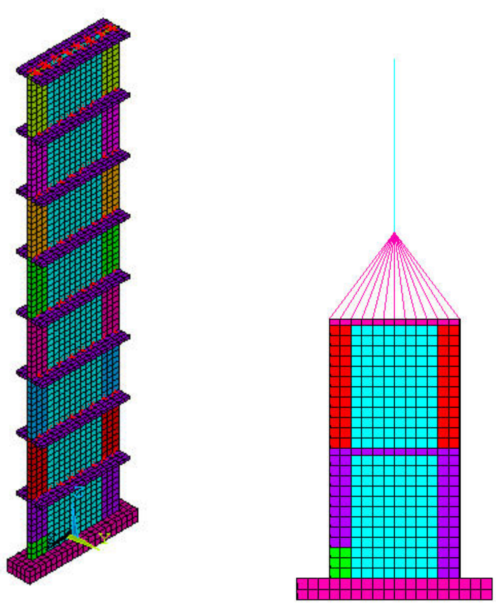

Figure 4.32 Finite element models of cantilever walls

CHAPTER 5

PERFORMANCE LIMITS OF STRUCTURAL WALLS

5.1 INTRODUCTION

Provisions for performance assessment of reinforced concrete structures, such as FEMA356 and ASCE/SEI 41, include modeling parameters and numerical acceptance criteria for both flexure and shear controlled wall members at specific limit states to estimate the performance of components and structures. The criteria are defined in terms of plastic hinge rotations and total drift ratios for the governing behavior modes of flexure (ductile members) and shear (brittle members), respectively. Strain limits are defined for concrete in compression and steel in tension at serviceability and damage-control limit states as a vital component of direct displacement-based design procedures (Priestley et al., 2007). The recently revised Turkish Seismic Code (TSC, 2007) specifies limiting strain values associated with different performance levels. On one side deformations are specified in relation to global parameters, and on the other side local damage indicators in terms of strain limits are used to determine the expected performance. When results of nonlinear pushover analyses are evaluated according to either of the acceptance criteria whether the local and global response will imply similar performance states is a matter that must be established because calibration of the requirements is lacking.

Another criticism raised against the rotations associated with different limit states is that they are lower than the actual rotations expected to develop in actual reinforced concrete sections. So, it is postulated that the given limits may be unduly conservative. In a way this is a direct consequence of adaptations performed for the plastic hinge analyses method employed in the codes. Since in daily application of structural analysis the moment-curvature relation of a section is calculated with section analysis method using the plane section hypothesis, the limiting plastic rotations in codes were adjusted to conform to the resulting plastic rotations calculated by multiplying the assumed plastic hinge length and plastic curvature rather than the actual rotations. These problems will be investigated in this chapter that forms the crux of this dissertation. The principal tool is the nonlinear finite element analysis for reinforced concrete structural components that has been thoroughly verified by the benchmark problems presented in Chapter 2. An extension is made to dynamic response calculations in Chapter 6. This chapter deals with statically applied monotonic effects only.

5.2 CODE PERFORMANCE LIMITS

5.2.1 FEMA 356 Performance Limits and Proposed ASCE/SEI 41 Revisions

A performance level describes a limiting damage condition which may be considered likely to be brought into concrete existence for a given building under seismically induced deformations. In FEMA 356 (2000) three discrete Structural Performance Levels and two intermediate Structural Performance Ranges are defined as shown in Figure 5.1 to identify the performance level of a building. Limiting values of modeling parameters and numerical acceptance criteria are specified to determine the performance. The discrete Performance Levels are Immediate Occupancy (IO), Life Safety (LS), and Collapse Prevention (CP). The intermediate Structural Performance Ranges are designated as Damage Control Range and the Limited Safety Range. Acceptance criteria for performance within the Damage Control Structural Performance Range are to be obtained by interpolating the acceptance criteria provided for the Immediate Occupancy and Life Safety Structural Performance Levels. Acceptance criteria for performance within the Limited Safety Structural Performance Range are obtained by interpolating the acceptance criteria provided for the Life Safety and Collapse Prevention Structural Performance Levels.

As indicated in Figure 5.1, at the Collapse Prevention level (CP) member deformation capacities are taken at ultimate strength (CEB, 1997) or at lateral displacement demand at which the lateral force resisting capability of the structure begins to rapidly degrade (Hamburger, 1997) for primary components. At the Life Safety level (LS), member deformation capacities are reduced by a (safety) factor of 4/3 over those applying at Collapse Prevention.

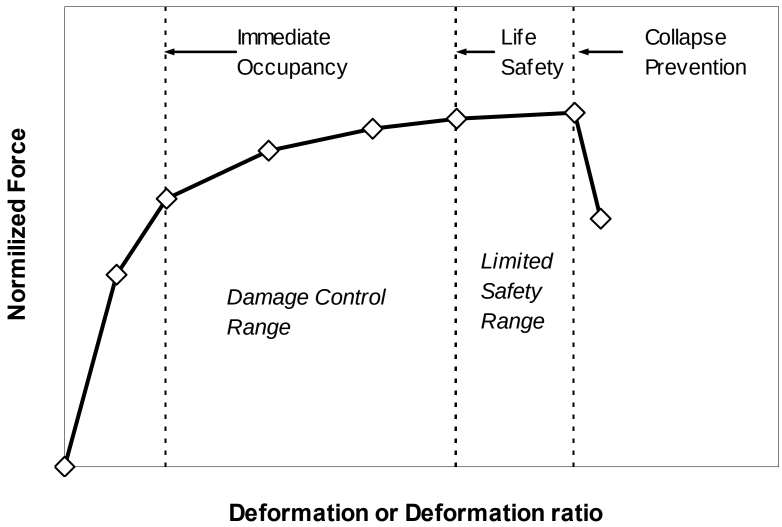

Figure 5.1 Structural Performance Levels

FEMA 356 states that monotonic load-deformation relationships for analytical models that represent shear walls and wall elements should be in accordance with the generalized relation shown in Figure 5.2. Depending on the behavior modes of shear walls different displacement criteria are used for the evaluation of the deformation capacity of shear walls. For walls having inelastic behavior under lateral loading that is governed by flexure, the rotation (θ) over the plastic hinging region at the end of member will be used as shown in Figure 5.3(a). The figure defines the behavior under monotonically increasing deformations. The hinge rotation at point B in Figure 5.2 corresponds to the yield point θ_y and shall be calculated in accordance with

$$\theta_y = \left(\frac{M_y}{E_c I}\right) L_p \tag{5.1}$$

where:

M_y = yield moment capacity of the shear wall or wall segment

E_c = concrete modulus

I = member moment of inertia for cracked section

L_p = assumed plastic hinge length

For reinforced concrete components, equivalent plastic-hinge length can be assumed as equal to one-half the member depth (Park and Paulay, 1975). FEMA 356 states that the value of L_p shall be set equal to 0.5 times the flexural depth of the element for analytical models of shear walls, but less than one story height. A similar estimate is applied to walls in Section 6.8.2.2 of FEMA 273 (1997), where L_p is "set equal to one half the flexural depth, but less than one story height." The 1997 UBC (ICBO, 1997) states that L_p "shall be established on the basis of substantiated test data or may be alternatively taken as $0.5L_w$." Based on research specifically applicable to walls, the equivalent plastic-hinge length, L_p, can be set at 0.2 times the wall length, L_w, plus 0.07 times the moment-to-shear ratio (also known as shear span), M/V (Paulay and Priestley, 1992). Equivalent plastic-hinge length, as calculated above, is used to relate plastic curvature to plastic rotation and tip displacement. The actual zone of nonlinear behavior may extend beyond the equivalent plastic-hinge zone.

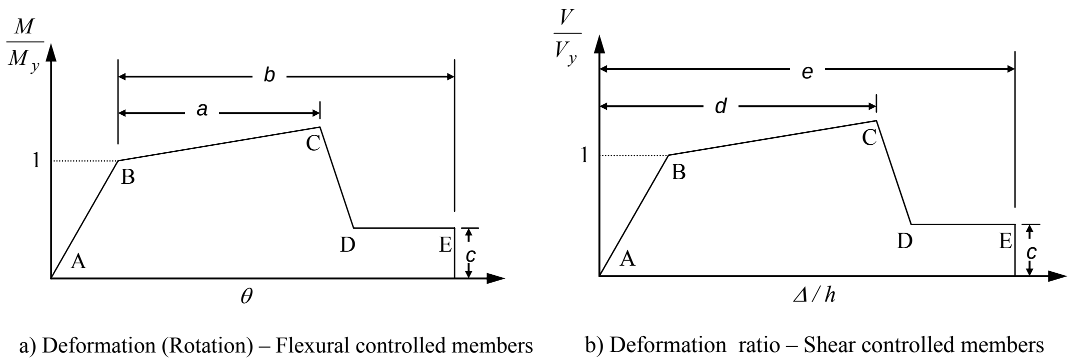

Figure 5.2 Generalized component force deformation relations for concrete elements

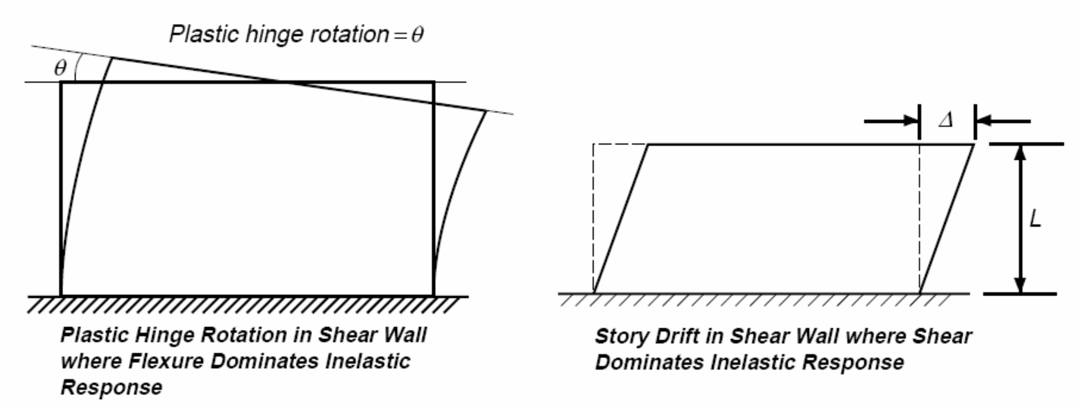

Figure 5.3 Deformation types of shear walls

For shear walls whose inelastic response is controlled by shear, the x-axis defining the load-deformation relation in Figure 5.2(b) will be taken as the lateral drift. For multi-story shear walls the drift shall be the story drift.

Values for the variables a, b, c, d and e, that are required to define the location of performance points C, D, and E in Figure 5.2(a) and Figure 5.2(b) , are given in *Table 6-18* and *Table 6-19* in FEMA 356. Table 5.1 and Table 5.2 summarize these modeling parameters and numerical acceptance criteria for flexure and shear controlled shear walls and wall elements, respectively. FEMA 356 adopts the ACI 318 (2008) requirements for the definition of a confined boundary. Linear interpolation between tabulated values shall be used if the member under analysis has conditions that are between the limits given in the tables. To eliminate the difficulties with the linear interpolation, the following functions have been derived to calculate the plastic hinge rotation limits related to each performance level for both conforming and nonconforming members whose response is controlled by flexure.

Immediate Occupancy:

Conforming members $$\theta_p = 0.007875 - 0.015\frac{P}{P_o} - 0.005v \tag{5.2a}$$

Nonconforming members $$\theta_p = 0.002667 - 0.00667\frac{P}{P_o} \tag{5.2b}$$

Life Safety:

Conforming members $$\theta_p = 0.01575 - 0.03\frac{P}{P_o} - 0.01v \tag{5.3a}$$

Nonconforming members $$\theta_p = 0.006417 - 0.01667\frac{P}{P_o} - 0.002v \tag{5.3b}$$

Collapse Prevention:

Conforming members $$\theta_p = 0.023 - 0.03667\frac{P}{P_o} - 0.018v \tag{5.4a}$$

Nonconforming members $$\theta_p = 0.01225 - 0.03\frac{P}{P_o} - 0.006v \tag{5.4b}$$

In the above equations, P/P_o is the axial load ratio and v is the member maximum average shear stress normalized with respect to $\sqrt{f_c}$ calculated as

$$v = \frac{V_{\max}}{t_w L_w \sqrt{f_c}} \tag{5.5}$$

where V_{max} is the maximum shear force carried by the member. Since the knowledge inherited in normalized shear stress expression given in Eq. (5.5) covers the parameters that affect the wall response significantly, normalized shear is a useful parameter that discriminates the distinct behavior modes of wall response.

Table 5.1 Modeling Parameters and Numerical Acceptance Criteria for Nonlinear Procedures-Members Controlled by Flexure

			Plastic Hinge Rotation (radians)		Residual strength ratio	Acceptable Plastic Hinge Rotation (radians)		
						Performance Level		
			a	*b*	*c*	IO	LS	CP
Shear walls and wall segments								
$\frac{(A_s - A_s^{'})f_y + P}{t_w l_w f_c^{'}}$	$\frac{Shear}{t_w l_w \sqrt{f_c^{'}}}$	Confined boundary						
≤ 0.10	≤ 0.25	Yes	0.015	0.020	0.75	0.005	0.010	0.015
≤ 0.10	≥ 0.50	Yes	0.010	0.015	0.40	0.004	0.008	0.010
≥ 0.25	≤ 0.25	Yes	0.009	0.012	0.60	0.003	0.006	0.009
≥ 0.25	≥ 0.50	Yes	0.005	0.010	0.30	0.0015	0.003	0.005
≤ 0.10	≤ 0.25	No	0.008	0.015	0.60	0.002	0.004	0.008
≤ 0.10	≥ 0.50	No	0.006	0.010	0.30	0.002	0.004	0.006
≥ 0.25	≤ 0.25	No	0.003	0.005	0.25	0.001	0.002	0.003
≥ 0.25	≥ 0.50	No	0.002	0.004	0.20	0.001	0.001	0.002

Table 5.2 Modeling Parameters and Numerical Acceptance Criteria for Nonlinear Procedures-Members Controlled by Shear

	Total Drift Ratio (%)		Residual strength ratio	Acceptable Total Drift Ratio (%)		
				Performance Level		
	d	*e*	*c*	IO	LS	CP
Shear walls and wall segments						
All shear walls and wall segments	0.75	2.0	0.40	0.40	0.60	0.75

A newly completed standard, ASCE/SEI 41-06 (2006), Seismic Rehabilitation of Existing Buildings, proposes changes to acceptance and modeling criteria for walls controlled by both flexure and shear in FEMA 356 (2000), and aims to enhance the accuracy and reliability of wall provisions. The main goal of the proposed changes to wall provisions of ASCE/SEI 41 (Section 6.7) was to update the modeling and acceptance parameters for walls to make them more consistent with experimental results (ASCE/SEI

41-06 update, 2007). For shear dominated wall members the proposed changes include subdividing the one category in FEMA, which encompasses all walls regardless of axial load, into two categories; one for walls with low axial loads and another for walls with significant axial load demands. For flexural walls the values for parameters a and b specified in Tables 6.18 and 6.20 in FEMA 356 were found to be very conservative (EERI/PEER, 2006) compared with experimental results on walls subjected to intermediate levels of shear stress (between $0.25\sqrt{f_c}$ and $0.4\sqrt{f_c}$, MPa). The limiting average shear stress was increased from $0.25\sqrt{f_c}$ to $0.33\sqrt{f_c}$, MPa to obtain a better match with experimental results (ASCE/SEI 41 update, 2007).

Using the results of recently completed experimental research (Hidalgo et al., 2002, EERI/PEER, 2006) ASCE/SEI Committee proposed changes to acceptance and modeling criteria for walls controlled by shear. While FEMA 356 classifies all shear controlled members in one category as given in Table 5.2, ASCE 41 subdivides shear-controlled walls into two categories; one for walls with low axial loads and another for walls with significant axial load demands as given in Table 5.3. Depending on very limited number of experimental studies (EERI/PEER, 2006), it was decided that for axial loads equal to or greater than $0.05 f_c' A_g$ shear controlled wall members exhibit reduced deformation and residual strength capacity. The backbone curve in Figure 5.2(b) used to model shear controlled members is replaced by the load deformation relationship given in Figure 5.4. The gradual degradation in the stiffness of shear controlled wall members was taken into account more realistically by this modification as investigated for the NUPEC wall specimen in Section 2.7.2.

Table 5.3 Modeling Parameters and Numerical Acceptance Criteria for Nonlinear Procedures-Members Controlled by Shear as proposed in ASCE/SEI 41

	Total Drift Ratio (%)			Strength ratio		Acceptable Total Drift Ratio (%)		
						Performance Level		
	d	*c*	*g*	*c*	*f*	IO	LS	CP
Shear walls and wall segments								
$\frac{(A_s - A_s')f_y + P}{t_w l_w f_c'} \le 0.05$	1.0	2.0	0.4	0.2	0.6	0.4	0.75	1.0
$\frac{(A_s - A_s')f_y + P}{t_w l_w f_c'} > 0.05$	0.75	1.0	0.4	0.0	0.6	0.4	0.55	0.75

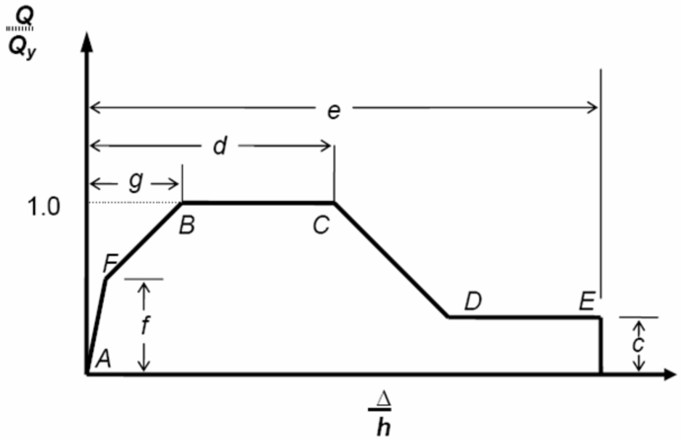

Figure 5.4 Modified load-deformation relationship for members controlled by shear in ASCE/SEI 41.

5.2.2 TSC 2007 Strain Limits

Turkish Seismic Code (2007) specifies strain limits to evaluate the performance of reinforced concrete members. Depending on the analysis tool, concrete compression and steel tension strain demands at a member section extreme fibers can be obtained directly (if the fiber section modeling technique is used) or must be transformed from member sectional rotations, which are obtained from pushover analyses or time history analyses (if generalized load-deformation models were used in the member modeling). When the later case holds the plastic rotations obtained at the member plastic hinge locations are used for calculating the plastic curvature demands at these critical sections followed by the calculation of total curvature, ϕ_t, by adding the yield curvature, ϕ_y.

$$\phi_p = \frac{\theta_p}{l_p}; \qquad \phi_t = \phi_p + \phi_y \tag{5.6}$$

Concrete compressive strains and steel tensile strain demands corresponding to the calculated total curvature demand at the plastic regions are calculated from the moment-curvature diagrams obtained by conventional sectional analyses of the critical section. Moment-curvature diagrams of the critical sections are obtained by using appropriate stress-strain rules for concrete and steel. Finally, the calculated strain demands are compared with the damage limits given below to determine the member damage states.

Concrete and steel strain limits at the fibers of a cross section for minimum damage limit (MN)

$$(\varepsilon_{cu})_{\mathrm{MN}} = 0.0035 \ ; \qquad (\varepsilon_s)_{\mathrm{MN}} = 0.010 \qquad (5.7)$$

Concrete and steel strain limits at the fibers of a cross section for safety limit (SF)

$$(\varepsilon_{cg})_{\mathrm{SF}} = 0.004 + 0.0095\ (\rho_s/\rho_{sm}) \leq 0.0135 \ ; \qquad (\varepsilon_s)_{\mathrm{SF}} = 0.040 \qquad (5.8)$$

Concrete and steel strain limits at the fibers of a cross section for collapse limit (CL)

$$(\varepsilon_{cg})_{\mathrm{CL}} = 0.004 + 0.013\ (\rho_s/\rho_{sm}) \leq 0.018 \ ; \qquad (\varepsilon_s)_{\mathrm{CL}} = 0.060 \qquad (5.9)$$

In Eqs. (5.7) to (5.9), ε_{cu} is the concrete strain at the outer fiber, ε_{cg} is the concrete strain at the outer fiber of the confined core, ε_s is the steel strain and (ρ_s/ρ_{sm}) is the ratio of existing confinement reinforcement at the section to the confinement required by the Code. In a radical break with tradition TSC has annexes that explain to code users how concrete and steel may be modeled by referring to particular material formulations. This approach is excessively vulnerable to improper treatment of different models by engineers who are not adequately familiar with nonlinear response of reinforced concrete components.

The limits utilized in TSC (2007) are mostly based on the studies and proposals of Priestley and his colleagues (Priestley et al., 2007). Priestley et al. (1996 and 2007) proposed strain limits for tension and compression in relation to serviceability and damage-control limit states to be used in moment-curvature analysis. Damage-control limit state corresponds to the collapse prevention performance level in TSC (2007) and will be discussed further in detail here since the evaluation of finite element analysis results depends significantly on these limits.

a) Damage-Control Tension Strain Limit: Priestley et al. (2007) suggest that it is not appropriate to use the ε_{su}, the strain at maximum stress of the reinforcing steel found from monotonic testing, as the maximum permissible tension strain for moment-curvature analysis. The reasons are:

- Under cyclic loading, the successive compressive and tensile reversal causes a reduction in the effective ultimate tensile strain that will be attained by the bar at failure.
- Reinforcing bars subjected to high tensile strains prior to compressive loading become more susceptible to buckling. This buckling typically occurs before the previously developed flexural cracks are closed, and while the bars are still subject to tensile strain but compressive stress. This endangers low-cycle fatigue of the reinforcing bar at levels of tensile strain significantly below ε_{su}.

- Finally, slip between the reinforcing steel and concrete at the critical section, and tension-shift effects result in reinforcement strain levels being lower than predicted by a "plane section" hypothesis.

Based on these considerations, the ultimate curvature of the section analyzed should be based on a steel tension strain limit of $\boldsymbol{\varepsilon_s = 0.6\varepsilon_{su}}$.

b) Damage-control Compression Strain: Priestley et al. (2007), assuming that the useful limit for confined concrete in compression is determined by the fracture of the transverse reinforcement confining the core derived the following expression by equating the strain energies of the concrete and confining steel absorbed in a unit volume of core concrete.

$$\varepsilon_{cu} = 0.004 + \frac{1.4\rho_s f_{yw}\varepsilon_{su}}{f_{cc}} \tag{5.10}$$

The equation was defined previously in APPENDIX C while explaining the Mander et al.'s (1988) concrete model. In the equation f_{yw} is the yield strength of transverse steel, ρ_s is the volumetric ratio of boundary element transverse reinforcement, f_{cc} is the compressive strength (peak stress) of confined concrete. Priestley et al. (2007) state that although Eq. (5.10) is approximate, it agrees well with the ultimate compressive strains measured in experiments (Mander et al., 1988). They state that the actual effective ultimate compression strains under combined axial force and flexure exceeds the predicted values by a factor of about 1.3 to 1.6. This degree of conservatism was found to be satisfactory for structures designed for damage control limit state.

5.2.3 Concrete Strain Limits in Reinforced Concrete

At this point it is useful to discuss concrete strain limits allowed in design and assessment of reinforced concrete structures.

In UBC 1997 it was declared that under no circumstances should designs be permitted in which compressive strains exceed 0.015. In portions, where compressive strains exceed 0.003, boundary zone requirements shall be met.

ACI 318-02 states in Section 10.2.3 that for members under axial load and flexure maximum usable strain at extreme concrete compression fiber shall be assumed equal to 0.003. Moreover, in the accompanying commentary it was noted that from tests it is observed that ε_{cult} varies from 0.003 to higher than 0.008 under special conditions. It was also cautioned that, the strain at which ultimate moments are developed is usually about 0.003 to 0.004 for members of normal proportions and materials.

While defining usable compressive strain limits for components without confining transverse reinforcement under flexural and axial loads, FEMA 356 defines the maximum strain at the extreme concrete compression fiber as 0.002 in nearly pure compression and 0.005 for other types of stress states unless larger strains are substantiated by experimental evidence and approved. For confined concrete, in the determination of maximum usable compressive strains the limits should conform to the limitations imposed by fracture of transverse reinforcement, buckling of longitudinal reinforcement, and degradation of component resistance at large deformation levels. Maximum compressive strains in longitudinal reinforcement shall not exceed 0.02, and maximum tensile strains in longitudinal reinforcement shall not exceed 0.05.

In previous studies, a limiting compressive strain of 0.004 has been suggested (Paulay, 1986; Wallace and Moehle, 1992) for no special transverse reinforcement required to confine concrete and found to yield favorable comparison with the test results of isolated walls. At this strain, only a minor deterioration in the cover concrete at wall boundary was reported (Wallace and Moehle, 1992). In addition, no effect of this deterioration on the overall structural integrity is noted. Therefore, Wallace (1995a), states that if the maximum wall compression strain is less than 0.004, no special transverse reinforcement may be required for concrete confinement. It is clear that, the maximum fiber strain at the extremities of a wall will be function of the displacements induced by earthquake ground motion excitation.

5.3 METHOD OF ANALYSIS TO INVESTIGATE THE PERFORMANCE LIMITS

5.3.1 Finite Element Model and Parameters of the Analytical Investigation

5.3.1.1 Parameters

Within the analytical framework described in the previous chapter, the results from a parametric study conducted to determine the relation between the local and global deformation demands will be presented here. The idealized cantilever models described in the previous chapter were used in the analyses. The variables of the parametric study have been also discussed in Chapter 4 and are summarized below. The schematic description of these variables is given in Figure 5.5. The parameters are

- Wall length (L_w): 3 m, 5 m and 8 m.
- Effective shear span (L_v): 5 m, 6 m, 9 m, 15 m, 24 m.
- Wall boundary element longitudinal reinforcement ratio (ρ_b): 0.5, 1, 2, 4 percent.
- Wall axial load ratio at the base ($P/f_c/A_w$): 0.02, 0.05, 0.1, 0.15, 0.5.

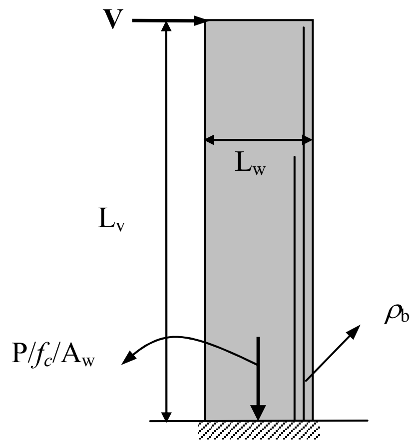

Figure 5.5 Illustration of variables of the parametric study

In the design of walls that were used for the parametric study, the design procedure defined in Section 4.4.1 was employed. Concrete strength was taken as 25 MP for all cases. Wall boundary elements were assumed to extend over a region of $0.2L_w$ at the edges. For any given combination of above parameters the wall yield moment (M_{wy}) is calculated using Eq. (4.33), where the section yield capacity is only function of wall length (L_w), ratio of boundary element longitudinal reinforcement area to the boundary region cross section area (ρ_b) and axial load ratio (P/P_o). In the following step, using the specified shear span length (L_v) the design shear force is calculated ($V_d=M_{wy}/L_v$). The ratio of the horizontal and vertical web reinforcement is assumed to be nominally 0.0025. If the factored shear force ($V_e=\lambda V_d$) exceeds the shear safety limit calculated with Eq. (4.35), the required amount of web horizontal reinforcement is recalculated employing the same equation. Since codes specify that the amount of vertical reinforcement should not be less than the horizontal reinforcement in the web, the same steel ratio of web reinforcement is used in the vertical as well. The design shear force is factored only for flexural over-strength. The amplification in the base shear due to higher mode effects was disregarded. Base shear amplification is studied in the following chapter.

5.3.1.2 Boundary element confinement

The deformation capacity of structural walls is controlled by the level of confinement in the boundary elements. TSC (2007) and ACI 318-08 (2008) calculates the amount of transverse reinforcement that is required at the wall boundaries with similar expressions. The expression in TSC was given in Eq. (4.36) as $A_{sh} = 0.05 s\, b_c f_{ck} / f_{ytk}$. This is 2/3 of the amount of transverse reinforcement used to confine the column elements. The same equation with a multiplier of 0.09 is given in ACI 318. In the models analyzed here the boundary region length were taken as $0.2L_w$ and the thickness of the walls as $t_w = 250$ mm ($b_c = 200$ mm). The yield strength of the longitudinal and transverse reinforcement was assumed to be 420 MPa. The boundary element transverse reinforcement calculated according to TSC was ϕ8/150 (assuming f_y = 420 MPa). Since TSC states that vertical spacing of hoops and/or crossties shall not be more than half the wall thickness and 100 mm, nor shall it be less than 50 mm, as transverse reinforcement ϕ8/100 is used. If the ACI 318 had governed the design, ϕ8 hoops at 85 mm spacing would have been required as confinement steel at the boundary elements. In conclusion wall boundaries can be considered as well confined for TSC and adequately confined for ACI 318. Obviously confinement should be considered among the variables of the parametric study, but since this would increase the analysis permutations significantly, the study will be limited to confined members.

It has been recently reported (ASCE/SEI41, 2006) that behavior of walls not fully conforming to ACI 318 is adequately represented by modeling and acceptance criteria for conforming elements in *Tables 6.18* (Table 5.1) and *6.20* of FEMA 356. ASCE/SEI 41 has revised the definition of a confined boundary from that having transverse reinforcement conforming to ACI 318-08 to include boundary elements in which the amount of transverse reinforcement exceeds 75% of that required in ACI 318-08, and spacing of transverse reinforcement does not exceed $8d_b$ for the purpose of evaluating the behavior of walls. In the proposed changes it also is permitted to take modeling parameters and acceptance criteria as 80% of confined values where boundary elements have at least 50% of the requirements given in ACI 318, and spacing of transverse reinforcement does not exceed 8*db*. Otherwise, boundary elements must be considered as not confined.

The stress strain curves of the confined concrete for different vertical reinforcement and boundary length combinations are given in Figure 5.6. As seen in the figures the modified Kent and Park model (1982) indicates a lower deformability at the wall boundaries. Although the Saatcioglu and Razvi (1992) and Mander et.al (1988) models produce similar curves, former yields a more realistic behavior in the descending part of the stress-strain curve as discussed in APPENDIX C.

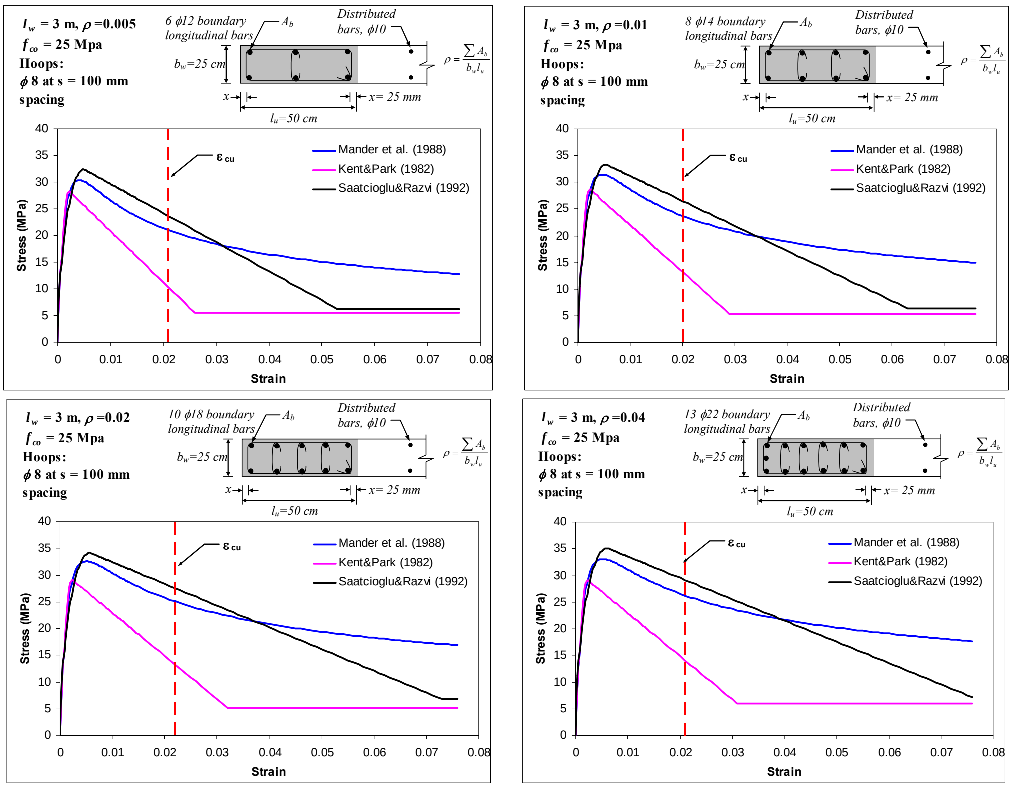

Figure 5.6 Stress-strains of confined region

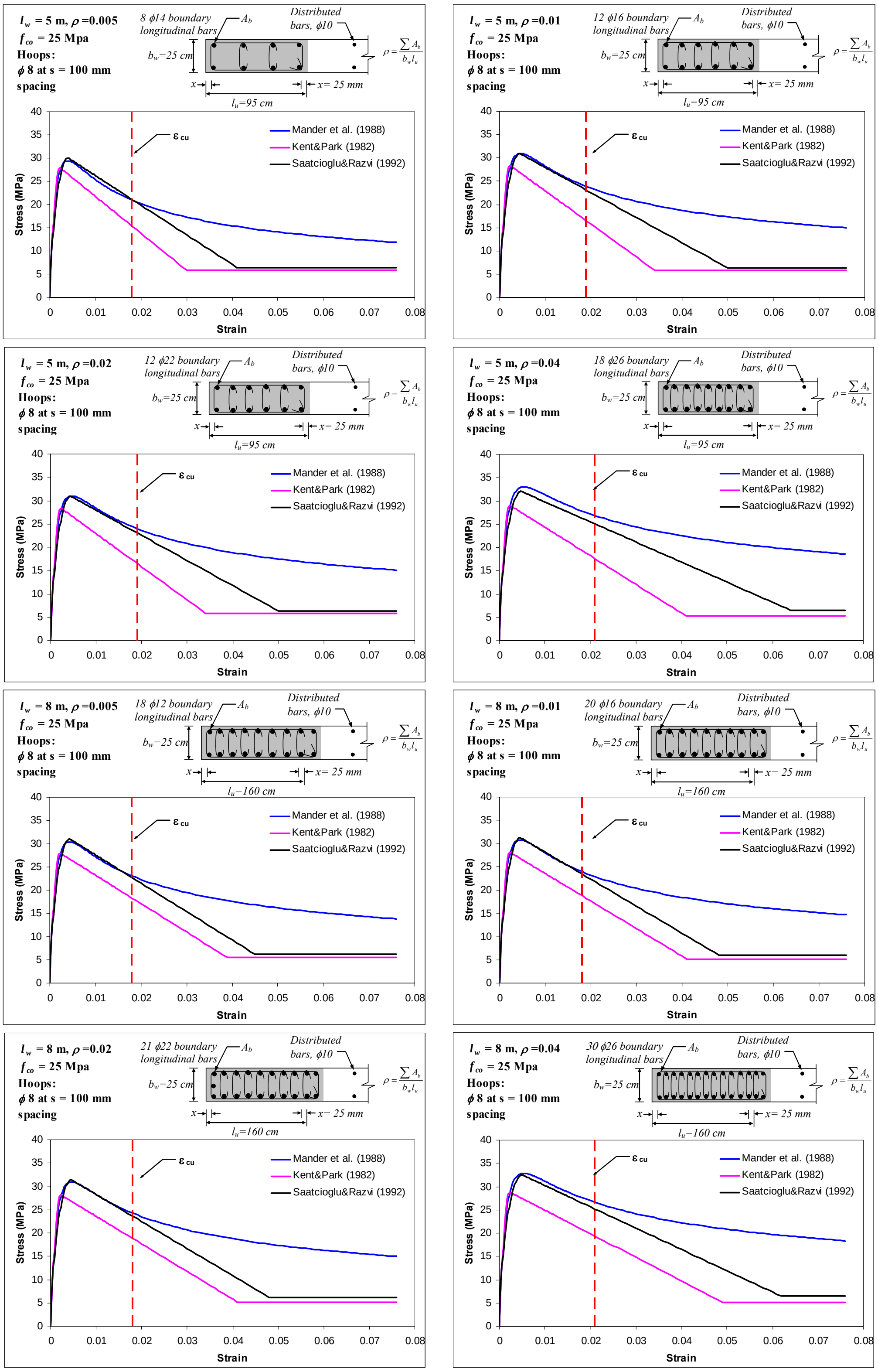

Figure 5.6 (Continued) Stress-strains of confined region

5.3.1.3 Finite Element Models

Trial analysis of cantilever walls under uniform and inverted triangular load patterns displayed that even when cracking may extend up to mid-height of the wall, significant steel yielding extends over only lower one or two stories. The upper stories can be effectively treated as a cracked beam. Using this analogy a finite element model is developed to reduce the computation time. As shown in the model in Figure 5.7, the first two stories of the cantilever wall was discreticized with solid continuum elements (SOLID65) whereas the upper stories is modeled with BEAM188 which is based on Timoshenko beam theory. The nonconformance between the nodal degree of freedoms of beam (d.o.f.'s: u_x, u_y, u_z, θ_x, θ_y, θ_z) and solid (d.o.f.'s: u_x, u_y, u_z) elements was overcome by providing the transition with constraint element MPC184 by utilizing the rigid beam option. BEAM188 takes into account the shear deformations. As described in Section 4.5.2, to define the behavior of beam elements generalized nonlinear section properties were used. The load deformation behavior of beam elements was assigned in the form of bilinear force-distortion angle (F-γ) and moment-curvature (M-ϕ) relation. The initial flexural rigidity was taken as $0.5EI_w$. This model proved to be adequate since all the response parameters under investigation is concentrated at the lower stories.

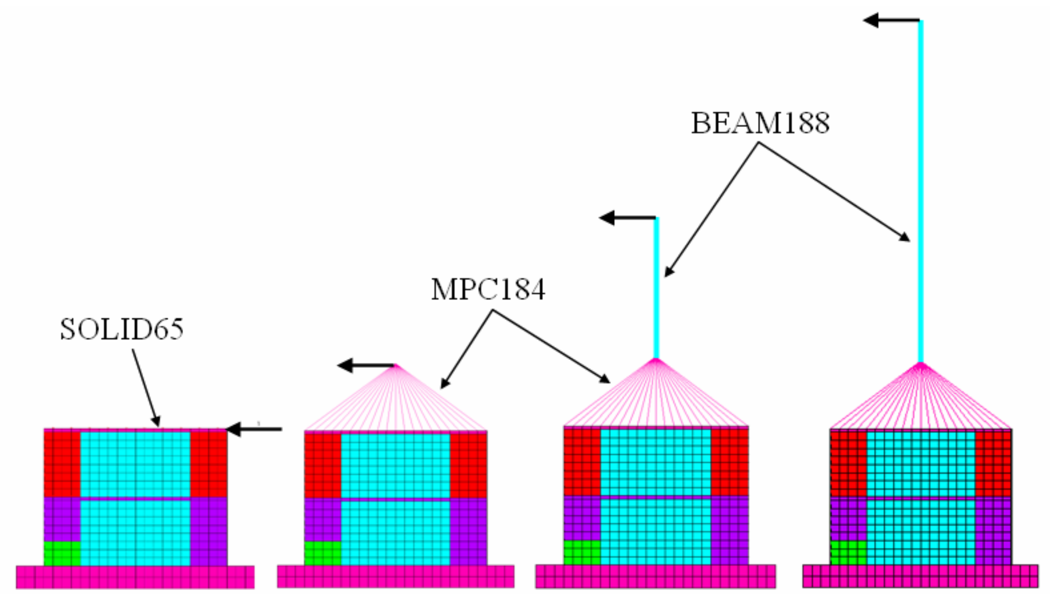

Figure 5.7 Reduced finite element model of cantilever walls

5.3.2 Calculated Response Parameters

The benefit of NLFEA lies in the fact that several response parameters in either global or local scale can be calculated accurately. At every point of the model strains and stresses can be obtained numerically and checked through graphics. Additionally crack pattern and strains calculated on the model reveal the governing behavior mode of the specimen.

5.3.2.1 Deformation Components

Calculation of the global and interstory drift demands on shear walls as an indicator of structural damage are not the same as the drift calculations on frames. A distinction is required between the two measures of interstory distortion. In shear wall buildings, interstory drift is not an appropriate measure of damage since significant portion of the global drift results from the rigid body rotation of lower stories. As shown in Figure 5.8, in isolated structural walls, that exhibit predominantly cantilever flexure type behavior, the interstory “tangential deviation”, (i.e., the deviation or horizontal displacement of a point on the axis of the wall at a given floor level measured from the tangent to the wall axis at the floor immediately below it), rather than the “interstory displacement”, provides a better measure of the distortion that the wall experiences. In fact, the tangential deviations vary in the same manner as, and are directly reflected in, the bending moments that are induced by the lateral deflection of the wall.

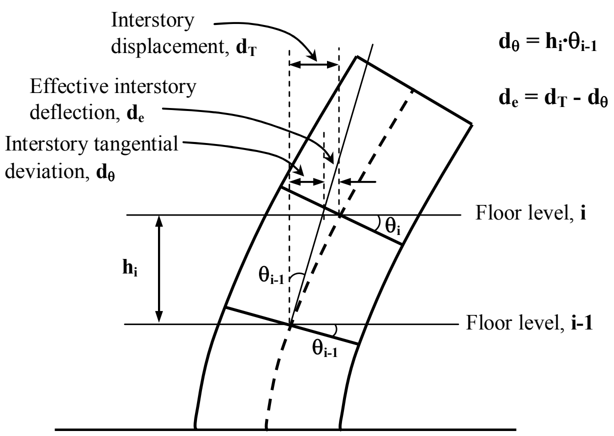

Figure 5.8 Computation of lateral drift of cantilever walls

The above figure can be used to describe the required calculations of interstory displacements and rotations for flexure dominated shear walls. However, in the calculation of shear deformations that results from significant shear actions like diagonal tension and compression on the web a different scheme is required. The procedure described in Figure 5.9 (Oesterle et. al, 1976) utilizes shear distortion angles in the calculation of the shear deformation component of the total deformation. The flexural component of the displacement can be calculated by subtracting the displacement components corresponding to diagonal and sliding shear from the total lateral displacement.

Another component of the deformation that has not been accounted for is due to slippage/pull-out of vertical bars from the foundation and bond slip. These deformation components have been neglected in all the analyses carried out in this study.

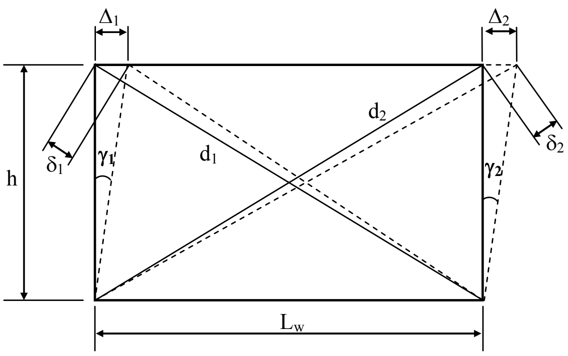

$$\gamma_1 = \frac{\Delta_1}{h}, \ \gamma_2 = \frac{\Delta_2}{h}, \ \gamma_{ave} = \frac{\Delta_1 + \Delta_2}{2h}$$

$$\frac{\Delta_1}{\delta_1} = \frac{d_1}{L_w}, \ \frac{\Delta_2}{\delta_2} = \frac{d_2}{L_w}$$

$$\gamma_{ave} = \frac{d_1\delta_1 + d_2\delta_2}{2hL_w}$$

$$\Delta_{shear} = \gamma_{ave} h$$

Figure 5.9 Computation of shear deformation component of the wall lateral displacement

5.3.2.2 Forces and Moments

In the finite element model shear force along a section is calculated by summing the horizontal nodal forces along the faces of the elements lying on that section. The summation can be done on the faces of elements lying along both sides of the section. Only the sign of the force will change. The bending moments are calculated by summing the moments of each element nodal force normal to the section surface around the section center.

5.3.2.3 *Strain Measurements*

Vertical strains at compression and tension boundary extremities of the wall were evaluated. Although stress and strain results can be obtained at element integration points or as average values at nodes in ANSYS, the vertical strains were computed by using the nodal vertical displacements. The vertical strain is calculated by dividing the difference between the vertical displacements at successive nodes to the distance between these nodes. These strains pair-wise in a row were used to calculate the curvature distribution along the height of the wall. Using both the tensile steel strain profile along the edge and the curvature distribution along the height of the wall the length of plastic zone (L_{pz}) is determined. Figure 5.10 provides the visual description about the location of the calculated strains.

At the lower 1 m of the each story (three elements in height) the vertical strains are extracted along the length of wall in the horizontal direction row-wise also. Using the strain distributions along the row neutral axis depth, c, is investigated.

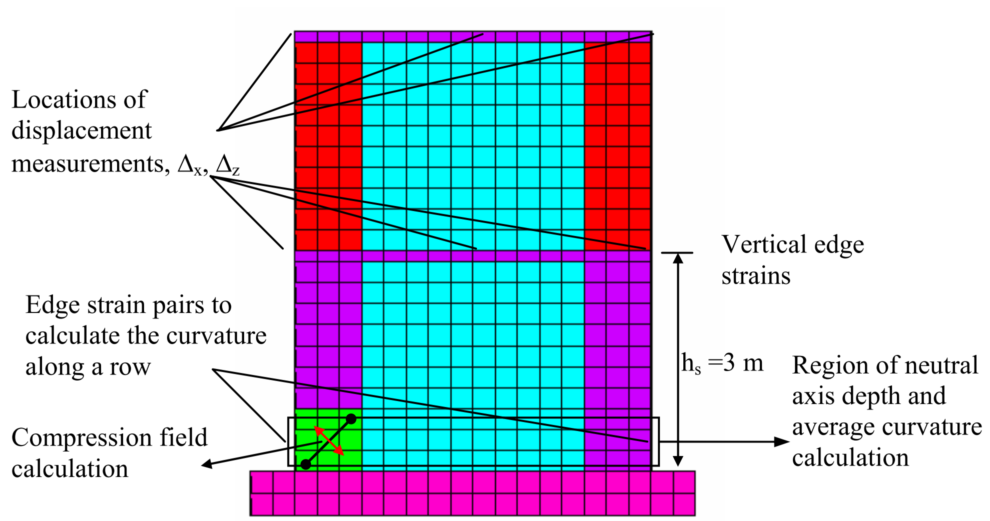

Figure 5.10 Locations of calculated strain quantities

5.3.2.4 *Curvatures and Rotations*

Curvatures were calculated in two different ways. The first type of curvature is calculated over a region of three element height at the base of the wall, which is approximately 1 m in height as shown in Figure 5.10. This curvature is an average value that can be used to get an estimate of the wall curvature when the actual curvature can not be obtained due to difficulties in the interpretation of extent of plastification over the wall height. The second type of curvatures is row curvatures that are computed from average element strains calculated at the same height (in the same row) at the two wall ends. These curvatures can be used to determine the spread of plasticity along the wall.

Rotations are calculated from the nodal vertical displacements along each end of the wall by using the triangulation calculations. The height over which the rotations are calculated depends on the spread of plasticity, which is discussed in detail in Section 5.4.

5.3.3 Results of FEM Analyses

In the light of FEM analysis several useful observations are made. Through Figures F.1 to F.14 in APPENDIX F, force-displacement responses of the analyzed walls are presented. The analyses are grouped according to the wall length (L_w) and effective shear span length (L_v). The vertical axis representing the shear force capacity of the walls is normalized with respect to $t_w L_w \sqrt{f_c}$. The second floor drift ratio is used to display the deformation capacity of the analyzed walls. As discussed previously in Section 5.3.2.1 and displayed in Figure 5.7, roof drift of cantilever walls is not a meaningful measure to investigate the deformation capacity of structural walls. Additionally, the base stories are the most critical regions when the deformability of the walls is considered. By this way the deformation components can be directly compared with code specified values. 2nd floor displacements were preferred over 1st floor values, because the total drift composed of shear and flexural deformation components can be calculated more representatively over two story height due to excessive diagonal cracking and localized damage at the base story. The presented data provides significant information about the deformation capacity of the structural walls. The summary of relations between the normalized shear capacity and ultimate deformation capacity of walls is given in Figure 5.11. The drift capacity of walls further decomposed into flexural and shear components were also presented in this figure. The shear stress limits used to arrange the plastic rotation limits in FEMA 356 were superposed on the graph. ACI 318-08 states that the normalized shear carried by a wall member should not exceed $0.66\sqrt{f_c}$.

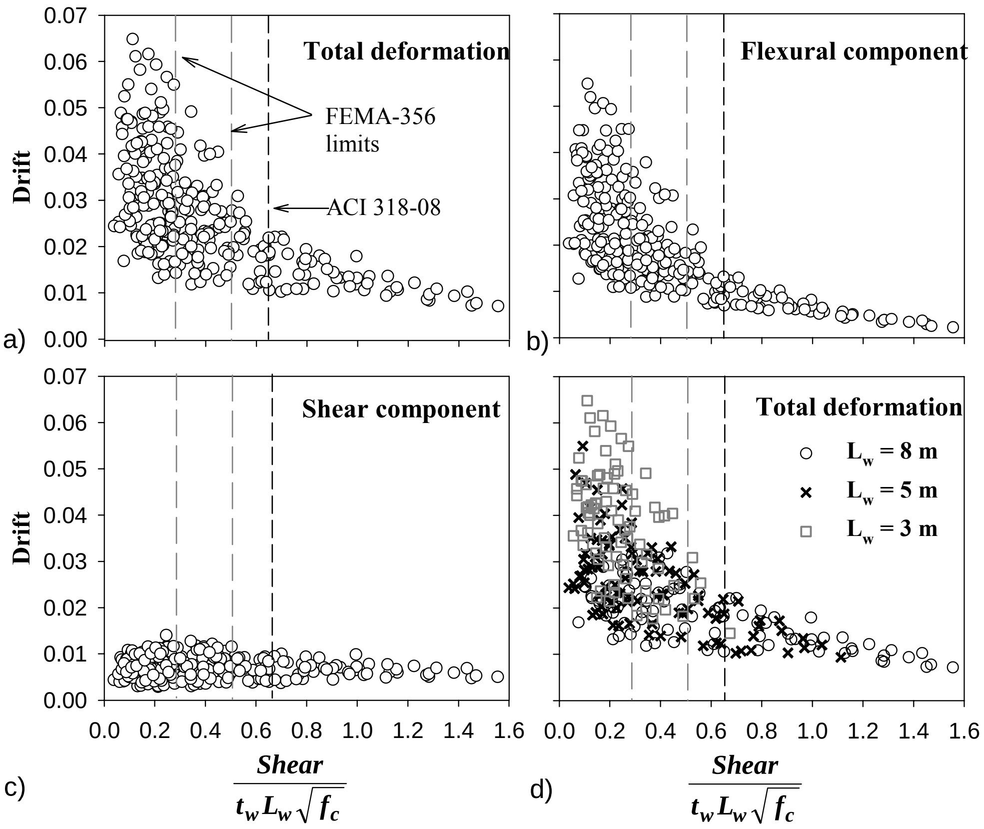

Figure 5.11 Ultimate drift capacities of wall models

As displayed in Figure 5.11(d) wall length significantly affects the deformation capacity of walls. Figure 5.12 reveals the effect of axial load ratio, the second important parameter, on the deformability of walls. As the wall length and axial load ratio increases deformation capacity of walls reduces. The FEMA normalized shear stress limits used to differentiate between the flexural and shear type of behavior correlates with the data presented here. For walls with $\nu < 0.25$ flexural type behavior governs. The drift capacities of walls that respond in flexural mode range from 2.5 to 6 percent depending on the level of axial load. Structural walls can exhibit significant displacement ductility capacity as seen in Figure 5.12(b). In codes, such as FEMA306 and FEMA356, the ductility capacity of members is classified as either low, moderate, or high. The following approximate relationship presented in Table 5.4 can be assumed for the classification. However, as seen in Figure 5.12(b) for low-to-moderate levels of axial load ratio the ultimate displacement ductility capacity of members may reach a value of 10 to 25. The ductility limits that were specified in codes seem to be too low and require to be adjusted for wall members.

Table 5.4 Classification of Displacement Ductility in FEMA 356

Displacement Ductility	Classification
$\mu_\Delta < 2$	Low Ductility
$2 \le \mu_\Delta \le 4$ (5)*	Moderate Ductility
$\mu_\Delta > 4$ (5)*	High Ductility

*Limits used in FEMA 306

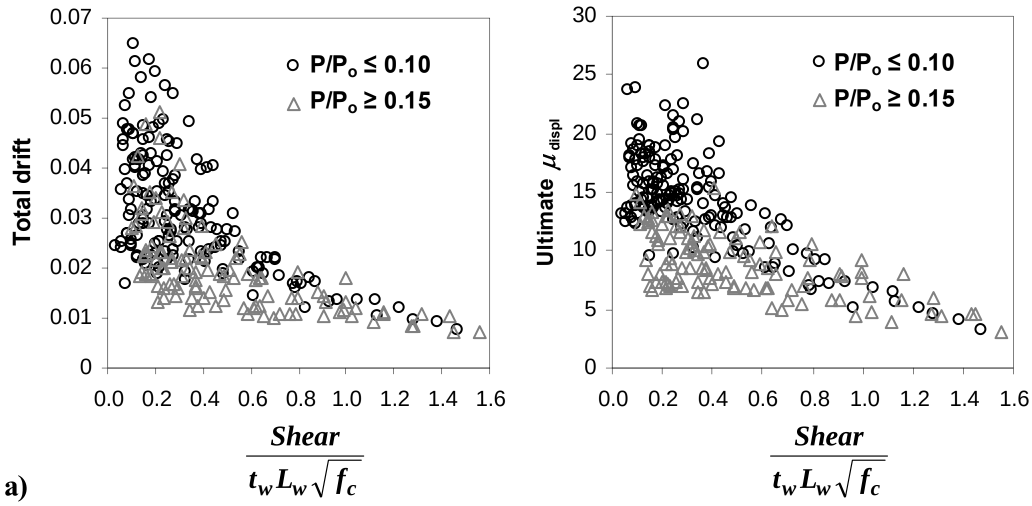

Figure 5.12 Effect of axial load level on the ultimate a) drift, and b) displacement ductility (μ_{displ}) capacities of wall models.

The ratio of shear deformation (Δ_s) to the total deformation (Δ_t) with respect to increasing shear capacity is displayed in Figure 5.13(a). The shear deformation may constitute a significant portion of the total deformation even though the shear stress carried by the walls is very low. The data in the figure points out that the shear deformations must be taken into account while modeling the lower stories of shear walls. Using the parameters that govern the response of shear walls an equation is derived to estimate the drift capacity of shear walls with moderately confined boundary elements. The equation from a regression analysis reads as

$$DR = A(\rho_b)^B \cdot \exp(-C \cdot \nu - D \cdot L_w) \qquad (5.11)$$

where A, B, C and D are coefficients defined in Table 5.5 as a function of axial load ratio, ρ_b is the boundary element reinforcement ratio, ν is the normalized shear stress and L_w is the wall length. The predictions are compared with the finite element results in Figure 5.13(b).

Table 5.5 Coefficients of Eq. (5.11) to calculate the ultimate drift capacity of walls

P/P_o	A	B	C	D
≤ 0.10	0.127	0.175	1.026	0.075
$= 0.15$	0.085	0.118	0.981	0.074
$= 0.25$	0.041	0.081	0.713	0.054

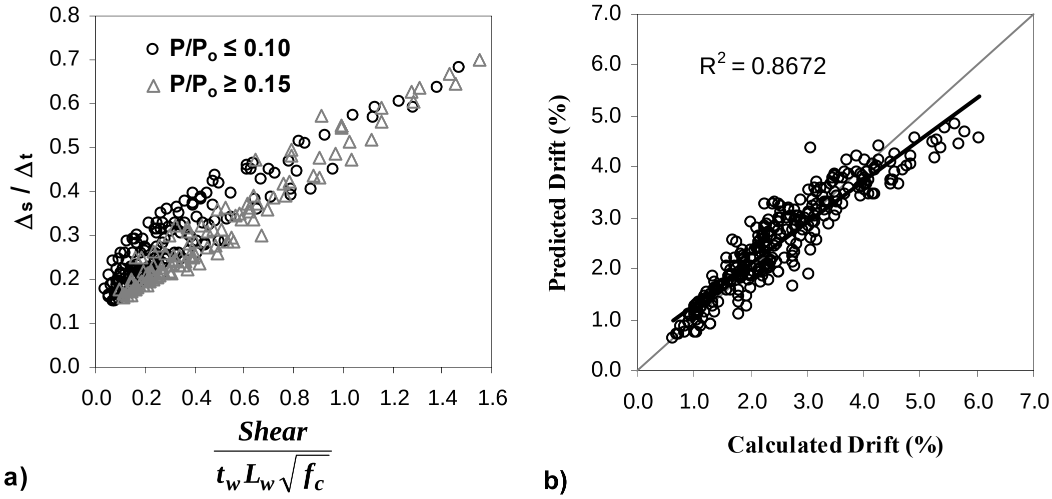

Figure 5.13 a) Ratio of shear component of displacement to the total displacement, b) comparison of calculated drift ratios predicted with Eq. (5.11)

It may be argued that the degrading effect of cyclic loading regimes on the stiffness and strength of reinforced concrete was not considered in the analysis. Past experimental studies have shown that the overall deformation under cycling loading may be at least 75% of the deformation reached under monotonic loading. This is due to deterioration of concrete, and the development of cyclic failure mechanisms associated with the load history and characteristics of the specimens. Vallenas et al. (1979) proposed that as a general rule the overall deformation capacity under a realistic ground motion could be expected to be over 75% of the deformation capacity under monotonic loading conditions. In this perspective, it may be useful and necessary to reduce the ultimate deformations obtained from the monotonic static analysis by a factor of 0.75~0.8.

Impropriety of conventional sectional analysis method in case of members under high shear condition is clearly revealed in the comparison of the vertical and principal compressive strain plots in Figure 5.14(b) and Figure 5.14(c). In flexure controlled member (Case2) the vertical strain and principal compressive strain distributions indicate to concentration of compressive strains at the edge of the wall. However, in the case of shear controlled member (Case1) while the vertical strain plot shows that only a limited region at the edge of the wall is under compression, the principal compressive strain plot indicates that the region under compression extends nearly over two thirds of wall length. Obviously these compressive strains are inclined, resulting from the compression strut action. Shear strain plots in Figure 5.14(d) indicate diagonal cracking in a flexural member and sliding shear failure above the base of a shear controlled member.

Accurate calculation of the spread of plasticity along the height of the wall is essential in deriving the plastic hinge length. Several factors such as the level of shear stress carried by the member, length of the wall plays fundamental role on the length of plastic hinge region. The effect of boundary element reinforcement on the spread of plasticity along the wall is displayed in Figure 5.15. The percentage of boundary element reinforcement takes the values of 0.5, 1, 2 and 4% in each figure. As seen in Figure 5.15, in lightly reinforced walls (ρ_b = 0.005~0.01) the flexural cracks concentrate at specific locations along the edge of wall. At the highest location, the flexural cracks rotate and turn into inclined shear cracks over the web region. As seen in Figure 5.16 both flexural and shear cracks are evident on the wall.

Case 1, $L_v = 5$ m, $\nu = 0.70\sqrt{f_c}$ **Case 2, $L_v = 24$ m, $\nu = 0.17\sqrt{f_c}$**

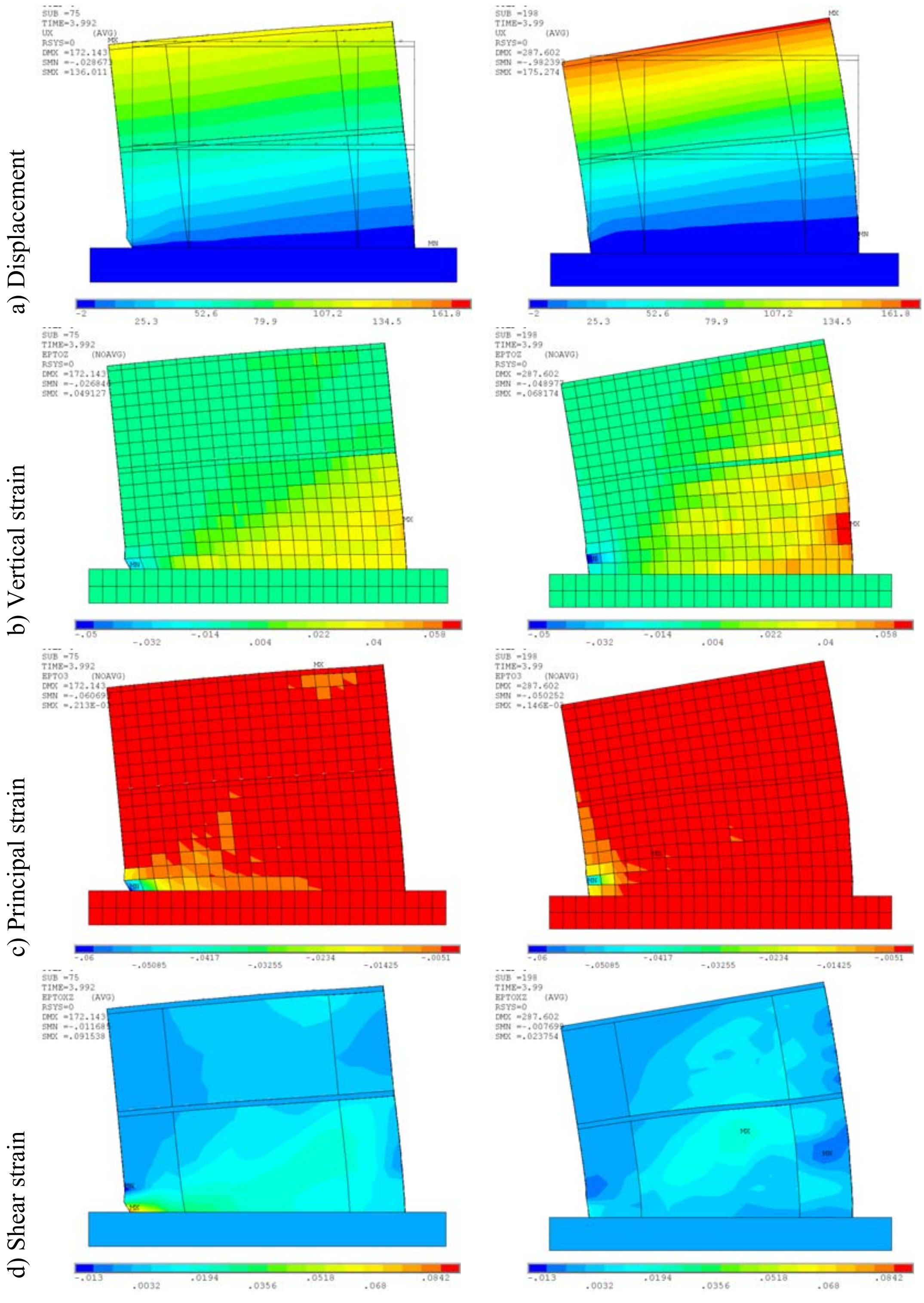

Figure 5.14 Contour plots displaying the distribution of a) Horizontal displacement b) Vertical strain c) Principal compressive strain d) Shear strain in the web

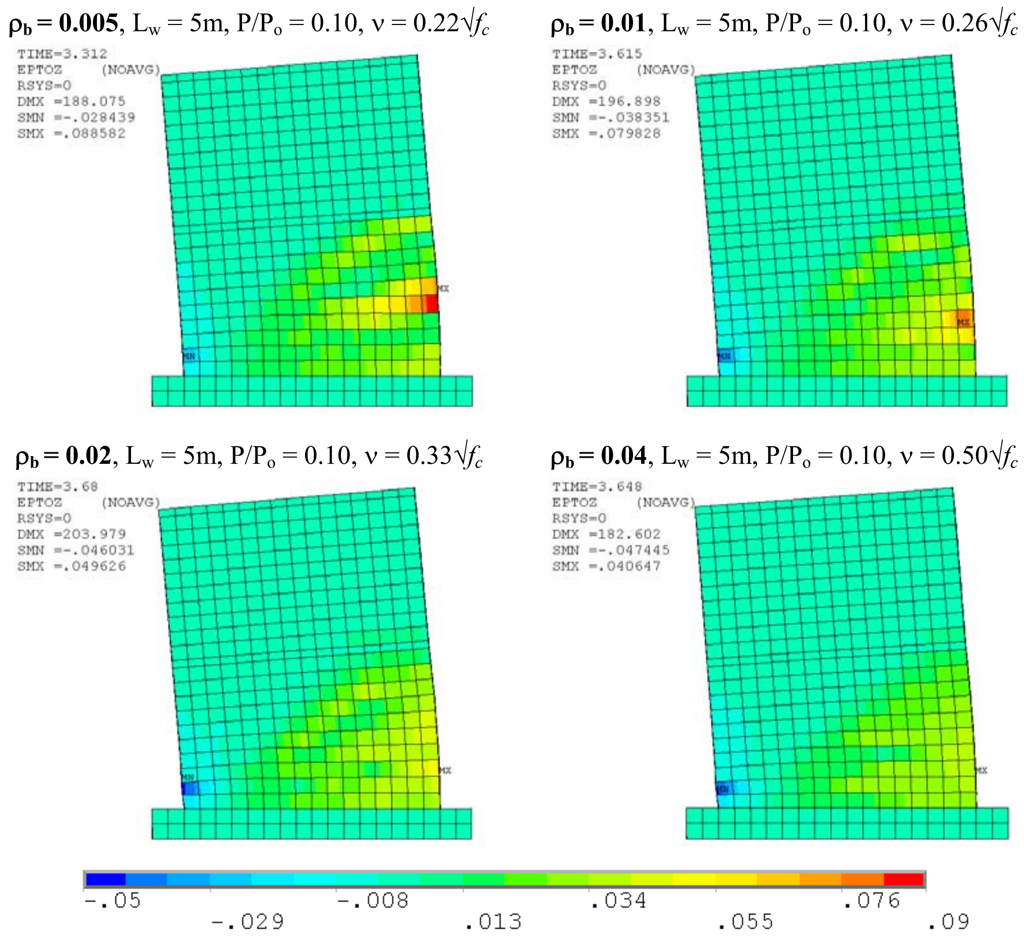

Figure 5.15 Effect of boundary element reinforcement on the spread of plasticity

As the amount of boundary element longitudinal reinforcement increase the cracking spreads over the edge of the wall along the plastic zone. Flexural cracks form a uniform pattern along the edge. The cracks that are initiated as flexural cracks directly propagate into the web as inclined shear cracks. Rather than a distinct shear crack passing diagonally through the web region, a diffused pattern of shear cracks appears on the lower half of the wall separated by the diagonal line as seen in Figure 5.16(d). In this case the wall is under high shear stress, and significant amount of this stress is concentrated at the compression boundary element. If the load was cyclic in nature, the load reversals would give rise to same situation in both boundaries. This weakens the base section and leads to sliding shear failure.

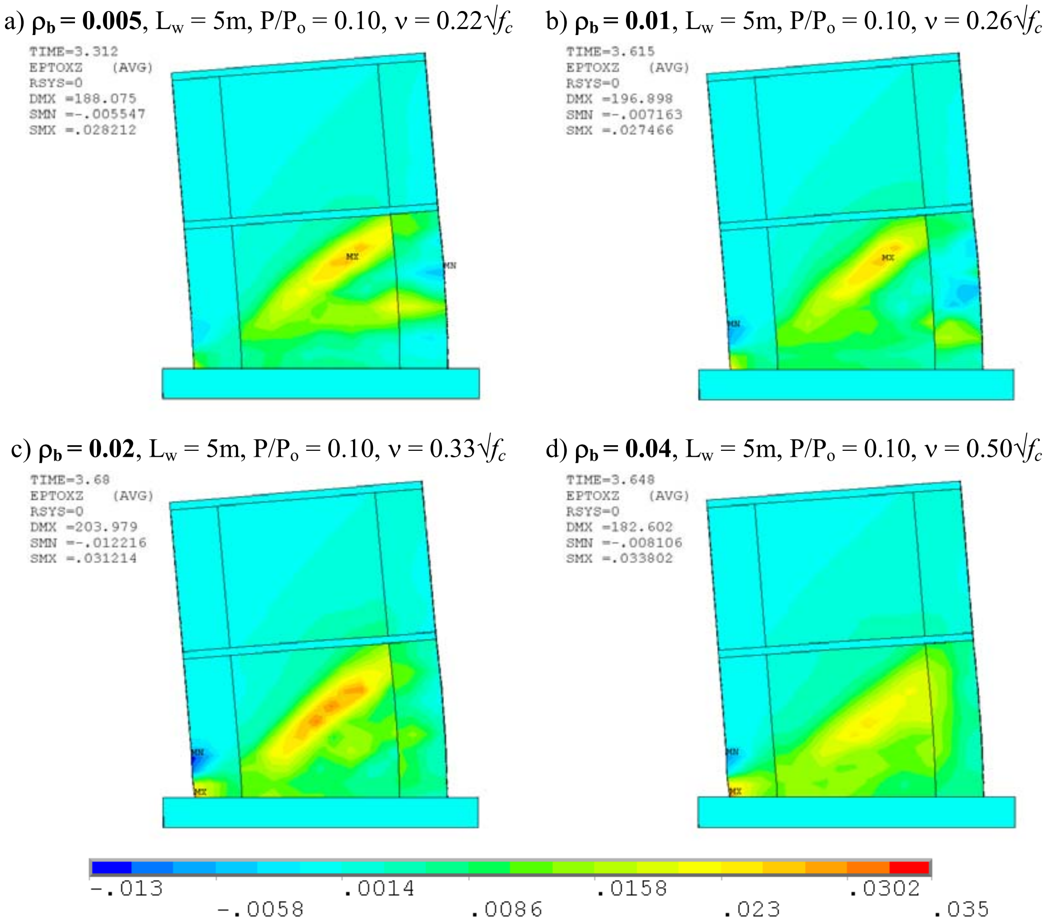

Figure 5.16 Effect of boundary element reinforcement on diagonal cracking and shear strain

5.4 PLASTIC HINGE ANALYSIS

Although advanced analyses tools and procedures are currently available to determine the seismic response of RC structural walls, the plastic hinge method and analyses derived from it (Park and Paulay, 1975) are still used extensively in the seismic design and assessment of structural walls to estimate the inelastic displacement capacity. Macro-modeling techniques most frequently used in the seismic assessment of structures also require the moment-rotation relation to be assigned to plastic hinges at member ends. The method is especially appealing for structural wall buildings, because it is simple and most of the time it is possible to idealize a wall member inside the building as isolated cantilevers as displayed in Figure 5.17. In the plastic hinge analyses the tip displacement of a cantilever is obtained as the sum of its yield displacement, Δ_y, and plastic displacement component, Δ_p. While the yield displacement is calculated by double integrating the curvature distribution along the cantilever, plastic displacement component is calculated by multiplying the height of the cantilever by the plastic rotation, θ_p, at the base as expressed in Eq. (5.12).

$$\Delta = \Delta_y + \Delta_p = \frac{\phi_y H^2}{3} + (\phi - \phi_y) L_p (H - 0.5 L_p) \tag{5.12}$$

The term, $(\phi\text{-}\phi_y)L_p$, in Eq. (5.12) refers to the plastic rotation θ_p and is based on the governing assumption that the plastic curvature is lumped in the center of the equivalent plastic hinge length, L_p. The actual physical length over which the plasticity spreads may be larger and referred as plastic hinge region, L_{pz}. The plastic hinge length that yields accurate plastic rotation can be easily determined from experimental data. Eq. (5.12) may be used to calculate the equivalent plastic hinge length from this data. This implies that if physical hinge length is unknown, inaccurate values of ϕ_p and L_p can be combined to yield an accurate value of θ_p.

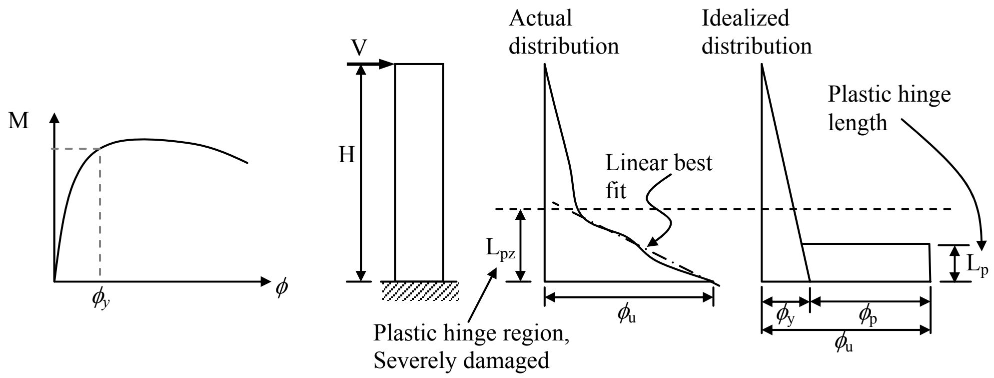

Figure 5.17 Definition of plastic hinge length (Park and Paulay, 1975)

Previous research has confirmed that in reinforced concrete members the spread of plasticity in the plastic hinge region is influenced by three distinct phenomena: moment gradient, tension shift and strain penetration. The term “moment gradient” reflects the fact that the transition between yield moment and ultimate moment in a member is proportional to the member's shear span. Therefore, a member with a shorter shear span has a smaller spread of plasticity. Occasionally the spread of plasticity (damage) on the member occurs over a larger region than anticipated by the effect of moment gradient. This is due to "tension shift" that can be described as the tendency of flexural tensile forces (steel tension forces) to decrease only minimally over a certain distance above the base of a wall until these forces can be transferred to the compression zone by adequately inclined struts (Hines et al., 2004). Additionally, strains near the base are significantly affected by the inclined flexure-shear cracks of the wall. As a consequence of the fanned crack pattern the compressive strains in the concrete are larger and the tensile strains in the reinforcement smaller than strains obtained from (plane) section analysis (Dazio et al., 2009, see Figure 1.1). These effects contravene the plane sections remain plane assumption. Hence, experimentally derived strains cannot be directly compared to strains obtained from section analysis. Although it is considered that the yielding takes place at the fixed end of member above the footing, the inelasticity in the longitudinal bars may extend some distance into the footing, which is referred as "strain penetration". The wall lifts off the footing as a result of accumulation of strains inside the footing. This deformation component at the base of the wall is named the fixed end rotation.

5.4.1 Discussion on the Components of Plastic Hinge Analysis

Relating the local deformation demands (strains) of the wall to the curvatures so as to flexural deformations requires correct interpretation of plastic hinge length or spread of plasticity along the member. Moreover, violation of the plane section remains plane after deformation hypothesis due to concentration of compression strains at the section of maximum moments at the base of the wall precludes a direct comparison of the base curvatures calculated from experimentally measured strains or strains obtained from FEM models such as here, or the curvatures obtained from moment-curvature based section analysis. It was stated previously that the methods based on section analysis, which are used to assess the force-displacement behavior of reinforced concrete members, generally provides conservative estimates of the structural performance levels. Curvature is the primary parameter used in the design and assessment of structural walls. Base curvature calculated in the plastic hinge length may provide a more appropriate means of linking local deformations measured experimentally (or as here results of FE analysis) at the base of the wall to the results from moment-curvature analysis. To do this plastic hinge length is required. The plastic rotations calculated above the plastic hinge length should be compatible with the modeling and acceptance criteria values tabulated in FEMA 356.

In experimental and analytical studies the length of the region (zone) over which the plasticity (damage) spreads should be discriminated from the plastic hinge length, which is a notional tool used to calculate the tip displacement of cantilever. Generally the length of plastic zone is larger than the value *assigned to* plastic hinge. It is an assignment because it does not matter what value is used for the plastic hinge length as long as it yields correct estimation of deformations.

Two different methods can be employed to evaluate the length of the plastic zone, L_{pz}. In the first method tensile strain profile along the edge reinforcement is used to determine the yielding region. It is assumed that when the bar strain at the extreme fiber reaches ε_s = 0.003 yielding takes place in the section (Kim, 2004). This limit is consistent with previously proposed bar strains to determine the section yielding. In members with more than one layer of vertical reinforcement, not all the tensile reinforcement yields simultaneously. The force displacement diagram does not indicate overall yielding until the middle reinforcement in the tensile boundary element yields. At limiting strain of ε_s = 0.06, the tensile strain profiles along the two story high region at the base are plotted in Figure 5.18 for walls with different lengths using the finite element analyses results. The plasticity spreads over much larger regions along the height of wall as the length of the wall increases. As the wall length increases they become more susceptible to shear effects leading to diagonal cracking, so as to increase the size of the damaged zone as opposed to concentrated flexural cracking at the base. The kink that can be clearly observed in the $0.2h_s$ level on the average tensile strain profile locates the position of the flexural deformation concentration on the wall. The anomaly on the strain profiles in the first story level is due to interrupting effect of the floor slab, and should be disregarded for a better interpretation of the message in the figure.

In the second method curvature profile computed from element strains calculated at the same height (in the same row as displayed in Figure 5.10) at the two wall ends can be used to determine the spread of plasticity along the wall. The limiting yield curvature can be calculated by the expression proposed by Priestley et al. (2007)

$$\phi_{wy} = 2\frac{\varepsilon_y}{L_w} \tag{5.13}$$

where ε_y is the yield strain of the reinforcement and L_w is the wall length. The calculated curvature profiles are plotted in Figure 5.19. Again the limiting tensile strain of 0.06 is used. Parallel to observations made in the tensile strain profiles, it is seen that damage extends over much larger region in walls with longer section lengths.

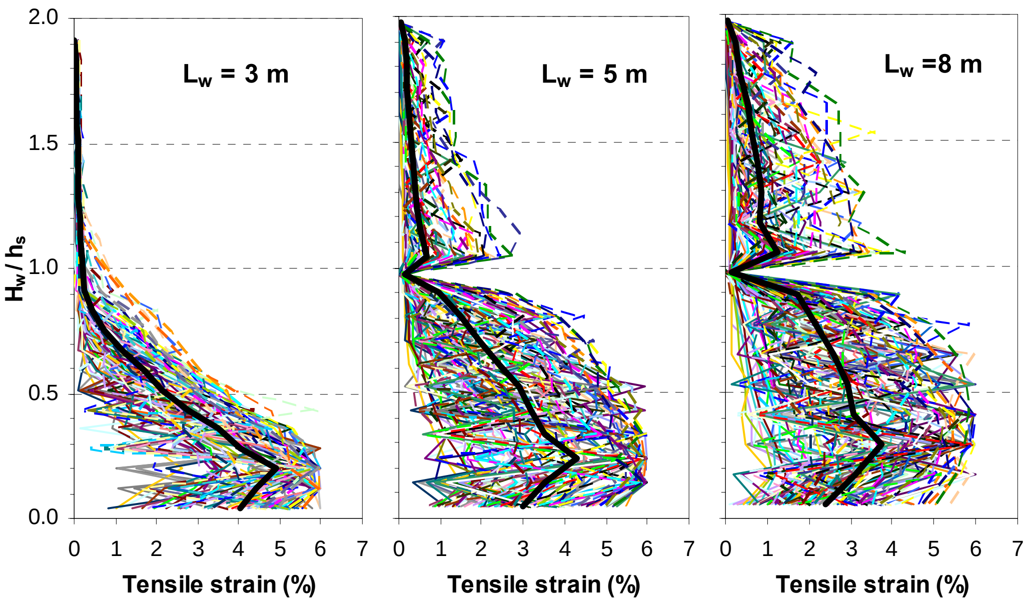

Figure 5.18 Tensile strain profiles along the tensile edge of the walls, all analyses

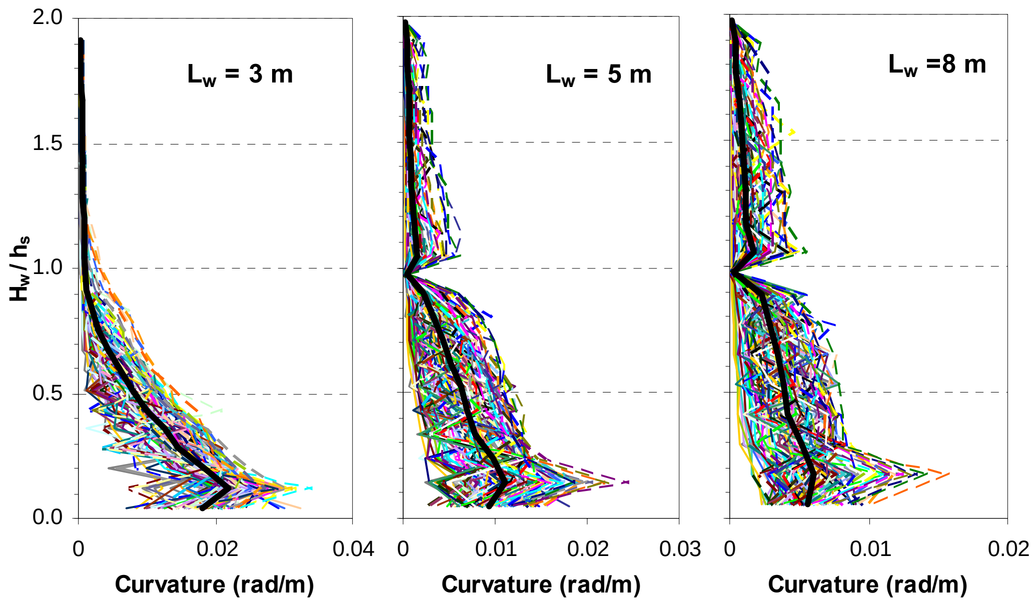

Figure 5.19 Curvature profiles along the height of the walls

The shortcomings of this procedure in case of inclined flexure-shear cracks were discussed in Section 5.3.3. Two different methods, each used for specimens with predominantly flexural cracking and for members exhibiting diagonal shear cracking at the hinging region, were presented by Oesterle et al. (1976) to determine the effective curvature distribution. Experimental studies (Dazio et al., 2009) have shown that within the plastic zone of the test units the curvature profiles were approximately linear in case of lightly reinforced wall members (flexural behavior). So the curvature calculated at the very bottom of the wall can be considered as the wall base curvature. Hence, to determine the base curvature a best-fit linear curvature profile over the height of the plastic zone L_{pz} was determined and extrapolated to the base of the wall as shown in Figure 5.17 previously and will be discussed in Figure 5.24 in greater detail.

5.4.1.1 Determination of Wall Yield Curvature

Yield curvature is a significant parameter that is used in the design of structural walls and is required to determine the spread of plasticity along the length of the wall. Paulay and Priestley (1992) stated that because ductility in design is based on the relationship between ductility and force reduction factors and the required ductility in design in reinforced concrete structures is evaluated on the basis of elastoplastic or bilinear approximation to the actual structural force-displacement response, in reinforced concrete sections ductility should be assessed on the basis of idealized elastoplastic or bilinear approximation of moment-curvature relation. As a result of bilinear idealization the yield curvature may not coincide with the first yield of the reinforcement or the actual global yield of the section, particularly in shear wall sections where the flexural reinforcement is distributed along the boundary element.

Paulay and Priestley (1992) and Priestley et al. (2007) defined an equivalent yield curvature, $\phi_y = (M_y/M'_y)\phi'_y$, that is obtained by factoring the yield curvature corresponding to the first yield of the tensile reinforcement at the extreme fiber (ε_y =0.0021) for elasto-plastic idealization of load-deformation curves. The coefficient is defined as the ratio of the equivalent yield moment (M_y) to the yield moment at first yield (M_y'). Here M_y holds for the nominal yield moment (M_N) that is defined as the moment where the extreme fiber strain in compression reaches 0.004 or extreme tension strain reaches 0.015, whichever occurs first. The bilinear curve is obtained by drawing the first line from origin to the point on the curve where the reinforcement yields for the first time extending up to the nominal yield moment.

The second line connects the first line at the top to ultimate point on the moment-curvature curve. The bilinearization procedure is illustrated in Figure 5.20.

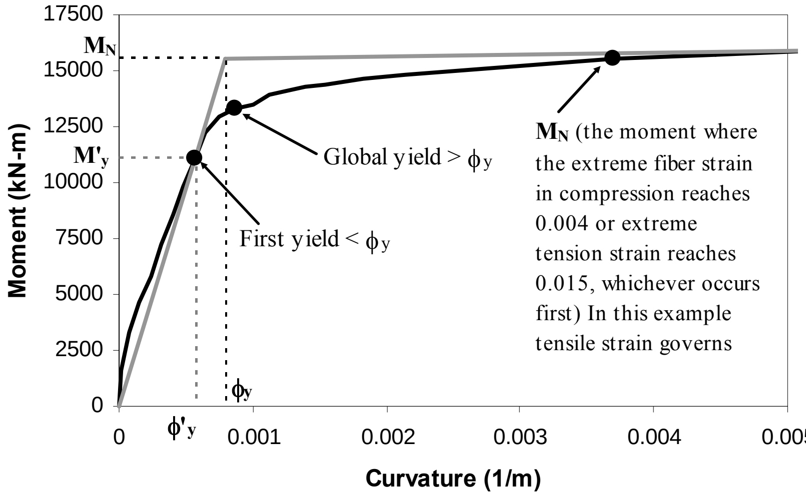

Figure 5.20 Example moment-curvature curve for wall section with L_w = 5m, initial section of moment-curvature response

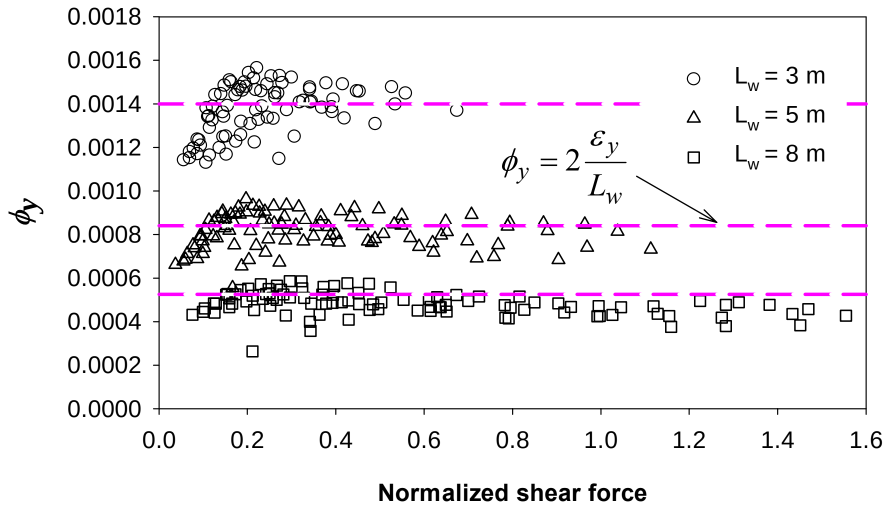

Figure 5.21 Correlation of Eq. (5.13) with FE analysis results

The yield curvatures obtained from the bilinearization of moment-curvature relations using the finite element analyses results are plotted in Figure 5.21. The curvature used in the moment-curvature relationship is the average curvature calculated over a 1 m high region above the base section. This effective length used to calculate curvatures was found to be in good agreement with the curvatures calculated with the described procedures. The presented data validates Eq. (5.13). It is found that the most significant parameter affecting the wall yield curvature is the wall length.

5.4.1.2 Plastic Region and Plastic Hinge Length

In view of the preceding discussion, the plastic zone length is calculated using the second method described above, i.e. the uppermost location where the yield curvature is encountered on the curvature profile was accepted as the plastic zone length, L_{pz}. The calculated plastic zone lengths at the ultimate response point are plotted in Figure 5.22. It is found that the spread of plasticity is strongly affected by the shear carried by the member and the wall length. While the plastic zone is constrained to first story in 3 m wide walls, it may extends over 2 stories height in 5 and 8 m wide walls as shown in Figure 5.22. Figure 5.22 also displays that the spread of plasticity along the wall decreases as the shear carried by the member increases. The plastic zone length normalized with respect to wall length is found to be slightly sensitive to boundary element reinforcement ratio, but it is significantly affected by the wall length as shown in Figure 5.23. The axial load level has also a slight reducing effect on the spread of plasticity along the wall.

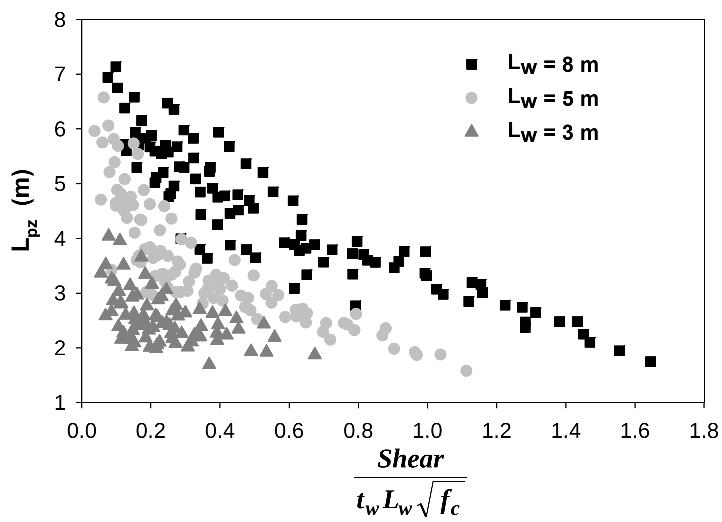

Figure 5.22 Variation of actual plastic zone length with normalized shear

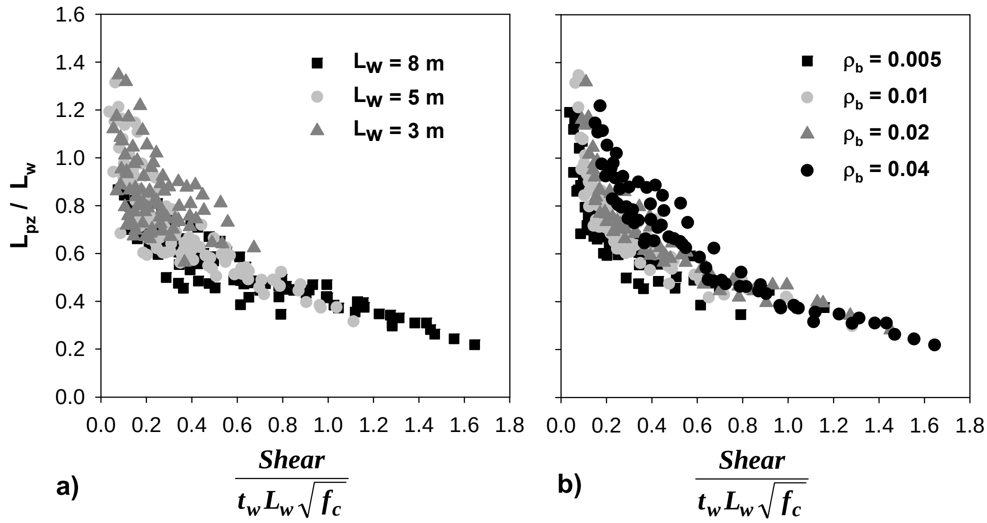

Figure 5.23 Variation of normalized plastic zone length with normalized shear arranged for a) wall length, b) boundary element reinforcement

As a second step, the base curvatures and rotations were calculated over the identified plastic zone lengths. The rotations, which are assumed to represent the rotation of the base section, were calculated just above the plastic zone length by using the vertical displacements calculated at tensile and compressive edges in the same row. The sketch in Figure 5.24 illustrates the calculation of the base section curvature and rotation. The ultimate base rotation capacity of wall specimens with respect to normalized shear force is plotted in Figure 5.25(a). The base curvature is calculated in two different ways to ensure the accuracy in the calculation of this parameter, since all the performance criteria and assessment procedure depends on it. ϕ_{b1} was obtained by using the moment-area theorem. Since the rotation above the plastic zone is known (θ_b) by integrating the curvature profile, which is assumed to be linear, along the plastic zone (length L_{pz}), ϕ_{b1} is obtained as $2\theta_b/L_{pz}$. ϕ_{b2} was obtained by fitting a best line to the curvature profile along the plastic zone length. The intercept of the best fit line equation at the base level was adopted as ϕ_{b2}. The comparison of the two curvatures is displayed in Figure 5.25(c). The two methods of curvature calculation yielded very similar results. The base curvatures used in this study are those calculated by best line fit method, i.e. ϕ_b = ϕ_{b2}. The ultimate curvature capacity of wall specimens is plotted in Figure 5.25(b).

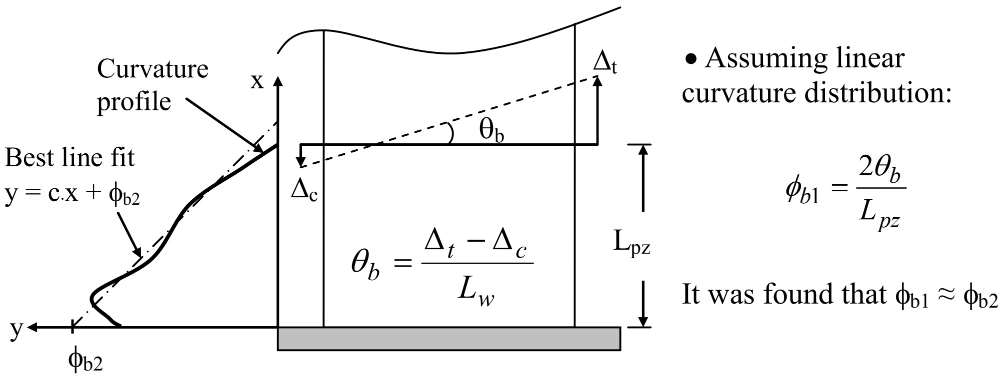

Figure 5.24 Schematic descriptions of base curvature and rotation calculation

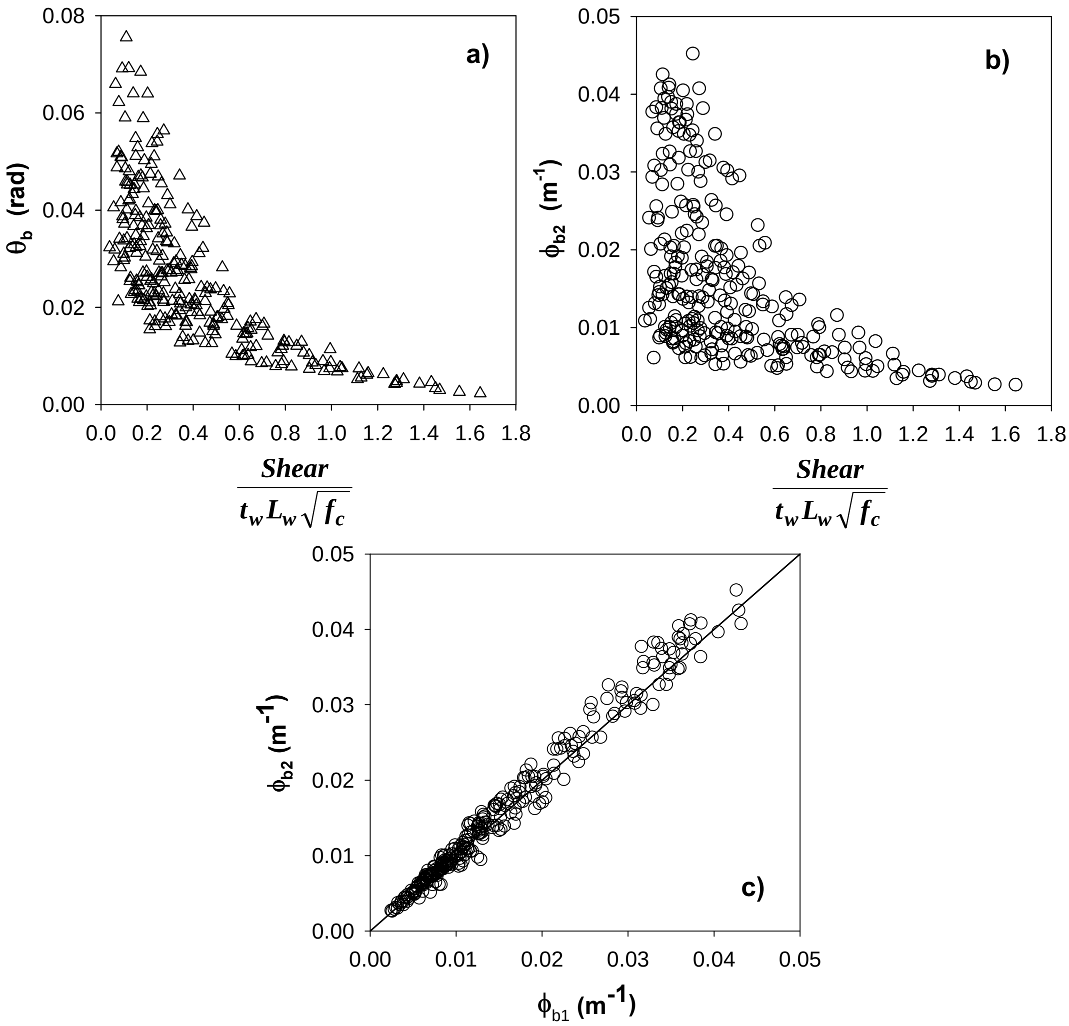

Figure 5.25 a) Ultimate base rotation, b) ultimate base curvature, plotted as a function of normalized shear force c) comparison of different base curvature schemes ultimate curvature results

As discussed in detail above, assuming a linear curvature profile over the height of the plastic zone length provides a consistent relation between the curvature (ϕ_b) and rotation (θ_b) that are adopted as the deformation attributes of the base section as described in Figure 5.24. Since the plastic hinge analysis is based on the condition that $\theta_p=L_p.\phi_p$ as illustrated in Figure 5.26, the plastic hinge length is $L_p = 0.5L_{pz}$ in the light of above discussion ($\theta_b=0.5L_{pz}.\phi_b$). Hines et al. (2004) and Dazio et al. (2009) reached a similar expression that reads as

$$L_p = 0.5L_{pz} + L_{sp} \tag{5.14}$$

where L_{sp} characterizes the contribution of strain penetration to the top displacement. The relation between the plastic zone length and shear stress was investigated in Figure 5.22 and Figure 5.23.

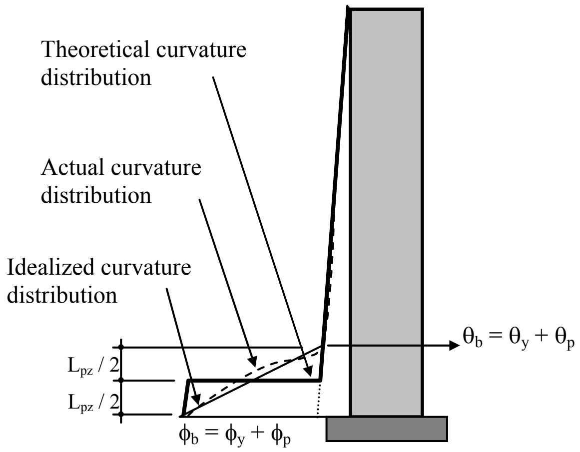

Figure 5.26 Plastic hinge analysis

The relation given in Eq. (5.14) for the calculation of the plastic hinge length can be verified by using Eq. (5.12). All the components of Eq. (5.12) are available to calculate the plastic hinge length. As discussed previously, the plastic hinge length calculated in this way is in a sense inaccurate, because it does not need to be in parallel with the actual spread of plasticity along the wall as long because it yields accurate estimation of wall displacements. However there is a consistent relation between the two lengths. The plastic hinge length calculated in two different ways and normalized with respect to plastic zone length was plotted as a function normalized shear in Figure 5.27(a). The procedure used to obtain L_p by substituting required values in Eq. (5.12) resulted in $L_p = 0.4L_{pz}$. It can be assumed that the plastic hinge length can be taken as the 40%~50% of region where plasticity spreads over the member. The plastic hinge length obtained by rearranging Eq. (5.12) is normalized with respect to wall length and plotted in Figure 5.27(b) as a function of shear stress. Other than the trend line which can be fitted to the relation on the figure, the data reveals that plastic hinge length is not a function of wall length multiplied with constant (such as $L_p = 0.5L_w$) as assumed by many codes and reported by other research..

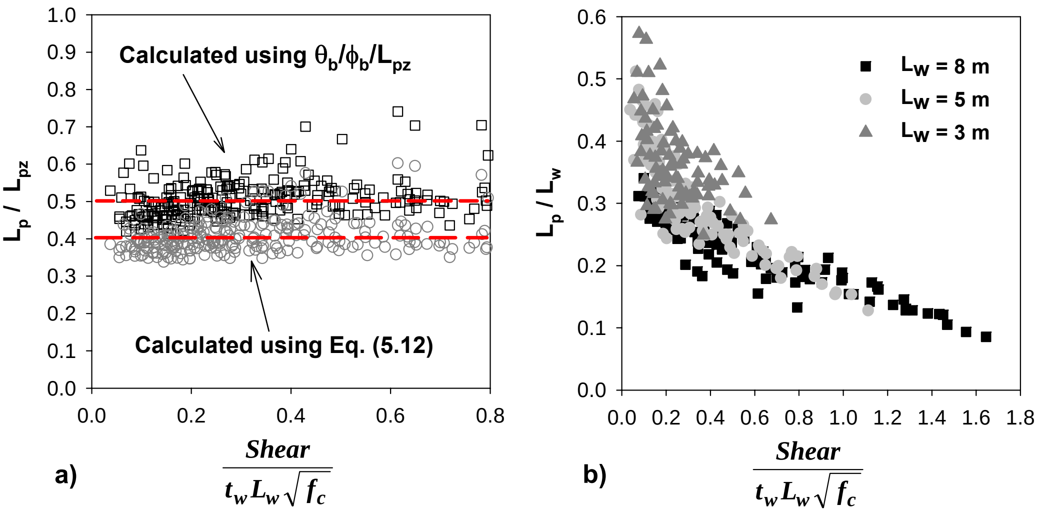

Figure 5.27 Plastic hinge length calculated as a function of a) plastic zone length, b) wall length.

An improved expression can be derived by regression analysis to calculate the plastic hinge length by using the variables of the parametric study. The plastic hinge length is found to be sensitive to the wall length and height, and axial load ratio. The proposed plastic hinge equation is given as

$$L_p = 0.4\left(1 - \frac{P}{P_o}\right)\left(H_w L_w\right)^{0.34} \tag{5.15}$$

in which L_w, H_w and L_p are in meters. The comparison of predictions with the simulation results are displayed in Figure 5.28. If typical story height is assumed to be 3 m, Figure

5.28 tells that the plastic hinge length is bounded within the first story height for low-to medium height walls.

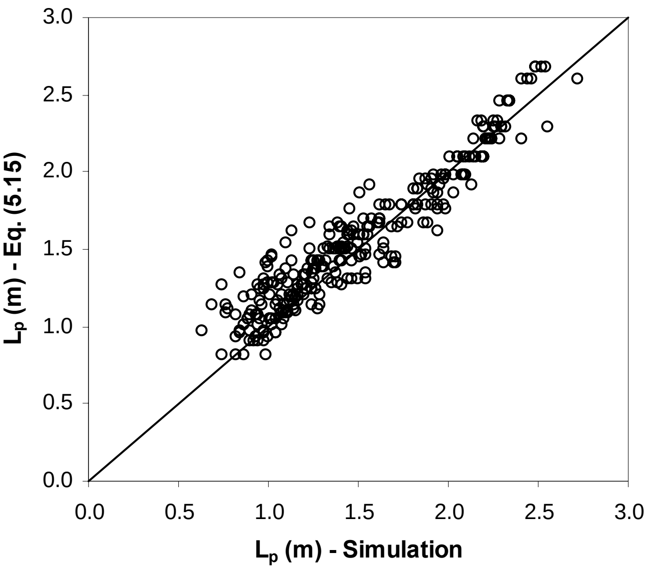

Figure 5.28 Comparison of plastic hinge length predicted by Eq. 5.15 with finite element simulation results

5.4.2 Relating Section Analysis Results with FEM Results

As discussed in the preceding sections, base curvature is the most appropriate means of establishing a relation between experimental and analysis results. The drift and rotation of the actual model (FEM model) corresponding to a given limit state can be related to the strains obtained from section analysis at equal curvatures. This way, a direct comparison of local and global deformation limits can be established. Comparison of typical moment-curvature relations obtained from section analyses and finite element analyses is shown in Figure 5.29. The curves agree in the initial segment and in terms of moment capacities, but the ultimate curvature capacities obtained from the two different analyses differ significantly. The ratio of ultimate curvatures obtained from section and finite element analyses are plotted as a function of normalized shear stress in Figure 5.30. It is seen from the figure that the sectional analysis results deviate from the finite element analysis results significantly in terms of curvature capacities as the wall length and the shear on the member increase. In most of the cases the sectional analysis results overestimate the deformation capacity of walls, which may lead to unconservative assessment of the structural walls. Even when section analyses indicate very large deformation capacities, the limiting value for the curvatures is adopted as the capacities obtained from FEM analysis in this study.

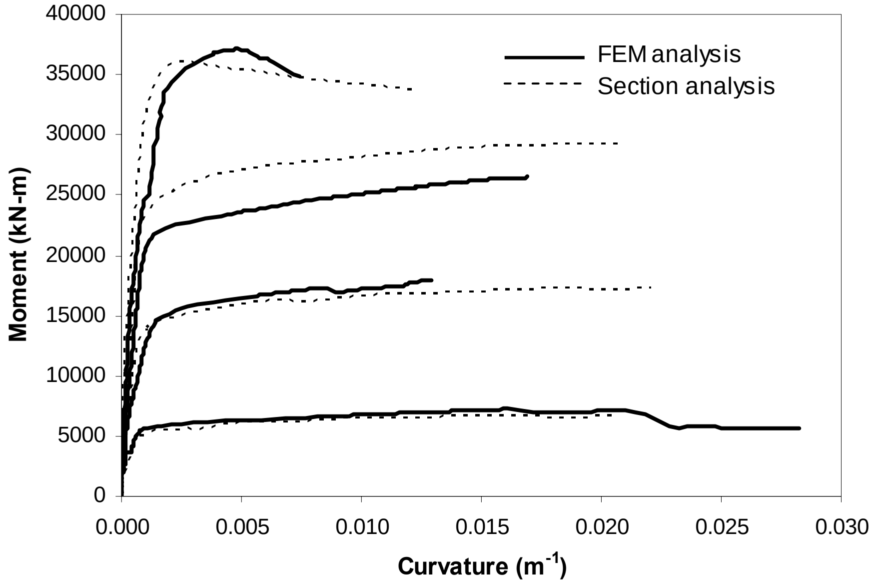

Figure 5.29 Comparison of typical moment-curvature relationships obtained from section and FEM analysis ($L_w = 5$ m)

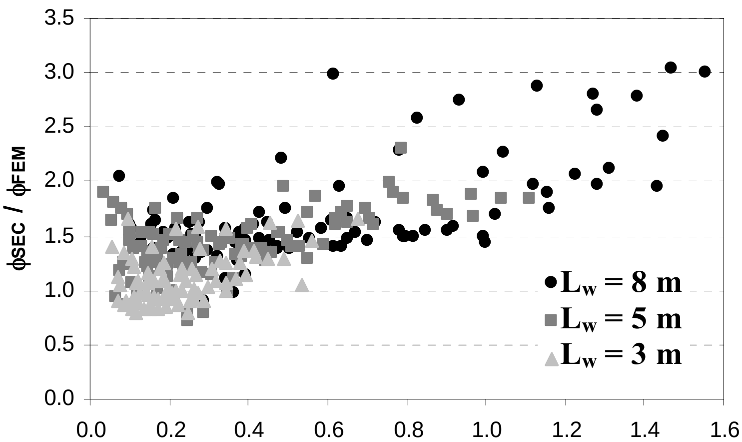

$$\frac{Shear}{t_w L_w \sqrt{f_c}}$$

Figure 5.30 Difference between the ultimate curvature capacities obtained from section and FEM analysis

5.5 EXPERIMENTAL DAMAGE PARAMETERS

There are a vast amount of experimental studies carried on shear walls to identify their structural characteristics and behavior, and dominant failure modes. These experiments were either carried at full scale, few story (generally one or two) wall components or scaled representative components and multistory walls. Static loads cyclic or monotonic in nature were applied. Figure 5.31 shows drift capacities versus maximum observed shear stress of walls tested by different researchers. Detailed information for each specimen in this figure is provided in Table G.1 of APPENDIX G. The test parameters of these structural walls were section shapes (rectangular, barbell, and flange shape), details of reinforcement distribution (concentrated or uniform distribution of longitudinal vertical reinforcement, and distribution of horizontal reinforcement), shear span ratio, existence of boundary element, ratio of axial load, etc. The experimental database covers wide range of test parameters and provides a good basis for the comparison with the range of applicability of the results of analyses cases here.

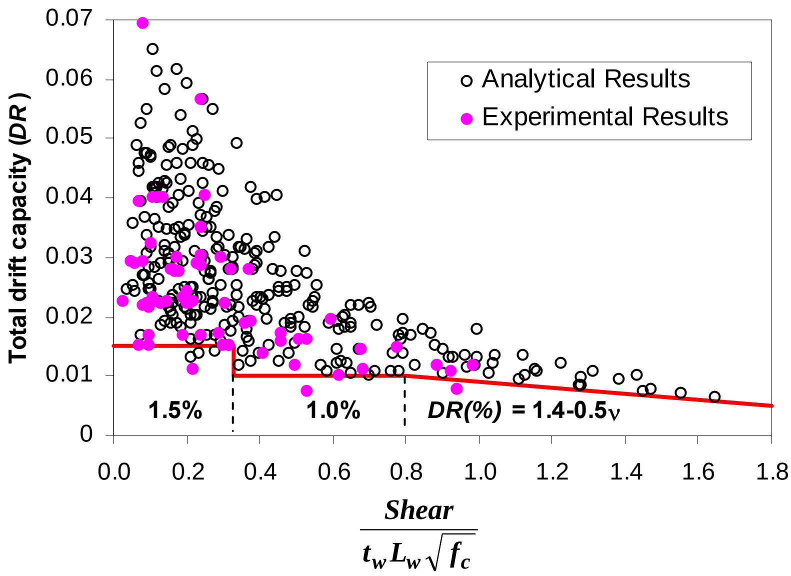

Figure 5.31 Maximum shear stress versus drift capacity relation of walls

As seen in Figure 5.31 the data produced in this study and the results of experimental studies show similar trends in the drift capacities under increasing shear stress condition. This supports the assertion that the analysis results here can be assumed to be representative for structural walls, either tested in the lab or existing in buildings. A drift ratio of 1·5% can be considered as an allowable limit value against a design earthquake in seismic provisions for the flexure controlled members. Thus, it is judged that most structural walls have satisfactory deformation capacities irrespective of the test variables (Han et al., 2002).

5.6 INVESTIGATION OF PERFORMANCE LIMITS

In this section the findings and results obtained from analyses up to this point are synthesized for comparison with the performance limits used to define modeling parameters and acceptance criteria in guidelines. The walls analyzed here represent the conforming members. The data presented about the deformation criteria here includes curvatures, drift ratios and strains in addition to rotations. With reference to Figure 5.1, the deformation limits at three performance levels are investigated. These are the immediate occupancy (IO), life safety (LS) and collapse prevention (CP) performance levels. For the collapse prevention performance level the ultimate point on the load deflection curve is selected. The ultimate point corresponds to initiation of strength degradation or rupture of tensile reinforcement or buckling of reinforcement at the compressive zone. Life safety is taken at the deformation level that is 75% of the collapse prevention level. The immediate occupancy level is calculated as the point on the load-deflection curve whichever of the concrete compressive strain and steel tensile strains at the extreme fibers reaches 0.0035 and 0.01 first, respectively. These strains are from the section analysis. The variables affecting the deformation limits was primarily considered as the normalized shear stress (ν) in the wall as defined in Eq. (5.5) and axial load ratio (P/P_o). These variables were considered in order to achieve uniformity with FEMA 356. Whenever additional parameters are required to define the data, they are included in the analyses.

Although FEMA 356 investigates structural walls under two groups as flexure controlled and shear controlled members, in this study the entire data was analyzed in the same bin. The clear trends observed in the data plotted in the preceding sections suggest that the whole range of wall behavior can be represented with a unique relation. ASCE/SEI 41 states that walls should be considered slender (normally controlled by flexure) if their aspect ratio (height/length) is greater than 3.0, and short or squat (normally controlled by shear) if their aspect ratio is less than 1.5. No such discrimination was used in this study. It will be shown that the expressions derived from regression analysis cover the entire behavior range satisfactorily.

5.6.1 Plastic Rotation Limits

The plastic rotations calculated above the plastic zone are plotted in Figure 5.32. Two vertical lines shown in Figure 5.32 correspond to values of limiting shear stress criteria for which the plastic rotation limits are specified for conforming members in FEMA 356 as defined by Eq. (5.4-a). Eq. (5.2) to (5.4) take the limiting plastic rotations values at the points given in FEMA and directly calculate the plastic rotation either within or outside of the region bounded by the limits without the need for interpolation. The solid lines displaying the FEMA limits are calculated for constant axial load ratios of 0.10 and 0.25.

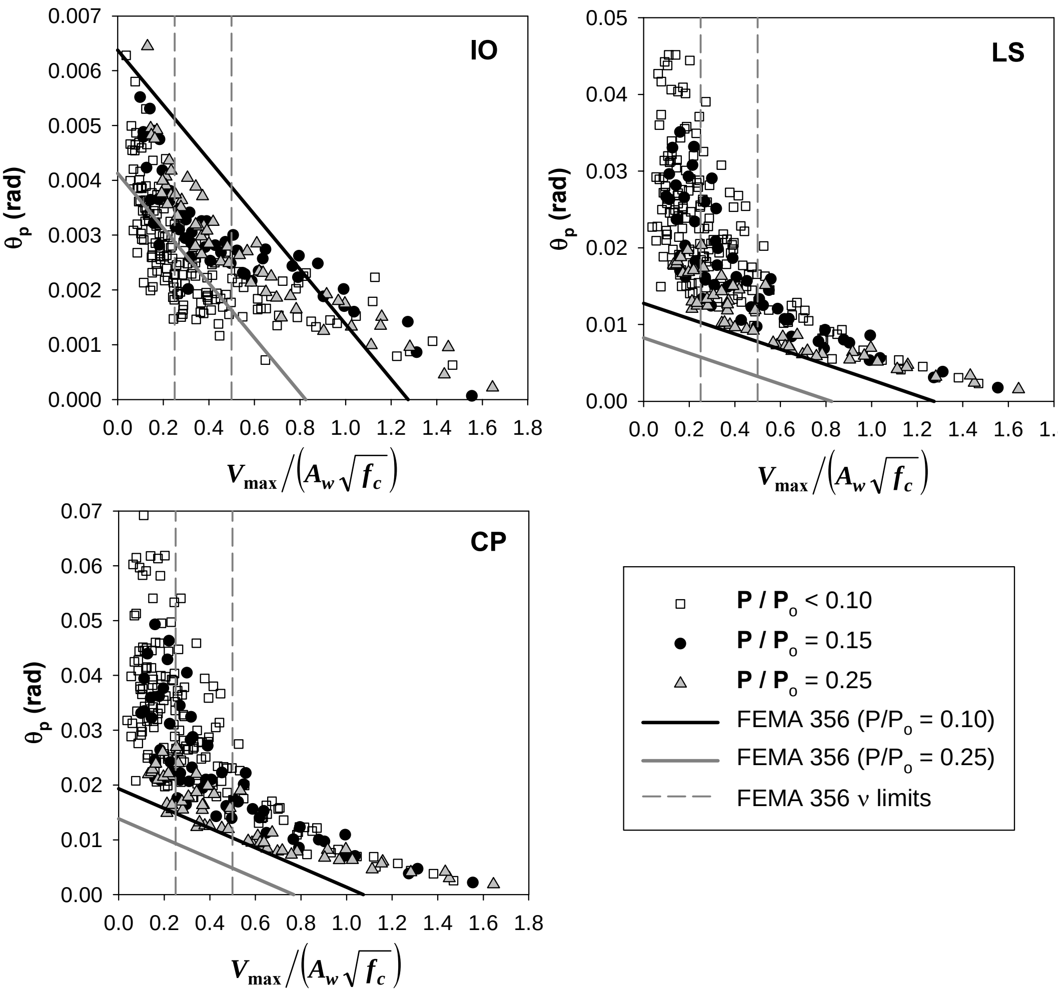

Figure 5.32 Calculated plastic rotations at specified performance levels

Figure 5.32 shows that the limits given in FEMA 356 are very conservative in comparison to limits calculated in this study for life safety and collapse prevention performance limits. The FEMA 356 curve defined for 10% axial load level defines the lower bound of the database. Typical ranges of normalized shear stress demand on structural walls are obtained from the design stage of the frame-wall structures investigated in the previous chapter and plotted in Figure 5.33. Design forces were obtained according to TSC 2007. The figure can be used to determine the useful range of normalized shear stress defined on the horizontal axis of Figure 5.32. Since most of the walls in Figure 5.33 are considered as slender according to definition in FEMA 356 and ASCE/SEI 41 ($H_w/L_w >$ 3), the shear stress on walls ranges between 0.2-0.6$\sqrt{f_c}$ when it is assumed that the typical values of wall index (p) ranges from 0.005 to 0.01 in buildings. In the range 0.2-0.6$\sqrt{f_c}$ the factor of safety in the given limits is around 2 to 3.

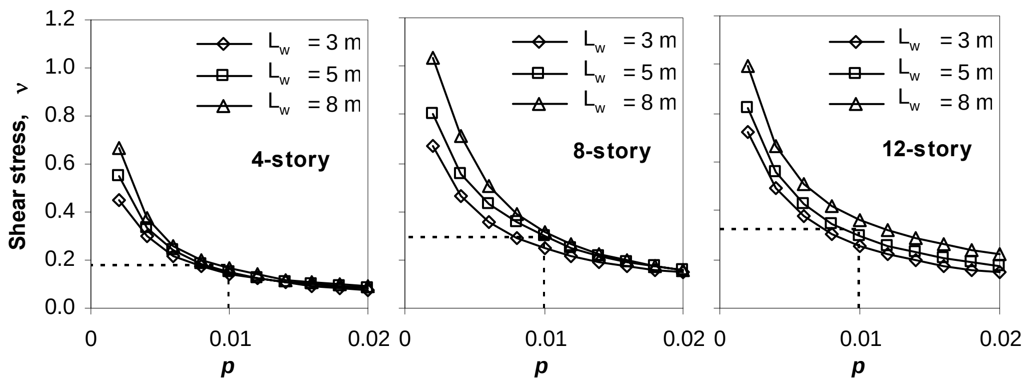

Figure 5.33 Typical normalized shear stress demands on walls as a function of wall index

A general expression is derived through regression analysis to calculate the rotation limits at collapse prevention performance level. The expression is in the same form as Eq. (5.11). The coefficients A, B, C and D that are adjusted for the calculation of plastic rotations are defined in Table 5.6 as a function of axial load ratio. The predictions were compared with the finite element results in Figure 5.34. The corresponding FEMA 356 limits were also plotted in the same figure. As seen in the figure the predicted values agree quite well with the finite element analyses results. If the predicted values are reduced by a factor of 0.75 the limits for life safety performance level is obtained.

Table 5.6 Coefficients of Eq. (5.11) to calculate the collapse prevention plastic rotation limit of structural walls with conforming boundary elements

P/P_o	A	B	C	D
≤ 0.10	0.183	0.220	1.814	0.071
= 0.15	0.117	0.148	1.779	0.066
= 0.25	0.046	0.037	1.485	0.037

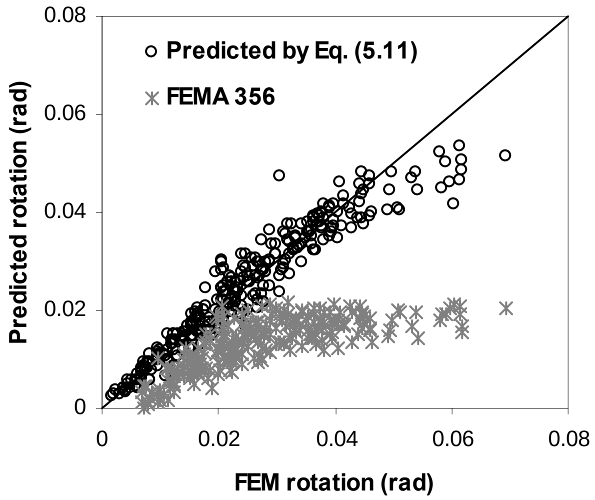

Figure 5.34 Correlation of predicted plastic rotations with analysis results

5.6.2 Total Curvature Limits

Although codes enforce the use of plastic rotations as assessment criteria, the section curvature may be a more appropriate means of drawing performance limits since curvature is the direct product of simple section analyses. This way, the uncertainty due to plastic hinge length assumption is eliminated. The total curvature performance limits obtained from the analyses are plotted in Figure 5.35. If desired the plastic curvatures can be obtained by the yield curvature calculated using Eq. (5.13). The scatter in the curvature data is more than the plastic rotation data presented in Figure 5.32. The data is classified for axial load level and wall length to distinguish the effect of these parameters on the scatter of curvature data. As seen in the second column of Figure 5.35 the wall length provides a much better classification parameter when compared to axial load.

.

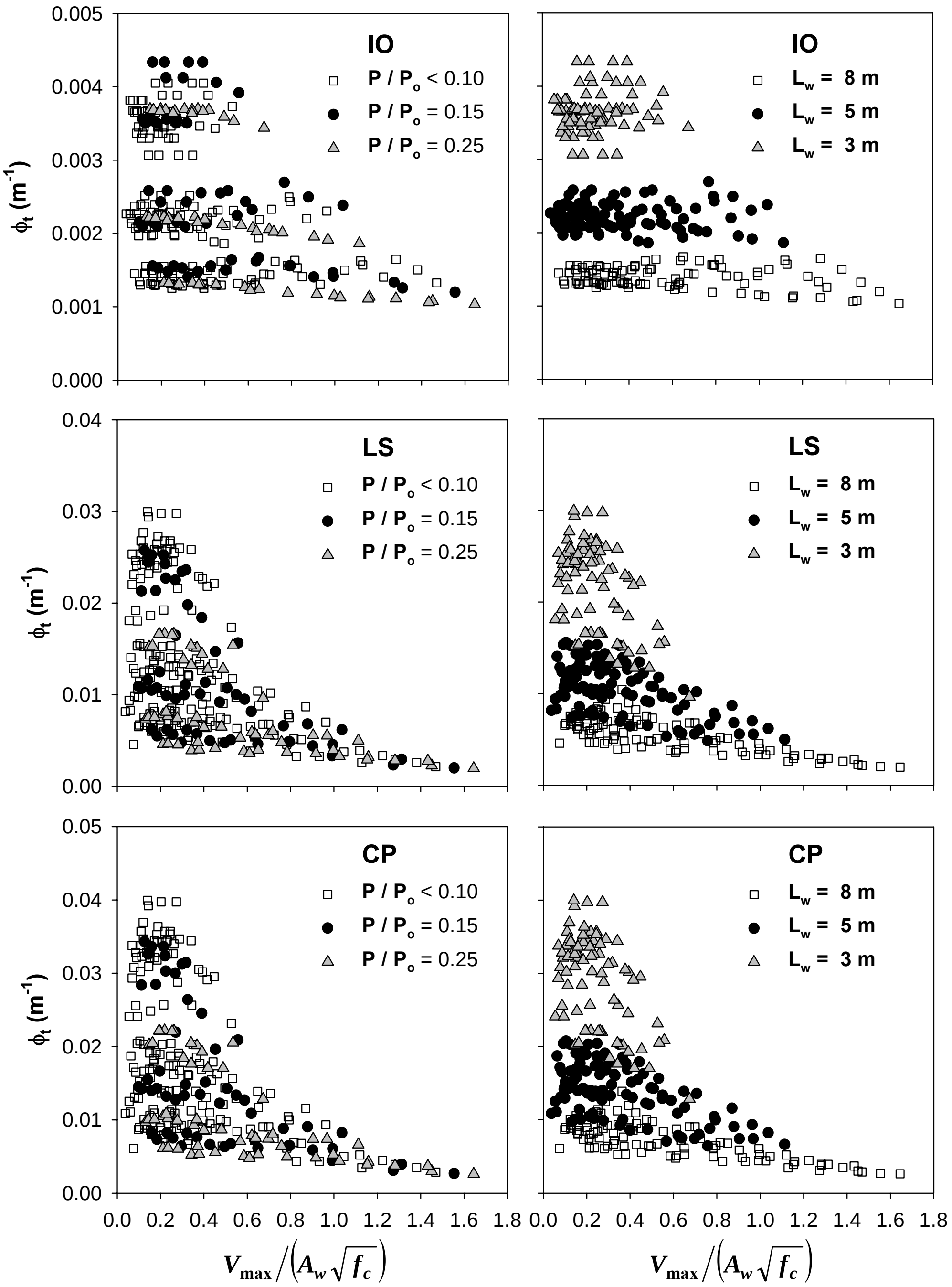

Figure 5.35 Calculated total curvatures at specified performance levels classified for a) Axial load level (first column), b) Wall length (second column)

5.6.3 Drift Limits

Drift ratio is the primary deformation criterion in shear controlled (squat) walls. In slender walls the drift ratio or, more correctly, the tangential interstory drift ratio, defined in Figure 5.8, should be interpreted as a secondary performance criterion when compared to rotations and curvatures because a significant percentage of the displacement in the upper stories is due to rotations at the base stories. Nevertheless, it should not be ignored that in frame-wall systems strong frame - weak wall interaction effects may gave rise to significant interstory displacement demands in the upper stories where it becomes crucial to know the damage state limits to assess the performance of the wall components.

The drift limits calculated at the second story level at different performance levels are plotted in Figure 5.36(a) as a function of normalized shear stress resisted by the wall. The drift ratios presented here should be interpreted as story drift. According to Figure 5.36(a), for drift values below 0.5% in average no damage is anticipated on the wall components. For flexural walls ($\nu < 0.25\sqrt{f_c}$) and walls under combined flexure and shear action ($0.25\sqrt{f_c} < \nu < 0.6\sqrt{f_c}$) the lower bound of story drift can be taken as 1% and 1.5% for life safety and collapse prevention performance levels, respectively, even under very high axial load conditions. Under moderate conditions ($\nu < 0.5\sqrt{f_c}$ and $P/P_o < 0.10$) the limiting story drift values can be extended to 1.5% and 2.5% for life safety and collapse prevention performance levels, respectively. These limits should be interpreted as the interstory drift ratio. The roof drift at these performance levels may take a little higher value. The story drift at collapse prevention performance level can be obtained by using Eq. (5.11). The life safety story drift limit can be taken as the 75% of the collapse prevention of the limit.

Wall length should be always considered as a significant constraint on the deformation limits of structural walls. A wall with 8 m length can seldom achieve a story drift of 2.5% in the most optimal conditions, i.e. under very low axial load and unit shear, as adopted by Sullivan et al. (2006). The drift limits categorized with respect to wall length is plotted in Fig. 5.36(b). As seen in Fig. 5.36, increased wall length and axial load ratio significantly reduce the deformation capacity of structural walls.

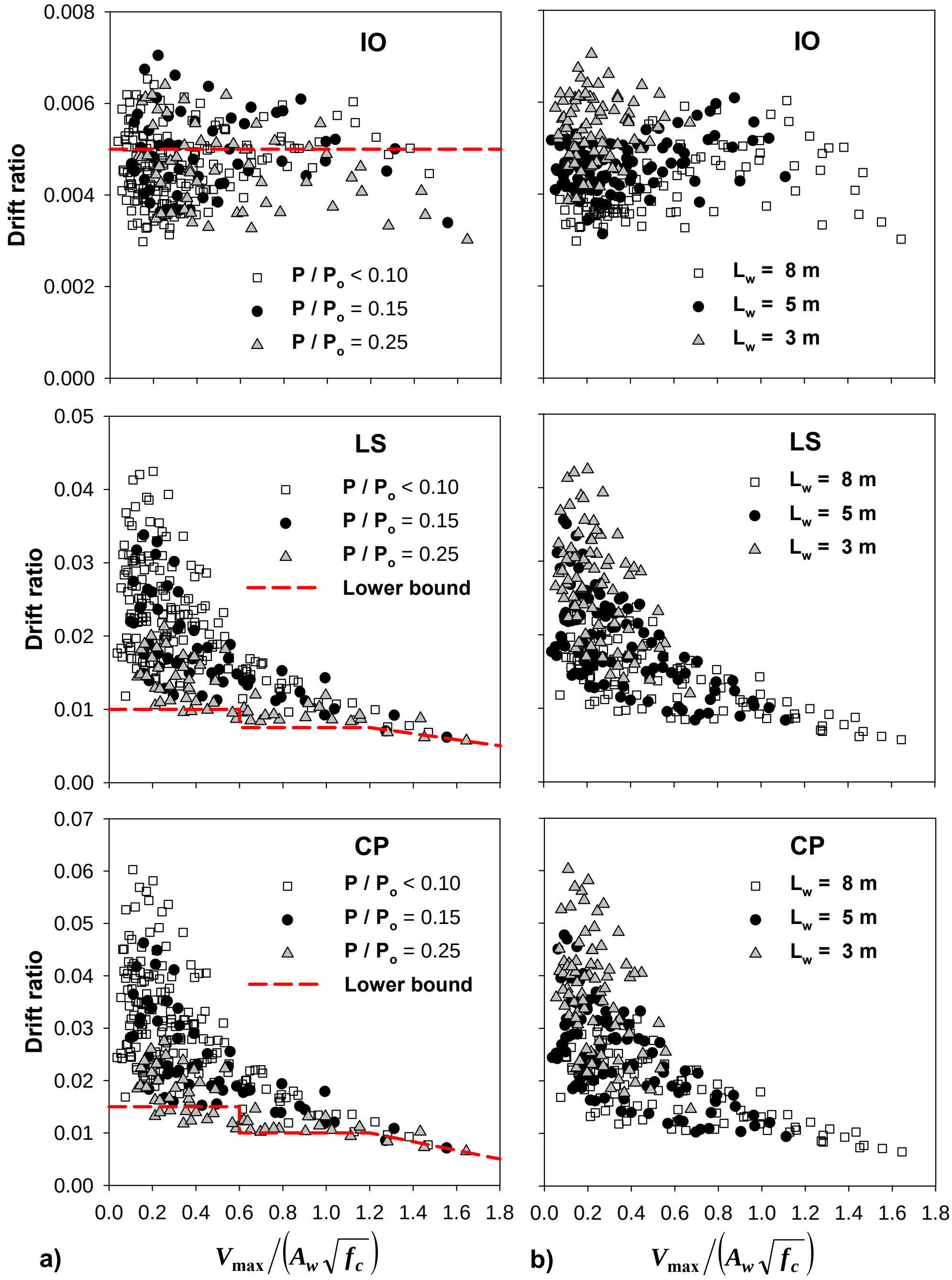

Figure 5.36 Drift ratio performance limits plotted as a function of a) axial load ratio (first column), b) wall length (second column)

5.7 COMPARISON OF TSC STRAIN LIMITS WITH ROTATION LIMITS

Up to this point performance limits with regard to rotations, curvatures and displacements were calculated and presented. The section extreme fiber compression and tension strains at these limit states are used frequently in the design and assessment of reinforced concrete members (Priestley et al., 2007; TSC, 2007). The extreme fiber strains in compression and tension at specified limit states are plotted in Figure 5.37 and Figure 5.38, respectively. The plots include strains obtained from section (ε_{SEC}) and finite element (ε_{FEM}) analyses superposed on the same figure to visualize the differences. The right set of frames gives the ratio of finite element analysis to section analysis strain ratios ($\varepsilon_{FEM}/\varepsilon_{SEC}$). This ratio is useful in evaluating the actual strains at the boundaries.

The first observation related to Figure 5.37 is that at the given limit states the section analysis strains are significantly lower than finite element analyses strains. The $\varepsilon_{FEM}/\varepsilon_{SEC}$ ratio takes the values 1.6, 1.8 and 2.1 for IO, LS and CP performance levels respectively. Priestley et al. (2007) specified the range of this ratio as 1.3 to 1.6 replacing the strains from finite element analyses with experimental strains, i.e. the ratio was defined as $\varepsilon_{EXP}/\varepsilon_{SEC}$. The difference may be due to two reasons. The ratio given by Priestley is applicable to column data and the strain measured in experiment varies significantly depending on the location of the measurement and gage length used to calculate the strain.

The TSC limits were also superposed on the same figure. Since the transverse reinforcement at the boundary elements of the finite element models conform adequately to TSC requirements as discussed previously, the TSC limits plotted in the figures can be taken as the upper bound values of strains allowed at the specified performance levels. The methodology adopted in this study allows the direct comparison of strain limits specified in TSC and section analyses results. The limit state strains obtained from section analyses are significantly lower than the limits defined in TSC (2007), so as given by Priestley et al. (2007). The analyses results clearly indicate that if the limits given in TSC are used as acceptance criteria in the assessment of reinforced concrete shear walls, they will yield unduly unconservative performance estimations of the structural walls.

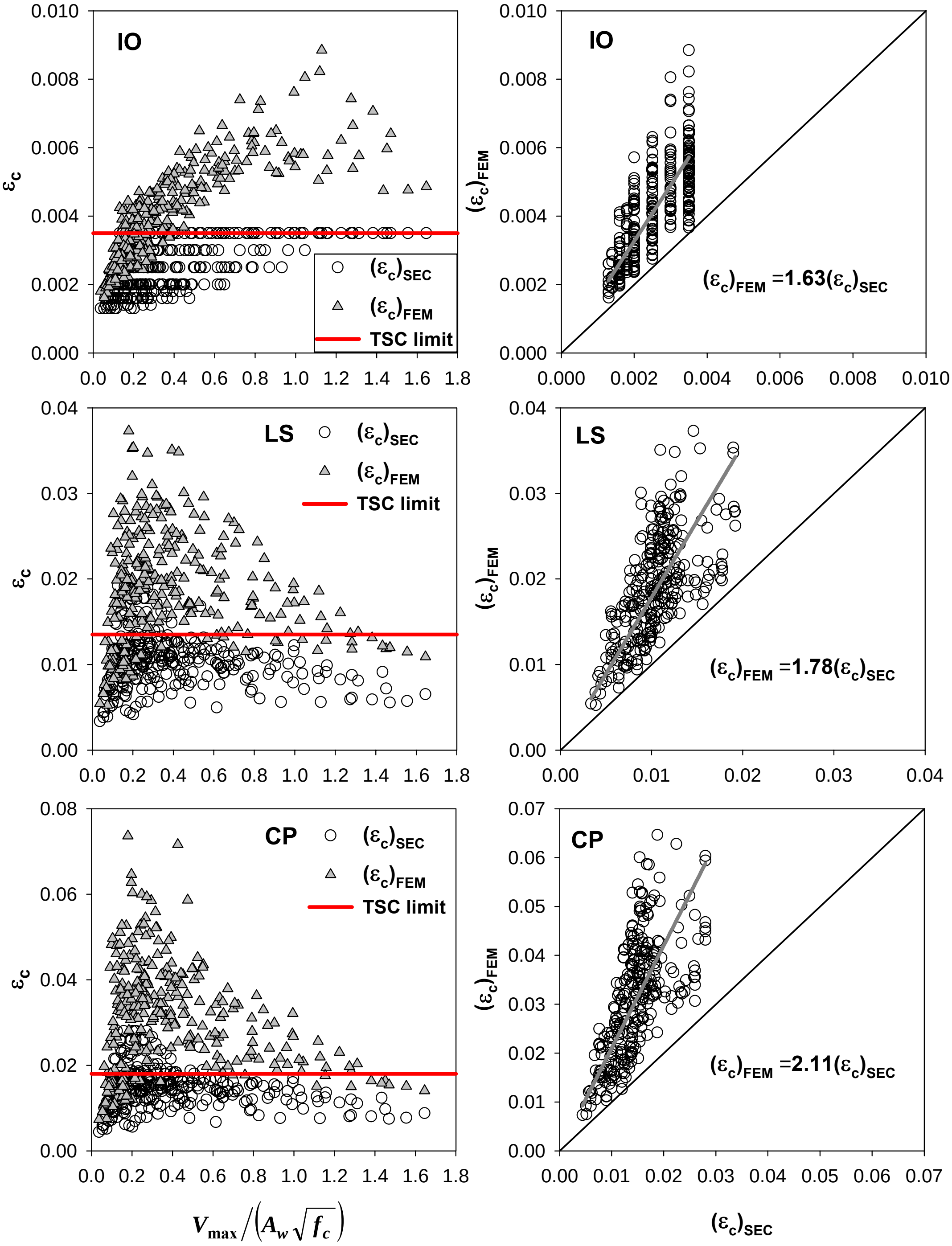

Figure 5.37 Extreme compression fiber strains at calculated limit states for section and finite element analyses

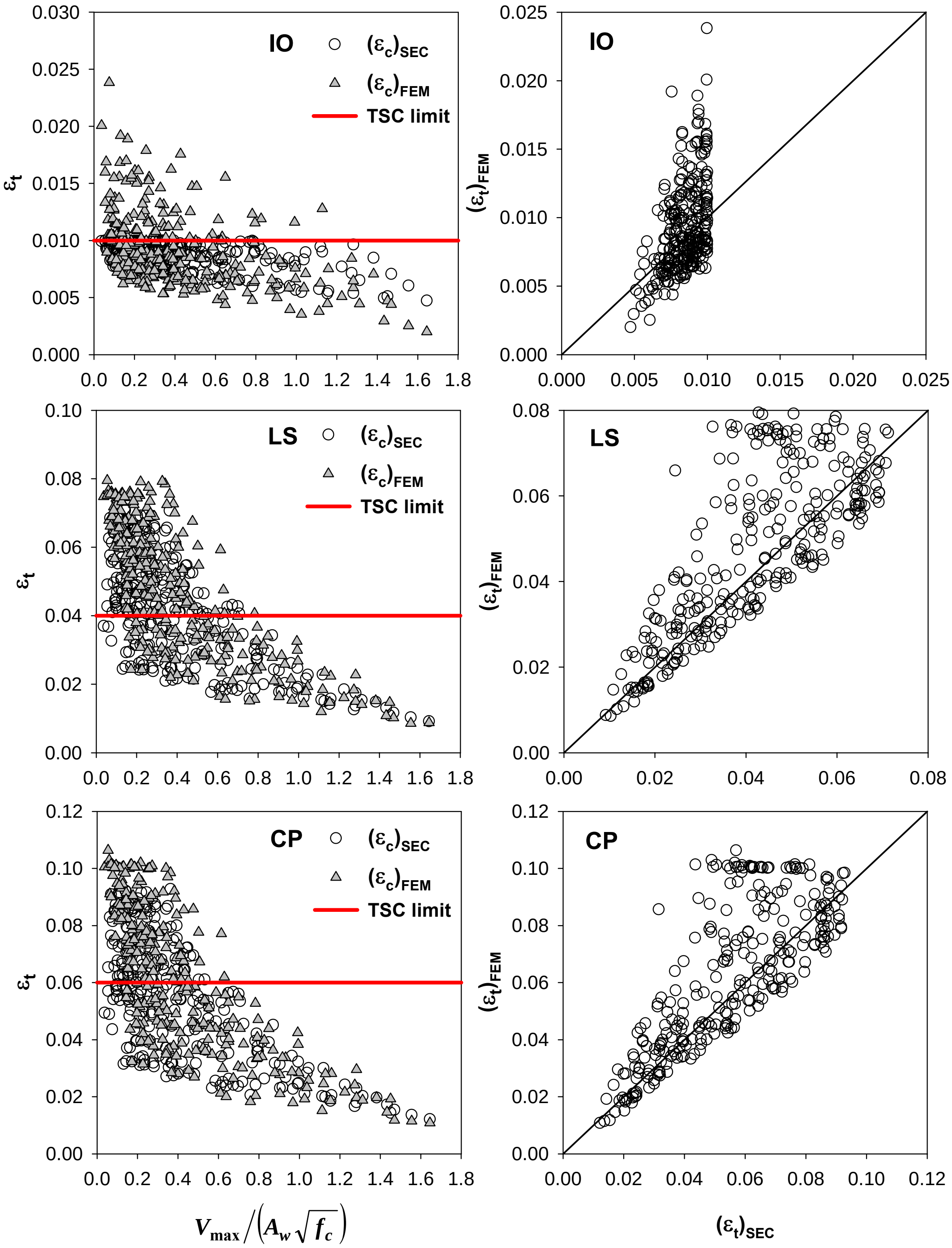

Figure 5.38 Extreme tension steel fiber strains at calculated limit states for section and finite element analyses

The compressive strains at different limit states obtained from section analyses and specified by the TSC are compared in Figure 5.39. The difference between the two formulations is defined by the ratio $\varepsilon_{SEC}/\varepsilon_{TSC}$. As seen in the figure, for most of the data points in the database the ratio is significantly lower than unity. The reason for this is certainly related to the modeling used in establishing the limit states in the requirements. It is demonstrated in Figure 5.30 that in general the ultimate curvature capacities of wall sections obtained from section analyses is larger than the ultimate curvatures obtained from FE analyses. In this study, ultimate curvature obtained from FE analysis is assumed as the ultimate curvature capacity of the section. In keeping with this, the limit states derived by running statistical analysis on the data from sectional analyses in codes should inevitably yield larger strain limits than the results presented here. It should be also admitted that the scarcity of comprehensive strain data measured in experiments impedes the improvement of such limits. Therefore, the results presented in this study should be considered to be more reliable because the shortfalls of the section analyses in determining the deformations of walls have been demonstrated throughout the text. The data in Figure 5.31 reinforces this assertion. Experimental and finite element results indicate the same ultimate deformations limits.

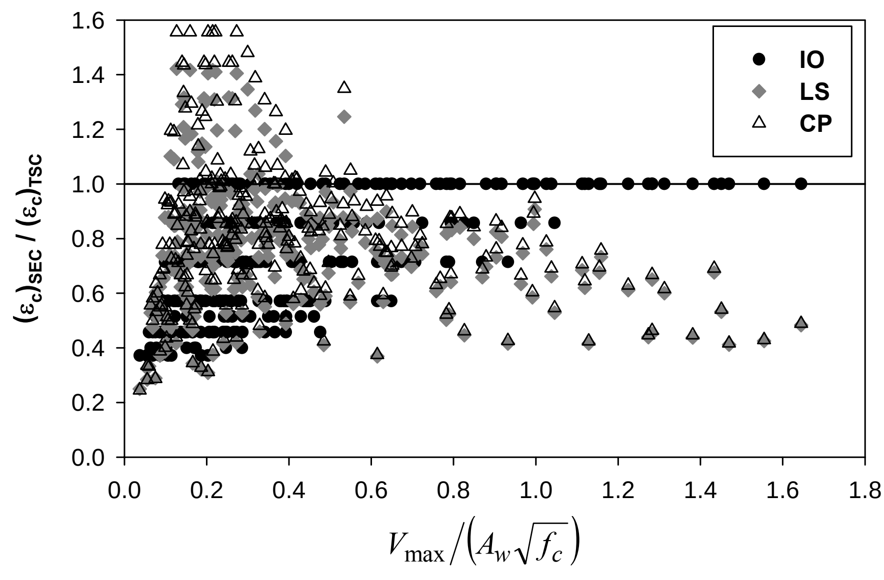

Figure 5.39 Ratio of limiting strains obtained from section analyses and specified by the TSC

Figure 5.40 illustrates the variation of compressive and tensile strain limits corresponding to plastic rotation limits in FEMA 356 against the normalized shear stress. As shown in Figure 5.40(b), the FEMA 356 equivalent compressive strains associated with each performance level are significantly lower than the strain limits specified in TSC. If the compressive strains are adapted to FEMA 356, they will take the values of 0.0035, 0.005 and 0.0075 in average for immediate occupancy, life safety and collapse prevention performance levels, respectively. For flexure controlled members even much lower limits apply. Although FEMA 356 equivalent tensile strains are also lower than TSC limits, the difference is not as large as that observed in compressive strains.

5.8 SHEAR STRENGTH

The nominal shear strength of reinforced concrete walls designed to resist seismic loads is defined in current design guidelines. The two quantities used to define nominal shear strength are the contribution of the web reinforcement and the contribution of concrete. TSC and ACI-318 employ quite similar expressions to calculate the nominal shear strength of walls. The TSC expression reads as

$$V_n = A_w\left(0.65 f_{ctd} + \rho_t f_{yd}\right) \tag{5.17}$$

where f_{ctd} and f_{yd} are the factored design cracking strength of concrete and the yield strength of reinforcement, respectively. The nominal shear strength of walls presented in ACI 318-08 is

$$V_n = A_w\left(\alpha_c \sqrt{f_c} + \rho_t f_y\right) \tag{5.18}$$

where f_c and f_y are the characteristic compressive strength of concrete and yield strength of steel reinforcement, respectively. The coefficient α_c is 0.25 for H_w / $L_w \leq 1.5$, is 0.17 for H_w / $L_w \geq 2.0$, and varies linearly between 0.25 and 0.17 for H_w / L_w between 1.5 and 2.0. In both equations, ρ_t is the ratio of area of distributed reinforcement parallel to the plane of A_w to gross concrete area perpendicular to that reinforcement.

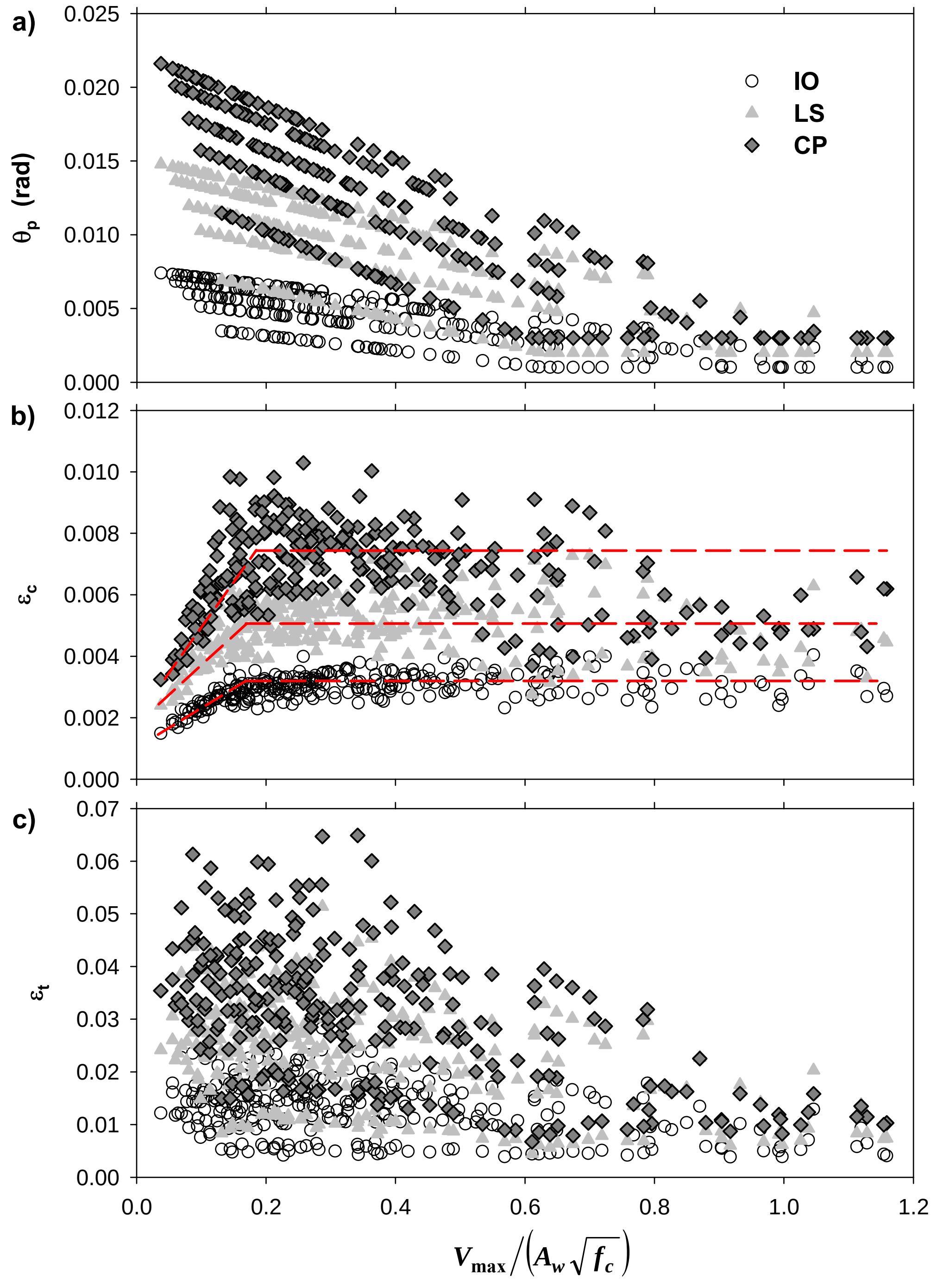

Figure 5.40 Variation of a) FEMA 356 plastic rotations and b) compressive, c) tensile strain limits adapted to FEMA 356 plastic rotation limits for conforming members with the normalized shear stress

The ratio of maximum shear force (V_{max}) obtained from the finite element analysis to the nominal shear strength (V_n) defined by Eqs. (5.17) and (5.18) is plotted as a function of normalized shear stress in Figure 5.411. Keeping in mind that the shear safety of the walls was adjusted according to TSC, it is seen that the shear strength calculated using the code formulation yields conservative estimates of the shear strength of walls for $\nu > \sim 0.4\sqrt{f_c}$. The linear trend in the initial portion of Figure 5.41 suggests that structural walls subjected to shear stress levels less than $0.4\sqrt{f_c}$ are not critical in terms of shear. Most of the data points in this region come from the walls that failed in flexure due to large wall slenderness ratio. Even though much less web shear reinforcement is required in most cases, the code minimum ρ_t = 0.25% was used in this region. The V_{max} calculated for flexural failure are much lower than the corresponding shear capacity of the members. This is the main reason of the observed behavior in this region. As expected the ACI-318-05 expression gives slightly less conservative estimation of the shear strength, because the nominal shear strength calculated using ACI expression yields larger values compared to the TSC equation.

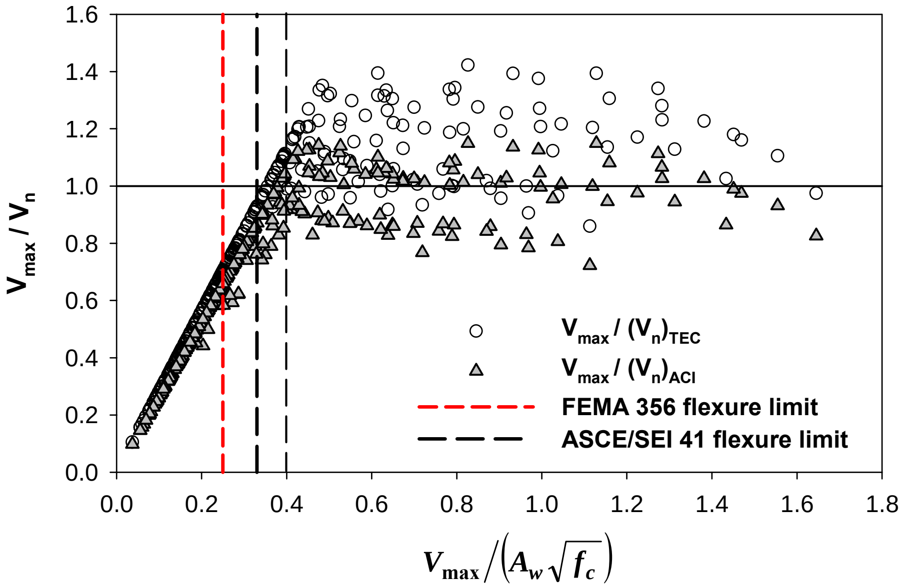

Figure 5.41 Variation of the ratio of shear strength calculated in FE analyses to shear strength calculated using code formulation with the normalized shear stress carried by the wall

5.9 DISCUSSION OF RESULTS

The analyses results displayed that the deformation capacity of shear wall members with confined boundary elements is larger than the limits given in FEMA 356 provisions. It is seen that FEMA 356 yields very conservative estimations of the structural performance. On the other hand, if the strain based performance criteria defined in TSC 2007 or as suggested by Priestley et al. (2007) is used in the determination of structural performance, unconservative estimations of performance are obtained for reinforced concrete rectangular walls. In reference to trends observed in Figure 5.32 and Figure 5.37 it can be concluded that plastic rotation is more stable parameter than the strains to establish the limit states of reinforced concrete members. The dispersion in the strain data in Figure 5.37 indicates that this measure of deformation is much more sensitive to member dimension, material properties, reinforcement amount and the level of axial load than the plastic rotations. So, as will be proposed next this study promotes the use of plastic rotations as performance limits in the assessment of reinforced concrete shear wall members.

The proposed limits for the modeling parameters and the acceptance criteria for shear wall members controlled by flexure are shown in Figure 5.42 and tabulated in Table 5.7. These limits, alternative to *Table 6.18* in FEMA 356, apply to conforming members. The limits are derived as a function of normalized shear stress (ν) and axial load level (P/P_o) for different ranges of these variables in order to obtain more accurate representation of plastic rotation limits at the specified performance levels. Limits in relation to mid range axial load levels (P/P_o = 0.15) are also introduced to increase the accuracy of the assessment procedure. The numbers written in parenthesis in bold letters in Table 5.7 is an adaptation for the FEMA 356 provisions. If the FEMA 356 provisions' format, as given in Table 5.1 previously, is preferred in the presentation of performance limits (such that limits only defined at specific ν and P/P_o values), while the underlined number corresponds to the existing FEMA 356 limit at the specified shear stress and axial load condition, the left side number is the value proposed by this study.

As seen in Figure 5.42 the proposed values correspond to lower bound limit of the results set. When more accurate values of the plastic rotation limits are required, Eq. (5.11) together with the coefficients defined in Table 5.6 can be employed to calculate plastic rotations at collapse prevention limit state. The limit obtained through Eq. (5.11) should be greater than the limit given in Table 5.7. If the limits obtained by this way are reduced by multipliying with a factor of 0.75, life safety performance criteria is obtained.

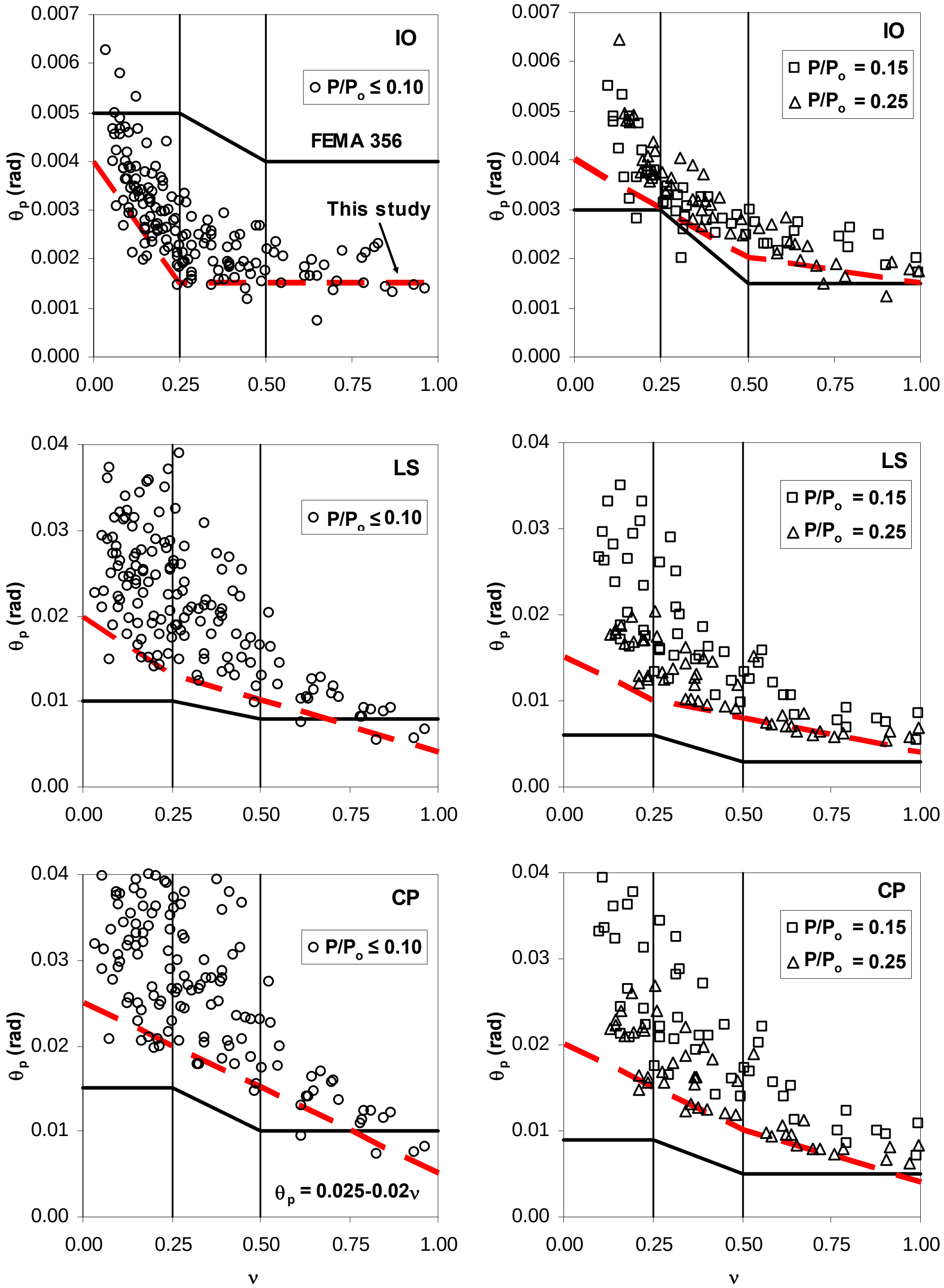

Figure 5.42 Lower bound plastic rotation limits at different performance levels

Table 5.7 The proposed modeling parameters and acceptance criteria for shear wall members controlled by flexure

		IO	LS	CP
$P/P_o <= 0.10$	**$\nu \leq 0.25$**	$0.004 - 0.01\nu$ **(0.0015 / <u>0.005</u>)**§	$0.02 - 0.028\nu$ **(0.013 / <u>0.01</u>)**	$0.025 - 0.02\nu$ **(0.02 / <u>0.015</u>)**
	$0.25 < \nu \leq 0.50$	0.0015	$0.016 - 0.012\nu$	$0.025 - 0.02\nu$
	$0.50 > \nu$	0.0015 **(0.0015 / <u>0.004</u>)**	$0.016 - 0.012\nu$ **(0.01 / <u>0.008</u>)**	$0.025 - 0.02\nu$ **(0.015 / <u>0.01</u>)**
$P/P_o = 0.15$	**$\nu \leq 0.25$**	$0.004 - 0.004\nu$	$0.02 - 0.032\nu$	$0.025 - 0.032\nu$
	$0.25 < \nu \leq 0.50$	$0.004 - 0.004\nu$	$0.016 - 0.016\nu$	$0.022 - 0.02\nu$
	$0.50 > \nu$	$0.0025 - 0.001\nu$	$0.011 - 0.006\nu$	$0.019 - 0.014\nu$
$P/P_o >= 0.25$	**$\nu \leq 0.25$**	$0.004 - 0.004\nu$ **(0.003 / <u>0.003</u>)**	$0.02 - 0.04\nu$ **(0.01 / <u>0.006</u>)**	$0.02 - 0.02\nu$ **(0.015 / <u>0.009</u>)**
	$0.25 < \nu \leq 0.50$	$0.004 - 0.004\nu$	$0.012 - 0.008\nu$	$0.02 - 0.02\nu$
	$0.50 > \nu$	$0.0025 - 0.001\nu$ **(0.0015 / <u>0.0015</u>)**	$0.012 - 0.008\nu$ **(0.008 / <u>0.003</u>)**	$0.016 - 0.012\nu$ **(0.01 / <u>0.005</u>)**

§**(This study / <u>FEMA 356</u>)**

CHAPTER 6

SEISMIC PERFORMANCE OF STRUCTURAL WALL BUILDINGS

6.1 INTRODUCTION

This chapter is devoted to investigation of seismic performance of structural wall buildings. The seismic demand characterized by the code spectrum compatible ground motions are applied on a set of generic frame-wall buildings that represents broad range of frame-wall combinations of relative strength. The effectiveness of walls in the structural system is characterized by wall index. This way behavior modes from purely flexure (cantilever model) to shear dominated (strong frame - weak wall systems) can be simulated. The purpose of the analysis in this chapter is to investigate the following parameters:

- The effect of wall amount (represented by wall index, p) on the deformation demands of reinforced concrete structures. The measures are the global roof drift ratio (DR) and maximum interstory drift ratio (MIDR).
- The performance of wall elements by evaluating the base rotations and strains with respect to code specified limits and the limits found in Chapter 5.
- The shear force to be used in the design of the walls to avoid shear failure. The amplification in the shear profile along the wall during a dynamic action due to higher mode effects has impelled codes to account for this excess shear in the design by a magnification factor (β_v) applied to design base shear obtained from static analysis (EC8, TSC 2007). The amplification of shear demand along the wall, especially at the base, has been recognized some time ago (Derecho et al., 1978b; Derecho and Corley, 1984). Several factors and expressions have been proposed to consider this amplification in the design stage (Paulay and Priestley, 1992; Ghosh and Markevicius, 1992; Seneviratna and

Krawinkler, 1997; Amaris, 2002; Rutenberg and Nsieri, 2006; Celep and Aydinoglu, 2006). Although there is a significant amount of work conducted on the base shear amplification factor, the presented results indicate significant variability on the proposed amplification values and expressions. This is particularly due to quantity (number) and quality (frequency content and amplitude) of the ground motion records used in the analysis and the structural idealization of wall models investigated in these studies. The ground motion database used in this study is carefully selected to represent the code specified seismic demand.

Using the stiffness and dynamic characteristics of the prototype frame-wall structures that were introduced in Chapter 4, the strength and stiffness characteristics of single wall-equivalent frame models that were created for the finite element analyses as shown in Figure 4.29 are determined. Each model is characterized with a particular wall index and αH parameter. Dynamic time history analyses are conducted on these models to investigate the aforementioned issues.

6.2 GENERIC SINGLE WALL-EQUIVALENT FRAME MODELS PRODUCED BY USING CHARACTERISTICS OF PROTOTYPE FRAME-WALL STRUCTURES

It is considered that the generic equivalent frame- single wall models cover a wall index range of 0.002 to 0.02. Models that represent 4, 8 and 12 story structures are developed. The primary variables in creating a model is the wall length (L_w) ,height (H_w), and wall index (p). Instead of wall height number of stories (N) can be used as well. The design procedure described in Section 4.5 is utilized. Table 6.1 to 6.3 summarize the complete set of parameters that emerge from the design process and are used to define wall-frame models.

The values for frame design shear force (V_f) and the boundary element longitudinal reinforcement ratio (ρ_b) in these tables require an explanation. The calculated frame shear force at the base story decreases considerably as the wall index (amount of wall) increases. This is directly related to elastic analysis employed in the design. Elastic lateral load analyses have demonstrated that nearly the entire lateral load resistance of frame-wall buildings is provided by the structural walls as the wall index increases in the system. The generic-frame wall structures that are composed of a single wall and equivalent frame system seem to require no frames to resist lateral loads as the wall index increases. If the frame component is ignored, the system resembles a cantilever wall and this situation engenders significant changes in the load resisting mechanism. Although walls are stiff elements and has a limiting effect on the deformations when elastic action is considered, in the inelastic range after plastic hinge formation at the base of the wall, system behavior changes completely to lead to significant deformation demands. This may have profound effects on the behavior of dual systems (Lu, 2002). Because of the rigid-body displacement of such walls, rotations along the height of the wall, of the same order as that at the foundation, will be introduced at every level. If the interaction effects are ignored, this will diminish the drift controlling effect of structural walls.

Although design analysis results point to negligible effect of frame elements in seismic resistance, in reality there usually exist a considerable number of frame elements (columns) in the system (considering prototype structures in Figure 4.20). Figure 6.1 displays the variation of number of columns per wall as the number of walls (wall index) increase in the prototype structure shown in Figure 4.20. These columns contribute to the lateral strength of the system even though the minimum requirements of the code governs their design (minimum amount of longitudinal reinforcement in a column is $(\rho_b)_{min} = 0.01$). This excess strength is not foreseen by the elastic analysis used in the design. So the frame forces calculated in Tables 6.1 to 6.3 should be adjusted in view of nonlinear analysis results where this substantial lateral strength is mobilized. One of the consequences of this situation is that the actual force reduction factor (R) in the system may turn out to be smaller than the one intended initially in the design of frame-wall systems.

In the light of above discussion an approximate rule may be developed for a "typical" situation. If it is considered that the minimum column dimension is 0.5x0.5 m^2 and minimum reinforcement amount is used ($(\rho_b)_{min} = 0.01$), the moment capacity of columns is found as 256, 305 and 345 kN-m for 5%, 10% and 15% axial load levels, respectively. If the contra flexure height is assumed to occur at the mid height of the column, the column shears are found as 170, 203 and 230 kN for the same set of axial load levels, respectively. Considering that two columns supplement a wall in the system, the minimum story yield shear force due to columns for generic frame-wall structures are calculated as 340, 406 and 460 kN for 4-, 8- and 12-story structures, respectively. If the frame shear found from elastic analysis is lower than the values given above they are replaced with these ones. Figure 6.1 is in favor of such a correction in frame shear. The relation between the number of columns per wall as the wall index increases in the system is derived for the prototype structures described in Chapter 4. It is clear that when the number of columns is considered the provided shear capacity is greater than that the elastic design forces on frame component have indicated. The story yield strength is not constant along the height of the structure. It is distributed to the upper stories in proportion to design forces resulting from code static lateral load pattern as shown in Figure 4.21 previously.

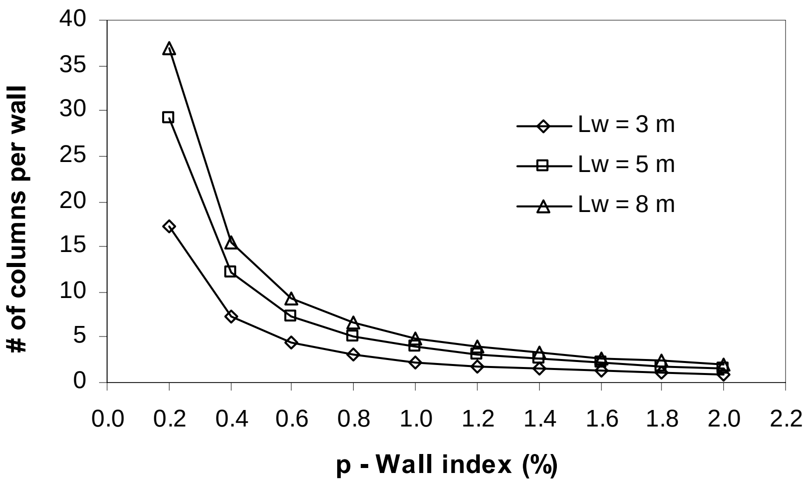

Figure 6.1 Relation between the wall index and number of columns per single wall extracted from prototype structures

The second explanation is with regards to longitudinal boundary element reinforcement, ρ_b. As seen in the Tables 6.1 to 6.3 the required boundary element reinforcement decreases as the wall index increases and it seems to take negative values after some point. This situation stems from design procedure defined in Section 4.5 of Chapter 4. As the wall index increases in the system the design moment of walls decreases significantly. The reinforcement ratio calculated by inserting the design moment into Eq. (4.33) then takes negative values, because the moment is smaller than the section capacity that is obtained with minimum reinforcement. In such case code specifies the use of minimum amount of ρ_b = 0.01 as in the column elements. In this study the minimum boundary element longitudinal reinforcement is set to be ρ_b = 0.005, which is lower than the code limit.

Table 6.1 Strength and stiffness characteristics of frame-wall models developed for dynamic analysis, 4-story structure

L_w (m)	H_w (m)	N_s	H_w/L_w	p (%)	αH	T_e (s)	A_f (m^2)	V_b (kN)	R	V_b/R (kN)	M_w (kN-m)	V_w (kN)	V_f (kN)	V_w/V_b	P/P_o	P_o (kN)	ρ_b	ρ_{sh}	M_{beam} (kN-m)	K_{frame} (kN/m)	K_{beam} kN-m/rad
3	12	4	4	0.2	2.85	0.39	375	14715	6	2453	6138	1341	1111	0.55	0.05	938	0.0263	0.0031	902	49381	225381
3	12	4	4	0.4	2.02	0.35	188	7358	6	1226	4431	886	340	0.72	0.05	938	0.0154	0.0025	706	15128	176554
3	12	4	4	0.6	1.65	0.32	125	4905	6	818	3515	654	164	0.80	0.05	938	0.0096	0.0025	598	7279	149525
3	12	4	4	0.8	1.43	0.29	94	3679	6	613	2938	517	96	0.84	0.05	938	0.0059	0.0025	523	4267	130830
3	12	4	4	1.0	1.28	0.28	75	2943	6	491	2535	428	63	0.87	0.05	938	0.0034	0.0025	467	2796	116728
3	12	4	4	1.2	1.17	0.26	63	2453	6	409	2236	364	44	0.89	0.05	938	0.0014	0.0025	422	1969	105570
3	12	4	4	1.4	1.08	0.25	54	2102	6	350	2004	318	33	0.91	0.05	938	0.0000	0.0025	386	1458	96462
3	12	4	4	1.6	1.01	0.23	47	1839	6	307	1817	281	25	0.92	0.05	938	-0.0012	0.0025	355	1121	88859
3	12	4	4	1.8	0.95	0.22	42	1635	6	273	1663	253	20	0.93	0.05	938	-0.0022	0.0025	330	887	82401
3	12	4	4	2.0	0.90	0.22	38	1472	6	245	1535	229	16	0.93	0.05	938	-0.0030	0.0025	307	718	76840
5	12	4	2.4	0.2	1.53	0.34	625	24525	6	4088	17061	2739	1349	0.67	0.05	1563	0.0243	0.0045	992	59934	247949
5	12	4	2.4	0.4	1.13	0.27	313	12263	6	2044	11000	1680	364	0.82	0.05	1563	0.0114	0.0025	671	16187	167646
5	12	4	2.4	0.6	0.94	0.23	208	8175	6	1363	8185	1200	163	0.88	0.05	1563	0.0054	0.0025	514	7236	128507
5	12	4	2.4	0.8	0.83	0.21	156	6131	6	1022	6542	931	91	0.91	0.05	1563	0.0019	0.0025	419	4028	104680
5	12	4	2.4	1.0	0.75	0.19	125	4905	6	818	5457	760	57	0.93	0.05	1563	-0.0005	0.0025	354	2539	88498
5	12	4	2.4	1.2	0.70	0.18	104	4088	6	681	4686	642	39	0.94	0.05	1563	-0.0021	0.0025	307	1734	76741
5	12	4	2.4	1.4	0.65	0.16	89	3504	6	584	4109	556	28	0.95	0.05	1563	-0.0033	0.0025	307	1253	76741
5	12	4	2.4	1.6	0.61	0.15	78	3066	6	511	3659	490	21	0.96	0.05	1563	-0.0043	0.0025	307	944	76741
5	12	4	2.4	1.8	0.58	0.15	69	2685	5.9	456	3312	439	17	0.96	0.05	1563	-0.0050	0.0025	307	737	76741
5	12	4	2.4	2.0	0.56	0.14	63	2349	5.7	413	3038	400	13	0.97	0.05	1563	-0.0056	0.0025	307	592	76741
8	12	4	1.5	0.2	0.84	0.26	1000	39240	6	6540	39936	5300	1240	0.81	0.05	2500	0.0259	0.0060	1002	55126	250614
8	12	4	1.5	0.4	0.66	0.19	500	19620	6	3270	22573	2976	294	0.91	0.05	2500	0.0096	0.0025	573	13077	143295
8	12	4	1.5	0.6	0.57	0.16	333	13080	6	2180	15799	2056	124	0.94	0.05	2500	0.0033	0.0025	405	5495	101174
8	12	4	1.5	0.8	0.51	0.14	250	9375	5.7	1654	12317	1587	67	0.96	0.05	2500	0.0000	0.0025	317	2982	79349
8	12	4	1.5	1.0	0.47	0.13	200	7064	5.3	1345	10193	1303	42	0.97	0.05	2500	-0.0020	0.0025	264	1863	65960
8	12	4	1.5	1.2	0.44	0.11	167	5615	4.9	1137	8721	1108	29	0.97	0.05	2500	-0.0034	0.0025	226	1267	56619
8	12	4	1.5	1.4	0.42	0.11	143	4631	4.7	986	7636	966	21	0.98	0.05	2500	-0.0044	0.0025	199	914	49707
8	12	4	1.5	1.6	0.40	0.10	125	3922	4.5	872	6802	857	15	0.98	0.05	2500	-0.0052	0.0025	177	688	44374
8	12	4	1.5	1.8	0.38	0.09	111	3390	4.3	783	6140	771	12	0.98	0.05	2500	-0.0058	0.0025	161	536	40125
8	12	4	1.5	2.0	0.37	0.09	100	2978	4.2	710	5601	701	10	0.99	0.05	2500	-0.0063	0.0025	147	428	36656

L_w = wall length; H_w = wall height; N_s = number of stories; H_w/L_w = aspect ratio of wall; p = wall index; αH = behavior factor; T_e = elastic period of structure; A_f = floor area per wall; V_b = unfactored total equivalent seismic base shear; R= force reduction factor; M_w = wall design bending moment; V_w = wall base shear; V_f = frame base shear; P_o = axial load; ρ_b = ratio of total boundary element longitudinal reinforcement area to boundary region area; ρ_{sh} = web reinforcement; M_{beam} = total bending effect of beams framing to walls; K =initial stiffness of beam and frame elements

Table 6.2 Strength and stiffness characteristics of frame-wall models developed for dynamic analysis, 8-story structure

L_w (m)	H_w (m)	N_s	H_w/L_w	p (%)	αH	T_e (s)	A_f (m^2)	V_b (kN)	R	V_b/R (kN)	M_w (kN-m)	V_w (kN)	V_f (kN)	V_w/V_b	P/P_o	P_o (kN)	ρ_b	ρ_{sh}	M_{beam} (kN-m)	K_{frame} (kN/m)	K_{beam} $\frac{kN\text{-}m}{rad}$
3	24	8	8	0.2	6.44	0.78	375	23905	6	3984	10831	1990	1995	0.50	0.1	1875	0.0495	0.0061	1895	88653	473812
3	24	8	8	0.4	4.56	0.75	188	12261	6	2044	8385	1388	655	0.68	0.1	1875	0.0339	0.0033	1587	29113	396773
3	24	8	8	0.6	3.73	0.73	125	8369	6	1395	7000	1063	332	0.76	0.1	1875	0.0250	0.0025	1405	14738	351174
3	24	8	8	0.8	3.23	0.71	94	6417	6	1069	6111	866	203	0.81	0.1	1875	0.0194	0.0025	1279	9023	319848
3	24	8	8	1.0	2.89	0.69	75	5242	6	874	5487	735	138	0.84	0.1	1875	0.0154	0.0025	1186	6153	296614
3	24	8	8	1.2	2.64	0.68	63	4455	6	743	5021	641	101	0.86	0.1	1875	0.0124	0.0025	1114	4497	278482
3	24	8	8	1.4	2.45	0.66	54	3891	6	649	4658	571	78	0.88	0.1	1875	0.0101	0.0025	1055	3449	263800
3	24	8	8	1.6	2.29	0.65	47	3467	6	578	4365	516	62	0.89	0.1	1875	0.0082	0.0025	1006	2741	251573
3	24	8	8	1.8	2.16	0.63	42	3135	6	522	4123	472	50	0.90	0.1	1875	0.0067	0.0025	965	2238	241163
3	24	8	8	2.0	2.05	0.62	38	2868	6	478	3918	436	42	0.91	0.1	1875	0.0054	0.0025	929	1868	232143
5	24	8	4.8	0.2	3.46	0.81	625	38638	6	6440	31873	3963	2477	0.62	0.1	3125	0.0494	0.0078	2182	110089	545447
5	24	8	4.8	0.4	2.55	0.72	313	21190	6	3532	23725	2759	772	0.78	0.1	3125	0.0321	0.0045	1701	34323	425164
5	24	8	4.8	0.6	2.14	0.66	208	15121	6	2520	19662	2136	384	0.85	0.1	3125	0.0234	0.0028	1459	17074	364720
5	24	8	4.8	0.8	1.88	0.62	156	11987	6	1998	17161	1764	233	0.88	0.1	3125	0.0181	0.0025	1305	10372	326217
5	24	8	4.8	1.0	1.71	0.58	125	9810	6	1635	15053	1480	155	0.91	0.1	3125	0.0136	0.0025	1166	6869	291413
5	24	8	4.8	1.2	1.57	0.55	104	8175	6	1363	13231	1255	108	0.92	0.1	3125	0.0097	0.0025	1039	4799	259774
5	24	8	4.8	1.4	1.47	0.53	89	7007	6	1168	11835	1088	80	0.93	0.1	3125	0.0067	0.0025	940	3535	235001
5	24	8	4.8	1.6	1.39	0.51	78	6131	6	1022	10726	961	61	0.94	0.1	3125	0.0044	0.0025	860	2709	214958
5	24	8	4.8	1.8	1.32	0.49	69	5450	6	908	9821	860	48	0.95	0.1	3125	0.0024	0.0025	793	2138	198338
5	24	8	4.8	2.0	1.26	0.47	63	4905	6	818	9066	779	39	0.95	0.1	3125	0.0008	0.0025	737	1729	184291
8	24	8	3	0.2	1.90	0.77	1000	64287	6	10715	88149	8199	2515	0.77	0.1	5000	0.0651	0.0110	2623	111786	655652
8	24	8	3	0.4	1.48	0.62	500	38443	6	6407	63718	5650	757	0.88	0.1	5000	0.0422	0.0066	1944	33645	486065
8	24	8	3	0.6	1.29	0.53	333	26160	6	4360	47449	4023	337	0.92	0.1	5000	0.0269	0.0039	1473	14961	368137
8	24	8	3	0.8	1.16	0.48	250	19620	6	3270	37634	3085	185	0.94	0.1	5000	0.0177	0.0025	1181	8229	295358
8	24	8	3	1.0	1.07	0.44	200	15696	6	2616	31307	2500	116	0.96	0.1	5000	0.0117	0.0025	991	5154	247764
8	24	8	3	1.2	1.01	0.41	167	13080	6	2180	26865	2101	79	0.96	0.1	5000	0.0075	0.0025	856	3508	213965
8	24	8	3	1.4	0.95	0.38	143	11211	6	1869	23563	1812	57	0.97	0.1	5000	0.0044	0.0025	754	2530	188611
8	24	8	3	1.6	0.91	0.36	125	9810	6	1635	21005	1592	43	0.97	0.1	5000	0.0020	0.0025	675	1904	168832
8	24	8	3	1.8	0.87	0.34	111	8720	6	1453	18963	1420	33	0.98	0.1	5000	0.0001	0.0025	612	1480	152938
8	24	8	3	2.0	0.84	0.33	100	7848	6	1308	17292	1281	27	0.98	0.1	5000	-0.0015	0.0025	559	1181	139869

L_w = wall length; H_w = wall height; N_s = number of stories; H_w/L_w = aspect ratio of wall; p = wall index; αH = behavior factor; T_e = elastic period of structure; A_f = floor area per wall; V_b = unfactored total equivalent seismic base shear; R= force reduction factor; M_w = wall design bending moment; V_w = wall base shear; V_f = frame base shear; P_o = axial load; ρ_b = ratio of total boundary element longitudinal reinforcement area to boundary region area; ρ_{sh} = web reinforcement; M_{beam} = total bending effect of beams framing to walls; K =initial stiffness of beam and frame elements

Table 6.3 Strength and stiffness characteristics of frame-wall models developed for dynamic analysis, 12-story structure

L_w (m)	H_w (m)	N_s	H_w/L_w	p (%)	αH	T_e (s)	A_f (m^2)	V_b (kN)	R	V_b/R (kN)	M_w (kN-m)	V_w (kN)	V_f (kN)	V_w/V_b	P/P_o	P_o (kN)	ρ_b	ρ_{sh}	M_{beam} (kN-m)	K_{frame} (kN/m)	K_{beam} $\frac{kN\text{-}m}{rad}$
3	36	12	12	0.2	10.04	1.14	375	26325	6	4387	12181	2135	2253	0.49	0.15	2813	0.0513	0.0067	2204	100117	550931
3	36	12	12	0.4	7.11	1.13	188	13318	6	2220	9476	1476	744	0.66	0.15	2813	0.0340	0.0037	1877	33056	469129
3	36	12	12	0.6	5.81	1.11	125	8977	6	1496	7923	1119	377	0.75	0.15	2813	0.0241	0.0025	1670	16766	417472
3	36	12	12	0.8	5.04	1.10	94	6804	6	1134	6911	903	231	0.80	0.15	2813	0.0177	0.0025	1522	10260	380437
3	36	12	12	1.0	4.51	1.08	75	5498	6	916	6193	759	157	0.83	0.15	2813	0.0131	0.0025	1409	6982	352135
3	36	12	12	1.2	4.12	1.07	63	4627	6	771	5651	657	114	0.85	0.15	2813	0.0097	0.0025	1318	5089	329598
3	36	12	12	1.4	3.81	1.06	54	4004	6	667	5226	580	88	0.87	0.15	2813	0.0069	0.0025	1244	3890	311113
3	36	12	12	1.6	3.57	1.05	47	3536	6	589	4881	520	69	0.88	0.15	2813	0.0047	0.0025	1182	3082	295605
3	36	12	12	1.8	3.36	1.03	42	3172	6	529	4595	472	56	0.89	0.15	2813	0.0029	0.0025	1129	2508	282360
3	36	12	12	2.0	3.19	1.02	38	2880	6	480	4353	433	47	0.90	0.15	2813	0.0014	0.0025	1084	2086	270882
5	36	12	7.2	0.2	5.39	1.24	625	41210	6	6868	36123	4076	2792	0.59	0.15	4688	0.0521	0.0081	2598	124093	649541
5	36	12	7.2	0.4	3.98	1.15	313	21921	6	3654	26687	2790	864	0.76	0.15	4688	0.0320	0.0046	2011	38395	502795
5	36	12	7.2	0.6	3.33	1.08	208	15280	6	2547	21913	2121	426	0.83	0.15	4688	0.0218	0.0028	1708	18921	426958
5	36	12	7.2	0.8	2.93	1.04	156	11885	6	1981	18974	1724	257	0.87	0.15	4688	0.0156	0.0025	1515	11403	378709
5	36	12	7.2	1.0	2.66	1.00	125	9813	6	1635	16952	1462	173	0.89	0.15	4688	0.0112	0.0025	1378	7691	344567
5	36	12	7.2	1.2	2.45	0.96	104	8410	6	1402	15458	1276	125	0.91	0.15	4688	0.0081	0.0025	1275	5574	318755
5	36	12	7.2	1.4	2.29	0.93	89	7394	6	1232	14300	1137	96	0.92	0.15	4688	0.0056	0.0025	1193	4246	298335
5	36	12	7.2	1.6	2.16	0.90	78	6623	6	1104	13369	1028	75	0.93	0.15	4688	0.0036	0.0025	1127	3355	281637
5	36	12	7.2	1.8	2.05	0.88	69	6016	6	1003	12599	941	61	0.94	0.15	4688	0.0020	0.0025	1071	2726	267635
5	36	12	7.2	2.0	1.96	0.86	63	5525	6	921	11950	870	51	0.94	0.15	4688	0.0006	0.0025	1023	2265	255659
8	36	12	4.5	0.2	2.96	1.29	1000	63779	6	10630	97624	7918	2712	0.74	0.15	7500	0.0679	0.0105	3047	120515	761796
8	36	12	4.5	0.4	2.31	1.09	500	36615	6	6102	69481	5300	802	0.87	0.15	7500	0.0415	0.0060	2227	35664	556632
8	36	12	4.5	0.6	2.00	0.97	333	26727	6	4455	56578	4065	390	0.91	0.15	7500	0.0293	0.0039	1847	17315	461739
8	36	12	4.5	0.8	1.81	0.89	250	21481	6	3580	48847	3347	233	0.93	0.15	7500	0.0221	0.0027	1616	10352	403875
8	36	12	4.5	1.0	1.67	0.83	200	18184	6	3031	43566	2874	156	0.95	0.15	7500	0.0171	0.0025	1455	6944	363729
8	36	12	4.5	1.2	1.57	0.78	167	15899	6	2650	39668	2537	113	0.96	0.15	7500	0.0134	0.0025	1335	5010	333695
8	36	12	4.5	1.4	1.48	0.74	143	14211	6	2368	36638	2283	86	0.96	0.15	7500	0.0106	0.0025	1240	3801	310084
8	36	12	4.5	1.6	1.41	0.71	125	12906	6	2151	34194	2084	67	0.97	0.15	7500	0.0083	0.0025	1163	2992	290862
8	36	12	4.5	1.8	1.36	0.68	111	11864	6	1977	32169	1923	55	0.97	0.15	7500	0.0064	0.0025	1099	2423	274800
8	36	12	4.5	2.0	1.31	0.65	100	11009	6	1835	30455	1790	45	0.98	0.15	7500	0.0048	0.0025	1044	2006	261106

L_w = wall length; H_w = wall height; N_s = number of stories; H_w/L_w = aspect ratio of wall; p = wall index; αH = behavior factor; T_e = elastic period of structure; A_f = floor area per wall; V_b = unfactored total equivalent seismic base shear; R= force reduction factor; M_w = wall design bending moment; V_w = wall base shear; V_f = frame base shear; P_o = axial load; ρ_b = ratio of total boundary element longitudinal reinforcement area to boundary region area; ρ_{sh} = web reinforcement; M_{beam} = total bending effect of beams framing to walls

6.2.1 Static Analysis on Generic Models with Elastic Properties

The relation between the wall index and vibration period is plotted in Figure 6.2. Based on the periods calculated and tabulated in Tables 6.1 to 6.3 and plotted in Figure 6.2 equivalent static seismic base shear is calculated according to the procedure defined previously in Section 4.5. Using triangular load pattern, static analyses was performed with reduced cracked section stiffness properties. No reduction was applied on the seismic base shear. The roof displacement was calculated using the expression given in Eq. (E.38) in APPENDIX E and normalized with respect to building height. The variation of roof drift with wall index is plotted in Figure 6.3.

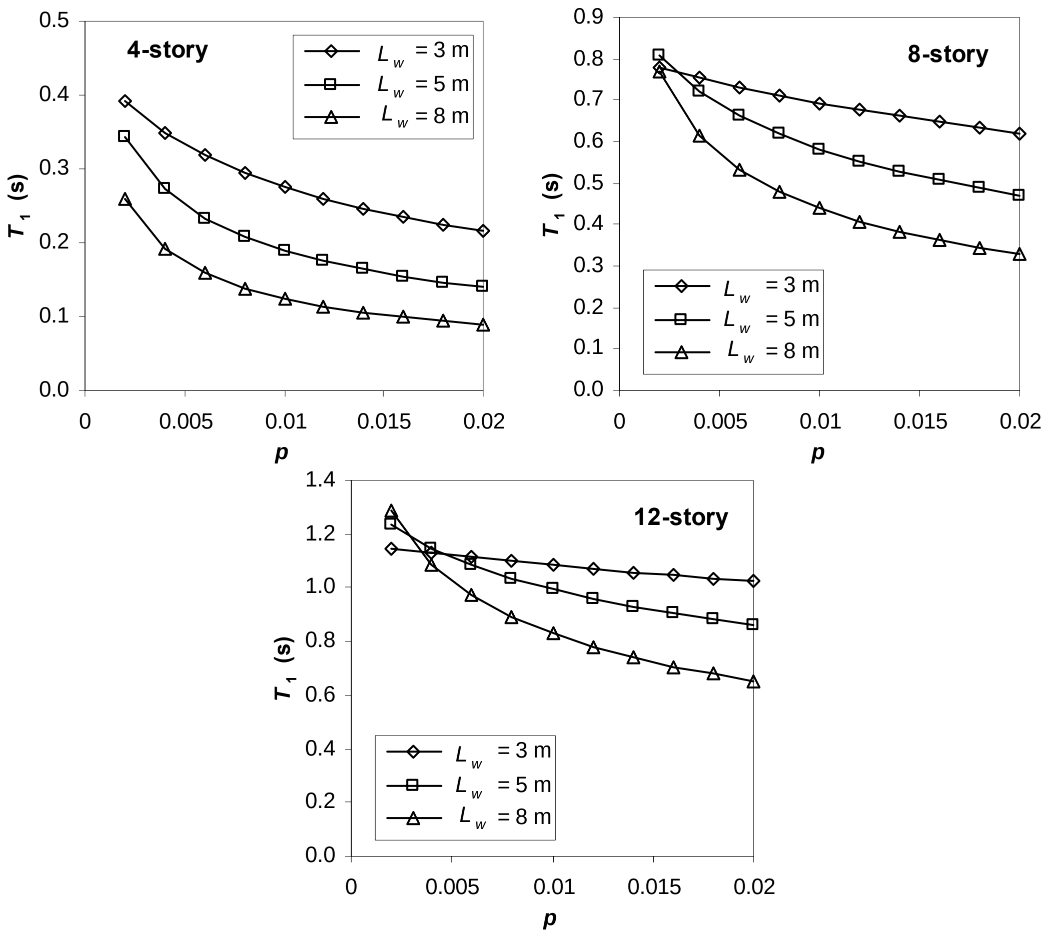

Figure 6.2 Change in the period of frame-wall system as a function of the amount of walls per floor area

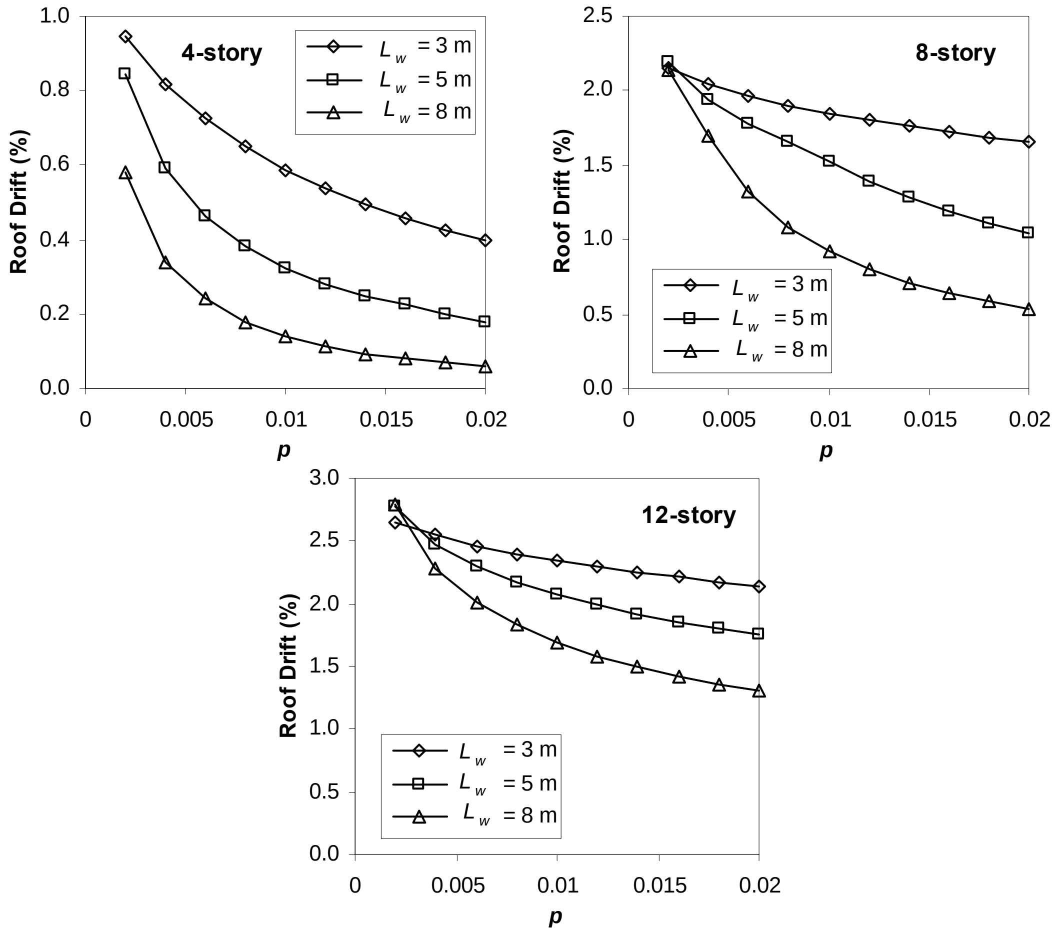

Figure 6.3 Drift of frame-wall system with an increase in the amount of walls per floor area

Although based on linear analyses useful observations emerge from the data presented in these figures. With reference to Figure 6.2, in low rise buildings (4-story) the wall amount provides significant stiffness improvement in the system regardless of comprising walls length as reflected in the reduction of fundamental vibration period. As the number of stories increase effect of wall length rather than the increased wall index become more pronounced in increasing the rigidity of the system. The effect of increased wall area in controlling the drift demands on frame wall-systems is displayed in Figure 6.3. It is seen in the figure that walls with larger length provide much better control and reduction on the drift demands. In reducing the seismic drift demands it is not the wall amount (area) but the stiffness provided by the increased moment of inertia that is more effective. So in the design using robust walls (L_w > 5m) should provide better control on the seismic drift demands. This is another argument against the use of “wall columns” that is common in Turkish practice.

The required boundary element reinforcement as function of strength reduction factors R = 4 and 6 is plotted in Figure 6.4. Increasing the strength reduction factor significantly increases the amount of boundary element flexural reinforcement required to resist the seismic moments even though the existing wall amount is quite large. These observations are valid for systems where walls only interact with frames in the direction of excitation. When wall-to-wall interaction exists (such as the case of coupled walls) the picture may change. For walls in low rise buildings (N = 4) designed as high ductility systems (R=6), when the wall index exceeds 0.5% the required amount of boundary element longitudinal reinforcement is satisfied with the minimum amount of 1% as specified in the code.

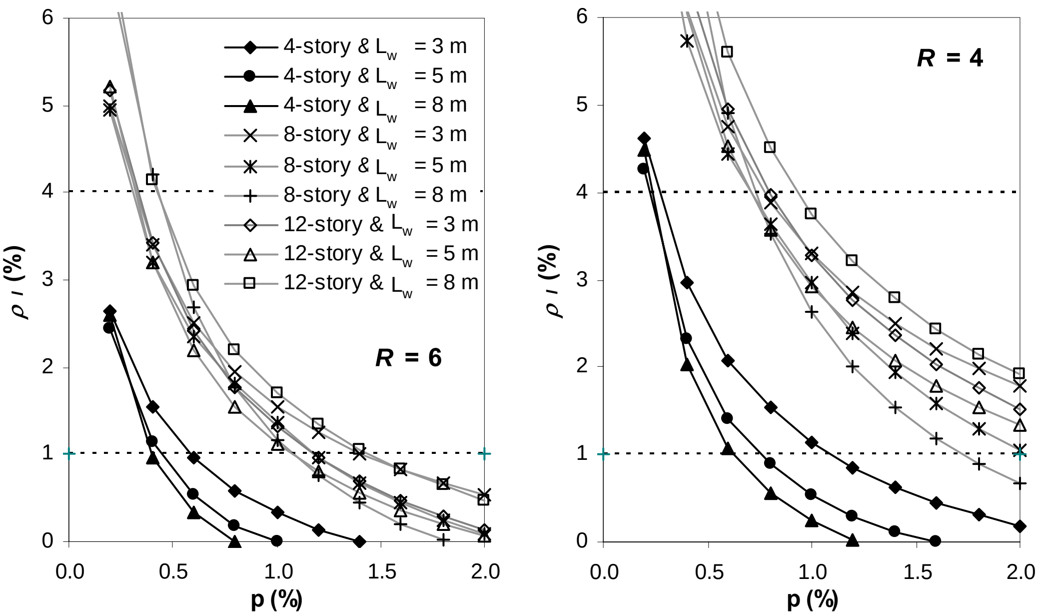

Figure 6.4 Boundary element reinforcement as a function of p and R

6.2.2 Nonlinear Dynamic Analysis of Generic Frame-Wall Models

Using the finite element model displayed in Figure 4.29 and the member strength and stiffness properties tabulated in Tables 6.1 to 6.3, nonlinear time history analyses were conducted. The nonlinear force-defromation relations were employed as defined in Section 4.6 of Chapter 4. As seismic input the ground motion data set composed of ten design spectrum compatible natural records were applied to the finite element models. The response parameters under investigation are plotted in Figure 6.5 to Figure 6.10. These parameters include maximum roof drift, maximum interstory drift, base rotation, base shear amplification factor and maximum compressive strain at the extreme fiber of the base section. The response parameters are mainly plotted as a function of wall index to see the effect of wall amount on these parameters.

Before commencing further, the key to the notation used on figures is given. As an example in “L3S4”, L3 indicates to wall with 3 m length and S4 refers to 4-story structure. The other labels should be read accordingly.

Figure 6.5 displays the maximum roof drift of model frame-wall structures. No profound effect of increased wall area is observed on the drift demands except for 4-story structures. For 8- and 12-story structures the mean drift reduces from 1% to 0.75% as the wall index increase from 0.2% to 2%. Although the reduction is not so significant considering the increase in the wall area, it can be seen that better control over the roof drift is achieved. For wall indexes greater than 0.75% the scatter of data around the mean drift ratio due to ground motion variability decreases significantly. The increased wall area affects significantly the seismic deformation demand on 4-story structures. The drift demands reduce from approximately 1.5% to below 0.5% as the wall area increases. Producing the same wall area in the system using larger walls also improves the drift control over 4-story structures. For the same wall index no effect of wall length on the drift demands is observed on 8 and 12-story structures. The trend between the wall index and the drift ratio observed in Figure 6.5 does not agree with the elastic analysis results plotted in Figure 6.3. Elastic analyses indicate much better control on the drift as the wall index increases. The difference may be attributed to change in the behavior of wall systems after formation of plastic hinge at the wall base.

The maximum interstory drift ratios (MIDR) are plotted in Figure 6.6. The figures indicate to same trends observed in the roof drift ratios (DR) in Figure 6.5, the only difference being the maximum interstory drift is generally 25 to 50 percent larger than the maximum roof drift in the 8- and 12-story models. The mean seismic MIDR decrease from 1.5% to 0.75% as the wall index increases from 0.2% to 2%. For wall indexes larger than 0.5% the MIDR is in the order of 1% or less.

Figure 6.7 presents the dynamic amplification at the base of the walls. The base shear amplification factor is calculated as

$$\beta_v = V_{dynamic} \big/ V_{static} \tag{6.1}$$

The static wall base shear is calculated by performing pushover analysis under code-specified equivalent static lateral load. Dynamic shear is the maximum value observed during the response history data. It is seen that the dynamic amplification decreases from approximately 1.5 to 1.15 as the wall index in the system increase. The increased wall index indicates reduced frame-wall interaction effects on the walls. TSC 2007 specifies that in the systems where the seismic force is completely carried by reinforced concrete structural walls the dynamic amplification factor can be taken as 1.0. This observation is in agreement with the code specification. However, there is one additional reason for this reduction observed in the dynamic amplification factor. As discussed in Section 6.2 in the design of frame-wall models due to code specified requirements and constructional restrictions the actual strength of the structure is higher than the strength calculated from elastic analysis. The structure happened to be designed for a lower force reduction factor than R= 6. It can be concluded that the dynamic amplification is also a function of expected inelasticity in the systems. The effect of force reduction factor is displayed in Figure 6.12 and will be discussed in the following sections.

Figure 6.8 displays the maximum plastic rotations calculated at the base of the walls as a function of wall index. Figure 6.9 displays only the mean base rotation plotted for wall index for more clear depiction of this type of deformation demand. The FEMA 356 rotation limits are also superposed on the same figure to facilitate estimating the likely performance of walls located in different structural systems. Before evaluating the results calculation of FEMA 356 limits is discussed. The limits for each model structure are calculated using normalized shear stress (ν) and the axial load ratio (P/P_o) on the wall element. The normalized shear stress is calculated according to Eq. (5.5) by factoring the design shear force of wall for flexural over-strength factor (ϕ_o = 1.25) and the dynamic amplification factor (β_v =1.5) as specified by the code. Eqs (5.2) to (5.4) are used to calculate the performance limits for immediate occupancy (IO), life safety (LS), collapse prevention

(CP). As seen in Figure 6.9 the calculated FEMA 356 plastic rotation limits indicate very low deformability at the base of the walls for low wall index systems ($p < 0.5\%$) especially for 8- and 12-story structures. This is due to high shear stress carried by the walls in this range of wall indexes. Above $p = 0.5\%$ nearly all walls in all systems assure at least life safety (LS) performance state.

The maximum compressive strains at the extreme fiber of wall base section are plotted in Figure 6.10. The pronounced effect of high shear stress is quite obvious on the increased strain demand in low wall index structures. The frame-wall interaction results in an increase in the slope of the moment profile along the lower stories of the wall, and thus increase the level of shear stress that must be resisted by the wall compared with cantilever walls. The base stories of walls in frame-wall structures with $p < 0.5$ % resemble squat wall in terms of loading conditions, so they inhabit very low deformation capacity (lower than 0.01 drift ratio) and most of the damage concentrates in the compression zone leading to concrete crushing and loss of concrete integrity at this region. The behavior of wall under high shear was discussed in Chapters 2 and 5 previously. As seen in Figure 6.10, concrete compressive strains in low wall index frame-wall structures are much higher than the limit allowed for design ($\varepsilon_c = 0.0035$), so it can be concluded that while allocating walls together with frames a minimum requirement must be sought on the amount of walls with respect to the total floor area. The limiting value can be recommended as $p = 0.5\%$.

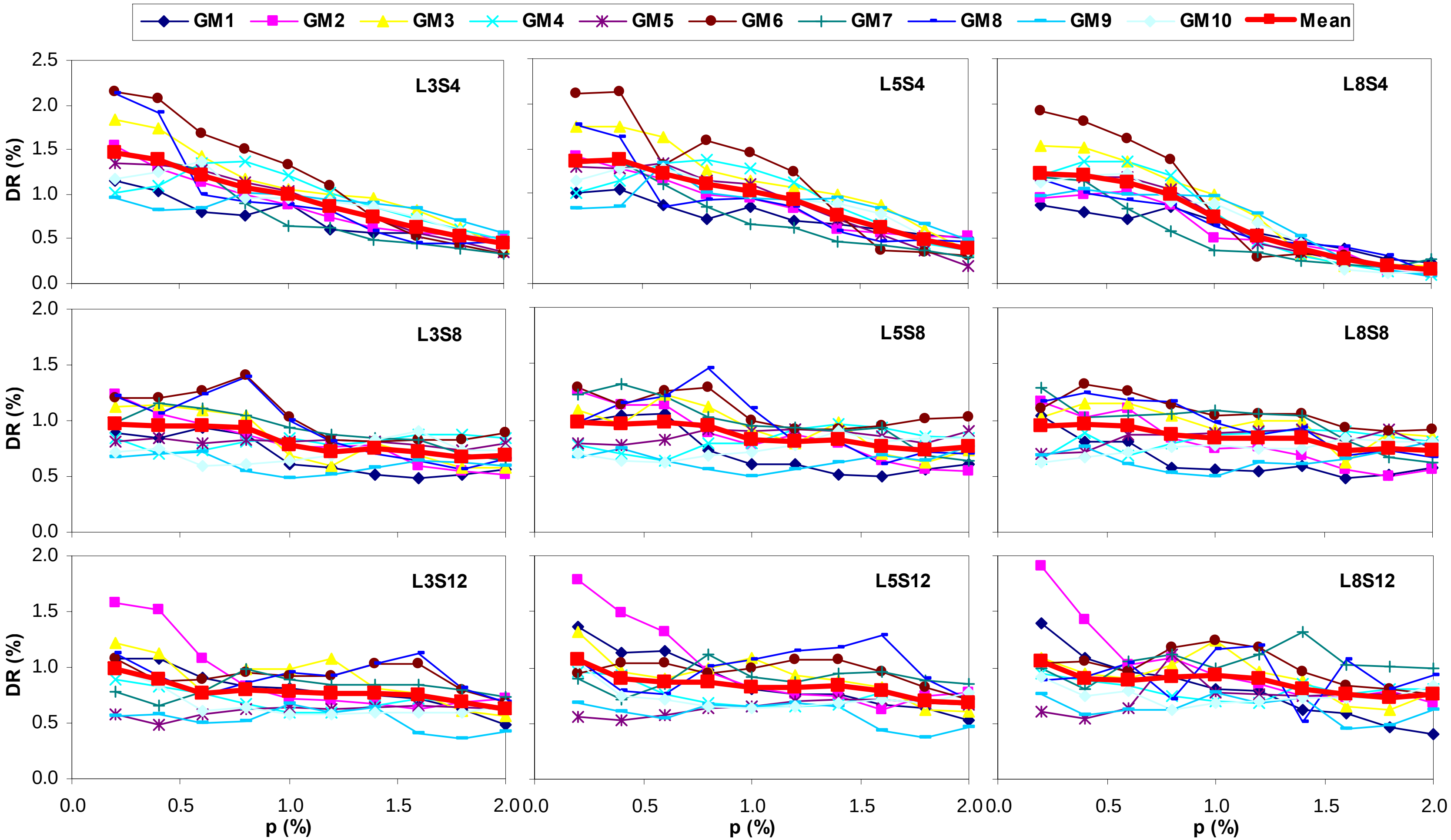

Figure 6.5 Variation of maximum roof drift with wall index and number of stories

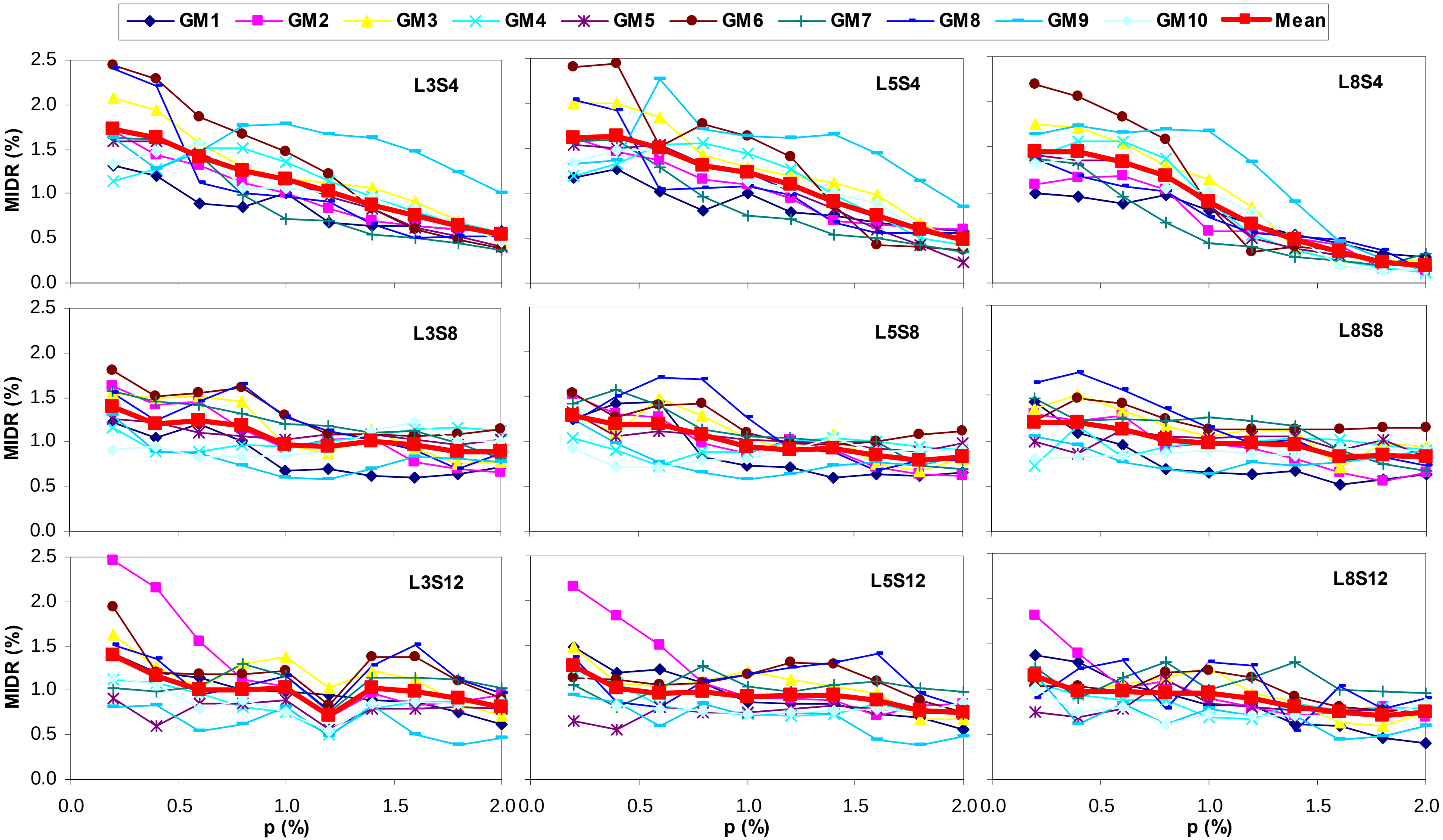

Figure 6.6 Variation of maximum interstory drift ratio with wall index and number of stories

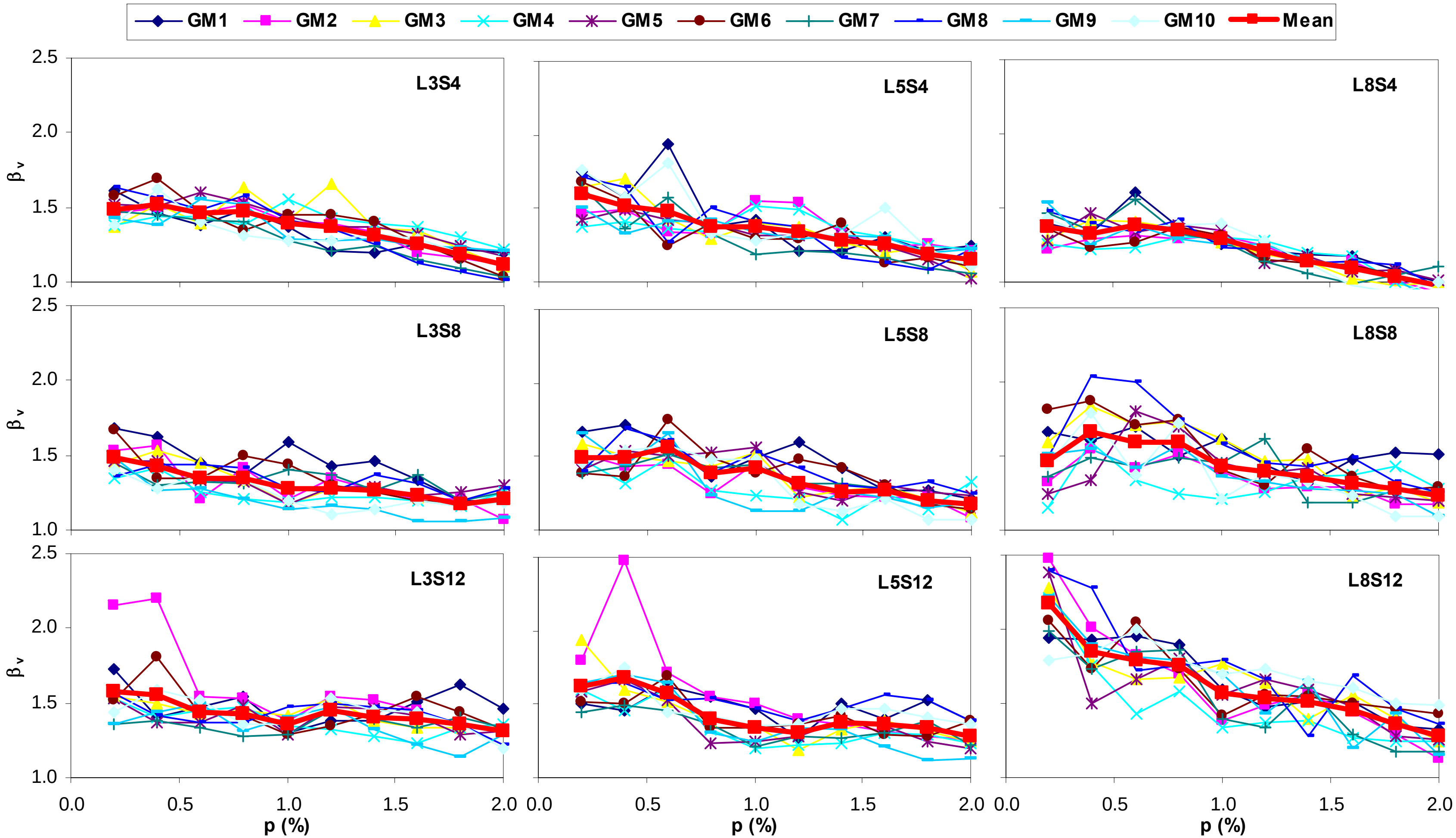

Figure 6.7 Variation of base shear amplification factor (β_v) with wall index and number of stories

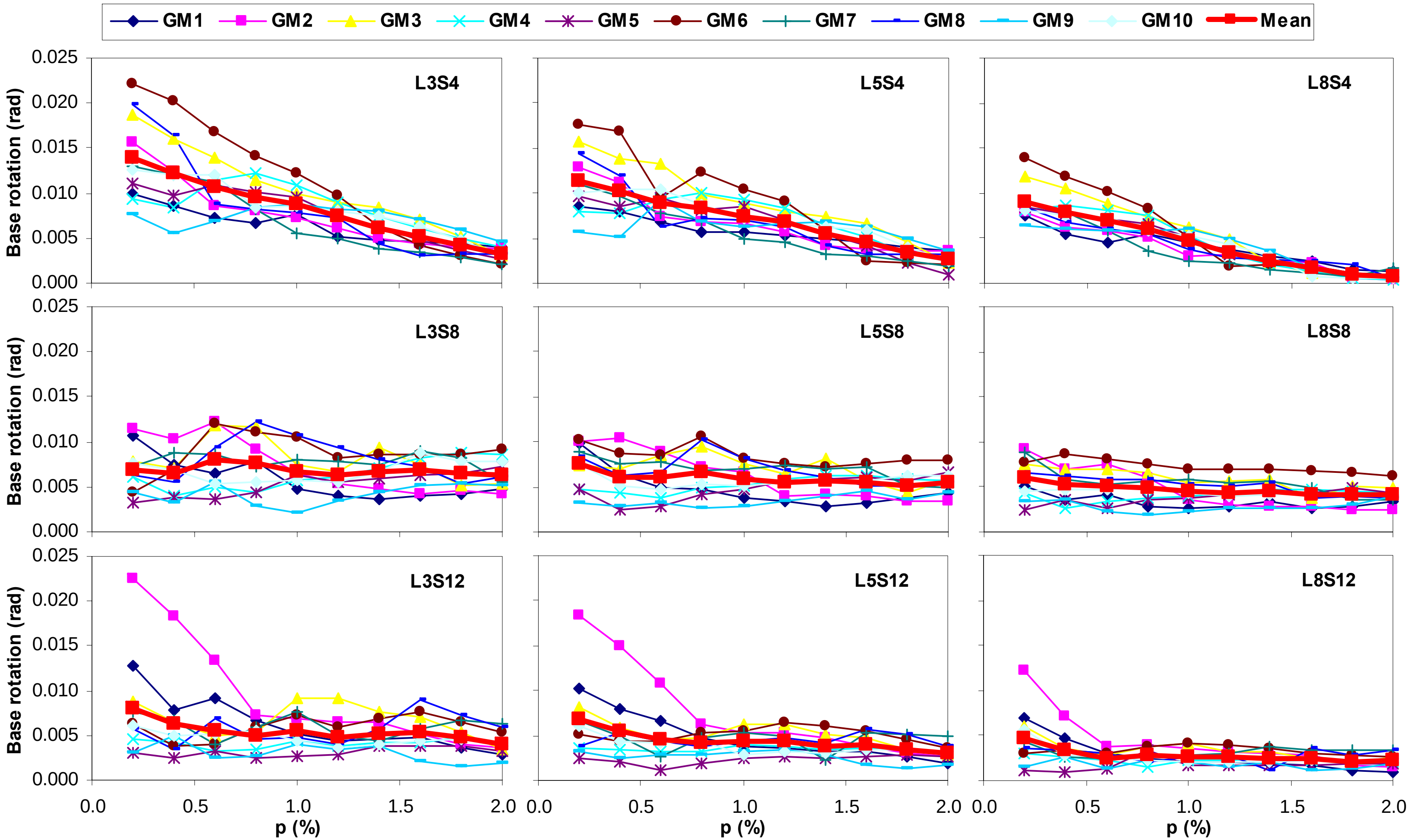

Figure 6.8 Maximum plastic rotation calculated at the base of the wall

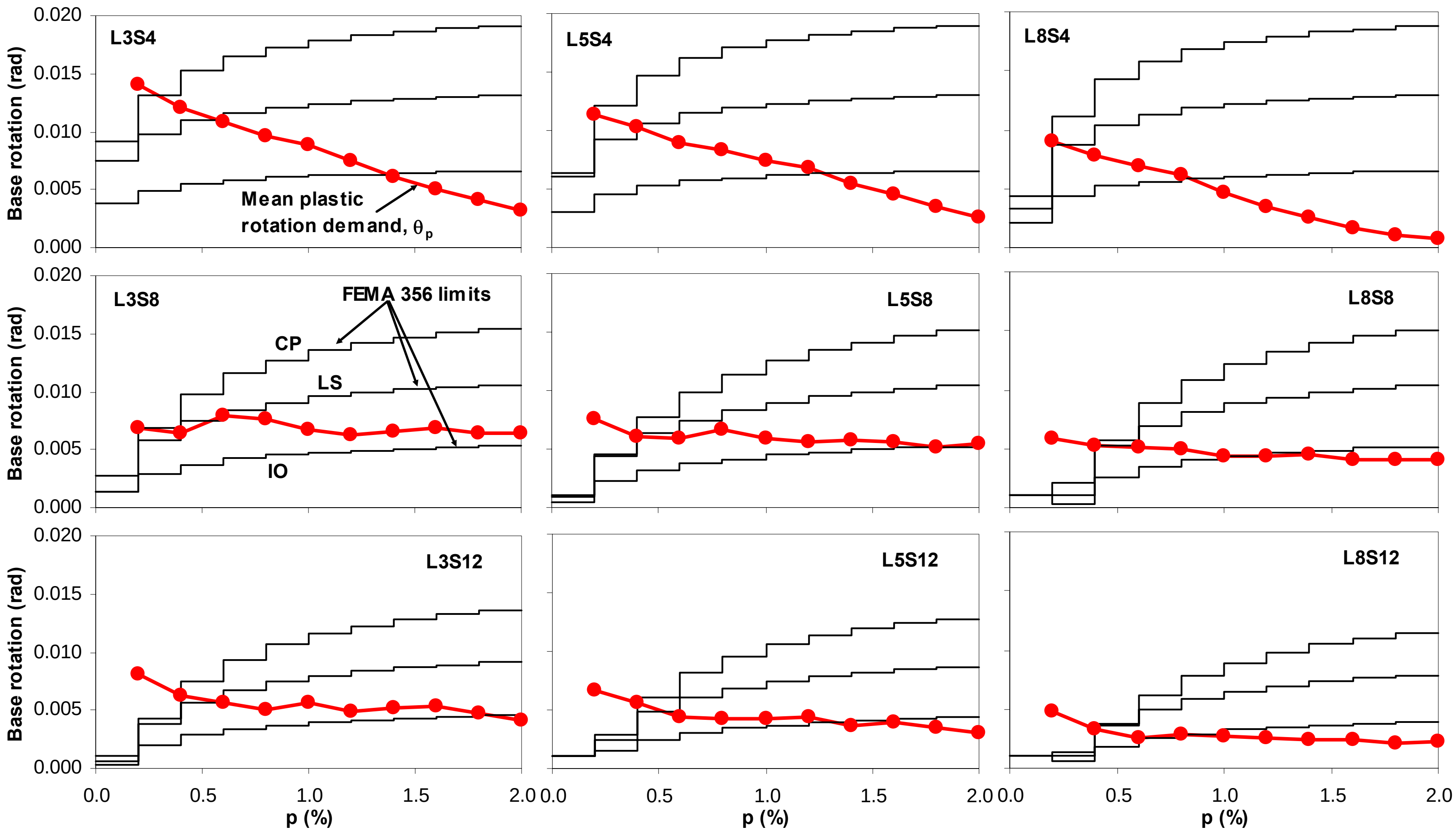

Figure 6.9 Comparison of mean base rotation demand at the wall base with FEMA 356 performance limits

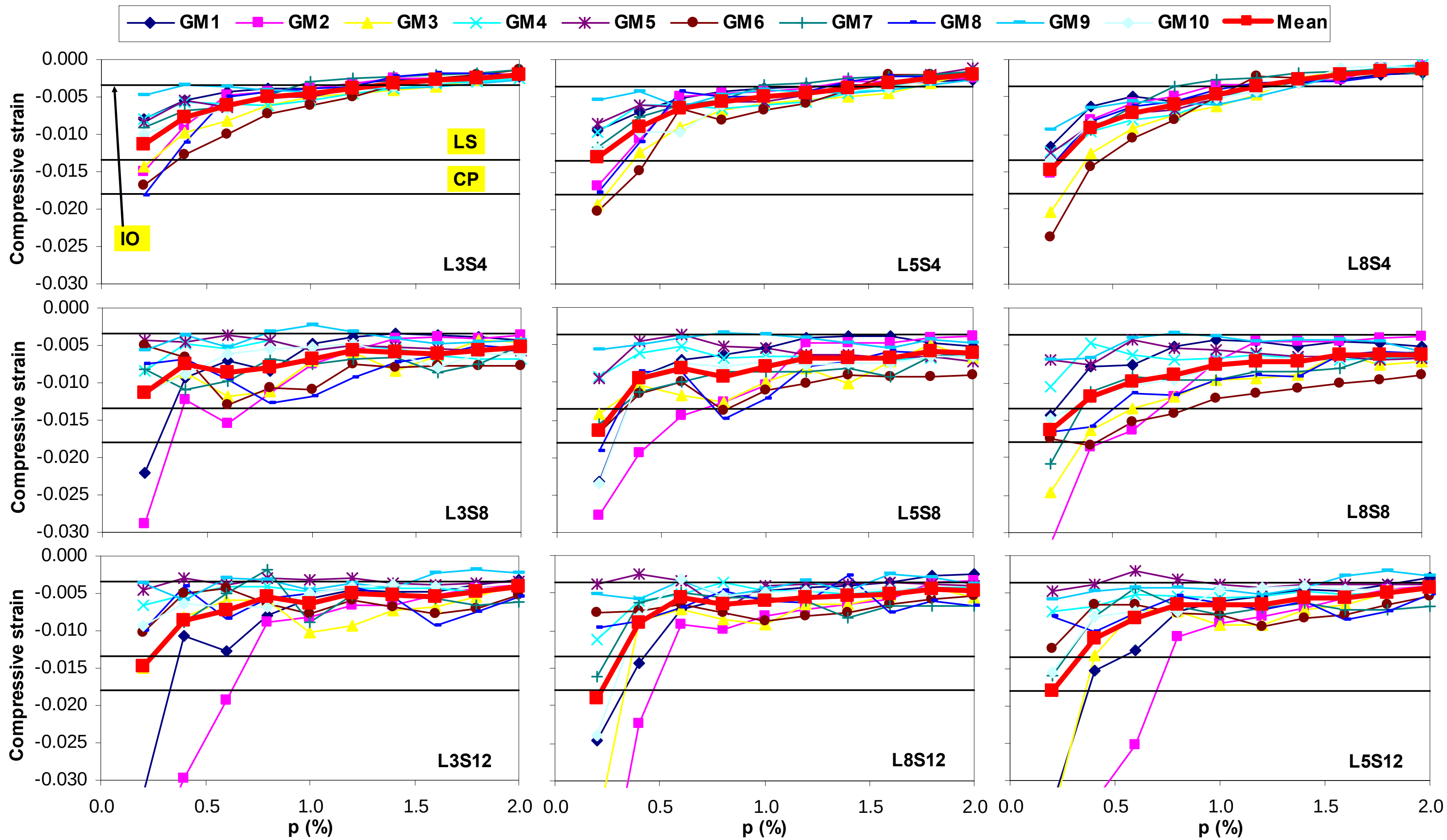

Figure 6.10 Maximum compressive strain at the base section and TSC 2007 strain limits

6.3 DYNAMIC AMPLIFICATION FACTOR

The code equivalent triangular lateral load pattern that represents the distribution of inertia forces along the building height locates the center of inertial forces at approximately $h_{eff} = 0.7H_w$ above the base. Thereafter, the formation of the plastic hinge at the base of the wall, introduces the contribution of higher modes of vibration, and the centroid of inertia forces over the height of the building may be in a significantly lower elevation than that predicted by the conventional static analysis method. The dynamic amplification factor is introduced into the design of structural walls to take into account this excess shear resulting from higher mode effects. It is known from structural dynamics that the contribution of higher modes to shear will increase as the number of stories increases. Depending on this argument Paulay and Priestley (1992) stated that the contribution of higher modes to shear will increase as the fundamental period of the structure increases since the period is proportional to the number of stories. The fundamental mechanism behind the shear amplification resulting from higher mode effects is the hinging of the wall base. This means that the criteria to be considered in the assessing the order of amplification should be associated with the level of nonlinearity in the systems. This in turn makes the force or strength reduction factor (R) as the most important variable in investigating dynamic amplification.

Earthquake resistant design codes employ expressions and constants to account the for the dynamic shear amplification in the design of walls. New Zealand 3101 (Standards New Zealand 2006) is one of the earliest codes that have included empirical amplifiers for wall shear. The expression for the dynamic shear amplification is given as

$$\beta_v = 0.9 + N/10 \tag{6.2a}$$

for buildings up to six stories, and

$$\beta_v = 1.3 + N/30 \tag{6.2b}$$

for buildings over six stories, where N is the number of stories. Eq. (6.2b) is valid for N<15 and the limiting value of amplification factor is given as $\beta_v < 1.8$.

Eurocode 8 adopts the equation initially proposed by Keintzel (1990)

$$\varepsilon = q\sqrt{\left(\frac{\gamma_{Rd}}{q}\cdot\frac{M_{Rd}}{M_{Ed}}\right)^2 + 0.1\cdot\left(\frac{S_e(T_c)}{S_e(T_1)}\right)^2} \le q \qquad (6.3)$$

wherein γ_{Rd} = 1.2 is a factor to account for overstrength due to steel strain-hardening, M_{Rd} is the design flexural resistance at the base of the wall and M_{Ed} the corresponding moment from analysis, T_1 is the fundamental period of vibration of the building, T_c is the upper limit period of the constant spectral acceleration region of the EC8 spectrum, and $S_e(T)$ is the ordinate of the elastic response spectrum. The equation is intended to account for the effects of both overstrength due to the development of a single plastic hinge at the base and higher modes (second term within the square root). The design envelope of shear forces is given in Figure 6.10.

TSC 2007 adopts a constant value for the dynamic amplification factor, β_v = 1.5.

Ghosh (1992) suggested the following equation giving the maximum dynamic base shear in isolated walls subjected to seismic excitation that is represented with the 1940 El Centro NS record (this record exhibited a peak ground acceleration of 0.33g)

$$V_{\max} = 0.25W\ddot{x}_{g\max}/g + M_y/0.67H_w \qquad (6.4)$$

where W is the total weight and $\ddot{x}_{g\max}$ is the peak ground acceleration.

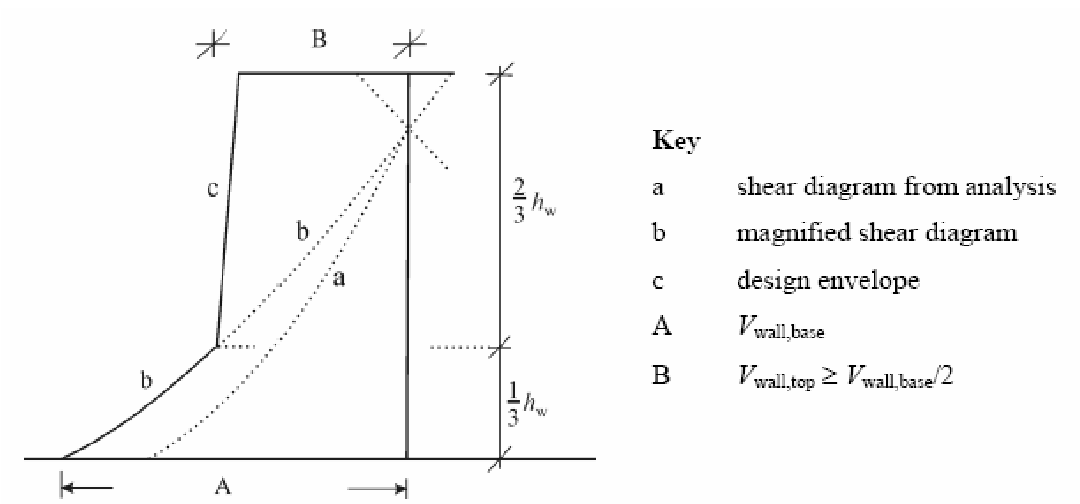

Figure 6.11 Design envelope of the shear forces in the walls of a dual system in EC8

Using the analysis results a new expression for the calculation of dynamic shear amplification is proposed. The calculated mean amplification factors at the base of wall are plotted as a function of wall index (p), strength reduction factor (R) and number of stories (N) in Figure 6.12. As seen in the figure, all of the parameters display a certain level of correlation with the dynamic amplification factor. As the number of stories and strength reduction factor increase, the amplification factors increase as well. Wall index is inversely proportional with amplification factor. At first sight it is considered that all three parameters influence the dynamic amplification. However, when the relation between the wall index (p) is plotted against the strength reduction factor (R) as in Figure 6.13 it is understood that the increased wall index leads to lower strength reduction factors as discussed in Section 6.2. These two parameters are the one and same in this study. So wall index is not a true parameter and may be ignored.

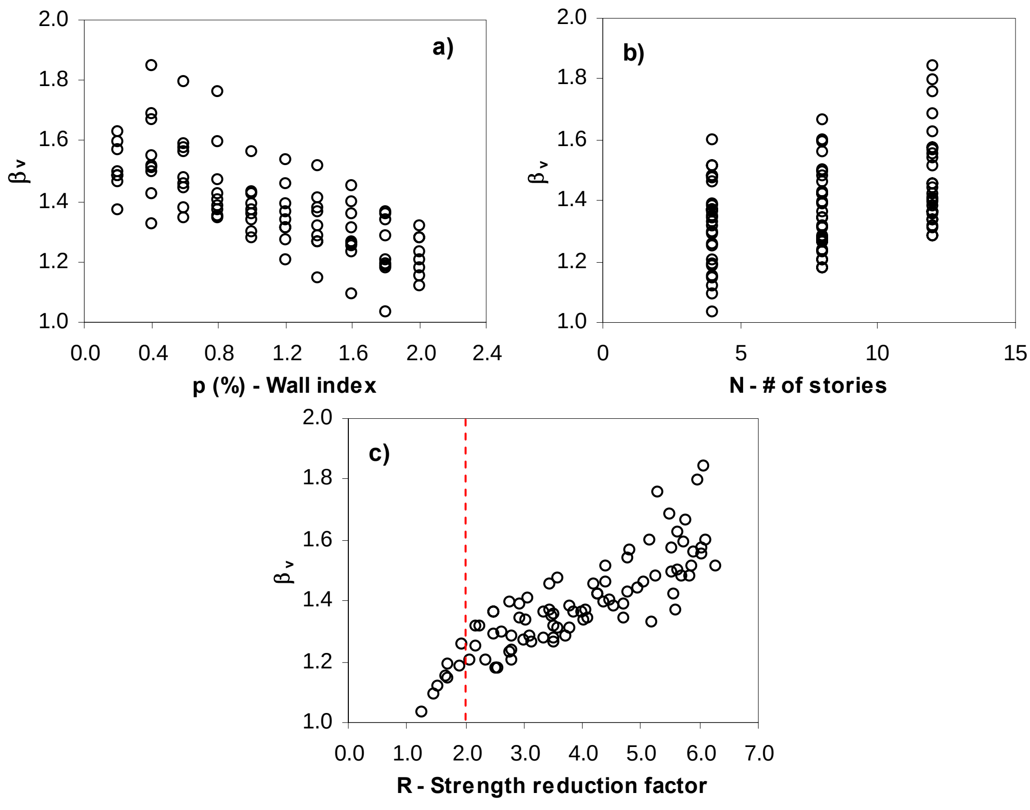

Figure 6.12 Variation of dynamic amplification factor with a) wall index, b) number of stories, c) strength reduction factor

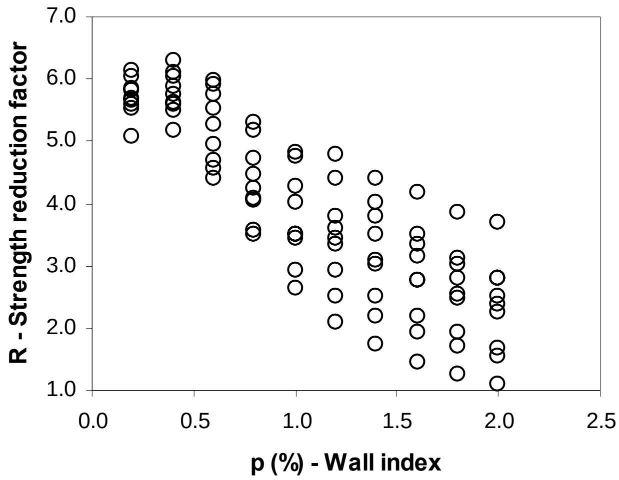

Figure 6.13 Relation between the strength reduction factor and wall index

A regression analysis is performed using the parameters R and N to estimate the β_v. Figure 6.12(c) suggests that the data must be investigated in two separate bins, because of the different linear trends observed on the left and right side of R=2 value. Using linear regression analysis method following expressions is proposed for the calculation of dynamic shear amplification factor

$$\beta_v = 0.95 + 0.01N + 0.1R \qquad \textit{for} \qquad R > 2 \tag{6.5a}$$

$$\beta_v = 1 + (R-1)(0.15 + 0.01N) \qquad \textit{for} \qquad R \leq 2 \tag{6.5b}$$

The comparison of predictions with the calculated amplification factors is plotted in Figure 6.14. The equation tells that the primary variable affecting the amplification factor is the expected level of nonlinearity in the system reflected by R. The number of stories or fundamental period is of secondary importance. Of course the regression analysis here cover number of stories up to 12 and structural period of 1.5 s at maximum. Beyond this limit the significance of these parameters may change, but we refrain from commenting on that.

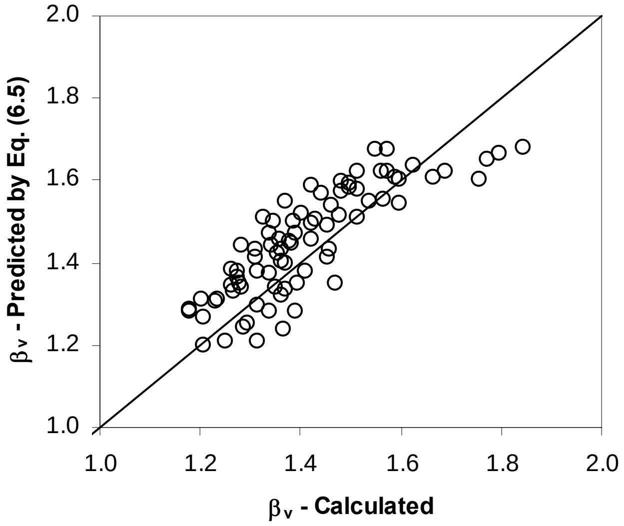

Figure 6.14 Comparison of predicted dynamic amplification factor by Eq. (6.5) with analysis results

CHAPTER 7

CONCLUSIONS AND RECOMMENDATIONS

7.1 SUMMARY

In this dissertation, seismic performance of structural walls has been investigated by evaluating the shortcomings of the existing seismic performance limits that are specified in certain codes as modeling and acceptance criteria for their seismic performance. The validity of strains over conventional drift and rotation limits in use of performance limits has been an area of focus. The seismic performance investigation of reinforced concrete structures requires certain level of accuracy and reliability in structural modeling and ground motion selection aspects, so these topics have been covered thoroughly in separate chapters. Verification of the finite element code used in the modeling and analysis of structural walls constitutes a significant tier of this study because reinforced concrete deformation limits can be only interrogated analytically if the utilized tool is able to estimate the actual strength and deformation capacity of reinforced concrete members accurately. In this work ANSYS finite element program has been used to analyze shear wall models. Realistic reduced finite element models of frame-wall structures have been developed to include structural interaction effects to the analysis process.

Results of several shear wall experiments conducted under dynamic, static cyclic and static monotonic loading conditions are used to establish the material and finite element aspects of nonlinear finite element analysis procedures. Calibration of concrete material model under different stress conditions, ranging from flexure to shear critical, is discussed in detail. The effect of solid finite element options, which is available in the ANSYS program, on the accuracy of calculated results is investigated by simulating the test results. Experimentally measured displacements, forces and strains are graphically compared with calculated values. The benchmark results are such that full confidence in the problem outputs is achieved.

The ground motions to be used as input in dynamic analysis have been selected from the four natural ground motion datasets that had been assembled by different researchers. Frequency content of ground motion is considered as the most significant parameter in selecting the ground motions. An existing and a newly developed ground motion intensity measures are used to identify the frequency content of the ground motion. The new spectral intensity measure is based on period elongation and area below the acceleration response spectrum. A/V ratio defined as the ratio of peak ground acceleration to velocity ratio is also used to describe the frequency content of the ground motion. The effect of frequency content on SDOF system deformation demands is analyzed using ground motion data sets classified according to A/V ratio. Ten out of 228 ground motions that conform to the frequency content of normal ground motions ($A/V \approx 8\ s^{-1}$) and yield code design spectrum compatible spectral shapes are selected for time history analyses.

The inadequacy of experimental setups used in the shear wall tests hinders the inclusion of 3D structural effects on the wall response. The actual loading conditions that develop during a dynamic event cannot be represented entirely either. An analytical framework that incorporates the selection of design parameters affecting wall response and accounts for significant interaction effects is developed to analyze structural walls in isolated form. Typically, finite element models of structural walls are discreticized with thousands of elements and nodes, so computationally efficient generic single wall-equivalent frame models reduced from real prototype frame-wall structure are required for use in finite element analyses. A straightforward design process based on linear shear-flexure beam continuum theory is developed. Derivation of an improved formulation for the shear-flexure beam model is presented.

While FEMA 356 relies on plastic rotations to be used as modeling parameters and numerical acceptance criteria for nonlinear procedures, TSC 2007 uses concrete and steel strains for the performance evaluation of reinforced concrete members. A parametric study including wall length, building height, axial load ratio, boundary element longitudinal reinforcement ratio as variables is conducted on model walls. Static analyses on isolated cantilever wall models are performed to determine the deformation limits of reinforced concrete conforming wall members in terms of drift, rotation and strains. Using the force-displacement responses obtained from analyses immediate occupancy, life safety and collapse prevention performance limits are determined. The FEMA 356 rotation limits and TSC 2007 strain limits are compared with the finite element analysis results. The limits defined in both documents are also crosschecked to examine the consistency among them. Expressions for drift and rotation are proposed to calculate the collapse prevention limit state. A thorough examination on the components of plastic hinge analysis is performed in parallel to investigation of performance limits. A discrete procedure is developed to establish the relation between the section responses obtained from experiments or equivalent methods and conventional section analysis. An expression is derived for the calculation of plastic hinge length. Reliance on simple calculations for strain is shown to produce false performance expectations.

Finally, the seismic performance of structural walls under different stress conditions represented with varying wall index (amount) in frame-wall systems is analyzed by performing nonlinear time history analysis. The generic frame-wall models is designed for strength reduction factor of R = 6. Ten design spectrum compatible ground motions are applied on each model. The deformation demands such as maximum roof drift and interstory drift ratio, base rotation and maximum compressive strain at the boundary element is compared with FEMA 356 and TSC 2007 performance limits. The dynamic amplification in the wall shear resulting form higher mode effects is investigated by comparing the seismic shear calculated at the base of wall during dynamic analysis with the one obtained from pushover analysis utilizing triangular lateral load pattern. A simple expression for the calculation of dynamic shear amplification is proposed.

7.2 CONCLUSIONS

The following conclusions in regards to seismic performance assessment of structural walls are reached on the basis of the results obtained in this study.

- Nonlinear finite element analysis procedures can be effectively used to calculate distinct response modes of shear walls ranging from flexure to shear dominated behavior. The deformation and strength characteristics of reinforced concrete structural walls can be calculated within reasonable accuracy. However, finite element programs, commercial or developed for research purposes, must be verified against benchmark problems as performed here for ANSYS code. The calibration of material models for each particular case is described in detail. The low order finite elements displaying shear locking behavior should be used with extensive care in regards to element options and mesh density in the model.

- The *frequency content* of a ground motion should be considered as an important parameter in the selection of ground motions to be used as input in nonlinear dynamic analysis. Two measures are used to determine the frequency content of a ground motion. A new spectral intensity measure (I_a) that is calculated as the area blow the acceleration response spectrum between the elastic fundamental period (T_i) and the elongated period (T_f) reflecting the effect of damage on the structure are found to correlate well with calculated seismic deformation demands. The second intensity measure is the A/V ratio. For the ground motions that has the same peak ground amplitude, the one that has lower A/V ratio found to be more destructive. It is also demonstrated that A/V ratio initially used to emphasize the effect of local soil conditions on the ground motion parameters also correlates well with the earthquake magnitude. Large earthquakes have lower A/V ratio reflecting the existence of low frequency wave components in the composition of the record. Most ground motions (design spectrum compatible) have A/V ratio of approximately 8 s^{-1}. Use of ground motions with low A/V ratio in time history analysis may cause overestimation of seismic demand. A/V is more useful in classifying ground motions data sets rather than selecting a single motion.

- A/V ratio may provide considerable insight in reducing discrepancies related to ground motion scaling based on peak ground amplitude parameters (PGA and PGV). If the ground motions classified in low, high and normal A/V ratio bins according to limits defined in this study are scaled to the same PGA, the highest deformation demands are obtained from low A/V ratio bin. If the scaling is done for the same PGV level, the highest deformation demands are obtained from high A/V ratio bin and lowest from the low A/V ratio bin. An interesting observation in regards to scaling of ground motions by peak ground amplitude values is that assuming the ground motions in a data set has narrow range of $(A/V)_{set}$ ratios, it does not matter whether the ground motions are scaled to same PGA or PGV level, similar mean deformation demands is obtained from both type scaling as far as the PGA/PGV ratio calculated using PGA and PGV values, for which the ground motions are scaled, yields an acceleration to velocity ratio in the same order of the data set's $(A/V)_{set}$ ratio. Factors that can be used to convert mean deformation demands among PGA and PGV based scaling procedures are derived as a function of A/V ratio of the data set and PGA/PGV ratio of the scaling.

- Derivation of a new shear-flexure beam formula introducing the two refinements into the otherwise well-known formulation for wall-frame systems is given. One is the correction of the shear force boundary condition at the base of the wall, and the other is the additional distributed moment transferred from link beam ends. The displacement, shear and moment profile along the wall calculated using the new formulation compares very favorably with finite element solutions.

- The methodology developed in this study for the parametric investigation of structural walls is one of the most comprehensive one available in the literature. Unlike the existing procedures utilizing simple isolated cantilever models, finite element models of generic frame-wall structures that can take into account structural interaction effects resulting from frames and link beams are developed. A design process is devised to calculate the required reinforcement at the boundary and web of walls.

- The plastic rotation limits given in FEMA 356 for conforming shear wall members controlled by flexure seem to yield very conservative estimations of structural performance. The existing plastic hinge rotation limits are in general lower than the limits found in this study in the order of two or more, especially for life safety and collapse prevention performance levels. The shear stress level (ν) and axial load ratio (P/P_o) that are used to calculate the plastic hinge rotation limits or to interpolate between the values effectively differentiates the deformation modes of structural walls. The proposed change to the limiting average shear stress value for flexural dominated response (increased from $0.25\sqrt{f_c}$ to $0.33\sqrt{f_c}$) by ASCE/SEI committee does not introduce a significant improvement to performance evaluation of the structural walls in this range. Instead of this change this study proposes to keep the shear stress limit as defined in FEMA 356 and increase the allowable plastic rotation for walls under low shear and normal stress (ν $< 0.25\sqrt{f_c}$ and $P/P_o < 0.1$). In this range walls has considerable plastic rotation capacity, 0.02 rad < θ_p < 0.06 rad.

- The calculated plastic hinge rotations display significant scatter above the lower limiting value of 0.02 radians for low shear stress conditions. It is seen that the scatter depends on the wall length. Although the shear stress incorporates the wall length in its calculation, it falls short in representing the deformation limits in case of low unit shear stress conditions. Walls with shorter length (slender walls) can exhibit very high plastic rotations in this range. So it may be proposed that in the low shear stress range the plastic hinge rotation performance limits should be based on slenderness of the wall.

- In the existing form the strain limits defined in TSC 2007 yield unconservative estimations for the performance assessment of structural walls. The local deformation demands obtained from finite element analysis is related to strains obtained from section analysis by means of base curvature. The compressive strains calculated at life safety and collapse prevention performance levels indicate strain values lower than specified in code nearly for all cases analyzed here. The limits defined in TSC 2007 are required to be adjusted for reinforced concrete rectangular walls. The actual compressive strains (finite element analysis results) are greater than the code specified limits.

- If the compressive strain limits in TSC 2007 are adapted to FEMA 356, under low to moderate stress conditions ($\nu < 0.50\sqrt{f_c}$) they take the values of 0.0035, 0.005 and 0.0075 for average upper bound limit of compressive strains at immediate occupancy, life safety and collapse prevention performance levels, respectively. These results for walls would raise concern for columns and other critical members.

- The plastic hinge length can be taken as the half of the height of the region over which the plasticity spreads on the wall ($L_p = 0.5L_{pz}$). As the wall length increases the spread of plasticity along the wall increases as well. As the shear stress increases the length of plastic zone decreases. The data reveals that plastic hinge length is mainly a function of wall length but is not a constant percentage of it (such as $L_p = 0.5L_w$) as assumed by many codes and reported by other research. The proposed Eq. (5.15) calculates the plastic hinge length within reasonable accuracy.

- Dynamic analysis results have demonstrated that when frame-wall systems resist lateral earthquake effects critical deformation demands may arise at the base of the walls for low wall index (ratio of total wall area to the floor area in plan) systems. In addition to the interaction between the frames and walls at story levels, the shear and moment transferred from link beams extending from frames directly to the ends of the walls can significantly change the moment profile causing a reduction in the inflection height of the wall and increase in the slope of the moment curve. The resulting high shear stress conditions at the lower stories lead to limited deformability of wall members. When walls are assessed according to limits defined in FEMA 356, it is seen that these walls can seldom survive the design earthquake without major damage. It is proposed that in the design of dual systems where frames and walls are connected by link beams, the minimum value of wall index should be 0.5%. Above p = 0.5% nearly all walls in all systems assure at least life safety (LS) performance state.

- The increased wall index leads to reduction in the top story and interstory displacement demands. The calculated roof drifts are in the order of 0.75-1.25%. However, the actual reduction effect of increased wall area is observed on the dispersion of the deformation demands. As the wall amount in the system increases the dispersion in the calculated roof drift due to ground motion uncertainty decreases considerably.

- It is found that the dynamic amplification of shear forces along the height of the building is a function of expected level of nonlinearity and number of stories (N). Since the desired level of nonlinearity in structural systems is introduced at the design stage by force (or strength) reduction factor, R, an expression [Eq.(6.5)] using R and N as parameters is proposed to calculate the dynamic amplification factor.

- In frame-wall structures the actual strength of the system after the code minimum reinforcement requirements has been provided may be larger than initial strength assignment. The strength assignment based on linear analysis with elastic member stiffness should be avoided in such cases since wall stiffness is much larger than the sum of column stiffnesses. A pushover analysis is required to determine the actual distribution of forces among each primary component for design verification.

7.3 RECOMMENDATIONS FOR FUTURE STUDIES

- This study focus on the investigation of deformation limits of conforming reinforced concrete shear wall members. The same methodology should be applied for the investigation nonconforming members. The parameter set used in the modeling of shear walls can be extended to investigate the influence other parameters as well.

- An extension can be made to investigation of framed-walls (barbell shape) and irregular shaped walls (T-, U-, H-shaped walls). This is important for walls where shear center location is strain-level dependent.
- Torsional effects have been disregarded in this study. The experimental studies investigating the torsional behavior of reinforced concrete shear walls are also very rare. Since the finite element and material models are also calibrated for shear critical conditions, the effect of torsion on the deformation capacity should be investigated.
- The modified shear-flexure beam formulation can be developed further to calculate the simple capacity curves of frame-wall systems. The results have shown that the significant stages in the frame-wall system response are the hinging of the wall base, yielding of beams framing to wall and the yielding of the frame. Characterizing each stage as a point on the capacity curve, the formulation can be adjusted by developing relevant mathematical models of these stages to calculate three or four point pushover curve. The procedure can be very useful in quick earthquake loss estimation procedures where total or inter-story drift are needed.

REFERENCES

ACI 318-08, 2008, "Building Code Requirements for Structural Concrete and Commentary", American Concrete Institute, Detroit, Michigan.

Akiyama H., 1987, "Earthquake-Resistant Limit-State Design for Buildings", University of Tokyo Press, Tokyo.

Akkar S. and Gülkan P., 2002, "A critical examination of near-field accelerograms from the sea of Marmara region earthquakes", Bulletin of the Seismological Society of America, Vol. 92, No. 1, pp. 428-447.

Akkar S., Sucuoğlu H. and Yakut A., 2005, "Displacement-based fragility functions for low- and mid-rise ordinary concrete buildings", Earthquake Spectra, Vol. 21, No. 4, pp. 901-927.

Akkar S., Yazgan U. and Gülkan, P., 2005, "Drift estimates in frame buildings subjected to near-fault ground motions", ASCE Journal of Structural Engineering, Vol. 131, No. 7.

Akkar S. and Özen Ö., 2005, "Effect of peak ground velocity on deformation demands for SDOF systems", Earthquake Engineering and Structural Dynamics, Vol. 34, pp. 151-1571.

Akkar S. and Bommer J.J., 2007a, "Empirical prediction equations for peak ground velocity derived from strong-motion records from Europe and the Middle East", Bulletin of the Seismological Society of America, Vol. 97, No. 2, pp. 511-530.

Akkar S. and Bommer J.J., 2007b, "Prediction of elastic displacement response spectra in Europe and the Middle East", Earthquake Engineering and Structural Dynamics, Vol. 36, pp. 1275-1301.

Ali A. and Wight J.K., 1991, "RC structural walls with staggered door openings", ASCE Journal of Structural Engineering, Vol. 117, No. 5, pp. 1514–1531.

Amaris A., 2002, "Dynamic amplification of seismic moments and shear forces in cantilever walls", Msc. Thesis, Rose School, Italy.

Ambraseys N.N., Douglas J., Rinaldis D., Berge-Thierry C., Suhadolc P., Costa G., Sigbjörnsson R. and Smit P., 2004, "Dissemination of European strong-motion data", Vol.

2, CD-ROM Collection, Engineering and Physical Sciences Research Council, United Kingdom.

Anderson J.C. and Bertero V.V., 1987, “Uncertainties in establishing design earthquakes”, ASCE Journal of Structural Engineering, Vol. 113, No. 8, pp. 1709-1724.

ANSYS R11.0. Swanson Analyses System. 2007.

ASCE-ACI Committee 445 on shear and Torsion, 1998, “Recent approaches to shear design of structural concrete”, ASCE Journal of Structural Engineering, Vol. 124, pp. 1375-1417.

ASCE-ACI Committee 447, 1982, “State-of-the-art report on finite element analysis of reinforced concrete”, ASCE, Reston, Virginia.

ASCE-ACI Committee 447, 1993, “Finite element analysis of reinforced concrete structures II”, by Jeremy Isenberg, (editor), Proceedings of the International Workshop held in New York City, New York, June 2-5, 1991.

ASCE/SEI 41-06, 2006, “Seismic rehabilitation of existing buildings”, American Society of Civil Engineers, Reston, Virginia.

ASCE/SEI 41 update, 2007, “Update to ASCE/SEI 41 Concrete Provisions”, Earthquake Spectra, Vol. 23, No. 3, pp. 493-523.

Aschheim M.A., 2002, “Seismic design based on the yield displacement”, Earthquake Spectra, Vol. 18ö No. 4, pp. 581-600.

ATC 40, 1996, “Seismic evaluation and retrofit of existing concrete buildings”, Applied Technology Council (ATC), Redwood City, California.

ASTM, 1999, “A615/A615M-96a: Standard specifications for deformed and plain billet-steel bars for concrete reinforcement”, Annual Book of ASTM Standards, ASTM international, Philadelphia.

Atkinson G.M. and Silva W., 2000, “Stochastic modeling of California ground motions”, Bulletin of the Seismological Society of America, Vol. 90, pp. 221 - 243.

Ayoub A and Filippou F.C., 1998, “Non-linear finite-element analysis of RC shear panels and walls”, ASCE Journal of Structural. Engineering, Vol. 124, No. 3, pp. 298-307.

Baker J.W. and Cornell C.A., 2005, “A vector valued ground motion intensity measure consisting of spectral acceleration and epsilon”, Earthquake Engineering and Structural Dynamics, Vol. 34, pp. 1193-1217.

Baker J.W. and Cornell C.A., 2006, “Spectral shape, epsilon and record selection”, Earthquake Engineering and Structural Dynamics, Vol. 35, pp. 1077-1095.

Balkaya C. and Kalkan E., 2003, "Estimation of fundamental periods of shear-wall dominant building structures", Earthquake Engineering and Structural Dynamics, Vol. 3, No. 7, pp. 985-998.

Balkaya C. and Kalkan E., 2004, "Seismic vulnerability, behavior and design of tunnel form building structures", Engineering Structures, Vol. 26, pp. 2081-2099.

Barbosa A.F. and Ribeiro G.A., 1998, "Analysis of reinforced concrete structures using ANSYS concrete model", In: Idelshon S, Onate E, Dvorkin E editors, Computational Mechanics, New Trends and Applications, Barcelona, Spain.

Barda F., Hanson J.M. and Corley W.G., 1977, "Shear strength of low-rise walls with boundary elements", Reinforced Concrete Structures in seismic zones, ACI SP-53, Detroit, Michigan, pp. 149-202.

Basham P.W., Weichert D.H., Anglin F.M. and Berry M.J., 1985, "New probabilistic strong seismic ground motion maps of Canada", Bulletin of the Seismological Society of America, Vol. 75, No. 2, 563-595.

Bazant Z.P., 1989, "Identification of strain-softening constitutive relation from uniaxial tests by series coupling model for localization", Cement and Concrete Research, Vol. 19, No. 6, pp. 973-977.

Belarbi A. and Hsu T.T.C., 1994, "Constitutive laws of concrete in tension and reinforcing bar stiffened by concrete", ACI Structural Journal, Vol. 91, No. 4, pp. 465-474.

Belarbi A. and Hsu T.T.C., 1995, "Constitutive laws of softened concrete in biaxial tension compression", ACI Structural Journal, Vol. 92, pp. 562-73.

Bentz E.C., 2005, "Explaining the riddle of tension stiffening models for shear panel experiments", ASCE Journal of Structural Engineering, Vol. 131, No. 9, pp. 1422-1425.

Berry M.P. and Eberhard M.O., 2005, "Practical performance model for bar buckling", ASCE Journal of Structural Engineering, Vol. 131, No. 7, pp. 1060-1070.

Binici B., 2003, "Punching shear strengthening of reinforced concrete slabs using fiber reinforced polymers", Ph.D. Dissertation, The University of Texas at Austin.

Blume J.A., 1968, "Dynamic characteristics of multi-story buildings", ASCE Journal of Structural Division, Vol. 94, No. 2, pp. 377-402.

Bommer J.J. and Acevedo A.B., 2004, "The use of real earthquake accelerograms as input to dynamic analysis", Journal of Earthquake Engineering, Vol. 8, Special Issue 1, pp.43-91.

Bommer J.J. and Pinho R. (2006). Adapting earthquake actions in Eurocode 8 for performance-based seismic design, Earthquake Engineering and Structural Dynamics, Vol. 35, 39–55.

Boore D.M. and Joyner W.B., 1997, "Site amplifications for generic rock sites", Bulletin of the Seismological Society of America, Vol. 98, No. 2, pp. 327-341.

Boore D.M. and Atkinson G.M., 2008, "Ground-motion prediction equations for the average horizontal component of PGA, PGV and 5%-damped PSA at spectral periods between 0.01 s and 10.0 s", Earthquake Spectra, Vol. 24, pp. 99-138.

Broderick B.M., Elnashai A.S. and Izzuddin B.A., 1994, "Observations on the effect of numerical dissipation on the nonlinear dynamic response of structural systems", Engineering Structures, Vol. 16, No. 1, pp. 51-62.

Brun M., Reynouard J.M. and Jezequel L., 2003, "A simple shear wall model taking into account stiffness degradation", Engineering Structures, Vol. 25, No. 1, pp. 1-9.

Carballo J.E. and Cornell C.A., 2000, "Probabilistic seismic demand analysis: spectrum matching and design", Report No. RMS-41, Department of Civil and Environmental Engineering, Stanford University.

Cardenas A.E., Russell H.G., and Corley W.G., 1980, "Strength of low-rise structural walls", in Reinforced Concrete Structures Subjected to Wind and Earthquake Forces, ACI Publication SP-63, pp. 221-241.

Carvajal O. and Pollner E., 1983, "Muros de concreto reforzados con armadura minima", Boletin Técnico Imme, Vol. 21, No 72-73.

Comite´ Euro-International Du Beton (CEB), 1996, "RC elements under cyclic loading-state of the art report", London.

CEB Bulletin d'Inlformation No. 236, 1997, "Seismic design of reinforced concrete structures for controlled inelastic response: recent advances in design concepts and codes", Comite Euro-International du Beton, Lausanne, Switzerland.

Celep U. and Aydinoglu M.N., 2007, "Dynamic shear amplification of cantilever wall systems", Sixth National Conference on Earthquake Engineering, 16-20 October 2007, Istanbul, Turkey (in Turkish).

Červenka J., Bažant Z.P. and Wierer M., 2005, "Equivalent localization element for crack band approach to mesh-sensitivity in microplane model", International Journal of Numerical Methods in Engineering, Vol. 62, pp. 700-726.

Cervenka V., 1970, "Inelastic finite element analyses of reinforced concrete panels", Ph.D. Dissertation, University of Colorado, Department of Civil Engineering, Boulder.

Cervenka V. and Gerstle K.H., 1972, "Inelastic analyses of reinforced concrete panels: experimental verification and applications", Intl. Assoc. Bridge Struct. Eng. Proc., Vol. 32, No. 2, pp. 25-39.

Chansawat K., 2003, "Nonlinear finite element analysis of reinforced concrete structures strengthened with FRP Laminates", Ph.D. Dissertation, Oregon State University.

Chansawat K., Yim S.C.S. and Miller T.H., 2006, “Nonlinear finite element analysis of a FRP-strengthened reinforced concrete bridge”, ASCE Journal of Bridge Engineering, Vol. 11, No. 1, pp. 21-32.

Charney F.A. and Bertero V.V., 1982, “An evaluation of the design and analytical seismic response of a seven-story reinforced concrete frame-wall structure”, UCB/EERC-82/08, Earthquake Engineering Research Center, University of California, Berkeley, 196 p.

Chen W.F., 1982, “Plasticity in reinforced concrete”, McGraw-Hill Book Co., New York.

Choi Y. and Stewart J.P., 2005, “Nonlinear site amplification as function of 30 m shear wave velocity”, Earthquake Spectra, Vol. 21, No. 1, pp. 1-30.

Chopra A., 2000, “Dynamics of structures: theory and application to earthquake engineering”, Prentice-Hall, 2nd edition.

Chung J. and Hulbert G.M., 1993, “A time integration algorithm for structural dynamics with improved numerical dissipation: The Generalized-α Method”, Journal of Applied Mechanics, Vol. 60, pp. 371.

Clough R.W. and Penzien J., 1993, “Dynamics of Structures”, McGraw-Hill, New York.

Collins M.P. and Mitchell D., 1980, “Shear and Torsion design of prestressed and non-prestressed concrete beams”, Journal of Prestressed Concrete Institute, Vol. 25, No. 5, pp. 32-100.

Colotti V., 1993, “Shear behavior of RC structural walls”, ASCE Journal of Structural Engineering, Vol. 119, No. 3, pp. 728-746,

Combescure D., 2002, “IAEA CRP-NFE Camus Benchmark: Experimental results and specifications to the participants”, Rapport DM2S. SEMT/EMSI/RT/02-047/A.

Cook R.D., Malkus D.S., Plesha M.E. and Witt R.J., 2001, “Concepts and applications of finite element analysis”, Fourth Edition, John Wiley and Sons, New York.

Cordova P.P., Deierlein G.G., Mehanny S.S.F. and Cornell C.A., 2000, “Development of a two-parameter seismic intensity measure and probabilistic assessment procedure”, The 2nd U.S.-Japan Workshop on Performance-Based Earthquake Engineering, PEER Report 2000 / 10, Hokkaido/Japan, pp. 195-214.

Corley W.G., Fiorato A.E. and Oesterle R.G., 1981, “Structural walls”, ACI SP 72-4, ACI, Detroit, Michigan, pp. 77–131.

Coull A., 1973, Discussion of "Approximate Analysis of tall wall-frame structures", ASCE Journal of Structural Division, Vol. 99, No. 11, pp. 2326.

Dazio A., Beyer K. and Bachmann H., 2009, “Quasi-static cyclic tests and plastic hinge analysis of RC structural walls”, Engineering Structures, Vol. 31, No. 7, pp. 1556-1571.

Derecho A.T., Ghosh S.K., Iqbal M., Freskakis G.N. and Fintel M., 1978a, “Structural walls in earthquake resistant buildings - Dynamic analyses of isolated structural walls - DEVELOPMENT OF DESIGN PROCEDURE –DESIGN FORCE LEVELS”, Report to the National Science Foundation, RANN, under Grant No. ENV74-14766, Portland Cement Association.

Derecho A.T., Ghosh S.K., Iqbal M., Freskakis G.N. and Fintel M., 1978b, “Structural walls in earthquake resistant buildings - Dynamic analyses of isolated structural walls - PARAMETRIC STUDIES”, Report to the National Science Foundation, RANN, under Grant No. ENV74-14766, Portland Cement Association.

Derecho A. and Corley W., 1984, “Design requirements for structural walls in multistory buildings”, Proceedings of Eigth World Conference on Earthquake Engineering, San Francisco, California, July, pp. 541-548.

Dhakal R.P. and Maekawa K., 2002, “Modeling for postyield buckling of reinforcement. ASCE Journal of Structural Engineering, Vol. 128, No. 9, pp. 1139-1147.

Drucker D.C. and Prager W., 1952, “Soil mechanics and plastic analysis or limit design”, Q. Appl. Math., Vol. 10, No. 2, pp. 157-65.

Duffey T.A., Farrar C.R., Goldman A., 1994, “Low-rise shear wall ultimate drift limits”, Earthquake Spectra, Vol. 10, pp. 655-74.

EERI/PEER, 2006, “New information on the seismic performance of existing concrete buildings”, Seminar Notes, EERC, Oakland, California.

Elmorsi M., Kianoush M.R. and Tso W.K., 1998, “Nonlinear analysis of cyclically loaded reinforced concrete structures” ACI Structural Journal, Vol. 95, No. 6, pp.725–739.

Emori K. and Schnobrich W.C., 1981, “Inelastic behavior of concrete frame-wall structures”, ASCE Journal of Structural Division, Vol. 107, No.1, pp. 145–164.

Eurocode 8, 1994, “Design provisions for earthquake resistance of structures, Part 1-1, 1-2 and 1-3”, CNE (Comite Europeen de Normalisation), European Pre-standard ENV 1998-1-1, 1-2, and 1-3, Bruxelles.

Farvashany F.E., Foster S.J., and Rangan, B.V., 2008, “Strength and deformation of high-strength concrete shearwalls”, ACI Structural Journal, Vol. 105, No. 1, pp. 21-29.

FEMA 273, 1997, “NEHRP Guidelines for the Seismic Rehabilitation of Buildings” Federal Emergency Management Agency Publication 273, Washington, D.C.

FEMA 306, 1999, “Evaluation of earthquake damaged concrete and masonry wall buildings-Basic Procedures manual”, Federal Emergency Management Agency, Washington, D.C.

FEMA 356, 2000, “NEHRP Guidelines for the seismic rehabilitation of buildings”, Federal Emergency Management Agency, Washington DC.

Franklin H.A., 1970, “Nonlinear analysis of reinforced concrete frames and panels”, Ph.D. dissertation, University of California, Berkeley, Department Civil Engineering, Rep. SESM 70-5.

Freeman S.A., Nicoletti J.P. and Tyrell J.V., 1975, “Evaluations of existing buildings for seismic risk - A case study of Puget Sound Naval Shipyard, Bremerton, Washington”, Proceedings of U.S. National Conference on Earthquake Engineering, Berkeley, U.S.A., pp. 113-122.

Ghobarah A., 2001, “Performance-based design in earthquake engineering: state of development”, Engineering Structures, Vol. 23, No. 8, pp. 878-884.

Ghosh S.K., 1992, "Required shear strength of earthquake-resistant reinforced concrete shearwalls", Nonlinear Seismic Analysis and Design of Reinforced Concrete Buildings, Elsevier Applied Science, London and New York.

Ghosh S.K. and Markevicius V.P., 1991, “Design of earthquake resistant shear walls to prevent shear failure”, Concrete Shear in Earthquake, (Proceedings of the International Workshop on Concrete Shear in Earthquake, Jan. 14-16, 1991, Houston), Elsevier Science Publishers, Inc., London-New York.

Gil-Martín L.M., Hernández-Montes H, Aschheim M. and Pantazopoulou S.J., 2008, “Approximate expressions for the simulated response of slender longitudinal reinforcement in monotonic compression”, Magazine of Concrete Research, Vol. 60, No. 6, pp. 391-397.

Goel R.K. and Chopra A.K., 1998, “Period formulas for concrete shear wall buildings, ASCE Journal of Structural Engineering, Vol. 124, No. 4, pp. 426-433.

Gupta B. and Kunnath S.K., 2000, “Adaptive specra-based pushover procedure for seismic evaluation of structures”, Earthquake Spectra, Vol. 16, pp.367-391.

Gülkan P. and Sözen M., 1974, “Inelastic responses of reinforced concrete structures to earthquakes motions”, Proceedings of the ACI, Vol. 71, No. 12, pp. 604-610.

Gülkan P. and Utkutuğ D., 2003, “Okul binalarının deprem güvenliği için minimum dizayn kriterleri”, Türkiye Mühendislik Haberleri, No. 425, pp. 13-22.

Hamburger R.O., 1997, “A framework for performance-based earthquake resistive design”, EERC-CUREe Symposium in Honor of Vitelmo V. Bertero, Berkeley, California.

Han D.J. and Chen W.F., 1988, “Plasticity for Structural Engineers”, Springer-Verlag, Virgina, USA.

Han S.W., Oh Y.H. and Lee L.H., 2002, “Seismic behavior of structural walls with specific details”, Magazine of Concrete Research, Vol. 54, No. 5, pp. 333–345

Heidebrecht A.C. and Stafford Smith B., 1973, "Approximate analyses of tall wall-frame structures." ASCE Journal of Structural Division, Vol. 99, No. 2, pp. 199-221.

Hemmaty Y., 1998, "Modeling of the shear force transferred between cracks in reinforced and fibre reinforced concrete structures", Proceedings of the ANSYS Conference, Vol. 1, Pittsburgh, Pennsylvania.

Hidalgo P.A., Ledezma C.A. and Jordan R.M., 2002, "Seismic behavior of squat reinforced concrete shear walls", Earthquake Spectra, Vol. 18, No. 2, pp. 287-308.

Hilber H.M., Hughes T.J.R. and Taylor R.L., 1977, "Improved numerical dissipation for time integration algorithm in structural dynamics", Earthquake Engineering and Structural Dynamics, Vol. 5, pp. 283.

Hines E.M., Restrepo J.I. and Seible F., 2004, "Force-displacement characterization of well-confined bridge piers", ACI Structural Journal, V. 101, No. 4, pp. 537-548.

Hofbeck J.A., Ibrahim I.O. and Mattock A.H., 1969, "Shear transfer in reinforced concrete", ACI Journal, Vol. 66, No. 2, pp. 119–128.

Hognestad E., 1951, "A study of combined bending and axial load in reinforced concrete members", Bulletin Series No. 399, Engineering Experiment Station, Urbana, USA: University of Illinois.

Housner G.W., 1959, "Behavior of structures during earthquakes", ASCE Journal of Engineering Mechanics Division, Vol. 85, No. 4, pp. 109-129.

Hsu T.T.C. and Zhu R.R.H., 2001, "Post yield behavior of reinforced concrete membrane elements – The Hsu/Zhu ratios", in Modeling of Inelastic Behavior of RC Structures Under Seismic Loads, By Pui-shum B. Shing, Tadaaki Tanabe, National Science Foundation (U.S.), Nihon, Published by ASCE Publications.

Hsu T.T.C. and Zhu R.R.H., 2002, "Softened membrane model for reinforced concrete elements in shear", ACI Structural Journal, Vol. 99, No. 4, pp.460-469.

Hudson D.E., 1979, "Reading and interpreting strong motion records", EERI, Berkeley,CA.

ICBO, 1997, "Uniform Building Code", International Conference of Building Officials, Whittier, California.

Iervolino I. and Cornell C.A., 2005, "Record selection for nonlinear seismic analysis of structures", Earthquake Spectra, Vol. 21, No. 3, pp. 685-713.

Iwan W.D., 1997, "The drift spectrum: a measure of demand for earthquake ground motions", ASCE Journal of Structural Engineering, Vol. 123, No. 4, pp. 397-404.

Jalayer F., 2003, "Direct probabilistic seismic analysis: Implementing non-linear dynamic assessments", Ph.D. Dissertation, Department of Civil and Environmental Engineering, Stanford University: Stanford, 244 p.

Jirasek M. and Bazant Z.P., 2001, “Inelastic analysis of structures”, Wiley.

Kabeyasawa T., Shiohara H., Otani S. and Aoyama, H., 1983, “Analysis of the full-scale seven-story reinforced concrete test structure”, Journal (B), The faculty of Engineering, University of Tokyo, Vol. 37, No. 2, pp. 432 - 478.

Kachlakev D.I., 2002, “Finite element analysis and model validation of shear deficient reinforced concrete beams strengthened with GFRP laminates”, Third International Conference on Composites in Infrastructure, San Francisco, California, paper 002.

Kadaş K., Yakut A. and Kazaz I., 2008, “Evaluation of spectral ground motion intensity parameters”, 8th International Congress on Advances in Civil Engineering, Eastern Mediterranean University, Famagusta, North Cyprus, 15-17 September.

Kadaş K., 2006, “Influence of idealized pushover curves on seismic response”, Master Thesis, Department of Civil Engineering, Middle East Technical University, Ankara, Turkey.

Kayal S., 1986, “Nonlinear interaction of RC frame-wall structure”, ASCE Journal of the Structural Division, Vo. 112, No. 5, pp. 1021-1035.

Kazaz I. and Yakut A., 2006, “Estimation of global displacement on the basis of spectral acceleration”, Seventh International Congress on Advances in Civil Engineering, Istanbul, Turkey, October 11-13.

Kazaz I., Yakut A. and Gülkan P., 2006a, “Numerical simulation of dynamic shear wall tests: A Benchmark Study”, Computers and Structures, Vol. 84, No. 8, pp. 549-562.

Kazaz I., Yakut A. and Gülkan P., 2006b, “Seismic response assessment of a stiff structure”, Earthquake Engineering and Structural Dynamics, Vol. 35, No. 6, pp. 737-759.

Keintzel E., 1990, “Seismic design shear forces in reinforced concrete cantilever shear wall structures”, European Journal of Earthquake Engineering, Vol. 3, pp. 7–16.

Khan F.R. and Sbarounis J.A., 1964, “Interaction of shear walls and frames”, Proceedings ASCE, Vol. 90, No. ST3, Part 1, pp. 285-335.

Kim T.W., 2004, “Performance assessment of reinforced concrete structural walls for seismic loads, Ph.D. thesis, University of Illinois at Urbana-Champaign, Illinois.

Kitada Y., Akino K., Terada K., Aoyama H., Miller A., 2000, “Report on seismic shear wall international standard problem organized by OECD/NEA/CSNI”.
http://www.nea.fr/html/nsd/docs/indexcsni.html (13.05.2006).

Kongoli X., Minami T. and Sakai Y., 1999, “Effects of structural walls on the elastic-plastic earthquake responses of frame-wall buildings”, Earthquake Engineering and Structural Dynamics, Vol. 28, No. 5, pp. 479-500.

Kotsovos M.D., Pavlovic M.N. and Lefas I.D., 1992, "Two-and three-dimensional nonlinear finite-element analysis of structural walls", Published in "Non-linear seismic analysis and design for reinforced concrete buildings" edited by P. Fajfar and H. Krawinkler, Elsevier Applied Science, pp. 521-528.

Kowalsky M.J, 2001, "RC structural walls designed according to UBC and displacement-based methods", ASCE Journal of Structural Engineering, Vol. 127, No. 5, pp. 506-516.

Kupfer H., Hilsdorf H.K., Rüsch H., 1969, "Behavior of concrete under biaxial stress", ACI Structural Journal, Vol. 66, No. 8, pp. 656-66.

Kwak H.G. and Kim D.Y., 2004a, "Material nonlinear analysis of RC shear walls subject to monotonic loadings", Engineering Structures, Vol. 26, pp. 1517–1533.

Kwak H.G. and Kim D.Y., 2004b, "Material nonlinear analysis of RC shear walls subject to cyclic loadings", Engineering Structures, Vol. 26, pp. 1423–1436.

Kwan W.P. and Billington S.L., 2001, "Simulation of structural concrete under cyclic load", ASCE Journal of Structural Engineering, Vol. 127, No. 12, pp.1391-1401.

Laible J.P., White R.N. and Gergely P., 1977, "Experimental investigation of seismic shear transfer across cracks in concrete nuclear containment vessels", ACI Special Publication 53, pp. 203-226.

Lee L.H., Chang K.K. and Chun Y.S., 2000, "Experimental formula for the fundamental period of RC buildings with shear-wall dominant systems", The Structural Design of Tall Buildings, Vol. 9, No. 4, pp. 295-307.

Lefas I.D., Kotsovos M.D. and Ambrasseys N.N., 1990, Behavior of RC structural walls: strength, deformation characteristics and failure mechanism", ACI Structural Journal, No. 87, No. 1, pp. 23-31.

Lefas I.D. and Kotsovos M.D., 1990, "NLFE analysis of RC structural walls", ASCE Journal of Structural Engineering, Vol. 116, No. 1, pp. 146-164.

Lertsrisakulrat T., Watanabe K., Matsuo M. and Niwa J., 2001, „Experimental study on parameters in localization of concrete subjected to compression", Journal of Materials, Concrete Structures, Pavements, JSCE, Vol. 50, No. 669, pp. 309-321

Lestuzzi P., Schwab P., Koller M. and Lacave C., 2004, "How to choose earthquake recordings for nonlinear seismic analyses of structures", 13th World Conference on Earthquake Engineering, Vancouver, B.C., Canada, paper no. 1241.

Li T., 2004, "Shear strengthening of unreinforced masonry (URM) walls with FRP composites", Ph.D. Dissertation, University of Missouri-Rolla.

Linde P., 1993, "Numerical modeling and capacity design of earthquake resistant reinforced concrete walls". Report no. 200 (Institute of Structural Engineering, Swiss Federal Institute of Technology, Zurich). Basel: Birkhauser.

Lowes L.N., 1999, “Finite element modeling of reinforced concrete beam-column bridge connections”, Ph.D. Dissertation, University of California, Berkeley.

Lu Y., 2002, “Seismic behavior of multistorey RC wall–frame system versus bare ductile frame system”, Earthquake Engineering and Structural Dynamics, Vol. 31, pp. 79–97.

Ma S.M., Bertero V.V. and Popov E.P., 1976, “Experimental and analytical studies on the hysteretic behavior of reinforce concrete rectangular and T-beams”, EERC Report 76-2, Earthquake Engineering Research Center, University of California, Berkeley.

MacGregor J.G., Majumdar S.N.G. Nikhed R.P. and Adams P.F., 1972, “Approximate inelastic analysis of shear wall-frame structures”, ASCE Journal of the Structural Division, Vol. 98, No. 11, pp. 2351-2361

Macleod I.A., 1971, “Shear wall-frame interaction: A design aid with commentary”, Portland Cement Association, Skokie, Illinois.

Maekawa K., Pimanmas A. and Okamura H., 2003, “Nonlinear mechanics of reinforced concrete”, Spon press, Newyork.

Maier J. and Thürlimann B., 1985, “Bruchversuche an Stahlbetonscheiben” IBK Bericht 8003-1. Zürich: ETH.

Malhotra P.K., 2002, “Cyclic-demand spectrum”, Earthquake Engineering and Structural Dynamics, Vol. 31, No. 7, pp. 1441-1457.

Malvar L.J. and Crawford J.E., 1998, “Dynamic increase factors for steel reinforcing bars”, Proceedings of the 28th DDESB Seminar, Orlando, Florida.

Mander J.B., Priestley M.J.N. and Park R., 1988, “Theoretical stress–strain model for confined concrete”, Journal of Structural Engineering, Vol. 114, No. 8, pp. 1804–1826.

Martirossyan A. and Xiao Y., 1996, “Seismic performance of high strength concrete columns”, USC Structural Engineering Research Program, Report No. USC-SERP-96/4.

Martínez-Rueda J.E., 1998, “Scaling procedure for natural accelerograms based on a system of spectrum intensity scales”, Earthquake Spectra, Vol. 14, No. 1, 135-152.

Martinez-Rueda J.E. and Elnashai A.S., 1997, “Confined concrete model under cyclic load”, Materials and Structures, Vol. 30, pp. 139-147.

Medina R. and Krawinkler H., 2003, “Seismic demands for non-deteriorating frame structures and their dependence on ground motions”, PEER Report 2003/15, University of California, Berkeley.

Meskouris K., Krätzig W.B. and Hanskötter U., 1992, “Seismic motion damage potential for R/C wall-stiffened buildings”, Nonlinear Seismic Analysis and Design of RC Buildings, Elsevier.

Miranda E., 1999, “Approximate lateral deformation demands in multistory buildings”, ASCE Journal of Structural Engineering, Vol. 125, No. 4, pp. 417–425.

Miranda E. and Reyes J.V., 2002, “Approximate lateral drift demands in multistory buildings with nonuniform stiffness”, ASCE Journal of Structural Engineering., Vol. 128, No. 7, pp. 840-849.

Miranda E. and Akkar S., 2006, “Generalized interstory drift demand spectrum”, ASCE Journal of Structural Engineering, Vol. 132, No. 6, pp. 840-852.

Mirmiran A., Zagers K., Yuan W., 2000, “Nonlinear finite element modeling of concrete confined by fiber composites”, Finite Elements in Analyses and Design, Vol. 3, pp. 79-96.

Mirza S.M. and Houde J., 1979, “Study of bond stress–slip relationships in reinforced concrete”, ACI Journal, Vol. 76, No. 1, pp.19–45.

Mohraz B., 1976, “A study of earthquake response spectra for different geological conditions”, Bulletin of the Seismological Society of America, Vol. 66, No. 3, 915 – 935.

Mohraz B., Hall W.J. and Newmark N.M., 1972, “A study of vertical and horizontal earthquake spectra”, Nathan M. Newmark Consulting Engineering Services, Urbana, Illinois (AEC Report WASH-1255).

Morgan B.J., Hiraishi H. and Corley W.G., 1986, “US-Japan quasi static test of isolated wall planar reinforced concrete structure”, PCA Report, Construction Technology Division, Skokie, Illinois, 111 pp.

Mwafy AM., 2000, “Seismic performance of code-designed RC buildings”, Ph.D. thesis, Imperial College, University of London.

Naeim F. and Lew M., 1995, “On the use of design spectrum compatible time histories”, Earthquake Spectra, Vol. 11, No. 1, 111-127.

Nau J.M. and Hall J., 1984, “Scaling methods for earthquake response spectra”, ASCE Journal of Structural Engineering, Vol. 110, No. 7, 1533-1548.

Newmark N.M. and Hall W.J., 1969, “Seismic design criteria for nuclear facilities”, Proc. of the Fourth World Conference on Earthquake Engineering, Santiago de Chile, Vol. 2, pp. B-4-31.

Newmark N.M. and Hall W.J., 1982, “Earthquake spectra and design”, in Engineering monographs on earthquake criteria, structural design and strong motion records, Earthquake Engineering Research Institute, University of California, Berkeley, CA.

New Zealand Standards Association (NZS 3101), 1995, “Code of Practice for the Design of Concrete Structures (Parts 1 & 2) 1982 and 1995”, Standards Association of New Zealand, Wellington.

Ngo D. and Scordelis A.C., 1967, “Finite element analysis of reinforced concrete beams”, Journal of the American Concrete Institute, Vol. 64, No.3, pp.152-163.

OECD/NEA/CSNI (1996). Seismic shear wall ISP NUPEC's seismic ultimate dynamic response test -Comparison Report. NEA/CSNI/R(96)10, OECD/GD(96)188.

Oesterle R.G., 1986, “Inelastic Analysis for In-Plane Strength of Reinforced Concrete Shear Walls”, Ph.D. dissertation, Northwestern Univ., Evanston, IL.

Oesterle R.G., Fiorato A.E., Johal L.S., Carpenter J.E., Russell H.G. and Corley, W.G., 1976, “Earthquake Resistant Structural Walls -- Tests of Isolated Walls, Report to National Science Foundation”, Portland Cement Association, Skokie, Illinois, 315 pp.

Oesterle R.G., Aristizabal-Ochoa J.D., Shiu K.N., and Corley W.G., 1980, “Hysteretic response of reinforced concrete structural walls”, In reinforced concrete structures subjected to Wind and Earthquake Forces, ACI Publication SP-63, pp. 231-241.

Okamura H. and Maekawa K., 1991, “Nonlinear analysis and constitutive models of reinforced concrete”, Giho-do Press, University of Tokyo.

Orakcal K., 2004, “Nonlinear modeling and analyses of slender reinforced concrete walls”, Ph.D. Dissertation, University of California, Los Angeles.

Orakcal K., Wallace J.W. and Conte J.P., 2004, “Flexural modeling of reinforced concrete walls – model attributes,” ACI Structural Journal, Vol. 101, No. 5, pp. 688 – 698.

Otani S., 1974, “Inelastic analysis of R/C frame structures, ASCE Journal of the Structural division, Vol. 100, ST7, pp. 1433 1449.

Palermo D. and Vecchio F.J., 2002, “Behavior of three-dimensional reinforced concrete shear walls”, ACI Structural Journal, Vol. 99, No. 1, pp. 81-89.

Palermo D. and Vecchio F.J., 2004, “Compression field modeling of reinforced concrete subjected to reversed loading: verification”, ACI Structural Journal, Vol. 101, No. 2, pp. 155-164.

Palermo D. and Vecchio F.J., 2007, “Simulation of cyclically loaded concrete structures based on the finite element method”, ASCE Journal of Structural Engineering, Vol. 133., No. 5, pp. 728-738.

Park R. and Paulay T., 1975, “Reinforced concrete structures”, New York: Wiley.

Park R., Priestley M.J.N. and Gill W.D., 1982, “Ductility of square confined concrete columns”, Journal of Structural Engineering, Vol. 108, No. 4, pp. 929–950.

Paulay T., 1986, “The design of ductile reinforced concrete structural walls for earthquake resistance”, Earthquake Spectra, Vol. 2, No. 4, pp. 695-687.

Paulay T., 2002, “An estimation of displacement limits for ductile systems”, Earthquake Engineering and Structural Dynamics, Vol. 31, pp. 583-599.

Paulay T. and Loeber P.J., 1977, “Shear transfer by aggregate interlock”, ACI Special Publication 42, No.1, pp. 1-15.

Popovics S., 1973, “A numerical approach to the complete stress-strain curve of concrete, Cement and Concrete Research, V. 3, No. 4, pp. 583-599.

Powanusorn S., 2003, “Effect of confinement on shear dominated reinforced concrete elements”, Ph.D. Dissertation, University of Texas, Austin.

Priestley M.J.N., 1993, “Myths and fallacies in earthquake engineering - conflicts between design and reality”, Bull. N. Z. Natl. Soc. Earthquake Eng., Vol. 26, No. 3, pp329-341.

Priestley M.J.N., Seible F. and Calvi G.M., 1996, “Seismic design and retrofit of bridges”, Wiley, New York, 686 p.

Priestley M.J.N., 2000, “Performance based seismic design”, in Proceedings of 12th World Conference on Earthquake Engineering, New Zealand.

Priestley M.J.N. and Kowalsky M.J., 1998, “Aspects of drift and ductility capacity of rectangular cantilever structural walls”, Bull. N. Z. Natl. Soc. Earthquake Eng. Vol. 31, No. 2, pp.73–85.

Priestley M.J.N., Calvi G.M. and Kowalsky M.J., 2007, “Displacement-based seismic design of structures”, IUSS Press, Pavia, Italy.

Rathje E.M., Abrahamson N.A. and Bray J.D., 1998, “Simplified frequency content estimates of earthquake ground motions”, ASCE Journal of Geotechnical and Geo-environmental Engineering, Vol. 124, No. 2, 150-159.

Riddell R., Wood S.L. and de la Llera J.C., 1987, “The 1985 Chile Earthquake: Structural Characteristics and Damage Statistics for the Building Inventory in Vina del Mar”, Civil Engineering Studies SRS-534, University of Illinois at Urbana-Champaign..

Riddell R. and Vasquez J., 1992, “Shear wall buildings: a type of construction less vulnerable to earthquakes?”, Proc. Int. Symp. Earthquake Disaster Prevention, Vol. III, Mexico City, pp. 37-51.

Rose B., Shing P.B. and Spacone E., 1999, “Modeling of shear behavior of RC column”, Proceedings of ASCE Structural Congress, ASCE, Reston, Va., pp.166–169.

Rosman R., 1973, Discussion of "Approximate Analysis of Tall Wall-Frame Structures", ASCE Journal of Structural Division, Vol. 99, No. 12, pp. 2501-2502.

Rutenberg A. and Nsieri E., 2006, “The seismic shear demand in ductile cantilever wall systems and the EC8 Provisions”, Bulletin of Earthquake Engineering, Vol. 4, pp. 1-21.

SAP2000, V. 11.0.8, Computers and Structures, Inc.

Saatcioglu M. and Razvi S.R., 1992, “Strength and ductility of confined concrete”, Journal of Structural Engineering, Vol. 118, No. 6, pp.1590–1607.

Sabetta F. and Pugliese A., 1996, “Estimation of response spectra and simulation of nonstationary earthquake ground motions”, Bulletin of the Seismological Society of America, Vol. 86, No. 2, 337 - 352.

Santhakumar R., Chandrasekaran E. and Dhanaraj R., 2004, “Analysis of retrofitted reinforced concrete shear beams using carbon fiber composites”, Electronic Journal of Structural Engineering, Vol .4, pp. 66-74.

Schnobrich W.C., Xu C. and Chesi C., 1992, “Computation of RC wall response”, Concrete Shear in Earthquake, Elsevier, New York, pp. 320–332.

SEAOC Vision 2000, 1995, “Performance based seismic engineering of buildings”, Vols. I and II: Conceptual framework, Structural Engineers Association of California, Sacramento (CA).

Seed H.B., Ugas C. and Lysmer J., 1976, “Site-dependent spectra for earthquake-resistant design”, Bulletin of the Seismological Society of America, Vol. 66, No. 1, pp.221 - 243.

Selby R.G. and Vecchio F.J., 1997, “A constitutive model for analysis of reinforced concrete solids”, Canadian Journal of Civil Engineering, Vol. 24, pp. 460–470.

Seneviratna G.D.P.K and Krawinkler H., 1997, “Evaluation of inelastic MDOF effects for seismic design”, The John A. Blume Earthquake Engineering Center, Report No. 120, Stanford University, Stanford.

Sheikh S.A. and Uzumeri S.M., 1982, “Analytical model for concrete confinement in tied columns”, ASCE Journal of the Structural Division, Vol.108, No. 12, pp.2703-2722.

Shibata A. and Sozen M., 1976, “Substitute structure method for seismic design in reinforced concrete”, ASCE Journal of the Structural Division., Vol. 102, No. 1, pp. 1–18.

Shimazaki, K. and Sozen M. A., 1984, “Seismic drift of reinforced concrete structures”, Hazama-gumi Ltd., Special Research Paper, Tokyo, Japan.

Shome N., Cornell C.A., Bazzurro P. and Carballo J.E., 1998, “Earthquakes, records, and nonlinear reponses”, Earthquake Spectra, Vol. 14, No. 3, pp. 469-500.

Sigfússon T., 2001, “Nonlinear analysis of reinforced concrete shear walls in low-rise Icelandic residential buildings”, Master Thesis, University of Iceland.

Sittipunt C. and Wood S.L., 1995, “Influence of web reinforcement on the cyclic response of structural walls”, ACI Structural Journal, Vol. 92, No. 6, pp. 745-56.

Somerville P., 2005, “Guidelines for the selection, modification and scaling of ground motion time histories”, URS, SCEC. COSMOS Annual Meeting. San Francisco.

Sozen M.A., 1989, “Earthquake response of buildings with robust walls”, Fifth Chilean Conference on Earthquake Engineering, Santiago, Chile.

Stewart J.P., Chiou S.J., Bray J.D., Graves R.W., Somerville P.G. and Abrahamson N.A., 2001, “Ground motion evaluation procedures performance-based design”, PEER Report 2001 / 09, University of California, Berkeley.

Stevens N.J., Uzumeri S.M. and Collins M.P., 1991, “Reinforced concrete subjected to reversed cyclic shear-experiments and constitutive model”, ACI Structural Journal, Vol. 88, No.2, pp.135–146.

Sucuoğlu H. and Nurtuğ A., 1995, “Earthquake ground motion characteristics and seismic energy dissipation”, Earthquake Engineering and Structural Dynamics, Vol. 24, 1195-1213.

Sucuoğlu H., Yücemen M.S., Gezer A. and Erberik M.A., 1998, “Statistical evaluation of damage potential of earthquake ground motions”, Structural Safety, Vol. 20, No. 4, pp. 357-378.

Sullivan T.J., Priestley M.J.N. and Calvi G.M., 2006, “Direct displacement-based design of frame-wall structures”, Journal of Earthquake Engineering, Vol. 10, Special Issue 1.

Swamy R.N. and Qureshi S.A., 1974, “An ultimate shear strength theory for reinforced concrete T-beams without web reinforcement”, Materials of Construction, Vol. 7, pp.181-9.

Takayanagi T., and Schnobrich W.C., 1976, “Computed behavior of reinforced concrete coupled shear walls”, University of Illinois, Urbana, Structural Research Series, No. 434.

Taucer F.F., Spacone E. and Filippou F.C., 1991, “A fiber-beam column element for seismic response analysis of reinforced concrete structures”, Report No. UCB/EERC-91/17, Earthquake Engineering Research Center, Berkeley.

Timoshenko S.P. and Goodier J.N., 1970, “Theory of Elasticity”, International addition, McGraw-Hill.

Toutanji A.H., 1997, “The effect of foundation flexibility on the interaction between shear walls and frames”, Engineering Structures, Vol. 19, No. 12, pp. 1036-1042.

TSC 2007, 2007, “Turkish Seismic Design Code for Buildings”, Ministry of Public Works and Resettlement, Ankara, Turkey.

TS 500, 2000, “Requirements for design and construction of reinforced concrete structures”, Turkish Standards Institute, Ankara.

Thomas J. and Ramaswamy A., 2006, “Finite element analysis of shear critical prestressed SFRC beams”, Computers and Concrete, Vol. 3, No. 1, pp. 65-77.

Thomsen J.H. and Wallace J.W., 1995, “Displacement-based design of reinforced concrete structural walls: an experimental investigation of walls with rectangular and T-shaped cross-sections”, CU/CEE-95/06, Dept. of Civil and Environmental Engineering, Clarkson University, Potsdam, N.Y.

Tremblay R., Léger P. and Tu J., 2001, “Inelastic seismic response of concrete shear walls considering P–delta effects”, Canadian Journal of Civil Engineering, Vol. 28, pp. 640–655.

Tso W.K., Zhu T.J. and Heidebrecht A.C., 1993, “Seismic energy demands on reinforced concrete moment-resisting frames”, Earthquake Engineering and Structural Dynamics, Vol. 22, pp. 533-545.

Tso W.K., Zhu T.J. and Heidebrecht A.C., 1992, “Engineering implication of ground motion A/V ratio”, Soil Dynamics&Earthquake Engineering, Vol. 11, No. 3, pp.133-144.

Vallenas M.V., Bertero V.V. and Popov E.P., 1979, “Hysteretic behavior of reinforced concrete structural walls”, EERC Report 79/20, Earthquake Engineering Research Center, University of California, Berkeley.

Vecchio F.J., 1998, “Lessons from the analysis of a 3-D concrete shear wall, Structural Engineering and Mechanics, Vol. 6, No. 4, pp. 439-55.

Vecchio F.J., 1999, “Towards cyclic load modeling of reinforced concrete”, ACI Structural. Journal, Vol. 96, No. 2, pp. 193–202.

Vecchio F.J. and Collins M.P., 1986, “Modified compression-field theory for reinforced concrete elements subjected to shear”, ACI Structural Journal, Vol. 83, pp. 219-231.

Vecchio F.J., 1989, “Nonlinear finite element analysis of reinforced concrete membranes”, ACI Structural Journal, Vol. 86, No. 1, pp. 26–35.

Vecchio F.J. and Collins M.P., 1993, “Compression response of cracked reinforced concrete”, ASCE Journal of Structural Engineering, Vol. 119, pp. 3590-3610.

von Mises. R., 1928, “Mechanik der plastischen Formänderung von Kristallen”, Z. Angrew. Math. Mech, Vol. 8, pp. 161-85.

Vulcano A., 1992, “Macroscopic modeling for nonlinear analysis of RC structural walls”, in H. Krawinkler and P. Fajfar (eds.), Nonlinear Seismic Analysis of RC Nonlinear seismic analysis and design of reinforced concrete buildings, Elsevier Applied Science, New York, pp. 181-190.

Vulcano A. and Bertero V.V., 1987, “Analytical models for predicting the lateral response of RC shear walls: evaluation of their reliability”, Report No. UCB/EERC-87/19, Earthquake Engineering Research Center, University of California, Berkeley.

Vulcano A., Bertero V.V. and Colotti V., 1988, “Analytical modeling of R/C structural walls”, Report No. UCB/EERC-88/17, arthquake Engineering Research Center, University of California, Berkeley.

Wallace J.W. and Moehle J.P., 1992, "Ductility and detailing requirements of bearing wall buildings", ASCE Journal of Structural Engineering, Vol. 118, No. 6, pp. 1625-1644.

Wallace J.W., 1994, "New methodology for seismic design of RC shear walls", ASCE Journal of Structural Engineering, Vol. 120, No. 3, pp. 863-884.

Wallace J.W., 1995a, "Seismic design of RC structural walls. Part I: New code format", ASCE Journal of Structural Engineering, Vol. 121, No. 1, January 1995.

Wallace J.W., 1995b, "Seismic design of RC structural walls. Part II: Applications", ASCE Journal of Structural Engineering, Vol. 121, No. 1, January 1995.

Wang T.Y., Bertero V.V., and Popov E.P., 1975, "Hysteretic behavior of reinforced concrete framed walls", Report No. EERC 75-23, Earthquake Engineering Research Center, University of California, Berkeley.

Watanabe K., Niwa J., Yokota H. and Iwanami M., 2004, "Experimental study on stress-strain curve of concrete considering localized failure in compression", Journal of Advanced Concrete Technology, Vol. 2 , No. 3, pp.395-407.

Willam K.J. and Warnke E.D., 1975, "Constitutive model for the triaxial behavior of concrete", Intl. Assoc. Bridge Struct. Eng. Proc., Vol. 19, pp. 174-203.

Wiradinata W. and Saatcioglu M., 1986, "Tests of squat shear walls under lateral load reversals", Proceedings of the Third U.S. National Conference on Earthquake Engineering, Charleston, South Carolina, U.S.A., Vol.2, pp.1395-1406.

Wood S.L., 1991, "Performance of reinforced concrete buildings during the 1985 chile earthquake: implications for the design of structural walls", Earthquake Spectra, Vol. 7, No. 4, pp. 607-638.

Yenier E., 2009, "Limitations on point-source stochastic simulations in terms of ground motions models", Master Thesis, Middle East Technical University, Ankara.

Zhu T.J., Tso, W.K. and Heidebrecht A.C., 1988a, "Effect of peak ground a/v ratio on structural damage", ASCE Journal of Structural Engineering, Vol. 114, No. 5, pp. 1019-1037.

Zhu T.J., Heidebrecht A.C. and Tso W.K., 1988b, "Effect of peak ground acceleration to velocity ratio on ductility demand of inelastic systems", Earthquake Engineering & Structural Dynamics, Vol. 16, No. 1, pp. 63-79.

APPENDIX A

DESCRIPTION OF THE FINITE ELEMENTS

1. Introduction

ANSYS is equipped with a special element SOLID65 that can be used in the 3-D modeling of reinforced concrete solids with or without reinforcing bars. In this study, structural walls have been modeled with this element. The reinforcing bars can be modeled either in a smeared manner by using the special rebar feature of the SOLID65 or can be modeled discretely using the three dimensional truss element LINK8. Additionally, MASS21 element is used to introduce mass to the system. In the following sections basic formulation and special features of these elements are described.

2. SOLID65 Element Description

Element SOLID65 has eight nodes with three translational degrees of freedom at each node. The solid element is capable of cracking (in three orthogonal directions) in tension and crushing in compression and also undergoing plastic deformations. If cracking occurs at an integration point, the cracking is modeled through an adjustment of material properties that effectively treats the cracking as a "smeared band" of cracks, rather than discrete cracks. The concrete material was assumed to be initially isotropic (ANSYS). Up to three different rebar specifications may be defined. Ties and stirrups can also be modeled by making use of this property. The rebars can carry tension and compression, but not shear. They are also capable of plastic deformation and creep. The geometry, node locations and the coordinate system for this element are shown in Figure A.1.

The eight-noded isoparametric brick element, SOLID65, employs linear interpolation functions for the geometry and displacements with eight integration points (2x2x2). The interpolation function for this element is given as follows:

$$N_i = \frac{1}{8}(1 \pm \xi)(1 \pm \eta)(1 \pm \zeta)\,, \qquad \text{where } i \in 1,\ldots,8. \qquad \text{(A.1)}$$

Depending on the given shape functions, the nodal displacements (u_i, v_i, w_i) calculated at the nodes are interpolated at any point (ξ, η, ζ) within the element as

$$\begin{aligned} u &= u_1 N_1 + u_2 N_2 + \ldots + u_8 N_8 \\ v &= v_1 N_1 + v_2 N_2 + \ldots + v_8 N_8 \\ w &= w_1 N_1 + w_2 N_2 + \ldots + w_8 N_8 \end{aligned} \tag{A.2}$$

The displacement field in the element is calculated at the integration points by utilizing a variable integration scheme (Gauss quadrature) of 2x2x2.

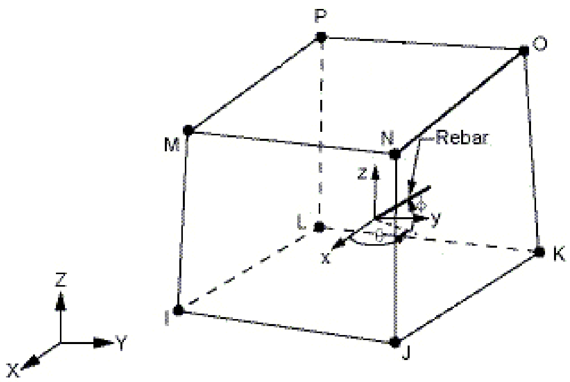

Figure A.1 SOLID65 geometry from ANSYS user manual (ANSYS, 2005)

2.1. Shear Locking and Extra Displacement Shapes:

Suppose that the surface of a block of material is divided into large number of small cubic elements with faces respectively parallel to the three coordinate planes as shown in Figure A.2. When this material is subjected to a pure bending moment, while the edges of these elements in the horizontal plane experience a curved shape change, the vertical edges remain straight. However, all the faces remains at 90^o to each other after deformation, so it is concluded that $\gamma_{xy} = \gamma_{xz} = 0$ and thus $\tau_{xy} = \tau_{xz} = 0$. Since the deformations involved do not require any interaction between the elements of a given transverse cross section σ_y, σ_z, τ_{yz} must be zero on the surface of the member.

When the continuum given in Figure A.2 is discretized with first order solid finite elements such as the SOLID65 discussed here, the deformed pattern of the same material block under pure bending moment should be as the one shown in Figure A.3. All the dashed lines remain straight, but the angle A can no longer stay 90^o. This is due to linear interpolation functions used for the element that leads to constant strain distribution within the element. The deformed pattern of the material block embodies that within the volume of material the strain energy of the elements is generating shear deformation instead of bending deformation. The artificial shearing stresses introduced to the material cause the element to become stiff under pure bending moment. Wrong displacements, false stresses, and spurious natural frequencies develop because of this phenomenon called shear locking.

A remedy for this problem is to add bending modes to element displacement fields. ANSYS provides "incompatible modes" formulation (also referred to as "extra shapes") for modeling bending applications because the eight-node solid element exhibits shear locking as the four-node plane element.

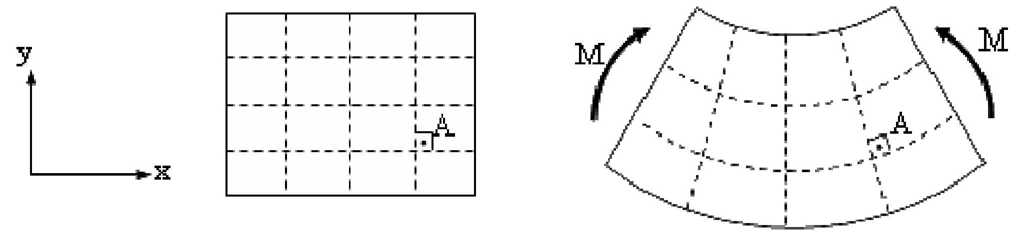

Figure A.2 Deformed shape of a material under pure bending

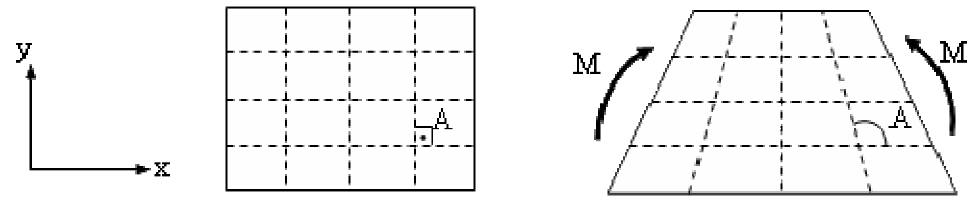

Figure A.3 Deformed shape of a material discretized with SOLID65 under pure bending

If the problem is predominantly bulk deformation, then you may choose to turn extra shapes off to reduce CPU/storage requirements and enhance convergence. However, doing so precludes the ability to model any bending. In such a case number of element in the bending direction must be increased. For structural analyses, this corner noded element with extra shape functions will often yield an accurate solution in a reasonable amount of computer time. Considering the extra shape functions (ESF), the displacement field is calculated as

$$
\begin{aligned}
u &= u_1 N_1 + u_2 N_2 + \ldots + u_8 N_8 + a_1(1-\xi^2) + a_2(1-\eta^2) + a_7(1-\zeta^2) \\
v &= v_1 N_1 + v_2 N_2 + \ldots + v_8 N_8 + a_3(1-\xi^2) + a_4(1-\eta^2) + a_8(1-\zeta^2) \\
w &= w_1 N_1 + w_2 N_2 + \ldots + w_8 N_8 + a_5(1-\xi^2) + a_6(1-\eta^2) + a_9(1-\zeta^2)
\end{aligned}
\tag{A.3}
$$

where the nine a_i are generalized d.o.f. or they may also be called as “nodeless” d.o.f. (Cook et al., 2001). The a_i are not associated with any node nor are they connected to d.o.f of any other element. Physically, displacement modes associated with the a_i are displacements *relative* to the displacement field dictated by the summations in Eq. (A.3).

The elements with extra shape functions called “incompatible” because of the behavior illustrated in Figure A.4. With the loading shown in Figure A.4(b), a gap appears between elements. If the forces are reversed, elements would overlap.

No gaps or overlaps appear in a physical continuum. Why then do incompatible elements provide a satisfactory model? It is because repeated mesh refinement causes elements to approach a state of constant strain. Initially straight lines, such as sides of undeformed elements, remain straight when deformation is such as to produce a state of constant strain. Thus an FE model composed of elements with extra shape functions (ESF) allows exact results to be approached as the mesh is refined. Convergence may be "from above" because a coarse mesh of elements with ESF may be overly flexible. In contrast, elements without ESF converge "from below" because they are always too stiff (or at best exact, in a field of constant strain) (Cook et al., 2001).

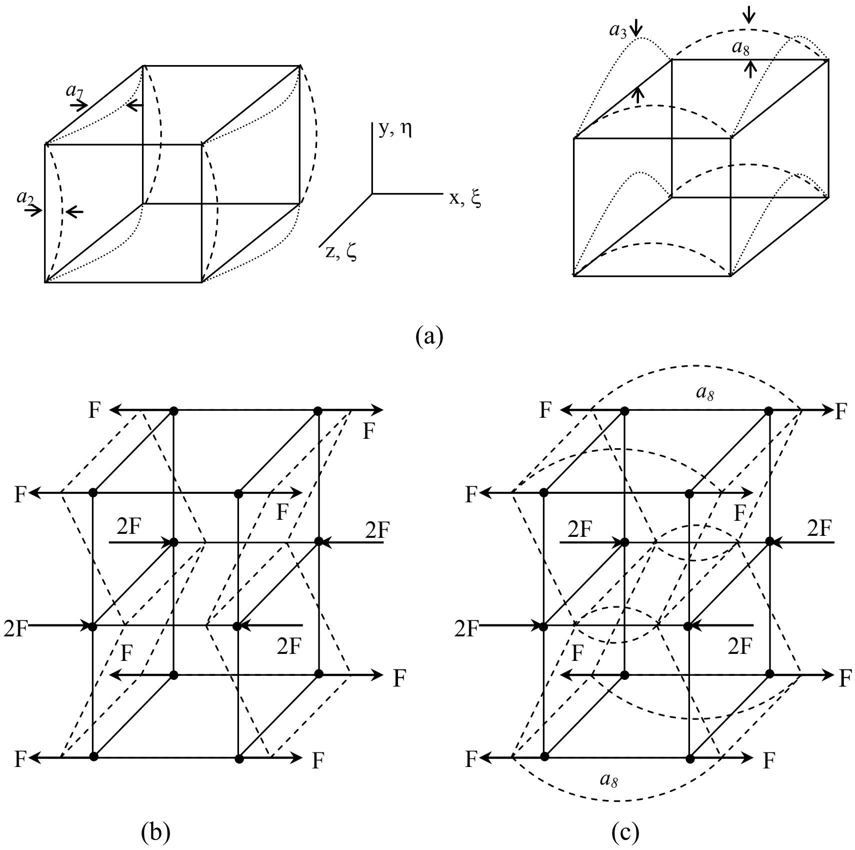

Figure A.4 Shear locking on the element (a) Displacement modes $u = (1-\eta^2)a_2 + (1-\zeta^2)a_8$ and $v = (1-\xi^2)a_3 + (1-\zeta^2)a_8$ (b) Elements with extra displacement shapes suppressed, no incompatibility between adjacent elements but having shear locking defect. (c) Elements with extra displacement shapes included, incompatibility between adjacent elements.

2.2 Assumptions and Restrictions:

The basic assumptions of the material model are as follows:

1. The concrete material is assumed to be initially isotropic.

The symmetric material stiffness matrix $[D^C]$ for concrete is given by

$$\left[D^C\right]=\frac{E}{(1+\upsilon)(1-2\upsilon)}\begin{bmatrix}(1-\upsilon) & \upsilon & \upsilon & 0 & 0 & 0\\ \upsilon & (1-\upsilon) & \upsilon & 0 & 0 & 0\\ \upsilon & \upsilon & (1-\upsilon) & 0 & 0 & 0\\ 0 & 0 & 0 & \frac{(1-2\upsilon)}{2} & 0 & 0\\ 0 & 0 & 0 & 0 & \frac{(1-2\upsilon)}{2} & 0\\ 0 & 0 & 0 & 0 & 0 & \frac{(1-2\upsilon)}{2}\end{bmatrix} \tag{A.4}$$

where E is the Modulus of Elasticity and υ is the Poisson's ratio for concrete.

2. Whenever the reinforcement capability of the element is used, the reinforcement is assumed to be "smeared" throughout the element. The reinforcement was entered as volumetric ratio of that element, defined as the rebar volume divided by the total element volume. In the formulation of stress-strain matrix, D, the relation given in Eq. (A.5) is used. The amount of reinforcement is used as a modification factor that calibrates the concrete's strain-stress matrix.

$$[D]=(1-\sum_{i=1}^{N_R}V_i^R)[D^C]+\sum_{i=1}^{N_R}V_i^R.[D^R]_i \tag{A.5}$$

In this equation, N_R denotes the number of different reinforcing materials, D^C is the stress-strain matrix of the concrete and D^R (given in Eq. (A.6)) is the stress-strain matrix of reinforcement material, V_i^R is the ratio of the volume of reinforcing material *"i"* to the total volume of the element.

$$\begin{Bmatrix}\sigma_{xx}^r\\ \sigma_{yy}^r\\ \sigma_{zz}^r\\ \sigma_{xy}^r\\ \sigma_{yz}^r\\ \sigma_{xz}^r\end{Bmatrix}=\begin{bmatrix}E_i^r & 0 & 0 & 0 & 0 & 0\\ 0 & 0 & 0 & 0 & 0 & 0\\ 0 & 0 & 0 & 0 & 0 & 0\\ 0 & 0 & 0 & 0 & 0 & 0\\ 0 & 0 & 0 & 0 & 0 & 0\\ 0 & 0 & 0 & 0 & 0 & 0\end{bmatrix}\begin{Bmatrix}\varepsilon_{xx}^r\\ \varepsilon_{yy}^r\\ \varepsilon_{zz}^r\\ \varepsilon_{xy}^r\\ \varepsilon_{yz}^r\\ \varepsilon_{xz}^r\end{Bmatrix}=\left[D^r\right]_i\begin{Bmatrix}\varepsilon_{xx}^r\\ \varepsilon_{yy}^r\\ \varepsilon_{zz}^r\\ \varepsilon_{xy}^r\\ \varepsilon_{yz}^r\\ \varepsilon_{xz}^r\end{Bmatrix} \tag{A.6}$$

In Eq. (A.6), E_i^r is the Young's modulus of reinforcement type i. It may be seen that the only nonzero stress component is σ_{xx}^r, the axial stress in the x_i^r direction of reinforcement type i. The orientation of the reinforcement i within the element is depicted in Figure A.5. The element coordinate system is denoted by (X, Y, Z,) and (x_i^r, y_i^r ,z_i^r) describes the coordinate system for reinforcement type i.

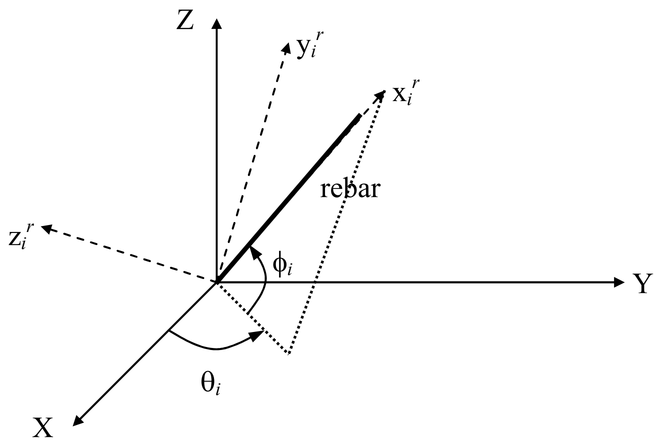

Figure A.5 Reinforcement orientation

Since the reinforcement material matrix is defined in coordinates aligned in the direction of reinforcement orientation, it is necessary to construct a transformation of the form

$$\left[D^R\right]_i = \left[T^r\right]^T \left[D^r\right]_i \left[T^r\right] \tag{A.7}$$

in order to express the material behavior of the reinforcement in global coordinates.

3. Cracking is permitted in three orthogonal directions at each integration point.

4. If cracking occurs at an integration point, the cracking is modeled through an adjustment of material properties which effectively treats the cracking as a "smeared band" of cracks, rather than discrete cracks. Once a crack occurs at an integration point, a plane of weakness is introduced in the direction normal to the crack face to modify the stress-strain relation of concrete.

The stress-strain relation of concrete in tension and the strength of cracked condition are explained in Figure A.6. In this figure f_t is the uniaxial tensile cracking strength and E is the modulus of elasticity of concrete. After cracking, a certain amount of stress relaxation can be included in the element stress formulation with the constant T_c which defaults to *0.6*. R_t is the secant slope defined as shown. It diminishes to zero as the solution converges. The stress relaxation after cracking is an option in the element formulation, so can be included or excluded when desired. But, including a certain amount of stress relaxation can help to achieve a better convergence behavior. Surpassing the tensile relaxation will equal R_t to 0.

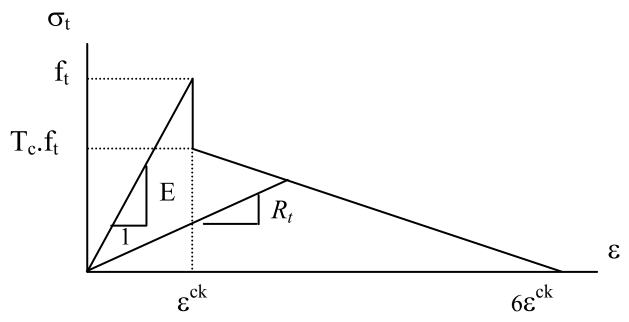

Figure A.6 Tensile behavior of concrete

Also, a shear transfer coefficient β_t is introduced which represents a shear strength reduction factor for those subsequent loads which induce sliding (shear) across the crack face. The stress-strain relations for a material that has cracked in one direction only become:

$$\left[D_c^{ck}\right] = \frac{E}{(1+\upsilon)} \begin{bmatrix} \frac{R_t(1+\upsilon)}{E} & 0 & 0 & 0 & 0 & 0 \\ 0 & \frac{1}{(1-\upsilon)} & 0 & 0 & 0 & 0 \\ 0 & 0 & \frac{1}{(1-\upsilon)} & 0 & 0 & 0 \\ 0 & 0 & 0 & \frac{\beta_t}{2} & 0 & 0 \\ 0 & 0 & 0 & 0 & \frac{1}{2} & 0 \\ 0 & 0 & 0 & 0 & 0 & \frac{\beta_t}{2} \end{bmatrix} \tag{A.8}$$

where the superscript *ck* signifies that the stress-strain relationship refers to a coordinate system parallel to the principal stress directions with x^{ck} being perpendicular to the crack direction. As can be observed from Eq. (A.8), the material stress-strain relationship is modified by R_t in the direction perpendicular to cracking, and by β_t for the shear terms. The term β_t represents the shear that can be transferred across a crack due to friction, aggregate interlock or dowel action. If the crack closes, then all the compressive stress normal to the crack plane are transmitted across the crack and only a shear transfer coefficient β_c for a closed crack is introduced. Then the corresponding stress-strain relationship for concrete with a closed crack takes the following form:

$$\left[D_c^{ck}\right]=\frac{E}{(1+\upsilon)(1-2\upsilon)}\begin{bmatrix} (1-\upsilon) & \upsilon & \upsilon & 0 & 0 & 0 \\ \upsilon & (1-\upsilon) & \upsilon & 0 & 0 & 0 \\ \upsilon & \upsilon & (1-\upsilon) & 0 & 0 & 0 \\ 0 & 0 & 0 & \beta_c\frac{(1-2\upsilon)}{2} & 0 & 0 \\ 0 & 0 & 0 & 0 & \frac{(1-2\upsilon)}{2} & 0 \\ 0 & 0 & 0 & 0 & 0 & \beta_c\frac{(1-2\upsilon)}{2} \end{bmatrix} \tag{A.9}$$

The stress-strain relations for concrete that has cracked in two directions are:

$$\left[D_c^{ck}\right]=E\begin{bmatrix} \frac{R_t}{E} & 0 & 0 & 0 & 0 & 0 \\ 0 & \frac{R_t}{E} & 0 & 0 & 0 & 0 \\ 0 & 0 & 1 & 0 & 0 & 0 \\ 0 & 0 & 0 & \frac{\beta_t}{2(1+\upsilon)} & 0 & 0 \\ 0 & 0 & 0 & 0 & \frac{\beta_t}{2(1+\upsilon)} & 0 \\ 0 & 0 & 0 & 0 & 0 & \frac{\beta_t}{2(1+\upsilon)} \end{bmatrix} \tag{A.10}$$

If both directions reclose,

$$\left[D_c^{ck}\right]=\frac{E}{(1+\upsilon)(1-2\upsilon)}\begin{bmatrix} (1-\upsilon) & \upsilon & \upsilon & 0 & 0 & 0 \\ \upsilon & (1-\upsilon) & \upsilon & 0 & 0 & 0 \\ \upsilon & \upsilon & (1-\upsilon) & 0 & 0 & 0 \\ 0 & 0 & 0 & \beta_c\frac{(1-2\upsilon)}{2} & 0 & 0 \\ 0 & 0 & 0 & 0 & \frac{(1-2\upsilon)}{2} & 0 \\ 0 & 0 & 0 & 0 & 0 & \beta_c\frac{(1-2\upsilon)}{2} \end{bmatrix} \tag{A.11}$$

The stress-strain relation for concrete that has cracked in all three directions are:

$$
\left[D_c^{ck}\right] = E\begin{bmatrix} \frac{R_t}{E} & 0 & 0 & 0 & 0 & 0 \\ 0 & \frac{R_t}{E} & 0 & 0 & 0 & 0 \\ 0 & 0 & 1 & 0 & 0 & 0 \\ 0 & 0 & 0 & \frac{\beta_t}{2(1+\upsilon)} & 0 & 0 \\ 0 & 0 & 0 & 0 & \frac{\beta_t}{2(1+\upsilon)} & 0 \\ 0 & 0 & 0 & 0 & 0 & \frac{\beta_t}{2(1+\upsilon)} \end{bmatrix} \tag{A.12}
$$

The transformation of $\left[D_c^{ck}\right]$ to element coordinates has the form

$$
[D_c] = \left[T^{ck}\right]^T \left[D_c^{ck}\right]\left[T^{ck}\right] \tag{A.13}
$$

where the terms composing $\left[T^{ck}\right]$ are the components of the principal direction vectors.

5. In addition to cracking and crushing, the concrete may also undergo plasticity, with the Drucker-Prager failure surface being most commonly used. In this case, the plasticity is done before the cracking and crushing checks.

3. Other Elements

Different elements, which are nonlinear in nature, were used in the model construction serving to different modeling purposes. The general characteristics of these elements are explained briefly below.

3.1. MASS21

MASS21 is a point element having up to six degrees of freedom: translations in the nodal x, y, and z directions and rotations about the nodal x, y, and z axes. A different mass and rotary inertia may be assigned to each coordinate direction.

3.2. LINK8 and LINK10

The 3-D bar element is a uniaxial tension-compression element with three degrees of freedom at each node: translations in the nodal x, y, and z directions. It is used when the reinforcing bars are modeled discretely. Plasticity, stress stiffening, and large deflection capabilities are included.

A special version of LINK8 is LINK10 that is a 3-D spar element having the unique feature of a bilinear stiffness matrix resulting in a uniaxial tension-only (or compression-only) element. With the tension-only option, the stiffness is removed if the element goes into compression (simulating a slack cable or slack chain condition).

3.3. COMBIN14

COMBIN14 has longitudinal or torsional capability in 1-D, 2-D, or 3-D applications. The longitudinal spring-damper option is a uniaxial tension-compression element with up to three degrees of freedom at each node: translations in the nodal x, y, and z directions. No bending or torsion is considered. The torsional spring-damper option is a purely rotational element with three degrees of freedom at each node: rotations about the nodal x, y, and z axes. No bending or axial loads are considered.

3.4. COMBIN39

COMBIN39 is a unidirectional element with nonlinear generalized force-deflection capability that can be used in any analysis. The element has longitudinal or torsional capability in 1-D, 2-D, or 3-D applications. The longitudinal option is a uniaxial tension-compression element with up to three degrees of freedom at each node: translations in the nodal x, y, and z directions. No bending or torsion is considered. The torsional option is a purely rotational element with three degrees of freedom at each node: rotations about the nodal x, y, and z axes. No bending or axial loads are considered.

The element is defined by two node points and a generalized force-deflection curve as shown in Figure A.7. The points on this curve (D1, F1, etc.) represent force (or moment) versus relative translation (or rotation) for structural analyses. The force-deflection curve should be input such that deflections are increasing from the third (compression) to the first (tension) quadrants. Adjacent deflections should not be nearer than 1E-7 times total input deflection range. The last input deflection must be positive. Segments tending towards vertical should be avoided. If the force-deflection curve is exceeded, the last defined slope is maintained, and the status remains equal to the last segment number. If the compressive region of the force-deflection curve is explicitly defined (and not reflected), then at least one point should also be at the origin (0,0) and one point in the first (tension) quadrant. Element can unload along same loading curve or along line parallel to slope at origin of loading curve depending on the application.

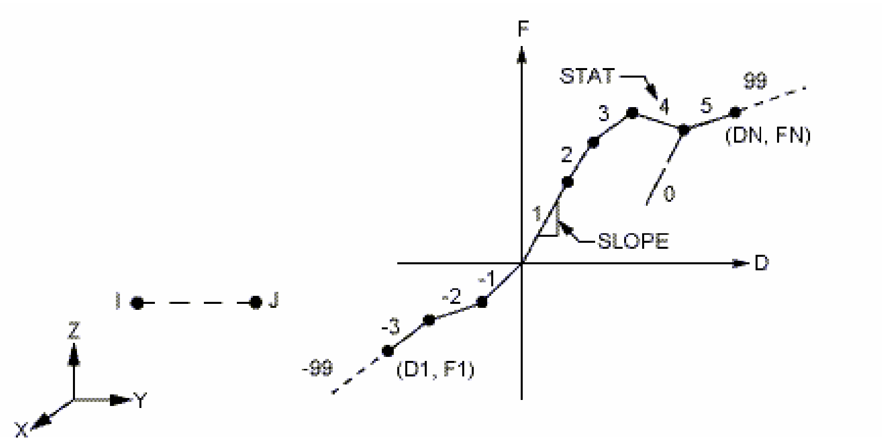

Figure A.7 COMBIN39 geometry (ANSYS manual)

3.5. BEAM188

BEAM188 is a linear (2-node) or a quadratic beam element in 3-D as shown in Figure A.8. BEAM188 has six or seven degrees of freedom at each node. These include translations in the x, y, and z directions and rotations about the x, y, and z directions. A seventh degree of freedom (warping magnitude) can also be considered. The beam element is based on Timoshenko beam theory, which is a first order shear deformation theory: transverse shear strain is constant through the cross-section; that is, cross-sections remain plane and undistorted after deformation.

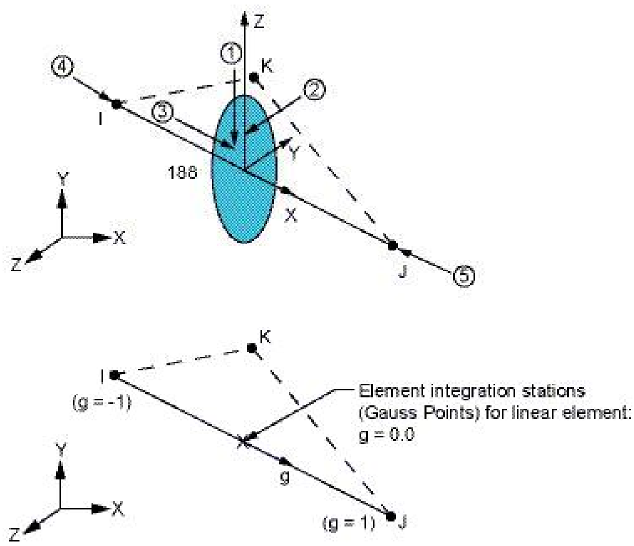

Figure A.8 BEAM188 element geometry and integration stations (ANSYS)

BEAM188/BEAM189 can be associated with either of these cross section types:

- Standard library section types or user meshes which define the geometry of the beam cross section. The material of the beam is defined either as an element attribute (MAT), or as part of section buildup (for multi-material cross sections).

- Generalized beam cross sections, where the relationships of generalized stresses to generalized strains are input directly.

When using nonlinear general beam sections, neither the geometric properties nor the material is explicitly specified. The nonlinear general beam section is an abstract cross section type that allows you to define axial, flexural, torsional, and transverse shear behavior as a function of axial strain, bending curvature, twist, and transverse shear strains. Generalized stress implies the axial force, bending moments, torque, and transverse shear forces. Similarly, generalized strain implies the axial strain, bending curvatures, twisting curvature, and transverse shear strains. This is an abstract method for representing cross section behavior; therefore, input often consists of experimental data or the results of other analyses. The behavior of beam elements is governed by the generalized-stress/generalized-strain relationship of the form:

$$\begin{bmatrix} N \\ M_1 \\ M_2 \\ \tau \\ S_1 \\ S_2 \end{bmatrix} = \begin{bmatrix} A_E(\varepsilon,T) & & & & & \\ & I_1^E(\kappa_1,T) & & & 0 & \\ & & I_2^E(\kappa_2,T) & & & \\ & & & J_G(\chi,T) & & \\ & 0 & & & A_1^G(\gamma_1,T) & \\ & & & & & A_2^G(\gamma_2,T) \end{bmatrix} \begin{bmatrix} \varepsilon \\ \kappa_1 \\ \kappa_2 \\ \chi \\ \gamma_1 \\ \gamma_2 \end{bmatrix} \qquad \text{(A.14)}$$

where

N = Axial force
M_1 = Bending moment in plane XZ
M_2 = Bending moment in plane XY
τ = Torque
S_1 = Transverse shear force in plane XZ
S_2 = Transverse shear force in plane XY
ε = Axial strain
κ_1 = Curvature in plane XZ
κ_2 = Curvature in plane XY
χ = Twist of the cross section
γ_1 = Transverse shear strain in plane XZ
γ_2 = Transverse shear strain in plane XY
$A_E(\varepsilon,T)$ = Axial stiffness as a function of axial strain and temperature
$I_1^E(\kappa_1,T)$ = Flexural rigidity as a function of curvature and temperature in plane XZ
$I_2^E(\kappa_2,T)$ = Flexural rigidity as a function of curvature and temperature in plane XY
$J_G(\chi,T)$ = Torsional rigidity, as a function of torsion and temperature
$A_1^G(\gamma_1,T)$ = Shear stiffness as a function of shear strain and temperature in plane XZ
$A_2^G(\gamma_2,T)$ = Shear stiffness as a function of shear strain and temperature in plane XY
T is the current temperature

APPENDIX B

CONCRETE MATERIAL MODELS

1. Introdcution

Complexity of concrete response under various loading regimes (uniaxial, biaxial or multi-axial) has been manifested long time ago (Chen, 1982). Due to highly nonlinear nature of concrete material including cracking, crushing, tension stiffening, compression softening and bond-slip, accuracy of response modeling of reinforced concrete structures and components is strongly dependent on the material models. The nonlinear response of reinforced concrete is caused by two major material effects, *cracking* of the concrete and the *plasticity* of the reinforcement and of the compression concrete. The tensile cracking reduces the stiffness of the concrete and is usually the major contributor to the nonlinear behavior of reinforced concrete structures, like walls, panels and shells, where the stress is predominantly the biaxial tension-compression type. For these structures, accurate modeling of cracking behavior of concrete is undoubtedly the most important factor (Chen, 1982).

ANSYS offers different material options to be used together with the solid reinforced concrete element. In the program, five parameter Willam-Warnke (1975) criterion was implemented to be used together with the SOLID65 element. The model assumes linear elastic stress-strain relationship until crushing. This is actually a failure surface. When used without a plasticity law it underestimates the deformation capacity of concrete because it neglects the slight nonlinearity in ascending branch and the post-crushing strength of concrete in compression (Barbosa and Ribiero, 1998). ANSYS offers a number of rate independent kinematic and isotropic hardening plasticity options that can be used with the concrete element to model the compression behavior. The Drucker-Prager plasticity model (DP), von Mises bilinear (BISO) and multi-linear isotropic work hardening plasticity (MISO) are combined with the tensile failure criteria of Willam-Warnke material model (CONC). The notation given in parenthesis is used to refer to plasticity models here as defined in ANSYS. These plasticity models require further discussion, especially the Drucker-Prager model, because parameters used to describe them differ for different loading conditions (stress states), since a combined yield surface is used.

2. Willam-Warnke Failure Criterion

The general characteristics of the failure surface of concrete can be determined by experiments. Experimental results indicate that the failure curve in the deviatoric plane has the following general characteristics (Chen, 1982)

1. The failure curve is *smooth*.
2. The failure curve is *convex*, at least for compressive stresses.
3. The failure curve's cross-sectional shape has threefold symmetry.
4. The failure curve is nearly triangular for tensile and small compressive stresses (corresponding to small ξ values near the π plane), and becomes increasingly bulged (more circular) for higher compressive stresses (corresponding to the increase of ξ values or high hydrostatic pressures).

It follows from these conditions that, shape of a failure surface in a three dimensional (Haigh-Westergaard) stress space can be best described by its cross sectional shapes in the deviatoric planes and its meridians in the meridian planes (planes containing the hydrostatic axis with θ= constant). In Figure B.1, the general geometrical representation of the failure surface was given depending on the characteristics listed above.

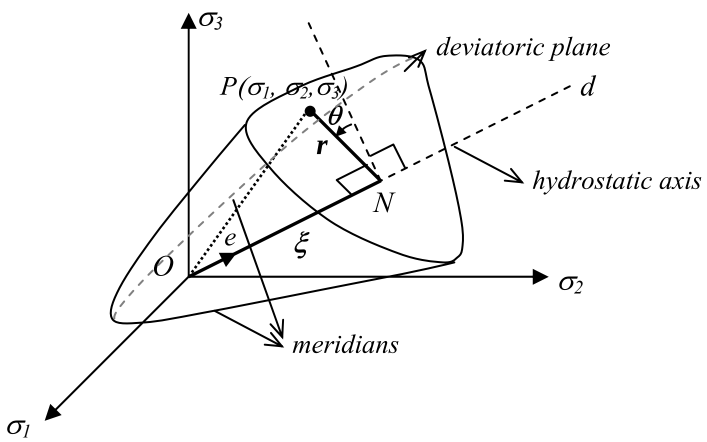

Figure B.1 Failure surface in 3-dimensional stress space

The concrete material model predicts the failure of brittle materials. Both cracking and crushing failure modes are accounted for. The criterion for failure of concrete due to a multiaxial stress state can be expressed in the form (Willam and Warnke, 1975):

$$\frac{F}{f_c^{'}} - S \geq 0 \tag{B.1}$$

where F is a function of the principal stress state (σ_{xp}, σ_{yp}, σ_{zp}- principal stresses in principal directions), S is the failure surface (to be discussed) expressed in terms of principal stresses and five input parameters f_t, f_c, f_{cb}, f_1 and f_2 defined in Table B.1 and f_c is the uniaxial compressive strength of concrete. If Eq. (B.1) is satisfied, the material will crack or crush.

Table B.1 Determination of the parameters of Willam-Warnke model

Test	σ_m / f_c'	τ_m / f_c'	θ, deg	$r(\sigma_m, \theta)$
1. $\sigma_1 = f_t'$	$\frac{1}{3}\bar{f}_t'$	$\sqrt{\frac{2}{15}}\bar{f}_t'$	0	$r_t = \sqrt{\frac{2}{3}}f_t'$
2. $\sigma_2 = \sigma_3 = -f_{bc}'$	$-\frac{2}{3}\bar{f}_{bc}'$	$\sqrt{\frac{2}{15}}\bar{f}_{bc}'$	0	$r_t = \sqrt{\frac{2}{3}}f_{bc}'$
3. $f_1 = (-\bar{\xi}_1, \bar{r}_1)$	$-\bar{\xi}_1$	$\bar{r}_1$	0	$r_t = \sqrt{5}\bar{r}_1 f_c'$
4. $\sigma_3 = -f_c'$	$\frac{1}{3}$	$\sqrt{\frac{2}{15}}$	60	$r_t = \sqrt{\frac{2}{3}}f_c'$
5. $f_2 = (-\bar{\xi}_2, \bar{r}_2)$	$-\bar{\xi}_2$	$\bar{r}_2$	60	$r_c = \sqrt{5}\bar{r}_2 f_c'$

A total of five input stress parameters are required to define the failure surface in function S, which are uniaxial tensile strength, uniaxial compressive strength, biaxial compressive strength, strength from triaxial compression test, and strength from triaxial extension test. The failure surface is as shown in Figure B.1 in the principal stress space. It can be observed that the failure surface has curved meridians (parabola in this case) and presents symmetry on the deviatoric plane as seen in Figure B.2.

\

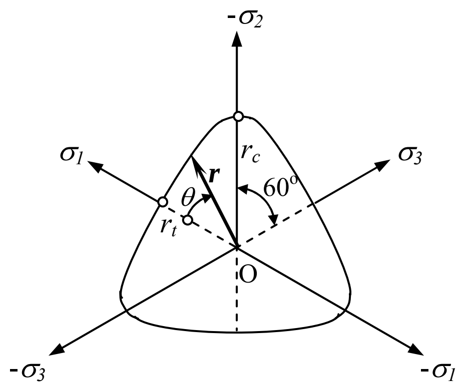

Figure B.2 Failure surface on the deviatoric plane

This cone shaped surface shown in Figure B.1 can be defined by two quadratic curves, one on the tension meridian plane, $r_t(\sigma_m)$ (where $\theta = 0^\circ$), and the other, on the compression meridian plane, $r_c(\sigma_m)$ (where $\theta = 60^\circ$) as shown in Eq. (B.2).

$$\frac{\tau_{mt}}{f_c^{'}} = \frac{r_t}{\sqrt{5} f_c^{'}} = a_0 + a_1 \frac{\sigma_m}{f_c^{'}} + a_2 \left(\frac{\sigma_m}{f_c^{'}} \right)^2 \quad \text{at } \theta = 0° \tag{B.2a}$$

$$\frac{\tau_{mc}}{f_c^{'}} = \frac{r_c}{\sqrt{5} f_c^{'}} = b_0 + b_1 \frac{\sigma_m}{f_c^{'}} + b_2 \left(\frac{\sigma_m}{f_c^{'}} \right)^2 \quad \text{at } \theta = 60° \tag{B.2b}$$

By this way, the variations of the average shear stresses, τ_{mt} and τ_{mc}, along the tensile ($\theta = 0°$) and compressive ($\theta = 60°$) meridians, respectively, are approximated by second-order parabolic expression in terms of the average normal stress, σ_m where

$$\sigma_m = \frac{1}{3}(\sigma_x + \sigma_y + \sigma_z) = \frac{1}{3}\sigma_{ii} = \frac{1}{3} I_1 \tag{B.3}$$

represents the *mean stress* or the *pure hydrostatic stress.*

Any point between the tension and compression curves can be interpolated from the assumed elliptical polar equation, $r(\theta)$, on the deviatoric plane. The radius of the cone, r, is determined by substituting the calculated values of r_t and r_c into Eq. (B.4).

$$r(\sigma_m, \theta) = \frac{2r_c\left(r_c^2 - r_t^2\right)\cos\theta + r_c(2r_t - r_c)\left[4\left(r_c^2 - r_t^2\right)\cos^2\theta + 5r_t^2 - 4r_t r_c\right]^{1/2}}{4\left(r_c^2 - r_t^2\right)\cos^2\theta + \left(r_c - 2r_t\right)^2} \tag{B.4}$$

The angle of similarity or the Lode angle, θ, is defined as the angle between the deviatoric component of stress vector and the projection of σ_3 axis on the deviatoric plane (Figure B.2) and is given by:

$$\theta = \cos^{-1}\left[\frac{3(\sigma_3 - \sigma_m)}{\sqrt{6}\sqrt{\sigma_1^2 + \sigma_2^2 + \sigma_3^2 - 3\sigma_m^2}} \right] \qquad \text{for } \sigma_3 \geq \sigma_2 \geq \sigma_1 \tag{B.5}$$

where σ_i (i = 1–3) is the principal normal stress in the i$^{\text{th}}$ direction.

As the failure surface exhibits three-fold symmetry, it suffices to define this equation for a sector between 0° and 60°. In this manner, the entire surface is completely defined. By expressing Eq. (B.4) in terms of cartesian coordinates, the three principal stresses at failure are obtained from Eq. (B.6).

$$\begin{bmatrix} \sigma_1 \\ \sigma_2 \\ \sigma_3 \end{bmatrix} = r(\sigma_m, \theta) \begin{bmatrix} -\dfrac{\cos\theta}{\sqrt{6}} - \dfrac{\sin\theta}{2} \\ -\dfrac{\cos\theta}{\sqrt{6}} + \dfrac{\sin\theta}{2} \\ \dfrac{2\cos\theta}{\sqrt{6}} \end{bmatrix} + \begin{bmatrix} \sigma_m \\ \sigma_m \\ \sigma_m \end{bmatrix} \quad \text{where } \sigma_m = \frac{1}{3} I_1 \tag{B.6}$$

Since Eq. (B.6) is defined in the domain of $0 < \theta < 360°$ while Eq. (B.4) is only valid for $0 < \theta < 60°$, it is necessary to convert any angle of similarity outside the latter range to an equivalent angle within this range before substituting into Eq. (B.4).

Through the use of Eq. (B.4), the failure surface can be degenerated for the purpose of analyzing biaxial load cases by considering the intersection of the surface with any of the three principal planes. Due to the threefold symmetry of the failure surface, the biaxial failure envelopes on the three planes are identical. The biaxial failure envelope obtained from the experimental data presented by Kupfer et al. (1969) is depicted in Figure B.3.

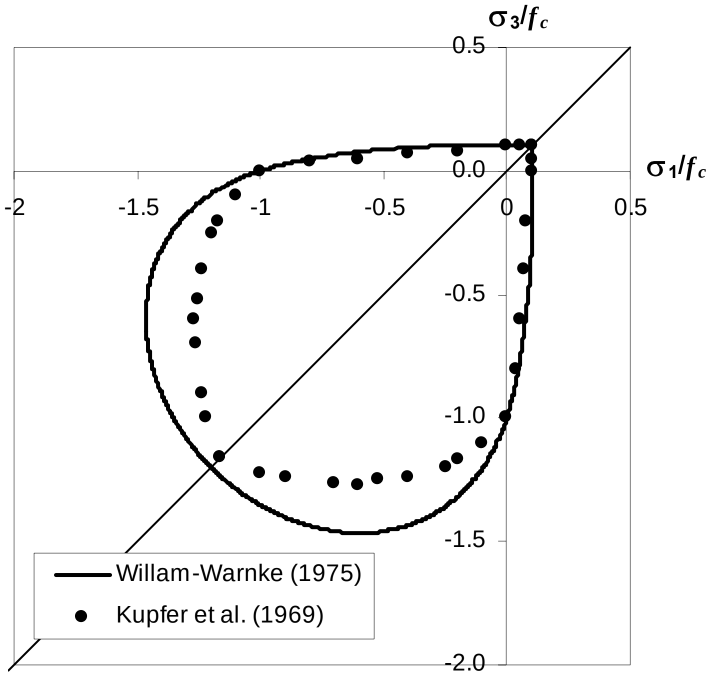

Figure B.3 Biaxial failure envelope degenerated from 3D failure surface. For Willam-Warnke model, $\bar{f}_t = f_t / f_c = 0.1$, high compressive stress point on tensile meridian $(\bar{\xi}_1, \bar{r}_1) = (1.97, 0.53)$, and high compressive stress point for on compressive meridian $(\bar{\xi}_2, \bar{r}_2) = (1.58, 0.63)$

If the failure criterion of Willam-Warnke is not combined with a plasticity rule, the behavior of concrete is linear up to crushing and once the crushing stresses are reached element stiffness contribution to the global stiffness diminishes to zero resulting in a premature failure due to strength loss (ANSYS). The uniaxial stress-strain relation is plotted in Figure B.4. So it is recommended that combining the failure criterion with a plasticity rule will give better results.

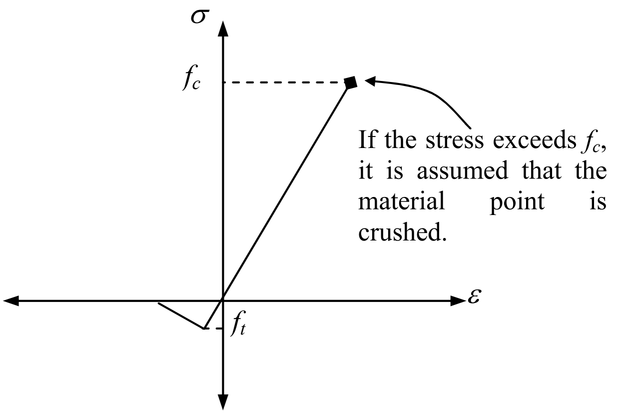

Figure B.4 Uniaxial behavior in Willam-Warnke criterion in ANSYS.

3. Von Mises Yield Criterion

In early finite element applications of concrete to simulate the behavior in compression, the von Mises plasticity model with isotropic hardening (BISO "ANSYS" designation), kinematic hardening or combined hardening was widely used. The von Mises yield criteria with isotropic hardening defined as:

$$F = \sqrt{J_2} - \sigma(\varepsilon_p) = 0 \tag{B.7}$$

where J_2 is the second stress invariant which can be expressed in the principal stress space as

$$J_2 = \frac{1}{6}\left[(\sigma_1 - \sigma_2)^2 + (\sigma_1 - \sigma_3)^2 + (\sigma_2 - \sigma_3)^2\right] \tag{B.8}$$

In Eq. (B.7) $\sigma(\varepsilon_p)$ is the hardening stress as a function of equivalent plastic strain, ε_p which is expressed as follows:

$$\varepsilon_p = \sqrt{\sum_{i=1}^{6}\sum_{j=1}^{6}\frac{2}{3}\varepsilon_{ij}^{p}\varepsilon_{ij}^{p}} \tag{B.9}$$

where ε_{ij}^{p} is the plastic part of the corresponding strain component. Since this model is independent of the magnitude of the hydrostatic stresses, it may not be a suitable plasticity model for concrete in high compression (Han and Chen, 1988). The use of BISO material model in ANSYS is quite straightforward, since the model is directly calibrated with concrete strength in compression (f_c) and post elastic modulus (E_{cp}) of the bilinear curve. This model is also used for the modeling of reinforcing steel.

4. Drucker-Prager Plasticity Model

The second material model available in ANSYS for modeling compressive behavior of granular materials is the Drucker-Prager yield criterion. In this study special emphasize is given to Drucker-Prager model since determination of its parameters is not as simple as bilinear isotropic hardening plasticity model for accurate response prediction of concrete response. A smooth approximation to the Mohr-Coulomb surface was proposed by Drucker and Prager (1952) is a simple modification of the von Mises yield criterion in the form

$$f(I_1, J_2) = \alpha I_1 + \sqrt{J_2} - \tau_0 = 0 \tag{B.10}$$

in which α and τ_0 are positive material parameters. $I_1 = \sigma_1 + \sigma_2 + \sigma_3$ is the first invariant of the stress tensor and J_2 is given in Eq. (2.8). Or identically, using $\xi = I_1 / \sqrt{3}$ and $r = \sqrt{2J_2}$ for clear geometric interpretation of the stress state and the yield surface can be represented as

$$f(\xi, r) = \sqrt{6}\alpha\xi + r - \sqrt{2}\tau_0 = 0 \tag{B.11}$$

where r is the deviatoric and ξ is the hydrostatic components of stress tensor.

The Drucker-Prager criterion represents moderately well the response of plain concrete subjected to multiaxial compression and provides a smooth yield surface. Comparison of the Drucker-Prager criterion with experimental data shows that while the criterion may be used to represent the response of concrete subjected to multiaxial compression, the model overestimates the capacity of concrete subjected to compression-tension or tension-tension type loading (Lowes, 1999).

In ANSYS the input parameters of Drucker-Prager criterion (α and τ_0) are interpreted in terms of c and ϕ of the Mohr-Coulomb (MC) model. Parameter c is called the cohesion and ϕ is the angle of internal friction. The general expression for Mohr-Coulomb criterion is given by

$$(1 + \sin\phi)\sigma_1 - (1 - \sin\phi)\sigma_3 = 2c\cos\phi\,. \tag{B.12}$$

Characteristic strengths values at uniaxial tensile and compressive failure of concrete is defined with the following relations in Mohr-Coulomb stress,

$$f_t = \frac{2c\cos\phi}{1 + \sin\phi} \tag{B.13}$$

$$f_c = \frac{2c\cos\phi}{1 - \sin\phi} \tag{B.14}$$

DP constants can be related to MC constants c and ϕ in several ways. The size of the cone of Drucker-Prager criterion can be adjusted to either surround the Mohr-Coulomb hexagon from the vertices corresponding to compressive meridians or tensile meridians as shown in Figure B.5.

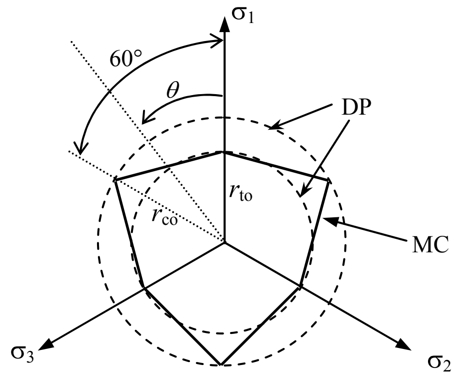

Figure B.5 Drucker-Prager criterion matched to Mohr-Coulomb failure surface

In the case of three dimensional matching, if the two failure surface decided to meet on the compressive meridian which can be followed from Figure B.6, the two sets of material constants are related by

$$\alpha = \frac{2\sin\phi}{\sqrt{3}(3-\sin\phi)} \qquad \tau_0 = \frac{6c\cos\phi}{\sqrt{3}(3-\sin\phi)} \tag{B.15}$$

If the tensile meridian is used similarly

$$\alpha = \frac{2\sin\phi}{\sqrt{3}(3+\sin\phi)} \qquad \tau_0 = \frac{6c\cos\phi}{\sqrt{3}(3+\sin\phi)} \tag{B.16}$$

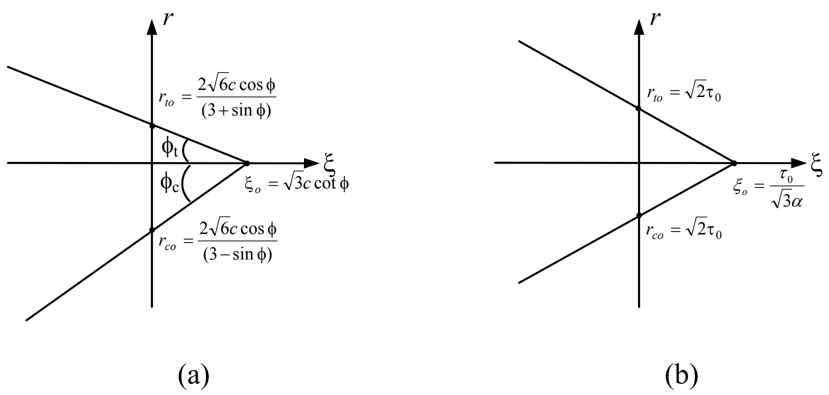

Figure B.6 Meridian representation in deviatoric stress vs. hydrostatic stress plane (a) Mohr-Coulomb and (b) Drucker-Prager yield surfaces

Variation in concrete response under various load regimes leads to different definitions of material constants at each regime. To relate the Drucker-Prager constants α and τ_0 with the Mohr-Coulomb constants c and ϕ in the biaxial stress space, two points from material tests are required.

Under plane stress condition (σ_2 = 0), the invariants of the stress tensor can be expressed as $I_1 = \sigma_1 + \sigma_3$ and $J_2 = (\sigma_1{}^2 + \sigma_3{}^2 - \sigma_1\sigma_3)/3$. Considering the uniaxial compression and tension tests and biaxial compression test conditions, the values of principal stresses, invariants I_1 and J_2, and Haigh-Westergaard coordinates ξ, r and θ are listed in Table B.2.

For the case of Drucker-Prager criterion, substituting the values at peak stress under uniaxial compression (f_c) and tension (f_t) and solving for the model parameters (Eq.'s (B.13) and (B.14)) we get

$$\alpha = \frac{f_c - f_t}{\sqrt{3}(f_c + f_t)} \tag{B.17}$$

$$\tau_0 = \frac{2 f_c f_t}{\sqrt{3}(f_c + f_t)} \tag{B.18}$$

Under the plane stress condition, the criterion in Eq. (B.10) can be presented in the form

$$4(\sigma_1{}^2 + \sigma_3{}^2) + \left(2 - 3\frac{f_c{}^2 + f_t{}^2}{f_c + f_t}\right)\sigma_1\sigma_3 + 4(f_c - f_t)(\sigma_1 + \sigma_3) - 4 f_c f_t = 0 \tag{B.19}$$

Table B.2 Principal stresses, stress invariants, and Haigh-Westergaard coordinates at failure

Stress state	σ_1	σ_3	I_1	J_2	ξ	**r**	***θ, deg.***
Uniaxial tension	f_t	0	f_t	$f_t^2/3$	$f_t/\sqrt{3}$	$f_t\sqrt{2/3}$	0
Uniaxial compression	0	$-f_c$	$-f_c$	$f_c^2/3$	$-f_c/\sqrt{3}$	$f_c\sqrt{2/3}$	60
Equibiaxial compression	$-f_{bc}$	$-f_{bc}$	$-2f_{bc}$	$f_{bc}^2/3$	$-2f_{bc}/\sqrt{3}$	$f_{bc}\sqrt{2/3}$	0

Depending on the ratio f_t / f_c, Eq. (B.19) can be an ellipse, parabola or hyperbola. By matching the uniaxial strengths in tension and in compression, we would obtain quite a reasonable approximation of the actual failure envelope in the quadrants that correspond to biaxial tension and to tension-compression. However, the equibiaxial strength in the compression-compression quadrant becomes infinite as f_t / f_c ratio decreases. On the other hand, a good approximation in the biaxial compression range can be obtained by matching the uniaxial and equibiaxial compressive (f_{bc}) strengths (Jirasek and Bazant, 2001). This leads to

$$\alpha = \frac{f_{bc} - f_c}{\sqrt{3}(2f_{bc} - f_c)} \tag{B.20}$$

$$\tau_0 = \frac{f_{bc} f_c}{\sqrt{3}(2f_{bc} - f_c)} \tag{B.21}$$

Similar to Eq. (B.19), under plane stress, the criterion can be expressed in the form as given below to give a better approximation in the compressive region

$$\begin{aligned} &\left(2 - 3\frac{f_{bc}}{f_c}\right)(\sigma_1^2 + \sigma_3^2) + \left(3\frac{(2f_{bc}^2 + f_c^2)}{f_c f_{bc}} - 8\right)\sigma_1\sigma_3 \\ &\qquad - 2(f_{bc} - f_c)(\sigma_1 + \sigma_3) + f_c f_{bc} = 0 \end{aligned} \tag{B.22}$$

5. Multilinear Work Hardening Plasticity Models (MISO and MKIN)

The greatest shortcomings of the BISO and DP plasticity models used to model concrete in compression is due to fact that while the concrete softening can not be modeled with the former, neither hardening nor softening can be modeled with the latter model. To model the descending branch of the concrete stress-strain curve multi-linear plasticity models available in ANSYS material library can be used. The Multilinear Isotropic Hardening (MISO) option is similar to the bilinear isotropic hardening option, except that a multilinear curve is used instead of a bilinear curve.

When the softening property in the post-peak response is used in constitutive models, the finite element solutions are known to have spurious sensitivity to the mesh size and have difficulty in converging since low order elements such as the one used here is utilized in the finite element analysis (Maekawa et al., 2003; Cervenka et al., 2005; Bazant and Jirasek, 2001). Additionally, NLFEA analysis under force type loading can not track the softening branch of the stress-strain curve after the ultimate (peak) force level of the model is reached. To achieve convergence after the ultimate load capacity of reinforced concrete member displacement controlled loading is applied.

APPENDIX C

CONCRETE MODELS FOR CONFINED CONCRETE

1. Model by Mander et al. (1988)

Due to wide recognition and since the recent version of TSC (2007) recommends the use of it, the confined concrete model proposed by Mander et al. (1988) is adopted in this study. Modeling of the confined concrete is essential in order to enable accurate modeling of critical (plastic hinge) zones up to very large deformations for the evaluation of ductility demand.

For monotonic loading, the compressive concrete stress f_c is given by the Popovics (1973) curve expressed as

$$f_c = \frac{f_{cc} x r}{r - 1 + x^r} \tag{C.1}$$

where the parameters of Eq. (C.1) are defined by Eqs. (C.2) through (C.7) as

$$f_{cc} = \lambda_c f_{co} \tag{C.2}$$

$$x = \varepsilon_c / \varepsilon_{cc} \tag{C.3}$$

$$\varepsilon_{cc} = \varepsilon_{co}\left[1 + 5\left(\frac{f_{cc}}{f_{co}} - 1\right)\right] \tag{C.4}$$

$$r = \frac{E_c}{E_c - E_{\sec}} \tag{C.5}$$

$$E_c = 5000\sqrt{f_{co}} \tag{C.6}$$

$$E_{\sec} = \frac{f_{cc}}{\varepsilon_{cc}} \tag{C.7}$$

where λ_c is the confinement factor, f_{co} is the compressive strength of unconfined concrete, f_{cc} is the compressive strength (peak stress) of confined concrete, ε_c is the longitudinal concrete strain, ε_{co} (~0.002) is the strain at unconfined stress f_{co}, ε_{cc} is the strain at maximum concrete stress f_{cc}, E_c is the initial modulus of elasticity of concrete and E_{sec} is the secant modulus of elasticity of concrete at peak stress.

The confinement factor can be calculated as

$$\lambda_c = 2.254\sqrt{1 + 7.94\frac{f_e}{f_{co}}} - 2\frac{f_e}{f_{co}} - 1.254 \tag{C.8}$$

The effective confinement strength, f_e, can be calculated as the average of values in two perpendicular directions for rectangular cross sections as:

$$f_{ex} = k_e \rho_x f_{yw} \qquad ; \qquad f_{ey} = k_e \rho_y f_{yw} \tag{C.9}$$

In these equations f_{yw} is the yield strength of transverse steel, ρ_x and ρ_y are the ratio of the volume of transverse reinforcement in two directions to the volume of concrete core measured to outside of stirrups, and k_e is the confinement effectiveness coefficient given as,

$$k_e = \left(1 - \frac{\sum a_i^2}{6b_o h_o}\right)\left(1 - \frac{s}{2b_o}\right)\left(1 - \frac{s}{2h_o}\right)\left(1 - \frac{A_s}{b_o h_o}\right)^{-1} \tag{C.10}$$

where a_i is the distance between the axes of longitudinal reinforcements, b_o and h_o are the distance between the axis of transverse reinforcement confining the concrete core, s is transverse reinforcement vertical spacing, A_s is the area of longitudinal reinforcement.

The maximum compressive strain in the extreme fiber of confined concrete can be calculated from (Paulay and Priestly, 1992)

$$\varepsilon_{cu} = 0.004 + \frac{1.4\rho_s f_{yw}\varepsilon_{su}}{f_{cc}} \tag{C.11}$$

where ρ_s is the volumetric ratio of transverse reinforcement and calculated as $\rho_s = \rho_x + \rho_y$ in rectangular sections.

The model is valid only within a certain range of confinement steel; otherwise the results are not realistic or valid. Also there is a deficiency in the model regarding the descending part of the confined concrete stress-strain curve. The experimental results (Martirossyan and Xiao, 1996) show that some modifications as proposed by Martirossyan and others are required to make it more realistic. Also, as already mentioned, the model may be applied only for a confinement range for which f'_l is between zero and about 2.3; otherwise the method will not yield realistic behavior.

2. Saatcioglu and Razvi (1992) Model

Another model proposed by Saatcioglu and Razvi (1992) to construct a stress-strain relationship for confined concrete remedy to the problem in the descending (softening) part of the curve in the Mander et al. (1988) model. The model consists of a parabolic ascending branch, followed by a linear descending branch. Lateral reinforcement in the sense of equivalent uniform lateral pressure in both circular and rectangular columns was used to develop the model characteristics for the strength and ductility of the confined concrete. The model has been compared with different types of column tests, including circular, square, and rectangular, as well as welded wire fabric. Spirals, rectilinear hoops, and cross ties have been used as lateral reinforcement in confined columns. The following expression is suggested for the parabolic ascending portion

$$f_c = f_{cc}' \left[2\left(\frac{\varepsilon_c}{\varepsilon_1}\right) - \left(\frac{\varepsilon_c}{\varepsilon_1}\right)^2 \right]^{\frac{1}{1+2K}} \qquad \leq f_{cc}' \qquad \text{(C.12)}$$

The expressions to calculate necessary parameters in constructing the ascending branch of stress-strain curve are given below in consideration with a rectangular section plotted in Figure C.1.

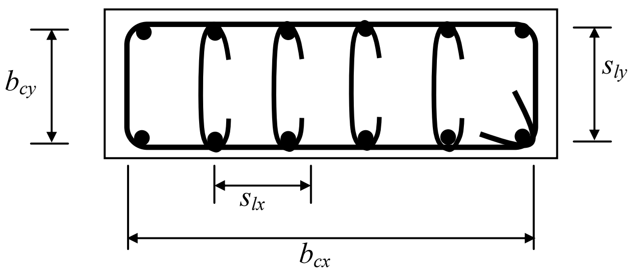

Figure C.1 Rectangular cross-section of a column

Eqs. (C.13) and (C.14) calculates the average uniform lateral pressures in x and y directions together with the reduction factor, k_2, applied to reduce average pressures since these values results in overestimation of the actual effect of lateral pressure.

$$f_{lx} = \frac{\sum A_{sx} f_{yt} \sin\alpha}{s b_{cy}} \qquad k_{2x} = 0.26\sqrt{\left(\frac{b_{cx}}{s}\right)\left(\frac{b_{cx}}{s_{lx}}\right)\left(\frac{1}{f_{lx}}\right)} \qquad \leq 1.0 \qquad \text{(C.13)}$$

$$f_{ly} = \frac{\sum A_{sy} f_{yt} \sin\alpha}{s b_{cx}} \qquad k_{2y} = 0.26\sqrt{\left(\frac{b_{cy}}{s}\right)\left(\frac{b_{cy}}{s_{ly}}\right)\left(\frac{1}{f_{ly}}\right)} \qquad \leq 1.0 \qquad \text{(C.14)}$$

The average lateral pressure in Eq. (C.13) and (C.14) is in MPa; k_2 = 1.0 for spirally reinforced circular columns as well as square columns with closely spaced lateral and laterally supported longitudinal reinforcement; and α = the angle between the transverse reinforcement and b_c, and is equal to 90^o if the transverse reinforcement is perpendicular to b_c. b_{cy} and b_{cy} are measured center to center of perimeter hoop, and s_{lx} and s_{ly} is the spacing between the laterally supported longitudinal reinforcement in x and y directions, respectively, as defined in Figure C.1. s is the center to center spacing between the ties. The overall equivalent uniform pressure obtained by combining the equivalent pressures in x and y directions can be established by

$$\left.\begin{aligned} f_{lex} &= k_{2x} f_{lx} \\ f_{ley} &= k_{2y} f_{ly} \end{aligned}\right\} \rightarrow f_{le} = \frac{f_{lex} b_{cx} + f_{ley} b_{cy}}{b_{cx} + b_{cy}} \tag{C.15}$$

The triaxial strength of concrete in terms of uniaxial strength and lateral confinement pressure is given by

$$f_{cc}' = f_{co}' + k_1 f_{le} \tag{C.16}$$

where f_{cc} and f_{co} are the confined and unconfined strengths of concrete in a member, respectively. Coefficient k_1 varies with different values of lateral pressure f_{le}. Based on the test data, a relationship between these two parameters has been established as:

$$k_1 = 6.7\left(f_{le}\right)^{-0.17} \tag{C.17}$$

where f_{le} is the uniform confining pressure in MPa. Finally, the following expression was proposed to calculate K.

$$K = \frac{k_1 f_{le}}{f_{co}'} \tag{C.18}$$

The strain corresponding to the peak stress of confined concrete (f_{cc}) is denoted as ε_1 and is calculated as similar to that found by previous researchers (Balmer 1949; Mander et al. 1988):

$$\varepsilon_1 = \varepsilon_{01}(1 + 5K) \tag{C.19}$$

In the above equation, ε_{01} is the strain corresponding to the peak stress of unconfined concrete, which should be determined under the same rate of loading used for the confined concrete. In the absence of experimental data the value 0.002 may be appropriate for ε_{01}. This concludes the first part of the model, i.e., the ascending branch of the stress-strain curve.

The descending branch of the curve is linear and connects the points (f_{cc}', ε_1) and ($0.85 f_{cc}', \varepsilon_{85}$) on the plane of the stress-strain curve. The value of strain corresponding to 85% of confined concrete strength is calculated as:

$$\varepsilon_{85} = 260\rho\varepsilon_1 + \varepsilon_{085} \tag{C.20}$$

where ρ is the volumetric ratio of transverse reinforcement and is expressed as:

$$\rho = \frac{\sum A_s}{s\left(b_{cx} + b_{cy}\right)} \tag{C.21}$$

and ε_{085} is the strain corresponding to 85% of the strength level beyond the peak stress of unconfined concrete. Again it should be determined under the same rate of loading as for the confined concrete specimen. If no test data are available the value 0.0038 might be used.

The equation for the descending branch is

$$f_c = f_{cc}\left[1 - \frac{0.15(\varepsilon - \varepsilon_1)}{\varepsilon_1(260\rho - 1) + \varepsilon_{085}}\right] \tag{C.22}$$

APPENDIX D

TIMES SERIES OF SELECTED CROUND MOTIONS

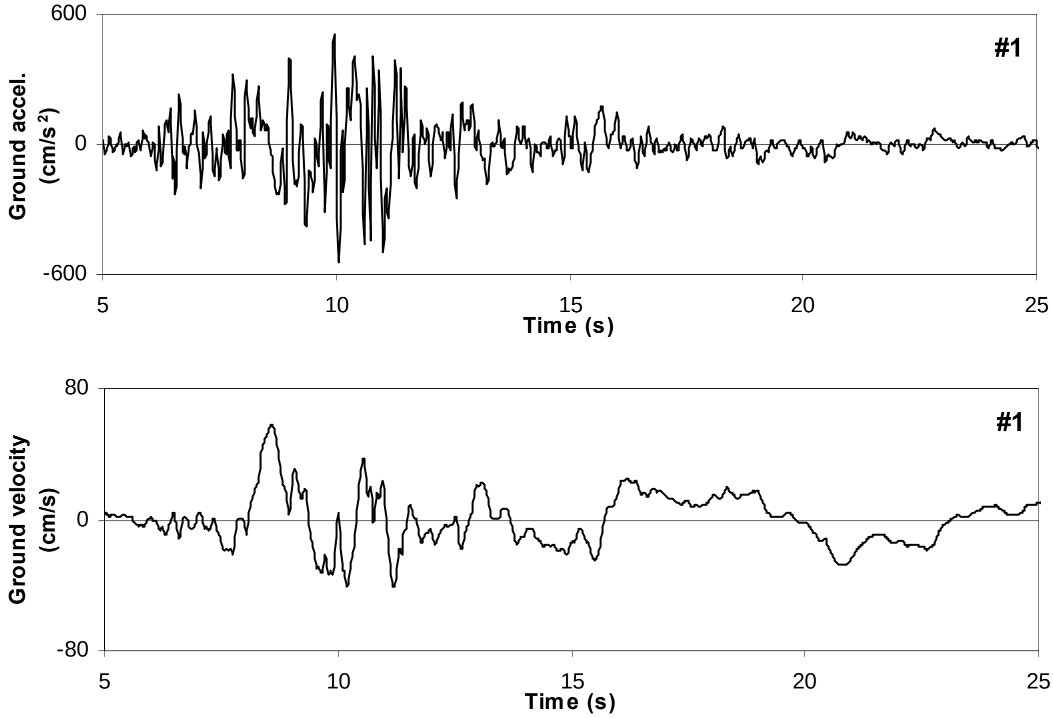

Figure D.1 The scaled ground acceleration and velocity time series of selected ground motion #1.

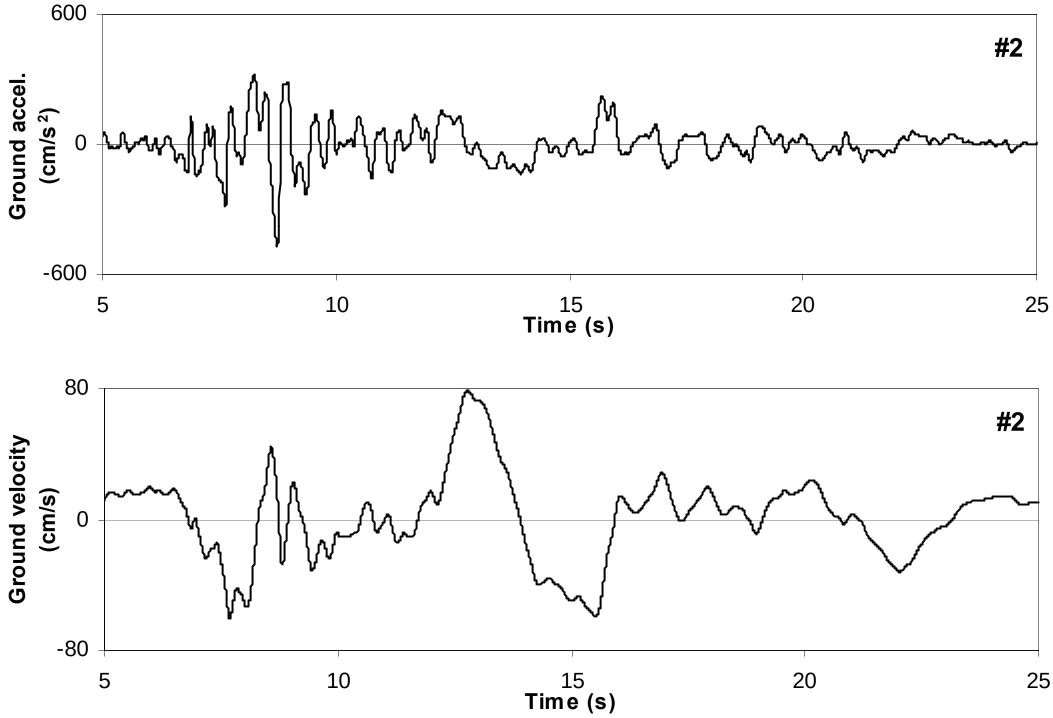

Figure D.2 The scaled ground acceleration and velocity time series of selected ground motion #2.

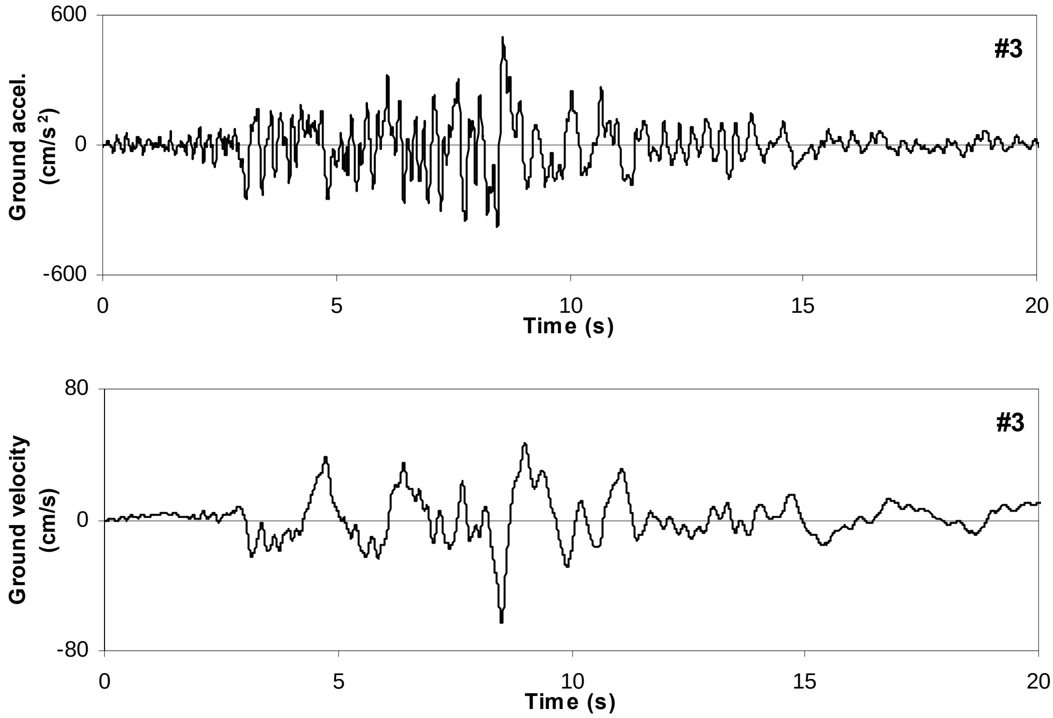

Figure D.3 The scaled ground acceleration and velocity time series of selected ground motion #3.

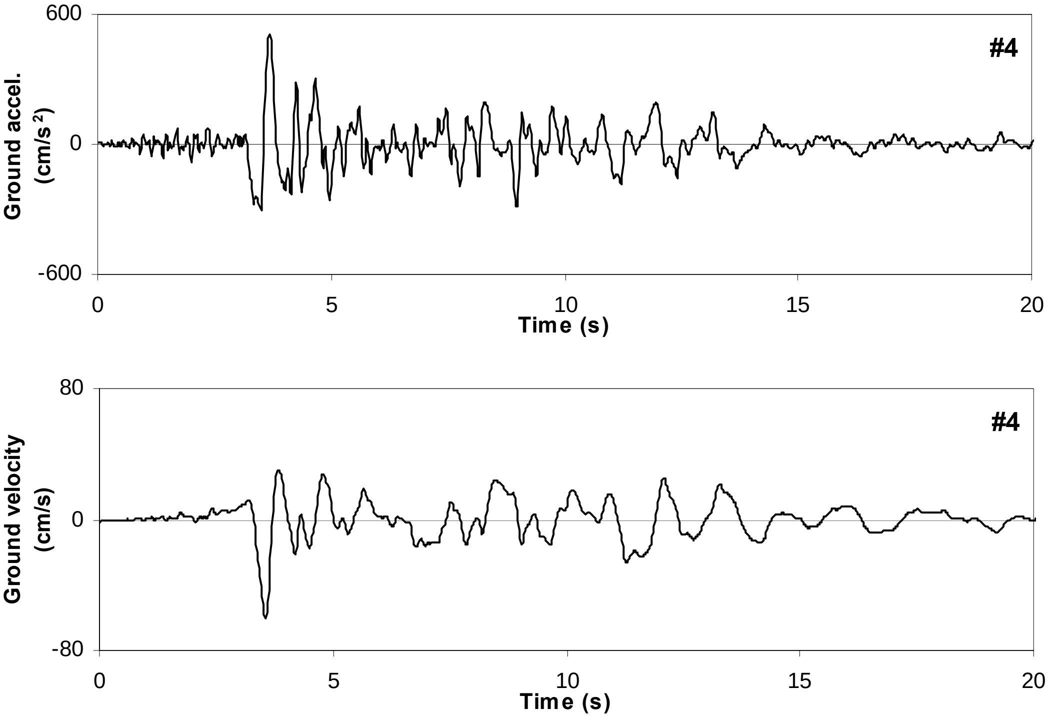

Figure D.4 The scaled ground acceleration and velocity time series of selected ground motion #4.

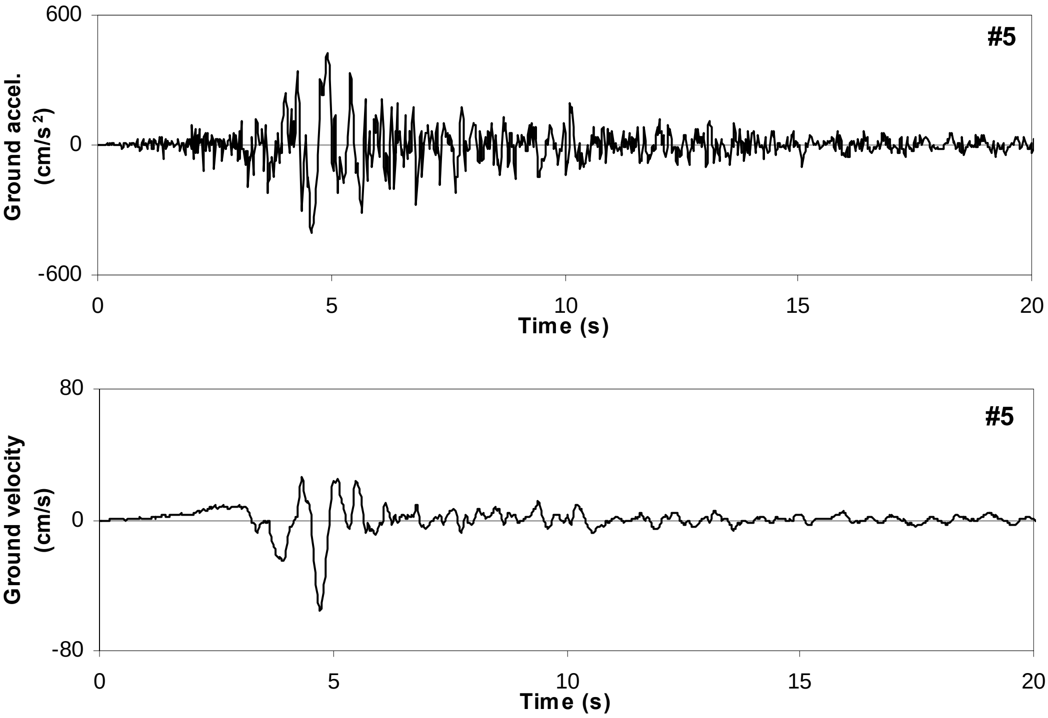

Figure D.5 The scaled ground acceleration and velocity time series of selected ground motion #5.

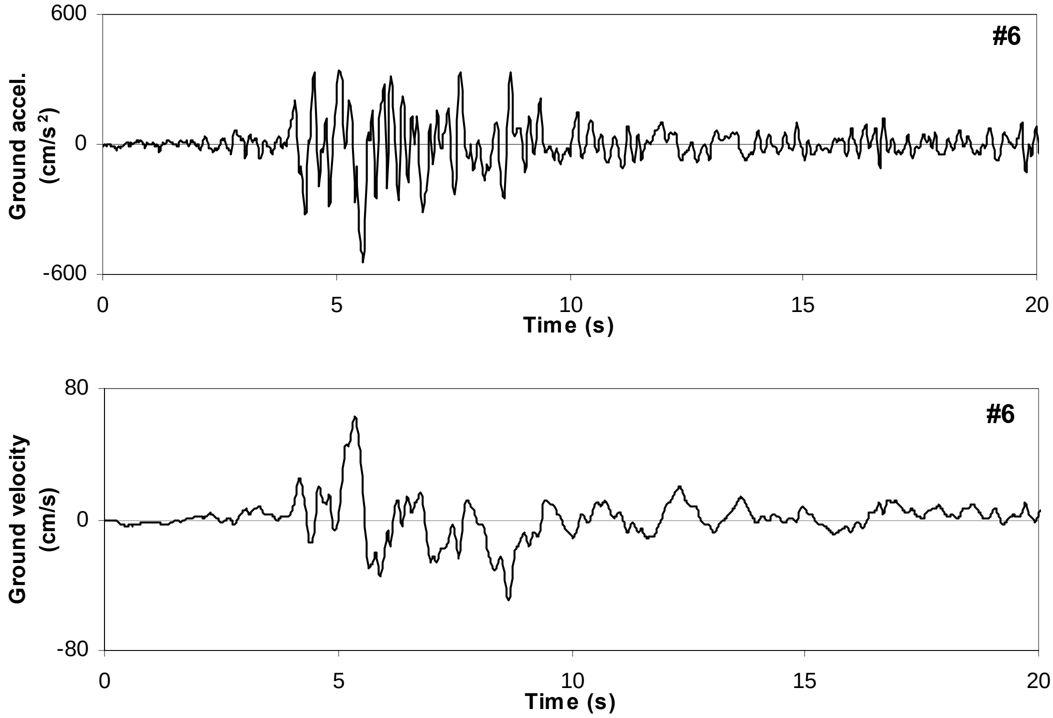

Figure D.6 The scaled ground acceleration and velocity time series of selected ground motion #6.

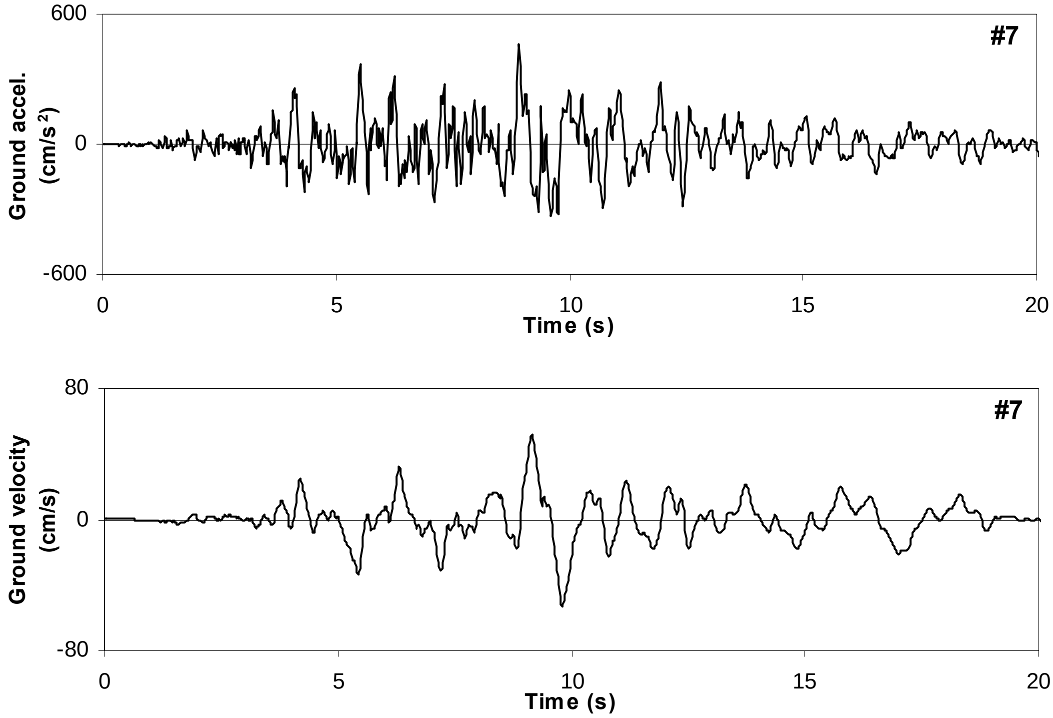

Figure D.7 The scaled ground acceleration and velocity time series of selected ground motion #7.

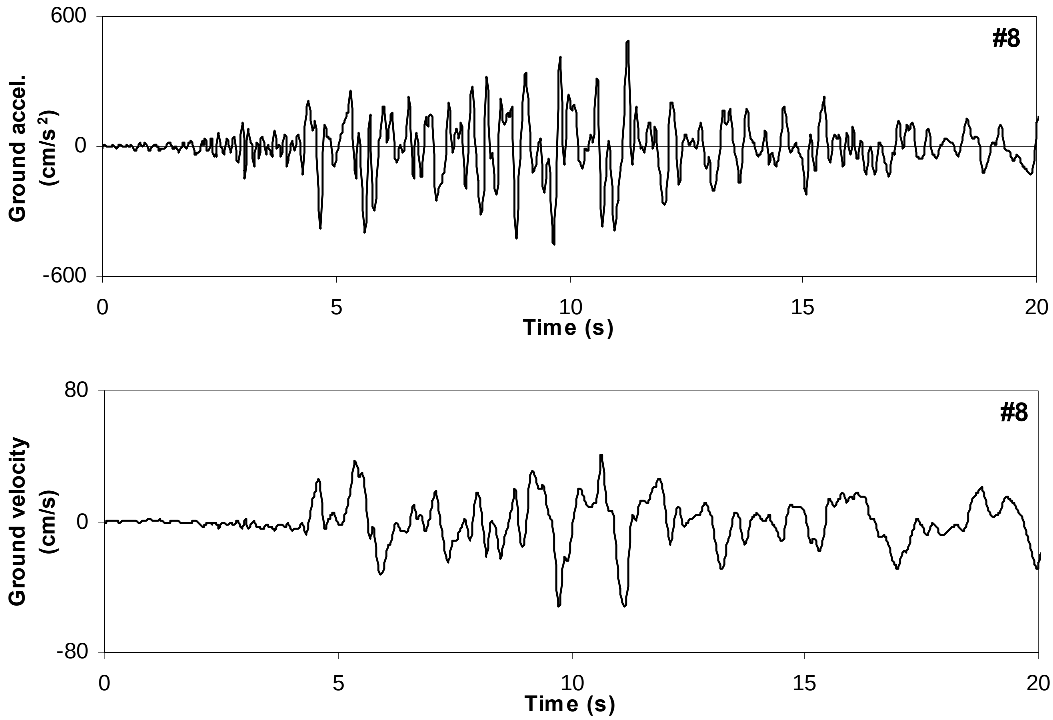

Figure D.8 The scaled ground acceleration and velocity time series of selected ground motion #8.

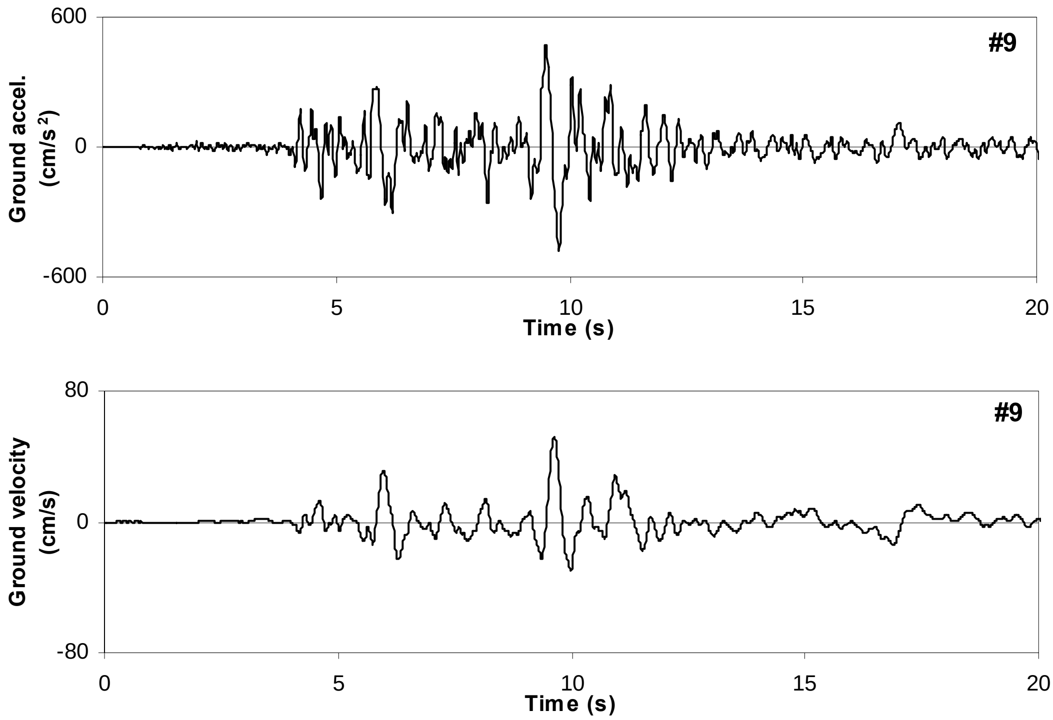

Figure D.9 The scaled ground acceleration and velocity time series of selected ground motion #9.

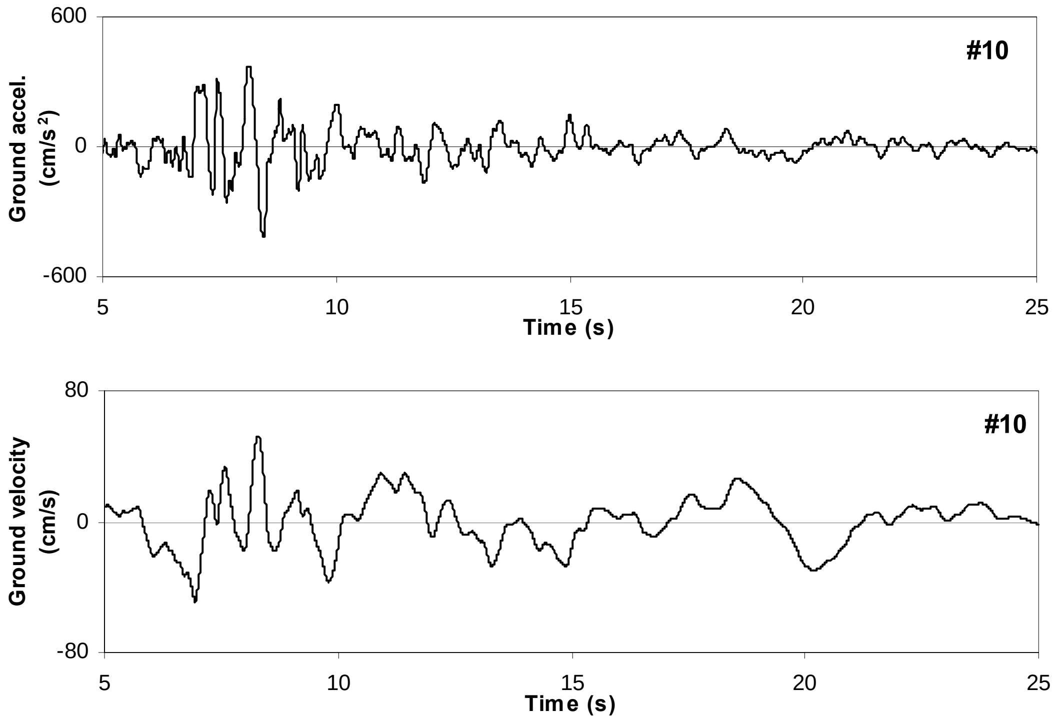

Figure D.10 The scaled ground acceleration and velocity time series of selected ground motion #10.

APPENDIX E

AN IMPROVED FRAME-SHEAR WALL MODEL: CONTINUUM APPROACH

1. Introduction

The governing equation of the combination beam in Figure 4.15 is given by

$$\frac{d^4 y}{dx^4} - \alpha^2 \frac{d^2 y}{dx^2} = \frac{w(x)}{EI} \tag{E.1}$$

where *w(x)* is the distributed lateral loading function and

$$\alpha^2 = \frac{GA}{EI} \tag{E.2}$$

in which *GA* and *EI* are the shear and flexural rigidities, respectively.

A tall structural wall can be considered as vertical cantilever beam, with zero deflection and rotation at the base and free at the top, so the boundary conditions that apply to the solution of the differential equation are $y(0) = y'(0) = M(H) = V(H) = 0$, where H is the height of the structure. The shear force in the shear component (frame) is calculated as

$$V_S(x) = GA \frac{dy}{dx} \tag{E.3}$$

so the shear force at the base of this member becomes zero, which is not correct.

Frame-wall structures can be composed of either (i) walls and frames connected by floor slabs, or (ii) link-beams extending from frames directly to the ends of the walls. The interaction between the frames and walls of structures with link beams is more significant than the form of frame-wall structure where walls and frames connected by floor slabs. The shear and moment transferred from beams can significantly change the moment profile causing a reduction in the inflection height of the wall. The beam shear forces transferred from both side of the wall affect the axial load on the wall. If the problem is idealized by assuming beams of equal strength and equal length that frame into the wall from both sides, the axial load will not be affected by the beam shears since they will cancel out. However, the beam shears from both sides will form a moment couple which must be added to moments transferred from beams. Additional 3D effects such as transverse beams shear forces also contribute to the moments created by the link beams connecting to shear wall.

This article introduces the two refinements into the otherwise well-known formulation for wall-frame systems. One is the correction of the shear force boundary condition at the base of the wall, and the other is the additional distributed moment transferred from link beam ends.

Before presenting the details of mathematical model of the continuum model dealing with the items defined above, the stress resultant-displacement relations derived from flexural and shear beam theories will be given next. Then following the derivation of the differential equations for the deflection of the combined beam, the findings will be verified on a sample frame-wall structure.

2. Stress resultant-displacement relations

Each component in a frame-wall system is forced to deflect in a hybrid mode that is different from their inherent deflected shapes due to frame-wall interaction effects acting through the floor diaphragms. Individually considered, the inherent deflected shapes of frame and shear wall components of a dual system can be represented with beams deforming dominantly in shear and bending modes, respectively. While Euler-Bernoulli beam theory serves well for calculating the elastic deflection of most of the beams assuming pure bending moment, Timoshenko beam theory, a refined version of the former, considers the deflections due to transverse shear, which is the case in deep beams or sandwich beams with low shear modulus. The difference between these fundamental beam theories lies in that, while in the Euler-Bernoulli beam its is assumed that plane cross sections perpendicular to the neutral axis of the beam remain plane and perpendicular to the neutral axis after deformation, in the Timoshenko beam plane sections remain plane but not necessarily normal to the longitudinal axis after deformation, thus causing a nonzero transverse shear strain. The illustration in Figure E.1 can be used to describe this phenomenon graphically.

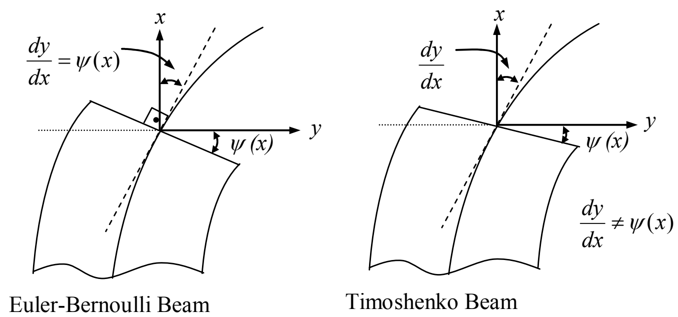

Figure E.1 Schematic representation of deflections according to two fundamental beam theories

Figure E.2 displays the element of a beam used in deriving the relationships between loads, shear forces and bending moments. All loads and stress resultants are shown in their positive directions. In a real structure the forces and moments occur at floor levels at discrete locations, which cause the finite increments (step changes) in shear and moment.

However, since a continuum medium is assumed to be exist between two beam components, the loads are also assumed to be distributed along the members, so increment in V and M can be considered infinitesimal, denoted by dV and dM, respectively. Considering the equilibrium in the y direction yields,

$$\frac{dV}{dx} = -w(x) \tag{E.4}$$

where $w(x)$ is the lateral load on the beam. Then, summing up the moments about the z axis at the left end of the beam element of length dx gives

$$\frac{dM}{dx} = -V(x) + m(x) \tag{E.5}$$

where $m(x)$ describes the action of distributed moments.

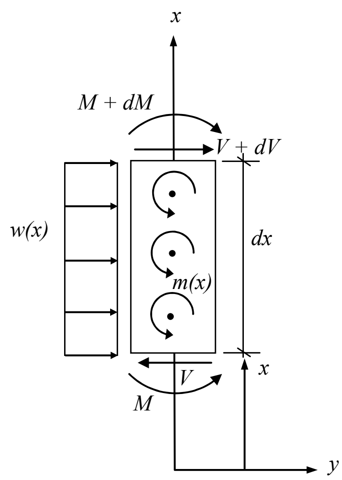

Figure E.2 Element of beam used in deriving the relationships between loads, shear forces and bending moments

Considering these fundamental relationship and a prismatic beam of length L, cross-sectional area A, second moment of area I, elastic modulus of E, and shear modulus of rigidity G under any transverse loading action of $w(x)$ and distributed bending moment $m(x)$, according to the Euler-Bernoulli beam, the stress-displacement relations are given by

$$M = EI\frac{d\psi}{dx} = EI\frac{d^2y}{dx^2} \quad \text{and} \quad V = -EI\frac{d^3y}{dx^3} + m(x) \tag{E.6, 7}$$

where EI is the flexural rigidity and ψ is the rotation of the beam section.

According to Timoshenko beam theory, the stress-displacement relations are given by the following,

$$M = EI\frac{d\psi}{dx} \qquad \text{and} \qquad V = -GAK_s\left(\psi(x) - \frac{dy}{dx}\right) \tag{E.8, 9}$$

where GA represents the shear rigidity and K_S is the shear correction coefficient.

3. Mathematical model for frame-wall interaction problem

In the classical formulation, an equivalent shear stiffness term (GA) that is based on the deformed pattern of the frame components is defined. This stiffness depends on the frame member stiffnesses, the frame configuration and the rigidity of joints, as shown in Figure E.3.

In reference to model in Figure E.4, the contribution of the single column to the total GA parameter of the equivalent shear-flexure beam is given by (Heidebrecht and Stafford Smith, 1973)

$$GA = \frac{12EI_h}{h^2}\frac{1}{1+\dfrac{2I_h}{h\left(\dfrac{I_{b1}}{b_1}+\dfrac{I_{b2}}{b_2}\right)}} \tag{E.10}$$

in which I_h = moment of inertia of column; h = story height; b_1, b_2 = total lengths of adjacent beams; I_{b1}, I_{b2} = moment of inertia of corresponding beams. E is the modulus of elasticity of the concrete material. The total GA contribution of a planar frame is the arithmetic sum of the GA terms for each of the columns in a typical story of the frame.

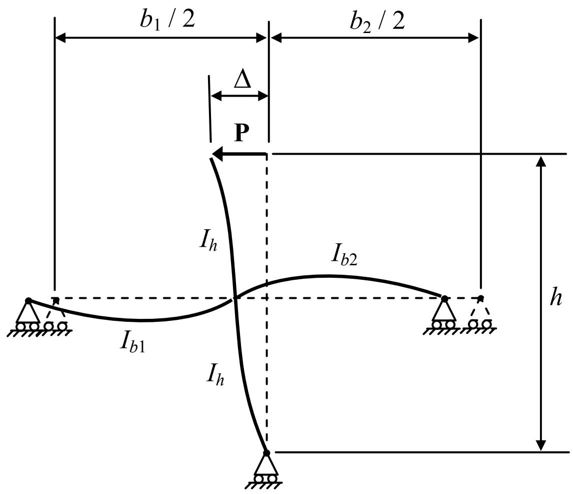

Figure E.3 Modeling of “shearing” behavior in frame

In the deformed representation of one-story beam column assembly of a multi-bay frame shown in Figure E.3, it is assumed that the points of contraflexure occur at midheight of the columns and at midspan of the beams. On the other hand, the restraining system of base story columns below the point of contraflexure is different and the members deform in flexure as shown in Figure E.4. It is assumed here that the entire structure consists of two substructures. The part above the contraflexure point of the base columns is named as Substructure 1 and the below portion as Substructure 2. Section forces at contraflexure points of the columns (h_{cc}) are displayed in Figure E.4. The portion of the columns and shear walls below the contraflexure height can be modeled as cantilevers with point loads applied at the tip. However, since the height to width ratio (h_{cc} / l_w) of the shear wall segment will be very low, Timoshenko beam theory taking into account shear effects will be a better choice to model the shear walls in this region. Figure E.5 displays the ratio of the flexural deformation to total deformation of a cantilever beam with variable height to length ratios under different loading conditions. It is seen in this figure that for typical height to length ratios of shear walls at the ground story (h_{cc}/l_w < 1) the contribution of shearing deformations to total deformation can constitute a significant share. Unless columns cross sectional dimensions are of a level that invokes shear effects significantly, they can be modeled using classical beam theory.

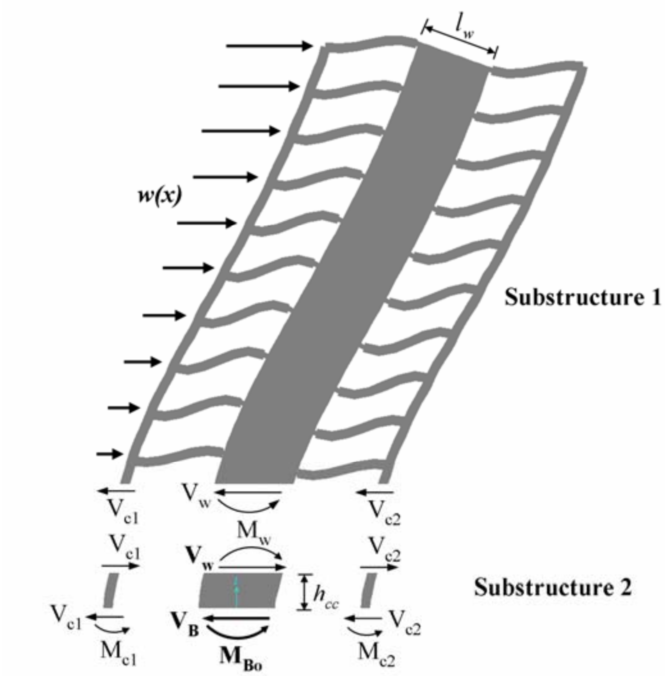

Figure E.4 Section forces on the base story columns and shear walls at the point of column contraflexure

Considering the frame and wall components individually under a distributed lateral load applied on the entire structure, the interaction forces that contribute to the lateral deformations are beam axial forces (coupled with slab forces) for frame component and floor interaction forces and moments transferred from beams for wall component. In the present method, the multistory structure will be modeled as an equivalent continuum structure composed of a flexural cantilever and a shear cantilever, the forces and moments in the actual structure will be assumed distributed along the continua. The continuum model for equivalent shear flexure beam is shown in Figure E.6. It has to be noted that the beam moments acting on the walls were disregarded in the frame component since they do not have any influence on the lateral deformation. In this figure, *q(x)* and *m(x)* represent the action of interaction forces and beam moments transferred on the shear wall, respectively. The subscripts, *B* and *S*, refer to the flexural and shear beams, respectively. Although it was assumed that the action of horizontal forces on the wall as distributed, a concentrated interaction force at the top is required to maintain the deformation compatibility and force equilibrium between the flexural and shear beams. A point load of magnitude *Q* is therefore included in the model shown in Figure E.6.

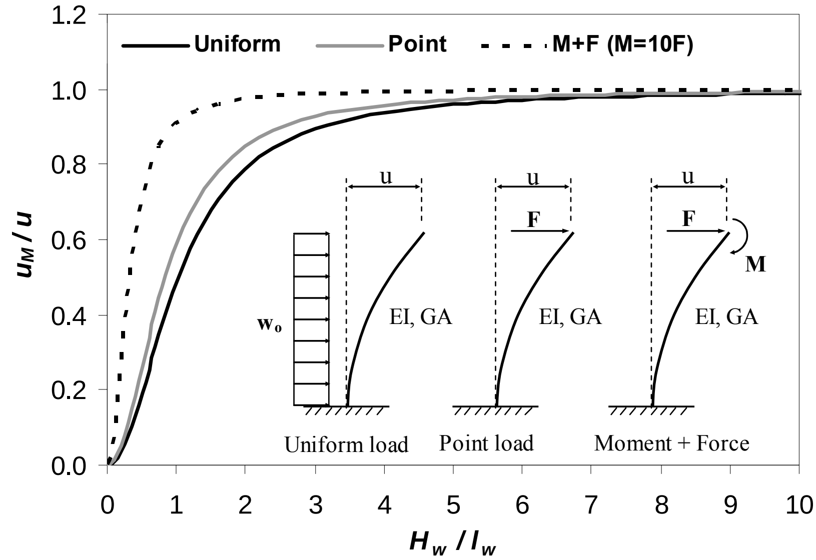

Figure E.5 Ratio of flexural deformation to total deformation on the base of a structural wall

3.1. Differential Equation of Substructure 1

The formula derived by Heidebrecht and Stafford Smith (1973) will be modified further to take into account the effects of link beams on shear walls. The differential equations governing the behavior of two types of beam, referring to Figure E.6, are: For flexural component, assuming uniform stiffness height wise and using Eq. (E.4) and (E.7)

$$EI\frac{d^4y}{dx^4}-\frac{dm}{dx}=w_B(x)-q(x) \tag{E.11}$$

and for shear (frame component) using Eq. (E.4) and (E.9) and ignoring shear correction factor,

$$GA\left(\frac{d\psi_S}{dx}-\frac{d^2y}{dx^2}\right)=w_S(x)+q(x) \tag{E.12}$$

in which subscripts, B and S, refer to flexural and shear beams, respectively.

In multistory structures consisting of tall slender frames, the axial deformations in the exterior columns of the frame will cause the floor diaphragms to rotate, which will contribute to the rotations of the elastic curve [$\psi_S(x)$]. A generalized theory for tall building structures, allowing for axial deformations of columns was proposed by Stafford Smith et al. (1984). However, the effect of such a situation is minor and limited to few structures, so that the rotation of floor slab is assumed to be zero along the height of the structure in this study [$\psi_S(x) = 0$].

Eqs. (E.11) and (E.12) are the governing equations of the flexural (shear wall) and shear (frame) components of the shear-flexure combination member, respectively. Adding these equations, the differential equation governing the response of frame-shear wall system under prescribed lateral load, $w(x)$, is obtained as

$$EI\frac{d^4y}{dx^4} - GA\frac{d^2y}{dx^2} - \frac{dm(x)}{dx} = w(x) \tag{E.13}$$

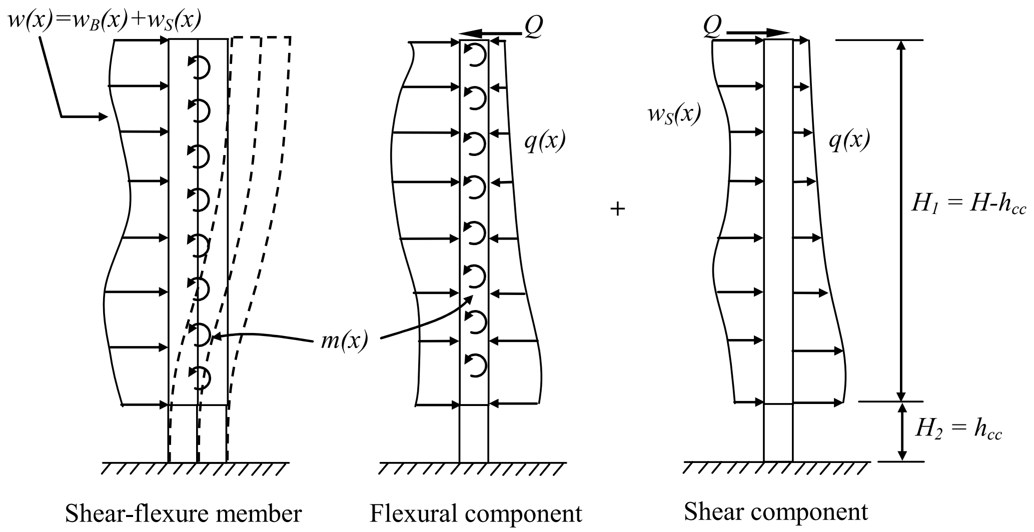

Figure E.6 Mathematical model of shear-flexural beam, interconnected frame and shear wall (equal deflections at each story levels)

3.1.1. Effect of link beams

Eq. (E.13) contains the first derivative of the distributed moment. The distributed beam moment resulting from the beam end moments and shear forces can be calculated using the free body diagram in Figure E.7. The rotation angle at the ends of link beams is the sum of joint and chord rotations. Slope deflection equations are used to calculate the beam end moments on the tension and compression side of the shear wall as given in Eq. (E.14).

$$\left.\begin{aligned} M_l^j &= \frac{2EI_b^j}{l_b}\left(2\theta_l^j + \theta_l^i + 3\phi_l\right) + M_{ij}^F \\ M_r^i &= \frac{2EI_b^i}{l_b}\left(2\theta_r^i + \theta_r^j + 3\phi_r\right) - M_{ij}^F \end{aligned}\right\} \tag{E.14}$$

The beam end joint rotation at the wall side will be equal to the wall rotation, $\theta_l^j = \theta_r^i = \theta_w$, from compatibility. It is also assumed that the beam end rotations at the column side can be equated to beam end rotation at the wall side, $\theta_l^i = \theta_r^j = \theta_w$. For a known value of neutral axis depth, c, the beam chord rotation due to uplift of the wall end is calculated as

$$\phi_l = \frac{\gamma\, l_w \theta_w}{l_b} \tag{E.15}$$

where γ is the ratio of length of the tension (crack) region, measured from the neutral axis to extreme tension fiber, to the wall length. For the linear analysis here γ is 0.5.

Distributing the calculated values in Eq. (E.14) yields

$$\left.\begin{aligned} M_l^j &= \frac{6EI_l^j}{l_b}\left(1 + \frac{\gamma\, l_w}{l_b}\right)\theta_w + M_{ji}^F \\ M_r^i &= \frac{6EI_r^i}{l_b}\left(1 + \frac{(1-\gamma) l_w}{l_b}\right)\theta_w - M_{ij}^F \end{aligned}\right\} \tag{E.16}$$

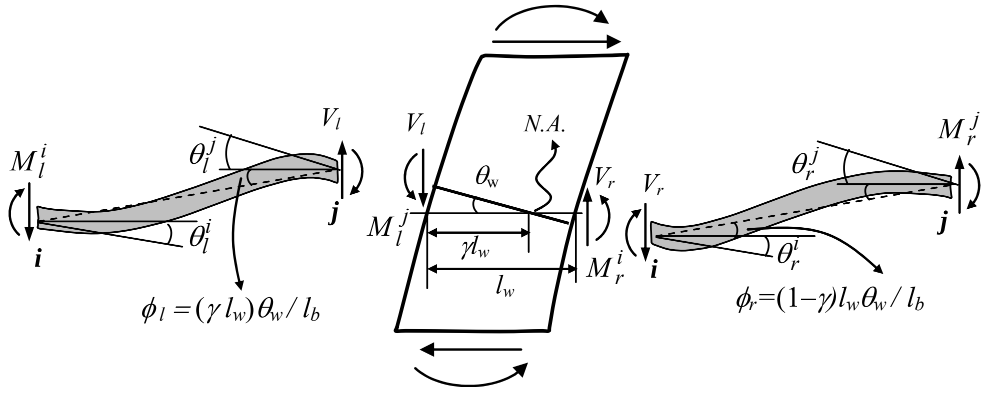

Figure E.7 Deformed configuration of shear wall beam assembly to derive the transmitted beam moments and distributed moment.

On the uplift side of the wall the beam flange and on the drop side of the wall the beam bottom are in tension, so flexural rigidities of beams in Eqs. (E.14) and (E.16) can be different while calculating M_l and M_r taking into account flanges if cracking is considered. These values can be calculated separately or an average value can be taken. For linear analysis, which assumes uncracked section, this does not matter, because the flexural rigidity is equal in both positive and negative bending directions.

Assuming beam rotations are equal at both ends, the beam end moments on the column side can be calculated accordingly. Then the beam end shear force transferred to the wall can be calculated as

$$V_l = \frac{M_l^i + M_l^j}{l_b} \qquad \text{and} \qquad V_r = \frac{M_r^i + M_r^j}{l_b} \tag{E.17}$$

Distributing the related expressions and summing the moments transmitted from beams and calculating the moment created by beam shears at the centerline of the wall axis, the net moment acting on the wall at the ith story is obtained as

$$M_{b,i} = M_l^j + M_r^i + \frac{l_w}{2}(V_l + V_r) \tag{E.18}$$

Considering equal beam length on both sides of the wall and an equal flexural rigidity at all ends of the beams (EI_b), which can taken as the average of flexural rigidities of a flanged section calculated when bent in two directions taking into account the cracking, and inserting $\theta_w = \frac{dy}{dx}$, Eq. (E.18) can be written in open form as

$$M_{b,i} = \frac{6EI_b}{l_b}\left(1 + \frac{l_w}{l_b}\right)\left(2 + \frac{l_w}{l_b}\right)\frac{dy}{dx} \tag{E.19}$$

Assuming this moment is uniformly distributed in between two half story heights (h), the expression giving the distributed moment is obtained as

$$m(x) = \frac{6EI_b}{l_b h}\left(1 + \frac{l_w}{l_b}\right)\left(2 + \frac{l_w}{l_b}\right)\frac{dy}{dx} = \eta \frac{dy}{dx} \tag{E.20}$$

Using the same analogy, the distributed moment action of beams in such a case where only one beam frames to the shear wall can be written as

$$m(x) = \frac{6EI_b}{l_b h}\left(1 + \frac{l_w}{l_b}\right)\left(1 + \frac{l_w}{2l_b}\right)\frac{dy}{dx} = \eta \frac{dy}{dx} \tag{E.21}$$

Inserting the relations obtained in Eqs. (E.20) and (E.21) into the governing differential equation given in Eq. (E.13) of the combined beam and rearranging, we have the expression

$$\frac{d^4 y}{dx^4} - \alpha^2 \frac{d^2 y}{dx^2} = \frac{w(x)}{EI} \tag{E.22}$$

where $w(x) = w_B(x) + w_S(x)$ and

$$\alpha^2 = \frac{GA + \eta}{EI} \tag{E.23}$$

3.2. Response of Substructure 2

The mathematical model describing the essential elements of the base story is given in Figure E.8. This figure represents the portion of the structure below the contraflexure height (h_{cc}). In multistory structures while the point of contraflexure can be taken at the midheight of columns and midspan of beams above the ground story, the contraflexure point of the base story columns (h_{cc}) does not develop at the midheight and moreover it is not constant for every structure. The contraflexure point of corner columns is also different from the interior columns' in the same structure. For a while the discussion on this issue will be postponed until the essential derivations of the new method are completed. The total column shear and the total wall shear are represented with V_c and V_w and they do not vary along the height of the base story. While the column moments are zero at this height, wall moment is equal to M_w.

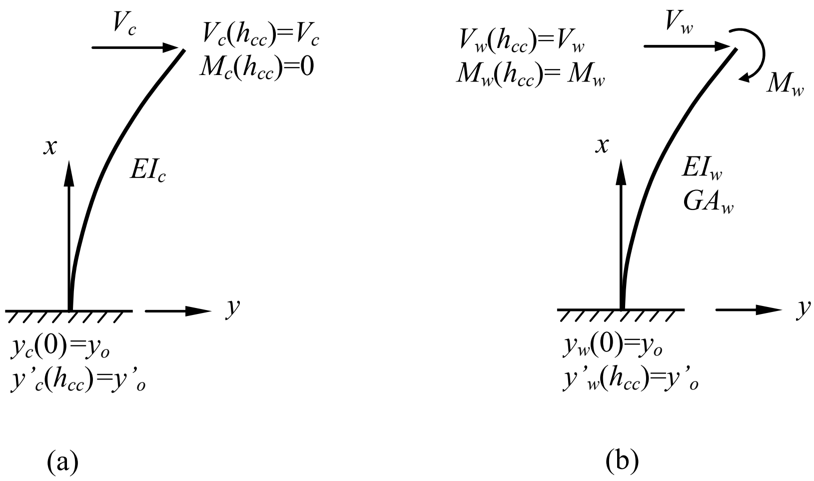

Figure E.8 Model of the base story

In Figure E.8, the flexural (EI_w and EI_c) and shear rigidities (GA_w) are the sum of member rigidities that are of same type at the base story. From Figure E.8(a) the following relationship can be written using the Euler-Bernoulli beam theory

$$EI_c \frac{d^2 y_c}{dx^2} = V_c\left(h_{cc} - x\right) \tag{E.24}$$

Integrating twice and using the prescribed boundary conditions at the base the deflection curve is calculated as

$$y_c(x) = \frac{V_c}{EI_c}\left(\frac{h_{cc}x^2}{2} - \frac{x^3}{6}\right) + y'_o x + y_o \tag{E.25}$$

The total base shear is the sum of wall and column shears, so the column shear can be represented as $V_c = V_o - V_w$ alternatively. Then Eq. (E.25) becomes

$$y_c(x) = \frac{(V_o - V_w)}{EI_c}\left(\frac{h_{cc}x^2}{2} - \frac{x^3}{6}\right) + y_o'x + y_o \tag{E.26}$$

Taking into account shear deformations and using Figure E.8(b), the shear wall component stress-displacements relations become

$$EI_w \frac{d\psi}{dx} = M_{Bo} - V_w x \tag{E.27}$$

where $$M_{Bo} = M_w(h_{cc}) + V_w h_{cc} \tag{E.28}$$

and $$V_w(x) = V_w = -GA_w\left(\psi(x) - \frac{dy_w}{dx}\right) \tag{E.29}$$

Integrating Eq. (E.27) once and using the boundary condition $\psi(0) = y_o'$ for the rotation of wall cross section we obtain,

$$\psi(x) = \frac{1}{EI_w}\left(M_{Bo}x - \frac{V_w x^2}{2}\right) + y_o' \tag{E.30}$$

Introducing Eq. (E.30) into the shear expression in Eq. (E.29) and rearranging, the slope of the deflection curve becomes

$$\frac{dy_w}{dx} = \frac{1}{EI_w}\left(M_{Bo}x - \frac{V_w x^2}{2}\right) + y_o' + \frac{V_w}{GA_w} \tag{E.31}$$

Integrating and using the boundary condition $y(0) = y_o$, the deflection curve of the shear wall is calculated as

$$y_w(x) = \frac{x^2}{2EI_w}M_{Bo} + \left(\frac{x}{GA_w} - \frac{x^3}{6EI_w}\right)V_w + y_o'x + y_o \tag{E.32}$$

The only unknowns in Eqs. (E.26) and (E.32) are M_{Bo} and V_w, the moment at the base of the shear wall and the wall shear force, respectively. The total base shear, V_o, is the sum of the applied lateral load at the base level. The force on the shear wall can be obtained in terms of M_{Bo} and V_o, if the resulting displacements calculated at the contraflexure height on columns and walls are related to each other as

$$\beta = y_c(h_{cc})/y_w(h_{cc}) \tag{33}$$

In the following β is taken as 1. Assuming displacement and rotation boundary conditions is applicable to both columns and walls, the relation defined in Eq. (E.33) yields

$$V_w = \frac{M_{Bo}\beta h_{cc}^2}{2fEI_w} - \frac{V_o h_{cc}^3}{3fEI_c} \tag{E.34}$$

where f is expressed as

$$f = \frac{\beta h_{cc}^3}{6EI_w} - \frac{h_{cc}^3}{3EI_c} - \frac{\beta h_{cc}}{GA_w} \tag{E.35}$$

After the wall shear force (F_w) is distributed into the expressions for the displacement, rotation and bending moment on the wall, we have

$$y_2(x) = y_o + y'_o x + M_{Bo}\left[\frac{x^2}{2EI_w} + \frac{h_{cc}^2\beta}{2fEI_w}\left(\frac{x}{GA_w} - \frac{x^3}{6EI_w}\right)\right] - \frac{V_o h_{cc}^3}{3fEI_c}\left(\frac{x}{GA_w} - \frac{x^3}{6EI_w}\right) \tag{E.36}$$

$$y'_2(x) = y'_o + M_{Bo}\left(\frac{x}{EI_w} - \frac{h_{cc}^2 x^2\beta}{4f(EI_w)^2}\right) + \frac{V_o h_{cc}^3 x^2}{6fEI_w EI_c} \tag{E.37}$$

$$M_w(x) = M_{Bo}\left(1 - \frac{h_{cc}^2 x\beta}{2fEI_w}\right) + \frac{V_o h_{cc}^3 x}{3fEI_c} \tag{E.38}$$

4. Solution of the governing differential equation for uniform stiffness along the height

For the case of a uniformly distributed load of intensity w_o, the solution for Eq. (E.22) can be written in the form

$$y_1(x) = c_1 + c_2 x + c_3\cosh(\alpha x) + c_4\sinh(\alpha x) - \frac{w_o x^2}{2EI\alpha^2} \tag{E.39}$$

where the coefficients c_1, c_2, c_3 and c_4 are the coefficients of the homogenous solution. These coefficients can be found by using the following boundary conditions

$$y_1(0) = y_2(h_{cc}) = y_o^* \tag{E.40a}$$

$$\frac{dy_1(0)}{dx} = \frac{dy_2(h_{cc})}{dx} = y'^*_o \tag{E.40b}$$

$$M_B(0) = M_w(h_{cc}) = M_{Bo}^* \tag{E.40c}$$

$$V(0) = V_o \tag{E.40d}$$

where the subscripts B and S refer to the flexural and shear beams components, respectively. The interval of the solution is $0 \le x \le (H_1 = H - h_{cc})$. The superscript, "*", is used to differentiate the boundary conditions that apply to the junction between two substructures from those that apply to Substructure 2 at the base.

The expressions for displacement, rotation, bending moment and shear force on the wall component then become

$$y_1(x) = y_o^* + y_o'^* \frac{\sinh(\alpha x)}{\alpha} + M_{Bo}^* \left[\frac{\cosh(\alpha x)-1}{\alpha^2 EI}\right] + V_o\left[\frac{\alpha x - \sinh(\alpha x)}{\alpha(\eta + GA)}\right] + \frac{w_o}{EI}\left[\frac{\cosh(\alpha x)-1}{\alpha^4} - \frac{x^2}{2\alpha^2}\right] \quad (E.41)$$

$$y_1'(x) = y_o'^* \cosh(\alpha x) + M_{Bo}^* \frac{\sinh(\alpha x)}{\alpha EI} + V_o\left[\frac{1-\cosh(\alpha x)}{\eta + GA}\right] + \frac{w_o}{EI}\left[\frac{\sinh(\alpha x)}{\alpha^3} - \frac{x}{\alpha^2}\right] \quad (E.42)$$

$$M_B(x) = y_o'^* \alpha EI \sinh(\alpha x) + M_{Bo}^* \cosh(\alpha x) - V_o \frac{\sinh(\alpha x)}{\alpha} + w_o\left[\frac{\cosh(\alpha x)-1}{\alpha^2}\right] \quad (E.43)$$

$$\begin{aligned} V_B(x) = -y_o'^* GA \cosh h(\alpha x) - M_{Bo}^* \frac{GA}{\alpha EI}\sinh(\alpha x) + \frac{V_o}{(\eta + GA)}\left[\eta + GA\cosh(\alpha x)\right] \\ - \frac{w_o}{\alpha(\eta + GA)}\left[\alpha x \eta + GA \sinh(\alpha x)\right] \end{aligned} \quad (E.44)$$

Equilibrium requires that the moment should be zero at the free end of each of the components of the shear-flexure cantilever, we can write

$$M_B(H_1) = y_o'^* \alpha EI \sinh(\alpha H_1) + M_{Bo}^* \cosh(\alpha H_1) - V_o \frac{\sinh(\alpha H_1)}{\alpha} + w_o\left[\frac{\cosh(\alpha H_1)-1}{\alpha^2}\right] = 0 \quad (E.45)$$

Using the compatibility condition at the junction between the two substructures, $y_o'^*$ and M_{Bo}^* can be calculated from Eq. (E.37) and (E.38) at x = h_{cc}. After inserting the calculated expressions in Eq. (E.45) and rearranging, the bending moment at the wall base can be derived as

$$M_{Bo} = \frac{V_o\left\{\frac{\sinh(\alpha H_1)}{\alpha} - \frac{h_{cc}^4}{3EI_c f}\left[\frac{1}{2}\alpha h_{cc}\sinh(\alpha H_1) + \cosh(\alpha H_1)\right]\right\} - \frac{w_o}{\alpha^2}\left[\cosh(\alpha H_1) - 1\right]}{\left(1 - \frac{h_{cc}^3 \beta}{4EI_w f}\right)\alpha h_{cc}\sinh(\alpha H_1) + \left(1 - \frac{h_{cc}^3 \beta}{2EI_w f}\right)\cosh(\alpha H_1)} \quad (E.46)$$

Here V_o can be written alternatively as $w_o H_1$ for uniformly loaded cantilever beam. Once the bending moment at the base of the wall is obtained, all the quantities at any point of the both substructures can be calculated by using the derived expressions because all the expressions depend only on M_{Bo}. Using Eq. (E.34) the shear force on the wall at the base story can be calculated accordingly. The expression for wall base moment and relations for displacement, rotation, wall bending moment and shear force is derived and given at the end of this Appendix for the case of triangular load distribution.

4.1. The contraflexure height in base story columns (h_{cc})

For typical frame wall structures, double curvature can be assumed for columns and beams with a fixed point of contraflexure. Single curvature can be assumed for walls, with some moment gradient along the member. A common choice will locate the point of contraflexure between 55% and 65% of the storey height above the base. As the system behavior approaches the flexural mode ($\alpha H \rightarrow 0$), the contraflexure height moves away from the base. There are cases where the behavior of lower story columns is dominated by cantilever action. This occurs when the columns are considerably stiffer than the beams that frame into it. In such case the contraflexure point can move to upper story columns.

When the derived expressions are used to calculate the shear profile in any of the components, the transition between the substructures should be smooth. The easiest way of estimating the contraflexure height is to perform graphical solution. The wall shear force calculated at the base of the substructure 1 (upper part of the model) should be equal to or slightly less than that calculated at the base substructure given in Eq. (E.34). In Figure E.9 for a structural system with αH = 3.81, the location of contraflexure height is determined by trial and error. The ratio of contraflexure height at base story column to the base story height (h_{cc} / $h_{basestroy}$) was found approximately as 0.75, so that the force compatibility is provided at the junction. It has to be notified that this procedure should not be perceived as a trial-and error method, it is a graphical solution since each structure is characterized by a unique (h_{cc} / $h_{basestroy}$) ratio. An interesting observation with regard to Figure E.9 is that the location of contraflexure height does not influence the distribution of displacement and moment along the height and the shear distribution at the upper substructure. Since the expression for the base substructure is not expressed in dimensionless form, which is to say the response can only be calculated for specific values of EI_w, EI_c and GA_w, a general expression for h_{cc} / $h_{basestroy}$ ratio can not be derived.

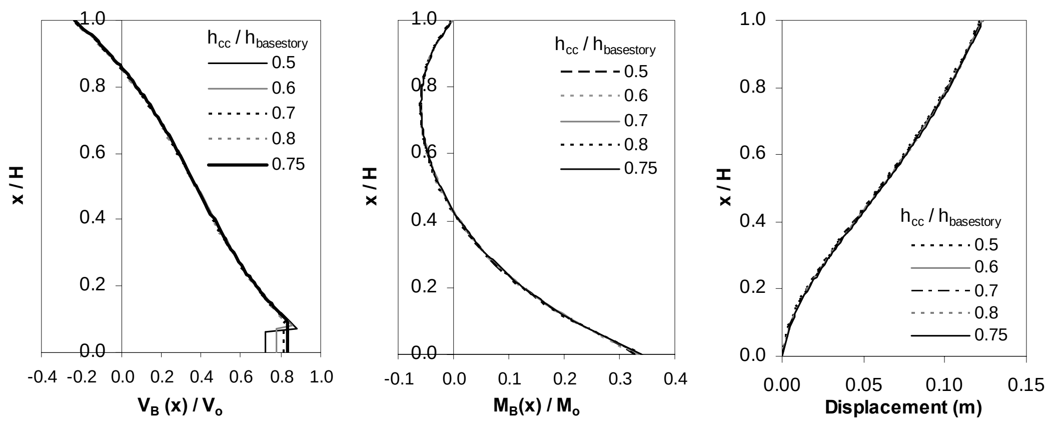

Figure E.9 Graphical determination of column contraflexure height for a specific case (αH = 3.81, EI = 8.0825E+10 Nm^2, GA_w = 1.594E+10 N, GA = 8.315E+8 N, EI_b = 2.384E+8 Nm^2)

5. Calculation of the response through the continua by transfer matrix method in consideration with nonuniform stiffness and arbitrary loading

The two principal deficiencies noted in the formulation given in Heidebrecht and Stafford Smith (1973) are that the moments from link beams were not considered and zero rotation condition, $y'_o = 0$, imposed at the base leads to frame shear calculated by Eq. (E.3) to vanish. Both of these deficiencies can be eliminated by incorporating beam moment effects into Eq. (E.22) and developing a new formulation for the base story that now yields nonzero frame shear at the base.

In case of nonuniform stiffness and lateral loads that do not have regular pattern along the height of the structure, obtaining a closed form solution from Eq. (E.22) becomes difficult. In such cases, the transfer matrix method adopted by Heidebrecht and Stafford Smith (1973) provides an elegant way of solving the problem. A nonuniform building is considered to consist of a number of uniform segments. The shear and flexural rigidities and intensity of loading may change from segment to segment but must be uniform in the segment. The basic expression defining the deflection of a particular segment is of the same form as Eq. (E.39). For known values of boundary conditions defined in terms of the displacement, rotation, bending moment and shear at the base of the segment, values of these quantities can be calculated anywhere within the segment using the derivatives of Eq. (E.39):

$$y(0) = y_o^* \tag{E.47a}$$

$$\frac{dy(0)}{dx} = y'^*_o \tag{E.47b}$$

$$M_B(0) = M_{Bo}^* \tag{E.47c}$$

$$V(0) = V_o^* \tag{E.47d}$$

If the expressions defining the displacement, rotation and bending moment are arranged and put in matrix form, they define the state vector of these quantities at any position in the segment which can be written in the form

$$\{z(x)\} = [T(x)]\{z_o\} + \{B(x)\} \tag{E.48}$$

where

$$\{z(x)\} = \begin{Bmatrix} y(x) \\ \dfrac{dy(x)}{dx} \\ EI\dfrac{dy^2(x)}{dx^2} \end{Bmatrix} \tag{E.49}$$

$$[T(x)] = \begin{bmatrix} 1 & \dfrac{\sinh(\alpha x)}{\alpha} & \dfrac{\cosh(\alpha x)-1}{EI\alpha^2} \\ 0 & \cosh(\alpha x) & \dfrac{\sinh(\alpha x)}{EI\alpha} \\ 0 & EI\alpha\sinh(\alpha x) & \cosh(\alpha x) \end{bmatrix} \tag{E.50}$$

and

$$\{B(x)\} = \begin{Bmatrix} \dfrac{V_o^*}{\alpha(\eta+GA)}[\sinh(\alpha x)-\alpha x] + \dfrac{w_o}{EI\alpha^4}\left[\cosh(\alpha x)-1-\dfrac{(\alpha x)^2}{2}\right] \\ \dfrac{V_o^*}{(\eta+GA)}[1-\cosh(\alpha x)] + \dfrac{w_o}{EI\alpha^3}[\sinh(\alpha x)-\alpha x] \\ -\dfrac{V_o^*}{\alpha}\sinh(\alpha x) + \dfrac{w_o}{\alpha^2}[\cosh(\alpha x)-1] \end{Bmatrix} \tag{E.51}$$

The matrices [*T(x)*] and {*B(x)*} are known quantities for any value of *x* in the segment. The quantities w_o and V_o^*, representing the intensity of the uniform lateral loading in the segment and the shear force at the base of the segment, can be calculated by static equilibrium for any segment in the structure.

A different formulation was derived for the bottom segment (Substructure 2), which is measured from the base to the contraflexure height of the columns, the transfer matrices used for this segment are obtained from Eqs. E.36-E.37-E.38:

$$[T(x)] = \begin{bmatrix} 1 & x & \dfrac{x^2}{2EI_w} + \dfrac{h_{cc}^2}{2fEI_w}\left(\dfrac{x}{GA_w} - \dfrac{x^3}{6EI_w}\right) \\ 0 & 1 & \dfrac{x}{EI_w} - \dfrac{h_{cc}^2 x^2}{4f(EI_w)^2} \\ 0 & 0 & 1 - \dfrac{h_{cc}^2 x}{2fEI_w} \end{bmatrix} \tag{E.52}$$

$$\{B(x)\} = \begin{Bmatrix} \dfrac{V_o h_{cc}^3}{3fEI_c}\left(\dfrac{x^3}{6EI_w} - \dfrac{x}{GA_w}\right) \\ \dfrac{V_o h_{cc}^3 x^2}{6fEI_w EI_c} \\ \dfrac{V_o h_{cc}^3 x}{3fEI_c} \end{Bmatrix} \tag{E.53}$$

Starting from the bottom segment, with boundary conditions given in Eq. (E.47 a-b-c-d), the conditions can be calculated at the other end of the segment using Eq. (E.48). For two adjacent segments compatibility conditions imply that the boundary conditions calculated at the upper end of the bottom segment become the base boundary conditions for the top segment to start. If this sequence is followed from base to top of the structure for each segment, the following recursive relationships result:

$$\left[\overline{T}_n\right] = \left[T_n\right]\left[\overline{T}_{n-1}\right] \tag{E.54}$$
$$\left[\overline{B}_n\right] = \left[T_n\right]\left[\overline{B}_{n-1}\right] + \left[B_n\right] \tag{E.55}$$
$$\text{for } \{z\} = \left[\overline{T}_n\right]\left[z_o\right] + \left[\overline{B}_n\right] \tag{E.56}$$
$$\text{and } \{z_n\} = \left[T_n\right]\left[z_{n-1}\right] + \left[B_n\right] \tag{E.57}$$

in which $\{z_n\}$=the state vector at the top of the n^{th} segment, and $\{z_o\}$ = the state vector at the base of the structure. If the bottom substructure consists of only one segment, the matrices $\{B_o(0)\}$, $[T_o(0)]$, $\{B_1(h_{cc})\}$, $[T_1(h_{cc})]$ are calculated using Eqs. (E.52) and (E.53).

Assuming a clamped (fixed) base structure, the boundary conditions at the base of the structure to start with are known except the bending moment (M_{Bo}) at the base of the flexural component. For a structure of N segments, using the final equation, which has the same form as Eq. (E.55), the unknown parameter M_{Bo} can be calculated. As the displacement and rotation at the very base and $M_B(H_l)$ are all zero, the third row of the matrices yields

$$M_{Bo} = -\frac{\overline{B}_{N_3}}{\overline{T}_{N_{33}}} \tag{E.58}$$

in which $\overline{B}_{N_3}$ is the third element of the vector $\left\{\overline{B}_N\right\}$ and $\overline{T}_{N_{33}}$ is the (3,3) element of matrix $\left[\overline{T}_N\right]$.

Once M_{Bo} has been computed, the state vector $\{z_o\}$ is known, and Eq. (E.57) can be applied successively to each segment to determine the state vectors at each segment boundary. Eq. (E.48) can then be used to evaluate the state vector $\{z(x)\}$ at any position, x, within any segment.

6. Numerical examples

6.1. Uniform Structure

In order to verify the accuracy and effectiveness of the proposed procedure, ten-story prototype frame-wall structure was created. A general plan view is shown in Figure E.10. The structure consists of three-bay frames, (frames A, B and C) parallel to the loading direction, and four two-bay frames, (frames 1, 2, 3 and 4) in the perpendicular direction. The span widths are 6.0, 5.0 and 6.0 m, respectively in the longitudinal direction, and 6.0 m each in the transverse direction. Frame B has a shear wall in the central bay continuous from the first to the tenth story. While the height of ground story is 3.75 m, the story height for the stories above is 3 m yielding a total height of 30.75 m.

The columns are 0.6mx0.6m and the wall is 5mx0.3m in plan dimensions. Beams are 0.6 m in depth and 0.3 m in width. Four different cases are designed for analysis purposes. In some cases, the slab contribution to the beam resistance is considered, so flanged beam cross section was used. In these cases flange width was taken as 1.2 m. While the structures in Cases 1, 3 and 4 consist of flanged beams, Case 2 structure is composed of rectangular beams. The wall in Case 4 is 3mx0.3m. By changing member cross sectional properties and the pattern of the lateral loads both approximate and exact stiffness matrix method structural analyses of the systems were carried out. The analysis cases with different member properties and applied loading are summarized in Table E.1. The modulus of elasticity of the concrete (E) was taken as 25’000 MPa and the shear modulus is assumed to be equal to G=0.425E.

The flexural component of the shear-flexure beam in this analysis consists of the shear wall (I_w=3.125 m^4). The shear component consist of the frames A, B and C. Joints A2&A3 and C2&C3 are framed by two beams and joints A1&A4, B1&B4 and C1&C4 are framed from only one side in the direction of loading. The contribution of single joint to the GA parameter of the equivalent shear flexure beam is calculated and tabulated in Table E.2.

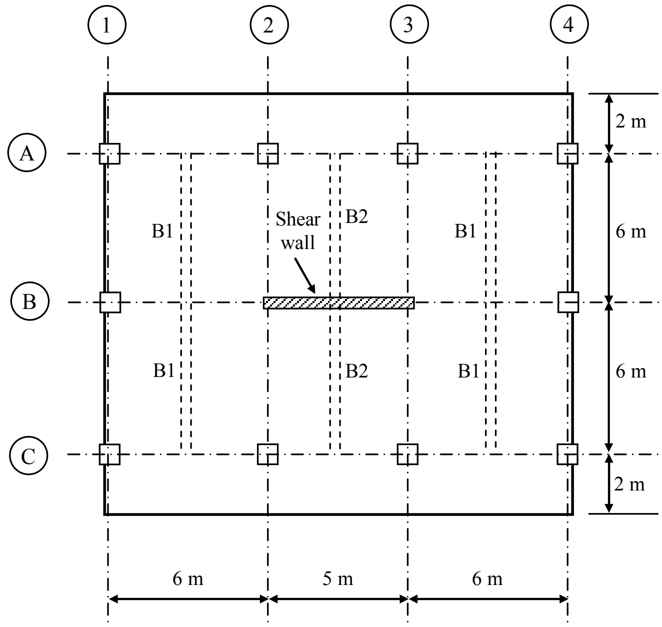

Figure E.10 General plan view and frame properties

Table E.1 Member rigidities used in different analyses cases

Cases	EI_c (Nm^2)	EI_w (Nm^2)	EI_b (Nm^2)	GA_w (N)	EI (Nm^2)	GA (N)	η (N)	αH	Loading
Case 1	2.700E9	7.813E10	2.384E8	1.594E10	8.083E10	8.315E8	4.127E8	3.815 3.119*	Triangular w=720 kN/m
Case 2	2.700E9	7.813E10	1.350E8	1.594E10	8.083E10	5.280E8	2.338E8	2.985 2.485*	Triangular w=720 kN/m
Case 3	2.700E9	7.813E10	2.384E8	1.594E10	8.083E10	8.315E8	4.127E8	3.815 3.119*	Uniform w=355 kN/m
Case 4	2.700E9	1.688E10	2.384E8	9.563E9	1.958E10	8.315E8	4.127E8	7.752 6.337*	Triangular w=720 kN/m

*The values are calculated according to Heidebrecht and Stafford Smith (1973).

Table E.2 Contribution of single joint to the *GA* parameter of the equivalent shear-flexure beam. Units in Newtons

	Joints A2&3 and B2&3	Joints A1&4, B1&4 and C1&4	Total
***GA* (Case 1,3&4)**	1.100E+08	6.510E+07	8.315E+08
***GA* (Case 2)**	7.200E+07	4.000E+07	5.280E+08

The results of the analyzed cases are given in Figure E.11 and used for the verification of proposed method in comparison with the results of Heidebrecht and Stafford Smith (1973) and those calculated with more exact finite element method. It is clearly seen in these figures that the present method not only provides improved estimates over the results of the method due to Heidebrecht and Stafford-Smith, but also calculates the wall shear at the base accurately. The new method provides far better results in terms of shear force distribution in the system compared with the previous method, especially when the relative rigidity of frames increases.

6.2. Nonuniform Structure

The performance of the proposed method was also checked for a nonuniform structure. The same model with abrupt changes in the stiffness along the height of the structure was considered. The structure has the same plan form given in Figure E.10 but the first four stories consist of 0.6mx0.6m columns and 5m long and 0.3m thick shear walls. The beams are rectangular with 0.7mx0.4m in dimension up to the fifth story. Stories from five to ten consist of 0.45mx0.45m columns and 3mx0.25m shear walls. The beams are weaker at these stories, with dimensions of 0.5mx0.3m. Such an arrangement results in three distinct stiffness regions along the height. The first region reaches to 11.25 m height, corresponding to mid-height of the fourth story. A story height region between the fourth and fifth stories midheights provides a transition region. Above 14.25 m the final stiffness region starts. The global flexural (*EI*) and shear rigidity (*GA*) terms at the transition region were taken as the average of upper and bottom part values. A triangular load distribution that totals 16’500 kN at the base is applied. The computed displacement profile, shear force and bending of the nonuniform structure are plotted in Figure E.12.

As seen in Figure E.12, the displacement profile was calculated accurately. In terms of moment distribution, while the presented method and former method by Heidebrecht and Stafford Smith (1973) yield the same profile due to weak beams at the upper stories, at the lower stories the present method provides far better predictions because the effects of link beams are considered. The share of walls from the total base shear is also calculated accurately. Abrupt changes occur in the shear force profile since the stiffness changes drastically from one stiffness region to another.

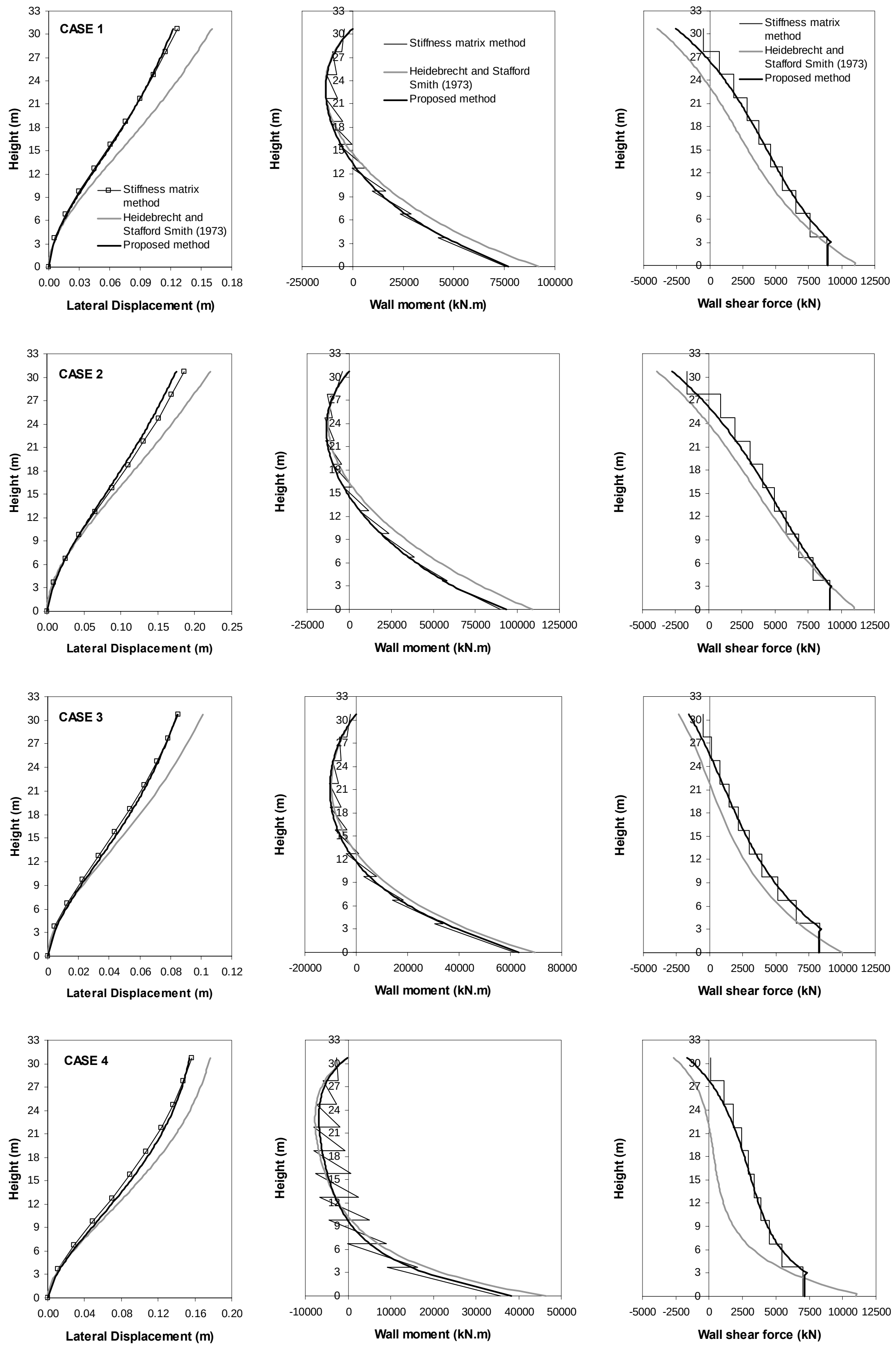

Figure E.11 Comparison of displacements, wall shear forces and bending moments calculated using different methods. Uniform stiffness was assumed along the height.

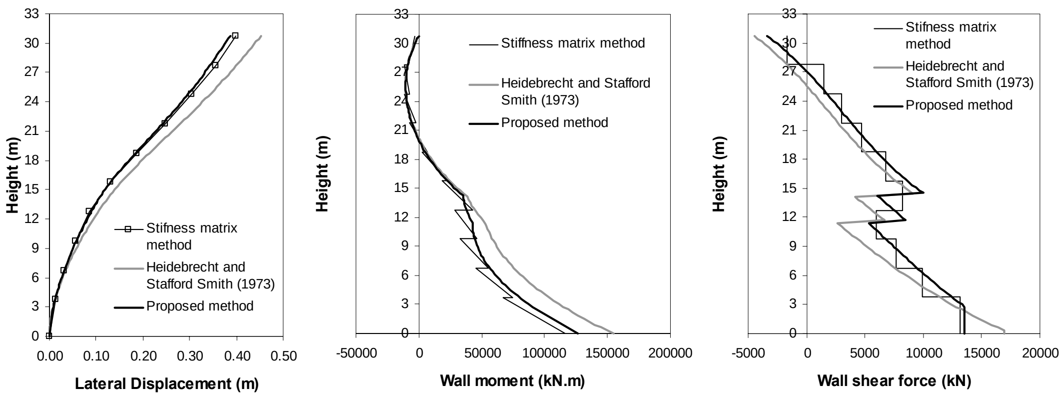

Figure E.12 Comparison of displacements, wall shear forces and bending moments calculated with different methods for nonuniform stiffness.

7. Displacement, rotation and stress resultants for triangular load, uniform structure

Although the lateral load is applied on the entire beam, only the portion acting on the Substructure 1 is considered. This yields the following lateral load distribution applied on the continuum model

$$w(x) = \frac{w_1}{H}(x + h_{cc}) \qquad \text{for } \; 0 \le x \le H_1 \;\; \text{where } \; H_1 = H - h_{cc} \tag{E.59}$$

The expressions for displacement, rotation, bending moment and shear force on the wall component for triangular distribution of lateral loads are

$$\begin{aligned} y_1(x) = y_o^* + y_o'^* \frac{\sinh(\alpha x)}{\alpha} + M_{Bo}^* \left[\frac{\cosh(\alpha x) - 1}{\alpha^2 EI}\right] + \frac{V_o}{\alpha^3 EI}\left[\alpha x - \sinh(\alpha x)\right] \\ + \frac{w_1}{\alpha^5 HEI}\left[\alpha h_{cc}\cosh(\alpha x) + \sinh(\alpha x) - \alpha(x + h_{cc})\right] - \frac{w_1}{2\alpha^2 HEI}\left(\frac{x^3}{3} + x^2 h_{cc}\right) \end{aligned} \tag{E.60}$$

$$\begin{aligned} y_1'(x) = y_o'^* \cosh(\alpha x) + M_{Bo}^* \frac{\sinh(\alpha x)}{\alpha EI} + \frac{V_o}{\alpha^2 EI}\left[1 - \cosh(\alpha x)\right] \\ + \frac{w_1}{\alpha^4 HEI}\left[\alpha h_{cc}\sinh(\alpha x) + \cosh(\alpha x) - 1\right] - \frac{w_1}{2\alpha^2 HEI}\left(x^2 + 2x h_{cc}\right) \end{aligned} \tag{E.61}$$

$$\begin{aligned} M_B(x) = y_o'^* EI\alpha \sinh(\alpha x) + M_{Bo}^* \cosh(\alpha x) - V_o \frac{\sinh(\alpha x)}{\alpha} \\ + \frac{w_1}{\alpha^3 H}\left[\alpha h_{cc}\cosh(\alpha x) + \sinh(\alpha x)\right] - \frac{w_1(x + h_{cc})}{\alpha^2 H} \end{aligned} \tag{E.62}$$

$$V_B(x) = -y_o'^{*} GA \cosh h(\alpha x) - M_{Bo}^{*} \frac{GA}{\alpha EI} \sinh(\alpha x) + V_o \left[\frac{\eta + GA \cosh(\alpha x)}{\alpha^2 EI} \right]$$
$$+ \frac{w_1 GA}{\alpha^2 H(\eta + GA)} \left[1 - \cosh(\alpha x) - \alpha h_{cc} \sinh(\alpha x) \right] - \frac{w_1 \eta}{2\alpha^2 HEI} \left(x^2 + 2x h_{cc} \right) \quad \text{(E.63)}$$

where $y_o'^{*}$ and M_{Bo}^{*} can be calculated from Eq. (E.37) and (E.38) at $x = h_{cc}$. The bending moment at the base of the shear wall for triangular load distribution is given as

$$M_{Bo} = \frac{\frac{V_o \sinh(\alpha H_1)}{\alpha} - \frac{V_o h_{cc}^4}{3EI_c f} \left[\frac{\alpha h_{cc} \sinh(\alpha H_1)}{2} + \cosh(\alpha H_1) \right] - \frac{w_1}{\alpha^3 H} \left[\alpha h_{cc} \cosh(\alpha H_1) + \sinh(\alpha H_1) - \alpha H \right]}{\left(1 - \frac{h_{cc}^3 \beta}{4EI_w f} \right) \alpha h_{cc} \sinh(\alpha H_1) + \left(1 - \frac{h_{cc}^3 \beta}{2EI_w f} \right) \cosh(\alpha H_1)} \quad \text{(E.64)}$$

where for a given intensity of lateral load (w_1), V_o can be expressed as

$$V_o = \frac{w_1 (H^2 - h_{cc}^2)}{2H} \quad \text{(E.65)}$$

APPENDIX F

FORCE-DEFORMATION RELATIONS OF WALL SPECIMENS

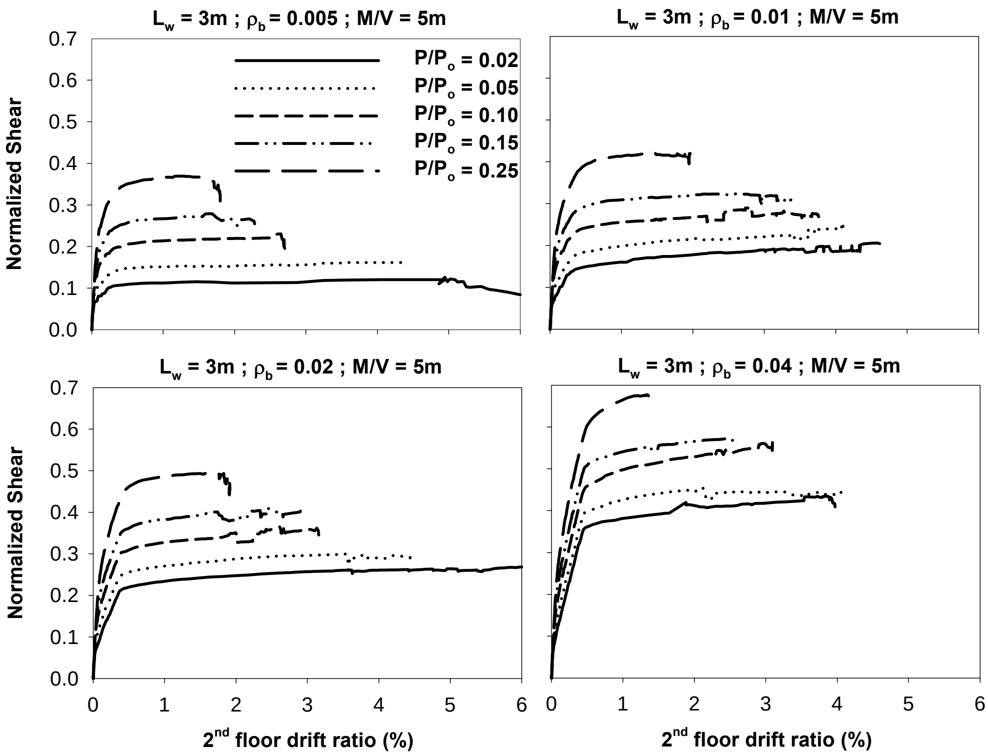

Figure F.1 Force-displacement relations of wall models (L_w = 3 m; L_v = 5 m)

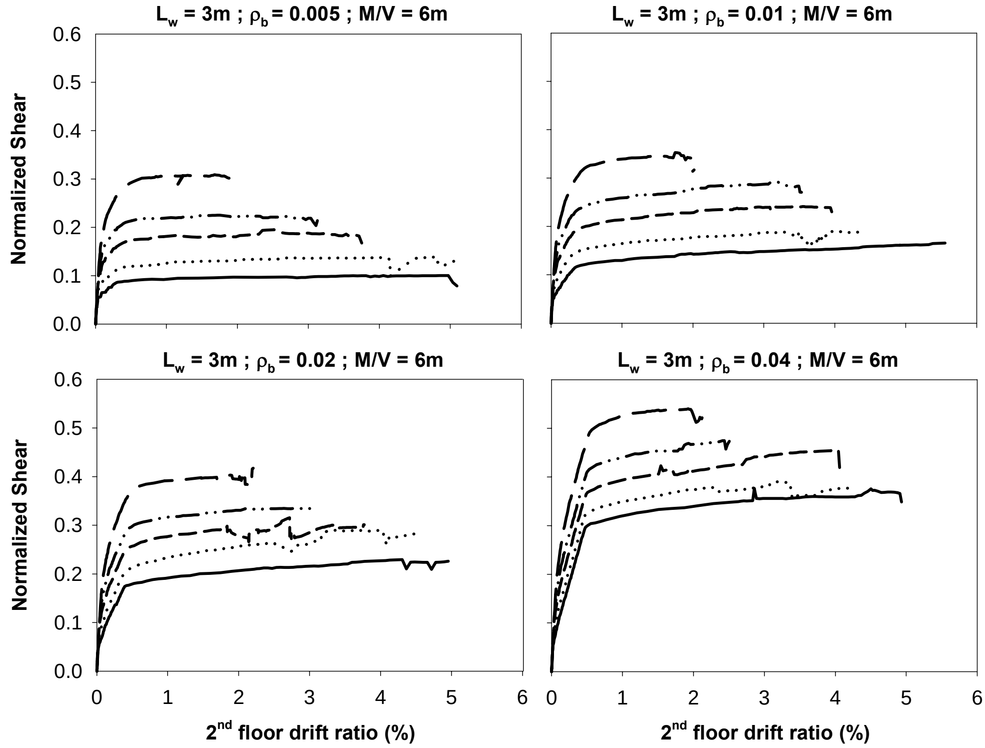

Figure F.2 Force-displacement relations of wall models (L_w = 3 m; L_v = 6 m)

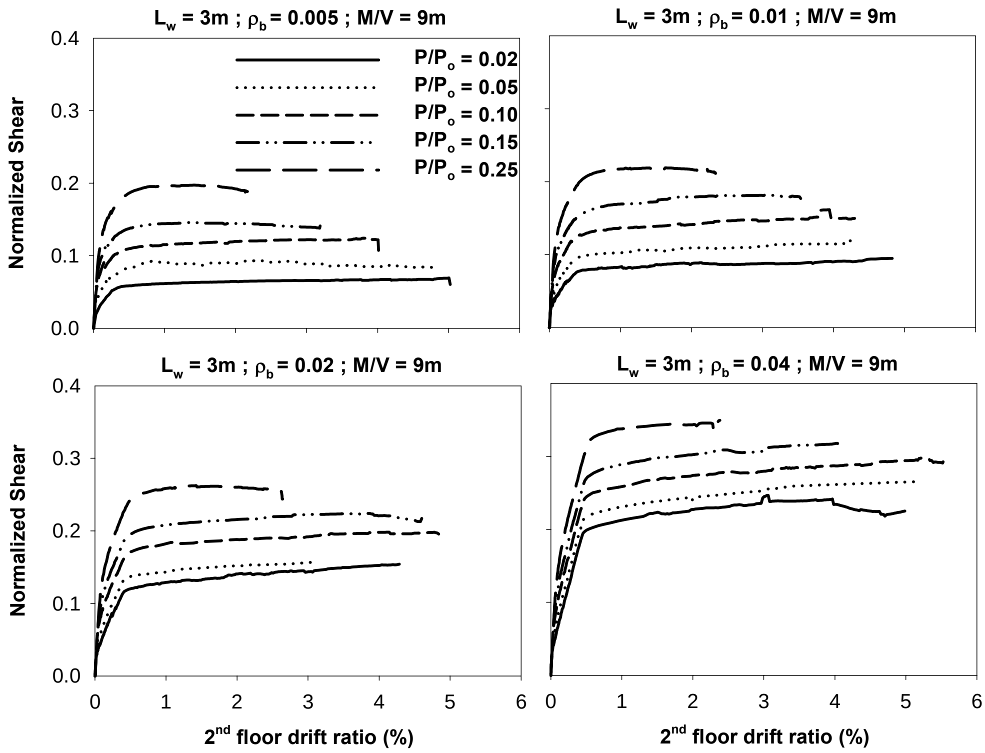

Figure F.3 Force-displacement relations of wall models (L_w = 3 m; L_v = 9 m)

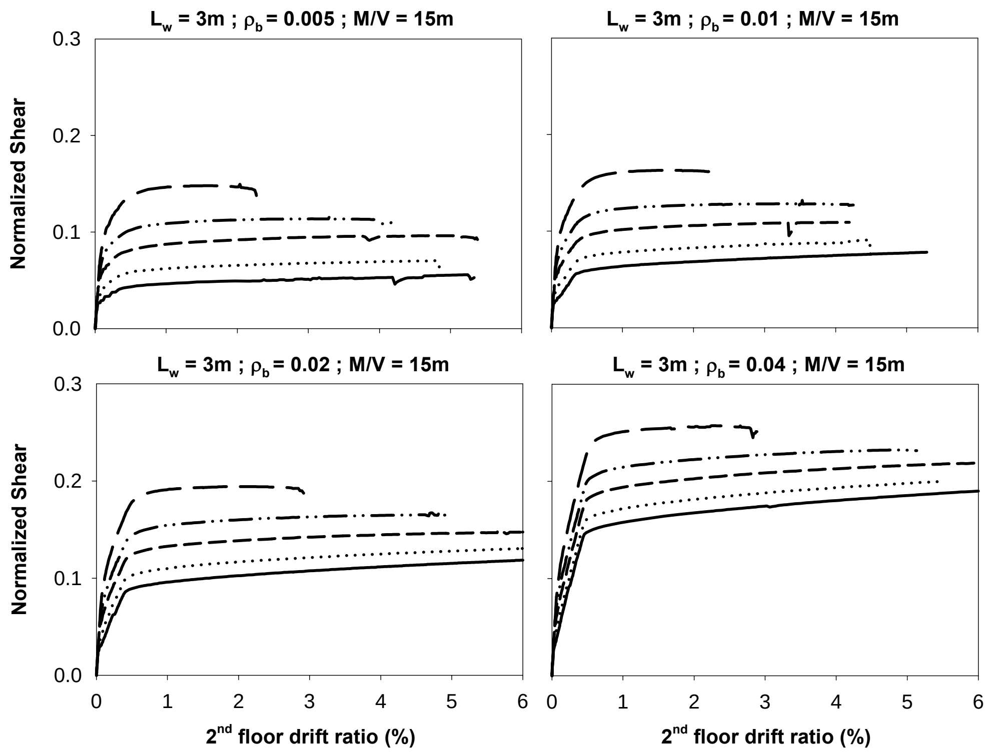

Figure F.4 Force-displacement relations of wall models (L_w = 3 m; L_v = 15 m)

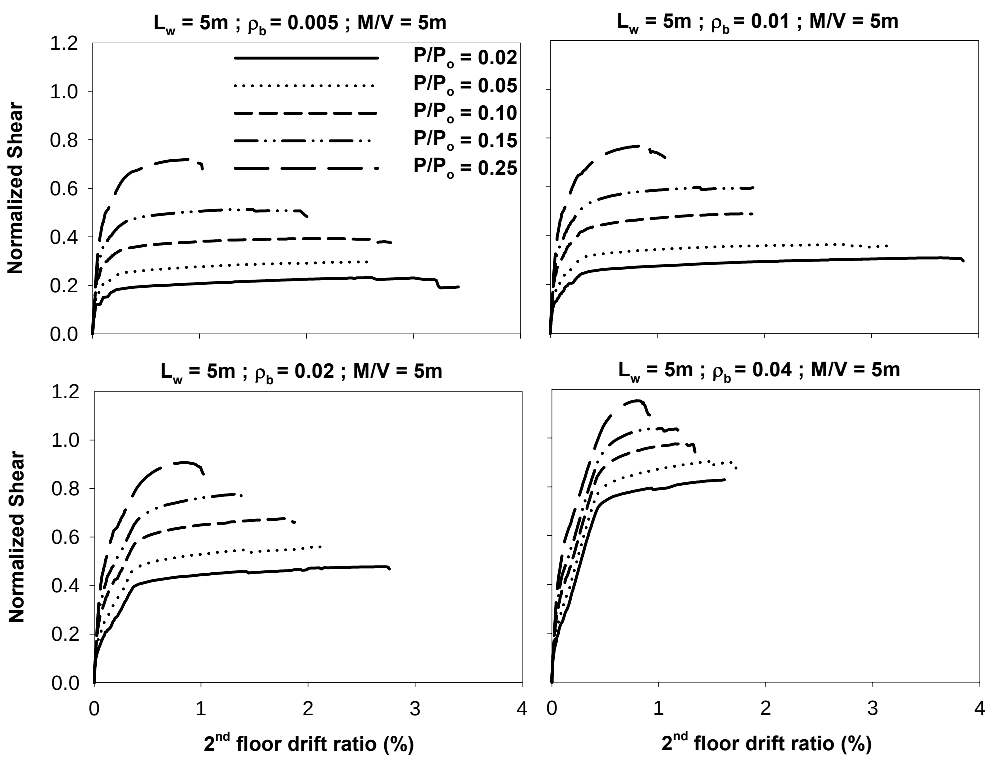

Figure F.5 Force-displacement relations of wall models (L_w = 5 m; L_v = 5 m)

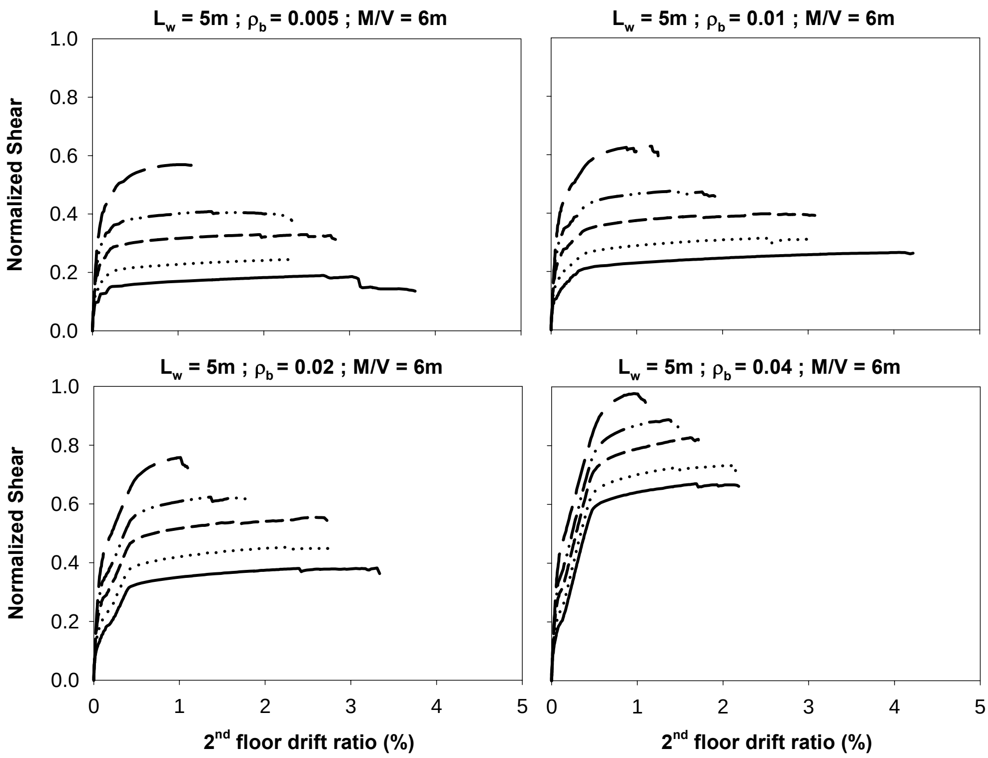

Figure F.6 Force-displacement relations of wall models (L_w = 5 m; L_v = 6 m)

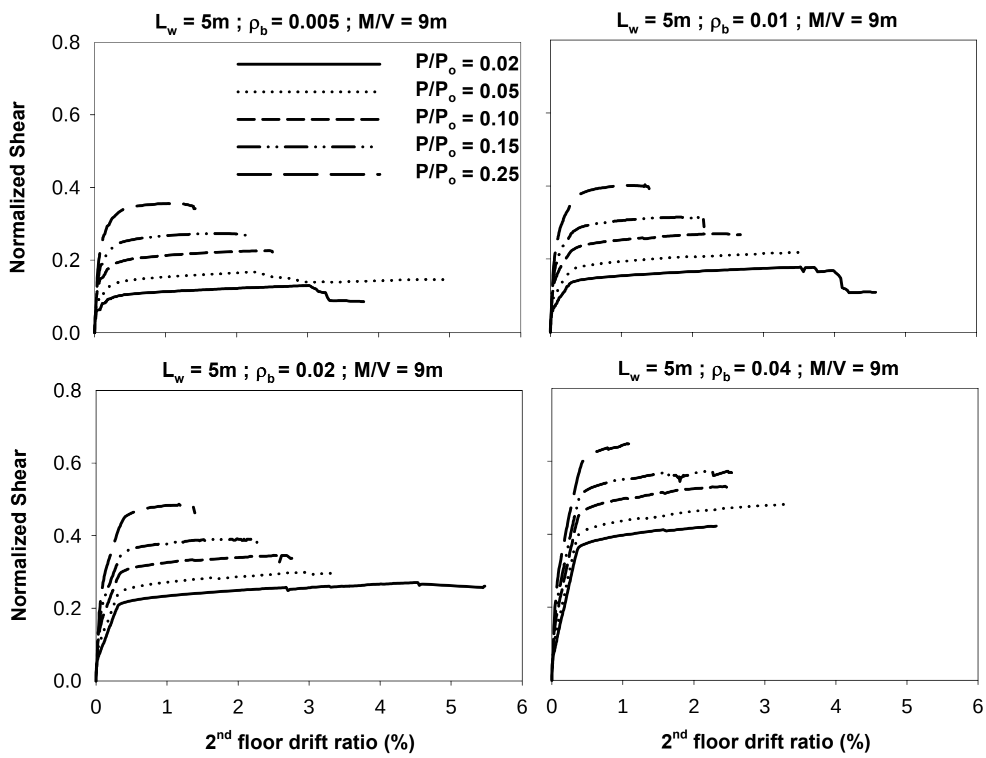

Figure F.7 Force-displacement relations of wall models (L_w = 5 m; L_v = 9 m)

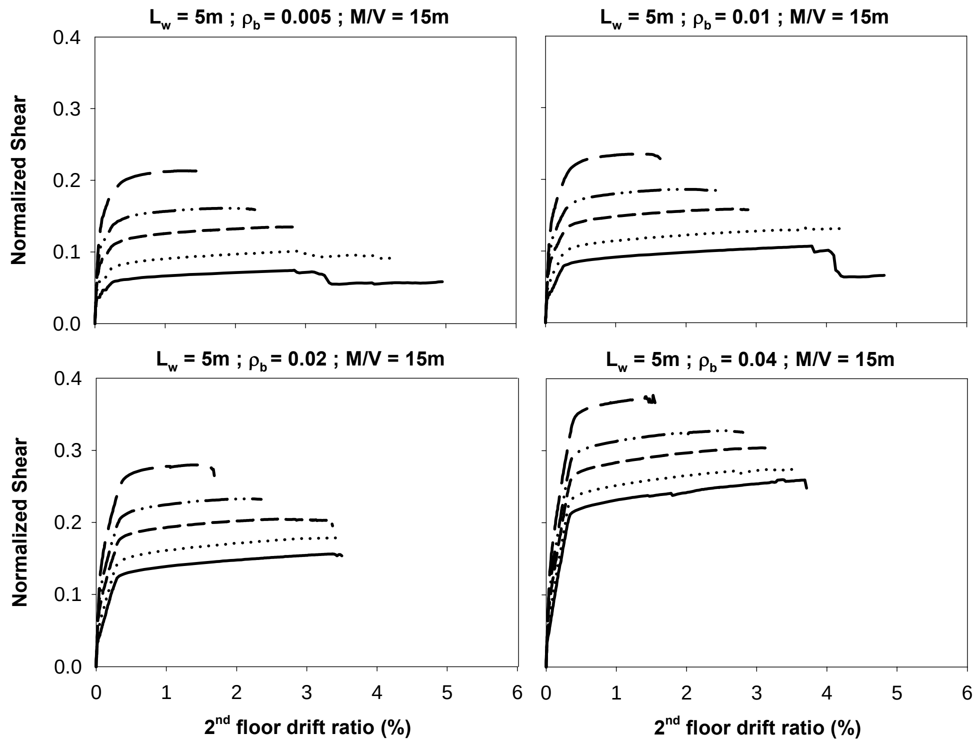

Figure F.8 Force-displacement relations of wall models (L_w = 5 m; L_v = 15 m)

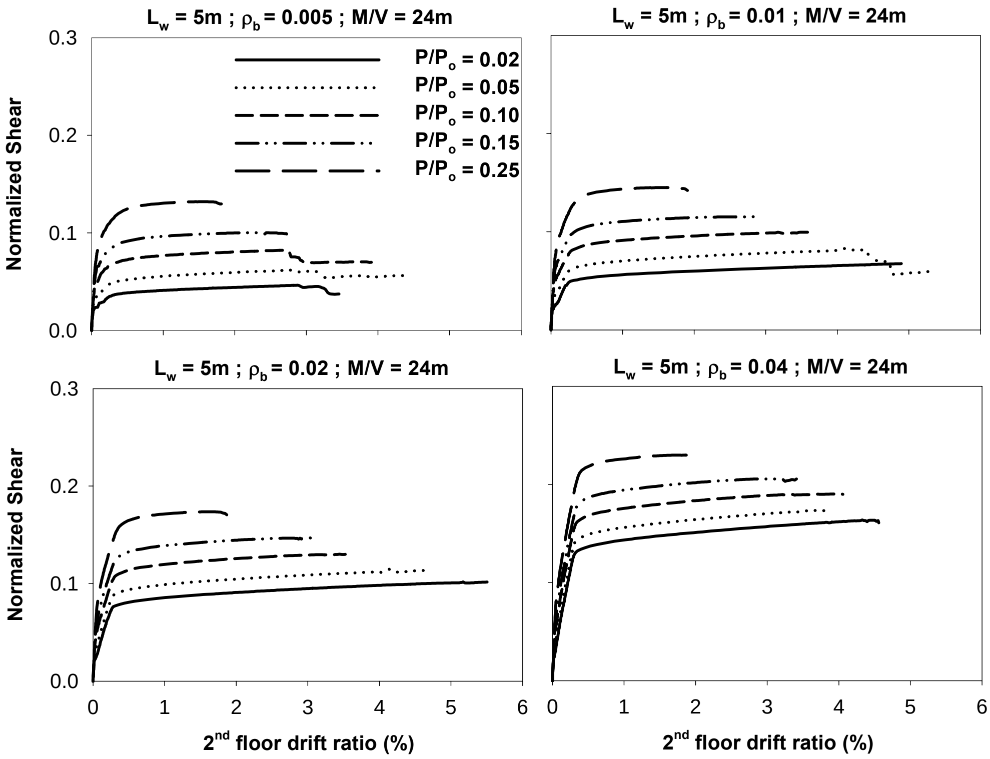

Figure F.9 Force-displacement relations of wall models (L_w = 5 m; L_v = 24 m)

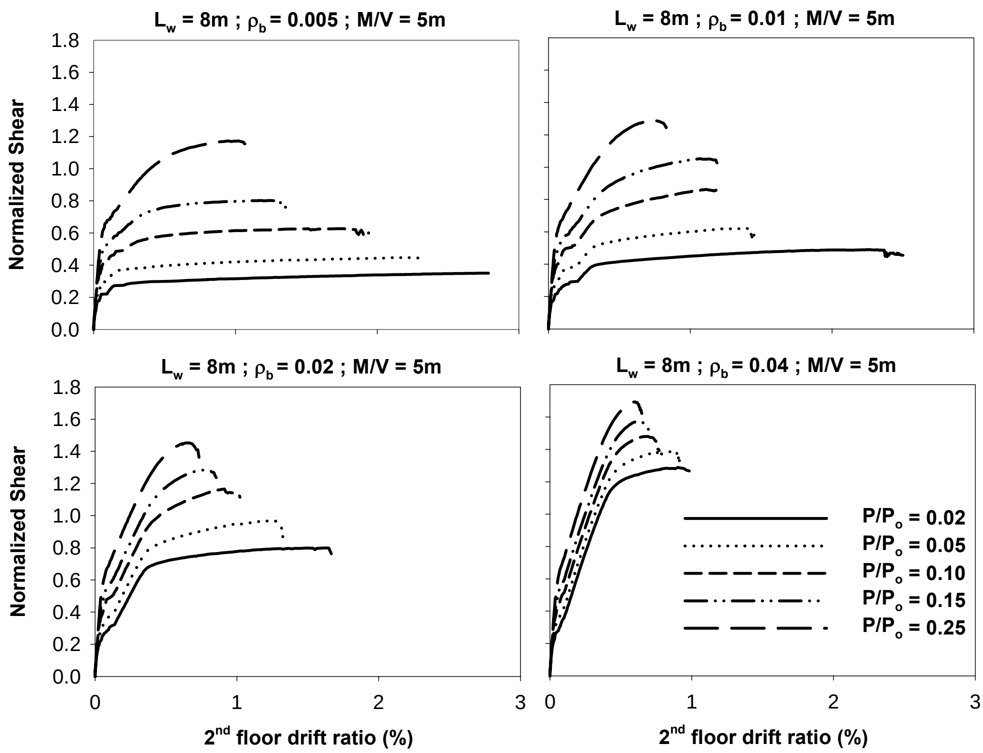

Figure F.10 Force-displacement relations of wall models (L_w = 8 m; L_v = 5 m)

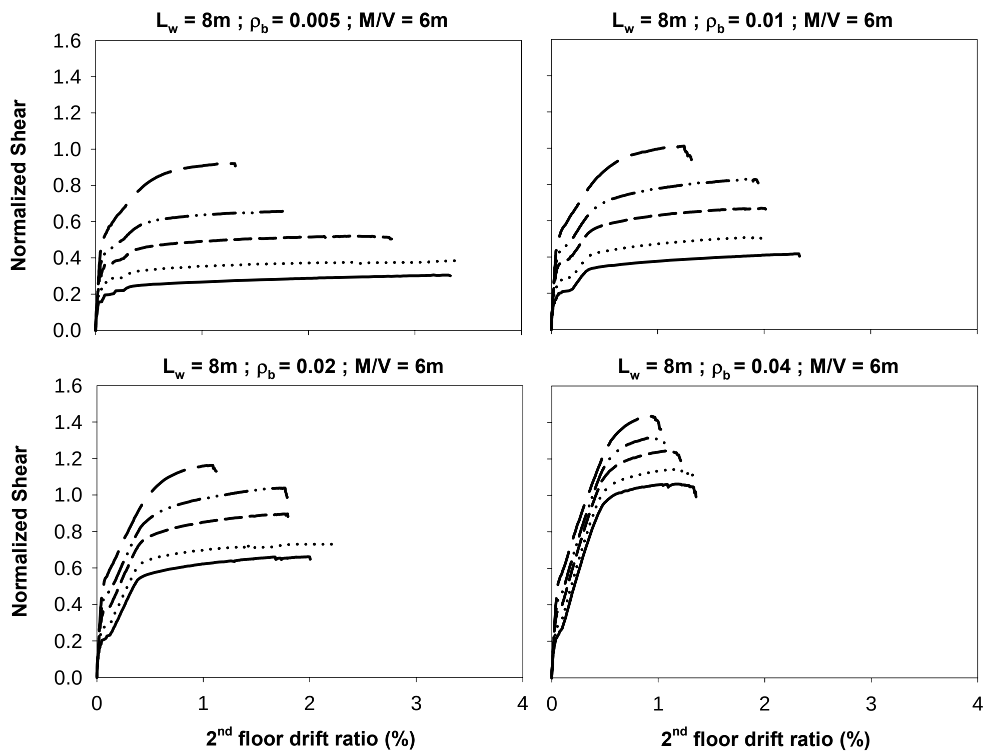

Figure F.11 Force-displacement relations of wall models (L_w = 8 m; L_v = 6 m)

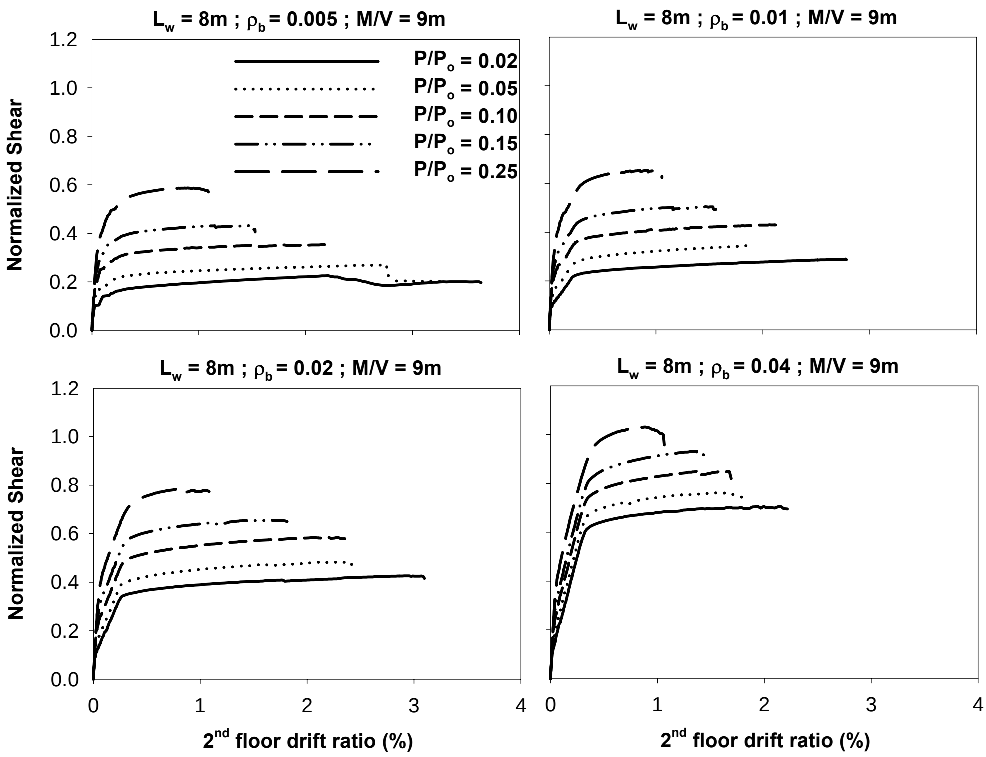

Figure F.12 Force-displacement relations of wall models (L_w = 8 m; L_v = 9 m)

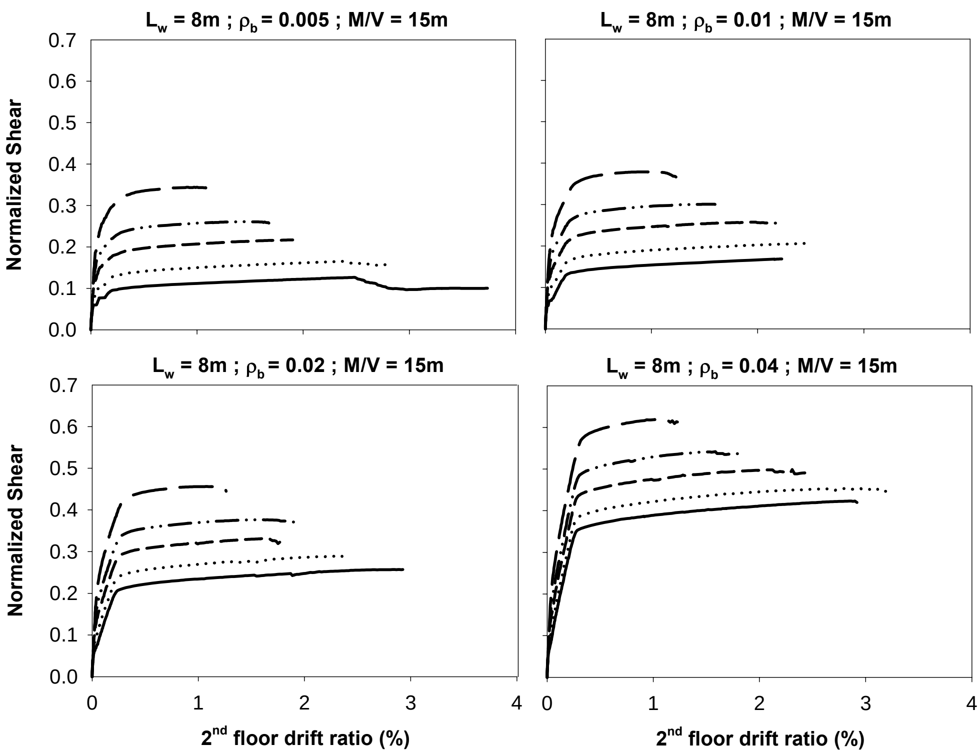

Figure F.13 Force-displacement relations of wall models (L_w = 8 m; L_v = 15 m)

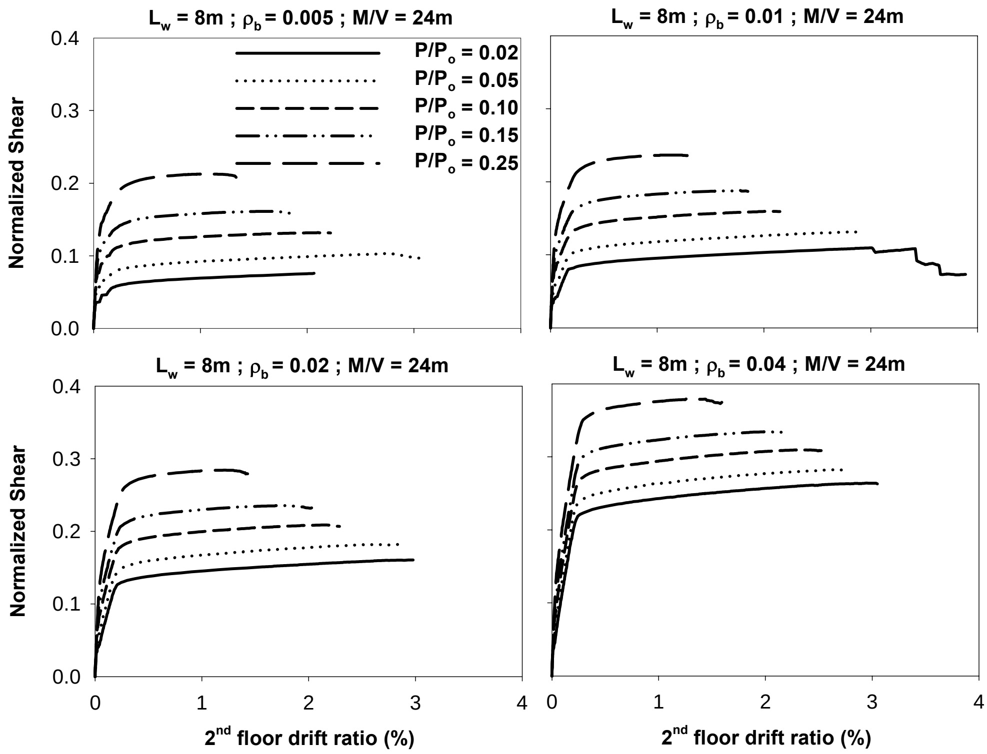

Figure F.14 Force-displacement relations of wall models (L_w = 8 m; L_v = 24 m)

APPENDIX G

SHEAR WALL EXPERIMENTS

Table G.1 Roof Drift and shear stress of test specimens by other researchers

Reference	H_w (m)	L_w (m)	t_w (mm)	P/P_o (%)	V_{max} (kN)	f_c (Mpa)	ν^* (Mpa)	H_w/L_w	δ_u (mm)	δ_u/H_w (%)
Corley et al. (1981)	4.57	1.905	102	7.0	182.4	24.4	0.19	2.4	76.4	1.67
Corley et al. (1981)	4.57	1.905	102	7.5	92.6	22.7	0.10	2.4	76.4	1.67
Corley et al. (1981)	4.57	1.905	102	14.1	263.1	21.8	0.29	2.4	78.2	1.71
Corley et al. (1981)	4.57	1.905	102	7.9	313.8	49.3	0.23	2.4	132.1	2.89
Corley et al. (1981)	4.57	1.905	102	9.3	302.2	42	0.24	2.4	130.8	2.86
Corley et al. (1981)	4.57	1.905	102	8.9	309.7	44.1	0.24	2.4	138.1	3.02
Corley et al. (1981)	4.57	1.905	102	8.6	223.1	45.6	0.17	2.4	126.6	2.77
Corley et al. (1981)	4.57	1.905	102	0.4	265.2	38.5	0.22	2.4	50.7	1.11
Corley et al. (1981)	4.57	1.905	102	7.6	275.2	45.5	0.21	2.4	101.5	2.22
Corley et al. (1981)	5.49	1.905	102	1.0	103.2	23.3	0.11	2.88	126.7	2.31
Morgan et al. (1986)	4.38	1.575	57	4.9	35.4	31.7	0.07	2.78	66.1	1.51
Oesterle et al., 1978	4.57	1.905	102	0.4	39.0	44.7	0.03	2.4	103.3	2.26
Oesterle et al., 1978	4.57	1.905	102	0.4	66.2	46.4	0.05	2.4	133.5	2.92
Oesterle et al., 1978	4.57	1.905	102	0.3	84.9	53	0.06	2.4	132.1	2.89
Oesterle et al., 1978	4.57	1.905	102	0.3	213.4	53.6	0.15	2.4	103.8	2.27
Oesterle et al., 1978	4.57	1.905	102	0.3	93.5	47.3	0.07	2.4	179.7	3.93
Oesterle et al., 1978	4.57	1.905	102	0.3	104.3	45	0.08	2.4	317.3	6.94
Oesterle et al., 1978	4.57	1.905	102	0.3	235.4	45.3	0.18	2.4	126.6	2.77
Vallenas et al. (1979)	3.06	2.388	102	7.8	344.9	34.8	0.24	1.28	173.3	5.67
Vallenas et al. (1979)	3.09	2.413	102	7.3	284.5	33.4	0.20	1.28	74.7	2.42
Wang et al. (1975)	3.06	2.388	102	7.9	343.4	34.5	0.24	1.28	107.0	3.5
Wang et al. (1975)	3.06	2.388	102	7.6	348.8	35.6	0.24	1.28	51.0	1.67
Wang et al. (1975)	3.06	2.388	102	7.5	321.1	35.9	0.22	1.28	68.8	2.25
Wang et al. (1975)	3.09	2.413	102	7.0	274.7	34.5	0.19	1.28	72.0	2.33
Oesterle (1986)	4.57	1.905	102	0.3	227.8	53.7	0.16	2.4	127.1	2.78
Oesterle (1986)	4.57	1.905	102	0.4	251.0	41.7	0.20	2.4	101.5	2.22
Oesterle (1986)	4.57	1.905	102	5.9	133.4	27.9	0.13	2.4	101.5	2.22

Table G.1 (Continued) Roof Drift and shear stress of test specimens by other researchers

Reference	H_w (m)	L_w (m)	t_w (mm)	P/P_o (%)	V_{max} (kN)	f_c (Mpa)	ν* (Mpa)	H_w/L_w	δ_u (mm)	δ_u/H_w (%)
Thomsen&Wallace (1995)	3.82	1.22	102	7.0	65.8	43.7	0.08	3.13	83.6	2.19
Thomsen&Wallace (1995)	3.82	1.22	102	10.0	69.3	31	0.10	3.13	82.5	2.16
Han et al. (2002)	2.00	1.50	200	10.0	442.90	34.2	0.25	1.3	80.9	4.05
Han et al. (2002)	2.00	1.50	200	10.0	573.30	34.5	0.33	1.3	55.9	2.80
Han et al. (2002)	2.00	1.50	200	10.0	321.40	36.9	0.18	1.3	59.6	2.98
Shiu et al. (1981)	5.49	1.91	101.6	1.0	349.3	23.3	0.37	2.9	152.6	2.78
Ali and Wigth (1991)	3.56	1.22	76.2	7.4	160.6	34.0	0.30	2.9	106.8	3.00
Ali and Wigth (1991)	3.56	1.22	76.2	9.3	166.4	32.3	0.31	2.9	53.4	1.50
Ali and Wigth (1991)	3.56	1.22	76.2	9.1	169.5	33.0	0.32	2.9	53.4	1.50
Ali and Wigth (1991)	3.56	1.22	76.2	8.8	163.3	34.2	0.30	2.9	53.4	1.50
Carvajal&Pollner (1983)	1.55	0.50	101.6	8.4	36.9	28.1	0.14	3.1	62.1	4.00
Carvajal&Pollner (1983)	1.55	0.50	101.6	8.3	34.3	28.2	0.13	3.1	62.1	4.00
Carvajal&Pollner (1983)	1.55	0.50	101.6	9.2	28.5	25.6	0.11	3.1	62.1	4.00
Carvajal&Pollner (1983)	1.55	0.50	101.6	8.2	28.0	28.7	0.10	3.1	50.0	3.22
Carvajal&Pollner (1983)	1.55	0.50	101.6	11.3	27.1	20.8	0.12	3.1	34.9	2.25
Lefas&Kotsovos (1990)	1.3	0.65	65	0.0	117.7	30.1	0.51	2.0	20.9	1.61
Lefas&Kotsovos (1990)	1.3	0.65	65	0.0	115.8	35.2	0.46	2.0	22.2	1.71
Lefas&Kotsovos (1990)	1.3	0.65	65	0.0	111	53.6	0.36	2.0	24.5	1.88
Lefas&Kotsovos (1990)	1.3	0.65	65	0.0	111.5	49.2	0.38	2.0	25.0	1.92
Lefas et al. (1990)	0.75	0.75	70	0.0	260	52.3	0.68	1.0	8.3	1.10
Lefas et al. (1990)	0.75	0.75	70	10.0	340	53.6	0.88	1.0	8.9	1.18
Lefas et al. (1990)	0.75	0.75	70	20.0	330	40.6	0.99	1.0	8.9	1.18
Lefas et al. (1990)	0.75	0.75	70	0.0	265	42.1	0.78	1.0	11.2	1.49
Lefas et al. (1990)	0.75	0.75	70	10.0	320	43.3	0.93	1.0	8.1	1.07
Lefas et al. (1990)	0.75	0.75	70	20.0	355	51.7	0.94	1.0	5.8	0.77
Lefas et al. (1990)	0.75	0.75	70	0.0	247	48.3	0.68	1.0	10.8	1.43
Lefas et al. (1990)	1.3	0.65	65	0.0	127	42.8	0.46	2.0	20.6	1.59
Lefas et al. (1990)	1.3	0.65	65	10.0	150	50.6	0.50	2.0	15.3	1.18
Lefas et al. (1990)	1.3	0.65	65	20.0	180	47.8	0.62	2.0	13.2	1.01
Lefas et al. (1990)	1.3	0.65	65	0.0	120	48.3	0.41	2.0	18.1	1.39
Lefas et al. (1990)	1.3	0.65	65	20.0	150	45	0.53	2.0	9.5	0.73
Lefas et al. (1990)	1.3	0.65	65	0.0	123	30.1	0.53	2.0	20.9	1.61

*v is the member maximum average shear stress normalized with respect to $\sqrt{f_c}$ calculated as

$$v = \frac{V_{\max}}{t_w L_w \sqrt{f_c}}$$

CURRICULUM VITAE

PERSONAL INFORMATION

Surname, Name: Kazaz, İlker
Nationality: Turkish (TC)
Date and Place of Birth: 31.05.1977
Marital Status: Married
Phone: +90 (312) 210 7458
Fax: +90 (312) 210 1328
Email: ikazaz@metu.edu.tr

EDUCATION

2002-2010 Ph.D., Civil Engineering, METU

1996-2001 BS, Civil Engineering, METU

1988-1995 Trabzon Kanuni Anatolian High School

WORK EXPERIENCE

2002-Present Research Assistant, Department of Civil Engineering, METU

PUBLICATIONS

1. **Kazaz İ.** and Gülkan P., 2010, "An improved frame-shear wall model: continuum approach", Accepted for publication in The Structural Design of Tall and Special Buildings.
2. Kadaş K., Yakut A. and **Kazaz İ.**, 2010, "Ground motion intensity based on period elongation", Accepted for publication in ASCE Journal of Structural Engineering.
3. **Kazaz İ.**, Yakut A. and Gülkan P., 2006, "Numerical simulation of dynamic shear wall tests: A benchmark study", Computers & Structures, Vol. 84, No. 8, pp. 549-562.

4. **Kazaz İ.**, Yakut A. and Gülkan P., 2006, "Seismic response assessment of a stiff structure", Earthquake Engineering and Structural Dynamics, Vol. 35, No. 6, pp. 737-759.

5. **Kazaz İ.** and Yakut A., 2010, "Evaluation of period formula for shear wall buildings", 9th US National and 10th Canadian Conference on Earthquake Engineering, Toronto, Canada, Accepted.

6. **Kazaz İ.**, Akansel V. and Gülkan P., 2009, "A Unique Example for Earthquake Durability: Four- Legged Minaret in the "Şeyh Mutahhar" Mosque, Diyarbakir", Symposium with International Participation on Strengthening and Preserving Historical Buildings and Cultural Heritage – II, 15-17 October 2009, Diyarbakır, Turkey. (in Turkish)

7. Kadaş K., Yakut A. and **Kazaz İ.**, 2008, "Evaluation of spectral ground motion intensity parameters", 8th International Congress on Advances in Civil Engineering, Eastern Mediterranean University, Famagusta, North Cyprus, 15-17 September.

8. **Kazaz İ.** and Gülkan P., 2007, "Pushover analyses of squat shear walls", International Symposium on Advances in Earthquake & Structural Engineering, October 24-26, Süleyman Demirel University, Antalya, Turkey.

9. **Kazaz İ.**, 2007, "Lineer Ötesi Dinamik Analizler İçin Yer İvmesi Kaydi Seçimi", Sixth National Conference on Earthquake Engineering, 16-20 October 2007, Istanbul, Turkey (in Turkish).

10. **Kazaz İ.** and Yakut A., 2006, "Estimation of Global Displacement on the Basis of Spectral Acceleration", Seventh International Congress on Advances in Civil Engineering, October 11-13, Istanbul, Turkey.

11. Yamaguchi N., **Kazaz İ.** and Minowa C., 2004, "Ground motions with static displacement derived from strong-motion accelerogram records by a new baseline correction method", Proceedings Third UJNR Workshop on Soil-Structure Interaction, March 29-30, Menlo Park, California, USA.

12. Gülkan P., Yakut A. and **Kazaz İ.**, 2006, "Evaluation of approximate nonlinear procedures for observed response of a shear wall structure", Advances in Earthquake Engineering for Urban Risk Reduction (eds. Wasti, S. T. and Ozcebe, G.), Springer.

13. Gülkan P., **Kazaz İ.** and Yakut A., 2005, "Caveats for Nonlinear Response Assessment of Short-Period Structures", EE-21C International Conference on Earthquake Engineering, Skopje-Ohrid, Macedonia.